NASA/TM—2016–218229

Natural Environments Definition for Design

H.L. Justh (Ed.), K.M. Altino, R.K. Decker, H.M. Koehler, F.B. Leahy, J.I. Minow, B.C. Roberts, R.M. Suggs, R.J. Suggs, and P.W. White
Marshall Space Flight Center, Huntsville, Alabama

R.E. Barbre, Jr., J.W. Howard, and L.N. Parker
Jacobs ESSSA Group, Huntsville, Alabama

L. Burns
Raytheon/Jacobs, ESSSA Group, Huntsville, Alabama

R.D. Leach
Dynetics, Huntsville, Alabama

S.K. Noble
NASA Headquarters, Washington, DC

W.M. Farrell
Goddard Space Flight Center, Greenbelt, Maryland

J.B. Plescia
Applied Physics Laboratory, Johns Hopkins University, Laurel, Maryland

October 2016

The NASA STI Program…in Profile

Since its founding, NASA has been dedicated to the advancement of aeronautics and space science. The NASA Scientific and Technical Information (STI) Program Office plays a key part in helping NASA maintain this important role.

The NASA STI Program Office is operated by Langley Research Center, the lead center for NASA's scientific and technical information. The NASA STI Program Office provides access to the NASA STI Database, the largest collection of aeronautical and space science STI in the world. The Program Office is also NASA's institutional mechanism for disseminating the results of its research and development activities. These results are published by NASA in the NASA STI Report Series, which includes the following report types:

- TECHNICAL PUBLICATION. Reports of completed research or a major significant phase of research that present the results of NASA programs and include extensive data or theoretical analysis. Includes compilations of significant scientific and technical data and information deemed to be of continuing reference value. NASA's counterpart of peer-reviewed formal professional papers but has less stringent limitations on manuscript length and extent of graphic presentations.

- TECHNICAL MEMORANDUM. Scientific and technical findings that are preliminary or of specialized interest, e.g., quick release reports, working papers, and bibliographies that contain minimal annotation. Does not contain extensive analysis.

- CONTRACTOR REPORT. Scientific and technical findings by NASA-sponsored contractors and grantees.

- CONFERENCE PUBLICATION. Collected papers from scientific and technical conferences, symposia, seminars, or other meetings sponsored or cosponsored by NASA.

- SPECIAL PUBLICATION. Scientific, technical, or historical information from NASA programs, projects, and mission, often concerned with subjects having substantial public interest.

- TECHNICAL TRANSLATION. English-language translations of foreign scientific and technical material pertinent to NASA's mission.

Specialized services that complement the STI Program Office's diverse offerings include creating custom thesauri, building customized databases, organizing and publishing research results…even providing videos.

For more information about the NASA STI Program Office, see the following:

- Access the NASA STI program home page at <http://www.sti.nasa.gov>

- E-mail your question via the Internet to <help@sti.nasa.gov>

- Phone the NASA STI Help Desk at 757–864–9658

- Write to:
  NASA STI Information Desk
  Mail Stop 148
  NASA Langley Research Center
  Hampton, VA 23681–2199, USA

NASA/TM—2016–218229

Natural Environments Definition for Design

H.L. Justh (Ed.), K.M. Altino, R.K. Decker, H.M. Koehler, F.B. Leahy, J.I. Minow, B.C. Roberts, R.M. Suggs, R.J. Suggs, and P.W. White
Marshall Space Flight Center, Huntsville, Alabama

R.E. Barbre, Jr., J.W. Howard, and L.N. Parker
Jacobs ESSSA Group, Huntsville, Alabama

L. Burns
Raytheon/Jacobs, ESSSA Group, Huntsville, Alabama

R.D. Leach
Dynetics, Huntsville, Alabama

S.K. Noble
NASA Headquarters, Washington, DC

W.M. Farrell
Goddard Space Flight Center, Greenbelt, Maryland

J.B. Plescia
Applied Physics Laboratory, Johns Hopkins University, Laurel, Maryland

National Aeronautics and
Space Administration

Marshall Space Flight Center • Huntsville, Alabama 35812

October 2016

Available from:

NASA STI Information Desk
Mail Stop 148
NASA Langley Research Center
Hampton, VA 23681–2199, USA
757–864–9658

This report is also available in electronic form at
<http://www.sti.nasa.gov>

TABLE OF CONTENTS

TABLE OF CONTENTS (Continued)

TABLE OF CONTENTS (Continued)

TABLE OF CONTENTS (Continued)

TABLE OF CONTENTS (Continued)

TABLE OF CONTENTS (Continued)

TABLE OF CONTENTS (Continued)

TABLE OF CONTENTS (Continued)

TABLE OF CONTENTS (Continued)

TABLE OF CONTENTS (Continued)

LIST OF FIGURES

LIST OF FIGURES (Continued)

LIST OF FIGURES (Continued)

LIST OF FIGURES (Continued)

LIST OF FIGURES (Continued)

LIST OF FIGURES (Continued)

LIST OF FIGURES (Continued)

LIST OF FIGURES (Continued)

LIST OF FIGURES (Continued)

LIST OF FIGURES (Continued)

LIST OF FIGURES (Continued)

LIST OF FIGURES (Continued)

LIST OF FIGURES (Continued)

LIST OF TABLES

LIST OF TABLES (Continued)

LIST OF TABLES (Continued)

LIST OF TABLES (Continued)

LIST OF TABLES (Continued)

LIST OF TABLES (Continued)

LIST OF TABLES (Continued)

LIST OF ACRONYMS, SYMBOLS, AND ABBREVIATIONS

AFRL	(United States) Air Force Research Laboratory
Alb	albedo
Al_2O_3	aluminum oxide
ALSEP	Apollo lunar surface experiments package
Amb.	ambient
ANG	above natural grade
AO	atomic oxygen
Ar	argon
AU	astronomical unit
Au	gold
Ba	barium
Ca	calcium
CaO	calcium oxide
CC	cloud-to-cloud (lightning)
CCAFS	Cape Canaveral Air Force Station
CDIP	Coastal Data Information Program
CD–ROM	compact disk-read only memory
Ce	cerium
C-ERA40	40-year corrected-European Centre for medium-range weather forecasts reanalysis
CEV	crew exploration vehicle

CG	cloud-to-ground (lightning)
CGLSS	Cloud-to-Ground Lightning Surveillance System
CH_4	methane
CME	coronal mass ejection
CMOS	complementary metal oxide semiconductor
CO	carbon monoxide
Co	cobalt
CO_2	carbon dioxide
Comb	combined
COS	carbonyl sulfide
CPI	comprehensive plasma instrument
CPME	Charged Particle Measurement Experiment
Cr	chromium
Cr_2O_3	chromium(III) oxide
Cs	cesium
CS_2	carbon disulfide cation
DC	direct current
DD	displacement damage
DMSP	Defense Meteorological Satellite Program
DOL	day of launch
DRWP	Doppler radar wind profiler
Dy	dysprosium

E3	electromagnetic environmental effects
EAFB	Edwards Air Force Base
Earth-GRAM	Earth Global Reference Atmospheric Model
ECMWF	European Centre for Medium Range Weather Forecasts
ELDRS	enhanced low dose rate sensitivity
EMF	electromagnetic force
EOM	end of mission
ER	Eastern Range; electron reflectometer
Er	erbium
ERBE	Earth Radiation Budget Experiment
ERBS	Earth Radiation Budget Satellite
ESD	Exploration Systems Development; electrostatic discharge
Eu	europium
EUV	extreme ultraviolet
EVA	extravehicular activity
Fe	iron
FeO	ferrous oxide
Ga	giga years ago
GCR	galactic cosmic rays/radiation
Gd	gadolinium
GEO	geosynchronous orbit
GN&C	guidance, navigation, and control

GPS	Global Positioning System
GRACE	Gravity Recovery and Climate Experiment
GRAM	Global Reference Atmospheric Model
GRC	Glenn Research Center
GRS	gamma ray spectrometer
GSE	ground support equipment
H	hydrogen
H^+	hydrogen ion
H_2O	water
H_2S	hydrogen sulfide
H_2SO_4	sulfuric acid
HCl	hydrogen chloride
He	helium
He^+	helium ion
HEO	high Earth orbit
Hf	hafnium
Hg	mercury
HNO_3	nitric acid
Ho	holmium
HRMP	Harvard Radio Meteor Project
HWM	Harmonic Wind Model
IC	intracloud (lightning)

IGRF	International Geomagnetic Reference Field
IMF	interplanetary magnetic field
IMP-8	Interplanetary Monitoring Platform-8 (satellite)
IR	infrared radiation
Ir	iridium
IRI	International Reference Ionosphere
Is	ratio of the intensity in arbitrary units of the ferromagnetic resonance to the iron oxide conecentration
ISEE	International Sun-Earth Explorer (satellite)
ISS	International Space Station
K	potassium
K_2O	potassium oxide
Kr	krypton
KSC	Kennedy Space Center
La	lanthanum
LCC	Launch Commit Criteria
LDAR	Lightning Detection and Ranging (system)
LDEF	Long Duration Exposure Facility
LEAM	Lunar Ejecta and Meteorite (experiment)
LEO	low Earth orbit
LET	linear energy transfer
Li	lithium
LM	lunar module

LP	Lunar Prospector (satellite)
LPLWS	Launch Pad Lightning Warning System
LRO	Lunar Reconnaissance Orbiter
LROC	Lunar Reconaissance Orbiter Camera
LST	local standard time
Lu	lutetium
M/OD	meteoroid and orbital debris
MAP	Middle Atmosphere Program
MARECS	Maritime European Communications Satellite
Max.	maximum
MEEC	Mars Experiment on Electrostatic Charging
MEM	Meteoroid Engineering Model
MEO	Meteoroid Environment Office; middle Earth orbit
MET	Marshall Engineering Thermosphere (model)
Mg	magnesium
MgO	magnesium oxide
mho/m	measurement of conductivity, replaced by Siemens
MIL-SPEC	Military Specification
MIL-STD	Military Standard
Min.	minimum
MLT	magnetic local time
Mn	manganese

MnO	manganese (II) oxide
M/OD	meteoroid and orbital debris
MSFC	Marshall Space Flight Center
MSIS	Mass Spectrometer Incoherent Scatter (model)
MSL	mean sea level
MVWP	monthly vector wind profile (model)
N_2	nitrogen
N_2^+	nitrogen ion
N_2O	nitrous oxide
Na	sodium
Na_2O	sodium oxide
NAC	nacreous cloud
NASCAP	NASA/Air Force Spacecraft Charging Analyzer program
NASCAP-2k	NASA/Air Force Spacecraft Charging Analyzer Program-2000
Nb	niobium
NCEP	National Centers for Environmental Prediction
Nd	neodymium
NDBC	National Data Buoy Center
NH_3	ammonia
NH_4^+	ammonium ion
Ni	nickel
NLC	noctilucent cloud
NLDN	National Lightning Detection Network

NO	nitric oxide
NO^+	nitrous oxide ion
NO_2	nitrogen dioxide
NO_3	nitrogen trioxide
NOAA	National Oceanic and Atmospheric Administration
NOZOMI	Martian orbiter spacecraft (Japanese for “HOPE”)
NS	neutron spectrometer
O^+	atomic oxygen ion
O_2	molecular oxygen
O_2^+	molecular oxygen cation
O_2^-	molecular oxygen anion
O_3	ozone
OLR	outgoing long-wave radiation
ORDEM2000	Orbital Debris Engineering Model 2000
P	phosphorus
P_2O_5	phosphorus pentoxide
POLAR	Potentials of Large Spacecraft in Auroral Regions (satellite)
POR	period of record
Pr	praseodymium
PSC	polar stratospheric cloud
PSE	Passive Seismic Experiment
RADAR	radio detection and ranging

Rb	rubidium
RMP	R_e for the magnetopause
RRA	Range Reference Atmosphere
S	sulfur
SAA	South Atlantic Anomaly
SAE	Society of Automotive Engineers
SAM	statistical analysis mode
Sc	scandium
SCATHA	spacecraft charging at high altitudes
SEE	single event effect
SEU	single event upset
Si	silicon
SIDE	Superthermal Ion Detector Experiment
SiO_2	silcon dioxide
Sm	samarium
SO_2	sulfur dioxide
SO_4^{2-}	sulfate ion
SPE	solar particle event
Sr	strontium
SSA	specific surface area
SSP	Space Shuttle Program; Space Station Program
SST	sea surface temperature

STEM	Simple Thermal Environment Model
STS	Space Transportation System
SWH	significant wave height
SZA	solar zenith angle
Ta	tantalum
Tb	terbium
Th	thorium
Ti	titanium
T_iO_2	titanium dioxide
TID	traveling ionospheric disturbance; total ionizing dose
TLP	transient lunar phenomena
TM	Technical Memorandum
TOA	time of arrival
TPS	Thermal Protection System
U	uranium
UN	United Nations
U.S.	United States
USAF	United States Air Force
UTC	universal coordinated time
UV	ultraviolet
V	vanadium
VAGSC	Vehicle Ascent Guidance Steering Commands

W	tungsten
WSMR	White Sands Missile Range
WTS	westward traveling surge
Y	yttrium
Zn	zinc
Zr	zirconium
Yb	ytterbium

NOMENCLATURE

A	orbital altitude; fitting parameter; cross-sectional area normal to fluid flow direction (m^2); constant; ratio of electron density to ion density (n_e/n_i)
$[A_i(\mu_i)]^2$	energy spectrum (m^2/Hz)
A_p	daily planetary geomagnetic index
$A(\mu)$	directional hemispherical albedo (reflectivity)
$\overline{a}$	average lunar normal bolometric albedo = 0.15
a_c	reference radius of the Moon
a_p	planetary geomagnetic activity index
B	magnetic field strength; constant; square foot of the ratio of electron to ion temperatures $(T_e/T_i)^{1/2}$
B_y	component
B_z	component
C	heat capacity; constant; square root of the ratio of ion-to-electron mass $(m_i/m_e)^{1/2}$; constant (7.4)
C_c	compression index
C_{nm}	harmonic coefficient
C_p	heat capacity (J/kg K)
C_r	recompression index
c	parameter; cohesion (kPa)
$D_{0-\lambda}$	percentage of the solar constant (1,366.1 W•m^{-2}) associated with wavelengths shorter than λ
D_a	diameter (km)

NOMENCLATURE

D_R	relative density
d	distance; particle diameter
d_m	gust half-width
E	electron energy (MeV); activation energies; energy of incident electron
$E_{\max}$	energy at which the maximum yield occurs
E_λ	solar spectral irradiance averaged over small bandwidth centered at λ ($W \bullet m^{-2} \bullet m^{-1}$)
e	void ratio of regolith
$e_{\max}$	maximum void ratio at which the regolith can be placed
$e_{\min}$	minimum void ratio at which the regolith can be placed
$erfc$	complementary error function
F	flux (No./cm^2-s-ster-MeV)
$\vec{F}$	vector force acting on a particle (N)
$F_{10.7}$	solar radio noise flux
$F_{10.7}B$	centered solar radio noise flux averaged over six rotations
F_a	error
f	frequency
$f_{\max}$	maximum frequency (Hz)
G	gust factor (function of peak wind speed); specific gravity
g	gravity (m/s^2)
$\vec{g}$	accelerator vector
g_m	gravity (m/s^2)

NOMENCLATURE

H	wave height; reference altitude
$\overline{H_{1/10}}$	average height of the highest one-tenth of the waves
$\overline{H_{1/100}}$	average height of the highest one-hundredth of the waves
H_{max}	maximum wave height
H_p	highest desired fraction of the wave
$\overline{H_p}$	average height of the highest desired fraction of the waves
H_{rms}	root mean square wave height
h	height (m ANG)
I	inertia (J/(m^2 s$^{1/2}$ K)
I^*	omnidirectional slope variance
I_{DH}	direct horizontal solar radiation
I_{DI}	direct incident solar radiation
$I_{DN}(0)$	intensity of solar radiation normal to surface at the Earth's surface assuming clear skies
$I_{DN}(Z)$	intensity of solar radiation normal to surface at required height Z
$I_{D\beta}$	direct incident solar radiation
I_{TH}	total horizontal diffuse radiation
I_{dH}	horizontal diffuse sky radiation
i	solar incidence angle; hydraulic gradient
K	absolute permeability (m^2); thermal conductivity (J/(smK))
K_0	coefficient of lateral stress
k	thermal conductivity; modulus of subgrade reaction parameter Boltzmann's constant

NOMENCLATURE

k_p	logarithm of a_p, the planetary geomagnetic activity index
L	integral scales of turbulence; smallest wavelength (m); turbulence length scale; size of spacecraft; vector along the length of the conductor
M	percent $FeO + TiO_2$
M_p	mass of the particle (g)
M_x	mean of the Rayleigh random variable, x (m)
m	moment of wave spectrum; mass of particle (kg)
m_0	zeroth moment of wave spectrum
m_i	mass, ith series
N	number of recorded wave cycles
n	number of standard deviations away from the mean; total number of frequency bins; porosity
n_e	electron number
n_i	number density
P_{nm}	associated Legendre functions of the first kind of degree n and order m
p	nondimensional parameter; highest fraction of interest
$p(x)$	density function
Q	flow rate (m^3/s)
Q_{in}	radiative heat input into the surface
q	nondimensional parameter; aerodynamic pressure
R	autocorrelation
R_a	depth (km), relative to external surface

NOMENCLATURE

R_e	Earth radii
R_L	lunar radii
r	distance between particle and center of Earth (m)
$\hat{r}$	unit vector pointing from the center of the Earth to the particle
r_c	unit variance Gaussian random variable
rud	zero-mean variable
S	solar constant (W/m^2)
$S(f)$	spectral density function
Snm	harmonic coefficient
So	average solar constant at 1 AU
T	temperature (K)
T,t	time
T_i	temperature, *i*th series
T_m	mean zero up-crossing wave period
T_p	peak spectral wave period
T_s	lunar surface temperature at the subsolar point
T_v	virtual temperature
U_4	peak wind speed at the 4-m reference height
$\bar{U}_h$	steady state wind at height h (m/s)
U_h	peak wind at height h (m/s)
$\bar{U}_z$	steady state wind speed (m/s)

NOMENCLATURE

u	longitudinal component of turbulence; wind speed
u_i	bulk flow velocity, ith species; instantaneous wind speed
V	random gust; spacecraft velocity vector; gravitational potential
V_1	initial gust
V_2	random gust
V_m	gust magnitude
v	lateral component; particle velocity
w	vertical component; annual mean and $+–2\sigma$ mixing ratio
$X\chi$	compression index
x	random variable; desired frequency (Hz)
x_m	mean of x in the distribution
x_N	normalized variate
y	resulting energy (m^2/Hz)
z	height
α	Sun's azimuth (measured from the south direction toward positive west); angle of attack
β	tilt angle; angle of sideslip
γ	fitting parameter
Δ	size of particle (cm)
Δe	change in void ratio
$\Delta \log \sigma_v$	log change of applied vertical stress

NOMENCLATURE

ΔQ	amount of heat
ΔT	temperature change
$\Delta\mu_i$	energy spectrum (m^2/Hz)
δ	number of secondary electrons emitted per incident electron
$\delta_{\max}$	maximum number of secondary electrons emitted per incident electron
ε	long-wave emissivity of the surface (assumed to equal 1)
θ	solar zenith angle; angle relative to surface normal
κ	thermal conductivity (W/mK)
λ	wavelength (μm); longitude
μ	total water surface slope (deg); fluid viscosity (Ns/m^2)
μ_c	crosswind water surface slope component (rad)
μ_E	gravitational constant for the Earth
μ_{ud}	upwind-downwind water surface slope component (rad)
μ_V	mean of random gusts
ρ	density of meteoroid; bulk density; density of the fluid (kg/m^3); density (g/m^3)
ρ_S	atmospheric density at sea level (kg/m^3)
ρ_w	density of water
ρ_Z	atmospheric density at required height (kg/m^3)
σ	standard deviation; Stefan-Boltzmann constant (5.67×10^{-8} W/m^2K^4); normal stress (kPa); conductivity
σ^2	variance

NOMENCLATURE

σ^2_c	crosswind slope variance
σ^2_{ud}	upwind-downwind slope variance
σ_h	horizontal stress
σ_V	standard deviation of random gusts; vertical stress
σ_x	standard deviation
τ	average period
ϕ	geocentric declination; latitude; friction angle (º)
$\phi(\Omega)$	gust spectral density function $(m^2/s^2\ (cGy/m)^{-1}$
Ω	wave number

TECHNICAL MEMORADUM

NATURAL ENVIRONMENTS DEFINITION FOR DESIGN

1. INTRODUCTION

Planning for future National Aeronautics and Space Administration (NASA) missions will encompass a variety of operational and engineering activities that involve a multitude of issues, constraints, and influences derived from the natural environment. This Technical Memorandum (TM) presents a definition of the natural environment, i.e., a description in engineering handbook format of models and data specifically selected to support the architecture development, engineering design, and technology development for NASA's Exploration Systems Development (ESD) initiatives.

1.1 Purpose

This TM provides a uniform description of the natural environment to serve as a support framework for missions under ESD initiatives. It is intended to support engineering and analysis, requirements development, and verification involved in the development of exploration concepts and architectures, flight hardware, and new technologies. Presenting a single benchmark definition of natural environment parameters provides an easily accessible and uniform baseline for competitive studies, independent analyses, and concept studies.

Since the definitions specified herein are, for the most part, definitions developed and used on prior programs, they are well understood by NASA and significant portions of the contractor community. Thus, use of this TM enables a better understanding of program technical risk than would be possible without a baselined definition document.

1.2 Scope

Natural environment, as the term is used here, is intended to include all environmental factors that are independent, i.e., outside the influence, of the program. Orbital debris and some other manmade environments are included because they are beyond program control. All induced environments, contamination, and aeroheating, for example, are excluded because they are dependent on system design. Likewise, 'environmental impact,' the effects of a program on the environment, is not within this scope.

This TM provides all natural environments needed to support aerospace vehicle design and development activities. The material is divided as follows:

- Introduction (sec. 1).

- Terrestrial ground and aloft environments (secs. 2 and 3). The terrestrial environments sections include the natural environments from the Earth's surface to the edge of the thermosphere, approximately 90 km (295.3×10^3 ft) altitude. These environments will be experienced at ground facilities at the primary launch and landing sites, and during ground operations and processing, launch, and landing. Examples include surface and upper level winds, severe weather, lightning, and thermodynamic parameters.

- Near and low Earth space environments, and medium and high Earth orbits (HEOs) (secs. 4–6). The near Earth space environments sections describe the Earth orbital environments, including thermosphere density, ionizing radiation, plasma, solar activity, geomagnetic fields, orbital debris, and meteoroids, etc.

- Cislunar and lunar space and surface environments (secs. 7–9). The cislunar and lunar environments sections focus on the lunar orbital and surface environments.

This TM is a handbook and source document for the environment models and data needed to support a program throughout the development phase. It is not a science text.

The Natural Environments Branch at Marshall Space Flight Center (MSFC), Huntsville, Alabama, should be notified when environment information is needed that has not been provided in this TM. They will work with appropriate NASA programs to provide the information and update this TM as appropriate. Clarification and interpretation of the information contained herein is also the responsibility of the Natural Environments Branch.

The application of the models and data provided herein, and documentation of the applications, is the responsibility of the user. The intent of this TM is to support design and development phases.

1.3 Format and Use of This Technical Memorandum

Each section within this TM contains an explanation and description of the natural environment phenomenon to which it is devoted.The physics of the phenomenon and its dynamics are briefly described. Key data describing the environment are presented in handbook style format. Any analysis and models that are applicable and available for providing the key data are listed. Graphs and diagrams, unless otherwise noted, are for illustration purposes only and should not be used for specifications. Finally, lessons learned concerning the potential impacts of the environmental factors are discussed and mitigation techniques are suggested for consideration.

In recent years it has become popular to express requirements in terms of probabilities, e.g., probability of loss of crew or loss of vehicle, probability of launch delay, etc. For this reason, this TM defines the probability distribution functions for the various natural environment parameters wherever possible, i.e., the intensity as a function of probability of occurrence over some period of record (POR). This is intended to allow architecture developers to trade robust design against

operational mitigation and/or acceptable risks wherever the environmental parameters affect architecture performance against one of the key requirements. Unfortunately, the format and detail of the probability distribution varies from parameter to parameter, depending on the quality and amount of data available for the particular environment. In some cases, a complete distribution function is available either directly or within a model. For other cases, only a few points can be provided (estimates of a 95th or 96th percentile, for example). In some cases, there is inadequate information available about the environment to define the distribution, e.g., orbital debris. In any case, the manner and limitations of data presentation are not intended to define the design points.

2. TERRESTRIAL GROUND ENVIRONMENTS

This section provides a baseline description of the natural terrestrial environment for the ground surface. Definitions and descriptions of terrestrial environmental phenomena for the surface, zero to 150 m (zero to 492.1 ft), are provided in this section. Definitions and descriptions for aloft environments, 150 m to 90 km (492.1 to 295.3×10^3 ft), are provided in section 3. Environment definitions are given for the following surface locations: Eastern Range (ER) (28.90 °N., 80.55 °W.) and Edwards Air Force Base (EAFB) (34°54′ N., 117°52′ W.).

Introductions to various statistical models and their databases that are pertinent to the vehicle design are presented. It is important to remember that the interdependence of the various parameters in this section is critical when evaluating launch/landing probability. A summary of key design factors for ground environments is displayed in table 1.

Table 1. Summary of key design factors.

Parameter	Source	Select Based On
Winds	Sections 2.1, 2.1.1, 2.1.1.1– 2.1.1.4, and 2.1.2	Location, altitude, steady state winds, peak wind profile, wind gusts
Solar radiation	Section 2.2; tables 10 and 11	Location, season, time of day, altitude, cloudiness
Temperature means/extremes	Figures 5 and 7	Location, month
Pressure means/extremes	Figures 9 and 11	Location, month
Humidity	Figures 13 and 14	Location, temperature, dew point temperature
Aerosols	Section 2.6; table 31	Location, humidity, wind speed, altitude
Precipitation: rain	Tables 33 and 35	Location, altitude
Precipitation: hail	Tables 34 and 36	Location, altitude
Atmospheric electricity/lightning	Tables 38, 40, and 42	Location, month
Tropical cyclones	Sections 2.9.1 and 2.9.2	Location, season
Sea state statistics	Tables 43–46	Location, month, wind speed, and direction
Ocean temperatures	Tables 47 and 48	Location, season, depth in ocean
Earthquakes	Sections 2.11.1, 2.11.4.2, and 2.11.5.2	Location
Tsunamis and seiches	Sections 2.11.2 and 2.11.4.3	Location
Volcanic hazards	Sections 2.11.3, 2.11.3.1, 2.11.3.2, 2.11.4.4, and 2.11.5.3	Location
Ionizing radiation: Secondary neutron environment	Sections 2.12.1, 2.12.2, and 2.12.3	Critical device LET threshold

2.1 Ground Winds

Ground winds are defined in this TM as the winds from the surface up to 150 m (492.1 ft). This layer is referred to as the boundary layer. The winds within the boundary layer are characterized by very complicated three-dimensional (3D) flow patterns with turbulent accelerations in both space and time. Turbulent circulations generated by surface heating during the daytime influence the surface winds by transferring momentum vertically throughout the depth of the boundary layer. Turbulence is small during nighttime conditions as the wind speeds are typically light within the statically stable boundary layer. Winds in the boundary layer will affect not only the vehicle, but also the ground support equipment (GSE) and facilities. Natural environmental factors influencing the magnitude and direction of the winds range from synoptic, large-scale (>1,000 km (539.9 nmi)), steady state wind to localized weather phenomena, such as thunderstorm downdrafts and thermally induced circulations, which tend to induce peak winds and/or turbulent gusts.

Note: Standard meteorology convention is adopted for wind direction, i.e., north is designated as 0°, east as 90°, etc. An east wind is therefore directed from east to west.

2.1.1 Eastern Range

The ER as defined in this TM is the region that comprises Cape Canaveral Air Force Station (CCAFS), which includes NASA's Kennedy Space Center (KSC) and Patrick Air Force Base. All areas of the region are situated along the eastern shore in central Florida.

The weather station elevation at the ER is approximately 5 m (16.4 ft) above mean sea level (MSL).[1] Some measured atmospheric variables, such as pressure and density, are a function of station elevation. For standardization purposes, these values are reduced to the value at MSL.

Note that since the ER elevation is only 5 m (16.4 ft) MSL, all data reported from the ER are in terms of MSL values, except the 18.3-m- (60-ft-) tall pad light pole that is reported above natural grade (ANG).

The ER is exposed to a variety of synoptic-scale weather patterns during a year. In the winter, cold front passages can result in steady state northerly winds at speeds from 5 to 10 m/s (16.4 to 32.8 ft/s) for consecutive days. In the summer, an expansive high-pressure system typically develops in the central Atlantic, resulting in 5 to 10 m/s (16.4 to 32.8 ft/s) easterly flow at the ER. During the autumn months, northeasterly winds of approximately 10 to 15 m/s (32.8 to 49.2 ft/s) typically occur and are associated with a continental high-pressure system over the central United States. These northeasterly winds introduce a crosswind component on the runways and could affect vehicle landings. The proximity of the ER to the Atlantic Ocean also makes it susceptible to tropical storms and hurricanes, which produce strong winds over long durations. The hurricane season extends from June through November. Further discussion of tropical storms and hurricanes is presented in section 2.9.

Locally, the ER proximity to the Atlantic Ocean and tropical latitudes results in a large dispersion of winds in the boundary layer. Thermally induced circulations develop due to differential heating of land versus sea. These circulations cause boundary layer winds to blow from the sea

during the day and from the land at night, and are known as sea breezes and land breezes, respectively. The circulations that develop act to either accelerate or reduce the prevailing wind speed and can change the direction of the wind. When acting against the prevailing wind, convergent boundaries can form at the boundary between the thermally induced circulation and the prevailing wind. These convergent zones can act as a trigger mechanism for thunderstorm development that can produce downdrafts with vertical velocities up to 15 m/s (49.2 ft/s) and horizontal velocity components of approximately 25 m/s (82 ft/s). Thunderstorm initiation from sea breeze circulations tends to occur over the central Florida peninsula and move eastward with the mean wind; whereas, land breeze-initiated thunderstorms develop off the Florida Atlantic coast in the early morning hours, 03:00 to 06:00 local standard time (LST), and move inland.

From the brief description of the natural wind environment for the ER, engineers need to account for steady state winds in addition to the peak winds with the associated turbulent spectra and discrete gusts when designing an aerospace vehicle, GSE, and facilities. Peak wind speed is the fundamental measure of wind instead of steady state wind speed since the loads placed on the vehicle are greater for peak winds versus steady state winds.[1]

Exposure duration to the natural environment is also important in the design of the vehicle, GSE, and facilities. For example, the aerospace vehicle's exposure time will likely be less than the GSE and facilities. Therefore, the design requirements for withstanding a single-occurrence peak ground wind will differ between the vehicle and the GSE or facilities.

Due to these natural environment conditions, NASA has developed empirical formulas for peak wind and steady state wind profiles based on extensive observations of winds measured at NASA's ground wind tower at the ER. From these formulas, wind speed envelopes are calculated at a specified risk level, based on probability distributions for either peak or steady state wind values, during a specified exposure period (e.g., 1 hr, 30 day, 3 mo, or 1 yr) at the ER. In order to perform loading and response calculations resulting from steady state and random turbulence drag loads and von Karman vortex shedding loads, the engineer requires information about the vertical variation of the mean wind and the structure and turbulence in the atmospheric boundary layer. The philosophy is to extrapolate the peak wind statistics up in height via a peak wind profile model or empirical formula. The associated steady state or mean wind profile is obtained by applying a gust factor that is a function of wind speed and height.

2.1.1.1 Peak Wind Profile. The peak wind profile empirical formula was developed at discrete heights, 18 m (59.1 ft) , 30 m (98.4 ft), 60 m (196.9 ft), 90 m (295.3 ft), 120 m (393.7 ft), and 150 m (492.1 ft), and is defined with a power law relationship as:[1]

$$u(z) = u_{18.3}\left(\frac{z}{18.3}\right)^{k}, \tag{1}$$

where $u(z)$ is the peak wind speed at height z in meters ANG, $u_{18.3}$ is a known peak wind speed at 18.3 m (60 ft), and for $u_{18.3}$ >2 m/s (6.6 ft/s), k is defined as:

$$k = c\left(u_{18.3}\right)^{-3/4}, \tag{2}$$

where parameter c is normally distributed with a mean of 0.52 $(m/s)^{3/4}$ and standard deviation (σ) of 0.36 $(m/s)^{3/4}$; thus, $c = 0.52 + 0.36n$ $(m/s)^{3/4}$, where n is the number of standard deviations away from the mean. For example, when $n = 3$ (3σ), $c = 1.6$ $(m/s)^{3/4}$, corresponding to a risk level of 0.135%.[2] The peak wind is referenced to the 18.3-m (60-ft) level, which is the base height of the launch pad at the ER.

Referencing a standard level in the discussion of ground winds avoids confusion in the interpretation of risk statements and structural load calculations. For a given σ level, the peak wind speed profile will envelope the appropriate percentage of wind speed profiles for a given peak wind at the reference level. The reference level wind and the peak wind speed profile can have different levels of risk. For example, a reference level wind can have a 5% risk of being exceeded, but one can build a 3σ ($n = 3$) profile that will envelope 99.865% of wind speeds given that particular reference level wind. This formula for peak wind provides an envelope of the peak winds in the boundary layer associated with a reference peak wind at 18.3 m (60 ft) at a specified standard deviation. The formula does not provide instantaneous wind profiles.

Figure 1, along with the raw data in table 2, is an example of peak wind speed profile envelopes ($n = 3$) for the 5% risk of exceeding the 10 m (32.8 ft) peak wind speed for various exposure periods.[1]

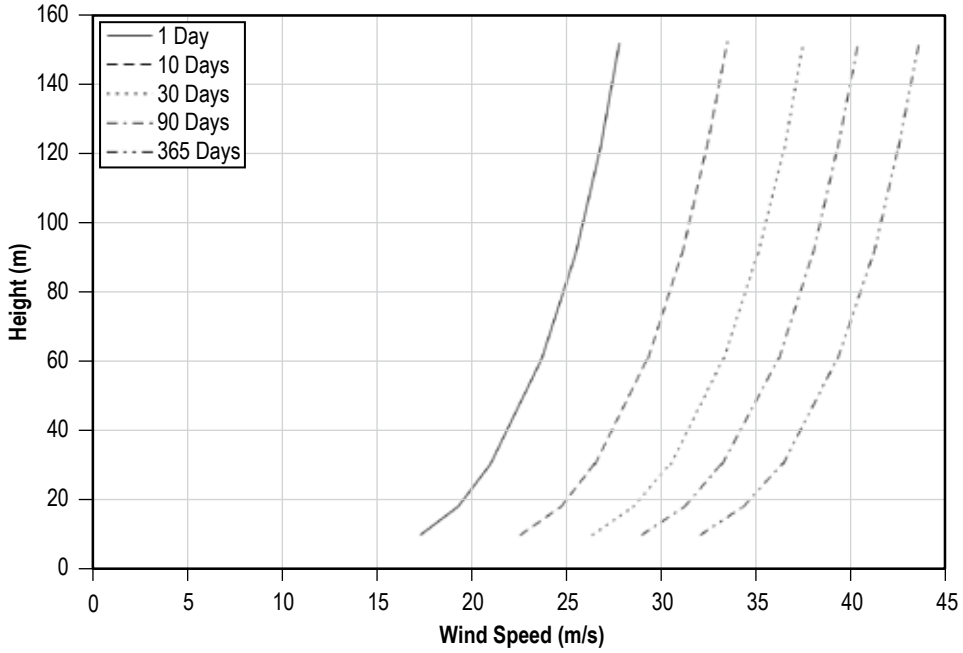

Figure 1. Peak wind speed profile envelopes for a 5% risk of exceeding 10 m (32.8 ft) peak wind speeds for various exposure periods for the ER.

Table 2. Peak wind speed profile envelopes for a 5% risk of exceeding 10 m (32.8 ft) for various exposure periods for the ER.

Height		Exposure Days									
		1		10		30		90		365	
(m)	(ft)	(m/s)	(ft/s)	(m/s)	(ft/s)	(m/s)	(ft/s)	(m/s)	(ft/s)	(m/s)	(ft/s)
10	33	17.3	56.8	22.6	74.1	26.4	86.6	29	95.1	32.1	105.3
18.3	60	19.3	63.3	24.7	81	28.5	93.5	31.2	102.4	34.3	112.5
30.5	100	21	68.9	26.5	86.9	30.5	100.1	33.2	108.9	36.4	119.4
61	200	23.7	77.8	29.3	96.1	33.3	109.3	36.2	118.8	39.3	128.9
91.4	300	25.5	83.7	31.1	102	35.1	115.2	38	124.7	41.2	135.2
121.9	400	26.8	87.9	32.4	106.3	36.5	119.8	39.3	128.9	42.5	139.4
152.4	500	27.8	91.2	33.5	109.9	37.5	123	40.4	132.5	43.6	143

From figure 1, as the exposure time increases, so does the peak wind speed throughout the depth of the boundary layer. The steady state wind profiles obtained from the peak wind profile for design purposes are based on the following:[2]

$$\bar{U}(z) = u(z)\left(1+\left(\frac{\left(\frac{18.3}{z}\right)^{\left(0.283-0.435e^{-0.2u_{18.3}}\right)}}{1.98-1.887e^{-0.2u_{18.3}}}\right)\right), \tag{3}$$

where $u(z)$ is the peak wind found in equation (1), z is height in meters ANG, and $u_{18.3}$ is the known peak wind speed at 18.3 m (60 ft).

2.1.1.2 Ground Wind Gust Factors. The gust factor (G) is defined as:

$$G = \frac{u}{\bar{u}}, \tag{4}$$

where u is the maximum wind speed at height z within an average period (τ), and $\bar{u}$ is the mean wind speed associated with τ, given by:

$$\bar{u} = \frac{1}{\tau}\int_0^{\tau} u_i(t)\,dt, \tag{5}$$

where $u_i(t)$ is the instantaneous wind speed at time (t), and t is the time reckoned from the beginning of the averaging period.

If $\tau = 0$, then $\bar{u} = u$ according to equation (5), and it follows from equation (4) that $G = 1$. As τ increases, $\bar{u}$ departs from u, $\bar{u} \le u$, and $G > 1$. Also, as τ increases, the probability of finding a maximum wind of a given magnitude increases. In other words, the maximum wind speed

increases as τ increases. In the case of $\bar{u} \to 0$ and $u \geq 0$ ($\bar{u} = 0$ might correspond to windless free convection), $G \to \infty$. As $\bar{u}$ or u increases, G tends to decrease for fixed $\tau > 0$, while for very high wind speeds, G tends to approach a constant value for given values of z and τ. Finally, as z increases, G decreases. Thus, the gust factor is a function of the averaging time (τ) over which the mean wind speed is calculated, the height (z), and wind speed (mean or maximum).

Investigations of gust factor data have revealed that the vertical variation of the gust factor can be described with the following relationship:[3]

$$G = 1 + \frac{1}{g_0}\left(\frac{18.3}{z}\right)^p , \tag{6}$$

where z is the height in meters ANG. The parameter (p), a function of the 18.3 m (60 ft) peak wind speed in m/s, is given by:

$$p = 0.283 - 0.435e^{\left(-0.2u_{18.3}\right)} . \tag{7}$$

The parameter g_0 depends on the averaging time and the 18.3 m (60 ft) peak wind speed and is given by:

$$g_0 = 0.085\left(\ln\frac{\tau}{10}\right)^2 - 0.329\left(\ln\frac{\tau}{10}\right) + 1.98 - 1.887e^{-0.2u_{18.3}} , \tag{8}$$

where τ is given in minutes and $u_{18.3}$ is given in m/s.

These relationships are valid for $u_{18.3} \geq 4$ m/s (13.1 ft/s) and $\tau \leq 10$ min. In the interval 10 min $\leq \tau \leq$ 60 min, G is a slowly increasing monotonic function of τ, and for all engineering purposes, the 10-min gust factor ($\tau = 10$ min) can be used as an estimate of the gust factors associated with averaging times >10 min and <60 min.

The calculated 10-min gust factors for values of $u_{18.3}$ in the interval 4.63 m/s (15.2 ft/s) $\leq u_{18.3} \leq \infty$ are presented in table 3 in the metric and U.S. customary units for $u_{18.3}$ and z. As an example, the gust factor profile for $\tau = 10$ min and $u_{18.3}$ = 9.3 m/s (30.5 ft/s) is given in table 4. Since the basic wind statistics are given in terms of hourly peak wind, the $\tau = 10$-min gust factors are used to convert the peak winds to mean winds by dividing by G. All gust factors in these sections are expected values for any particular set of values for u, τ, and z.

Table 3. Ten-minute gust factors for the ER.

Reference Height 18.3 m (60 ft) Peak Wind		Height ANG in Meters (ft)						
(m/s)	(ft/s)	10 (32.8)	18.3 (60)	30.5 (100)	61 (200.1)	91.4 (299.8)	121.9 (399.9)	152.4 (500)
4.63	15.2	1.868	1.812	1.767	1.71	1.679	1.658	1.642
5.15	16.9	1.828	1.766	1.718	1.657	1.624	1.602	1.585
5.66	18.6	1.795	1.729	1.678	1.614	1.58	1.556	1.539
6.18	20.3	1.768	1.699	1.645	1.579	1.544	1.52	1.502
6.69	21.9	1.746	1.674	1.618	1.552	1.514	1.489	1.471
7.21	23.7	1.727	1.652	1.595	1.525	1.488	1.464	1.446
7.72	25.3	1.712	1.634	1.576	1.505	1.467	1.442	1.424
8.24	27	1.698	1.619	1.559	1.487	1.449	1.424	1.409
8.75	28.7	1.686	1.606	1.545	1.472	1.424	1.409	1.39
9.27	30.4	1.676	1.594	1.532	1.459	1.421	1.395	1.377
9.78	32.1	1.668	1.584	1.522	1.447	1.409	1.384	1.365
10.3	33.8	1.66	1.575	1.512	1.437	1.399	1.374	1.355
12.9	42.3	1.634	1.545	1.48	1.403	1.365	1.339	1.321
15.4	50.5	1.619	1.528	1.462	1.385	1.346	1.321	1.302
∞	∞	1.599	1.505	1.437	1.359	1.32	1.295	1.277

Table 4. Gust factor profile for $\tau = 10$ min and $u_{18.3} = 9.27$ m/s (30.4 ft/s).

Height		
(m)	(ft)	Gust Factors
10	32.8	1.676
18.3	60	1.594
30.5	100	1.532
61	200.1	1.459
91.4	299.8	1.421
121.9	399.9	1.395
152.4	500	1.377

2.1.1.3 Spectral Gust Environment. At any moment in time, in a fully developed turbulent flow, there will exist a departure in the instantaneous wind vector from the quasi-steady state wind vector. This departure will have two horizontal turbulent components, longitudinal and lateral, which are, respectively, parallel and perpendicular to the quasi-steady state wind vector. The vertical turbulence component is assumed to equate to the lateral component. Because of these departures from the quasi-steady state wind vector, design of the launch vehicle must take into consideration the vehicle's ability to withstand either the spectral gust environment or the discrete gust environment from any azimuth induced by the turbulent flow.[2]

The longitudinal, lateral, and vertical turbulent components at height z ANG are given by:

$$S(f) = \frac{A\left(\frac{z}{18.3}\right)^{a} z\left(\frac{\bar{U}_{18.3}^{2}}{\bar{U}_{z}}\right)}{\left(1 + B\left(\left(\frac{18.3}{z}\right)^{C_2}\left(\frac{fz}{\bar{U}_{z}}\right)\right)^{C_4}\right)^{b}}, \tag{9}$$

where the values for the nondimensional constants A, B, a, b, C_2, and C_4, given in table 5, are a function of the turbulent components, z is height in meters ANG, $\bar{U}_z$ is the steady state wind speed (m/s) at height z, and $\bar{U}_{18.3}$ is the steady state wind speed (m/s) at 18.3 m (60 ft).The quantity $S(f)$ is a spectral density function of frequency f. $S(f)$ is defined such that integration over the frequency domain, $0 \le f \le \infty$, yields the variance of the component of turbulence of concern. The units of $S(f)$ are m^2/s^2 $(cycle/s)^{-1}$ and the units of f are cycles/s.

Table 5. Nondimensional constraints for the longitudinal, lateral, and vertical components of turbulence for the vehicle on-pad, transportation, and launch operation phases at the ER.

Component	A	B	a	b	C_2	C_4
Longitudinal	1.35	29.035	–1.1	1.972	1	0.845
Lateral and vertical	0.258	9.059	–0.93	2.134	0.58	0.781

2.1.1.4 Discrete Gust Model. The discrete gust model consists of longitudinal, lateral, and vertical discrete gusts given by:

$$V = \frac{V_m}{2}\left(1 - \cos\left(\pi \frac{d}{d_m}\right)\right), 0 \le d \le 2d_m, \tag{10}$$

where V_m is the gust magnitude, d_m is the gust half-width, and d is distance. The discrete gusts are applied individually, and the resulting loads and responses are combined with the loads and responses resulting from the steady state wind profile with appropriate statistical procedures to determine design loads and responses.[2] Refer to section 3.2 for a more complete description and application of the discrete gust model.

The Natural Environments Branch at MSFC has an extensive database consisting of surface observations from meteorological towers measuring wind speed and direction from the surface up to 150 m (492.1 ft) that can be utilized in support of vehicle development. These observations can be used to determine peak/steady state wind speed profile envelopes for a specified risk level, reference period, and spectral/discrete gust moments for input into load simulations.

2.1.2 Edwards Air Force Base

EAFB is located on the western edge of the Mojave Desert approximately 145 km (78.3 nmi) northeast of Los Angeles, CA, at 34°54′ N., 117°52′ W. The field elevation is 701.6 m (2,302 ft). EAFB lies on a desert plateau, averaging 731.5 m (2,400 ft) above sea level. The plateau is generally flat and sandy with typical cacti and scrub vegetation, and no open water. The Rogers and Rosamond dry lakes on base are the only truly flat surfaces in the area. Sudden moderate to heavy rainfall can cover the dry lakes with water up to 0.3 m (1 ft) deep, which can be a source of fog after frontal passages. EAFB is surrounded southeast through northwest by mountain ranges. The low Garlock Range lies north of the base a few kilometers, but rises only approximately 152.4 m (500 ft). More significant are the Tehachapi Mountains, 55.6 km (30 nmi) to the west and northwest, with peaks to 2,438.4 m (8,000 ft). Also, the San Gabriel Mountains lie 48 km (25.9 nmi) to the south with peaks to 3,048 m (10,000 ft). The topography changes little in character to the east, but several large mountains of the Sierra Nevadas, oriented north-south, lie 48 km (25.9 nmi) to the north of the base.[4]

Wind becomes a complex problem at EAFB as speeds and directions may vary greatly in time and space. Speeds to 20.6 m/s (67.6 ft/s) are not uncommon with frontal passage but are usually of short duration. Topography also affects the local wind. During the late spring and summer, a daily temperature and pressure differential develops between the high desert and the coastal basins, which causes a heating wind to occur during the late afternoon and evening. The direction is southwesterly and speed can be up to 20.6 m/s (67.6 ft/s). Because of the blocking effect of the Tehachapi Mountains, EAFB rarely experiences northwest winds. Northeast winds are expected to be funneled through the Owens Valley.[4]

Wind data and risk levels are based upon the concept of providing comprehensive coverage and minimizing risk and cost, while maximizing operational capability. For deorbit, descent, and landing/post-landing phases, where EAFB wind conditions can be monitored, the design risk is generally 5% for the worst month. This provides for adequate operational capability and scheduling flexibility and, combined with the wind monitoring, results in very low-risk operations. For those flight regimes where the atmospheric conditions cannot be monitored, the design risk must necessarily be significantly lower and is set at 1%.

Table 6 shows the 5% risk peak wind speeds for various exposure periods at EAFB at the 4 m (13.1 ft) ANG reference height.[5]

Table 6. EAFB 5% risk, peak wind speeds versus exposure period at 4 m (13.1 ft) ANG reference height.

Exposure Period (hr)	5% Risk Wind Speed	
	(m/s)	(ft/s)
1	18	59.1
2	19	62.3
3	20	65.6
24	23	75.5

Equation (11) can be used to calculate peak wind speeds above the 4 m (13.1 ft) reference height:[5]

$$U_h = U_4\left(\frac{h}{4}\right)^{0.085} , \tag{11}$$

where U_h is in m/s, U_4 is the peak wind speed at the 4 m (13.1 ft) reference height, and h is height in m ANG. The EAFB peak wind speed profile, as calculated with equation (11), is shown in table 7.

Table 7. EAFB peak wind speed profile for 5% risk, 1 hr exposure, 4 m (13.1 ft) ANG reference height.

Height ANG		U_h Peak Wind Speed	
(m)	(ft)	(m/s)	(ft/s)
4	13.1	18	59.1
30.5	100.1	21	68.9
61	200.1	23	75.5
91.4	299.8	24	78.7
121.9	399.9	24	78.7
152.4	500	25	82
295	967.8	26	85.3

Equation (12) can be used to calculate the steady state wind profile that is associated with the peak wind profile given by equation (11):[5]

$$\bar{U}_h = \frac{U_h}{G\left(U_h\right)} , \tag{12}$$

where $\bar{U}_h$ is the steady state wind at height h, U_h is the peak wind at height h, and G is the gust factor which is a function of peak wind speed. The gust factor (G) is calculated by equation (13):[5]

$$G = 0.9936 + 0.895e^{(-0.05U_hC)} + 10.09(U_hC)^{(-1.19)} , \tag{13}$$

where U_h is in m/s and C is 1.94254 s/m.

Table 8 contains selected values of the steady state wind profile at various heights ANG for the worst month.[5]

Table 8. EAFB steady state wind speed profile for 5% risk, 1 hr exposure, 4 m (13.1 ft) ANG reference height.

Height ANG		Wind Speed	
(m)	(ft)	(m/s)	(ft/s)
4	13.1	14	45.9
30.5	100.1	17	55.8
61	200.1	19	62.3
91.4	299.8	20	65.6
121.9	399.9	20	65.6
152.4	500	21	68.9
295	967.8	22	72.2

Wind shear below the 295 m (967.8 ft) level can be computed first by selecting a point (shear computation point) on the steady state wind profile and then linearly interpolating (not to exceed 0.25/s shear rate) to a zero wind (or higher if constrained by 0.25/s limit) condition at the surface of the Earth. The mean (steady state) wind profile will then be used above the shear computation point with the linear extension below. A necessary number of shear computation points must be used up to the 295 m (967.8 ft) level for a sufficient number of design steady state wind envelopes to ensure an adequate vehicle control system design study.[1]

The 5% risk vector wind shear in the worst month for heights below approximately 762 m (2,500 ft) ANG is 15 m/s (49.2 ft/s).[5] This wind shear should be representative of low-level jet conditions since the shear calculations were made from 04:00 LST observations, a time when that phenomenon is most likely to be present.

The Dryden Spectral gust environment with longitudinal (u), lateral (v), and vertical (w) spectral density functions is given by:

• Longitudinal:
$$\phi_u(\Omega) = \sigma^2 \frac{2L}{\pi} \frac{1}{1+(L\Omega)^2} \tag{14}$$

and

• Lateral vertical:
$$\phi_{v,w}(\Omega) = \sigma^2 \frac{L}{\pi} \frac{1+3(L\Omega)^2}{\left[1+(L\Omega)^2\right]^2}\ , \tag{15}$$

where $\phi(\Omega)$ is the gust spectral density function with units of m^2/s^2 $(cGy/m)^{-1}$ at wave number Ω with units of cGy/m.

The quantities σ and L denote the standard deviation and integral scales of turbulence. The longitudinal component of turbulence (u) is defined as the component of turbulence parallel to the horizontal projection of the flight path of the vehicle. The lateral component (v) lies in the horizontal plane and is perpendicular to the longitudinal component, and the vertical component

(w) is perpendicular to the other two components and is assumed to equal v. The spectral density functions are defined such that integration over the domain $0 \leq \Omega \leq \infty$ yields the variance. In order to define the design input forcing function for spectral response calculations and the simulation of forcing function time histories along the flight path of the vehicle, the turbulent velocity vector must be added to the steady state wind vector to define the instantaneous wind vector. To generate atmospheric turbulence time sequences, apply equations (14) and (15) in conjunction with the procedures and equations given in sections 2.3.14 and 2.3.14.1 of Johnson.[1]

Atmospheric turbulence below the 295 m (967.8 ft) ANG level is anisotropic so that the statistical properties of turbulence will vary from component to component, i.e., the standard deviations and integral scales of turbulence vary from component to component. The longitudinal, lateral, and vertical components of turbulence are as defined above. The vertical profiles of the standard deviations and the integral scales of turbulence requirements for the flight phases below the 295 m (967.8 ft) ANG level are given by:

$$\sigma_h = \sigma_4 \left(\frac{h}{4} \right)^p \tag{16}$$

and

$$L_h = L_4 \left(\frac{h}{4} \right)^q \ , \tag{17}$$

where h denotes height ANG in m, and σ_4 and L_4 denote the 4 m (13.1 ft) level values of σ and L, and p and q are nondimensional parameters.

The design values of these parameters (σ, L, p, and q) for each component of turbulence, which are used to establish design spectral gust requirements for the vehicle descent and landing, below the 295 m (967.8 ft) ANG level, are given in table 9.[2]

Table 9. Dryden turbulence spectra parameters for altitudes below the 295 m (967.8 ft) ANG level.

	σ_4			L_4		
Component	(m/s)	(ft/s)	p	(m)	(ft)	q
Longitudinal	2	6.6	0.16	11.7	38.39	0.65
Lateral	1.33	4.4	0.25	5.2	17.06	0.83
Vertical	0.83	2.7	0.36	2	6.56	1.05

2.2 Solar Radiation

The total (global) solar radiation measured on a horizontal plane at the surface is a function of the intensities of direct solar radiation from the Sun and diffuse radiation from the total sky atmosphere. The total amount of direct solar radiation striking the surface is dependent on the

solar zenith angle (SZA) (θ). Maximum intensity of direct solar radiation to a horizontal plane on a daily basis will occur when the SZA is the smallest. Seasonally, the maximum intensities of direct solar radiation are a function of the Earth's distance to the Sun. For example, the maximum intensity of direct solar radiation occurs in December, near perihelion, in the early afternoon hours, when θ is the smallest.

A diffuse radiation incident at the surface depends upon the humidity and the amount of scattering particles present in the atmosphere. When the atmosphere is clear and dry, diffuse radiation is minimized and increases with increasing humidity and/or scattering particles.

For design studies, when radiation data are used, direct solar radiation is assumed to emanate from a single point source (the Sun) and travel in parallel rays. Since absorbed solar radiation is converted to heat, differential heating of surfaces occurs (due to differential absorption, e.g., direct sun versus shade, or differences in surface absorptivity of different system components). Unequal heating may result in stresses or deformations to the vehicle or GSE.

Computations of total (direct plus diffuse) horizontal solar radiation (I_{TH}) require measurements of direct horizontal radiation (I_{DH}) and diffuse sky radiation (I_{dH}) on a horizontal surface.[1] The relationship is as follows:

$$I_{TH} = I_{DH} + I_{dH} \ . \tag{18}$$

After subtracting out the horizontal diffuse radiation (I_{dH}) from the total horizontal solar radiation (I_{TH}), the resultant direct horizontal solar radiation (I_{DH}) can be used to compute the direct incient solar radiation (I_{DI}) by the following:

$$I_{DI} = \frac{I_{DH}}{\cos\theta} \ , \tag{19}$$

where I_{DI} is the direct incident solar radiation, I_{DH} is the direct horizontal solar radiation, and θ is the SZA.

To determine the amount of solar radiation on a south-facing surface, with tilt angle β, the following equations may be used:

$$I_{D\beta} = I_{DH}(\cos\beta + \tan\theta\cos\alpha\sin\beta) \ , \tag{20}$$

where $I_{D\beta}$ = intensity of direct solar radiation on a (more or less) south-facing surface with tilt angle β, I_{DH} the direct horizontal solar radiation = $I_{TH} - I_{dH}$, α the Sun's azimuth measured from the south direction (toward west positive), θ , the SZA (angle between local zenith and direction to Sun), and β the tilt angle of surface (angle between local zenith and normal to plane of surface).

Solar radiation data for the locations in this section were obtained from the National Solar Radiation Database, 1991–2005.[6] The database consists of modeled values and, when available, measured data of total (global) horizontal solar radiation (I_{TH}), direct incident solar radiation to

a plane normal to the Sun (I_{DI}), and diffuse horizontal radiation (I_{dH}). Extreme values of direct incident solar radiation (I_{DI}) were first calculated, and the corresponding values of total horizontal (I_{TH}) and diffuse (I_{dH}) associated with the extreme direct values were then determined.

2.2.1 Eastern Range

Table 10 shows the frequency distributions for the maximum and the 95th percentile values for the different types of solar radiation as a function of LST for the ER in June and December. Table 11 shows the same, but for the minimum and 5th percentile values.

Table 10. Extreme high values of solar radiation for the ER.

Time of Day (LST)	Total (Direct+Diffuse) Solar Radiation to a Horizontal Surface* (W/m^2)		Diffuse Radiation to a Horizontal Surface* (W/m^2)		Direct Incident Solar Radiation Normal to the Sun (W/m^2)	
	Max	95%	Max	95%	Max	95%
June						
05:00	–	–	–	–	–	–
06:00	11	2	8	1	56	49
07:00	144	157	51	97	440	280
08:00	341	296	82	73	613	528
09:00	535	536	106	144	701	637
10:00	777	713	130	152	833	722
11:00	901	852	161	166	823	766
12:00	965	939	146	178	844	782
13:00	995	954	169	168	833	793
14:00	1,007	921	203	167	835	784
15:00	836	822	125	160	819	758
16:00	686	660	123	133	766	718
17:00	516	463	91	97	753	639
18:00	287	265	62	79	621	515
19:00	105	90	41	46	376	268
20:00	3	3	3	3	20	3
21:00	–	–	–	–	–	–
December						
07:00	–	–	–	–	–	–
08:00	53	11	19	4	373	185
09:00	236	255	39	77	731	631
10:00	422	399	53	73	864	768
11:00	536	535	56	82	927	833
12:00	651	615	70	85	952	862
13:00	667	628	71	84	957	875
14:00	614	583	67	82	942	859
15:00	497	476	59	82	899	814
16:00	327	314	46	57	808	723
17:00	161	144	34	40	630	538
18:00	4	12	2	8	122	85
19:00	–	–	–	–	–	–

* Associated with corresponding direct incident solar radiation values.

Table 11. Extreme low values of solar radiation for the ER.

Time of Day (LST)	Total (Direct+Diffuse) Solar Radiation to a Horizontal Surface* (W/m^2)		Diffuse Radiation to a Horizontal Surface* (W/m^2)		Direct Incident Solar Radiation Normal to the Sun (W/m^2)	
	Min	5%	Min	5%	Min	5%
June						
05:00	–	–	–	–	–	–
06:00	–	–	–	–	–	–
07:00	19	52	19	52	–	–
08:00	50	115	50	115	–	–
09:00	86	191	86	191	–	–
10:00	108	265	108	265	–	–
11:00	131	257	131	257	–	–
12:00	140	349	140	349	–	–
13:00	150	363	150	363	–	–
14:00	142	276	142	276	–	–
15:00	127	139	127	139	–	–
16:00	107	108	107	108	–	–
17:00	71	76	71	76	–	–
18:00	40	56	40	56	–	–
19:00	11	22	11	22	–	–
20:00	–	–	–	–	–	–
21:00	–	–	–	–	–	–
December						
07:00	–	–	–	–	–	–
08:00	–	–	–	–	–	–
09:00	32	42	32	42	–	–
10:00	61	77	61	77	–	–
11:00	77	102	77	102	–	–
12:00	92	117	92	117	–	–
13:00	96	108	96	108	–	–
14:00	93	115	93	115	–	–
15:00	73	95	73	95	–	–
16:00	47	68	47	68	–	–
17:00	21	37	21	37	–	–
18:00	–	–	–	–	–	–
19:00	–	–	–	–	–	–

* Associated with corresponding direct incident solar radiation values.

These 2 months were selected because they best represent the periods of year with the longest (June) and shortest (December) durations of daylight.[1] Maximum intensity of direct normal incident solar radiation in the early afternoon hours is greater in December, even though the SZA is larger than in June. However, the length of exposure to solar radiation for the vehicle and/or GSE in June is longer than in December. The actual radiation absorbed by a surface is a function of the surface optical properties and the surface geometry relative to the Sun vector. Figure 2 shows the 95th percentile value of the direct incident solar radiation to a plane normal to the Sun for June and December.

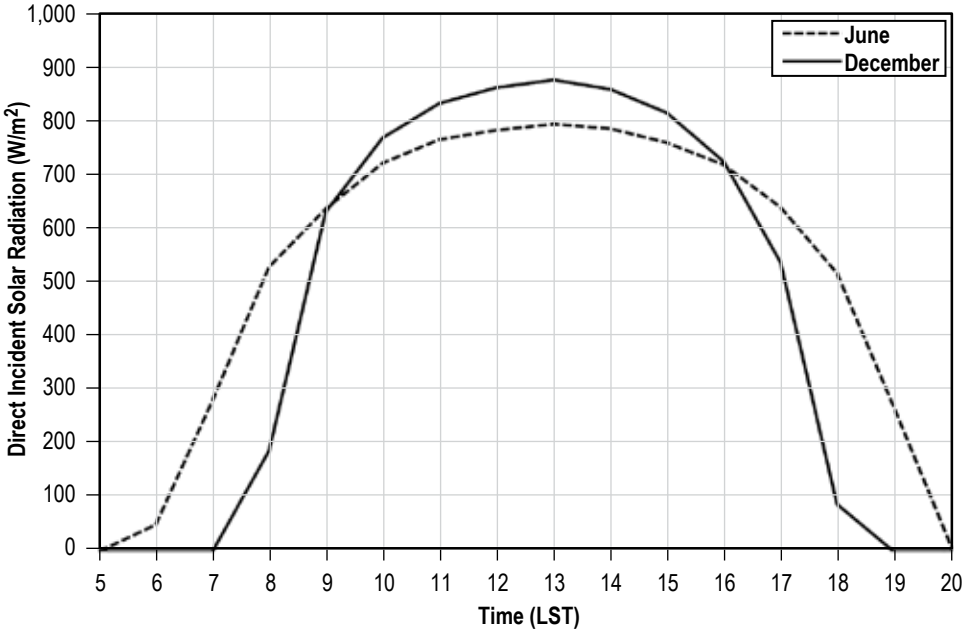

Figure 2. 95th percentile value of direct incident solar radiation on a plane normal to the Sun for the ER.

2.2.2 Edwards Air Force Base

Table 12 shows the frequency distributions for the maximum and the 95th percentile values for the different types of solar radiation as a function of LST for EAFB in June and December.[1] Table 13 shows the same information, but for the minimum and 5th percentile values. The actual radiation absorbed by a surface is a function of the surface optical properties and the surface geometry relative to the Sun vector. Figure 3 shows the 95th percentile value of the direct incident solar radiation to a plane normal to the Sun for June and December.

Table 12. Extreme high values of solar radiation for EAFB.

Time of Day (LST)	Total (Direct+Diffuse) Solar Radiation to a Horizontal Surface* (W/m^2)		Diffuse Radiation to a Horizontal Surface* (W/m^2)		Direct Incident Solar Radiation Normal to the Sun (W/m^2)	
	Max	95%	Max	95%	Max	95%
June						
04:00	0	0	0	0	0	0
05:00	4	4	2	2	85	59
06:00	109	102	24	24	551	499
07:00	313	307	41	47	774	738
08:00	528	522	56	64	875	847
09:00	724	720	68	81	929	905
10:00	884	867	80	88	961	938
11:00	995	981	86	88	979	961
12:00	1,049	1,023	89	82	986	966
13:00	1,039	1,036	86	102	985	964
14:00	974	964	81	95	980	952
15:00	848	841	74	87	956	930
16:00	681	664	65	77	925	895
17:00	477	500	52	89	859	829
18:00	261	274	35	57	741	705
19:00	71	67	20	26	462	369
20:00	–	–	–	–	30	14
21:00	–	–	–	–	–	–
December						
06:00	–	–	–	–	–	–
07:00	4	2	1	2	98	30
08:00	104	81	21	18	605	513
09:00	274	236	31	36	828	781
10:00	427	407	41	44	917	895
11:00	549	496	58	50	959	935
12:00	596	590	68	70	979	961
13:00	589	541	79	51	978	958
14:00	509	483	59	62	962	930
15:00	398	349	63	38	918	899
16:00	248	214	61	46	842	806
17:00	24	14	6	3	341	263
18:00	–	–	–	–	–	–

* Associated with corresponding direct incident solar radiation values.

Table 13. Extreme low values of solar radiation for EAFB.

Time of Day (LST)	Total (Direct+Diffuse) Solar Radiation to a Horizontal Surface* (W/m^2)		Diffuse Radiation to a Horizontal Surface* (W/m^2)		Direct Incident Solar Radiation Normal to the Sun (W/m^2)	
	Min	5%	Min	5%	Min	5%
June						
04:00	–	–	–	–	–	–
05:00	–	–	–	–	–	–
06:00	34	48	34	40	–	51
07:00	75	211	75	146	–	185
08:00	137	364	137	220	–	266
09:00	195	512	195	304	–	294
10:00	242	650	242	356	–	351
11:00	343	808	343	435	–	402
12:00	362	788	362	361	–	438
13:00	359	604	359	260	–	355
14:00	339	680	339	394	–	314
15:00	147	579	147	364	–	269
16:00	122	364	122	227	–	205
17:00	151	206	151	151	–	116
18:00	54	108	54	83	–	88
19:00	–	–	–	–	–	–
20:00	–	–	–	–	–	–
21:00	–	–	–	–	–	–
December						
06:00	–	–	–	–	–	–
07:00	–	–	–	–	–	–
08:00	10	28	10	28	–	–
09:00	33	84	33	84	–	–
10:00	61	149	61	149	–	–
11:00	84	179	84	177	–	6
12:00	90	191	90	187	–	6
13:00	89	171	89	171	–	–
14:00	77	165	77	165	–	–
15:00	58	123	58	123	–	–
16:00	30	69	30	65	–	21
17:00	1	15	1	15	–	–
18:00	–	–	–	–	–	–

* Associated with corresponding direct incident solar radiation values.

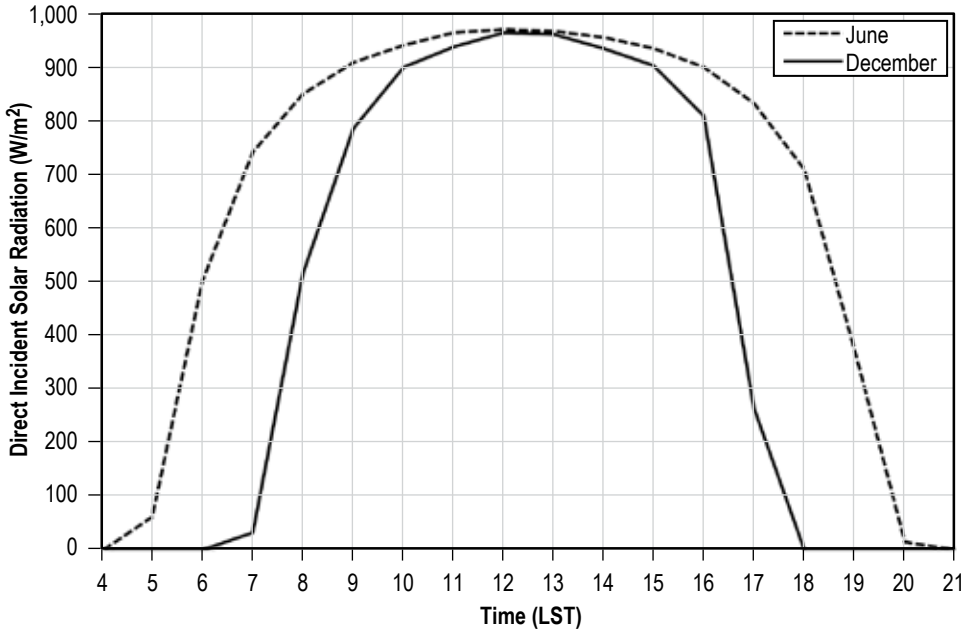

Figure 3. 95th percentile value for direct incident solar radiation on a plane normal to the Sun for EAFB.

2.2.3 White Sands Missile Range

Table 14 shows the frequency distributions for the maximum and the 95th percentile values for the different types of solar radiation as a function of LST for White Sands Missile Range (WSMR) in June and December.[1] Table 15 shows the same information, but for the minimum and 5th percentile values. The actual radiation absorbed by a surface is a function of the surface optical properties and the surface geometry relative to the Sun vector. Figure 4 shows the 95th percentile value of the direct incident solar radiation to a plane normal to the Sun for June and December.

Table 14. Extreme high values of solar radiation for WSMR.

Time of Day (LST)	Total (Direct+Diffuse) Solar Radiation to a Horizontal Surface* (W/m^2)		Diffuse Radiation to a Horizontal Surface* (W/m^2)		Direct Incident Solar Radiation Normal to the Sun (W/m^2)	
	Max	95%	Max	95%	Max	95%
June						
05:00	–	–	–	–	–	–
06:00	54	53	18	25	392	309
07:00	254	237	37	47	744	658
08:00	482	460	54	62	876	814
09:00	696	667	68	78	942	884
10:00	874	847	78	96	980	923
11:00	1,003	969	85	103	1,000	943
12:00	1,059	1,046	91	120	992	950
13:00	1,067	1,051	92	114	993	953
14:00	1,013	992	89	112	986	945
15:00	898	866	83	84	969	924
16:00	732	714	73	94	936	883
17:00	528	502	60	66	879	821
18:00	305	278	43	50	768	699
19:00	95	88	24	29	513	425
20:00	2	1	1	1	48	20
21:00	–	–	–	–	–	–
December						
06:00	–	–	–	–	–	–
07:00	1	–	–	–	56	7
08:00	138	123	54	43	712	676
09:00	307	257	53	57	875	835
10:00	472	430	60	58	955	921
11:00	575	543	61	49	990	961
12:00	646	597	66	54	1,019	982
13:00	620	606	52	54	1,007	985
14:00	571	552	59	60	987	969
15:00	447	416	46	49	940	907
16:00	282	254	38	41	843	811
17:00	80	66	17	18	571	499
18:00	1	–	–	–	49	11
19:00	–	–	–	–	–	–

* Associated with corresponding direct incident solar radiation values.

Table 15. Extreme low values of solar radiation for WSMR.

Time of Day (LST)	Total (Direct+Diffuse) Solar Radiation to a Horizontal Surface* (W/m^2)		Diffuse Radiation to a Horizontal Surface* (W/m^2)		Direct Incident Solar Radiation Normal to the Sun (W/m^2)	
	Min	5%	Min	5%	Min	5%
June						
05:00	–	–	–	–	–	–
06:00	–	–	–	–	–	–
07:00	40	96	40	93	–	12
08:00	76	80	76	76	–	8
09:00	104	358	104	321	–	55
10:00	132	310	132	252	–	71
11:00	154	538	154	439	–	109
12:00	164	636	164	524	–	115
13:00	293	730	293	647	–	85
14:00	159	338	159	242	–	103
15:00	138	386	138	335	–	61
16:00	112	271	112	236	–	49
17:00	75	194	75	188	–	12
18:00	44	69	44	69	–	–
19:00	10	26	10	26	–	–
20:00	–	–	–	–	–	–
21:00	–	–	–	–	–	–
December						
06:00	–	–	–	–	–	–
07:00	–	–	–	–	–	–
08:00	–	–	–	–	–	–
09:00	38	60	38	60	–	–
10:00	67	116	67	116	–	–
11:00	83	146	83	146	–	–
12:00	98	175	98	175	–	–
13:00	95	172	95	172	–	–
14:00	86	162	86	162	–	–
15:00	65	119	65	119	–	–
16:00	39	74	39	74	–	–
17:00	9	23	9	23	–	–
18:00	–	–	–	–	–	–
19:00	–	–	–	–	–	–

* Associated with corresponding direct incident solar radiation values.

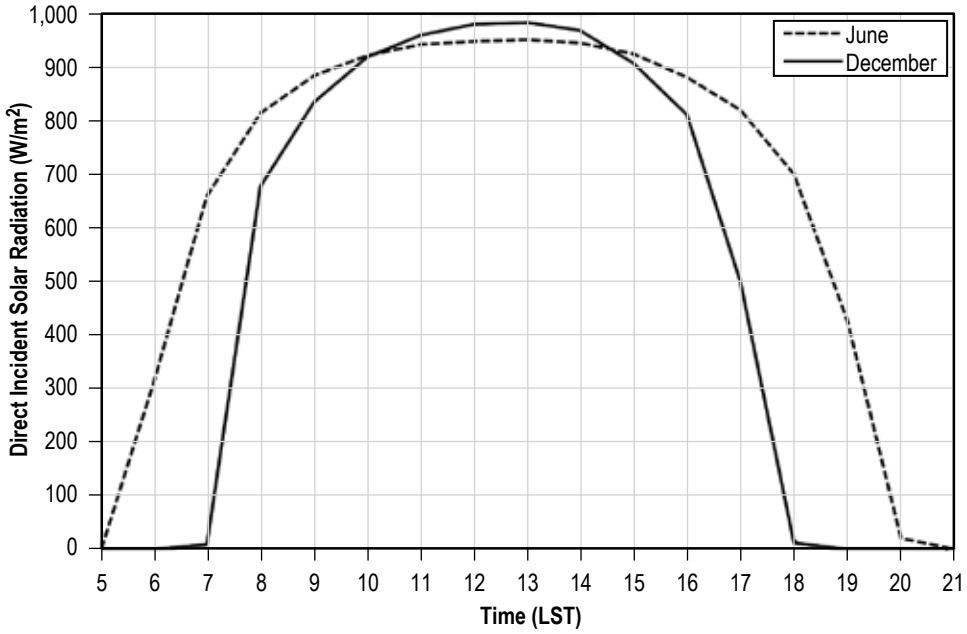

Figure 4. 95th percentile value of direct incident solar radiation on a plane normal to the Sun for WSMR.

2.3 Temperature

The normal thermodynamic definition of temperature, the derivative of energy with respect to entropy, applies to the atmospheric environment. The surface temperatures are primarily the result of a balance between incoming and outgoing radiative energy along with convection effects. As a black-body radiator, the clear sky is considered equivalent to a cold surface. The radiation temperature of the clear sky is the same during the day and night. It is the clear sky acting as a cold sink, without the incoming solar radiation heating of the surface, which causes near-surface air temperatures to be lower at night than during the day. At night, clouds act as a barrier to the outgoing radiation. Clouds absorb outgoing infrared radiation and emit radiation at a lower temperature, making the effective atmospheric temperatures warmer than the clear sky. Thus, the air near the ground will not cool off to as low a temperature on a cloud-covered night. Therefore, the greatest cooling of the Earth's surface occurs with calm winds (no mixing with warmer air) and clear skies.

2.3.1 Eastern Range

The intensity of incoming radiative energy has a seasonal dependence, hence the annual variability in surface temperature at the ER. The coldest temperatures observed at the ER have occurred in the early morning hours and were associated with calm winds and clear skies after the passage of a cold front. Maximum air temperatures observed occur in the summer months during the hours of 14:00 to 16:00 LST after prolonged exposure and absorption of radiative energy at the surface. Expected extreme surface temperatures and the sky radiation values for the ER are shown in table 16.[1]

Table 16. Surface air and sky radiation temperature extremes for the ER.

Area		Surface Air Temperature Extremes*				Sky Radiation	
		Maximum		Minimum		Extreme Minimum Equivalent Temperature	Equivalent Radiation (W/m^2)
		Extreme	95%**	Extreme	95%**		
KSC, Florida	°C	38	35	–6	0.6	–15	252
	°F	100.4	95	21.2	33.1	5	

* The extreme maximum and minimum temperatures will be encountered during periods of wind speeds less than or approximately 1 m/s (3.3 ft/s).

** Based on daily extreme (maximum or minimum) observations for worst month.

The monthly mean temperature and monthly temperature extremes for the ER are shown in figure 5 and table 17. The data are based on hourly surface observations at the ER from 1957 through 2002. It is possible that the true extreme temperature was slightly different from that shown in figure 5 and table 17 because the observations were taken on the hour, not necessarily at the time of extreme occurrence.

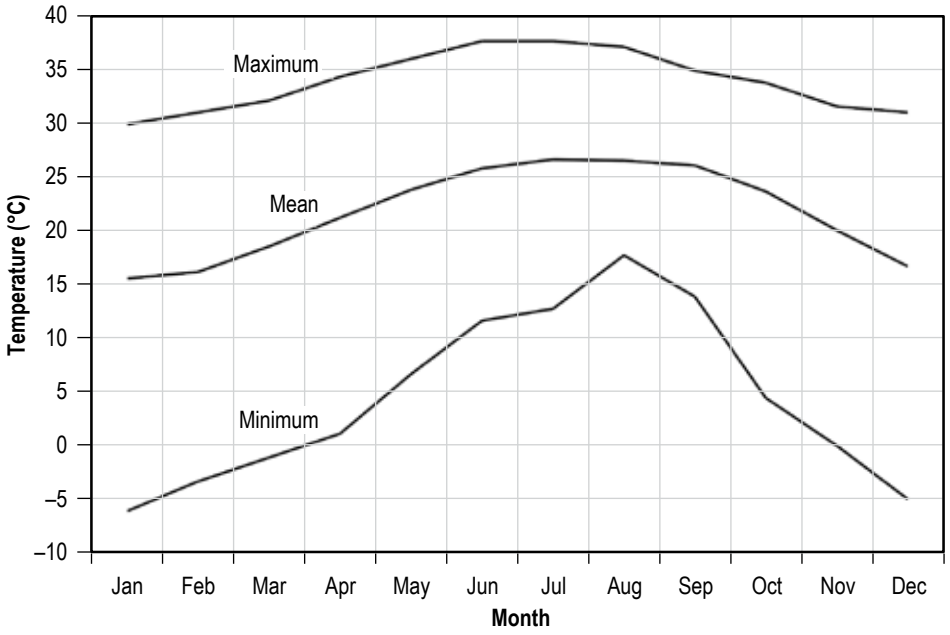

Figure. 5. Monthly maximum, mean, and minimum temperatures for the ER.

Table 17. Monthly mean and extreme (maximum and minimum) temperatures for the ER.

Month	Mean Temperature *, **		Maximum Temperature *, **		Minimum Temperature *, **	
	(°C)	(°F)	(°C)	(°F)	(°C)	(°F)
January	15.6	60.1	30	86	–6	21.2
February	16.2	61.2	31	87.8	–3	26.6
March	18.6	65.5	32	89.6	–1	30.2
April	21.3	70.3	34	93.2	1	33.8
May	23.9	75	36	96.8	7	44.6
June	25.9	78.6	38	100.4	12	53.6
July	26.7	80.1	38	100.4	13	55.4
August	26.6	79.9	37	98.6	18	64.4
September	26.2	79.1	35	95	14	57.2
October	23.7	74.7	34	93.2	4	39.2
November	20.1	68.2	32	89.6	–	32
December	16.7	62.1	31	87.8	–5	23

* Data from hourly surface observations at the ER.
** POR: 1957–2002.

Table 18 and figure 6 show the probability of a given maximum 3-, 6-, or 12-hr temperature change occurring at the ER. For example, from table 18, there is a 90% chance that the maximum 3-hr temperature change will be ≤4.1 °C (≤7.4 °F). The data in table 18 and figure 6 were obtained from hourly surface observations from 1957 through 2002.

Table 18. Cumulative probability for 3-, 6-, and 12-hr temperature change at the ER.

Percentile	Temperature Change Over Specified Period*					
	3-hr		6-hr		12-hr	
	(°C)	(°F)	(°C)	(°F)	(°C)	(°F)
25	0.1	0.2	0.8	1.4	1.8	3.2
50	1	1.8	2.3	4.1	3.8	6.8
75	2.4	4.3	4.4	7.9	6.1	11
90	4.1	7.4	6.6	11.9	8.3	14.9
95	5.4	9.7	8.1	14.6	9.7	17.5
99	8.1	14.6	11.4	20.5	12.4	22.3

* Based on hourly surface observations, 1957–2002.

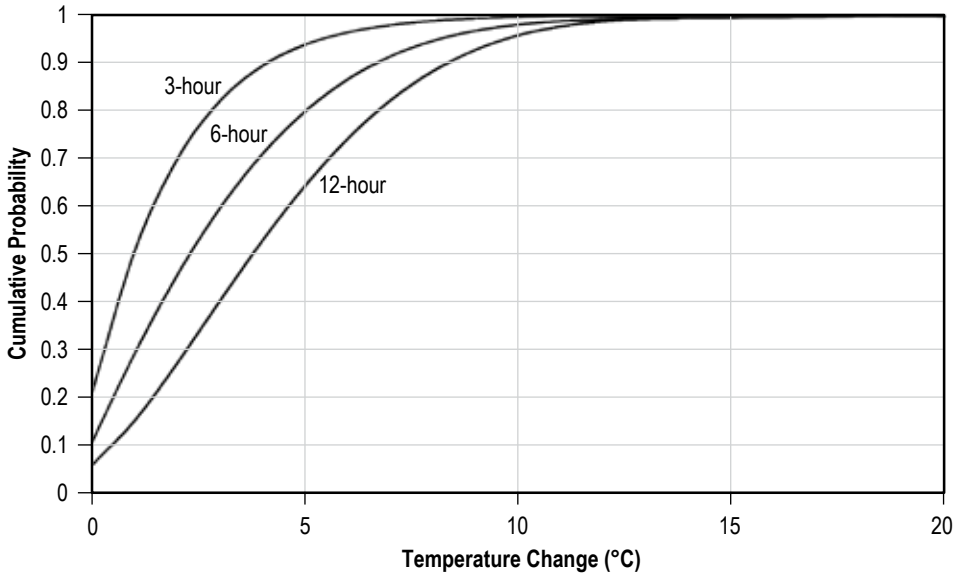

Figure 6. Cumulative probability for 3-, 6-, and 12-hr temperature change at the ER (based on hourly surface observations, 1957–2002).

2.3.2 Edwards Air Force Base

Expected extreme surface temperatures and the sky radiation values for EAFB are shown in table 19.[1]

Table 19. Surface air and sky radiation temperature extremes for EAFB.

Area		Surface Air Temperature Extremes*				Sky Radiation	
		Maximum		Minimum		Extreme Minimum Equivalent Temperature	Equivalent Radiation (W/m^2)
		Extreme	95%**	Extreme	95%**		
EAFB, California	°C	45	41.7	–15.6	–7.8	–30	198
	°F	113	107.1	3.9	17.9	–22	

* The extreme maximum and minimum temperatures will be encountered during periods of wind speeds less than or approximately 1 m/s (3.3 ft/s).

** Based on daily extreme (maximum or minimum) observations for worst month.

The monthly mean temperature and monthly temperature extremes for the EAFB are shown in figure 7 and table 20. These data are based on hourly surface observations at EAFB from 1971 through 2001. It is possible that the true extreme temperature was slightly different from that shown in figure 7 and table 20 because the observations were taken on the hour, not necessarily at the time of extreme occurrence.

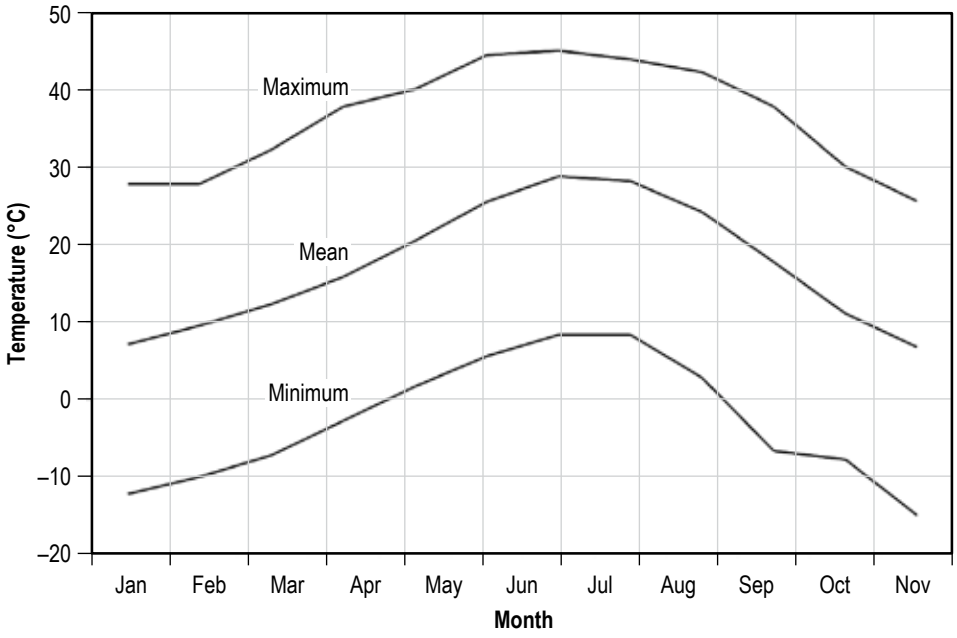

Figure 7. Monthly maximum, mean, and minimum temperatures for EAFB.

Table 20. Monthly mean and extreme temperatures for EAFB.

Month	Mean Temperature *, **		Maximum Temperature *, **		Minimum Temperature *, **	
	(°C)	(°F)	(°C)	(°F)	(°C)	(°F)
January	7.1	44.8	28	82.4	–12	10.4
February	9.5	49.1	28	82.4	–10	14
March	12.3	54.1	32	89.6	–7	19.4
April	15.8	60.4	38	100.4	–3	26.6
May	20.4	68.8	40	104	2	35.6
June	25.5	77.9	44	111.2	6	42.8
July	28.8	83.8	45	113	8	46.4
August	28.2	82.7	44	111.2	8	46.4
September	24.2	75.5	42	107.6	3	37.4
October	17.7	63.9	38	100.4	–7	19.4
November	11.1	51.9	30	86	–8	17.6
December	6.7	44.1	26	78.8	–15	5

* Data from hourly surface observations at EAFB.

** POR: 1971–2001.

Table 21 and figure 8 show the probability of a given maximum 3-, 6-, or 12-hr temperature change occurring at EAFB. For example, from table 21, there is a 90% chance that the maximum 3-hr temperature change will be ≤8 °C (≤14.4 °F). The data in table 21 and figure 8 were obtained from hourly surface observations from 1971 through 2001.

Table 21. Cumulative probability for 3-, 6-, and 12-hr temperature change at EAFB.

	Temperature Change Over Specified Period*					
	3-hr		6-hr		12-hr	
Percentile	(°C)	(°F)	(°C)	(°F)	(°C)	(°F)
25	1.4	2.5	3	5.4	3.5	6.3
50	3.3	5.9	6.1	11.0	8	14.4
75	5.7	10.3	9.9	17.8	12.9	23.2
90	8	14.4	13.4	24.1	16.7	30.1
95	9.3	16.7	15.5	27.9	18.5	33.3
99	11.5	20.7	18.7	33.7	21	37.8

* Based on hourly surface observations, 1971–2001.

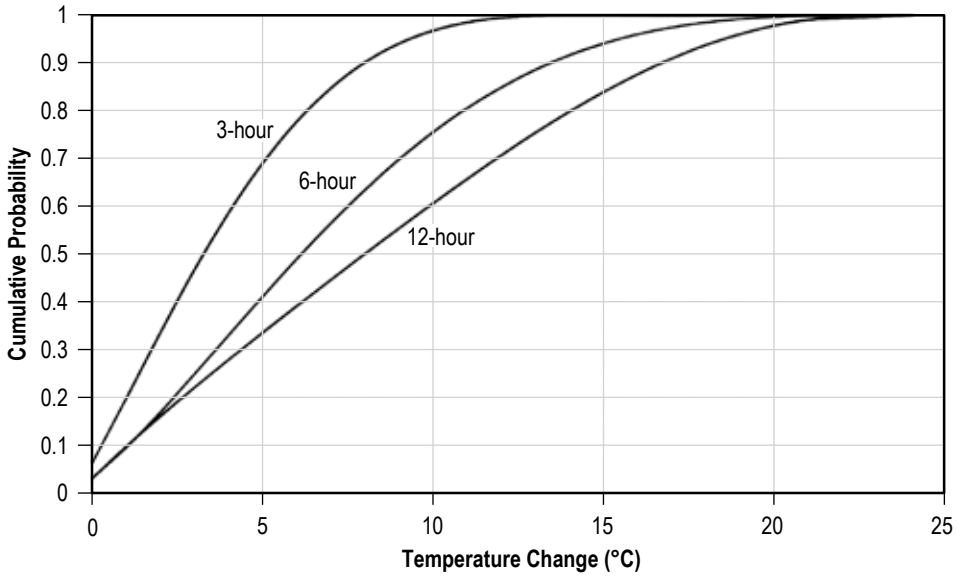

Figure 8. Cumulative probability for 3-, 6-, and 12-hr temperature change at EAFB (based on hourly surface observations, 1971–2001).

2.4 Pressure

Atmospheric pressure (also called barometric pressure) is the force exerted, resulting from gravitational attraction, by the mass of the column of air of unit cross section lying directly above the area in question. It is expressed as force per unit area and is typically defined in the unit of

hectopascals (hPa (lbf/in^2)). Because variations in surface elevation, and hence the volume of the air column over the area, surface pressures recorded are reduced to a standardized sea level pressure value for continuity purposes.

The total variation of pressure from day to day is relatively small. For example, a gradual rise or fall in pressure of 3 hPa (0.04 lbf/in^2) and then a return to original pressure can be expected within a 24-hr period. Diurnal, semidiurnal, and terdiurnal tidal variations can all affect the normal surface atmospheric pressure pattern. Rapid and slightly greater variations of pressure occur as the result of the passage of synoptic systems, and the passage of a hurricane can cause somewhat larger changes in the atmospheric pressure environment. Typically, a maximum pressure change of 6 hPa (0.09 lbf/in^2) (rise or fall) can be expected within a 1-hr period at all localities. Only the pressure drop in a tornado is significant and can exceed 20% of the ambient pressure during the few seconds of its passage.

2.4.1 Eastern Range

Pressure variations at the ER are representative of the descriptions given in the previous paragraph. However, due to the ER's susceptibility to tropical storm passages, extreme sea level pressure minimums observed are 1%–2% lower than extreme sea level pressure minimums at interior continental locations.[1] Figure 9 represents hourly sea level pressure mean and extreme values from the hourly measurements during each month observed at the ER for a period from 1957 to 2002. The extreme minimum in September was due to the passage of a tropical storm near the ER. Further discussion of hurricanes is presented in section 2.9. Values plotted in figure 9 are provided in table 22.

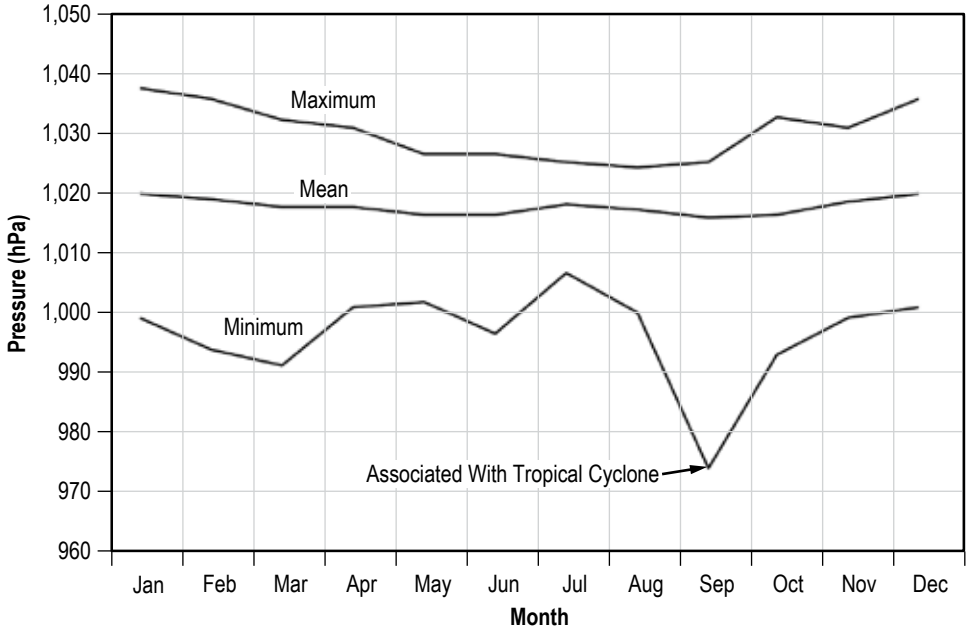

Figure 9. Maximum, mean, and minimum sea level air pressure at the ER (based on hourly surface observations, 1957–2002).

Table 22. Monthly sea level pressure at the ER (based on hourly surface observations, 1957–2002).

Sea Level Pressure Extreme		Jan	Feb	Mar	Apr	May	Jun
Min.	(hPa)	999.3	993.9	991.4	1,000.7	1,001.7	996.6
	(lbf/in^2)	14.494	14.416	14.379	14.514	14.529	14.455
Mean	(hPa)	1,020	1,018.9	1,017.7	1,017.8	1,016.5	1,016.4
	(lbf/in^2)	14.794	14.778	14.761	14.762	14.743	14.742
Max.	(hPa)	1,037.4	1,035.9	1,032.5	1,030.8	1,026.4	1,026.4
	(lbf/in^2)	15.046	15.025	14.975	14.951	14.887	14.887
Sea Level Pressure Extreme		**Jul**	**Aug**	**Sep**	**Oct**	**Nov**	**Dec**
Min.	(hPa)	1,006.8	1,000	973.9	992.9	999.3	1,000.7
	(lbf/in^2)	14.603	14.504	14.125	14.401	14.494	14.514
Mean	(hPa)	1,018	1,017.1	1,015.8	1,016.6	1,018.6	1,020.1
	(lbf/in^2)	14.765	14.752	14.733	14.745	14.774	14.796
Max.	(hPa)	1,025.4	1,024.5	1,025.1	1,032.9	1,031.1	1,035.9
	(lbf/in^2)	14.872	14.859	14.868	14.981	14.955	15.025

Table 23 and figure 10 show the cumulative probability of sea level pressure at the ER.

Table 23. Cumulative probability of sea level pressure at the ER (based on hourly surface observations, 1957–2002).

	Sea Level Pressure	
Percentile	(hPa)	(lbf/in^2)
1	1,007.1	14.607
5	1,010.8	14.661
10	1,012.5	14.685
25	1,015.2	14.724
50	1,017.9	14.764
75	1,020.3	14.798
90	1,023	14.838
95	1,024.7	14.862
99	1,027.8	14.907

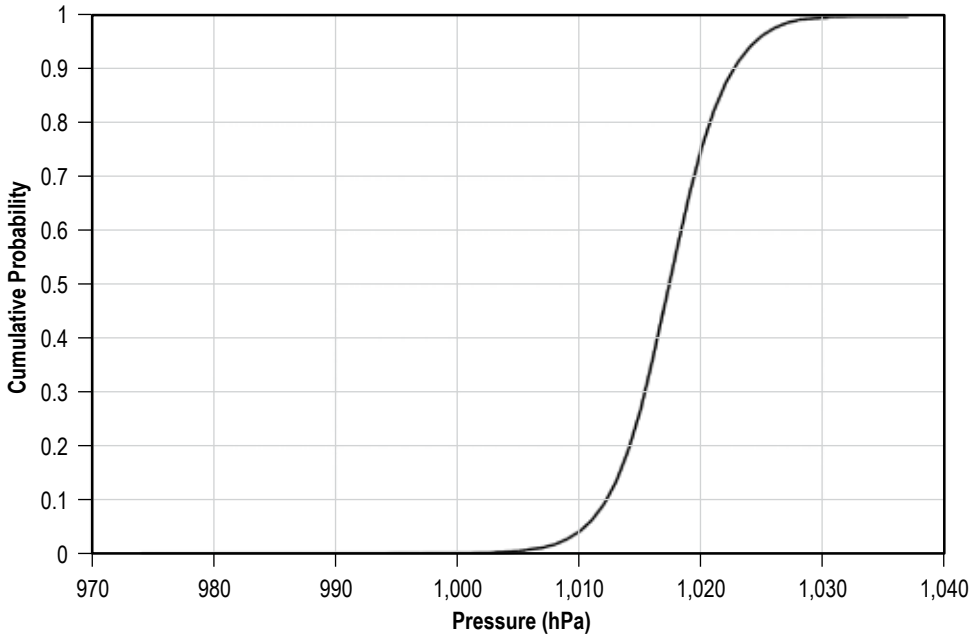

Figure 10. Cumulative probability of sea level pressure at the ER (based on hourly surface observations, 1957–2002).

2.4.2 Edwards Air Force Base

Figure 11 represents hourly sea level pressure mean and extreme values from the hourly measurements during each month observed at EAFB for a period from 1971 to 2001. Values plotted in figure 11 are provided in table 24.

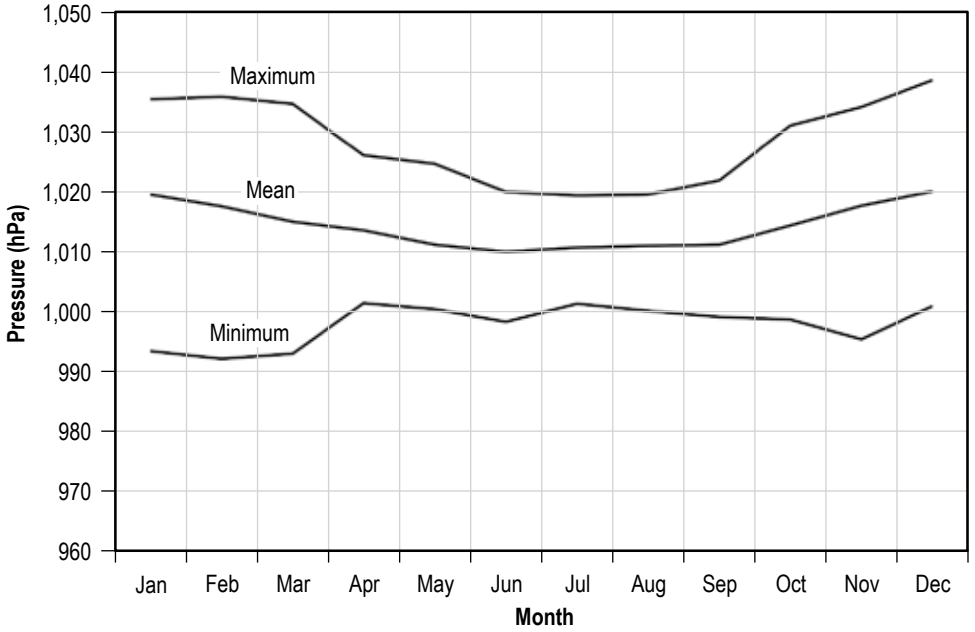

Figure 11. Maximum, mean, and minimum sea level air pressure at EAFB (based on hourly surface observations, 1971–2001).

Table 24. Monthly sea level pressure at EAFB (based on hourly surface observations, 1971–2001).

Sea Level Pressure Extreme		Jan	Feb	Mar	Apr	May	Jun
Min.	(hPa)	993.4	992.1	993	1,001.4	1,000.4	998.3
	(lbf/in^2)	14.408	14.389	14.402	14.524	14.510	14.479
Mean	(hPa)	1,019.6	1,017.6	1,015	1,013.6	1,011.2	1,010
	(lbf/in^2)	14.788	14.759	14.722	14.701	14.666	14.649
Max.	(hPa)	1,035.5	1,035.9	1,034.7	1,026.1	1,024.7	1,020
	(lbf/in^2)	15.019	15.025	15.007	14.882	14.862	14.794
Sea Level Pressure Extreme		**Jul**	**Aug**	**Sep**	**Oct**	**Nov**	**Dec**
Min.	(hPa)	1,001.3	1,000.1	999.2	998.7	995.4	1,000.9
	(lbf/in^2)	14.523	14.505	14.492	14.485	14.437	14.517
Mean	(hPa)	1,010.7	1,011	1,011.2	1,014.4	1,017.7	1,020.1
	(lbf/in^2)	14.659	14.664	14.666	14.713	14.761	14.796
Max.	(hPa)	1,019.4	1,019.6	1,021.9	1,031.1	1,034.2	1,038.7
	(lbf/in^2)	14.785	14.788	14.822	14.955	15	15.065

Table 25 and figure 12 show the cumulative probability of sea level pressure at EAFB.

Table 25. Cumulative probability of sea level pressure at EAFB (based on hourly surface observations, 1971–2001).

	Sea Level Pressure	
Percentile	(hPa)	(lbf/in^2)
1	1,004.3	14.566
5	1,007	14.606
10	1,008.2	14.623
25	1,010.4	14.655
50	1,013.3	14.697
75	1,017.5	14.758
90	1,022.1	14.824
95	1,024.7	14.862
99	1,029	14.925

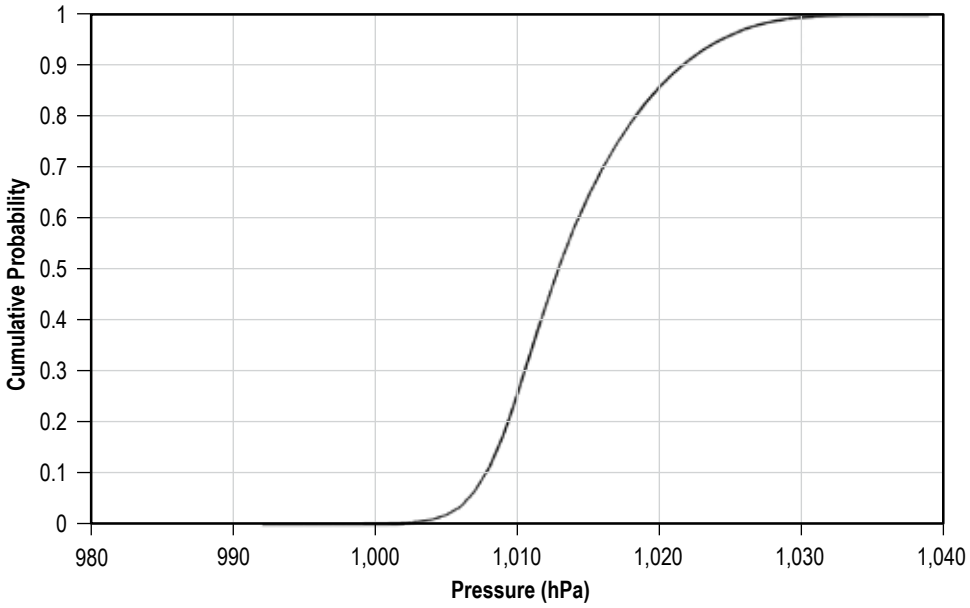

Figure 12. Cumulative probability of sea level pressure at EAFB (based on hourly surface observations, 1971–2001).

2.5 Humidity

The amount of water vapor the atmosphere can hold is a function of the air temperature and total atmospheric pressure (partial pressure of dry and moist air). Periods of high water vapor content in the atmosphere can have adverse effects on the vehicle and GSE components. Temperatures above 20 °C (68 °F) and relative humidity above 75% are conducive to high growth rates of fungi and bacteria.

2.5.1 Eastern Range

The Atlantic Ocean provides an unlimited source of water for evaporation into the atmosphere near the ER. Table 26 provides maximum vapor concentration for the ER.[1]

Table 26. Maximum vapor concentration for the ER.

Geometric Altitude		Maximum Vapor Concentration		Temperature Associated With Maximum Vapor Concentration	
(km)	(ft)	(g/m^3)	(lb/ft^3)	°C	°F
0.005 (SFC)	16.4	27	0.00169	30.6	87.1

Surface psychrometric data for the ER is presented in table 27 and figure 13. The surface psychrometric data are based on hourly surface observations from 1957 to 2002.

Table 27. Surface psychrometric data, dewpoint versus temperature envelope for the ER.

Temperature		Dewpoint	
(C°)	(F°)	(C°)	(F°)
–4	24.8	–14	6.8
–4	24.8	–4	24.8
28	82.4	28	82.4
36	96.8	28	82.4
40	104	15	59
11	51.8	–14	6.8

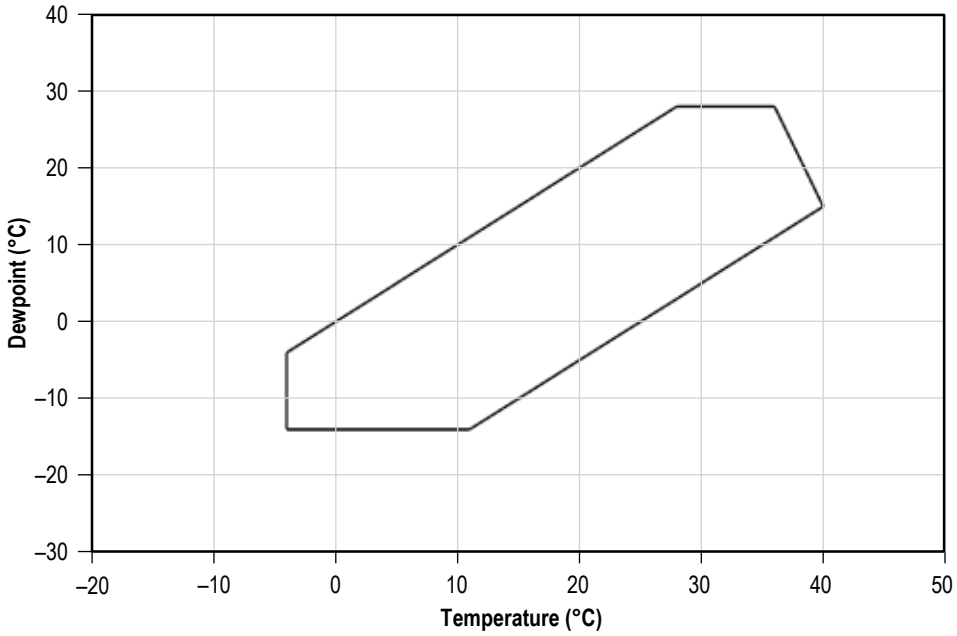

Figure 13. Surface psychrometric data for the ER (based on hourly surface observations, 1957–2002).

2.5.2 Edwards Air Force Base

Surface psychrometric data for EAFB is presented in table 28 and figure 14. The surface psychrometric data are based on hourly surface observations from 1971 to 2001.

Table 28. Surface psychrometric data, dewpoint versus temperature envelope for EAFB.

Temperature		Dewpoint	
(C°)	(F°)	(C°)	(F°)
–7	19.4	–26	–14.8
–16	3.2	–16	3.2
24	75.2	–24	75.2
44	111.2	13	55.4
44	111.2	–12	10.4

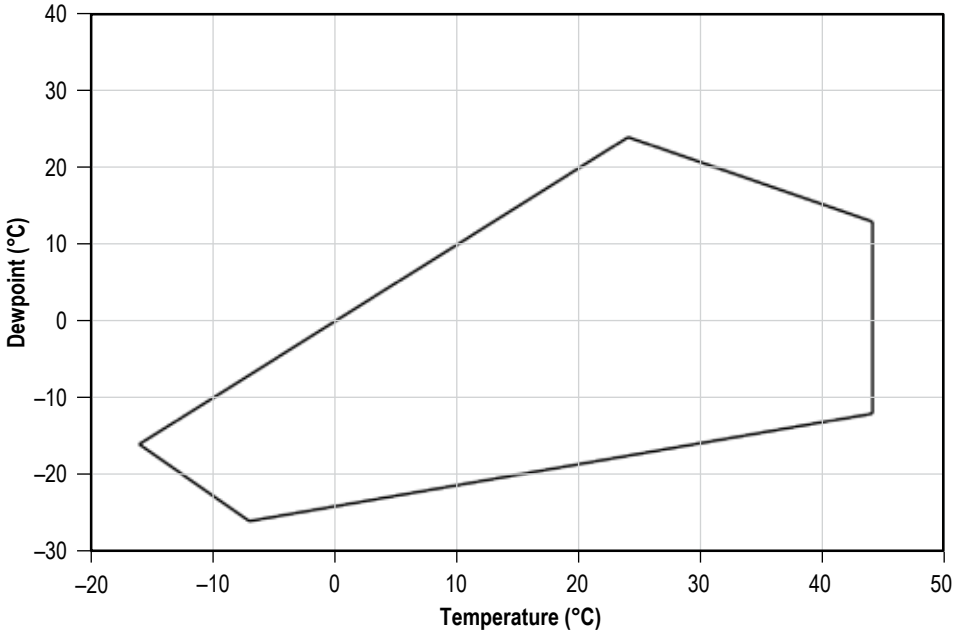

Figure 14. Surface psychrometric data for EAFB (based on hourly surface observations, 1971–2001).

2.5.3 Fog

Fog is a visible aggregate of minute water droplets suspended in the atmosphere near the Earth's surface or a cloud in contact with the Earth's surface. Fog is responsible for reducing visibility to <1 km (<0.6 mi). Several types of fog can be classified according to formation, which include advection fog, frontal fog, up-slope fog, and radiation fog.[7] Ground fog is usually a radiation fog with a depth of <6 m (19.7 ft), whereas a shallow ground fog has a depth of <2 m (<6.6 ft). Fogs are classified as either warm or supercooled fog based on whether the ambient temperature is above or below 0 °C (32 °F).

Figure 15 shows a photo of the Challenger (Space Transportation System-6 (STS)-6) rollout to pad 39A in fog, December 8, 1982.

Figure 15. Challenger (STS-6) rollout to pad 39a in fog, December 8, 1982 (courtesy of NASA).

The conditions most favorable for the formation of fog are high relative humidity, light surface winds, ground temperature colder than that of the air, no cloud overcast, and an abundance of condensation nuclei. Fog occurs more frequently in coastal areas than in inland areas because of an abundance of water vapor.

Fog is formed either by cooling the air until the water vapor condenses or by the evaporation of additional water vapor into the air. Common types of fog are: (a) radiation fog, (b) advection fog, (c) up-slope fog, (d) frontal fog, and (e) steam fog.

2.5.3.1 Radiation Fog. Radiation fog forms over land on clear nights when the Earth loses heat very rapidly to the atmosphere and the air temperature falls to or below its dewpoint. When humidity is high and cooling takes place rapidly, condensation occurs. If there are no winds, the fog will be very shallow or will be reduced to a dew or frost deposit. If winds are present (~0.5 m/s (1.6 ft/s)), then the fog will thicken and deepen. These fogs do not occur at sea since the sea surface does not cool as the land does.

2.5.3.2 Advection Fog. Advection fog is caused by the movement (advection) of mild, humid air over a colder surface, and the consequent cooling of that air to below its initial dewpoint. These fogs occur in coastal areas because the moist, warm air moves inland by breezes over the colder land in the winter. In summer, the warm, moist air may be carried out to sea, where it forms a fog over the cool water (sea fog) and then the sea breeze advects the fog inland. These summer fogs are common along the coast of California.

2.5.3.3 Up-Slope Fog. Up-slope fog forms when stable, moist air moves up sloping terrain and is adiabatically cooled by expansion to or below its original dewpoint. This cooling produces condensation, and fog forms. An up-slope wind is necessary for the formation and maintenance of this type of fog. Usually these fogs produce low stratus-type clouds.

2.5.3.4 Frontal Fog. Frontal fog forms in the cold air mass of the frontal system. The precipitation from the warm air mass, overrunning the cold air mass, evaporates as it falls through and saturates the cold air, thus producing the frontal-type fog. These fogs form rapidly, cover large areas, occur frequently in winter, and are associated with slow-moving or stationary fronts.

2.5.3.5 Steam Fog. Steam fog forms by the movement of cold air over a warmer water surface. Steam fog rises from the surface of lakes, rivers, and oceans and has the appearance of rising streamers.

2.5.3.6 Ice Fog. Although not classified as a common type fog, ice fog is a fog type referred to as ice (crystal) fog that is of interest. This fog normally occurs at high latitudes under calm conditions when the air temperature is approximately less than –30 °C (–22 °F), and as water vapor from the exhaust of aircraft engines, automobiles, etc., is produced, the vapor changes directly to ice particles (crystals) instead of condensing directly to liquid drops. The suspension of the ice crystals (10 to 100 μm (3.9×10^{-4} to 3.9×10^{-3} in) in diameter) in the atmosphere produces the ice fog. Ice fog can persist from a few minutes to several days and is quite a problem in arctic or polar regions.

Some typical microphysical characteristics of radiation and advection types of fogs are as follows:

- Radiation fog (inland):
  - Diameter of drops (average): 10 μm (3.9×10^{-4} in)
  - Typical drop size: 5 to 35 μm (2×10^{-4} to 1.4×10^{-3} in)
  - Liquid water content: 110 mg/m^3 (6.9×10^{-6} lb/ft^3)
  - Droplet concentration: 200/cm^3 (3,278.7/in^3)
  - Vertical depth:
    - Typical: 100 m (328 ft)
    - Severe: 300 m (984.3 ft)
  - Horizontal visibility: 100 m (328 ft)

- Advection fog (coastal):
  - Diameter of drops (average): 20 μm (7.9×10^{-4} in)
  - Typical drop size: 7 to 65 μm (2.7×10^{-4} to 2.6×10^{-3} in)
  - Liquid water content: 170 mg/m^3 (1.1×10^{-5} lb/ft^3)
  - Droplet concentration: 40/cm^3 (655.7/in^3)
  - Vertical depth:
    - Typical: 200 m (656.1 ft)
    - Severe: 600 m (1,968.5 ft)
  - Horizontal visibility: 300 m (984.3 ft)

2.5.3.7 Eastern Range Probability of Fog. Figure 16, showing the percentage frequency of precipitation or fog with visibility ≤0.8 km (≤0.5 mi) at KSC was developed from historical records of hourly observations. Unfavorable climatic conditions occur mainly during summer afternoons due to the high frequency of fog from summer afternoon showers in central Florida.

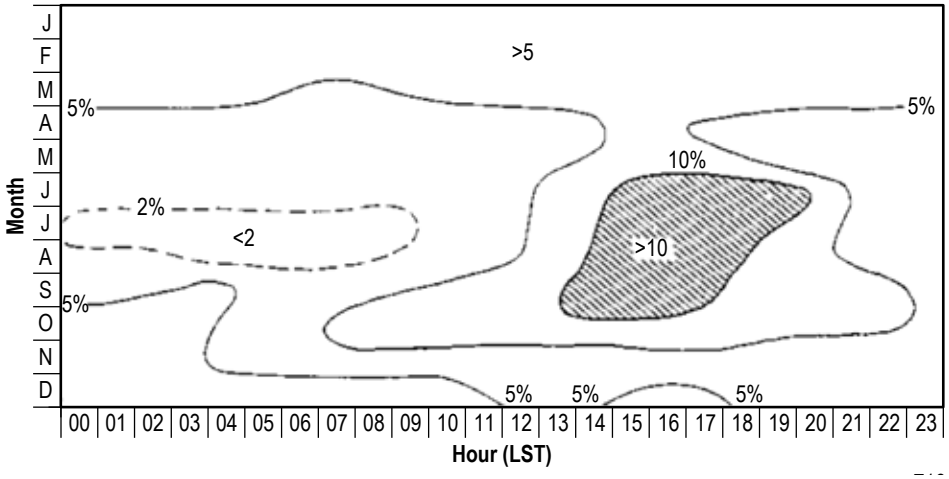

Figure 16. Probability of precipitation or fog with visibility ≤0.8 km (≤0.5 mi) at KSC.

For climatological studies useful in operational design data for spacecraft and aircraft operations, the Department of Transportation, Federal Aviation Administration has produced a tabulation of ceilings, visibilities, wind, and weather data by various periods of the day and by various temperature and wind categories for 41 airports.[8]

2.5.3.8 Eastern Range Fog Climatology. A 5-year (1986–1990) study was conducted at KSC that was to improve the 90-min forecasts made in support of the Space Shuttle landing at KSC. This concerns rapid fog development that would affect the <7 statute mile visibility flight rule (4-64) for end-of-mission shuttle landings at KSC. Space Shuttle Program (SSP) flight rule 4-64 also stated that <5 statute mile can be used as the GO/NO GO decision visibility constraint under certain other measurement conditions. Therefore, fog statistics for <7 statute miles and <5 statute miles were developed for these two visibility criteria. Over the 5-year study period, 335 fog events occurred at KSC for the <7 mile criteria, and 267 fog events occurred for the <5 mile criteria.

The KSC fog season is normally defined as October 1 through April 30, although fog occurs there during other months of the year (table 29). The fog climatology for the KSC area is complicated due to the Cape Canaveral topography which includes numerous water bodies (rivers, ocean), its land mass, and land/sea breeze effects. Of all the fog cases, only 36 fog events were completely analyzed, resulting in KSC fog events falling into three categories: (1) Advection fog (21/36 = 58%), (2) prefrontal fog (13/36 = 36%), and (3) radiation fog (2/36 = 6%).

Table 29. Normally expected fog days at KSC.[9]

Jan	Feb	Mar	Apr	May	Jun	Jul	Aug	Sep	Oct	Nov	Dec	Annual
13	10	9	7	7	6	4	6	4	7	8	12	93 Days

However, using all the fog event cases, the time of fog onset and dissipation are given in table 30.

Table 30. KSC fog onset and dissipation time: range and peak hour.[10]

Parameter	Number of KSC Fog Cases	
	335	267
Visibility criteria	<7 statute miles	<5 statute miles
Fog onset time: Range of hours	05:00 – 14:59 UTC	05:00 – 14:59 UTC
Fog onset time: Peak hour (peak hour percent frequency)	09:00 – 09:59 UTC 95/335 = 28.4%	10:00 – 10:59 UTC 46/267 = 17.2%
Fog dissipation time: Range hours	10:00 – >20:00 UTC	10:00 – >20:00 UTC
Fog dissipation time: Peak hour (peak hour percent frequency)	13:00 – 13:59 UTC 75/335 = 22.4%	12:00 – 12:59 UTC 62/267 = 23.2%

2.6 Surface Aerosols

The distribution of aerosols is regionally dependent. However, particles may have a 'local' distribution as well as a 'regional' distribution. The local aerosol occurs in the area surrounding factories, wild fires, oceans, arid/semiarid regions, and terrestrial biota. Factors such as wind speed, distance from source, altitude, and particle size play an important part in determining the makeup and concentration of aerosols. On a regional scale, number concentrations of particles in the atmosphere increase rapidly with decreasing particle size to sizes smaller than 0.1 μm (3.9×10^{-6} in) radius.

Dust and sand particles are transported through the air by wind blowing across a disturbed soil area. Strong winds are required to uplift the submicron sand and dust particles because strong adhesive forces exist between the particles and the ground. Dense vegetation and ground cover also provide considerable protection from strong winds. The concentration of these particles is highly dependent on wind speed (the higher the speed, the greater the volume of sand and dust), the nature of the soil, and the amount of moisture in the soil and in the air. Threshold air velocities for the input of soil particles into the air increase with different types of soil surfaces in the following order: disturbed soils (except disturbed heavy clay soils), sand dunes, alluvial and Aeolian sand deposits, disturbed playa (dry lake) soils, skirts of playa centers, and desert pavements (alluvial deposits).[1]

The larger, more abrasive particles in dust and sand storms are mostly in the lower 2 km (1.2 mi) of the atmosphere, although fine dust can reach great heights and travel great distances.

Measurements of aerosols in the central Atlantic has shown aerosols of continental origin up to at least 1,500 km (809.9 nmi) from land. California has two general regions of dust activity. One region extends into southwestern Arizona and covers all of southeastern California with a maximum aerosol measurement occurring north of the Salton Sea and the western Mojave Desert. The second region is situated in central California.

Salt particles, whether from the ocean or from areas where salt occurs in nature may be detrimental to space vehicles and associated systems because of their corrosive actions and their ability to coat transparent areas until they become opaque. Salt attacks many metals, and the corrosion is especially rapid at high humidity and high temperature. Salt solutions also provide a conductive path that can alter or short electrical circuits.

2.6.1 Eastern Range

In the region around the ER, sea salt particles are the most common aerosol component.[1] The Corrosion Technology Laboratory Web site <http://corrosion.ksc.nasa.gov/index.htm>[11] includes two documents that contain data on the salt contents of the atmosphere at the ER: Local Atmosphere Salt Profiles, July 1974, <http://corrosion.ksc.nasa.gov/lasp.htm>[12] and the corrosion rate at various locations at ER including the launch pad area <http://corrosion.ksc.nasa.gov/pubs/099-74.pdf>.[13]

Most airborne sea salt droplets are formed by the breaking of myriads of air bubbles at the surface of the sea. Sea salt particle concentration is also dependent on the wind speed, as stronger winds will increase the particle concentration as shown in figure 17.[1] The suspended droplets are also sensitive to the atmospheric relative humidity; droplets evaporate when the humidity falls below 75%. If humidity measurements above 75% occur, the sea salt particles become droplets again.

Atmospheric temperature inversions over the oceans, such as the tropical inversion, tend to keep sea salt particles below a few kilometers in altitude. Above such inversions, the particles are largely of continental origin, except near clouds or near the residues from dissipated clouds. Table 31 lists three average concentrations of sea salt with respect to altitude.[1]

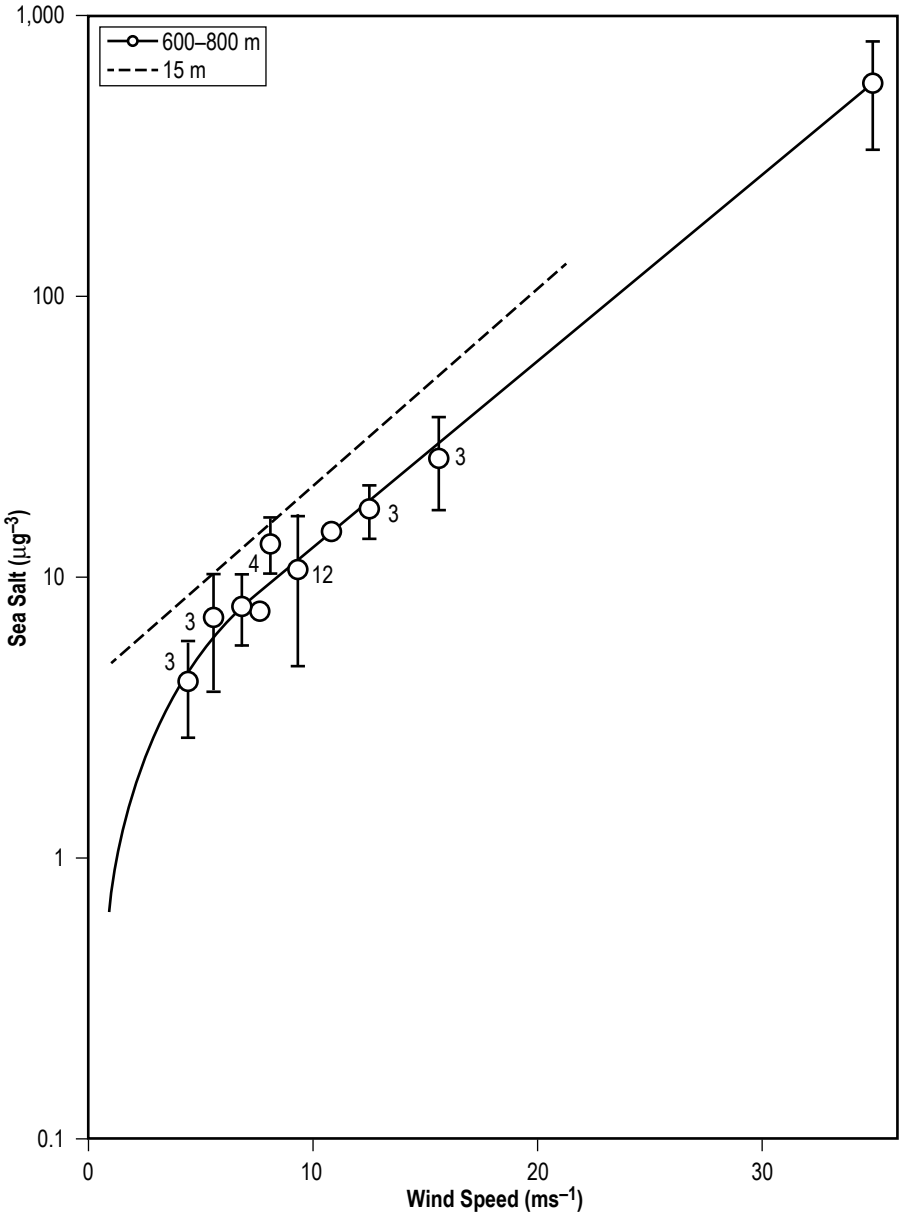

Figure 17. Sea salt concentration at two altitudes as a function of wind speed near the surface of the sea: 600–800 m altitude (Woodcock)[14] and 15 m altitude (Lovett).[15] (The number of observations averaged for each data point is given, as well as standard deviation.)

Table 31. Mean sea salt particle concentrations in maritime air masses and corresponding altitudes.

Altitude		Concentration	
(m)	(ft)	(particles/cm^3)	(particles/in^3)
Sea level	Sea level	200–300	3,277–4,916
600–800	1,968.5–2,624.6	10–20	164–328
1,200	3,937	2–4	33–66

2.6.2 Edwards Air Force Base

The terrain around EAFB causes some unique phenomena. The range to the south blocks much of the pollution from the Los Angeles basin and virtually all the marine effects prevalent there. However, with moderate to strong southwesterly winds, the pollutants can be seen coming through the passes and at times, over the mountains. The advection of pollutants from the Los Angeles basin is the primary cause of degraded visual ranges at EAFB.[4]

2.7 Precipitation

Precipitation is defined as all forms of hydrometeors, liquid or solid, which are free in the atmosphere and reach the ground. Because precipitation does occur in discrete events, statistical representation may be misleading.

Hail is precipitation in the form of balls or irregular lumps of ice and is always produced by convective clouds. By definition, hail has a diameter of 5 mm (0.2 in) or more. Hail falls are small-scale area phenomena, with a relatively infrequent occurrence at any given geographical point. The resulting time and space variability of hail is its prime characteristic. A generally accepted value for the density of hail at all locations is 0.89 g/cm^3 (55.56 lb/ft^3).[1]

Hail characteristics estimated for use in evaluating hail protection needs and requirements are:

- Hailstone size
- Terminal velocity
- Number of hailstones per hail fall
- Horizontal velocity of hailstones
- Density of hailstones.

These estimated characteristics are provided for the ER and EAFB.[1]

2.7.1 Eastern Range

Rainfall rates of various durations for the 50th, 95th, and 99th percentile, on a given day with rain in the month that has the highest average of rain, also referred to as the highest rain month, are given in table 32 for the ER.[1] The precipitation amounts should not be interpreted that the rain fell uniformly for the entire reference periods. As an example, the 99th percentile total of 49 mm (1.93 in) for a 1-hr duration as shown in table 32 could have occurred as follows: 25 mm (0.98 in) could have fallen during a 5-min period within a particular hour with an additional 24 mm (0.95 in) of rainfall for another 5-min period, making a total of 49 mm (1.93 in) for a total of ~10 min. Subsequently, no rain would have fallen for 50 min of the hypothetical 1-hr period. The 99th percentile rainfall data are referenced in that such extremes are important to consider in vehicle and facility design studies. Extremes in rainfall totals can also be associated with tropical storm passages. More information on tropical storms is given in section 2.9. Table 33 has rainfall rates listed as well as total accumulation, raindrop size, etc. for various periods for the ER.[1] Table 34 shows the estimated hail characteristics for the ER.[1]

Table 32. Highest rainfall rate versus duration for various probabilities, given a day with rain for the highest rain month at the ER.

Duration	Percentile											
	50th				95th				99th			
	(mm)	(in)	(mm/hr)	(in/hr)	(mm)	(in)	(mm/hr)	(in/hr)	(mm)	(in)	(mm/hr)	(in/hr)
5 min	5.6	0.22	66	2.6	18	0.72	221	8.7	25	1	305	12
15 min	5.8	0.23	24	0.93	22	0.88	89	3.5	33	1.3	132	5.2
1 hr	6.4	0.25	6.4	0.25	30	1.17	30	1.17	49	1.93	49	1.93
6 hr	7.1	0.28	1.3	0.05	39	1.55	6.6	0.26	81	3.18	13	0.53
24 hr	10.9	0.43	0.5	0.02	67	2.62	2.8	0.11	127	5	5.3	0.21

Table 33. Design rainfall at the ER based on yearly largest rate for stated periods. (Use average rate of fall for raindrops of 6.5 m/s (21.3 ft/s) for all times.)

Time Period	Rainfall Rate		Rainfall Total Accumulation		Raindrop Diameter	
					Average	Largest
	(mm/hr)	(in/hr)	(mm)	(in)	(mm)	(mm)
1 min	492	19.4	8	0.3	2	6
5 min	220	8.7	18	0.7	2	5.8
15 min	127	5	32	1.3	2	5.7
1 hr	64	2.5	64	2.5	2	5
6 hr	26	1	156	6.1	1.8	5
12 hr	18	0.7	220	8.7	1.6	4.5
24 hr	13	0.5	311	12.2	1.5	4.5

Table 34. Estimated hail characteristics for the ER (reference height = 61 m (200.1 ft)).

Estimated Hail Characteristics	
Exposure time risk (%)	
Worst month reference period	1
Worst 6 months reference period	7
Mean number of hailstorm days per year	0.1
Average point of duration of hail fall	5 min
Average number of hailstones per 929 cm^2 (1 ft^2)	24
Density of hailstones	0.9 g/cm^3 (56.1 lb/ft^3)
Diameter and terminal velocity	
Representative diameter (50% risk)	0.9 cm (0.4 in)
Terminal velocity	11 m/s (36 ft/s)
Large diameter (5% risk)	2.2 cm (0.9 in)
Terminal velocity	17 m/s (55.8 ft/s)
Horizontal velocity—all directions	
Mean speed	9 m/s (29.5 ft/s)
5% risk speed	15 m/s (49.2 ft/s)
Month of maximum frequency	May
POR—years	22

2.7.2. Edwards Air Force Base

The major effect of the topography around EAFB is on precipitation. The orographic uplift and subsequent dynamic descent over the mountains, which happens to storms moving towards EAFB from the northwest, tends to dry out storms. Systems moving from the west and southwest are also affected in the same manner but with a lesser influence. With only 96 km (51.8 nmi) of mountains between EAFB and the coast, there is usually enough moisture left to provide significant rainfall. Occasional summer air mass thunderstorms develop almost exclusively over the higher terrain in the area, even over the relatively small ranges scattered throughout the Mojave Desert. A few cells may advect over EAFB, primarily in the late afternoon. Table 35 contains the EAFB design rain rates, drop size, and rate of fall values versus time period.[1] Table 36 shows estimated hail characteristics for EAFB.[1]

Table 35. EAFB design ground-level rainfall based on yearly largest rate for stated durations.

Time Period	Rainfall Rate		Rainfall Total Accumulation		Raindrop Diameter				Average Rate of Fall*	
					Average		Largest			
	(mm/hr)	(in/hr)	(mm)	(in)	(mm)	(in)	(mm)	(in)	(m/s)	(ft/s)
1 min	197	7.7	3	0.1	2	0.08	5.6	0.22	6.5	21.3
5 min	88	3.5	7	0.3	2	0.08	5.3	0.21	6.5	21.3
15 min	51	2	13	0.5	2	0.08	5	0.2	6.5	21.3
1 hr	25	1	25	1	1.8	0.07	5	0.2	6.5	21.3
6 hr	10	0.4	62	2.4	1.5	0.06	4.6	0.18	6	19.7
12 hr	7	0.3	88	3.5	1.3	0.05	4.3	0.17	5.8	19
24 hr	5	0.2	124	4.9	1.3	0.05	4	0.16	5.5	18

*Average size raindrops.

Table 36. Estimated hail characteristics for EAFB (EAFB reference height=18 m (59.1 ft)).

Estimated Hail Characteristics	
Exposure time risk (%)	
Worst month reference period	5
Worst 6 months reference period	25
Mean number of hailstorm days per year	0.6
Average point of duration of hail fall	5 min
Average number of hailstones per 929 cm^2 (1 ft^2)	24
Density of hailstones	0.9 g/cm^3 (56 lb/ft^3)
Diameter and terminal velocity	
Representative diameter (50% risk)	0.9 cm (0.4 in)
Terminal velocity	11 m/s (36.1 ft/s)
Large diameter (5% risk)	2.2 cm (0.9 in)
Terminal velocity	17 m/s (55.8 ft/s)
Horizontal velocity—all directions	
Mean speed	13.m/s (42.7 ft/s)
5% risk speed	22 m/s (72.2 ft/s)
Months of maximum frequency	February to April
POR—years	28

2.8 Lightning

Atmospheric electricity must be considered in the design, transportation, and operation of aerospace vehicles. Inadequately protected aerospace vehicles can be upset, damaged, or destroyed by a direct lightning stroke to the vehicle or launch support equipment before or after launch. Damage can also result from current induced in the vehicle from changing electric fields produced by a nearby lightning stroke.[16] Direct (physical) and indirect (electromagnetic) effects of lightning on vehicle systems, along with mitigation techniques, are described in MPCV 70080, Cross Program Electromagnetic Environmental Effects (E3) Requirements Document and SLS-RQMT-040, Space Launch System Program Electromagnetic Environmental Effects (E3) Requirements.

All clouds are electrified to some degree. In some convective clouds, updrafts can lead to sufficient electrical charge separation to give rise to thunderstorms. The processes involved in this charge separation are yet to be fully understood. Several electrification mechanisms have been theorized, including charge transfer from colliding polarized cloud particles, thermoelectric effects where positive ions migrate toward colder cloud particles, and the gathering of charge from riming graupel and ice crystals. The result of these electrification mechanisms is a thunderstorm with a net positive charge in the upper regions of the cloud (~20 C) and a net negative charge (~20 C) in the lower regions.

As electrical charges become separated in a cloud, the potential gradient between the cloud and the ground, and between various regions of the cloud, increases and eventually exceeds the critical breakdown potential for air. The resulting dielectric breakdown becomes a lightning flash. A typical ground flash consists of a first return stroke followed by several subsequent strokes separated in time by ~50 ms. The subsequent ground strokes are the cause of the 'flicker' typically seen in ground flashes. The peak current in the first return stroke is usually twice as large as the current in subsequent strokes. Each stroke can eliminate the 20 C of charge in the lower region of the thundercloud. The charge-generating mechanisms within the cloud must then replenish the charge before another stroke can occur. Lightning flashes also occur within thunderstorms neutralizing the main positive and negative charge centers. Instead of consisting of several discrete strokes, an intracloud discharge generally consists of a single stroke. Studies have shown that the ratio of intracloud (IC) to cloud-to-ground (CG) (IC:CG) lightning is approximately 2 to 1 for the ER area.[17]

2.8.1 Eastern Range

The formation of cumulonimbus clouds is strongly dependent upon the time of day and season in the ER region. During the summer months, convergence zones develop within the boundary layer between the sea breeze winds and the large-scale flow. These zones are focal points for thunderstorm formation as updrafts are intensified. Also, the presence of light wind shears aloft allows the thunderstorms to grow vertically, which intensifies the charge gradient within the cloud. Studies have shown that these warm season convergence zones develop more frequently in the ER area when there is a southwest flow in the low-level wind pattern.[18] For the other months, frontal passages are the primary cause of thunderstorm formation and do not depend on time of day.

Figure 18 and table 37 provide insight into the diurnal variation of lightning flashes that occur near the ER. The data displayed are from the National Lightning Detection Network (NLDN), which has a detection efficiency of 90% for ER versus the Cloud-to-Ground Lightning Surveillance System (CGLSS) detection efficiency of 98%; NLDN and CGLSS only record the first CG return stroke from a lightning flash. Lighting flashes often have multiple return strokes. It is estimated (Personal Communication, Dr. V.A. Rakov, University of Florida, Gainesville) that the actual numbers could be increased by 70%.

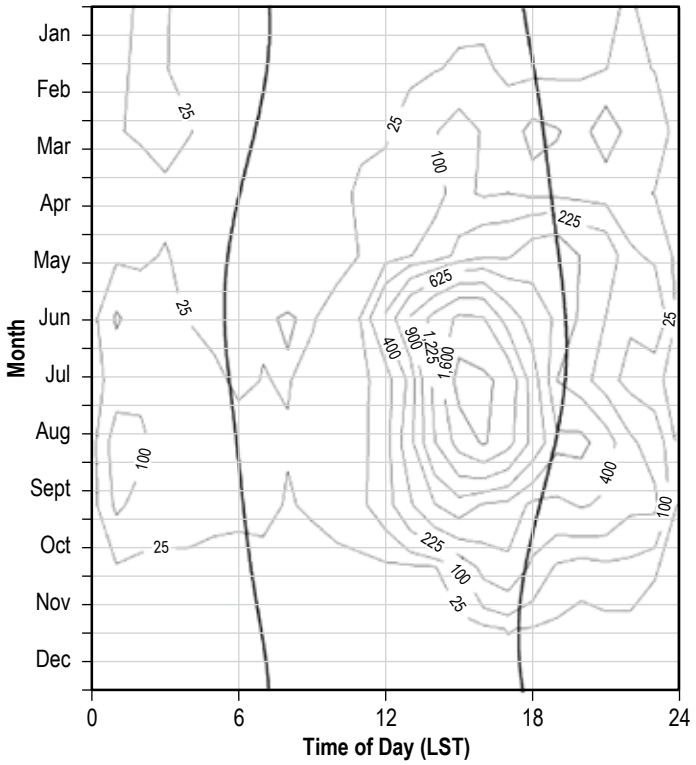

Figure 18. Diurnal/monthly variation of yearly average lightning flashes within a 50 km (26.9 nmi) radius of the ER, 1988–2001.

Table 37. Diurnal variation of lightning flashes for the ER.*

Hour (LST)	Jan	Feb	Mar	Apr	May	Jun	Jul	Aug	Sep	Oct	Nov	Dec	Annual
0	3	16	22	4	12	111	51	147	116	20	11	–	513
1	35	33	31	3	15	59	70	122	72	11	11	–	462
2	29	26	56	10	29	41	51	52	65	8	14	–	381
3	7	17	27	7	8	20	82	29	62	8	9	–	276
4	6	9	12	2	3	13	34	31	45	5	3	1	164
5	3	3	4	2	4	8	17	41	40	6	2	2	132
6	8	5	8	1	6	21	26	30	38	13	3	1	160
7	4	2	5	2	1	28	22	28	22	19	3	2	138
8	7	–	3	2	1	20	40	37	31	7	2	1	151
9	12	–	7	6	2	52	41	52	50	9	2	7	240
10	3	–	11	37	28	103	78	76	82	8	2	5	433
11	9	2	13	59	56	435	145	163	158	13	4	9	1,066
12	9	5	67	37	97	925	448	537	371	13	12	3	2,524
13	8	22	93	78	132	1,336	1,346	1,203	612	20	9	2	4,861
14	10	33	139	127	270	1,679	2,221	1,749	776	92	4	8	7,108
15	8	36	93	86	365	1,617	2,108	2,081	597	277	8	4	7,280
16	7	11	63	101	375	1,058	1,904	1,733	549	351	27	2	6,181
17	8	7	123	73	522	757	1,060	1,137	350	199	20	4	4,260
18	6	9	106	68	582	589	398	682	354	84	12	–	2,890
19	8	16	71	64	386	361	282	697	418	45	9	1	2,358
20	18	25	152	49	336	223	145	495	371	74	5	2	1,895
21	30	35	70	42	114	118	61	251	257	71	6	2	1,057
22	9	23	60	23	85	179	38	162	257	30	7	5	878
23	1	43	35	6	26	156	42	168	234	23	9	–	743
Totals	248	378	1,271	889	3,455	9,909	10,710	11,703	5,927	1,406	194	61	46,151

* Numbers represent the 14-yr (1988–2001) average numbers of flashes, separated by month and hour of the day, occurring within 50 km (26.9 nmi) of the ER. The bottom row indicates the average number of flashes by month, independent of time of day. The far right column indicates the average number of flashes by time of day, independent of month.

The Air Force's 45th Weather Squadron uses several systems to monitor lightning activity at the ER. The Launch Pad Lightning Warning System (LPLWS) is a network of ~30 ground-based electric field mills that measure the electric field at the surface and detect electric discharges near the ER. Data from the LPLWS are used for evaluation of lightning Launch Commit Criteria (LCC) electric field rules. The effective range of the LPLWS is approximately 20 km (10.8 nmi). The CGLSS is a network of six ground-based magnetic direction finders (MDFs).The MDFs use the magnetic field from a CG lightning flash to determine the azimuth to the CG strike point. The CGLSS determines location by direction finder and time of arrival (TOA) techniques. The effective range of the CGLSS is approximately 100 km (53.9 nmi). The Lightning Detection and Ranging (LDAR) system is a network of seven sensors that detect cloud-to-cloud (CC), IC, and CG lightning pulses. The LDAR uses a TOA technique to determine the location of lightning pulses. With this method, locations are established by taking the difference between the arrival times of the same lightning pulse signal to different LDAR sensors. The effective range of the LDAR system is approximately 100 km (53.9 nmi).[19]

The NLDN is a commercially owned network of more than 100 ground-based sensors distributed across the continental United States. The network consists of a mixture of magnetic direction finder and TOA sensors used to detect CG flashes. Along with lightning ground strike locations, the NLDN provides data on the number of strokes (first return and subsequent) and the peak current (in units of kiloamps) of the first return stroke for each CG lightning flash.

Table 38 shows the monthly and annual 50th and 99th percentile and maximum values for first return stroke peak current obtained from the NLDN for the years 1988–2001. Also given is the risk (%) of exceeding a 200 kA lightning flash. The CG lightning test waveform typically used for vehicle design has a first return stroke peak current of 200 kA. Lightning test waveforms for design are described in section 2.8.4.

Table 38. Lightning statistics for the ER, 1988–2001.*

Parameter	Jan	Feb	Mar	Apr	May	Jun	Jul	Aug	Sep	Oct	Nov	Dec	Annual
50th percentile peak current (kA)	50th percentile peak current (kA)	23.2	19.5	19.9	23.8	22.2	24.9	25.3	26.6	26.4	26.9	27.1	26.9
99th percentile peak current (kA)	99th percentile peak current (kA)	113.9	87.7	90.3	91.2	74.8	84.7	81.5	89.2	110	97.2	128.8	144.2
Maximum peak current (kA)	Maximum peak current (kA)	187.8	200.1	226	170.9	191.3	236.8	738.3	260.1	250.3	385.7	178.8	208.7
Risk (%) of peak currents >200 kA	Risk (%) of peak currents >200 kA	–	0.018	0.023	–	–	0.006	0.032	0.013	0.019	0.02	–	0.118

* Only flashes within 50 km (26.9 nmi) of the ER are considered. Peak current values are the absolute value of the first return stroke only. Values are determined from NLDN.

The average lightning flash density, i.e., the number of lightning ground flashes per square kilometer per year is an important phenomenological parameter that aids in the design of lightning protection systems. This parameter is critical in almost all lightning protection designs (such as the lightning over voltage protection of a utility power line), since the number of power outages or related failures is directly proportional to the number of CG discharges per unit area per year.

Figure 19 shows the mean annual CG lightning flash density (in units of flashes/km^2/yr) for the ER and KSC area. Data were obtained from the NLDN for the years 1988–2001. Standards for lightning protection of ground equipment and facilities at KSC are presented in a NASA Standards document.[20] The data displayed are from the NLDN, which has a detection efficiency of 90% for the ER versus CGLSS detection efficiency of 98%. Both NLDN and CGLSS only record the first CG return stroke from a lightning flash. Lighting flashes often have multiple return strokes. It is estimated (by Dr. Rakov, University of Florida) that the actual numbers could be increased by 70%. Figure 19 shows a local maximum in flash density (approximately 12 flashes/km^2/yr) just west of Cape Canaveral due to the sea breeze convergence zone.

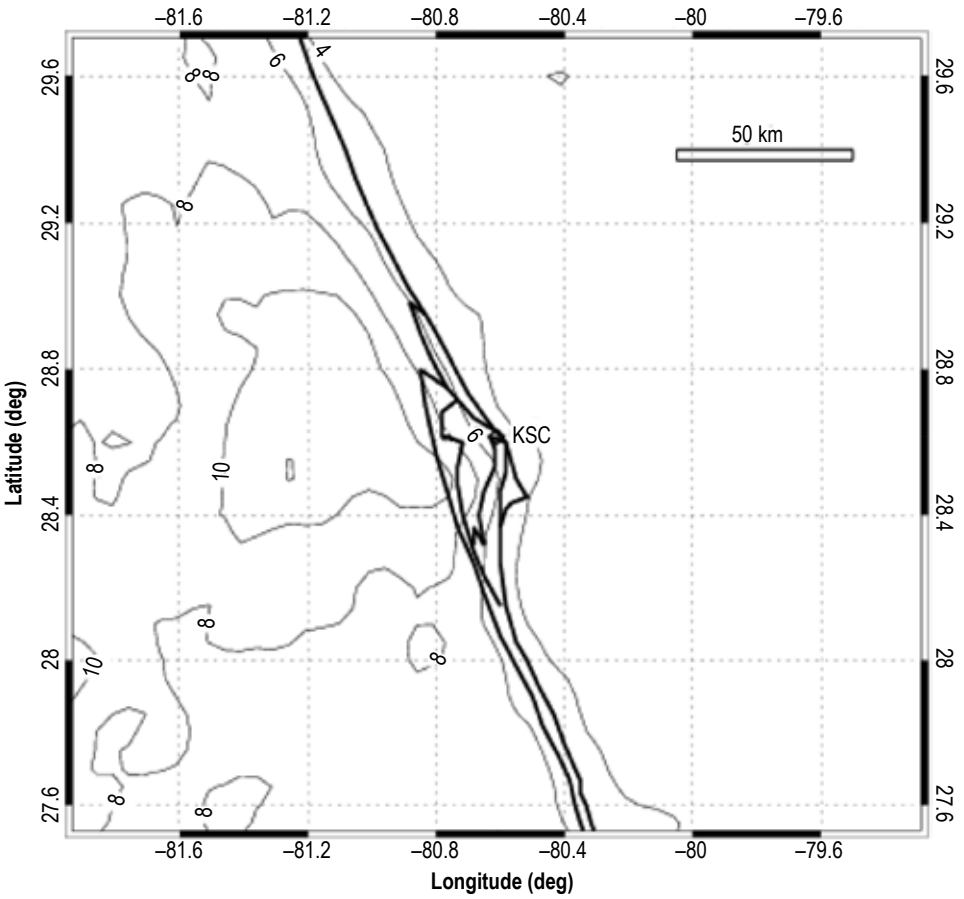

Figure 19. Mean annual CG lightning flash (flashes/km^2/yr) for the ER area.

Triggered lightning is one threat to aerospace vehicles after launch, and is caused when the vehicle and its electrically conductive exhaust plume passes through a sufficiently strong preexisting ambient electric field and spans a potential voltage difference across that field. As the vehicle passes through such a high electric field, electrical charges are induced on the vehicle's extremities, which produce a locally enhanced electric field sufficient to exceed the local breakdown strength of the air surrounding the vehicle. This local enhancement in the high preexisting ambient field leads to the growth of electric streamers at the vehicle extremities which support the initiation of conductive leaders and the resultant triggered lightning event.[21]

The danger of rocket-triggered lightning was first realized moments after the launch of Apollo 12 in 1969 at KSC. The rocket triggered two lightning strikes during a nonlightning producing weather situation. The lightning strikes produced major system upsets but only minor permanent damage. The vehicle and crew survived, and the crewmembers were able to complete their mission. This event led to the implementation of a set of lightning LCC, which are rules designed to avoid lightning threats to launch vehicles.

The next major event was the 1987 Atlas/Centaur-67 accident at KSC. The rocket caused a triggered lightning strike in nonlightning weather similar to the Apollo 12 incident that disrupted

the vehicle guidance electronics. As a result, the rocket yawed unexpectedly and Range Safety was forced to destroy the vehicle. In subsequent years, several studies and working groups produced many lightning LCC revisions and recommendations.[21] The most recent lightning LCC revision occurred in 2005 by the Lightning Advisory Panel, which advises the United States Air Force (USAF) and NASA on LCC issues.[22] These criteria consist of 11 rules used to protect against the natural and triggered lightning threat to in-flight vehicles. The lightning LCC include rules for cloud thickness, attached and detached electrified anvil clouds, and surface electric fields. Electrified anvil clouds can be particularly troublesome during the warm season due to the abundance of sea and land breeze-induced thunderstorms.[23] A total of 4.7% of the launches from October 1, 1988 to September 1, 1997 were scrubbed and 35% were delayed due to the lightning LCC.[21]

2.8.2 Edwards Air Force Base

Figure 20 and table 39 provide insight into the diurnal variation of lightning flashes that occur near EAFB. Figure 21 shows the mean annual CG lightning flash density (in units of flashes/ km^2/yr) for EAFB. Data were obtained from the NLDN for the years 1988–2001.

Table 40 shows the monthly and annual 50th and 99th percentile and maximum values for first return stroke peak current obtained from the NLDN for the years 1988–2001. Also given is the risk (%) of exceeding a 20 kA lightning flash.The CG lightning test waveform typically used for vehicle design has a first return stroke peak current of 200 kA. The lightning test waveform for design is described in section 2.8.4.

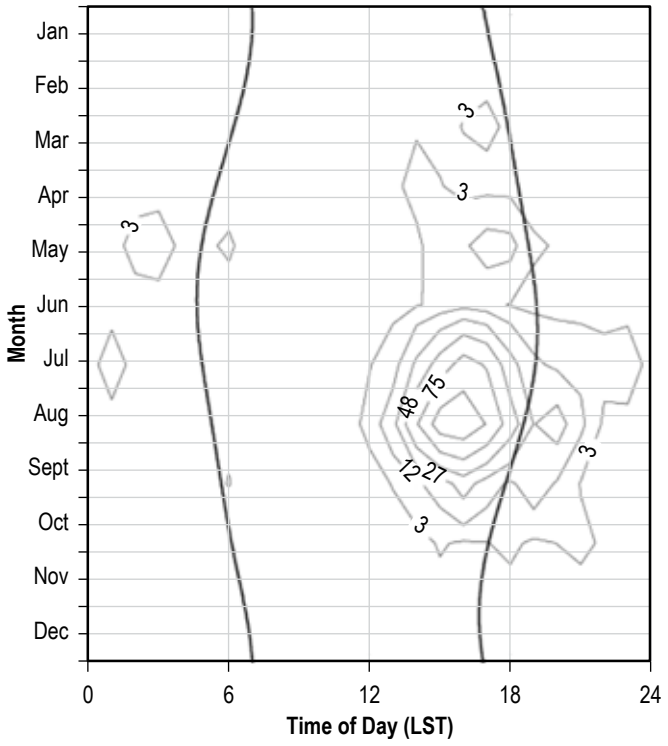

Figure 20. Diurnal/monthly variation of yearly average lightning flashes within a 50 km (26.9 nmi) radius of EAFB, 1988–2001.

Table 39. Diurnal variation of lightning flashes for EAFB.*

Hour (LST)	Jan	Feb	Mar	Apr	May	Jun	Jul	Aug	Sep	Oct	Nov	Dec	Annual
0	–	–	–	–	–	–	7	–	2	–	–	–	9
1	–	–	–	–	6	–	–	1	–	–	–	–	7
2	–	–	–	–	7	–	1	1	–	–	–	–	9
3	–	–	–	–	1	–	2	–	1	–	–	–	4
4	–	–	–	–	2	–	–	2	2	1	–	–	7
5	–	–	–	–	4	–	–	2	3	–	–	–	9
6	–	–	–	–	–	–	1	1	1	1	–	–	4
7	–	–	–	–	–	–	1	–	2	–	–	–	3
8	–	–	–	–	–	–	–	–	–	–	–	–	–
9	–	–	–	–	–	–	–	–	–	–	–	–	–
10	–	–	–	–	–	–	1	–	–	–	–	–	1
11	–	–	–	–	3	–	3	5	–	–	–	–	11
12	–	–	1	2	1	2	6	21	3	–	–	–	36
13	–	1	3	5	2	3	30	72	10	–	–	–	126
14	–	1	1	3	6	4	58	126	17	4	–	–	220
15	–	1	3	1	11	8	88	133	35	2	–	–	282
16	–	1	5	1	17	5	72	106	18	3	–	–	228
17	–	3	2	–	15	3	33	60	10	5	–	–	131
18	–	2	1	–	4	1	14	26	20	2	–	–	70
19	–	–	–	–	2	1	9	35	11	3	–	–	61
20	–	–	–	–	1	–	9	14	3	5	–	–	32
21	–	–	–	–	1	–	6	1	1	2	–	–	11
22	–	–	–	–	–	–	8	–	2	1	1	–	12
23	–	–	–	–	–	–	12	–	2	–	–	–	14
Total	–	9	16	12	83	27	361	606	143	29	1	–	1,287

* Numbers represent the 14 yr (1988–2001) average numbers of flashes, separated by month and hour of the day, occurring within 50 km (26.9 nmi) of the EAFB. The bottom row indicates the average number of flashes by month, independent of time of day. The far right column indicates the average number of flashes by time of day, independent of month.

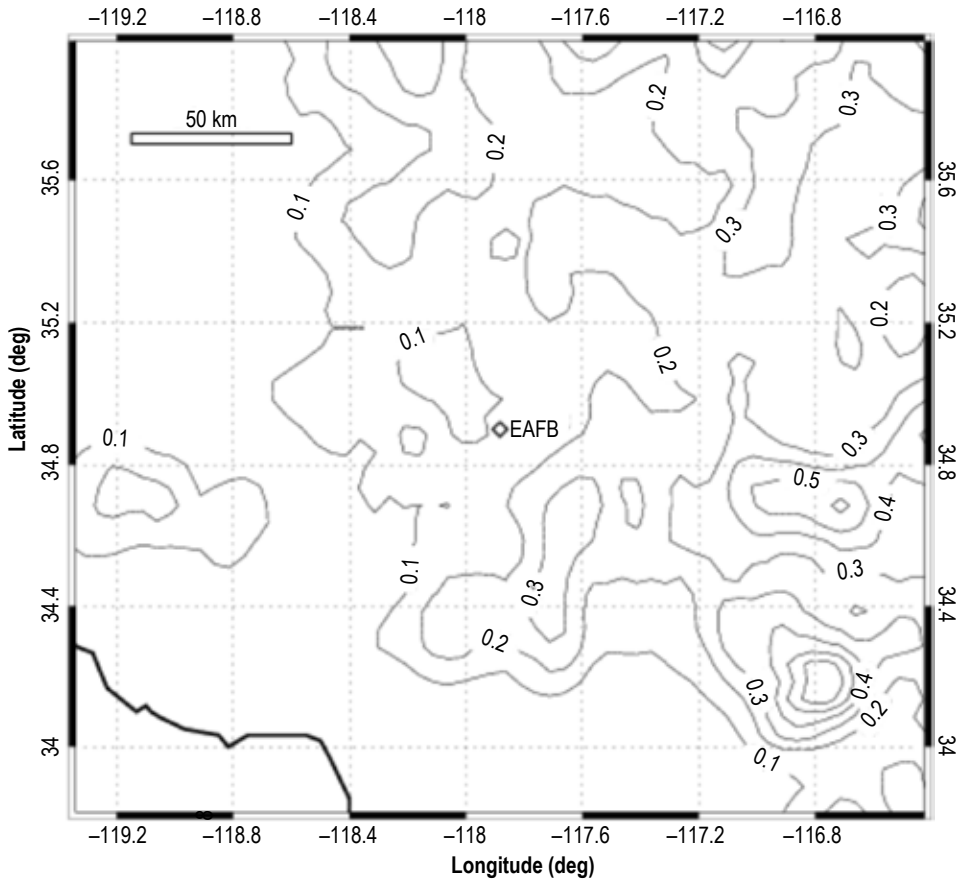

Figure 21. Mean annual CG lightning flash density (flashes/km^2/yr) for EAFB.

Table 40. Lightning statistics for EAFB, 1988–2001.*

Parameter	Jan	Feb	Mar	Apr	May	Jun	Jul	Aug	Sep	Oct	Nov	Dec	Annual
50th percentile peak current (kA)	65.9	32.2	24.8	22.4	20.3	20.3	18	18.5	17.9	24.6	29	33.1	18.6
99th percentile peak current (kA)	119.2	241.3	197.8	223.3	96.7	79.8	52.8	49.1	55	91.5	68.3	73.3	60.4
Maximum peak current (kA)	119.2	241.3	212.2	223.3	297.4	171.2	94.8	177.3	115.6	156	68.3	73.3	297.4
Risk (%) of peak currents >200 kA	–	2.632	0.495	0.599	0.084	–	–	–	–	–	–	–	0.033

* Only flashes within 50 km (26.9 nmi) of EAFB are considered. Peak current values are the absolute value of the first return stroke only. Values were determined from NLDN data.

2.8.3 Lightning Design and Test Criteria

The lightning environment at or external to the vehicle is characterized by composites of several voltage and current waveform components in accordance to the specified zone. The lightning environment within the vehicle is characterized by voltage and current waveforms, induced by the external lightning environment, in accordance with levels or electromagnetic regions specified within the vehicle.

Vehicle lightning strike zones are defined and described in Society of Automotive Engineers (SAE) ARP5414, Aircraft Lightning Zoning.[24]

2.8.3.1 External Lightning Design.

2.8.3.1.1 Voltage Waveforms. Voltage waveforms used to characterize the (external) lightning environment simulate electric fields, which increase until breakdown occurs either by puncture or flashover. They are intended for evaluation of possible vehicle lightning attachment locations and dielectric breakdown paths through nonconducting surfaces and structures.[25] Voltage waveforms A–D are displayed in figures 22–25.

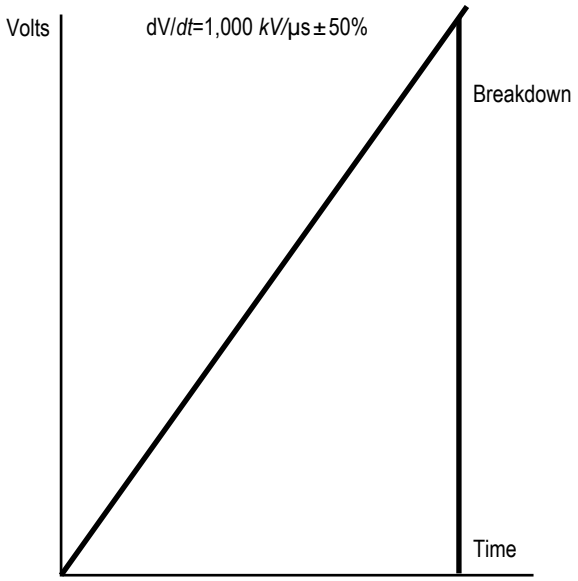

Figure 22. Voltage waveform A is characterized by a rise at the rate of 1,000 kV/µs (±50%) until its increase is interrupted by puncture or flashover.

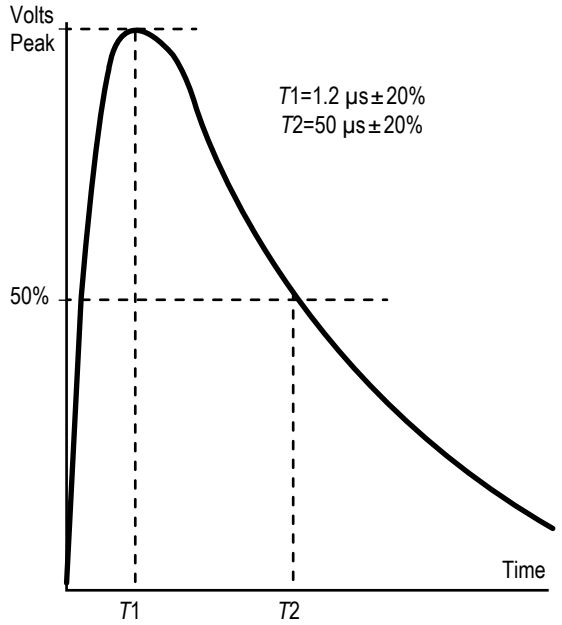

Figure 23. Voltage waveform B is a 1.2 × 50 µs waveform that crests at 1.2 µs (±20%) and decays to half of crest amplitude 50 µs (±20%).

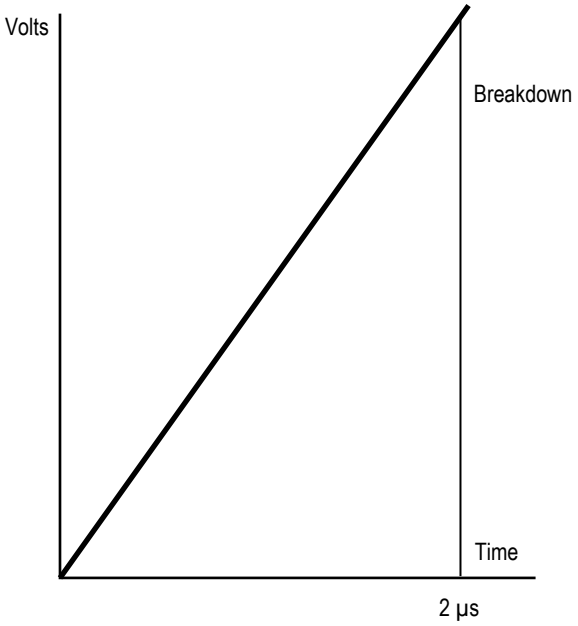

Figure 24. Voltage waveform C ramps up to breakdown voltage in 2 µs (±50%).

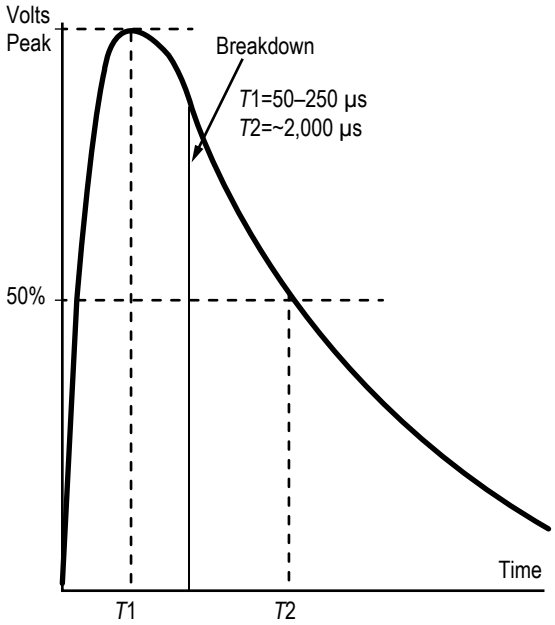

Figure 25. Voltage D slow-fronted waveform with a rise time between 50 and 250 µs.

2.8.3.1.2 Current Waveforms. The external lightning environment comprises current components A, Ah, B, C, D, and H, and the multiple stroke and multiple burst waveform sets. The multiple stroke and multiple burst comprise current components D (and D/2) and H, respectively.

Current components A–D are compositely used to evaluate direct effects; whereas, current component A and waveform sets multiple stroke (current component D and multiple D/2 current components) and multiple burst (multiple H current components) are applicable for evaluating indirect effects.

2.8.3.1.3 Direct Effects. Lightning environment direct effects for current components A–D (displayed in fig. 26):

- Current component A (first return stroke)
  Peak amplitude: 200 kA (±10%)
  Action integral: $2\times10^6 A^2s$ (±20%) (in 500 µs)
  Time duration: ≤500 µs

- Current component B (intermediate current)
  Maximum charge transfer: 10 C (±10%)
  Average amplitude: 2 kA (±20%)
  Time duration: ≤5 ms

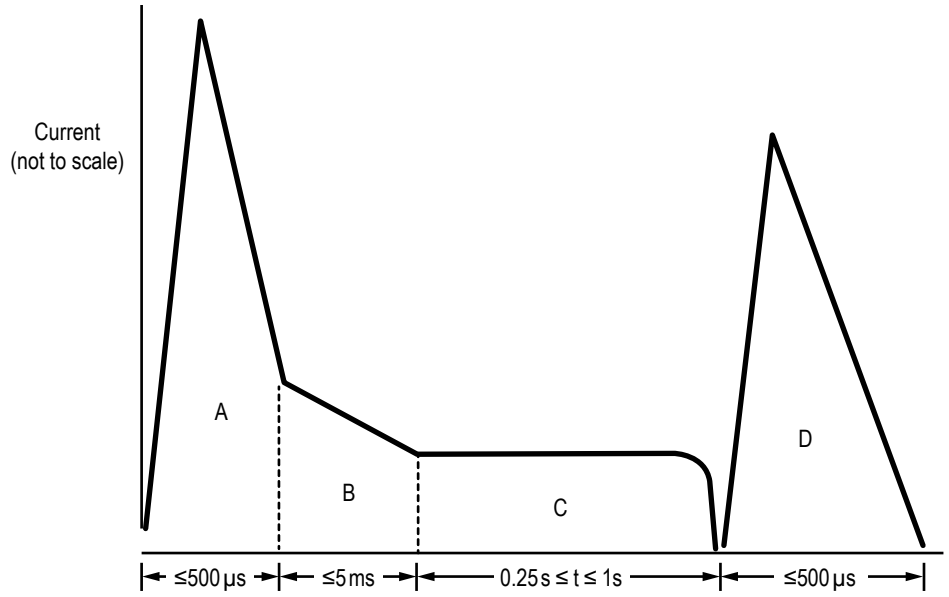

Figure 26. Lightning environment direct effects current components A through D.

- Current component C (continuing current)
  Amplitude: 200–800 A
  Charge transfer: 200 C (±20%)
  Time duration: 0.25–1 s

- Current component D (subsequent return stroke)
  Peak amplitude: 100 kA (±10%)
  Action integral: 0.25×10^6 $(A)^2s$ (±20%) (in 500 µs)
  Time duration: ≤500 µs

2.8.3.1.4 Indirect Effects. Lightning environment indirect effects for current component A (displayed in fig. 27).

- Current component A (first return stroke)
  Peak amplitude: 200 kA
  10% rise time: 0.15 µs
  90% rise time: 3 µs
  Peak crest: 6.4 µs
  50% fall time: 69 µs

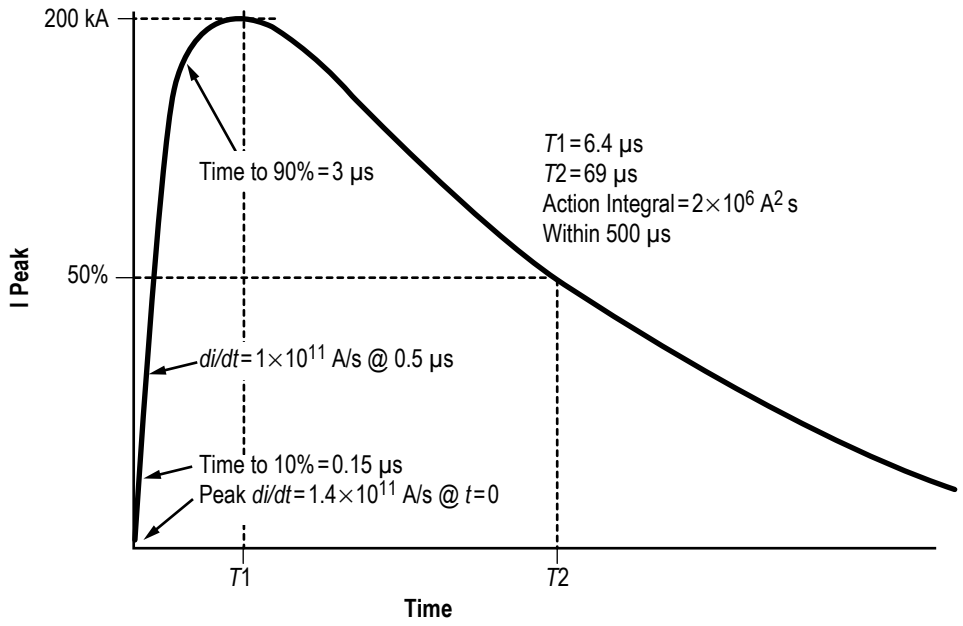

Figure 27. Lightning environment indirect effects current component A.

Lightning environment indirect effects for multiple stroke waveform set (displayed in fig. 28):

- Multiple stroke waveform set (current component D followed by 13 component D/2s)
  Duration (total): ≤1.5 s
  Time between components: 10–200 ms

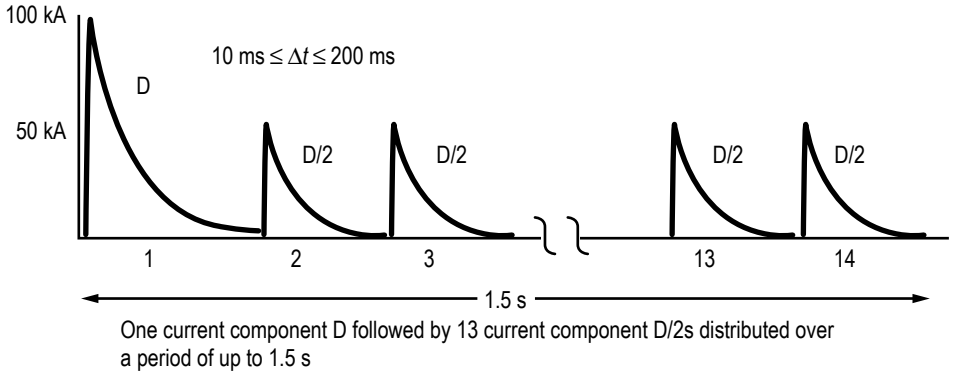

Figure 28. Lightning environment indirect effects multiple stroke waveform set.

Lightning environment indirect effects for current component D (displayed in fig. 29):

- Current component D (subsequent return stroke)
  Peak amplitude: 100 kA
  10% rise time: 0.08 µs
  90% rise time: 1.5 µs
  Peak crest: 3.18 µs
  50% fall time: 34.5 µs

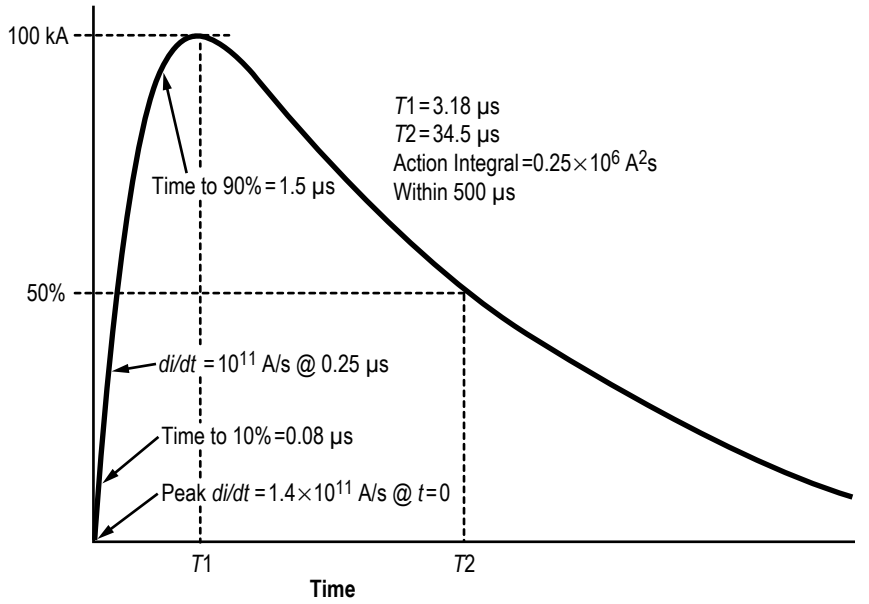

Figure 29. Lightning environment indirect effects current component D.

Lightning environment indirect effects for multiple burst waveform set (displayed in fig. 30).

- Multiple burst waveform set (repetitive current component H waveforms in three bursts of 20 pulses each)
  Duration (total): ≤0.62 s
  Time between bursts: 30–300 ms
  Time between pulses: 50–1,000 µs

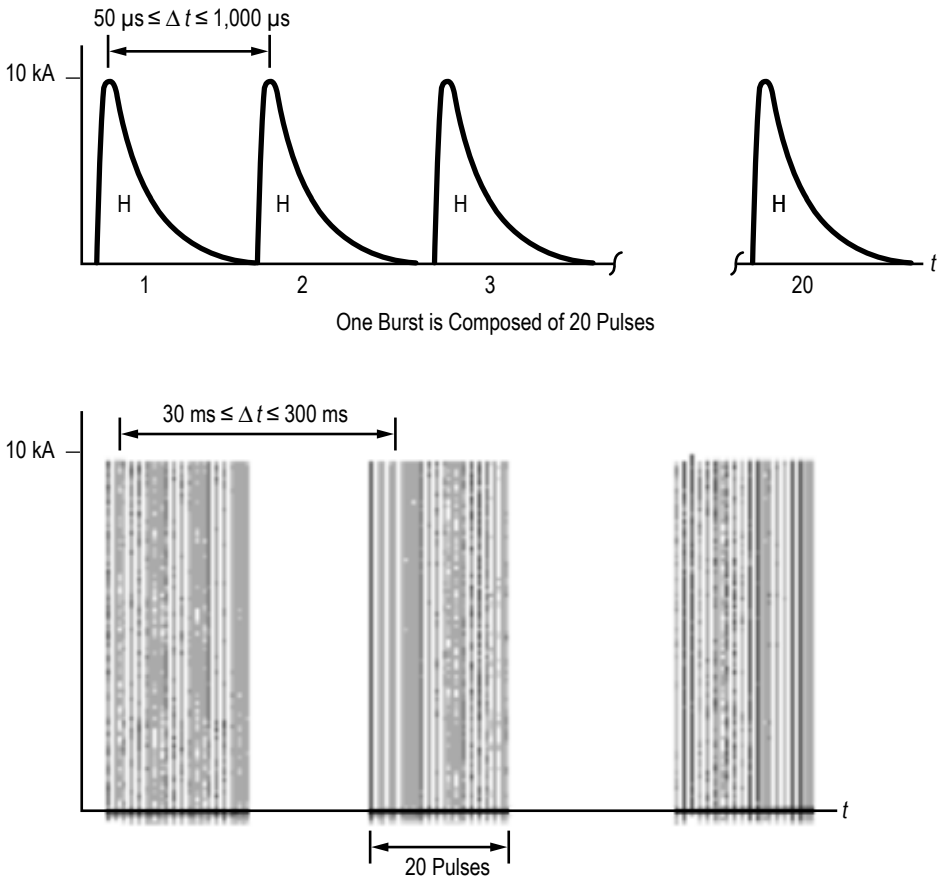

Figure 30. Lightning environment indirect effects multiple burst waveform set.

Table 41 displays the application of external lightning environment to vehicle zones.[24]

Table 41. Application of external lightning environment to vehicle zones (includes direct and indirect effects).

Vehicle Zone	Voltage Waveform Components	Current Waveform Components
1A	A, B, D	A, B, C, H
1B	A, B, D	A, B, C, D, H
1C	A	Ah, B, C, D, H
2A	A	D, B, C, H
2B	–	D, B, C, H
3	–	A, B, C, D, H
Lightning strike model tests	C	–

2.8.3.2 Internal Lightning Design Environment. High amplitudes and high rates of change of the external lightning environment current components A, D, and H induce major transients internal to the vehicle.

Magnetic fields penetrating through vehicle apertures induce currents and voltages inside the vehicle with waveforms similar to the current component A waveform (waveform 1), and similar to the derivative of the current component A waveform (waveform 2), respectively. Internal lightning environment amplitudes are not as severe as those of the external environment, varying with the electromagnetic regions designated within the vehicle and summarized in table 42.

Table 42. Maximum induced environment for electromagnetic regions.

Electromagnetic Region	Waveform 1 (A)	Waveform 2 (V)	Waveform 3 (V/A)	Waveform 4 (V)	Waveform 5 (A)
Level 1	100	50	100/20	50	150
Level 2	250	125	250/50	125	400
Level 3	600	300	600/120	300	1,000
Level 4	1,500	750	1,500/300	750	2,000
Level 5	3,200	1,600	3,200/640	1,600	5,000

Descriptions and conditions for the application of lightning environment waveforms are detailed in the following documents:

- SAE ARP5412, Aircraft Lightning Environment and Related Test Waveforms.[25]

- Radio Technical Commission for Aeronautics DO-160E, Environmental Conditions and Test Procedures for Airborne Equipment, section 22, Lightning Induced Transient Susceptibility, and section 23, Lightning Direct Effects.[26]

Electric and magnetic fields penetrating vehicle apertures create resonance, in the form of damped sinusoidal voltages and currents (waveform 3), on cables internal to the vehicle.

Structural IR voltage and diffusion flux coupling produce loop voltages, which have the shape of current component A (waveform 4). If the vehicle structure is highly resistive, the current waveform is lengthened (longer rise and fall times), but still similar to current component A (waveform 5).

All the induced transient waveform responses (waveforms 1–5) can occur during multiple stroke mode.

The multiple burst waveform set induces a voltage waveform 3 response or a current waveform 6 response, which has the same shape as the external environment component H:

- Waveform 1 (current waveform):
  Peak amplitude: (varies according to electromagnetic region)
  10% rise time: 0.15 μs
  90% rise time: 3 μs
  Peak crest: 6.4 μs (±20%)
  50% fall time: 69 μs (±20%)

- Waveform 2 (derived voltage waveform):
  Peak amplitude: (varies according to electromagnetic region)
  Peak crest: 100 ns
  Zero crossover: 6.4 μs (±20%)

- Waveform 3 (voltage or current waveform):
  Peak amplitude: (varies according to electromagnetic region)
  Range of resonance: 1–50 MHz

- Waveform 4 (voltage waveform):
  Peak amplitude: (varies according to electromagnetic region)
  10% rise time: 0.15 μs
  90% rise time: 3 μs
  Peak crest: 6.4 μs (±20%)
  50% fall time: 69 μs (±20%)

- Waveform 5A (current waveform):
  Peak amplitude: (varies according to electromagnetic region)
  10% rise time: 1.44 μs
  90% rise time: 23.7 μs
  Peak crest: 40 μs (±20%)
  50% fall time: 120 μs (±20%)

- Waveform 5B (current waveform):
  Peak amplitude: (varies according to electromagnetic region)
  10% rise time: 1.21 μs
  90% rise time: 23.9 μs
  Peak crest: 50 μs (±20%)
  50% fall time: 500 μs (±20%)

- Waveform 6 (current waveform):
  Peak amplitude: (varies according to electromagnetic region)
  10% rise time: 5.3 ns
  90% rise time: 0.11 μs
  Peak crest: 0.244 μs (±20%)
  50% fall time: 4 μs (±20%)

2.9 Tropical Cyclones

2.9.1 Eastern Range

The occurrence of hurricanes and tropical storms near the ER increases the risk and potential damage to the vehicle by surface winds and the induced loads placed on the vehicle. Extreme maxima in rainfall rates and total rainfall along with extreme minima in MSL atmospheric pressure are also associated with tropical cyclones. For this TM, the term tropical cyclone includes hurricanes and tropical storms. By definition, a hurricane is a storm of tropical origin with maximum sustained (1-min mean) surface winds ≥33.5 m/s (≥109.9 ft/s). A tropical storm is a storm whose origin is in the tropics with sustained wind speeds ranging between a maximum of 33.5 m/s (109.9 ft/s) and a minimum of 18 m/s (59 ft/s).[1] Tropical cyclone season in the Atlantic basin typically lasts from June 1 to November 30, but tropical cyclones have been reported as early as February and as late as December.[15]

Development of tropical cyclones typically occurs in two regions: the tropical western Atlantic or Gulf of Mexico/Caribbean Sea. In the months of July through September, tropical storms have a tendency to develop over the tropical western Atlantic; whereas, in the early season (May–June) and late season (October–December), cyclones tend to develop in the Gulf of Mexico/Caribbean Sea region. A report by Turpin,[27] for a POR from 1886 to 1997, showed that 92.2% of the storms that passed within 333 km (179.8 nmi) of the ER originated in the regions from the east down through the southwest of the ER.

The potential threat of a tropical cyclone to near the ER is presented from data contained in Johnson and Rawlins [28] for the tropical seasons from 1871 to 1999, a POR of 129 years. Over the POR, there have been 1,076 tropical cyclones in the Atlantic basin. Of those cyclones, 856 storms (79.6%) occurred during the 3 months of August–October with September accounting for 387 (36% of the total), the most of any single month during tropical cyclone season. Of the 1,076 tropical cyclones in the Atlantic Basin, 47% reached a radial distance of <928 km (<501.1 nmi) from the ER. The number decreased as the radial distance from the ER decreased. Only 9.1% were within a radial distance of 185 km (99.9 nmi). The conditional probability a tropical cyclone with a radial distance of 928 km (501.1 nmi) from the ER would track to within 185 km (99.9 nmi) of the ER was 19.3%. Specifically for September, the month with the greatest number of storms, the conditional probability of a storm initially within a radial distance of 928 km (501.1 nmi) moving to within a radial distance of 185 km (99.9 nmi) was only 16.2%.[28]

Maximum sustained winds within a tropical cyclone present a threat to the vehicle and facilities. Tropical cyclones, in addition to air mass thunderstorms, have produced the strongest winds measured at the ER.[29] In general, tropical cyclones approaching the ER from the east produce higher winds than those approaching the ER from over the Florida peninsula.[1] Over a POR of 55 years, 1945 to 1999, 12 tropical cyclones have produced sustained winds exceeding 17.5 m/s (57.4 ft/s) at the ER. From an annual perspective, this means that there is a 0.06% chance of encountering sustained winds that exceed 17.5 m/s (57.4 ft/s) annually. During tropical cyclone season, the probability increases to 0.10%, and during the months August to October, it is 0.24%.[28]

2.9.2 Edwards Air Force Base

The only impact to EAFB from tropical cyclones is from tropical cyclone remnants yielding large amounts of rainfall over the site. From 1900 to 1997, there have been 42 occurrences of tropical cyclones in the southwestern United States. Only one of those cyclones has ever made landfall at tropical storm strength. This storm occurred in September 1939 and made landfall at Long Beach, with sustained winds of 22.4 m/s (73.5 ft/s).[29] The majority of systems track along the Baja California peninsula and make landfall in southwestern Arizona.

2.10 Sea State

Knowledge of sea state characteristics and probabilities are important to aerospace vehicle design and trade studies in the development of detailed design requirements and specifications, and for operational analyses. It is important to characterize the sea conditions for landing and recovery zones (including pad and ascent abort, normal, and off-nominal zones), launch availability, and the possible sea recovery and tow back of reusable components. Some of the site-specific information contained in this section is based on the work done by the MSFC Natural Environments Branch for the Orion Multi-Purpose Crew Vehicle. Though certain information is specific to the anticipated Orion configuration and splashdown zones, the general information provided within this section can be applied to other aerospace vehicles. Additional information can be provided in the future as needed.

2.10.1 Sea State Data

2.10.1.1 C-ERA 40 Hindcast Global Database. The 40-year Corrected-European Centre for Medium-Range Weather Forecasts Re-Analysis (C-ERA40)[30] is developed from the European Centre for Medium-Range Weather Forecasts (ECMWF) over a 45-year POR (September 1957–August 2002), making the C-ERA40 the longest and most complete global wave data set presently available.

The products provided by the C-ERA40 were constructed through the reanalysis of historical data using an atmospheric numerical model coupled with a wave hindcast numerical model and were validated with in situ and satellite measurements.[30,31] The databases include six hourly (00, 06, 12, and 18 coordinated universal time (UTC)) reports of wind speed at a 10 m (32.8 ft) height, significant wave height (SWH), and mean zero up-crossing wave period with a $1.5^{\circ} \times 1.5^{\circ}$ spatial resolution. Each individual SWH, wind speed, and wave period report represents an average of the last 20 min of the given 6-hr time period over the entire grid box centered on the corresponding latitude and longitude provided in the database. It has also been found that model errors in SWH and wind speed are consistent with, or better than, previous scientific and engineering studies which compared model and buoy data.[31,32]

Several limitations do exist with the database. The C-ERA40 reanalysis only applies to deep water. Tropical cyclones cannot be resolved properly; therefore, data in regions where tropical cyclones are prevalent may not fully represent the true environment.[33]

2.10.1.2 Buoy Networks. Several buoy networks exist which provide both real-time and historical observations. The National Data Buoy Center (NDBC) provides hourly meteorological and wave data such as wind speed, air temperature, and SWH. In addition, some buoys in the NDBC network have the capability to record spectral wave data. While the NDBC buoys range in size and shape (3 to 12 m (9.8 to 39.3 ft) discus hulls to a 6-m (19.7-ft) boat-shaped hull), the buoys owned by the Coastal Data Information Program (CDIP) are spherical and 0.9 m (2.9 ft) in diameter. The CDIP buoys not only record data on a finer temporal resolution than the NDBC buoys (every 30 min), but the upper frequency limit that the wave spectra are reported to is also higher. Unfortunately, the CDIP buoys do not have the instrumentation to make meteorological observations, which only allows the buoys to record wave data.

A limitation that both networks share is the greater concentration of buoys along coastlines versus the open ocean. While this is helpful for data needed for Orion pad aborts at KSC in Florida, or within the normal end-of-mission (EOM) landing zone near San Clemente Island, California, archived observations for ocean locations that could potentially see ascent aborts over open ocean or off-nominal EOM zones are sparse or do not exist.

An overview of the ECMWF can be found at <www.ecmwf.int>.[34] Recent and archived observations from the NDBC and CDIP buoy networks can be accessed online by the public at <http://www.ndbc.noaa.gov/> and <http://cdip.ucsd.edu/>, respectively. [35,36]

2.10.2 Significant Wave Height and Extreme Wave Height Values

A regular sea surface is considered nearly sinusoidal with constant wave height, period, and direction, but natural waves are often associated with an irregular sea surface where the observable waves move in different directions and the associated heights and periods can vary.[37,38] This variability in wave height from wave to wave leads to a more statistical definition of the parameter, where wave height is the distance from the crest to trough. Wave height measurements tend to follow a Rayleigh distribution, as shown in figure 31.[37] Given enough recorded wave cycles exist to create a distribution, the Rayleigh distribution may be used to determine the average height of the highest desired fraction of the waves ($\overline{H_p}$), or the wave height exceeded by the highest desired fraction of the waves (H_p):

$$\overline{H_p} = \left[\sqrt{\ln\left(\frac{1}{p}\right)} + \frac{\sqrt{\pi}}{2p} \cdot erfc\left(\sqrt{\ln\left(\frac{1}{p}\right)} \right) \right] \cdot H_{\text{rms}} \tag{21}$$

and

$$H_p = \sqrt{\ln\left(\frac{1}{p}\right)} \cdot H_{\text{rms}} \ , \tag{22}$$

where p equals the highest fraction of interest and *erfc* is the complementary error function. An estimation of various wave heights includes SWH, which corresponds to the average height

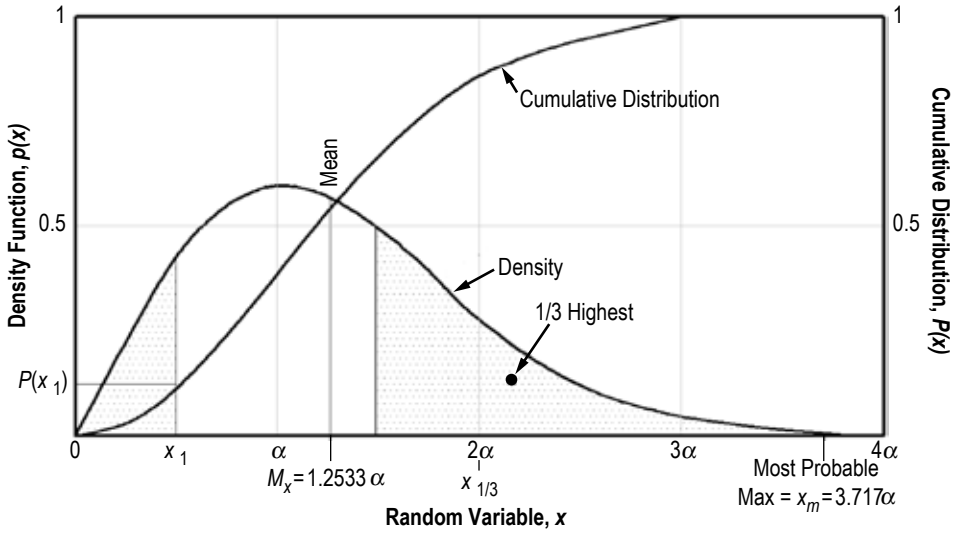

Figure 31. Rayleigh probability density and cumulative probability distribution ($x = \alpha$ corresponds to the mode).[37]

of the highest one-third of the waves, and maximum wave height ($H_{\max}$) which depends on the number of observed waves and the SWH. While estimated wave heights from the middle of the Rayleigh distribution, like SWH and root-mean-square wave height (H_{rms}), are <u>not</u> dependent on the total waves observed, maximum wave height ($H_{\max}$) is dependent on the number of recorded wave cycles:[39]

$$\text{SWH} \approx 4 \cdot \sqrt{m_0} = 1.416 \cdot H_{\text{rms}} , \tag{23}$$

$$\overline{H_{1/10}} = 1.27 \cdot \text{SWH} = 1.8 \cdot H_{\text{rms}} = 5.091 \cdot \sqrt{m_0} , \tag{24}$$

$$\overline{H_{1/100}} = 1.67 \cdot \text{SWH} = 2.36 \cdot H_{\text{rms}} = 6.672 \cdot \sqrt{m_0} , \tag{25}$$

and

$$H_{\max} = 1.86 \cdot \text{SWH} \quad \text{(for 1,000 wave cycles in the record)} , \tag{26}$$

where

m_0 = zeroth moment of the wave spectrum

$\overline{H_{1/10}}$ = average height of the highest one-tenth of the waves

$\overline{H_{1/100}}$ = average height of the highest one-hundredth of the waves.

If the average of the highest 1/N waves $\left(\overline{H_{\max}}\right)$ is desired instead:

$$\overline{H_{\max}} = \left[\sqrt{\ln(N)} + \frac{\sqrt{\pi}}{2} \cdot erfc\left(\sqrt{\ln(N)}\right) \right] \cdot H_{\text{rms}} \ , \tag{27}$$

where N is the number of recorded wave cycles.

Although Rayleigh distributions are usually adequate for deep water, they tend to overestimate the number of larger wave heights in coastal waters. Currently, no other distribution exists that better fits the waves in shallow water, therefore the Rayleigh is still used with the assumption that waves will likely be overpredicted.

2.10.3 Wave Height and Wind Speed Durations and Intervals

The time an episode of SWH or wind speed persists above a given threshold is referred to as the duration of the event. The time between two episodes is termed an interval. The length of time an episode is likely to last once it has begun is important to such aerospace applications as launch operations, rescue, and recovery.

The United States (U.S.) Navy has compiled a historical data set in the form of a wind and wave climatology called the U.S. Navy Hindcast Spectral Ocean Wave Model Climatic Atlases for both the North Atlantic Ocean[39] and the North Pacific Ocean.[40] Duration and interval tables are provided for various grid points across the oceans at various months of the year. Information on the construction and use of these tables including examples of their applications are provided in the Navy Atlases.[40,41] A subset of the tables for the ER and a brief description of their use was also provided in the reference 42. Since these tables are rather voluminous and have not been updated since their inclusion in NASA/TM—2008–215633,[41] they are not duplicated here. Note that as indicated in NASA/TM—2008–215633, the Spectral Ocean Wave Model underestimates wind speed and wave height near U.S. east coast areas. However, the Spectral Ocean Wave Model is the only known source for duration/interval statistics.

2.10.4 Wave Period

Wave period can have different definitions depending on which wave assumption is used to characterize the sea surface. In cases where the sea surface is assumed to have regular waves, or constant wave properties, the wave period is defined as the amount of time between two successive crests or troughs at a given point. Realistically, the sea contains irregular, or random, waves where the variability in wave height and period from wave to wave leads to more statistical definitions of the wave properties. In random seas, the more common definitions of wave period, like zero up- or down-crossing period, take into account the zero (or mean) water line which represents the mean level of the water surface. Figure 32 illustrates the differences between regular and irregular seas where the zero line is represented by the x-axis in each wave profile.[37]

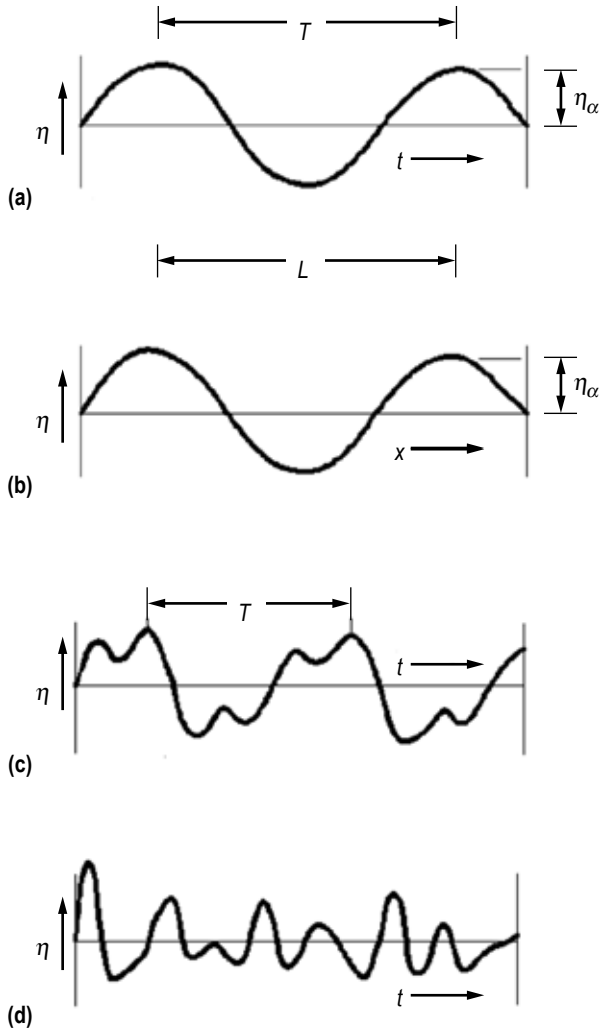

Figure 32. Examples of regular and irregular waves: (a) Regular wave (temporal), (b) regular wave (spatial), (c) irregular wave, and (d) random wave.[37]

While the zero up-crossing period is defined as the time it takes a point on a water surface to cross the zero line in an upward direction and continue along the wave profile to the next zero up-crossing, the zero down-crossing is described as the amount of time between successive down-crossings. Although both zero crossing methods tend to provide statistically similar mean values of wave period, the mean zero up-crossing wave period (T_m) is the quantity that is utilized in the C-ERA40 database and is given by:

$$T_m = \sqrt{\frac{m_0}{m_2}}\ , \tag{28}$$

where m_0 and m_2 are the zeroth and second moments of the wave spectrum.[37,41] Wave period can also be represented by the peak spectral wave period (T_p), which is defined as the period associated with the largest wave energy in a wave record, or the spectral peak frequency, $f_p = 1/T_p$.

Using the products from the C-ERA40 database, minimum wave period design specifications are determined by analyzing the distribution of T_m in 1-s time intervals within specified half-meter SWH ranges. In each SWH and T_m range, the first value is included in the range, while the second value is not. According to Sorensen,[42] as wave height increases, the wave period distribution narrows. This narrowing is visible in table 43, which shows the percentage of T_m reports in 1-s intervals that are within a specified SWH range. The sum of the T_m probabilities within each SWH range equals 100%.

Table 43. Percentage of wave period observations in 1-s intervals that are within a specified SWH range (0.5 m) from January–December 1971–2001.

Significant Wave Height		Mean Zero Up-Crossing Wave Period (s)														
(m)	(ft)															
≥7	≥23	–	–	–	–	–	–	*	0.7	23.5	53.1	18.7	3.6	0.4	–	–
6.5–7	21.3–23	–		–	–	–	–	*	4.3	57.4	30.6	5.9	1.5	0.3	–	–
6–6.5	19.7–21.3	–	–	–	–	–	*	0.1	11.2	62.1	19.6	5.2	1.5	0.3	–	–
5.5–6	18–19.7	–	–	–	–	–	*	0.3	25.6	52.6	14.6	5.1	1.4	0.3	–	–
5–5.5	16.4–18	–	–	–	–	–	*	1.5	43.2	36.6	12.1	5	1.3	0.3	–	–
4.5–5	14.8–16.4	–	–	–	–	–	*	6.6	50.7	24.8	11.3	4.9	1.3	0.3	–	–
4–4.5	13.1–14.8	–	–	–	–	*	0.2	19.7	43	19.5	11.4	4.6	1.3	0.2	–	–
3.5–4	11.5–13.1	–	–	–	*	*	1.2	33	30.6	17.7	11.5	4.5	1.3	0.2	–	–
3–3.5	9.8–11.5	–	–	*	*	*	6.1	35.6	23.7	17.4	11.5	4.6	0.9	0.1	–	–
2.5–3	8.2–9.8	–	–	*	*	0.3	14.7	29.6	20.7	18.3	12	3.8	0.6	0.1	–	–
2–2.5	6.6–8.2	–	*	*	*	2.2	19.2	22.9	20.9	21.3	10.8	2.3	0.3	–	–	–
1.5–2	4.9–6.6	–	–	*	0.2	7.2	17.2	21.2	27.2	20	5.4	1.2	0.2	–	–	–
1–1.5	3.3–4.9	–	*	*	3.8	12.6	17.6	26.9	26.2	9.1	2.8	0.8	0.2	–	–	–
0.5–1	1.6–3.3	–	*	2.6	19.8	17.7	18.2	19.4	12.9	6.2	2.3	0.6	0.1	–	–	–
0–0.5	0–1.6	–	0.2	22.7	33.6	18.9	11.1	7	3.9	1.7	0.6	0.1	–	–	–	–
		0–1	1–2	2–3	3–4	4–5	5–6	6–7	7–8	8–9	9–10	10–11	11–12	12–13	13–14	≥14

Significant Wave Weight (m)

Note:
– Indicates no report existed for the specific T_m range within the SWH range.

* Indicates that reports existed, but the probability is <1/10 of a percent.

The minimum average wave periods indicated in table 44 are selected by determining which 1-s wave period range contains the first percentile of wave periods observed for the given SWH range. Since the first percentile falls between two values within a wave period range, the lower of the two wave period values is used to be conservative. Therefore, the minimum average wave period is approximately the lowest mean zero up-crossing wave period associated with the specified SWH range and the dashed line in table 43 is used to indicate this boundary across all the given SWH ranges.

Table 44. Minimum average wave period corresponding to given significant wave height.

Significant Wave Height		Minimum Average Wave Period
(m)	(ft)	(s)
0–0.5	0–1.6	2
0.5–1	1.6–3.3	2
1–1.5	3.3–4.9	3
1.5–2	4.9–6.6	4
2–2.5	6.6–8.2	4
2.5–3	8.2–9.8	5
3–3.5	9.8–11.5	5
3.5–4	11.5–13.1	5
4–4.5	13.1–14.8	6
4.5–5	14.8–16.4	6
5–5.5	16.4–18	6
5.5–6	18–19.7	7
6–6.5	19.7–21.3	7
6.5–7	21.3–22.9	7
≥ 7	22.9	8

Values of T_m associated with the Orion normal and off-nominal design maximum SWH (2 and 4 m (6.6 and 13.1 ft), respectively) are displayed in table 44.

2.10.5 Water Surface Slope

Several different methods for calculating wave slope for Orion were examined. These methods included: (1) Wave height divided by wave length, which provided a gross overestimate and assumed that the water surface was a straight line without any curve to it, (2) the Neumann spectrum, which was the ocean model used by the Apollo program but it lacked advancements in wave theory that more current spectra contained, (3) the Pierson-Moskowitz (PM) spectrum, which replaced analyses conducted with the Neumann spectrum but did not provide the steeper 3σ slopes seen by real ocean data.

The approach that was eventually used to calculate wave slope is based on historical wave spectrum databases, which allows for the calculation of water surface slopes based on measured data.

The energy spectrum associated with the Orion normal and off-nominal design maximum SWH (2 and 4 m (6.6 and 13.1 ft), respectively) are provided in table 45 (for 2 m (6.6 ft) SWH) and table 46 (for 4 m (13.1 ft) SWH). Each energy spectrum may be truncated on the high-frequency end to limit the calculated water surface slope to the dimensions of interest to the engineering application. The limit of the high-frequency end of the energy spectrum can be determined using the following equation:

$$f_{\max} = \sqrt{\frac{g}{2 \cdot \pi \cdot \left(\frac{L}{2}\right)}}\ , \tag{29}$$

where $f_{\max}$ is the maximum frequency (Hz), g is gravity (m/s^2), and L is the smallest wavelength (m) of interest for the engineering application. The energy spectrum is used to derive the Orion normal and off-nominal water surface slope distributions using the following equations:

$$I^* = \sum_{i=1}^{n} \left[\left(\frac{\mu_i^2}{g} \right) \times \left[A_i\left(\mu_i\right) \right]^2 \times \Delta\mu_i \right], \tag{30}$$

where I^* is the omnidirectional slope variance, n represents the total number of frequency bins, g is gravity, and $[A_i(\mu_i)]^2$ and $\Delta\mu_i$ are the energy spectrum (m^2/Hz) and bandwidth (Hz), respectively, associated with the ith frequency bin.

The directional components of slope variance are determined by multiplying slope variance by the constants $f(\theta) = 0.625$ and $g(\theta) = 0.375$,[43] which are representative values of how the slope variance is divided into its directional components:

$$\sigma_{ud}^2 = I^* \cdot f(\theta) \tag{31}$$

and

$$\sigma_c^2 = I^* \cdot g(\theta), \tag{32}$$

where σ_{ud}^2 is the upwind-downwind slope variance component and σ_c^2 is the crosswind slope variance component. Each directional slope standard deviation component is used to run a 10,000 case (typical) Monte Carlo Simulation, assuming the water surface slope fits a Gaussian distribution. The directional water surface slope components are determined using the following equations:

$$\mu_{ud} = \arctan\left(\sigma_{ud} \cdot r_{ud}\right) \tag{33}$$

and

$$\mu_c = \arctan\left(\sigma_c \cdot r_c\right), \tag{34}$$

Table 45. Energy spectrum for 2 m (6.6 ft) SWH.

Frequency (Hz)	Energy (m^2/Hz)	Bandwidth (Hz)	Frequency (Hz)	Energy (m^2/Hz)	Bandwidth (Hz)
0.025	0.0033	0.005	0.38	0.101	0.01
0.03	0.0069	0.005	0.39	0.135	0.01
0.035	0.0121	0.005	0.4	0.131	0.01
0.04	0.0113	0.005	0.41	0.1227	0.01
0.045	0.0289	0.005	0.42	0.0737	0.01
0.05	0.0946	0.005	0.43	0.0869	0.01
0.055	0.1462	0.005	0.44	0.0715	0.01
0.06	0.129	0.005	0.45	0.0865	0.01
0.065	0.2023	0.005	0.46	0.0583	0.01
0.07	0.3837	0.005	0.47	0.0477	0.01
0.075	0.3455	0.005	0.48	0.0489	0.01
0.08	0.3837	0.005	0.49	0.0517	0.01
0.085	0.4284	0.005	0.5	0.0543	0.01
0.09	0.614	0.005	0.51	0.0379	0.01
0.095	0.3799	0.005	0.52	0.0298	0.01
0.1013	0.2611	0.0075	0.53	0.0343	0.01
0.11	0.0961	0.01	0.54	0.0325	0.01
0.12	0.1051	0.01	0.55	0.0198	0.01
0.13	0.169	0.01	0.56	0.0183	0.01
0.14	0.4548	0.01	0.57	0.0259	0.01
0.15	0.9438	0.01	0.58	0.0203	0.01
0.16	1.0642	0.01	0.59	0.01829	0.01
0.17	1.1356	0.01	0.6	0.0167	0.01
0.18	1.3596	0.01	0.61	0.01524	0.01
0.19	1.2059	0.01	0.62	0.01392	0.01
0.2	0.9438	0.01	0.63	0.0127	0.01
0.21	1.1076	0.01	0.64	0.0116	0.01
0.22	0.5929	0.01	0.65	0.01058	0.01
0.23	0.5639	0.01	0.66	0.00966	0.01
0.24	0.7314	0.01	0.67	0.00882	0.01
0.25	0.7499	0.01	0.68	0.00805	0.01
0.26	0.464	0.01	0.69	0.00735	0.01
0.27	0.4241	0.01	0.7	0.00671	0.01
0.28	0.4199	0.01	0.71	0.00612	0.01
0.29	0.3668	0.01	0.72	0.00559	0.01
0.3	0.4458	0.01	0.73	0.0051	0.01
0.31	0.16	0.01	0.74	0.00466	0.01
0.32	0.2064	0.01	0.75	0.00425	0.01
0.33	0.2484	0.01	0.76	0.00388	0.01
0.34	0.1179	0.01	0.77	0.00354	0.01
0.35	0.1329	0.01	0.78	0.00323	0.01
0.36	0.1624	0.01	0.79	0.00295	0.01
0.37	0.0985	0.01	0.8	0.0027	0.01

Table 46. Energy spectrum for 4 m (13.1 ft) SWH.

Frequency (Hz)	Energy (m^2/Hz)	Bandwidth (Hz)	Frequency (Hz)	Energy (m^2/Hz)	Bandwidth (Hz)
0.025	0.0353	0.005	0.38	0.1336	0.01
0.03	0.0477	0.005	0.39	0.0951	0.01
0.035	0.1419	0.005	0.4	0.1046	0.01
0.04	0.1608	0.005	0.41	0.0951	0.01
0.045	0.8124	0.005	0.42	0.0856	0.01
0.05	4.9392	0.005	0.43	0.0985	0.01
0.055	5.9132	0.005	0.44	0.067	0.01
0.06	2.0693	0.005	0.45	0.0641	0.01
0.065	0.349	0.005	0.46	0.0398	0.01
0.07	0.8329	0.005	0.47	0.0341	0.01
0.075	1.3128	0.005	0.48	0.0546	0.01
0.08	2.2416	0.005	0.49	0.0525	0.01
0.085	3.041	0.005	0.5	0.0501	0.01
0.09	2.0693	0.005	0.51	0.0375	0.01
0.095	3.7516	0.005	0.52	0.0468	0.01
0.1013	4.6515	0.0075	0.53	0.0364	0.01
0.11	7.8632	0.01	0.54	0.0313	0.01
0.12	10.1472	0.01	0.55	0.0242	0.01
0.13	7.0794	0.01	0.56	0.0277	0.01
0.14	7.3683	0.01	0.57	0.0225	0.01
0.15	6.4378	0.01	0.58	0.024	0.01
0.16	4.9392	0.01	0.59	0.01906	0.01
0.17	3.1336	0.01	0.6	0.01741	0.01
0.18	2.9072	0.01	0.61	0.01591	0.01
0.19	2.1005	0.01	0.62	0.01453	0.01
0.2	1.9782	0.01	0.63	0.01327	0.01
0.21	1.6606	0.01	0.64	0.01212	0.01
0.22	1.3128	0.01a	0.65	0.01107	0.01
0.23	1.0857	0.01	0.66	0.01012	0.01
0.24	0.9922	0.01	0.67	0.00924	0.01
0.25	0.5639	0.01	0.68	0.00844	0.01
0.26	0.4481	0.01	0.69	0.00771	0.01
0.27	0.5958	0.01	0.7	0.00704	0.01
0.28	0.5668	0.01	0.71	0.00643	0.01
0.29	0.2637	0.01	0.72	0.00588	0.01
0.3	0.4014	0.01	0.73	0.00537	0.01
0.31	0.2843	0.01	0.74	0.0049	0.01
0.32	0.1552	0.01	0.75	0.00448	0.01
0.33	0.1648	0.01	0.76	0.00409	0.01
0.34	0.2192	0.01	0.77	0.00374	0.01
0.35	0.1716	0.01	0.78	0.00341	0.01
0.36	0.1934	0.01	0.79	0.00312	0.01
0.37	0.1227	0.01	0.8	0.00285	0.01

where μ_{ud} is the upwind-downwind water surface slope component (rad), μ_c is the crosswind water surface slope component (rad), and r_{ud} and r_c are zero-mean, unit variance Gaussian random variables. Each pair of directional water surface slope component values is applied to the following equation to create a water surface slope distribution:

$$\mu = \arctan\left(\sqrt{\tan^2 \mu_{ud} + \tan^2 \mu_c} \times \frac{180}{\pi}\right), \tag{35}$$

where μ is the total water surface slope (degrees).

The normal (off-nominal) energy spectrum for the Orion landing zones in tables 45 and 46 was developed using 5-m wind speed data from buoys 46047 and 46069, near San Nicolas Island, California, in the NDBC network along with spectral data from buoy 067 near San Nicolas Island in the CDIP buoy network. The spectral data ranges from 0.025 to 0.58 Hz and is reported every half hour, along with the corresponding SWH. These archived buoy data, when compared with the NDBC spectral data, provide spectral data at higher frequencies in the area of interest. The energy spectrum for Orion normal water landings is the enveloping spectrum during August over a 9-year POR (1999–2007), where SWH is ≤2 m (6.6 ft) and wind speed is ≤8.2 m/s (26.9 ft/s). The energy spectrum in table 45 represents a single spectrum from August 23, 2001, at 0349 UTC and is created using (1) the energy in each frequency bin from 0.025 to 0.58 Hz and (2) energy that is extrapolated from 0.58 to 0.8 Hz with an exponential curve ($y = 3.9708 \cdot \exp^{-9.1189x}$) that is fit to the energy found in each frequency bin from 0.3 to 0.58 Hz. The variable x is the desired frequency (Hz) and y is the resulting energy (m^2/Hz).

The energy spectrum for the Orion off-nominal landing zone is the enveloping spectrum during March over a 6-year POR (2000–2005), where SWH is ≤4 m (≤13.1 ft) and wind speed is ≤13.9 m/s (≤45.6 ft/s). The energy spectrum in table 46 represents a single spectrum from March 29, 2001, at 0013 UTC and is created using (1) the energy in each frequency bin from 0.025 to 0.58 Hz and (2) energy that is extrapolated from 0.58 to 0.80 Hz with an exponential curve ($y = 3.9773 \cdot \exp^{-9.052x}$) that is fit to the energy found in each frequency bin from 0.30 to 0.58 Hz.The variable x is the desired frequency (Hz) and y is the resulting energy (m^2/Hz).

A water surface slope distribution for the normal Orion landing zone was derived from the full energy spectrum and is illustrated in figure 33. A water surface slope distribution for the off-nominal Orion landing zone was derived from the full energy spectrum and is illustrated in figure 34. The figures show the probability that the water surface slope is below a given value. The normal and off-nominal slope distributions represent the extreme case of 5,422 and 5,934 energy spectra, respectively. The normal spectrum was selected based on the distributions seen in figure 33, and the off-nominal spectrum was selected based on the distributions seen in figure 34. Both spectra not only cover the higher probabilities of steeper water surface slopes, but they also cover the water surface slopes seen at higher frequencies when the energy spectrum is extrapolated.

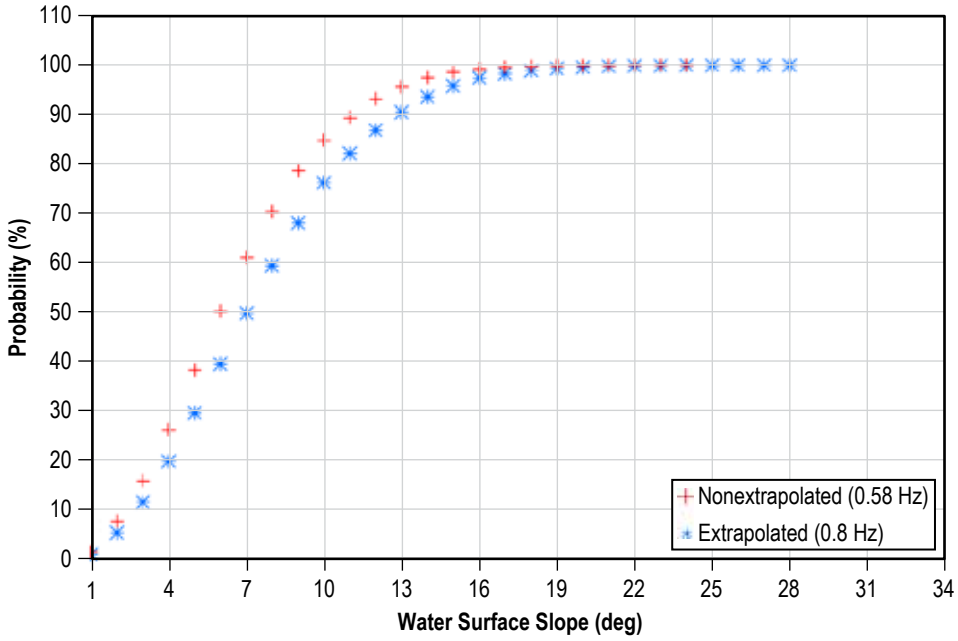

Figure 33. Cumulative distributions of water surface slope for 2 m (6.6 ft) SWH.

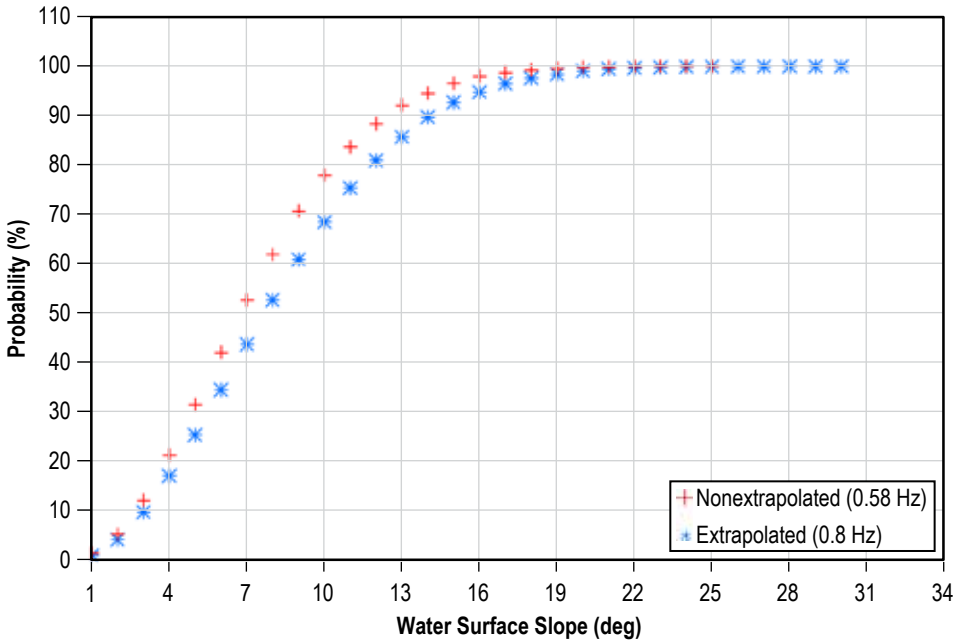

Figure 34. Cumulative distributions of water surface slope for 4 m (13.1 ft) SWH.

2.10.6 Ocean Temperature and Salinity

Physical properties of seawater are dependent primarily upon salinity and temperature. Differences in salinity and/or temperature throughout the ocean cause density differences that drive subsurface water masses. These subsurface water mass movements are called thermohaline currents.

Salinity is defined as the total amount of solid material in grams contained in 1 kg of seawater when carbonate has been converted to oxide, bromine, and iodine replaced by chlorine, and all organic material completely oxidized. While coastal waters can exhibit a wide range of salinity as a result of freshwater runoff, most of the world's ocean water lies in the narrow salinity range of 33.8 to 36.8 g of dissolved salts per kilogram of seawater. The North Atlantic is the most saline of the world's oceans, having a mean salinity of 35.09 g/kg compared to the global average of 34.72 g/kg. At any given temperature and pressure, seawater is denser than freshwater.

Temperature in the ocean varies widely, both horizontally and with depth. Some of the warmest sea surface temperatures (SSTs) on Earth have been recorded at the surface in the Persian Gulf in summer. The lowest possible temperature values hover around –2 °C (28.4 °F), the usual minimum freezing point of seawater. Freshwater reaches its maximum density at 4 °C (39.2 °F) and then expands (becomes less dense) as it cools to 0 °C (32 °F) and freezes. This is why freshwater ponds in cold climates convectively turn over every season. Saltwater, on the other hand, continues to become denser as it cools to its freezing point. When saltwater freezes, the salt impurities (primarily composed of sodium chloride) are not easily incorporated into the ice crystal lattice structure and the newly formed ice is composed primarily of freshwater. The solution rejected when seawater freezes is even higher in salt content, and denser as well, and has an even lower freezing point than the original solution. Therefore, the greatest changes in density of seawater occur near the surface where density is decreased by either precipitation, water runoff from land surfaces, melting ice, or heating. Density is increased by the formation of sea ice, cooling, and by evaporation. The greatest increase in density occurs in the polar regions, where the water is cold and great quantities of ice form. This cold, dense polar water sinks and spreads to lower latitudes via thermohaline currents.

At depths more than a couple hundred meters (600 to 700 ft) below the surface of the ocean, the temperature and salinity of water normally change very slowly. When it does change rapidly, it is because a 'new' water mass (with new salinity and temperature values) advects into, and displaces, the original water from that location. In this case, both temperature and salinity are conservative properties of a fluid (i.e., changed only by advection) and, as a result, the movement of water mass can be traced by its temperature and salinity. Origin regions and relative depths characterize water masses. Four depths, beginning at the surface and extending to the ocean bottom, are used: surface, intermediate, deep, and bottom.

The greatest known depth of water in the oceans is 11,524 m (37,808.4 ft) in the Marianas Trench in the Pacific. The average ocean depth worldwide is 3,795 m (12,450.8 ft). By way of comparison, the highest land on Earth—Mount Everest—is 8,840 m (29,002.6 ft) tall and the average height of land is 840 m (2,755.9 ft) above sea level. About 23% of the ocean is shallower than 3,000 m (9,842.5 ft); about 76% is between 3,000 and 6,000 m (9,842.5 and 19,685 ft); and a little more than 1% is deeper than 6,000 m (19,685 ft). In addition, about 77% of the world ocean volume is colder than 4 °C (39.2 °F), with salinities in the relatively narrow range 34.1 to 35.1 g of dissolved salts per kilogram of seawater.

Maximum, mean, and minimum water temperatures for 3-month periods from the surface to depths of 50 m (164 ft) for the waters off the coast of the KSC ER areas are given in tables 47 and 48.

Table 47. Ocean temperatures (°C) in the ER booster recovery areas.

Months	Jan to Mar			Apr to Jun			Jul to Sep			Oct to Dec		
Depth (m)	Max.	Mean	Min.	Max.	Mean	Min.	Max.	Mean	Min.	Max.	Mean	Min
0	26	23	16	29	26	21	31	29	27	29	26	19
10	26	23	16	29	26	20	30	29	26	29	26	19
20	26	23	16	29	26	19	30	28	23	29	26	20
30	26	23	17	28	26	17	29	28	21	29	28	21
50	26	23	17	28	25	17	29	27	19	28	26	22

Table 48. Ocean temperatures (°F) in the ER booster recovery areas.

Months	Jan to Mar			Apr to Jun			Jul to Sep			Oct to Dec		
Depth (ft)	Max.	Mean	Min.	Max.	Mean	Min.	Max.	Mean	Min.	Max.	Mean	Min
0	78.8	73.4	60.8	84.2	78.8	69.8	87.8	84.2	80.6	84.2	78.8	66.2
33	78.8	73.4	60.8	84.2	78.8	68	86	84.2	78.8	84.2	78.8	66.2
66	78.8	73.4	60.8	84.2	78.8	66.2	86	82.4	73.4	84.2	78.8	68
98	78.8	73.4	62.6	82.4	78.8	62.6	84.2	82.4	69.8	84.2	78.8	69.8
164	78.8	73.4	62.6	82.4	78.8	62.6	84.2	80.6	66.2	84.2	78.8	71.6

2.10.6.1 Sea Surface Temperature Data. Although most NDBC and CDIP buoys have the instrumentation to record sea surface temperature (SST), the observations only cover a limited area of the globe. This makes it difficult to analyze certain ocean regions, especially those that are in open water since most buoys are located in coastal areas. Several databases exist which provide better global SST coverage through gridded reanalysis. The National Centers for Environmental Prediction (NCEP) optimum interpolation provides weekly mean SST observations on a 1° latitude×1° longitude global grid dating back to November 1981. This database was created using in situ and satellite SST observations, with the satellite data corrected for biasing, and simulated SST from sea ice cover.[44] This database was used to look at the global water temperatures for the Orion project. Using a POR from November 1981 through December 2006, it was found that the

warmest SSTs were seen in the Persian Gulf and Arabian Sea areas. The warmest temperature of approximately 36 ºC (96.8 ºF) occurred in the Persian Gulf during the summer months.

2.10.7 Ocean Surface Currents

Ocean currents transport seawater from one location of the ocean to another. They also transport momentum, chemicals (such as salts, oxygen, and carbon dioxide), biological species (such as plankton and fish), and any objects purposely or inadvertently inserted into the ocean. Knowledge of ocean currents is important to marine navigation, to dispersal of pollutants, and to aerospace applications such as search and rescue at sea or recovery of space-borne objects. Ocean currents are composed of both surface and subsurface currents. Since subsurface currents are primarily driven by differences in the density of the sea water, they generally travel at much slower speeds (2 to 3 orders of magnitude slower) than surface flows and are typically of less interest to aerospace applications. Ocean surface currents are primarily driven by atmospheric wind above the surface waters. Frictional stress at the interface between the ocean and the wind causes the water to move in the direction of the wind. Steady winds cause the sea surface to slope as water is piled up in the direction the wind is blowing. The maximum difference in water surface height due to this effect is generally about 1 m per 100 km (3.3 ft per 54 nmi).

Water flows from the region of higher pressure to the region of lower pressure. The Coriolis force, which results from the Earth's rotation, causes the current to move to the right of the pressure gradient path in the Northern Hemisphere and to the left in the Southern Hemisphere. On small scales, water flows from high to low pressure (the pressure gradient force) in the ocean, but for large-scale motion, the Earth's rotation leads to flow along lines of constant pressure (isobars). Such water flows that are controlled by a balance between the pressure gradient force and the Coriolis deflection result in currents called geostrophic currents that flow along isobars. Large-scale, mid-latitude ocean flow is an approximate geostrophic current. On a global scale, large ocean currents are constrained by the continents that border the three major oceanic basins. Continental borders cause these currents to develop large-scale, almost closed circular patterns called gyres. These gyres actually result from a combination of wind forcing, buoyancy forcing, and the Coriolis acceleration. Since Coriolis acceleration varies with latitude, gyre circulations are not symmetric and the ocean surface flow on western boundaries of a gyre is generally stronger. Figure 35 is a simplified illustration of the major ocean surface currents of the world.[45]

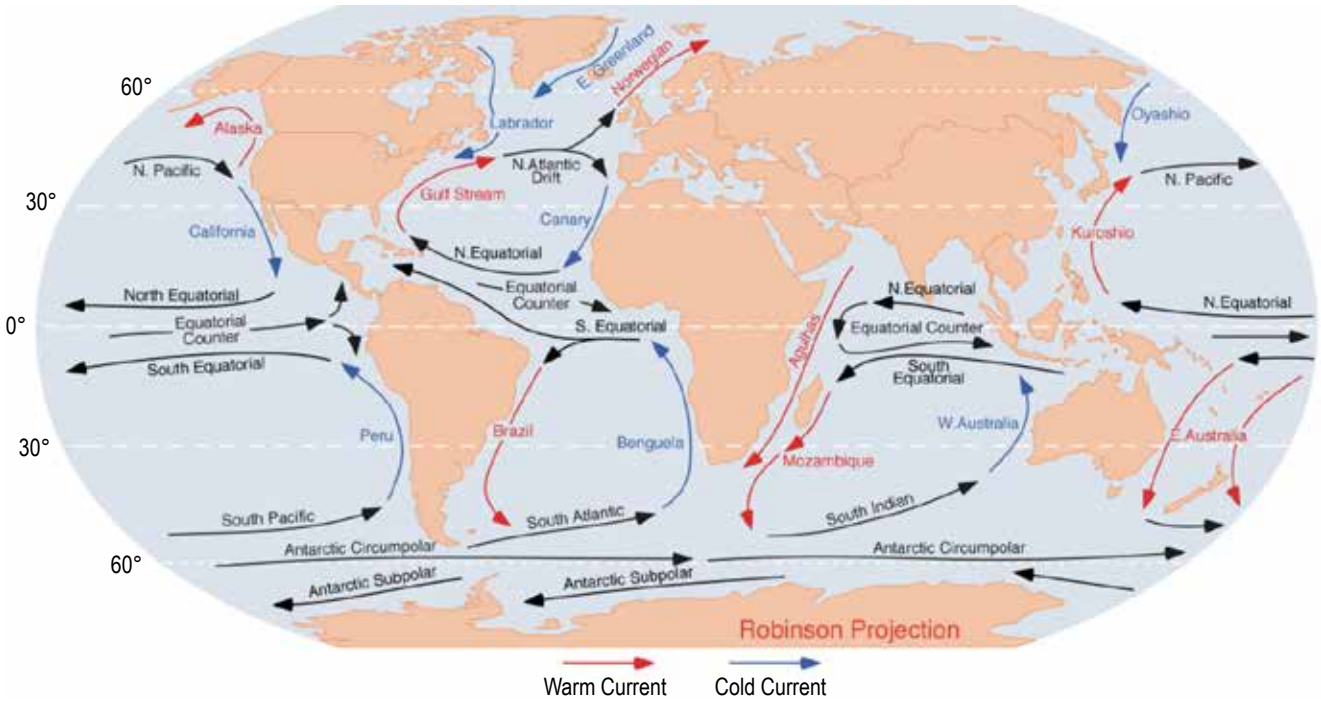

Figure 35. Major ocean surface currents of the world[45] (courtesy of Scott Jones).

On either side of the equator, in all ocean basins, there are two west-flowing currents: the North and South Equatorial. These currents flow between 3 and 6 km (1.6 and 3.2 nmi) per day and usually extend 100 to 200 m (328.1 to 656.1 ft) in depth below the ocean surface. The Equatorial Counter Current, which flows towards the east, is a partial return of water carried westward by the North and South Equatorial currents. In El Niño years, this current intensifies in the Pacific Ocean.

Flowing from the equator to high latitudes are the western boundary currents. These warm water currents have specific names associated with their location: North Atlantic—Gulf Stream, North Pacific—Kuroshio, South Atlantic—Brazil, South Pacific—East Australia, and Indian Ocean—Agulhas. All of these currents are generally narrow, jet-like flows that travel at speeds between 40 and 120 km (21.6 and 64.8 nmi) per day. Western boundary currents are the deepest ocean surface flows, usually extending 1,000 m (3,280.8 ft) below the ocean surface. The largest and most prominent of the western boundary currents is the Gulf Stream in the North Atlantic Ocean (fig. 36).The warmer water (red thermal image) of the current is a good indicator of the path it takes on its journey north (J. Bosch, Coastal Ocean Observation Laboratory, Institute of Marine and Coastal Sciences, Rutgers University, Personal Communication). The component of the Gulf Stream that flows through the Florida Straits up to Cape Hatteras, North Carolina, is called the Florida Current. The near surface current speed off the coast of Florida is typically 2 m/s (6.6 ft/s). The Florida Current mean northward transport is approximately 30×10^6 m^3/s ($1{,}059.4\times10^6$ ft^3/s). This is more than the total flow of all the rivers in the world combined. For comparison, the Mississippi River is approximately 0.02×10^6 m^3/s (0.71×10^5 ft^3/s). The width of the Florida Current is approximately 80 km (43.2 nmi) at 27 ºN. and 120 km (64.8 nmi) at 29 ºN. As the Florida Current

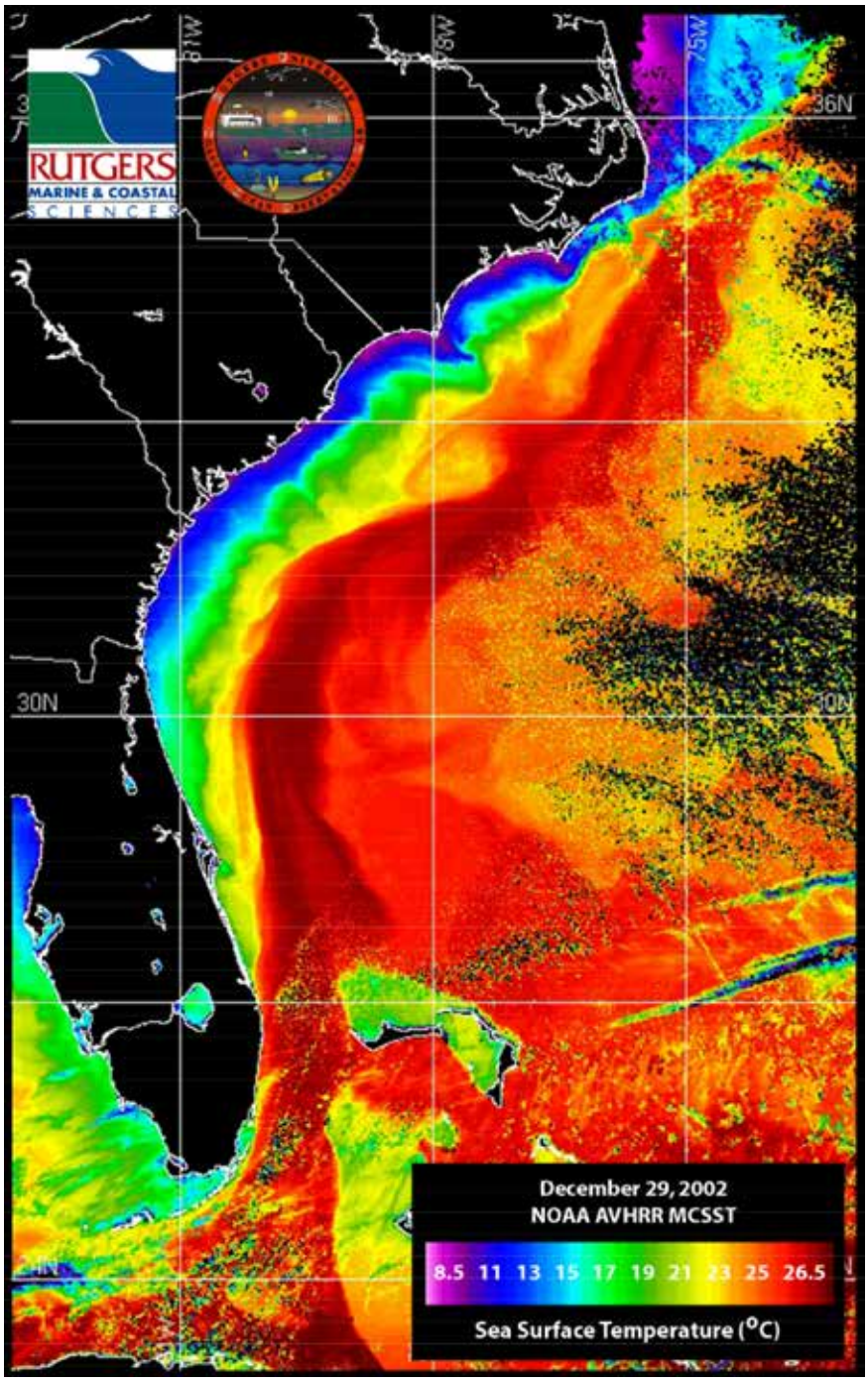

Figure 36. Satellite image of the Gulf Stream that shows the temperature differential of the ocean water off the coast of Florida (courtesy of Coastal Ocean Observation Laboratory, Institute of Marine and Coastal Sciences, Rutgers University).

is joined by other northward-flowing currents, the volume transport of the Gulf Stream increases to approximately 85×10^6 m^3/s ($3{,}001.7 \times 10^6$ ft^3/s) near Cape Hatteras.

Flowing from high latitudes to the equator are the eastern boundary currents. These cold water currents also have specific names associated with their location: North Atlantic—Canary, North Pacific—California, South Atlantic—Benguela, South Pacific—Peru, and Indian Ocean—West Australia. All of these currents are generally broad, shallow moving flows that travel at speeds between 3,000 and 7,000 m (9,842.5 to 22,965.9 ft) per day.

In the Northern Hemisphere, the east flowing North Pacific Current and North Atlantic Drift move the waters of western boundary currents to the starting points of the eastern boundary currents. The South Pacific Current, the South Indian Current, and the South Atlantic Current provide the same function in the Southern Hemisphere. These currents are associated with the Antarctic Circumpolar. Because of the absence of land masses at this latitude zone, the Antarctic Circumpolar flows in continuous fashion around Antarctica and only provides a partial return of water to the three southern hemispheric ocean basins.

In addition to water density gradients and atmospheric winds, another driving mechanism for ocean flow is the ocean tides generated by the Moon and Sun. For open ocean currents, the contribution to the flow from this source is generally considered noise. However, in coastal areas, tidal flow is usually the dominant flow component. Therefore, tidal forecasts are very important for many marine applications such as shipping, but less so for most aerospace applications.

General information on ocean currents is available from National Oceanic and Atmospheric Administration's (NOAA's) National Ocean Data Center at <http://nodc.noaa.gov>.[46]

2.11 Geologic Hazards

2.11.1 Earthquakes

Earthquakes are due to sudden releases of tectonic stresses that result in relative movement of rocks on opposite sides of a fault plane, as well as shaking of ground in areas near and sometimes far from the actual fault movement. Ground movement and shaking can trigger numerous other disasters, including landslides; liquefaction and sliding of unconsolidated sediments; destruction of buildings, dams, and roads; fires; tsunamis; seiches; changes in ground water level; and uplift or subsidence. They can also bring about far-reaching atmospheric pressure changes, sound waves, and oscillations of the ionosphere.[47]

Relative movement of different sections, plates, of the Earth's crust causes stresses to build up near the boundaries between them. Movement along faults, which releases seismic waves, takes place when the effective stresses exceed either the strength of the solid rock or the frictional resistance between rocks on either side of a preexisting break or fault. This movement takes place along preexisting fault surfaces because they usually have lower strength than the surrounding rock.

Many microearthquakes take place along active faults, such as in parts of the San Andreas Fault, but a greater number do not correspond to any known surface fault. Many of the earthquakes that are not associated with surface faults occur under folds called anticlines, geologic structures formed when layered sediments are buckled upward in a broad arch. The presence of an anticline reflects crustal compression as two moving tectonic plates collide in the same way a carpet wrinkles when pushed across the floor. An unanswered question is whether these active folds conceal large faults that could provide the sites for large shocks.[48]

Earthquakes have proven to be one of the most disastrous and insurmountable of geologic hazards. Buildings constructed to withstand them have crumbled under their forces.[47] Prediction of earthquake likelihood, intensity, and timing for a given location has not yet proved reliable. Experience has shown that the best protection against earthquakes is identification of high-risk areas and avoiding construction in those areas.

Definition of high-risk areas is a complicated process which includes mapping faults, dating movement on them to determine whether they are or might still be active, calculating theoretical maximum possible earthquake intensity for active faults, and predicting effects of possible earthquakes on sediments and rocks in the area. This information is then used to judge the safety of the area for construction.

Beginning in 1996, the U.S. Geological Survey prepared a new series of national seismic hazard maps. These maps show the severity of expected earthquake shaking for a particular level of probability. An example of such a map is shown in figure 37, which shows peak acceleration levels (% g, where g is the acceleration due to gravity) with a 10% chance of being exceeded in a 50-year period.[49]

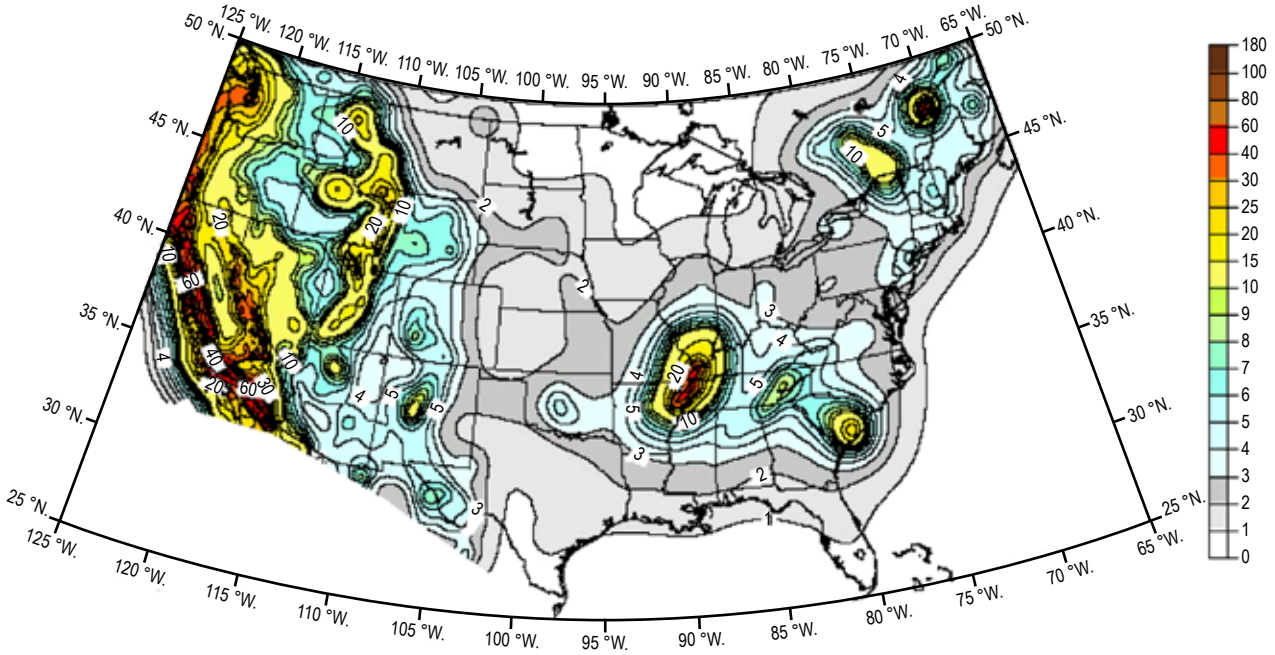

Figure 37. Peak acceleration with 10% probability of exceedance in 50 years (courtesy of the U.S. Geological Survey).

2.11.2 Tsunamis and Seiches

Tsunamis are seismic sea waves. Submarine earthquakes that suddenly elevate or lower portions of the sea floor, submarine landslides, or submarine volcanic eruptions can generate tsunamis. Tsunamis travel on the order of 500 km/hr (1,640.4×10^3 ft/hr) and can cross an ocean in <1 day. Their wavelengths are long: 100 to 200 km (53.9 to 107.9 nmi). Their amplitudes in deep water are low (<1 m (<3.3 ft)) but, as they approach a shoreline, their large volume of water piles up into sizable tidal waves. Configuration of the shoreline and tidal and wind conditions can help to form waves over 10 m (32.8 ft) high. In 1948, the U.S. Coast and Geodetic Survey established a seismic sea wave warning system for the Pacific Ocean. As a result of this warning system, the arrival of tsunamis from distant sources can now be anticipated by a few hours.

A seiche is a long surface wavelength standing wave occurring in an enclosed body of water. Its period can vary from a few minutes to several hours and is very dependent on the dimensions of the basin, pond, lake, or enclosed bay. Commonly, seiches are low in amplitude and are not noticeable. Large-amplitude waves occur when a large-scale disturbance takes place and can continue to be reflected back and forth across the body of water for hours or days. Large seiches can be caused when tsunamis arrive in bays, or when earthquakes and large slope movements initiate them in an enclosed body of water. Seiches can also cause the piling up of water at one end of a lake or bay, given the proper steady wind conditions blowing over the lake. Near enclosed bodies of water, investigation of possible damaging seiche activity should be considered as a part of earthquake and slope movement studies.

2.11.3 Volcanic Hazards

Volcanic hazards fall into two categories: hazards near the volcanic activity and hazards distant from it.[50,51]

2.11.3.1 Hazards Near Volcanic Activity. Within a few tens of miles of a volcanic center, hazards include: lava flows, nuées ardentes (hot ash flows) and poisonous gases, ash falls and bombs, earthquakes, debris, and mud flows.

Some lava flows are much more dangerous to man than others. Lava flows vary a great deal in viscosity, depending on their chemistry and temperature. They can be up to 10 m (32.8 ft) thick, traveling 1 m (3.3 ft) per hour, or they can form a sheet as thin as 1 m (3.3 ft) that travels up to 50 km/hr (1.6×10^5 ft/hr). The latter type has been the most hazardous to man in the past. A trained geologist can predict, to some extent, the type of flow most likely to occur in a given volcanic area. If fast fluid flows are likely, guiding levees can be built to shunt them away from populous or otherwise valuable areas.

Nuées ardentes are heavier-than-air gasborne flows of incandescent volcanic ash released during explosive volcanic eruptions. Temperatures in the flows reach 800 °C (1,472 °F) and the gases that carry them may be poisonous. The gasborne flows are extremely dense. Their physical force is great enough to snap large trees and crumble strong buildings. It was a nuée ardent from Mt. Pelée that devastated St. Pierre, Martinique, in 1902, completely destroying the town and killing an estimated 40,000 people. Hot, dense, poisonous gases can also be emitted without ash.

Ash falls in the immediate vicinity of a volcano can be up to a few tens of meters deep and very hot. Near the eruption center, ash falls may contain sizable volcanic bombs of solid or solidifying rock, as well as pebble-sized fragments of pumice. They may give off gases for some time.

Earthquakes usually accompany volcanic activity and often trigger debris flows and mud flows. Debris flows and mud flows form from the unconsolidated material that makes up the flanks of active stratovolcanoes (composite volcanoes). The material becomes unstable because of doming of the volcano, rapid melting of snow by hot ash or lava, and/or percolation of hot volcanic gases through snow masses. Volcanic mud and debris flows have been known to travel 80 km (43.2 nmi) at speeds of several tens of kilometers per hour. Some flows from major volcanoes contain on the order of 2 to 4 km^3 (0.5 to 0.9 mi^3) of material. Dams in the paths of mud flow may break and contribute to the volume of flows that overtop them. In some places, where a mudslide hazard has been recognized, dams have been built and reservoirs kept empty to absorb them. In addition to downstream damage, volcano-caused landslides can cause instability at their point of origin. When a large volume of material is removed suddenly from the flank or summit of an active volcano, pressure is released and an eruption may be triggered (as in the May 18, 1980, eruption of Mount St. Helens).

2.11.3.2 Hazards Distant From Volcanic Activity. Far from volcanic centers, volcanic ash and tsunamis can still be serious hazards. An ash falls' total volume depends on the size of the eruption that caused it. Its distribution depends on the elevation reached by the volcanic cloud

and on wind conditions at the time of the eruption. A sizable ash fall can damage areas several hundred kilometers from the eruption site. Ash is detrimental to human health and damaging to mechanical equipment. It reduces visibility if there is wind or traffic and must be removed from buildings and pavement. Fine ash, if it reaches the stratosphere, may remain there for months or years, affecting climate by reducing insulation.

Tsunamis can result from submarine volcanic explosions and debris slides, which can travel thousands of kilometers from the volcanism that caused them. They endanger life and all coastal construction within 40 m (131.2 ft) of sea level.

When considering volcanic hazards, it is important to realize that, in any area, volcanism is sporadic. A volcanic area that has been inactive throughout historic times may reawaken to violent activity in a few days or weeks or it may remain inactive for centuries into the future. Earthquakes, almost always felt or recorded several days or weeks before activity commences, serve as a warning of impending danger. Once volcanism commences, the danger is greatest within a few tens of kilometers of the eruption. The effects of volcanism can easily be catastrophic, especially since volcanoes are virtually uncontrollable by man. Important construction should not be located in the immediate vicinity of active or dormant volcanoes or in areas likely to be affected by distant volcanism.

2.11.4 Geology and Geologic Hazards at the Eastern Range

2.11.4.1 Geology. The ER, on the eastern coast of the Florida peninsula, covers an expanse of barrier bars, swamps, and lagoons between the Atlantic Ocean and the mainland. The entire area of KSC lies within 80 m (262.5 ft) of sea level. Surficial deposits on the center of the ER are roughly 30 m (98.4 ft) of Miocene to recent shelly sand and clay and medium- to fine-grained sand and silt.[52] These sediments overlie Eocene limestone and dolomite.

2.11.4.2 Earthquakes. Earthquakes are extremely unlikely in this area of the United States.

2.11.4.3 Tsunamis and Seiches. Tsunamis (sea waves) induced by earthquakes and/or volcanism elsewhere could be a hazard to the entire ER because of its low elevation. However, tsunamis are not common in the Atlantic Ocean and, although not impossible, are considered unlikely. The lagoons and rivers are also unlikely to develop seiches.

2.11.4.4 Volcanic Hazards. Volcanism near the ER is unknown in recent times. The only volcanic hazards to the ER are tsunamis caused by distant volcanism.

2.11.4.5 Summary. The ER is a low-risk area for geologic hazards. Only flooding due to hurricanes or seismically-induced waves is considered to be of possible importance. Dikes can protect crucial structures that would not survive high water.

2.11.5 Geology and Geologic Hazards at Edwards Air Force Base

2.11.5.1 Geology. Rock materials of three distinct age groups[53] cover EAFB. The oldest rocks are pre-Tertiary (formed more than 65 million years ago) granite intrusive and metamorphic units. These rocks are similar in age and composition to the Sierra Nevada Batholith. They form most of the ridges and hills within the Air Force Base boundaries.

Minor amounts of Tertiary age rocks (2.6 to 65 million years old) are exposed at EAFB. Most of these rocks are dikes and sills of fine-grained rock. A few volcanic flows and pyroclastics, with interbedded sediments, crop out along the eastern boundary of the base. Some bentonite layers occur within the sedimentary units. Although the dikes and sills form stable slopes, some of the slopes covered by the pyroclastic and sedimentary interbeds are unstable.

Most of the terrain within the boundaries of EAFB is covered with thick units of Quaternary and Recent (less than 2.6 million years old) unconsolidated and weakly consolidated materials, which include alluvial sand and gravel, beach dunes and bars, playa clays, windblown sands, and older, partly consolidated gravels. These deposits generally occupy areas of low relief.

Alluvial sand and gravel, deposited by flowing water, form channel and fan deposits. Wave-deposited bars and wind-deposited dunes occur along the northern 'shore' of Rogers Lake. Minor clay balls occur in the wave-deposited bars. Windblown sand forms small dunes elsewhere within the base and also covers parts of the desert floor with a thick veneer of sand.

The playa clays are mudflat facies of the alluvium. They are hard when dry but become soft and sticky when wet. Studies by Droste[54] found that playa clays from Rogers Lake consist of 40% to 50% montmorillonite and 40% to 50% illite. Clays from Rosamond Lake consist of 20% to 30% montmorillonite, 50% illite, and 20% to 30% chlorite. Although in the desert climate thorough wetting of the playas is rare, these high-montmorillonite clays are subject to severe swelling and shrinking, which should be considered when planning construction activities near the dry lake beds.

Several high-angle, northwest-trending faults have been mapped in the southern and eastern parts of the EAFB. They have small displacements and seem to edge granitic domal features. The faults are at present inactive.

2.11.5.2 Earthquakes. There were no recorded earthquakes with epicenter magnitude of 4 or greater at EAFB or within 40 km (21.6 nmi) of the base between 1910 and 1974.[55,56] The base is located on a relatively stable wedge between the San Andreas and Garlock Faults, both of which are less than 64 km (34.6 nmi) from the base. The proximity of these major active faults indicates regional tectonic instability.

The likelihood of surface fault rupture at the EAFB Dryden site is considered to be very remote. However, it cannot be dismissed completely because it is not presently known if any buried faults underlie the site which may belong to the group of Mojave block faults. Another risk, albeit a low one, is the possibility of sympathetic movement of these possible underlying faults in response to large motions from a great earthquake on the San Andreas Fault, including fault rupture extending to the ground surface.[48]

It is recommended that facilities that are to be constructed at EAFB be evaluated for their resistance to the two following types of earthquakes:[57]

(1) A magnitude 8.5 event on the nearest approach of the San Andreas Fault, approximately 47 km (25.4 nmi), would impose an acceleration of 0.4 g on the site with a bracketed duration of 40 s. It is suggested that a scaled trace of the N21E component of the Taft accelerogram of the 1952 Kern County earthquake is an adequate model.

(2) A near-field magnitude 4.5 event from a Mojave Block Fault would impose an acceleration of 0.2 g at the site with a short-bracketed duration of 6 s. It is suggested that the unscaled trace of the Lake Hughes No. 4 S69E component from the San Fernando Valley earthquake of 1971 be used as an appropriate model.

2.11.5.3 Volcanic Hazards. No volcanic hazards are expected to affect this area.

2.11.5.4 Conclusions. EAFB, though mostly underlain by granite, is 65% covered by Pleistocene and recent unconsolidated sand, clay, and gravel. Despite the proximity of major active faults, seismic risk is low. Slopes are generally <10%; as a result, geologic hazards from slope processes are localized and most likely restricted to steep slopes consisting of weakly consolidated fanglomerate.

Approximately 30% of the Air Base is covered by unconsolidated clay-rich material. The clays include a high proportion of montmorillonite and are susceptible to expansion and shrinking. However, low precipitation of the Mojave Desert region greatly reduces the potential for such problems.

In summary, EAFB is located in a geologically low-risk area.

2.12 Terrestrial Ionizing Radiation Environments and Effects

In the course of performing any space mission, whether manned or unmanned, the electronics systems will be exposed to various forms of ionizing radiation. This exposure not only varies with the physical location of the spacecraft, but can also vary with time. So knowledge of the dynamic ionizing radiation environments, both terrestrial and in space, and their effect on electronic systems is critical to a successful mission.

There are various sources of ionizing radiation around the Earth; these are divided into trapped and transient environments. Surrounding the Earth is a magnetic field that traps electrons and protons, forming what are called the Van Allen Belts. Since these belts only exist in the space region surrounding the Earth, the discussion on this source of ionizing radiation will be covered in more detail in the appropriate sections later in this TM.

The transient ionizing radiation environments are ones that can impact the terrestrial environments. These sources are solar particle events (SPEs) and galactic cosmic radiation (GCR) and are sources of protons and heavier ions that can impact systems flying in space and also impinge on the upper atmosphere and generate the natural environment of ionizing radiation that is seen in the atmosphere and on the ground.

In addition to the solar particle event (SPE), the Sun does produce another ionizing radiation environment called the solar wind. The solar wind consists of significantly lower energy electrons and protons than seen in SPE, GCR, and the trapped belts. While the solar wind environment is important for spacecraft charging issues, it is not energetically significant for electronic systems and does not yield any significant ionizing radiation environments in space or the atmosphere.

The source for solar ionizing radiation environments pertinent to the terrestrial ionizing radiation environment are SPEs. When a magnetic disruption in the solar photosphere occurs, a variety of radiation types and energies will erupt into space from the Sun. SPEs can produce energetic protons and heavy ions that will produce effects in electronics. An important influence on solar particle radiation, and all transient environments, is the Earth's magnetic field. The magnetic forces that cause charged particles to be trapped will also act on charged particles in an event from the Sun. For a given magnetic field strength, a particle of sufficient energy is required to penetrate that magnetic field. All lower energy particles are deflected along the magnetic field lines. This magnetic screening can offer significant protection for satellites in low inclination, low altitude Earth orbits. This screening is not seen at higher inclinations as the magnetic field lines terminate at the Earth's poles and the low energy particles that are deflected along the field lines will eventually reach these regions.

The next source of ionizing radiation is GCR consisting of electrons, protons, and heavy ions (charged particles with atomic numbers >1) that are believed to have an origin outside the solar system and to be omnidirectional in all regions of space. This radiation source can be significant in the near-Earth environment. The GCR is affected in the same manner as solar particles due to the effects of the Earth's magnetic field (i.e., low altitude equatorial orbits will receive significant screening, while higher inclination or altitude receive less).

Detailed descriptions of SPE and GCR environments can be found in references 58 and 59.

2.12.1 Terrestrial Ionizing Radiation Environments

As pointed out above, there are sources of high-energy protons and heavy ions that are constantly hitting the upper atmosphere of the Earth. These ions can undergo collisional interactions with nuclei of the atmosphere and generate a cascade of secondary particles that will continue to transit the atmosphere and possibly produce additional secondary and tertiary particles. A cartoon depiction of a typical cascade is shown in figure 38. Open circles in this figure show a location where an interaction occurs and the spray of particles that exit are shown by the labeled solid lines. An important take-away from figure 38 is that the production of neutrons can be significant.

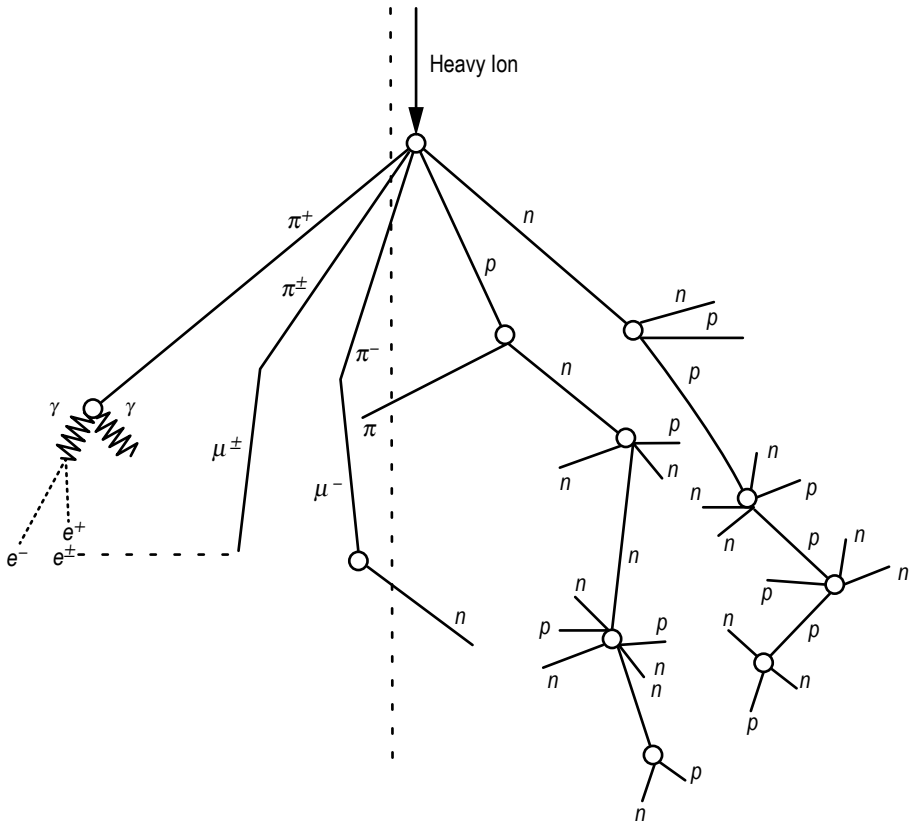

Figure 38. Cartoon depiction of a nuclear cascade event initiated by a high-energy heavy ion and yielding a distribution of atmospheric neutrons.

A second point to take away is that there are a number of interaction locations that yield these 'atmospheric' neutrons; therefore, it is expected that there will be a distribution of the quantity of these neutrons as a function of altitude. If it is also considered that the quantity of the atmospheric neutrons is directly dependent on the quantity of incident particles producing the cascade, then there are two other parameters that drive the atmospheric neutron population.

The first parameter that is considered in addition to altitude when evaluating the atmospheric neutron population is latitude. As discussed previously, the Earth's geomagnetic field provides a shield for the Earth from the high-energy heavy ions that are incident on it. The magnetic field lines can be approximated as a dipole magnet with the filed lines terminating at the Earth's north and south magnetic poles. Using this model, the magnetic field strength diminishes as the poles are approached which would yield less shielding. Therefore, the quantity of the incident ions would be larger as the magnetic poles of the Earth are approached. Or stated another way, the higher in latitude, the larger the incident ion population and therefore the larger the atmospheric neutron population.

In addition to altitude and latitude, the atmospheric neutron population is also driven by the solar activity. The solar activity impacts the incident ion population in two manners. The first, and most obvious, is when the Sun produces a solar particle event. In addition to the significant

increase in the incident ion population, depending on the type and strength of the SPE, the geomagnetic field can be impacted, allowing for deeper penetration at lower latitudes. The second way the solar activity has an effect is through the Sun's 11-year cycle of solar activity. The Sun has an 11-year cycle that for 7 of the 11 years, the activity of the Sun is at a high level and is referred to as solar maximum conditions. This is the time period where SPE probability is at their highest levels. Also during this time, due to the high energy output of the Sun, the GCR population incident on the Earth is reduced due to an increased solar wind population and a stronger solar magnetic field. Similarly, during the solar minimum conditions, the low energy output of the Sun does not provide the same level of shielding for the Earth, and the GCR population incident on the Earth is increased.

A simplistic model[60] was initially developed to predict the atmospheric neutron flux by assuming that the three factors affecting it (altitude, latitude, and solar activity) could be addressed independently.

A plot of how the neutron population varies as a function of altitude in this simplistic model is shown in figure 39. It can be seen from this figure that the neutron flux is a peaked function of altitude. This can be understood using the cartoon from figure 38. This figure shows that the significant portion of the neutron production occurs in the secondary and tertiary cascade events that occur lower in the atmosphere. This accounts for the rise in flux going from high to lower altitudes. The decrease in flux beyond the peak for lower altitudes is due simply to the range the incident ions have in the upper atmosphere. Only the highest energy incident ions can penetrate the atmosphere to sufficient depths to produce neutrons at low altitudes and on the Earth's surface. The population of these ions is significantly smaller than lower energy particles and therefore would yield a lower neutron flux.

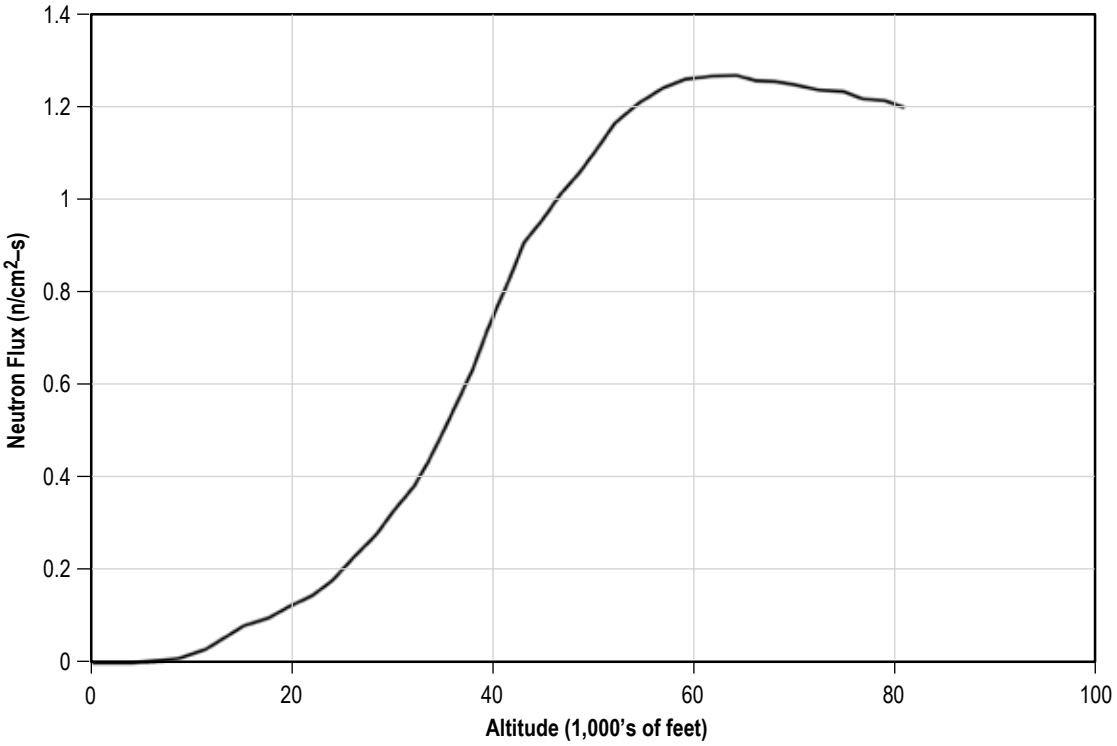

Figure 39. Plot of the atmospheric neutron population as a function of altitude. The peak environment is at an altitude of approximately 18.3 km.

The effect of the second parameter, latitude, is shown in figure 40. The effect shown here is what is expected based on the understanding geomagnetic field strength as a function of latitude. Up to about 30–40 deg of latitude, there is little increase in the neutron flux since the magnetic field strength is near maximum to this point. Also, above about 55 deg latitude, the magnetic field strength has diminished sufficiently to allow maximum neutron production, so little change is seen above that level. The middle region is just the transition between these two extremes.

The final parameter in the simplistic model is the solar activity. Since the three parameters are being considered independent, the effect of solar activity on the magnetic field strength is ignored. This allows the effect of solar activity to be nothing more than a scaling factor since the only effect is a higher incident ion rate.

This simplistic model gives a good qualitative understanding of the atmospheric neutron production. Since the three parameters are not really independent and the fact that the neutron flux is not just a single number but is a neutron energy spectrum at each location, a more detailed model is needed to properly predict the environment. Details of the measurement techniques and the modeled ground neutron energy spectra are contained in reference 61.

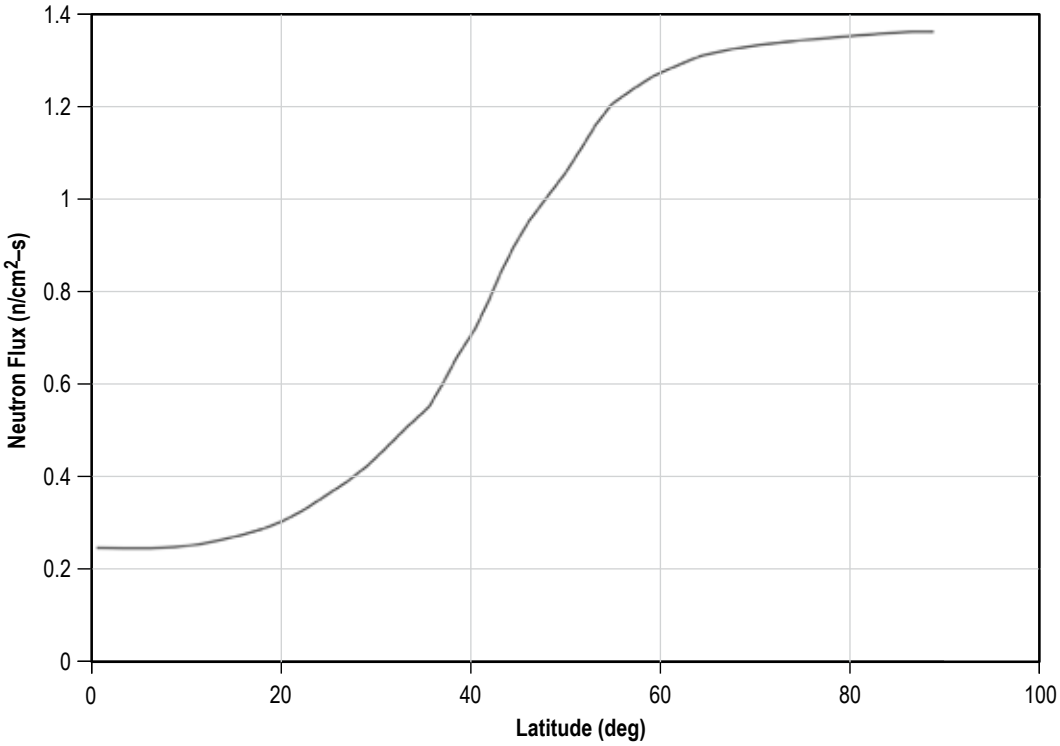

Figure 40. Plot of the atmospheric neutron population as a function of latitude. The peak environment is at high latitudes where the incident heavy ions have less geomagnetic screening.

2.12.2 Ground Environments

The average flux at sea level for the latitude/longitude of New York City (Joint Electron Device Engineering Council reference location) for >10 MeV neutrons is approximately 13 n/cm^2-hr. Differential energy spectra for selected energy ranges for any location can be estimated from the spectra available for the reference location.[61,62] SPEs generate an increase in neutron flux but do not generate direct ionization on the ground. However, measurements show increases of neutron flux as much as a factor of 30 from a large solar event in polar latitudes.[63]

2.12.3 Terrestrial Ionizing Radiation Effects

The effects of ionizing radiation on electronic systems can be divided into two categories: cumulative effects and transient effects. Cumulative effects are those that require exposure to the environments over time to produce an effect. Transient effects are those that can be induced at any time during a mission and can require nothing more than a single particle passing through an electronic device to produce the effect (that can either be temporary or permanent). Since the exposure time in the terrestrial environments is short and the ionizing radiation levels are small as compared to those in space, the cumulative effects for the terrestrial segments of a mission are negligible and will not be discussed here.

The only transient effect that is applicable to space systems is a single event effect (SEE). SEEs are effects in microelectronics that are induced by the passage of a single particle through the part. This is the area where neutrons, protons (both from trapped environment and solar particle events), and galactic cosmic radiation are important. SEE is a generic term encompassing all possible effects. Over the years that effects of single particles have been investigated, many acronyms were devised to indicate the effects caused by these single particles. The most common of these are single event upset (SEU) and single event latchup. With the wide range of effects and associated acronyms, it is accepted in the radiation effects community to refer to SEE, then draw the distinction between destructive and nondestructive events.

For protons and heavier ions the primary means of producing SEE is through interaction with the electrons of the material in the electronic component. This interaction occurs as the ion deposits energy in the material and the electron in the semiconductor material are raised sufficiently that they become available for conduction across the various junctions that are the structure of the electronic component.In short, the energy deposited produces stray currents within the device that may or may not produce an effect.

Neutrons and high-energy protons have another means of depositing energy in the devices, i.e., through direct nuclear interaction with the materials in the electronic component. In this case, the neutron or proton is captured into a nucleus where its energy is deposited. The most likely result of this interaction is that the nucleus expels the incident particle (at a lower energy) and recoils with the remaining energy. The recoiling nucleus does not have sufficient energy to produce a SEE but this type of interaction can be a significant contributor to a cumulative effect that will be discussed later. However, in approximately 1 in 10^4 nuclear interactions, the energy deposited in the nucleus will be sufficient to produce a spallation event, where the nucleus splits into larger atomic number fragments that can have sufficient energy to produce a SEE by the same ionization process described above for ions. More detailed descriptions of SEEs and the means by which they are produced can be found in reference 64.

Therefore, for the terrestrial environments that a space vehicle will encounter, the cumulative effects of ionizing radiation will not be significant. However, the electronic systems will be exposed to environments that can produce SEEs either through direct ionization interactions or through spallation events. Since this type of effect can occur at any time during a mission, and the effect may be nondestructive or destructive, it is imperative that these environments be considered for systems exposed during this segment of a mission.

2.12.4 Ground-Based Effects

While on the ground the only environment that a space vehicle will be exposed to is that population of atmospheric neutrons that reach the ground. While this is a relatively small environment, the electronics will be susceptible to these effects at any time they are powered. This can be a substantial amount of time during all the prelaunch operations. These types of events have been observed during the testing of the shuttle flight computers. Since current technology devices are much more susceptible to these types of effects than those used during the shuttle program, it is important that the electronic systems be analyzed for the effects of atmospheric neutrons while on the ground. Detailed treatment of atmospheric neutron effects on avionics can be found in reference 65.

3. TERRESTRIAL ALOFT ENVIRONMENTS

This section provides a baseline description of the natural terrestrial aloft environment (150 m to 90 km (492.1 to 295.3×10^3 ft)). A summary of key design factors for the aloft environment is displayed in table 49.

Table 49. Summary of key design factors.

Parameter	Source	Select Based On
Winds aloft: ascent/descent trajectories	Sections 3.1, 3.1.1, 3.1.1.1, and 3.1.2.1; figures 41 and 42	Location, season, altitude
Turbulence/wind gusts: In-flight wind perturbations	Sections 3.2, 3.2.1, and 3.2.2	Altitude, length scale
Solar radiation	Section 3.3	Altitude
Temperature	Figures 48 and 49; tables 55 and 56	Location, altitude
Pressure	Figures 50 and 51; tables 57 and 58	Location, altitude
Density	Figures 52 and 53; tables 59 and 60	Location, altitude
Humidity	Figures 55 and 56; tables 61 and 62	Location, altitude
Concentrations, altitude	Section 3.8.1; table 63	Altitude
Particle type, characteristics	Section 3.8.2; table 64	Altitude
Atmospheric models	Sections 3.9, 3.9.1–3.9.6; Earth-GRAM 2010: GUACA, MAP, MET, and RRA	Location, season, altitude
Clouds	Section 3.10	Location, season, altitude
Ionizing radiation: atmospheric neutron environment	Section 3.11.3	Critical device neutron upset threshold, latitude, altitude
Ionizing radiation: atmospheric GCR environment	Section 3.11.2	Critical device upset or latch threshold, latitude, altitude

3.1 Winds Aloft

The winds aloft are a critical factor in the design and performance of vehicles. In-flight wind profiles are needed for all stages of the vehicle design process. A basic requirement is to define an annual design reference wind profile that will be applied (along with the annual design reference atmosphere) in the development of the design reference ascent and descent reference trajectories. The databases for this basic requirement are included in NASA/TM—2008–215633.[1] When system component designs have been integrated to define a vehicle for the selected architecture, wind profile databases are required for application in design vehicle ascent trajectory simulations to establish the dispersion of trajectory variables relative to winter and summer month design reference trajectories. Developers of the vehicle's guidance and control systems and structural elements either design the vehicle to withstand the trajectory dispersions, protect the vehicle from dispersions using

operational constraints, or accept the risk of encountering the dispersions. If aerodynamic dispersion attributed to the wind environment cannot be safely accommodated with available technology, the vehicle design process will determine the need for operational constraints to achieve vehicle performance objectives. Likewise, the risk of encountering the wind environment can be accepted if neither vehicle design nor operational constraints mitigate the dispersion.

Analyses and models of in-flight winds are included in NASA/TM—2008–215633.[1] Selected information in the handbook could be useful for special engineering studies other than vehicle trajectory simulations to establish the capability of vehicle systems to withstand certain characteristics of the wind profile. This extensive information, which includes historical and alternative methods for defining characteristics of ascent wind profiles, may not be universally applicable to methodologies used in the vehicle design process.

When trajectory simulations are based on a representative sample of wind profiles, all the characteristics of the wind profiles are included and need not be analyzed piecemeal, independent of the vehicle flight simulation. Computational speed, which was a serious impediment to multiple simulations of vehicle trajectories in the early history of spacecraft development, now permits a trajectory simulation in seconds on a desktop computer compared to 'overnight' during the NASA Saturn/Apollo program.

3.1.1 Eastern Range

Wind profiles for in-flight design studies are either modeled or measured. Both are available for the ER. The monthly vector wind profile (MVWP) model, outlined in section 3.1.1.1, has been developed for ascent from the ER (0 to 27 km (0 to 88.6×10^3 ft)) and EAFB (0 to 25 km (0 to 82×10^3 ft)), and could be developed for any proposed launch site that has a statistically representative sample of rawinsonde profiles. A sample of measured high-resolution Jimsphere wind profiles has been traditionally applied in design evaluation flight simulations to determine the operational capability of a launch system. An adequate sample of Jimsphere wind profiles for this application exists only for the ER. In addition, the MSFC Natural Environments Branch has developed an archive of measurements from the KSC 50-MHz and 915-MHz Doppler radar wind profiler (DRWP) network, which contains high temporal and spatial resolution measurements from 0.3 to 18.6 km (656 to 61×10^3 ft). The utility of modeled or measured profiles, to be established by consultation with the design community, is related to (1) the complexity of wind representation required for the vehicle design application and (2) the flexibility for use in design trade studies.

Extensive measurements of winds aloft have been made at the ER through the use of rawinsondes, Jimspheres, and DRWPs to provide vertical profiles of winds. A sample wind profile contains mean wind, fine structures, and turbulence/gusts superimposed over a general trend. These measurements have provided insight into the temporal variability in winds aloft and aid in defining the wind environment the vehicle will be exposed to along a flight trajectory. Research has been performed to study the lifetime of wind features aloft measured by the instruments listed above for the purpose of determining how long before launch the measured winds accurately depict the environment through which the vehicle will travel.[66,67] The length scale of features that are above a predetermined coherence scale increases as the time between measurements increases.

3.1.1.1 Monthly Vector Wind Profile Model (0 to 27 km (0 to 88.6×10^3 ft)). The basic application of the MVWP model is for evaluation of design vehicle aerodynamic load indicator dispersion attributable to wind profile dispersion during the ascent phase.[66,67] The February and July MVWP model profile dispersion encompasses the wind profile dispersion for the entire year. These profiles are used in vehicle rigid body trajectory simulations for vehicle trade studies, development of vehicle guidance and control systems, and establishment of propellant requirements and reserves. For a selected reference altitude H, the model constructs 12 wind profiles that envelope the monthly wind vector dispersion at that altitude for a selected probability level. The construction process, based on quadravariate normal statistical probability functions, produces vectors at all the adjacent altitudes.

Note: For indicators, as used above, $q\alpha$ and $q\beta$, where q is aerodynamic pressure, α is angle of attack, and β is angle of sideslip.

Given a wind vector at H, the wind vectors at each altitude above or below H are conditional bivariate normal distributed. The given wind vectors at H are defined at 30° increments on the 99th percentile monthly wind vector ellipse relative to the vector of the monthly means at H. The conditional wind vectors at all adjacent altitudes that intercept the 99th percentile conditional wind vector ellipse 180° from the direction of the given wind vector approximate the largest wind vector shear between H and each selected adjacent altitude. The 12 profiles (zero to 27 km (zero to 88.6×10^3 ft)) for the ER illustrated in figure 41 are the in-plane and out-of-plane wind components, x and y, for a 90° flight azimuth during February for $H=9$ km (29.5×10^3 ft). In-plane and out-of-plane components are defined in reference to the vehicle pitch plane. The wind components, x and y, are calculated from the u and v wind components. These profiles are constructed for the 99th percentile wind vector dispersion at 9 km (29.5×10^3 ft) and from the 99th percentile conditional probability ellipses at all other adjacent altitudes. Similarly, but not illustrated herein, a total of 336 profiles are constructed from the ER rawinsonde statistical database, when all 28 of the available reference altitudes (zero to 27 km (zero to 88.6×10^3 ft)) are used.

The extreme profiles of the February and July mean in-plane and out-of-plane wind components can be applied in the development of the monthly Vehicle Ascent Guidance Steering Commands (VAGSC) used in the trajectory simulations for the corresponding monthly sets of MVWP model profiles. The trajectory simulation using either of these profiles of mean wind components produces the baseline aerodynamic load indicators at each altitude for the selected month. The aerodynamic load indicators (12 values of q, α, and β) derived from trajectory simulations using the 12 vector wind profiles for a selected reference altitude (for a particular month) represents the dispersion from the baseline at that altitude.

As evidenced by Space Shuttle and Department of Defense launch vehicle operational procedures, the aerodynamic load indicator dispersion can be greatly reduced by using a day of launch (DOL) wind profile for the VAGSC. The reduction of aerodynamic loads dispersion attributable to wind profile dispersion has allowed present vehicle programs to achieve performance and operability objectives.

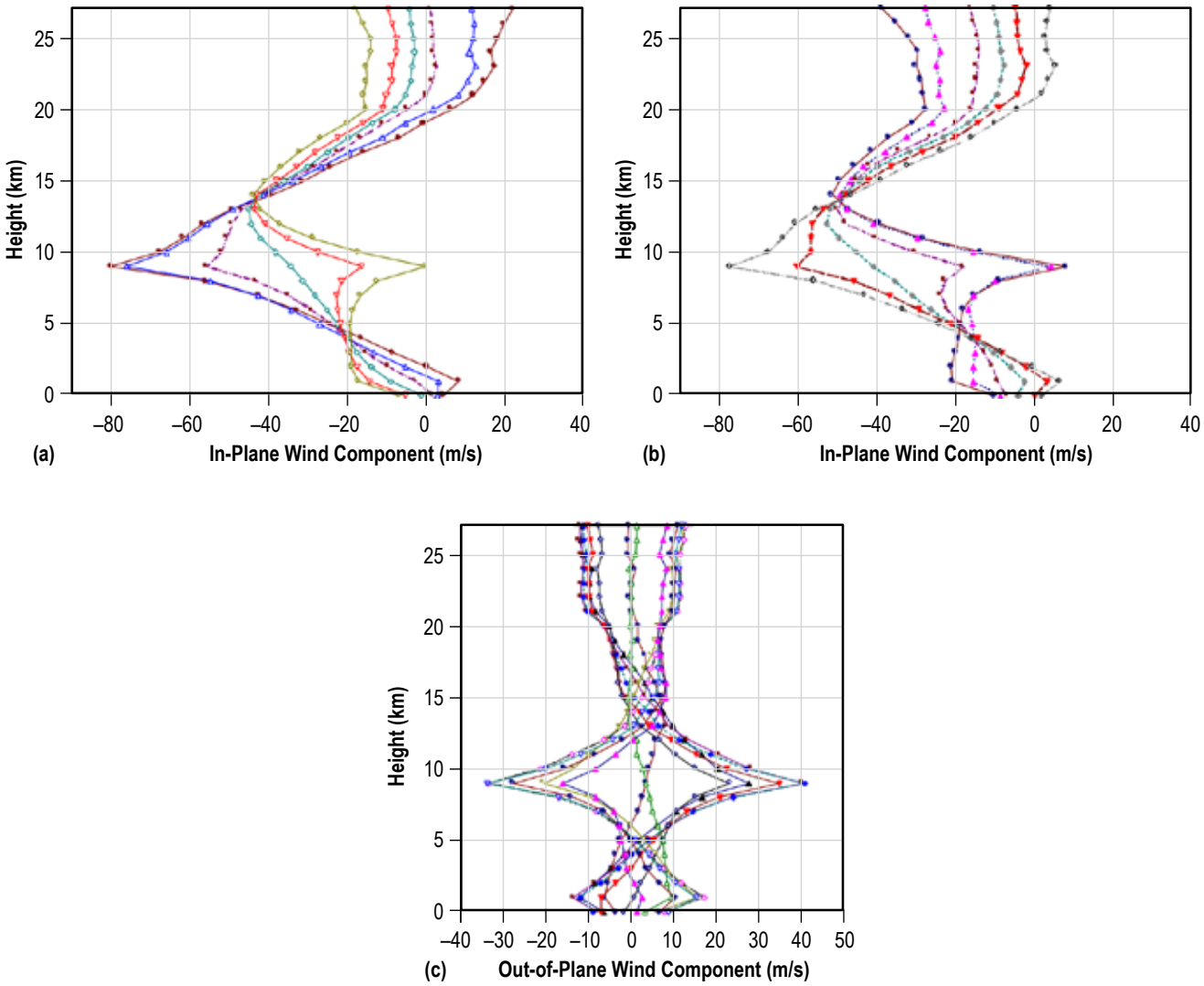

Figure 41. Twelve vector wind model profiles, the ER, February, reference height = 9 km (29.5×10^3 ft), wind components (m/s), flight azimuth = 90°: (a) In-plane (x), profiles 1–6, (b) in-plane (x), profiles 7–12, and (c) out-of-plane (y), profiles 1–12.

The wind profiles generated with the MVWP model contain wavelengths as small as 2 km. As illustrated in figure 42, it has been demonstrated, in an application of the original MVWP model during the Space Shuttle program,[68] that adding smaller wavelength wind perturbations or gusts to the model profiles will result in excessive dispersion of rigid body aerodynamic load indicators. This was verified in an application of a later version of the MVWP model.[69] Gusts are treated separately in elastic body dynamic loads analyses using discrete gust models or with simulated gust time series. Gust models are described in section 3.2.

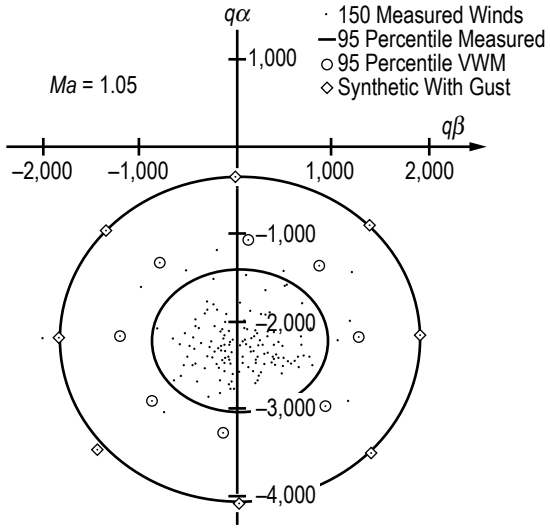

Figure 42. STS-1 pitch and yaw aerodynamic load indicators, $q\alpha$ and $q\beta$ (lb/ft^2 deg), Mach = 1.05, 150 April Jimsphere profiles, ER (addition of gusts to the synthetic wind profiles yields an overconservative result compared to the measured rates).

3.1.1.2 Jimsphere Wind Profile Database (0 to 20 km (0 to 65.6×10^3 ft)). Profiles from the Jimsphere balloon measurement system have been archived for use in flight vehicle ascent loads and trajectory assessments. The database contains sets of individual profiles for each month and profile pairs for the winter, summer, and transition seasons. Individual profiles can be used to examine vehicle loading from both large- and small-scale wind features due to the high resolution of Jimsphere measurements. The Jimsphere pairs database contains wind profiles separated by either 2 or 3.5 hr, and can be used to characterize the effect of wind changes over these intervals to the vehicle during the ascent phase. The Jimsphere archive provides output from zero to 20 km (zero to 65.6×10^3 ft) every 25 m (82 ft).

3.1.1.3 Kennedy Space Center Doppler Radar Wind Profiler Database (0.2 to 18.6 km (656 to 61×10^3 ft)). The MSFC Natural Environments Branch has developed an extensive archive of wind profiles from the KSC 50-MHz and 915-MHz DRWP network.[70] The archive contains wind profiles from 0.2 to 18.6 km (656 to 61×10^3 ft) every 100 m (328.1 ft), and serves the same purpose as the Jimsphere database described in section 3.1.1.2. However, the near-continuous measurement capability of the DRWP systems provides two major advantages to using the DRWP archive over the Jimsphere archive. First, the DRWP database contains a significantly greater number of profiles. Second, engineers can simulate the effects of wind changes to flight vehicles over any practical time interval.

3.1.1.4 High-Altitude Ascent Wind Model (up to 90 km (295.3×10^3 ft)). If required, the measured or MVWP model profiles can be appended with nominal or dispersed wind vectors derived from the Earth-Global Reference Atmosphleric Model (GRAM).[71] For more details on Earth-GRAM, refer to section 3.9.

3.1.2 Edwards Air Force Base

3.1.2.1 Monthly Vector Wind Profile Model (0 to 25 km (0 to 82×10³ ft)). An example MVWP model for EAFB is shown in figure 43. The 12 profiles illustrated in figure 43 are the in-plane and out-of-plane wind components, x and y, for a 90° flight azimuth during February for $H = 9$ km (29.5×10^3 ft). The 90° flight azimuth is shown for consistency with the other sites. Any desired flight azimuth can be produced from the MVWP model. The MVWP model is intended for use during the ascent phase only.

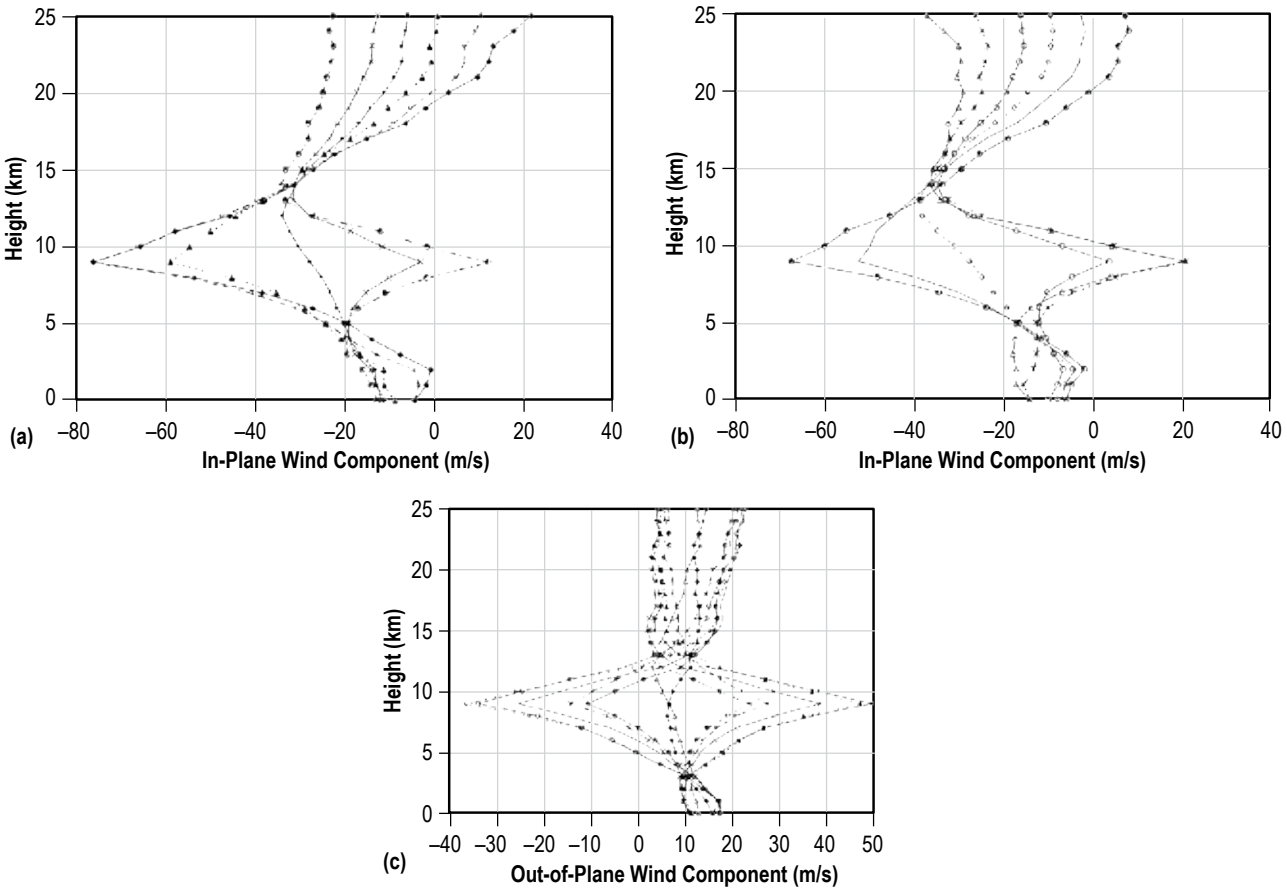

Figure 43. Twelve vector wind model profiles, EAFB, February, reference height = 9 km (29.5×10^3 ft), wind components (m/s), flight azimuth = 90°: (a) In-plane (x), profiles 1–6, (b) in-plane (x), profiles 7–12, and (c) out-of-plane (y), profiles 1–12.[68]

3.1.2.2 High-Altitude Ascent Wind Model (up to 90 km (295.3×10³ ft)). If required, the MVWP model profiles can be appended with nominal or dispersed wind vectors derived from Earth-GRAM.[71] For more details on Earth-GRAM, refer to section 3.9.

3.1.2.3 Low-Level Wind Shear, Eastern Range. An abrupt wind change through a ground-based temperature (radiation) inversion occurs at the ER, especially in winter. Most commonly, strong winds exist at the top of the inversion with light and variable winds existing immediately

below the top. These inversions develop at night, and endure until eroded by daytime surface heating, perhaps by 09:00 to 10:00 LST.

3.1.2.4 Low-Level Wind Shear, Edwards Air Force Base. An abrupt wind change through a ground-based temperature (radiation) inversion occurs frequently at EAFB, especially in winter. Most commonly, strong winds exist at the top of the inversion with light and variable winds existing immediately below the top. These inversions develop at night, and endure until eroded by daytime surface heating, perhaps by 09:00 to 10:00 LST. [72]

3.2 Discrete Gust Model

Idealized discrete gust models have been developed for vehicle design studies and other engineering applications in an attempt to represent, in a physically reasonable manner, characteristics of small-scale wind perturbations associated with vertical profiles of wind velocity. Evaluation of elastic body and buffeting response to in-flight wind perturbations or gusts is important in establishing vehicle design structural requirements and operational capability. In vehicle response analyses, the discrete gust is applied perpendicular to the launch vehicle longitudinal axis, and it is assumed that the vehicle is instantaneously immersed in the time-dependent gust profile.[69] Simulation of the autopilot response to the gust produces the loads that are responses to the gust-induced deviations of the angle of attack and angle of sideslip from the prelaunch programmed vehicle guidance commands. Launch vehicles can have significant response to gusts that are not observable with wind profile measurement systems. Since it is not practical to perform elastic body loads analyses for flight vehicles on DOL because of time constraints and other considerations, the commit to launch decision is protected for gust uncertainty contributions to elastic body loads uncertainties. This protection is in the form of an aerodynamic load increment (knockdown) that is developed in special engineering studies prior to the DOL. Development of the elastic body response to gust is also an important consideration during the vehicle design process, which is the initial intended application of material in this TM.

NASA has used two discrete gust models. The first model is the 'classical-NASA' 9 m/s (29.5 ft/s) quasi-square wave gust originally developed for Saturn/Apollo and certified for Shuttle program applications.[2] The second model[73] is an adaptation of the discrete gust model originally developed from Military Standard (MIL-STD-1797A) for the flying qualities of piloted aircraft,[74] and was developed to improve representation of gusts with half-widths (d_m) less than 100 m (328.1 ft) that had amplitudes that were overly conservative in the classical model. The classical NASA 9 m/s (29.5 ft/s) discrete gust model is considered to be the most conservative because of its quasi-square-wave form. In addition, no provision exists in the classical model for taking into account the expected variation of gust amplitude as a function of gust half-width and altitude. The MIL-STD model that includes such a variation yields smaller gust amplitudes than the classical model for gust half-widths less than 125 m (410.2 ft) at 8 km (26.2×10^3 ft) using severe turbulence criteria, and yields smaller gust amplitudes than the classical model for all gust half widths at all altitudes up to 90 km (295.3×10^3 ft) using moderate turbulence criteria.

3.2.1 NASA Discrete Gust Model

The basis for the derivation of gust magnitude as a function of gust half-width is given in MIL-STD-1797A[74] and its background information and users guide.[75] This MIL-STD is significant because it is based on the same aircraft turbulence data used in studies[76–78] that led to the establishment of the NASA classical 9 m/s (29.5 ft/s) gust. The gust model has the '1-cosine' shape (fig. 44) defined by MIL-STD-1797A:[74]

$$V = 0, d < 0 \text{ or } d > 2d_m, \quad V = \frac{V_m}{2}\left(1 - \cos\left(\frac{\pi d}{d_m}\right)\right), \quad \text{and } 0 \le d \le 2d_m \ , \tag{36}$$

where V_m is the gust magnitude, d_m is the gust half-width, and d is distance.

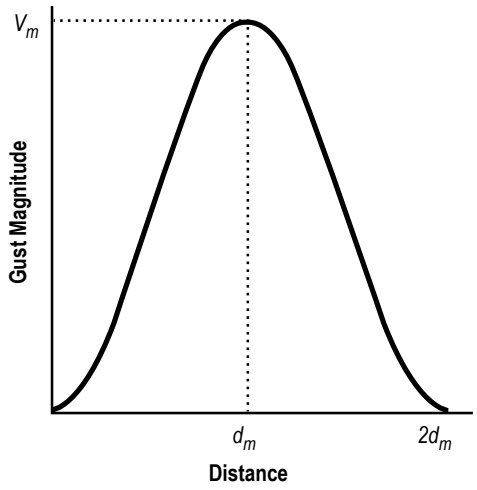

Figure 44. Discrete gust model (1-cosine).

The MIL-STD relationship between nondimensional longitudinal gust magnitude, Vm / σ, and nondimensional gust half-width, d_m /L is illustrated for the longitudinal gust component in figure 45, where σ is the standard deviation of atmospheric turbulence and L is the scale length of atmospheric turbulence. The most recent compilation[79] of these parameters (σ and L) as a function of altitude is presented in table 50 for moderate and severe turbulence. The relationship is derived by assuming gust perturbations are normally distributed about the steady state wind with:

$$f(V) = \frac{1}{\sqrt{2\pi\sigma_V^2}} \exp\left(-\frac{1}{2}\frac{\left(V - \mu_V\right)^2}{\sigma_V^2}\right), \tag{37}$$

where V is the random gust and μ_V and σ_V are the mean and standard deviation of the random gusts.[80,81] An initial gust (V_1) will be related to a gust (V_2) some distance (d) away by the conditional probability:

$$f\left(V_2 \mid V_1\right) = \frac{f\left(V_1, V_2\right)}{f\left(V_1\right)} \ . \tag{38}$$

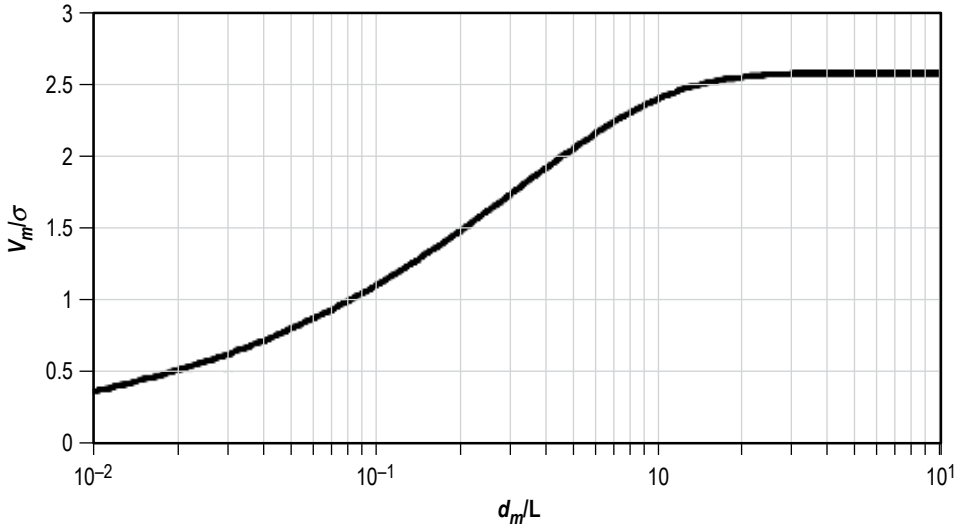

Figure 45. Nondimensional discrete gust magnitude V_m/σ as a function of nondimensional gust half-width, d_m/L, longitudinal component.[74]

Table 50. Mean horizontal (longitudinal) and vertical turbulence standard deviation (σ_h and σ_w) and length scale (L_h and L_w), as a function of altitude.

Altitude MSL		Moderate				Severe				L_h		L_w	
		σ_h		σ_w		σ_h		σ_w					
(km)	(ft)	(m/s)	(ft/s)	(m/s)	(ft/s)	(m/s)	(ft/s)	(m/s)	(ft/s)	(m/s)	(ft/s)	(m/s)	(ft/s)
1	3.28×10^3	1.65	5.41	1.36	4.46	3.9	12.79	3.21	10.53	0.832	2.73	0.624	2.05
2	6.56×10^3	1.65	5.41	1.43	4.69	4.35	14.27	3.78	12.4	0.902	2.96	0.831	2.73
4	13.12×10^3	2.04	6.69	1.68	5.51	6.24	20.47	5.13	16.83	1.04	3.41	0.972	3.19
6	19.69×10^3	2.13	6.99	1.69	5.54	7.16	23.49	5.69	18.67	1.04	3.41	1.01	3.31
8	26.25×10^3	2.15	7.05	1.69	5.54	7.59	24.9	5.98	19.62	1.04	3.41	0.98	3.21
10	32.81×10^3	2.23	7.32	1.73	5.68	7.72	25.33	6	19.69	1.23	4.03	1.1	3.61
12	39.37×10^3	2.47	8.1	1.79	5.87	7.89	25.89	5.71	18.73	1.8	5.9	1.54	5.05
14	45.93×10^3	2.62	8.59	1.91	6.27	6.93	22.74	5.05	16.57	2.82	9.25	2.12	6.96
16	52.49×10^3	2.44	8.01	2.1	6.89	5	16.4	4.31	14.14	3.4	11.15	2.6	8.53
18	59.06×10^3	2.21	7.25	2.07	6.79	4.07	13.35	3.81	12.5	5	16.4	3.34	10.96
20	65.62×10^3	2.26	7.41	1.99	6.53	3.85	12.63	3.38	11.09	8.64	28.35	4.41	14.47
25	82.02×10^3	2.71	8.89	2.09	6.86	4.34	14.24	3.34	10.96	12	39.37	6.56	21.52
30	98.43×10^3	3.73	12.24	2.39	7.84	5.6	18.37	3.59	11.78	28.6	93.83	8.88	29.13
35	114.83×10^3	4.59	15.06	2.58	8.46	6.89	22.6	3.87	12.69	35.4	116.14	8.33	27.33
40	131.23×10^3	5.26	17.26	2.87	9.42	7.89	25.89	4.3	14.11	42.6	139.76	6.2	20.34
45	147.64×10^3	6.22	20.41	3.25	10.66	9.33	30.61	4.88	16.01	50.1	164.37	5.2	17.06
50	164.04×10^3	7.27	23.85	4.21	13.81	10.9	35.76	6.31	20.7	57.9	189.96	5.3	17.39
55	180.45×10^3	8.7	28.54	4.4	14.44	13.1	42.98	6.6	21.65	66	216.54	6	19.69
60	196.85×10^3	10.1	33.14	4.42	14.5	15.1	49.54	6.63	21.75	74.4	244.09	6.8	22.31
65	213.25×10^3	11.3	37.07	4.05	13.29	16.9	55.45	6	19.68	83.2	272.96	7.5	24.61
70	229.66×10^3	15.9	52.17	5.04	16.54	23.8	78.08	7.5	24.61	92.3	302.82	8.2	26.9
75	246.06×10^3	19.2	62.99	6.3	20.67	28.7	94.16	9.5	31.17	102	334.64	9	29.53
80	262.47×10^3	22.6	74.15	8.3	27.23	33.8	110.89	12.4	40.68	111	364.17	9.7	31.82
85	278.87×10^3	27.3	89.57	10.3	33.79	40.9	134.19	15.4	50.52	121	396.98	10.4	34.12
90	295.28×10^3	33.2	108.92	11.8	38.71	49.8	163.39	17.7	58.07	132	433.07	11.2	36.75

Assuming the gust perturbations have zero means, and that the initial gust (V_1) begins at value 0, equation (38) becomes:

$$f\left(V_2 \mid V_1 = 0\right) = \frac{1}{\sqrt{2\pi\sigma^2\left(1-\rho^2\right)}} \exp\left(-\frac{1}{2}\frac{1}{1-\rho^2}\frac{V_2^2}{\sigma^2}\right), \tag{39}$$

where ρ is the correlation between V_1 and V_2. Letting $e^2 = \sigma^2(1-\rho^2)$ and upon integration, equation (39) becomes:

$$F\left(V_2\right) = P\left(x \le V_2\right) = \frac{1}{\sqrt{2\pi e^2}} \int_{-\infty}^{V_2} \exp\left(-\frac{1}{2} \frac{V^2}{e^2} \right) dV \ . \tag{40}$$

Since equation (40) cannot be integrated in closed form, computer routines are needed to compute the inverse of the normal cumulative distribution function. The inverse of equation (40) will provide the desired gust magnitude for a selected risk level.

Typically, computer routines require the probability level, the mean, and the standard deviation as inputs. Since most routines calculate the one-sided probability, the proper value to input for a desired risk level would be $P = 1 - (\text{risk}/2)$, where 'risk' represents the probability of exceeding a desired gust magnitude. A value of zero should be used for the mean and $e = \sqrt{[\sigma^2(1 - \rho^2)]}$ should be used for the standard deviation. To determine e, the value for σ is selected from table 50 for the desired altitude. The correlation ρ is determined by the inverse Fourier transform of the Dryden spectral turbulence model. The equations for the Dryden model for the longitudinal, lateral, and vertical component of atmospheric turbulence are:

• Longitudinal
$$\phi(\Omega) = \frac{2\sigma^2 L}{\pi} \left(\frac{1}{1 + (L\Omega)^2} \right) \tag{41}$$

• Lateral, Vertical
$$\phi(\Omega) = \frac{\sigma^2 L}{\pi} \frac{1 + 3(L\Omega)^2}{\left[1 + (L\Omega)^2 \right]^2} \ , \tag{42}$$

where $0 \le \Omega \le \infty$, σ^2 is the variance, and L is the turbulence length scale. Applying the inverse Fourier transform to equations (41) and (42) provides the autocorrelations:

• Longitudinal
$$R(d) = \exp\left(\frac{-d}{L} \right) \tag{43}$$

• Lateral, Vertical
$$R(d) = \left(1 - \frac{d}{2L} \right) \exp\left(\frac{-d}{L} \right) , \tag{44}$$

where R is the autocorrelation and d is the gust half-width (see eq. (36)). The value L is selected from table 50 for the desired altitude.

Values for V_m (m/s) at a selected altitude for a specified d_m (m) are calculated using the values of σ (m/s) and L (m) (σ_h and $10^3 L_h$, respectively) given in table 50 and the procedure described above. The values in table 50 are based on extensive published data gathered during the 30-year period since the data were gathered for and became the basis of the NASA classical discrete gust model. The authors caution the reader that the caption at the top of the original table (ref. 1, table 2.79b), the source of the values listed in table 50, refers to 'magnitudes (σ_h and σ_w),' but should read 'standard deviations (σ_h and σ_w).' The principal author of the original report[79] has verified this revision.

The derived gust magnitudes for the longitudinal gust component for severe and moderate turbulence as a function of altitude and gust half-width (d_m) are listed in table 51 and table 52, respectively. The longitudinal component is defined as the horizontal gust in the direction of the mean wind. The longitudinal gust is superimposed with the steady state wind to excite vehicle structures in an elastic body simulation model.

Table 51. Discrete longitudinal gust magnitude at the 1% risk level of exceedance as a function of altitude (km) and gust half-width, d_m (m), for severe turbulence.

Gust Magnitude (m/s)										
Altitude (km)	Gust Half-Width (m)									
	30	60	90	120	150	180	210	240	270	300
1	2.65	3.68	4.43	5.03	5.53	5.95	6.32	6.65	6.94	7.2
2	2.84	3.95	4.77	5.42	5.96	6.43	6.84	7.2	7.52	7.81
4	3.81	5.31	6.41	7.3	8.05	8.69	9.26	9.77	10.23	10.64
6	4.37	6.09	7.35	8.37	9.23	9.98	10.63	11.21	11.74	12.21
8	4.63	6.45	7.79	8.88	9.79	10.58	11.27	11.89	12.44	12.94
10	4.34	6.06	7.34	8.37	9.25	10.02	10.7	11.3	11.85	12.36
12	3.68	5.16	6.27	7.18	7.96	8.65	9.27	9.83	10.35	10.82
14	2.59	3.64	4.44	5.1	5.67	6.18	6.64	7.06	7.45	7.81
16	1.7	2.4	2.92	3.36	3.74	4.08	4.39	4.67	4.94	5.18
18	1.14	1.61	1.97	2.27	2.53	2.76	2.98	3.17	3.35	3.53
20	0.82	1.16	1.42	1.64	1.83	2	2.16	2.31	2.44	2.57
25	0.79	1.12	1.36	1.57	1.76	1.92	2.07	2.21	2.35	2.47
30	0.66	0.93	1.14	1.32	1.47	1.61	1.74	1.86	1.97	2.08
35	0.73	1.03	1.26	1.46	1.63	1.79	1.93	2.06	2.18	2.3
40	0.76	1.08	1.32	1.52	1.7	1.86	2.01	2.15	2.28	2.4
45	0.83	1.18	1.44	1.66	1.86	2.03	2.2	2.35	2.49	2.62
50	0.9	1.28	1.56	1.81	2.02	2.21	2.39	2.55	2.71	2.85
55	1.01	1.43	1.76	2.03	2.27	2.48	2.68	2.86	3.04	3.2
60	1.1	1.56	1.91	2.21	2.47	2.7	2.92	3.12	3.31	3.49
65	1.17	1.65	2.02	2.34	2.61	2.86	3.09	3.3	3.5	3.69
70	1.56	2.21	2.71	3.12	3.49	3.82	4.13	4.42	4.68	4.93
75	1.79	2.53	3.1	3.58	4.01	4.39	4.74	5.07	5.37	5.66
80	2.02	2.86	3.5	4.05	4.52	4.95	5.35	5.72	6.07	6.39
85	2.35	3.32	4.06	4.69	5.24	5.74	6.20	6.63	7.03	7.41
90	2.73	3.87	4.74	5.47	6.11	6.69	7.23	7.73	8.2	8.64

Table 52. Discrete longitudinal gust magnitude at the 1% risk level of exceedance as a function of altitude (ft) and gust half-width, d_m (ft), for severe turbulence.

Gust Magnitude (ft/s)										
Altitude (km)	Gust Half-Width (ft)									
	98.4	196.9	295.3	393.7	492.1	590.6	688.9	787.4	885.8	984.3
3.3	8.69	12.07	14.53	16.5	18.14	19.50	20.73	21.82	22.77	23.62
6.6	9.32	12.96	15.65	17.78	19.55	21.09	22.44	23.62	24.67	25.62
13.1	12.5	17.42	21.03	23.95	26.41	28.51	30.38	32.05	33.56	34.91
19.7	14.34	19.98	24.11	27.46	30.28	32.74	34.88	36.78	38.52	40.06
26.2	15.19	21.16	25.56	29.13	32.12	34.71	36.98	39.01	40.81	42.45
32.8	14.24	19.88	24.08	27.46	30.35	32.87	35.1	37.07	38.88	40.55
39.4	12.07	16.93	20.57	23.56	26.12	28.38	30.41	32.25	33.96	35.5
45.9	8.49	11.94	14.57	16.73	18.6	20.28	21.78	23.16	24.44	25.62
52.5	5.58	7.87	9.58	11.02	12.27	13.39	14.4	15.32	16.21	16.99
59.1	3.74	5.28	6.46	7.45	8.3	9.06	9.78	10.4	10.99	11.58
65.6	2.69	3.81	4.66	5.38	6	6.56	7.09	7.58	8	8.43
82	2.59	3.67	4.46	5.15	5.77	6.29	6.79	7.25	7.71	8.1
98.4	2.17	3.05	3.74	4.33	4.82	5.28	5.71	6.1	6.46	6.82
114.8	2.39	3.38	4.13	4.79	5.35	5.87	6.33	6.76	7.15	7.55
131.2	2.49	3.54	4.33	4.99	5.58	6.1	6.59	7.05	7.48	7.87
147.6	2.72	3.87	4.72	5.45	6.1	6.66	7.22	7.71	8.17	8.6
164	2.95	4.19	5.12	5.94	6.63	7.25	7.84	8.37	8.89	9.35
180.4	3.31	4.69	5.77	6.66	7.45	8.14	8.79	9.38	9.97	10.5
196.9	3.61	5.12	6.27	7.25	8.1	8.86	9.58	10.24	10.86	11.45
213.3	3.84	5.41	6.63	7.68	8.56	9.38	10.14	10.83	11.48	12.11
229.7	5.12	7.25	8.89	10.24	11.45	12.53	13.55	14.5	15.35	16.17
246.1	5.87	8.3	10.17	11.75	13.16	14.4	15.55	16.63	17.62	18.57
262.5	6.63	9.38	11.48	13.29	14.83	16.24	17.55	18.77	19.91	20.96
278.9	7.71	10.89	13.32	15.39	17.19	18.83	20.34	21.75	23.06	24.31
295.3	8.96	12.69	15.55	17.95	20.05	21.95	25.36	25.36	26.9	28.35

As shown in tables 51 and 52, the smallest gust half-width (d_m) associated with a 9 m/s (29.5 ft/s) gust assuming severe turbulence is approximately 130 m (426.5 ft) at 8 km (26.2×10^3 ft). This half-width is more than four times larger than the smallest half-width (30 m (98.4 ft)) of the NASA classical 9 m/s (29.5 ft/s) gust. This discussion emphasizes the conservatism of the NASA classical 9 m/s (29.5 ft/s) gust model for gust half-widths <130 m (426.5 ft). Application of the NASA discrete gust model for specification of gust magnitude requires that adequate protection exists for all vehicle response modes, including those for the gust half-widths greater than 130 m (426.5 ft) for which gust magnitudes can be larger than 9 m/s (29.5 ft/s) using severe turbulence. Tables 53 and 54 show that moderate turbulence magnitudes range from 2.7 to 3.7 m/s (8.9 to 12.1 ft/s) in the altitude and half-width regions where the severe turbulence magnitudes exceed 9 m/s (29.5 ft/s), which illustrates the conservatism of using severe turbulence relative to moderate turbulence.

Table 53. Discrete longitudinal gust magnitude at the 1% risk level of exceedance as a function of altitude (km) and gust half-width, d_m (m), for moderate turbulence.

Gust Magnitude (m/s)										
Altitude (km)	Gust Half-Width (m)									
	30	60	90	120	150	180	210	240	270	300
1	1.12	1.56	1.87	2.13	2.34	2.52	2.68	2.81	2.94	3.05
2	1.08	1.5	1.81	2.05	2.26	2.44	2.59	2.73	2.85	2.96
4	1.24	1.73	2.09	2.39	2.63	2.84	3.03	3.19	3.34	3.48
6	1.3	1.81	2.19	2.49	2.75	2.97	3.16	3.34	3.49	3.63
8	1.31	1.83	2.21	2.51	2.77	3	3.19	3.37	3.52	3.67
10	1.25	1.75	2.12	2.42	2.67	2.89	3.09	3.27	3.42	3.57
12	1.15	1.62	1.96	2.25	2.49	2.71	2.9	3.08	3.24	3.39
14	0.98	1.38	1.68	1.93	2.14	2.34	2.51	2.67	2.82	2.95
16	0.83	1.17	1.43	1.64	1.83	1.99	2.14	2.28	2.41	2.53
18	0.62	0.88	1.07	1.23	1.37	1.5	1.62	1.72	1.82	1.91
20	0.48	0.68	0.84	0.96	1.08	1.18	1.27	1.35	1.43	1.51
25	0.49	0.7	0.85	0.98	1.1	1.2	1.29	1.38	1.46	1.54
30	0.44	0.62	0.76	0.88	0.98	1.07	1.16	1.24	1.31	1.38
35	0.49	0.69	0.84	0.97	1.09	1.19	1.28	1.37	1.45	1.53
40	0.51	0.72	0.88	1.02	1.13	1.24	1.34	1.43	1.52	1.6
45	0.55	0.78	0.96	1.11	1.24	1.36	1.46	1.56	1.66	1.75
50	0.6	0.85	1.04	1.2	1.35	1.47	1.59	1.7	1.8	1.9
55	0.68	0.96	1.17	1.35	1.51	1.65	1.78	1.91	2.02	2.13
60	0.74	1.04	1.28	1.48	1.65	1.81	1.95	2.09	2.21	2.33
65	0.78	1.11	1.35	1.56	1.75	1.91	2.07	2.21	2.34	2.47
70	1.04	1.48	1.81	2.09	2.33	2.56	2.76	2.95	3.13	3.3
75	1.20	1.7	2.08	2.4	2.68	2.94	3.17	3.39	3.59	3.79
80	1.35	1.91	2.34	2.71	3.02	3.31	3.58	3.82	4.06	4.27
85	1.57	2.21	2.71	3.13	3.5	3.83	4.14	4.42	4.69	4.95
90	1.82	2.58	3.16	3.64	4.07	4.46	4.82	5.15	5.46	5.76

Table 54. Discrete longitudinal gust magnitude at the 1% risk level of exceedance as a function of altitude (ft) and gust half-width, d_m (ft), for moderate turbulence.

Gust Magnitude (ft/s)										
Altitude (km)	Gust Half-Width (ft)									
	98.4	196.9	295.3	393.7	492.1	590.6	688.9	787.4	885.8	984.3
3.3	3.67	5.12	6.14	6.99	7.68	8.27	8.79	9.22	9.65	10.01
6.6	3.54	4.92	5.94	6.73	7.41	8.01	8.5	8.96	9.35	9.71
13.1	4.07	5.68	6.86	7.84	8.63	9.32	9.94	10.47	10.96	11.42
19.7	4.27	5.94	7.19	8.17	9.02	9.74	10.37	10.96	11.45	11.91
26.2	4.3	6	7.25	8.23	9.09	9.84	10.47	11.06	11.55	12.04
32.8	4.1	5.74	6.96	7.94	8.76	9.48	10.14	10.73	11.22	11.71
39.4	3.77	5.31	6.43	7.38	8.17	8.89	9.51	10.1	10.63	11.12
45.9	3.22	4.53	5.51	6.33	7.02	7.68	8.23	8.76	9.25	9.68
52.5	2.72	3.84	4.69	5.38	6	6.53	7.02	7.48	7.91	8.3
59.1	2.03	2.89	3.51	4.04	4.49	4.92	5.31	5.64	5.97	6.27
65.6	1.57	2.23	2.76	3.15	3.54	3.87	4.17	4.43	4.69	4.95
82	1.61	2.3	2.79	3.22	3.6	3.94	4.23	4.53	4.79	5.05
98.4	1.44	2.03	2.49	2.89	3.22	3.51	3.81	4.07	4.3	4.53
114.8	1.61	2.26	2.76	3.18	3.58	3.9	4.2	4.49	4.76	5.02
131.2	1.67	2.36	2.89	3.35	3.7	4.07	4.4	4.69	4.99	5.25
147.6	1.8	2.56	3.15	3.64	4.07	4.46	4.79	5.12	5.45	5.74
164	1.97	2.79	3.41	3.94	4.43	4.82	5.22	5.58	5.91	6.23
180.4	2.23	3.15	3.84	4.43	4.95	5.41	5.84	6.27	6.63	6.99
196.9	2.43	3.41	4.2	4.86	5.41	5.94	6.4	6.86	7.25	7.64
213.3	2.56	3.64	4.43	5.12	5.74	6.27	6.79	7.25	7.68	8.1
229.7	3.41	4.86	5.94	6.86	7.64	8.4	9.06	9.68	10.27	10.83
246.1	3.94	5.58	6.82	7.87	8.79	9.65	10.4	11.12	11.78	12.43
262.5	4.43	6.27	7.68	8.89	9.91	10.86	11.75	12.53	13.32	14.01
278.9	5.15	7.25	8.89	10.27	11.48	12.57	13.58	14.5	15.39	16.24
295.3	5.97	8.46	10.37	11.94	13.35	14.63	15.81	16.9	17.91	18.9

3.2.2 Discrete Gust Summary

NASA has developed a rationale for derivation of a discrete gust magnitude that is a function of altitude and gust half-width. This rationale is based on established methods that are included in the military specification (MIL-SPEC) of requirements for the flying qualities of piloted aircraft. This prior specification is significant because it is based on the same aircraft turbulence data used in studies that established the classical NASA 9 m/s (29.5 ft/s) discrete gust model. The program application of the MIL-SPEC model is for protection of the vehicle from elastic body loads response to gust during severe turbulence. The MIL-SPEC model produces larger gust magnitudes for severe turbulence than the NASA classical model from roughly 6 to 10 km (19.7 to 32.8×10^3 ft) for gust half-widths between approximately 150 and 210 m (492.1 to 689 ft), and produces larger gust magnitudes than the NASA classical model from nearly 4 to 12 km (13.1 to

39.4×10^3 ft) for gust half-widths greater than approximately 210 m (689 ft). Conversely, the NASA classical model produces larger gust magnitudes than the MIL-SPEC model at all other altitudes and gust half-widths. Using the MIL-SPEC model for moderate turbulence further decreases the gust magnitudes by roughly a factor of 3 to 3.5 compared to using severe turbulence. The conservatism of the classical model is attributed to the lack of a relationship between gust magnitude and gust half-width, which is illustrated by the 'flat-top' quasi-square waveform and the larger gust gradients that result from constraining the classical gust model build-up and back-off to a 30 m (98.4 ft) interval (fig. 46). The MIL-SPEC model eliminates this conservatism by building up the gust magnitude from the start of the gust to the gust half-width, and by backing off the gust magnitude from the gust half-width to the end of the gust. In addition, the MIL-SPEC model is not constrained to peaking at 9 m/s (29.5 ft/s) at certain altitudes and half-widths, as shown in tables 51 and 52. An illustration of applying the two models for two gust half-widths at 8 km (26.2×10^3 ft) is provided in figure 46. The NASA classical model exceeds the MIL-SPEC model for severe turbulence at all relevant gust distances for d_m equals 60 m (196.9 ft), but the MIL-SPEC model for severe turbulence exceeds 9 m/s (29.5 ft/s) from roughly 120 to 180 m (393.7 to 590.6 ft) when d_m equals 150 m (492.1 ft) at the same altitude.

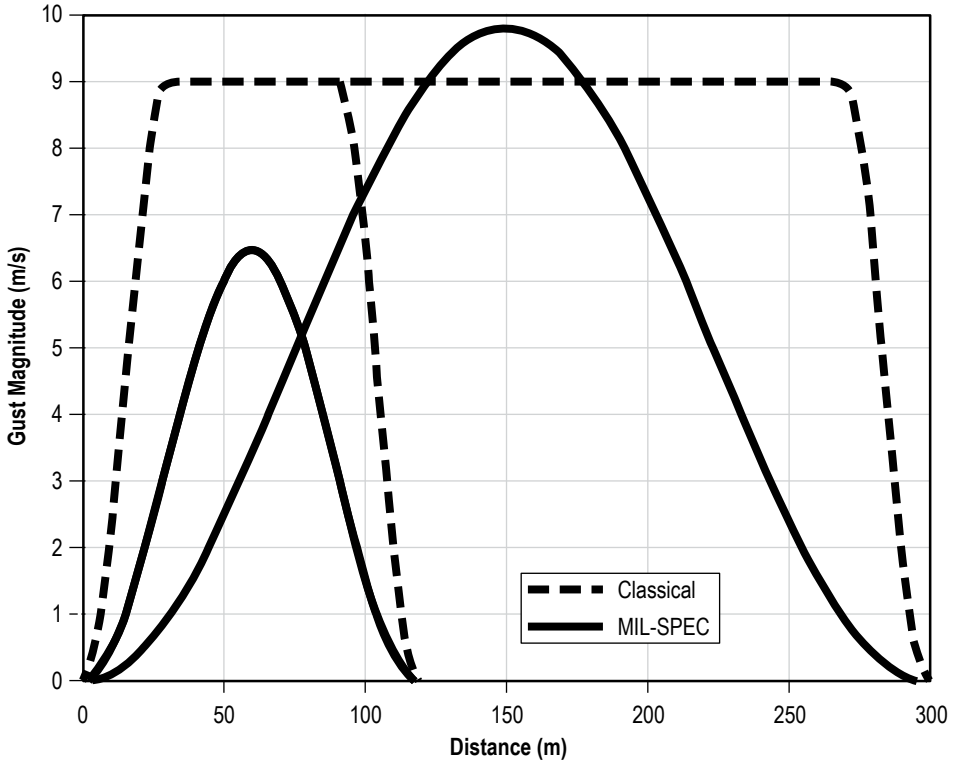

Figure 46. MIL-SPEC discrete gust at 8 km (26.2×10^3 ft) for severe turbulence (solid) and the NASA classical (dashed) discrete gust for half-widths of 60 and 150 m (196.9 and 492.1 ft).

3.3 Solar Radiation

Solar radiation intensity on a surface will increase with altitude above the Earth's surface, with clear skies, according to the following equation:

$$I_{DN}(Z) = I_{DN}(0) + \left(S - I_{DN}(0)\right)\left(1 - \frac{\rho_z}{\rho_s}\right), \tag{45}$$

where

$I_{DN}(Z)$ = intensity of solar radiation normal to surface at required height Z

$I_{DN}(0)$ = intensity of solar radiation normal to surface at the Earth's surface assuming clear skies ($I_{DN}(0)=I_{\mathrm{TN}}-I_{DH}(Z)$)

ρ_z = atmospheric density at required height (from 1976 U.S. Standard Atmosphere or 1966 U.S. Standard Atmosphere Supplements) (kg/m^3)

ρ_s = atmospheric density at sea level (from U.S. Standard Atmospheres or U.S. Standard Atmosphere Supplements) (kg/m^3)

S = solar constant (e.g., 1,367 W/m^2).

The diffuse solar radiation I_{dH} decreases with altitude above the Earth's surface. For clear skies, a good estimate of the value can be obtained from the following equation:

$$I_{dH}(Z) = 523 - 0.4076\, I_{DN}(Z)\ , \tag{46}$$

where

$I_{dH}(Z)$ = intensity of diffuse radiation (W/m^2) at height Z

$I_{DN}(Z)$ = intensity of solar radiation (W/m^2) normal to surface at height Z.

Equation (46) is valid for values of $I_{DN}(Z)$ from equation (45) up to 1,283 W/m^2. For values of $I_{DN}(Z)$ greater than 1,283 W/m^2, $I_{dH}=0$.

3.4 Temperature

The atmosphere from zero to 90 km (zero to 295.3×10^3 ft) has four distinct layers known as the troposphere, stratosphere, mesosphere, and thermosphere. The temperature profile contributes significantly to the characteristics of each layer. At the top of each layer, a transition zone exists where the temperature is quasi-isothermal with height. These transition zones are known as the tropopause, stratopause, mesopause, and thermopause.

The figures and tables in this section were derived from the 1983 Range Reference Atmosphere (RRA) for the particular site. Only the annual means are shown here. However, the designers are not constrained to using the annual means shown in this TM. Additional (monthly) data are available from the MSFC Natural Environments Branch and from the RRA documentation for each site.

3.4.1 Eastern Range

Seasonal variations in the temperature profile above the ER exist. For example, temperatures are colder in the layer from 70 to 90 km (229.7×10^3 to 295.3×10^3 ft) in the summer months than in the winter months above the ER. Figure 47 and table 55 show profiles of the annual mean and $\pm2\sigma$ values of temperature for the ER, as obtained from the Cape Canaveral RRA.[79] Spatial and temporal atmospheric temperature profiles for specific purposes, such as temperature along a time-varying flight trajectory, can be derived using Earth-GRAM,[71] which is discussed in section 3.9.

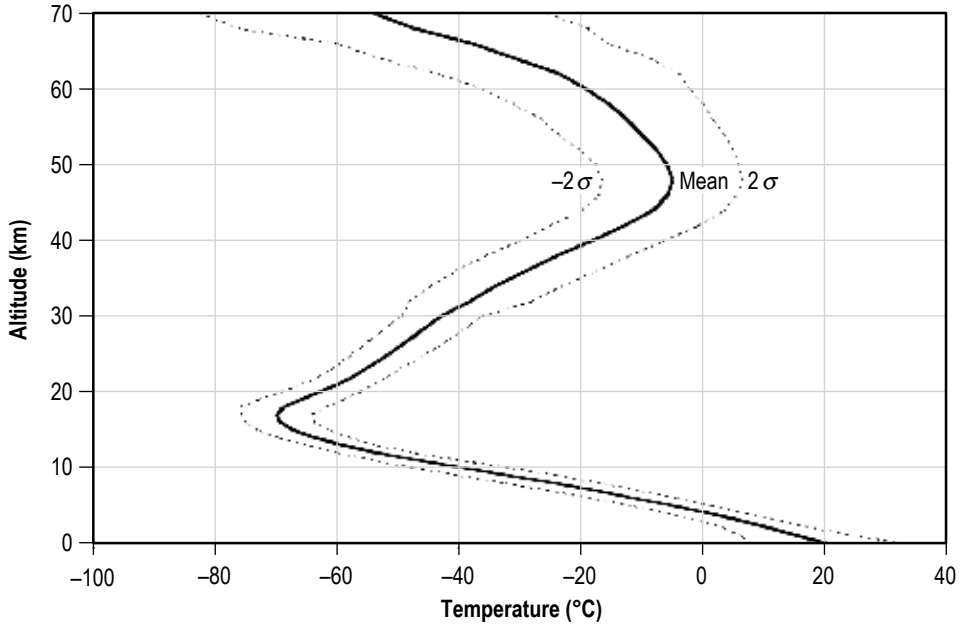

Figure 47. Annual mean and ±2σ of atmospheric temperature as a function of altitude at the ER.

Table 55. Annual mean and $\pm 2\sigma$ range of atmospheric temperature as a function of altitude at the ER.

Geometric Altitude		Mean		-2σ		2σ	
(km)	(ft)	(°C)	(°F)	(°C)	(°F)	(°C)	(°F)
–	–	20.81	69.46	8.45	47.21	33.17	91.71
0.003	9.8	20.45	68.81	7.91	46.24	32.99	91.38
1	3.3×10^3	15.88	60.58	6.48	43.66	25.28	77.5
2	6.6×10^3	11.17	52.11	3.71	38.68	18.63	65.53
3	9.8×10^3	6.41	43.54	–0.11	31.8	12.93	55.27
4	13.1×10^3	0.87	33.57	–5.51	22.08	7.25	45.05
5	16.4×10^3	–5.06	22.89	–11.72	10.9	1.6	34.88
6	19.7×10^3	–11.35	11.57	–18.41	–1.14	–4.29	24.28
7	23×10^3	–17.9	–0.22	–25.28	–13.5	–10.52	13.06
8	26.2×10^3	–24.79	–12.62	–32.71	–26.88	–16.87	1.63
9	29.5×10^3	–32.14	–25.85	–40.3	–40.54	–23.98	–11.16
10	32.8×10^3	–39.69	–39.44	–47.53	–53.55	–31.85	–25.33
12	39.4×10^3	–53.84	–64.91	–60	–76	–47.68	–53.82
14	45.9×10^3	–63.82	–82.88	–69.7	–93.46	–57.94	–72.29
16	52.5×10^3	–69.28	–92.7	–74.84	–102.71	–63.72	–82.7
18	59.1×10^3	–68.66	–91.59	–75.64	–104.15	–61.68	–79.02
20	65.6×10^3	–62.61	–80.7	–69.09	–92.36	–56.13	–69.03
22	72.2×10^3	–57.23	–71.01	–62.91	–81.24	–51.55	–60.79
24	78.7×10^3	–53.18	–63.72	–59.04	–74.27	–47.32	–53.18
26	85.3×10^3	–49.57	–57.23	–55.81	–68.46	–43.33	–45.99
28	91.9×10^3	–46.08	–50.94	–52.62	–62.72	–39.54	–39.17
30	98.4×10^3	–42.67	–44.81	–49.25	–56.65	–36.09	–32.96
34	111.5×10^3	–38.01	–36.42	–48.09	–54.56	–27.93	–18.27
38	124.7×10^3	–33.80	–28.84	–44.56	–48.21	–23.04	–9.47
42	137.8×10^3	–28.94	–20.09	–40.48	–40.86	–17.4	0.68
46	150.9×10^3	–23.71	–10.68	–35.49	–31.88	–11.93	10.53
50	164×10^3	–18.07	–0.53	–29.93	–21.87	–6.21	20.82
54	177.2×10^3	–12.68	9.18	–24.84	–12.71	–0.52	31.06
58	190.3×10^3	–7.99	17.62	–19.61	–3.3	3.63	38.53
62	203.4×10^3	–5.62	21.88	–16.96	1.47	5.72	42.3
66	216.5×10^3	–4.81	23.34	–16.39	2.5	6.77	44.19
70	229.7×10^3	–5.71	21.72	–17.41	0.66	5.99	42.78

3.4.2 Edwards Air Force Base

Figure 48 and table 56 show profiles of the annual mean and ±2σ values of temperature for EAFB. Spatial and temporal atmospheric temperature profiles for specific purposes, such as temperature along a time-varying flight trajectory, can be derived using the Earth-GRAM.[71] Temperature data used in figure 48 and table 56 were obtained from the EAFB RRA.[81]

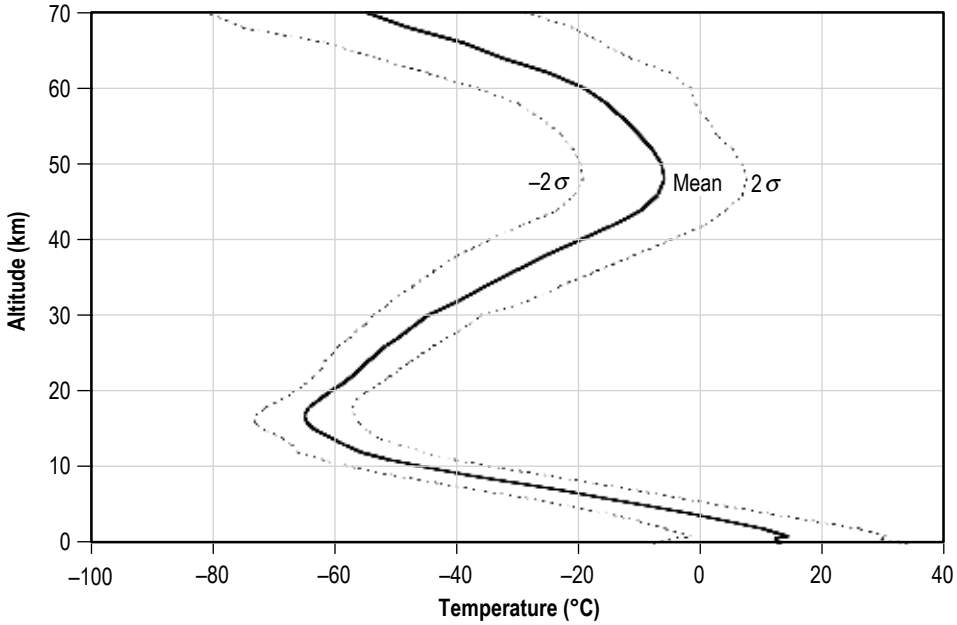

Figure 48. Annual mean and ±2σ of atmospheric temperature as a function of altitude at EAFB.

Table 56. Annual mean and ±2σ range of atmospheric temperature as a function of altitude at EAFB.

Geometric Altitude		Mean		–2σ		2σ	
(km)	(ft)	(°C)	(°F)	(°C)	(°F)	(°C)	(°F)
–	–	13.27	55.89	–7.55	18.41	34.09	93.36
0.705	2.3×10^3	12.34	54.21	–5.12	22.78	29.8	85.64
1	3.3×10^3	14.62	58.32	–1.42	29.44	30.66	87.19
2	6.6×10^3	10.3	50.54	–5.58	21.96	26.18	79.12
3	9.8×10^3	4.41	39.94	–9.95	14.09	18.77	65.79
4	13.1×10^3	–1.94	28.51	–15.22	4.6	11.34	52.41
5	16.4×10^3	–8.68	16.38	–21.5	–6.7	4.14	39.45
6	19.7×10^3	–15.63	3.87	–28.25	–18.85	–3.01	26.58
7	23×10^3	–22.84	–9.11	–35.6	–32.08	–10.08	13.86
8	26.2×10^3	–30.29	–22.52	–43.15	–45.67	–17.43	0.63
9	29.5×10^3	–37.8	–36.04	–50.32	–58.58	–25.28	–13.5
10	32.8×10^3	–44.84	–48.71	–56.68	–70.02	–33	–27.4
12	39.4×10^3	–55.48	–67.86	–65.88	–86.58	–45.08	–49.14
14	45.9×10^3	–60.59	–77.06	–68.41	–91.14	–52.77	–62.99
16	52.5×10^3	–64.5	–84.1	–73.06	–99.51	–55.94	–68.69
18	59.1×10^3	–63.99	–83.18	–71.09	–95.96	–56.89	–70.4
20	65.6×10^3	–60.68	–77.22	–66.68	–88.02	–54.68	–66.42
22	72.2×10^3	–57.11	–70.8	–63.37	–82.07	–50.85	–59.53
24	78.7×10^3	–54.4	–65.92	–61.5	–78.7	–47.3	–53.14
26	85.3×10^3	–51.41	–60.54	–59.21	–74.58	–43.61	–46.5
28	91.9×10^3	–47.93	–54.27	–56.29	–69.32	–39.57	–39.23
30	98.4×10^3	–44.78	–48.6	–53.62	–64.52	–35.94	–32.69
34	111.5×10^3	–34.97	–30.95	–47.01	–52.62	–22.93	–9.27
38	124.7×10^3	–25.27	–13.49	–39.73	–39.51	–10.81	12.54
42	137.8×10^3	–14.24	6.37	–29.26	–20.67	0.78	33.4
46	150.9×10^3	–6.88	19.62	–20.66	–5.19	6.9	44.42
50	164×10^3	–6.29	20.68	–19.55	–3.19	6.97	44.55
54	177.2×10^3	–10.09	13.84	–22.87	–9.17	2.69	36.84
58	190.3×10^3	–15.31	4.44	–29.67	–21.41	–0.95	30.29
62	203.4×10^3	–24.68	–12.42	–44.56	–48.21	–4.8	23.36
66	216.5×10^3	–38.74	–37.73	–61.28	–78.3	–16.2	2.84
70	229.7×10^3	–54.7	–66.46	–80.8	–113.44	–28.6	–19.48

3.5 Pressure

Atmospheric pressure decreases approximately exponentially with height from zero to 70 km (zero to 229.7×10^3 ft).

The figures and tables in this section were derived from the 1983 RRA for the particular site. Only the annual means are shown here. However, the designers are not to be constrained to use the annual means shown in this TM. Additional (monthly) data are available from the MSFC Natural Environments Branch and from the RRA documentation for each site.

3.5.1 Eastern Range

Pressure data used in figure 49 and table 57 were obtained from Cape Canaveral RRA.[79]

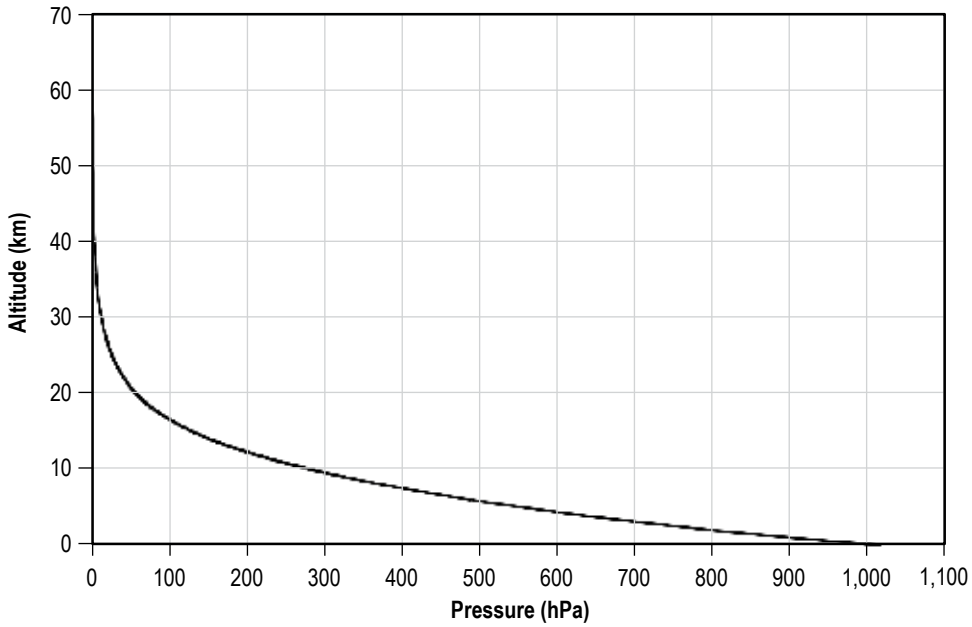

Figure 49. Annual mean atmospheric pressure as a function of altitude at the ER.

Table 57. Annual mean and ±2σ range of atmospheric pressure as a function of altitude at the ER.

Geometric Altitude		Mean		–2σ		2σ	
(km)	(ft)	(hPa)	(lbf/in^2)	(hPa)	(lbf/in^2)	(hPa)	(lbf/in^2)
–	–	1,017.4	14.7564	1,009.046	14.6352	1,025.754	14.8775
0.003	9.8	1,017.2	14.7535	1,008.736	14.6307	1,025.664	14.8762
1	3.3×10^3	906.15	13.1428	898.74	13.0353	913.56	13.2503
2	6.6×10^3	804.97	11.6753	797.296	11.564	812.644	11.7866
3	9.8×10^3	713.59	10.3499	705.426	10.2315	721.754	10.4683
4	13.1×10^3	631.03	9.1525	622.38	9.027	639.68	9.2779
5	16.4×10^3	556.63	8.0734	547.715	7.9441	565.545	8.2027
6	19.7×10^3	489.6	7.1012	480.303	6.9663	498.897	7.236
7	23×10^3	429.18	6.2248	419.66	6.0867	438.7	6.3629
8	26.2×10^3	374.92	5.4378	365.306	5.2984	384.534	5.5773
9	29.5×10^3	326.21	4.7313	316.537	4.5911	335.883	4.8716
10	32.8×10^3	282.63	4.0993	273.03	3.96	292.229	4.2385
12	39.4×10^3	209.22	3.0345	200.781	2.9121	217.659	3.1569
14	45.9×10^3	152.37	2.21	146.013	2.1178	158.727	2.3022
16	52.5×10^3	109.58	1.5893	105.383	1.5285	113.777	1.6502
18	59.1×10^3	78.532	1.139	75.494	1.095	81.57	1.1831
20	65.6×10^3	56.636	0.8214	54.194	0.786	59.078	0.8569
22	72.2×10^3	41.227	0.598	39.23	0.569	43.224	0.6269
24	78.7×10^3	30.211	0.4382	28.601	0.4148	31.821	0.4615
26	85.3×10^3	22.266	0.3229	20.972	0.3042	23.56	0.3417
28	91.9×10^3	16.495	0.2392	15.45	0.2241	17.54	0.2544
30	98.4×10^3	12.274	0.178	11.443	0.166	13.105	0.1901
34	111.5×10^3	6.871	0.0997	6.335	0.0919	7.407	0.1074
38	124.7×10^3	3.953	0.0573	3.618	0.0525	4.288	0.0622
42	137.8×10^3	2.328	0.0338	2.12	0.0308	2.536	0.0368
46	150.9×10^3	1.4	0.0203	1.272	0.0184	1.528	0.0222
50	164×10^3	0.848	0.0123	0.765	0.0111	0.931	0.0135
54	177.2×10^3	0.512	0.0074	0.457	0.0066	0.567	0.0082
58	190.3×10^3	0.306	0.0044	0.27	0.0039	0.342	0.005
62	203.4×10^3	0.179	0.0026	0.155	0.0022	0.203	0.003
66	216.5×10^3	0.1	0.0015	0.085	0.0012	0.115	0.0017
70	229.7×10^3	0.055	0.0008	0.043	0.0006	0.067	0.001

3.5.2 Edwards Air Force Base

Pressure data used in figure 50 and table 58 were obtained from EAFB RRA.[81]

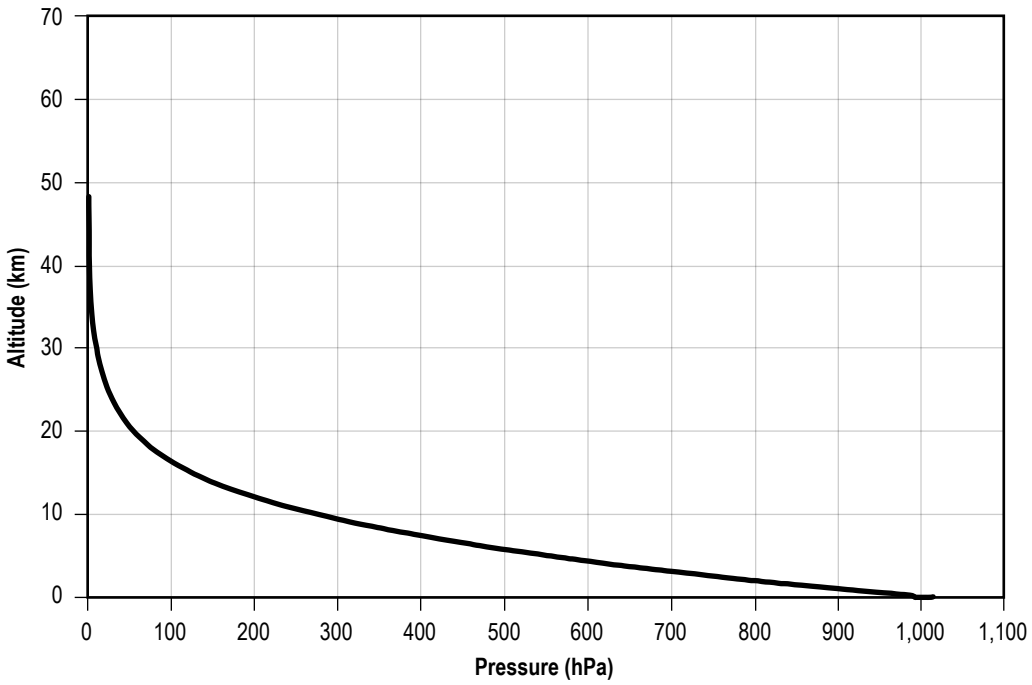

Figure 50. Annual mean atmospheric pressure as a function of altitude at EAFB.

Table 58. Annual mean and $\pm 2\sigma$ range of atmospheric pressure as a function of altitude at EAFB.

Geometric Altitude		Mean		-2σ		2σ	
(km)	(ft)	(hPa)	(lbf/in^2)	(hPa)	(lbf/in^2)	(hPa)	(lbf/in^2)
–	–	1,014.3	14.7114	1,000.979	14.5182	1,027.621	14.9046
0.705	2.3×10^3	932.26	13.5215	923.339	13.3921	941.181	13.6509
1	3.3×10^3	901.86	13.0806	893.422	12.9582	910.298	13.203
2	6.6×10^3	800.72	11.6136	791.585	11.4811	809.855	11.7461
3	9.8×10^3	709.17	10.2858	697.642	10.1186	720.698	10.453
4	13.1×10^3	626.21	9.0825	612.408	8.8824	640.012	9.2827
5	16.4×10^3	551.42	7.9978	536.094	7.7755	566.746	8.2201
6	19.7×10^3	484.23	7.0233	467.87	6.786	500.59	7.2606
7	23×10^3	423.33	6.14	406.476	5.8955	440.184	6.3844
8	26.2×10^3	368.76	5.3485	351.596	5.0995	385.924	5.5974
9	29.5×10^3	319.78	4.6381	302.747	4.391	336.813	4.8851
10	32.8×10^3	276.18	4.0057	259.558	3.7646	292.802	4.2468
12	39.4×10^3	203.5	2.9516	189.401	2.7471	217.599	3.1561
14	45.9×10^3	148.36	2.1518	138.014	2.0018	158.706	2.3019
16	52.5×10^3	107.36	1.5571	100.631	1.4595	114.089	1.6547
18	59.1×10^3	77.545	1.1247	73.042	1.0594	82.048	1.19
20	65.6×10^3	56.243	0.8157	52.887	0.7671	59.599	0.8644
22	72.2×10^3	41.074	0.5957	38.416	0.5572	43.732	0.6343
24	78.7×10^3	29.994	0.435	27.821	0.4035	32.167	0.4666
26	85.3×10^3	22.101	0.3206	20.345	0.2951	23.857	0.346
28	91.9×10^3	16.4	0.2379	14.986	0.2174	17.813	0.2584
30	98.4×10^3	12.196	0.1769	11.035	0.16	13.357	0.1937
34	111.5×10^3	6.84	0.0992	6.136	0.089	7.544	0.1094
38	124.7×10^3	3.925	0.0569	3.472	0.0504	4.378	0.0635
42	137.8×10^3	2.305	0.0334	2.007	0.0291	2.603	0.0378
46	150.9×10^3	1.381	0.02	1.187	0.0172	1.575	0.0228
50	164.0×10^3	0.835	0.0121	0.708	0.0103	0.962	0.0139
54	177.2×10^3	0.503	0.0073	0.42	0.0061	0.586	0.0085
58	190.3×10^3	0.3	0.0044	0.248	0.0036	0.352	0.0051
62	203.4×10^3	0.174	0.0025	0.143	0.0021	0.205	0.003
66	216.5×10^3	0.098	0.0014	0.081	0.0012	0.115	0.0017
70	229.7×10^3	0.054	0.0008	0.043	0.0006	0.065	0.0009

3.6 Density

Atmospheric mean density decreases exponentially with height, decreasing to half the MSL value at approximately 7 km (23×10^3 ft) above MSL. Density dispersions are of particular importance in the design of a launch vehicle. Dispersions at fixed altitudes have an influence on aerodynamic heating and dynamic pressure, and hence on trajectory designs and aerodynamic loads placed on a vehicle.

The figures and tables in this section were derived from the RRA for the particular site. Only the annual means are shown here. However, the designers are constrained to using the annual means shown in this TM. Additional (monthly) data are available from the MSFC Natural Environments Branch and from the RRA documentation for each site.

3.6.1 Eastern Range

Density data used in figure 51 and table 59 were obtained from the Cape Canaveral RRA.[79]

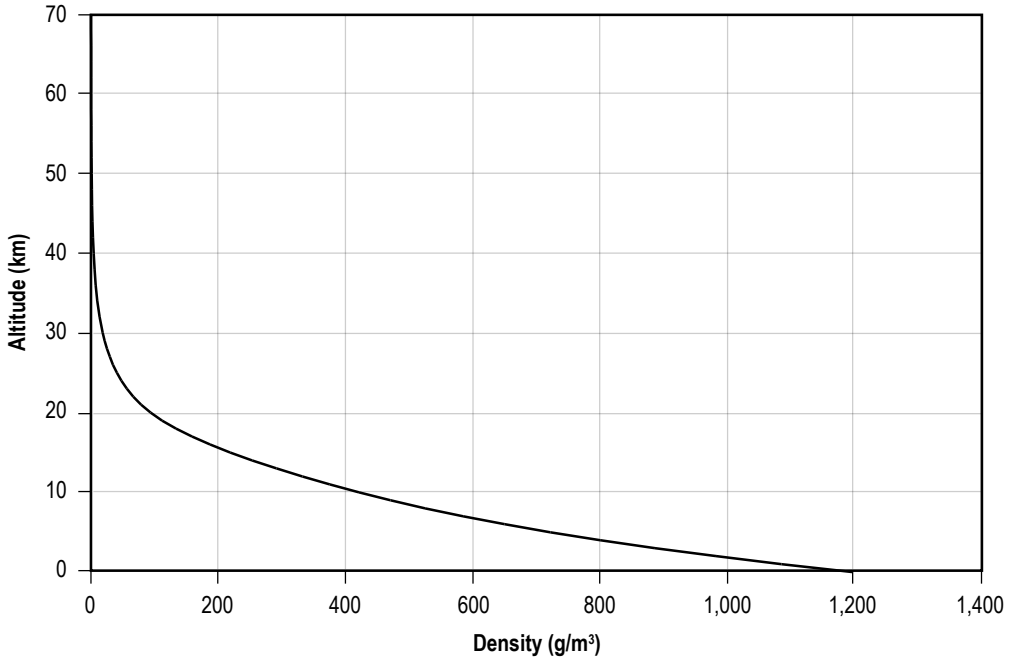

Figure 51. Annual mean atmospheric density as a function of altitude at the ER.

Table 59. Annual mean and $\pm 2\sigma$ range of atmospheric density as a function of altitude at the ER.

Geometric Altitude		Mean		-2σ		2σ	
(km)	(ft)	(g/m^3)	(lb/ft^3)	(g/m^3)	(lb/ft^3)	(g/m^3)	(lb/ft^3)
–	–	1,197	7.473×10^{-2}	1,136.88	7.098×10^{-2}	1,257.12	7.848×10^{-2}
0.003	9.8	1,198	7.479×10^{-2}	1,136.94	7.098×10^{-2}	1,259.06	7.86×10^{-2}
1	3.3×10^3	1,086	6.78×10^{-2}	1,047.04	6.537×10^{-2}	1,124.96	7.023×10^{-2}
2	6.6×10^3	982.7	6.135×10^{-2}	957.82	5.98×10^{-2}	1,007.58	6.29×10^{-2}
3	9.8×10^3	886.8	5.536×10^{-2}	869.85	5.43×10^{-2}	903.75	5.642×10^{-2}
4	13.1×10^3	800.6	4.998×10^{-2}	787.178	4.914×10^{-2}	814.022	5.082×10^{-2}
5	16.4×10^3	722.1	4.508×10^{-2}	710.38	4.435×10^{-2}	733.82	4.581×10^{-2}
6	19.7×10^3	650.6	4.062×10^{-2}	640.242	3.997×10^{-2}	660.958	4.126×10^{-2}
7	23×10^3	585.1	3.653×10^{-2}	575.902	3.595×10^{-2}	594.298	3.71×10^{-2}
8	26.2×10^3	525.4	3.28×10^{-2}	516.65	3.225×10^{-2}	534.15	3.335×10^{-2}
9	29.5×10^3	471.1	2.941×10^{-2}	462.876	2.89×10^{-2}	479.324	2.992×10^{-2}
10	32.8×10^3	421.5	2.631×10^{-2}	413.424	2.581×10^{-2}	429.576	2.682×10^{-2}
12	39.4×10^3	332.4	2.075×10^{-2}	321.168	2.005×10^{-2}	343.632	2.145×10^{-2}
14	45.9×10^3	253.6	1.583×10^{-2}	239.13	1.493×10^{-2}	268.07	1.674×10^{-2}
16	52.5×10^3	187.3	1.169×10^{-2}	177.526	1.108×10^{-2}	197.074	1.23×10^{-2}
18	59.1×10^3	133.8	8.353×10^{-3}	127.928	7.987×10^{-3}	139.672	8.72×10^{-3}
20	65.6×10^3	93.72	5.851×10^{-3}	90.212	5.632×10^{-3}	97.228	6.07×10^{-3}
22	72.2×10^3	66.52	4.153×10^{-3}	63.916	3.99×10^{-3}	69.124	4.315×10^{-3}
24	78.7×10^3	47.84	2.987×10^{-3}	45.802	2.859×10^{-3}	49.878	3.114×10^{-3}
26	85.3×10^3	34.69	2.166×10^{-3}	33.084	2.065×10^{-3}	36.296	2.266×10^{-3}
28	91.9×10^3	25.31	1.58×10^{-3}	23.996	1.498×10^{-3}	26.624	1.662×10^{-3}
30	98.4×10^3	18.55	1.158×10^{-3}	17.485	1.092×10^{-3}	19.615	1.225×10^{-3}
34	111.5×10^3	10.03	6.262×10^{-4}	9.268	5.786×10^{-4}	10.792	6.738×10^{-4}
38	124.7×10^3	5.534	3.455×10^{-4}	5.058	3.158×10^{-4}	6.01	3.752×10^{-4}
42	137.8×10^3	3.118	1.947×10^{-4}	2.82	1.761×10^{-4}	3.416	2.133×10^{-4}
46	150.9×10^3	1.823	1.138×10^{-4}	1.652	1.032×10^{-4}	1.994	1.245×10^{-4}
50	164×10^3	1.106	6.905×10^{-5}	1.005	6.275×10^{-5}	1.207	7.534×10^{-5}
54	177.2×10^3	0.678	4.233×10^{-5}	0.612	3.821×10^{-5}	0.744	4.645×10^{-5}
58	190.3×10^3	0.414	2.585×10^{-5}	0.369	2.301×10^{-5}	0.459	2.868×10^{-5}
62	203.4×10^3	0.25	1.561×10^{-5}	0.22	1.376×10^{-5}	0.28	1.746×10^{-5}
66	216.5×10^3	0.148	9.24×10^{-6}	0.127	7.941×10^{-6}	0.169	1.054×10^{-5}
70	229.7×10^3	0.087	5.431×10^{-6}	0.07	4.358×10^{-6}	0.104	6.505×10^{-6}

3.6.2 Edwards Air Force Base

Density data used in figure 52 and table 60 were obtained from EAFB RRA.[81]

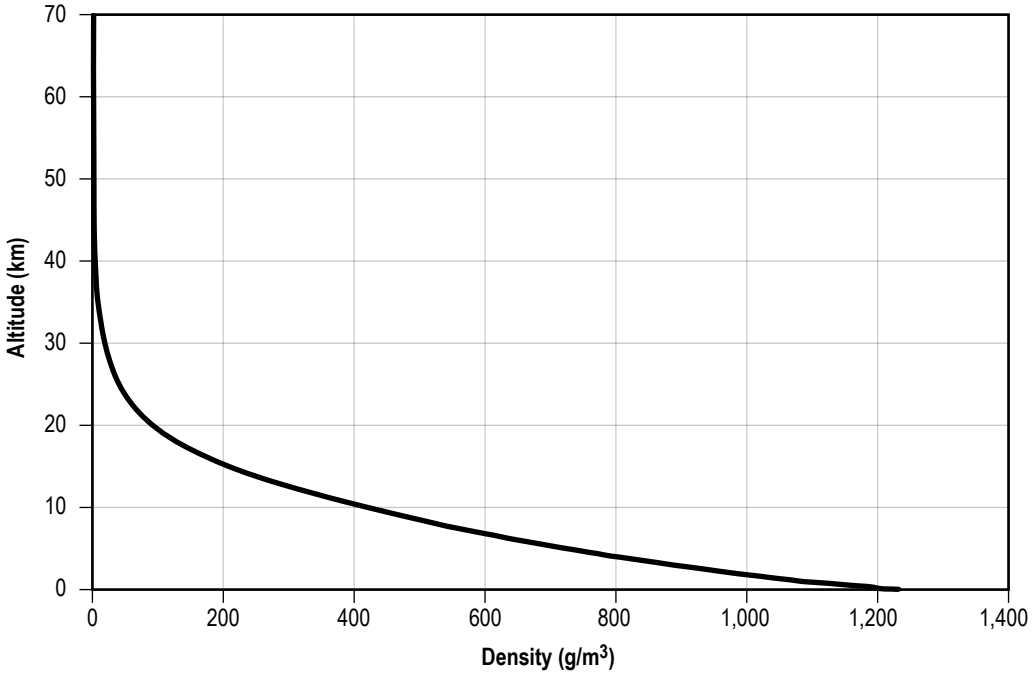

Figure 52. Annual mean atmospheric density as a function of altitude at EAFB.

Table 60. Annual mean and $\pm 2\sigma$ range of atmospheric density as a function of altitude at EAFB.

Geometric Altitude		Mean		-2σ		2σ	
(km)	(ft)	(g/m^3)	(lb/ft^3)	(g/m^3)	(lb/ft^3)	(g/m^3)	(lb/ft^3)
–	–	1,232	7.691×10^{-2}	1,126.46	7.032×10^{-2}	1,337.54	8.35×10^{-2}
0.705	2.3×10^3	1,136	7.092×10^{-2}	1,059.46	6.614×10^{-2}	1,212.54	7.57×10^{-2}
1	3.3×10^3	1,090	6.805×10^{-2}	1,026.44	6.408×10^{-2}	1,153.56	7.202×10^{-2}
2	6.6×10^3	983	6.137×10^{-2}	932.66	5.823×10^{-2}	1,033.34	6.451×10^{-2}
3	9.8×10^3	889.3	5.552×10^{-2}	853.4	5.328×10^{-2}	925.2	5.776×10^{-2}
4	13.1×10^3	803.8	5.018×10^{-2}	778.36	4.859×10^{-2}	829.24	5.177×10^{-2}
5	16.4×10^3	726	4.532×10^{-2}	707.002	4.414×10^{-2}	744.998	4.651×10^{-2}
6	19.7×10^3	654.8	4.088×10^{-2}	640.412	3.998×10^{-2}	669.188	4.178×10^{-2}
7	23×10^3	589	3.677×10^{-2}	577.306	3.604×10^{-2}	600.694	3.75×10^{-2}
8	26.2×10^3	528.8	3.301×10^{-2}	518.206	3.235×10^{-2}	539.394	3.367×10^{-2}
9	29.5×10^3	473.2	2.954×10^{-2}	461.79	2.883×10^{-2}	484.61	3.025×10^{-2}
10	32.8×10^3	421.3	2.63×10^{-2}	406.822	2.54×10^{-2}	435.778	2.721×10^{-2}
12	39.4×10^3	325.8	2.034×10^{-2}	303.88	1.897×10^{-2}	347.72	2.171×10^{-2}
14	45.9×10^3	243.3	1.519×10^{-2}	221	1.38×10^{-2}	265.6	1.658×10^{-2}
16	52.5×10^3	179.4	1.12×10^{-2}	162.918	1.017×10^{-2}	195.882	1.223×10^{-2}
18	59.1×10^3	129.2	8.066×10^{-3}	120.014	7.492×10^{-3}	138.386	8.639×10^{-3}
20	65.6×10^3	92.21	5.757×10^{-3}	87.35	5.453×10^{-3}	97.07	6.06×10^{-3}
22	72.2×10^3	66.23	4.135×10^{-3}	63.01	3.934×10^{-3}	69.45	4.336×10^{-3}
24	78.7×10^3	47.76	2.982×10^{-3}	45.324	2.83×10^{-3}	50.196	3.134×10^{-3}
26	85.3×10^3	34.71	2.167×10^{-3}	32.788	2.047×10^{-3}	36.632	2.287×10^{-3}
28	91.9×10^3	25.36	1.583×10^{-3}	23.786	1.485×10^{-3}	26.934	1.682×10^{-3}
30	98.4×10^3	18.6	1.161×10^{-3}	17.283	1.079×10^{-3}	19.917	1.243×10^{-3}
34	111.5×10^3	10.01	6.249×10^{-4}	9.109	5.686×10^{-4}	10.911	6.812×10^{-4}
38	124.7×10^3	5.519	3.446×10^{-4}	4.935	3.081×10^{-4}	6.103	3.81×10^{-4}
42	137.8×10^3	3.101	1.936×10^{-4}	2.75	1.717×10^{-4}	3.452	2.155×10^{-4}
46	150.9×10^3	1.806	1.127×10^{-4}	1.576	9.84×10^{-4}	2.036	1.271×10^{-4}
50	164×10^3	1.089	6.799×10^{-5}	0.944	5.895×10^{-5}	1.234	7.703×10^{-5}
54	177.2×10^3	0.665	4.152×10^{-5}	0.567	3.542×10^{-5}	0.763	4.761×10^{-5}
58	190.3×10^3	0.405	2.528×10^{-5}	0.339	2.119×10^{-5}	0.471	2.938×10^{-5}
62	203.4×10^3	0.244	1.523×10^{-5}	0.203	1.269×10^{-5}	0.285	1.778×10^{-5}
66	216.5×10^3	0.146	9.115×10^{-6}	0.12	7.504×10^{-6}	0.172	1.073×10^{-5}
70	229.7×10^3	0.086	5.369×10^{-6}	0.069	4.295×10^{-6}	0.103	6.443×10^{-6}

3.7 Humidity

In general, the vapor concentration decreases with altitude in the troposphere because of the decrease of temperature with altitude. Small amounts of moisture exist in the stratosphere and mesosphere. Figure 53 presents a reference model for the mean and variability of middle atmospheric water vapor.[1] It represents mean, Northern Hemisphere, mid-latitude, springtime, and number concentration (parts per million by volume (ppmv)) along with its variability (bars) and accuracies (brackets).

The figures and tables that follow in this section were derived from the 1983 RRA for the particular site. Only the annual means are shown here. However, the designers are not constrained to using the annual means shown in this TM. Additional (monthly) data are available from the MSFC Natural Environments Branch and from the RRA documentation for each site.

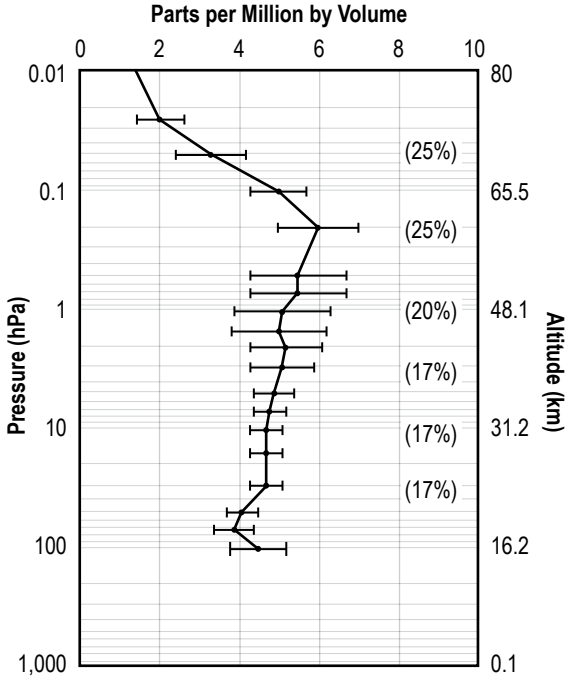

Figure 53. Reference profile of middle atmosphere number concentration mean, variability, and accuracy; representative of Northern Hemisphere, mid-latitude, springtime conditions.

3.7.1 Eastern Range

Annual mean mixing ratio data for the ER used in figure 54 and table 61 were obtained from the Cape Canaveral RRA.[79] The annual mean and $\pm 2\sigma$ mixing ratio (w) data were derived using equation (47):

$$w = \frac{\frac{T_v}{T} - 1}{0.61}, \tag{47}$$

where the virtual temperature (T_v) and temperature (T) are the mean, $\pm 2\sigma$ values for each calculation.

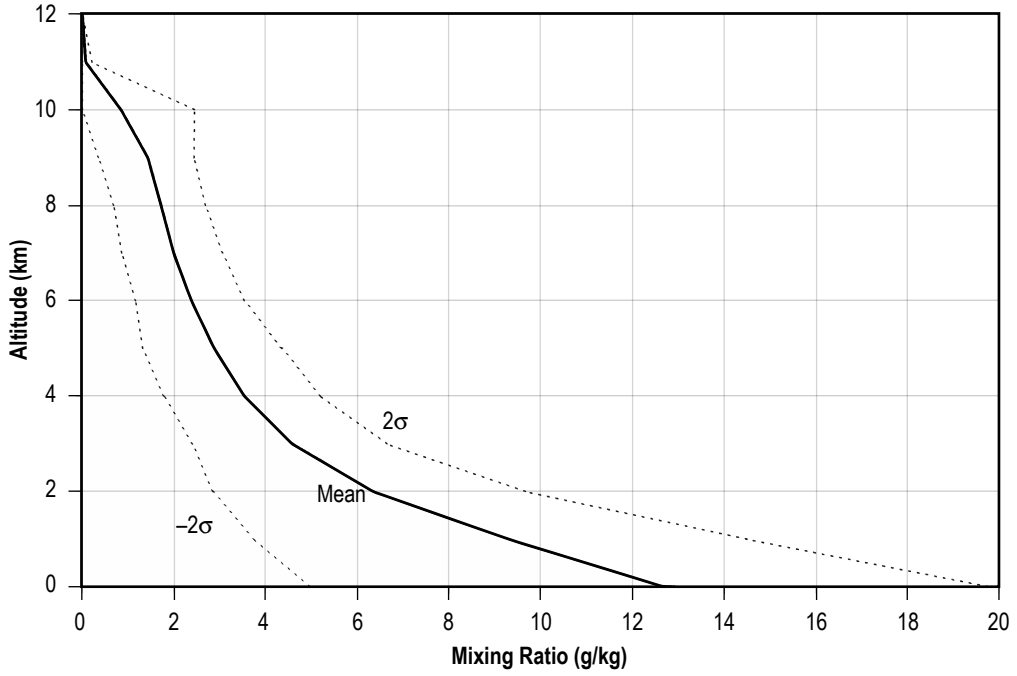

Figure 54. Annual mean and $\pm 2\sigma$ range of mixing ratio versus altitude about the annual mean for the ER.

Table 61. Annual mean and $\pm 2\sigma$ range of atmospheric mixing ratio versus altitude at the ER.

Geometric Altitude		Mean Mixing Ratio (g/kg)	-2σ Mixing Ratio (g/kg)	2σ Mixing Ratio (g/kg)
(km)	(ft)			
–	–	12.94	5.36	19.91
3×10^{-3}	9.8	12.67	4.96	19.76
1	3.3×10^{3}	9.3	3.75	14.5
2	6.6×10^{2}	6.34	2.84	9.66
3	9.8×10^{3}	4.57	2.4	6.65
4	13.1×10^{3}	3.53	1.78	5.2
5	16.4×10^{3}	2.87	1.32	4.36
6	19.7×10^{3}	2.38	1.16	3.54
7	23×10^{3}	1.99	0.86	3.06
8	26.2×10^{3}	1.72	0.68	2.69
9	29.5×10^{3}	1.43	0.35	2.43
10	32.8×10^{2}	0.84	< 0.001	2.45
11	36.1×10^{2}	0.07	< 0.001	0.21
12	39.4×10^{3}	<0.001	< 0.001	< 0.001

3.7.2 Edwards Air Force Base

Annual mean mixing ratio data for EAFB used in figure 55 and table 62 were obtained from EAFB RRA.[81] The annual mean and $\pm 2\sigma$ mixing ratio (w) data were derived using equation (47).

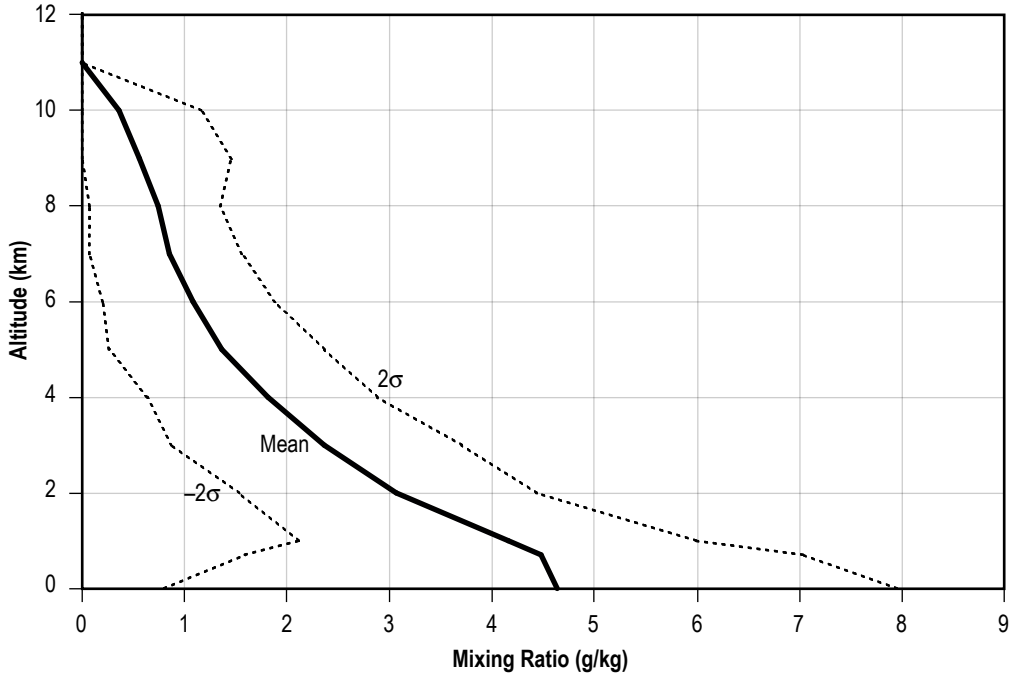

Figure 55. Annual mean and $\pm 2\sigma$ range of atmospheric mixing ratio versus altitude for EAFB.

Table 62. Annual mean and $\pm 2\sigma$ range of atmospheric mixing ratio versus altitude at EAFB.

Geometric Altitude		Mean Mixing Ratio (g/kg)	–2σ Mixing Ratio (g/kg)	2σ Mixing Ratio (g/kg)
(km)	(ft)			
–	–	4.64	0.8	7.95
0.71	2.3×10^3	4.48	1.59	7.03
1	3.3×10^3	4.16	2.11	5.99
2	6.6×10^2	3.07	1.53	4.44
3	9.8×10^3	2.36	0.87	3.71
4	13.1×10^3	1.81	0.64	2.88
5	16.4×10^3	1.36	0.26	2.36
6	19.7×10^3	1.08	0.2	1.88
7	23.0×10^3	0.85	0.07	1.56
8	26.2×10^3	0.74	0.07	1.35
9	29.5×10^3	0.56	<0.001	1.46
10	32.8×10^2	0.36	<0.001	1.16
11	36.1×10^2	<0.001	<0.001	<0.001
12	39.4×10^3	<0.001	<0.001	<0.001

3.8 Aloft Aerosols

Gases and particles in the atmosphere must be considered during vehicle development in order to avoid detrimental effects to the vehicle on the ground and in flight. Some of these effects include corrosion, abrasion, and optical hindrances. The intensity of damage depends on the source, location, and concentration of the particles. The particles, together with the air that suspends them, are termed aerosols.

3.8.1 Gaseous Constituents

Gaseous, as well as particulate matter, can cause detrimental effects on aerospace vehicles and ground equipment due to various chemical reactions/processes. Nitrogen (N_2) and molecular oxygen (O_2) make up approximately 99% by volume (98.6% by weight) of the lower atmosphere. These two atmospheric constituents, along with carbon dioxide (CO_2), water vapor, and ozone (O_3) are the gases of primary concern.

The variability of many atmospheric trace gases is quite large. However, table 63 provides the typical gas concentration values expected from the surface to 90 km (295.3×10^3 ft) altitude. Seasonal, diurnal, and location variations plus other changes can all add to the variability of the various atmospheric constituents. The mean values presented in table 63 are based on model information taken from references 82 and 83. The Earth-GRAM 2010 model, discussed in section 3.9, can be used to estimate atmospheric species concentrations.

3.8.2 Upper Atmospheric Aerosols

Atmospheric aerosols can exist at stratospheric levels (15 to 30 km, 49.2 to 98.4×10^3 ft) as well as in the troposphere.[1] The stratospheric aerosols, consisting mainly of liquid sulfuric acid droplets, are divided into three categories: (1) Background aerosols, (2) volcanic aerosols, and (3) polar stratospheric cloud (PSC) particles.[84] Table 64 presents the basic characteristics of stratospheric aerosols.[83]

Table 63. Average concentrations (standard atmosphere values) of various gaseous constituents from the Earth's surface up to 90 km (295.3×10^3 ft) altitude.*

Constituent	Typical Concentration		
	Altitude (km)	Altitude (ft)	ppbv
N_2	Zero and above	Zero and above	7.81×10^8
O_2	Zero and above	Zero and above	2.09×10^8
Rare gases	–	–	very small
O_3	–	–	27
	7	23.0×10^3	50
	22	72.2×10^3	3,650
	40	131.2×10^3	7,300
	75	246.1×10^3	250
	90	295.3×10^3	700
N_2O	–	–	320
	9	29.5×10^3	320
	32	104.9×10^3	117
	49	160.8×10^3	5
	90	295.3×10^3	0.5
NO**	–	–	0.3
	12	39.3×10^3	0.3
	18	59.1×10^3	0.2
	40	131.2×10^3	11
	70	229.6×10^3	11
	90	295.3×10^3	213
NO_2	–	–	0.02
	10	32.8×10^3	0.02
	18	59.1×10^3	0.8
	35	114.8×10^3	7.3
	50	164×10^3	0.4
	90	295.3×10^3	0.2
H_2S**	–	–	0.1
	2	6.6	0.03
	10	32.8×10^3	0.01
	26 and above	85.3×10^3 and above	10^{-15}
CS_2**	–	–	0.07
	14	45.9×10^3	0.03
	32 and above	104.9×10^3 and above	10^{-15}

* This table gives average values such that a constituent value at altitude can be obtained by linear interpolation between the listed altitude/concentration values. See references 80 and 81 for more exact curves.

** These gases have a very large latitudinal and longitudinal gradient, due to short lifetimes, causing a large range of local concentrations with altitude to exist.

Table 63. Average concentrations (standard atmosphere values) of various gaseous constituents from the Earth's surface up to 90 km (295.3×10^3 ft) altitude (Continued).*

Constituent	Typical Concentration		
	Altitude (km)	Altitude (ft)	ppbv
COS	–	–	<0.05
NH_3**	–	–	0.5
	12 and above	39.4×10^3 and above	<0.01
H_2	0 to 90	0 to 295.3×10^3	560
CH_4	–	–	1,700
	10	32.8×10^3	1,700
	40	131.2×10^3	564
	50	164×10^3	210
	90	295.3×10^3	140
SO_2 **	–	–	0.3
	30	98.4×10^3	0.01
	70	229.7×10^3	0.04
	90	295.3×10^3	0.002
CO	–	–	150
	10	32.8×10^3	100
	21	68.9×10^3	12
	50	164×10^3	46
	90	295.3×10^3	5,840
CO_2	–	–	3.3×10^5
	75	246.1×10^3	3.3×10^5
	90	295.3×10^3	3.1×10^5
HNO_3 (vapor)**	–	–	0.05
	15	49.2×10^3	0.45
	22	72.1×10^3	5.5
	50	164.0×10^3	0.06
	90	295.3×10^3	0.03
H_2SO_4 (vapor)	0 to 90	0 to 295.3×10^3	Small except in localized areas

* This table gives average values such that a constituent value at altitude can be obtained by linear interpolation between the listed altitude/concentration values. See references 80 and 81 for more exact curves.

** These gases have a very large latitudinal and longitudinal gradient, due to short lifetimes, causing a large range of local concentrations with altitude to exist.

Table 64. Characteristics of stratospheric aerosols.

Particle Type	Sulfate Aerosol	Type I PSC	Type II PSC	Meteoric Dust	Rocket Exhaust
Physical state	Liquid or slurry with crystals	Solid nitric acid trihydrate, solid solutions	Solid crystal, hexagonal, or cubic basis	Solid granular irregular or spherical	Solid spheres or irregular surface ablated debris
Particle radius (mm, 10^{-6} m)	0.01–0.5, ambient 0.01–10, volcanic	0.3–3	1–100	1–100, micro-meteorites 0.01–0.1, smoke	0.1–10
Number (No. cm^{-3})	~ 1–10	~ 0.1–10	<<1	10^{-6}, 100 mm 10^{-3}, 1 mm	10^{-4}, 10 mm 10^{-2}, 1 mm
Principal composition	H_2SO_4/H_2O ~ 70%/30%	HNO_3/H_2O ~ 50%/50%	H_2O	SiO_2, Fe, Ni, Mg; C	Al_2O_3
Trace composition	NH_4^+, NO_3	HCl, SO_4^{2-}	HNO_3, HCl	SO_4^{2-} (surface)	Cl^-, SO_4^{2-} (surface)
Physical characteristics	Dust inclusions, in solution	Equidimensional crystalline or droplets	Elongated crystals with polycrystalline structure	Irregular mineral grains, grain defects	Homogeneous composition; smooth spheres
Distribution	Global, ambient Regional, volcanic 12–35 km alt.	Polar winter 14–24 km altitude	Polar winter 14–24 km altitude	~ Global >12 km altitude	Global >12 km altitude
Residence time	~ 1–2 yr ambient ~ 1–3 yr volcanic	~ 1 day to weeks	~ Hours	<1 mo (micro-meteorites) 1–10 yr (meteoritic smoke)	<1 yr

3.9 Earth-Global Reference Atmospheric Model 2010

In the development of aerospace vehicles, standard or reference atmospheric models have been used to study the vehicle response to atmospheric variations in space and time. MSFC developed a GRAM, Version 2010 (Earth-GRAM 2010), that incorporates empirically-based models to provide complete global geographic variability, altitude coverage from the surface to orbital altitudes, and monthly and seasonal variability of wind components and thermodynamic variables. In addition to providing output of the monthly and seasonal mean atmospheric state, Earth-GRAM 2010 can also simulate spatial and temporal perturbations of these atmospheric parameters. The models that constitute Earth-GRAM 2010 are the National Centers for Environmental Prediction (NCEP) Database, the Middle Atmosphere Program (MAP), and a choice between three thermosphere models:

(1) Marshall Engineering Thermosphere (MET).

(2) Naval Research Labs Mass Spectrometer, Incoherent Scatter Radar Extended Model thermosphere (NRL MSIS-E-00) with the associated Harmonic Wind Model (HWM-93).

(3) Jacchia-Bowman 2008 thermosphere model (JB2008).

These are combined together for the purposes of providing a complete atmospheric profile. Figure 56 provides a graphical summary of the data sources and height regions.[71] Additional information about each component and other user options are discussed in the following section.

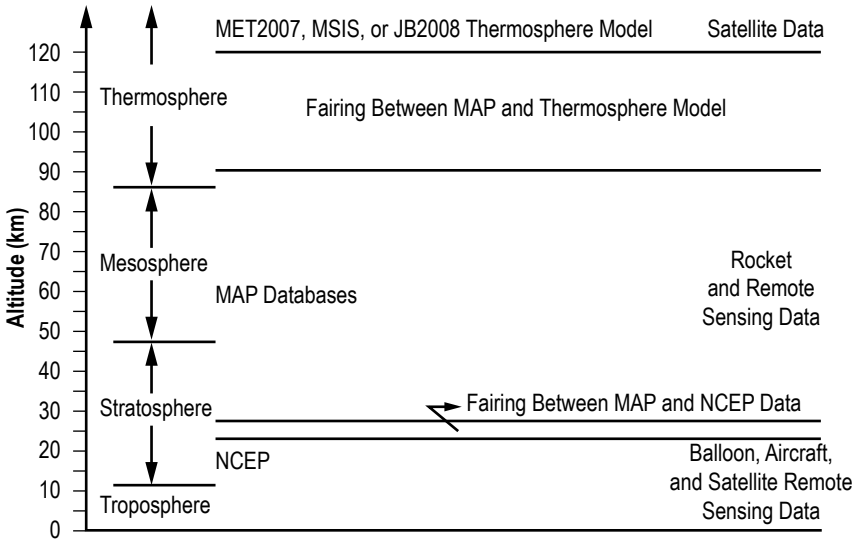

Figure 56. Graphical summary of the atmospheric regions in Earth-GRAM 2010 and sources for the model and the data from which the mean monthly values are based.

3.9.1 National Centers for Environmental Prediction Database (Surface to 10 mb (0.15 lb/in^2))

For the lower atmosphere, Earth-GRAM 2010 uses climatological data derived from an NCEP global reanalysis database. The NCEP data consist of means and standard deviations (at a global latitude-longitude resolution of 2.5°×2.5°) at four specific times of day (00, 06, 12, and 18 UTC) and for all four times of day combined at the surface and at each of 17 pressure levels. Averages and standard deviations are by month over a POR from 1990 through 2008. As part of validation studies conducted for Earth-GRAM 2010, NCEP hourly and daily averages of surface winds and temperatures were compared with statistics from more directly observed surface winds and temperatures. During these studies, it was found that NCEP average surface winds and temperatures did not have nearly as much variation with hour of day as did observed surface winds and temperatures. Consequently, a more detailed study of surface and near-surface NCEP data and observed winds and temperatures were undertaken. For more information on this study and the NCEP database, see Leslie and Justus.[71]

3.9.2 Middle Atmosphere Program (20 to 120 km (65.6×10^3 to 393.7×10^3 ft))

The MAP component of Earth-GRAM 2010 characterizes the monthly mean middle atmosphere from two data sets, the zonal mean and mean stationary wave patterns.[71] The zonal monthly mean data set is merged from six separate data sets over an altitude range of 20 to 120 km (65.6×10^3 to 393.7×10^3 ft). This data set contains pressure, density, temperature, and mean easterly wind component data. The data are gridded in 10° latitude (0° to 80°) and 5 km (16.4×10^3 ft) height increments. For zonal mean values at ±90° latitude, data set values are computed by an across-the-pole interpolation scheme.[71] The stationary perturbation data set contains pressure, density, temperature, and eastward and northward wind components gridded in the same latitude and

height increments as the zonal mean data and 20° longitude increments. This data set was merged from three sources of data on planetary-scale standing wave patterns. At the poles, the stationary wave perturbations are identically zero. At altitudes where irregularly spaced data overlap between the lowest altitude MAP value at 20 km (65.6×10^3 ft) and the highest altitude NCEP data at 10 mb (0.15 lb/in^2), fairing techniques are used to smooth the transition.

3.9.3 Marshall Engineering Thermosphere (Above 90 km (295.3×10^3 ft))

The MET (Jacchia) model calculates density, temperature, and pressure at altitudes above 90 km (295.3×10^3 ft). The MET model accounts for temperature and density variations due to solar and geomagnetic activity, diurnal, seasonal, and latitude-longitude variations at altitudes above 90 km (295.3×10^3 ft).[71] Geostrophic wind components are also evaluated by estimating horizontal pressure gradients. Fairing techniques are employed to ensure a smooth transition in the region of overlap, 90 to 120 km (295.3×10^3 to 393.7×10^3 ft), between the MAP and MET models.

3.9.4 Range Reference Atmosphere (0 to 70 km (0 to 229.7×10^3 ft))

Earth-GRAM 2010 can also incorporate RRA data as an alternative to Earth-GRAM climatology near RRA sites. Earth-GRAM 2010 uses a fraction of data contained within the RRA data set. The RRA data utilized in Earth-GRAM consists of an annual average data set and 12 monthly data sets for the following: height; mean and standard deviation E-W wind; mean and standard deviation N-S wind; mean and standard deviation pressure; mean and standard deviation temperature; mean and standard deviation density; and mean and standard deviation dewpoint temperature.

A practical application of using RRA data in Earth-GRAM 2010 is in vehicle trajectory simulations. For example, the vehicle can be launched from one RRA site (i.e., CCAFS), smoothly transition to an atmosphere characterized by the Earth-GRAM climatology, then smoothly transition into an atmosphere characterized by a different RRA site for landing (i.e., EAFB). Smooth transitions of an atmosphere characterized by an RRA site to Earth-GRAM climatology is based on user-selected inputs defining the size of the latitude-longitude region near any selected RRA site. Any latitude-longitude within a radius of 0.5° of any RRA site will use the RRA site data. If the location lies beyond a radius of 2.5°, the Earth-GRAM climatology is used. Between a radius of 0.5° and 2.5°, a weighted average of RRA data and Earth-GRAM data are used with the RRA data weighting factor smoothly changing from 1 at a radius of 0.5° to zero at a radius of 2.5°. The user can modify those values. If more than one RRA is located within a selected radius of influence, data from the nearest (highest weighted) site is used. Fairing techniques are used to transition from the RRA data to Earth-GRAM 2010 data near the top of the RRA site. For more information on how Earth-GRAM uses RRA data, refer to Leslie and Justus.[71]

3.9.5 Atmospheric Species Concentration Data

Earth-GRAM 2010 provides estimates of atmospheric species concentrations for water vapor (H_2O), O_3, nitrous oxide (N_2O), carbon monoxide (CO), methane (CH_4), CO_2, N_2, O_2,

atomic oxygen (AO), argon (Ar), helium (He), and hydrogen (H). Air Force Geophysics Laboratory[83] atmospheric constituent profiles are also used extensively for the constituents up to 120 km (393.7×10^3 ft) altitude. The MET (Jacchia) model provides the species concentrations for N_2, O_2, AO, Ar, He, and H above 90 km (295.3×10^3 ft). For more information on the atmospheric species concentration data in Earth-GRAM, see Leslie and Justus.[71]

3.9.6 Available Special Output

Earth-GRAM 2010 has the ability to calculate derived quantities at each grid point in addition to the standard output. Some examples of derived quantities are the speed of sound, pressure scale height, and mean free path. Refer to Leslie and Justus[71] for more information on derived quantities.

3.10 Stratospheric and Mesospheric Clouds

Due to a presence of high-altitude cloud systems/particles above the troposphere, designers and planners need to account for these factors when vehicle reentry, launch, or horizontal flight above 12 km (39.4×10^3 ft) altitude is desired. Stratospheric clouds typically develop in the lower altitudes of the stratosphere, 15 to 30 km (49.2×10^3 to 98.4×10^3 ft), while mesospheric clouds develop in the upper altitudes of the mesosphere, 80 to 85 km (262.5×10^3 to 278.9×10^3 ft). General characteristics will be presented in the following section.

PSCs are frozen aerosol particles observed in local winter over both polar regions whenever the ambient temperature falls below –78 °C (–108.4 °F). The clouds are layered with the maximum amount near 20 km (65.6×10^3 ft), close to the region of minimum stratospheric temperature. The layers are thin; <1 to 2 km (<3.3×10^3 to 6.6×10^3 ft) thick (thicker in the Antarctic). The PSC base descends over the local winter polar region, falling to an altitude of approximately 15 km (49.2×10^3 ft) at the end of winter. Antarctic PSCs generally occur at lower altitudes, <17 km (< 55.8×10^3 ft) than Arctic PSCs (17 to 25 km (55.8×10^3 to 82×10^3 ft)), due to the strong gradient across the polar vortex that develops over the nighttime Antarctic, which lasts until the springtime breakup. The clouds are much more prevalent in the Antarctic with their colder, stratospheric temperatures, by 3.5 °C (6.3 °F), than they are in the Arctic. Although different kinds of PSCs exist, which may have different compositions, they exist as highly supercooled/supersaturated liquid drops.[1]

Nacreous clouds (NACs), thin stratospheric clouds appearing brilliantly colored and stationary (lenticular), occur in wintertime over high latitudes in both hemispheres, i.e., Scandinavia, Alaska, and Antarctica, when the Sun is below the horizon. There are over 155 dates in which northern hemispheric sightings (for undisturbed stratosphere only, no aircraft contrails included) of NACs have been observed over 100 years during winter (December to February). Somewhat more frequent are NACs over the Antarctic winter (June to September) where over 140 sightings in 100 years have occurred in these sparse reporting areas.[1]

NACs have been sighted between 17 to 31 km (55.8×10^3 to 101.7×10^3 ft) altitude (average 23 km (75.5×10^3 ft)), and set up preferentially downwind of mountain ranges. This indicates

orographic origin with lee waves producing up to 40 km (131.2×10^3 ft) wavelengths present in the NAC bands. NACs are a special subset of PSCs, but it is not yet clear that the two-cloud phenomena are the same. NACs are composed of micrometer-sized water ice particles (crystals) with sizes of the order of 1 to 2 μm in radius, and lifetimes are >10 min at 20 km (65.6×10^3 ft) (1 ppm of water is equivalent to 5 particles/cm^3 (82 particles/in^3) of size 1.5 μm). An approximate maximum radius of approximately 4 μm at 20 km (65.6×10^3 ft) altitude may be determined, assuming 3 ppm of water condensing to form 1 particle/cm^3 (16 particles/in^3). It is generally believed that NACs form by deposition of H_2O on preexisting stratospheric aerosol particles (sulfate), when stratospheric temperatures are typically at or below –85 °C (–121 °F). Therefore, the number concentration of NAC particles should be equal to that of the stratospheric aerosols, approximately 5 to 20 cm^3 at 20 km (82 to 328.0/in^3 at 65.6×10^3 ft).[1]

Noctilucent clouds (NLCs) (also referred to as polar mesospheric clouds) were once thought to be very rare, especially in the Southern Hemisphere; however, observations from space have shown that they occur almost continuously during some periods of time.[1] In both hemispheres, their coverage can be quite extensive. NLCs are composed of submicron-sized water ice particles growing in supersaturated air and occurring in a few kilometers thick layer, only during summer, over higher latitudes, (poleward of 45 °N. and 50 °S.) at cold (< –133 °C (< –207.4 °F)) mesopause altitudes (85 km (278.9×10^3 ft)). These clouds have been observed only from the ground over the past 100 years, at twilight (morning or evening), when the Sun is between 6° and 16° below the horizon, so that the 80 to 85 km (262.5×10^3 to 278.9×10^3 ft) level is still in sunlight. Whether NLC and polar mesospheric clouds both represent the same phenomenon currently remains an open question.

3.11 Aloft (150 m to 90 km) Ionizing Radiation Environments and Effects

Once the space vehicle is aloft, it will continue to be exposed to the terrestrial ionizing radiation environments that were presented in section 2.12.

3.11.1 Aloft Ionizing Radiation Environments

Section 2.12.1 described the processes involved in understanding the ionizing radiation environments that will be encountered in the terrestrial segments. Variation from the ground environments to the aloft environments will be discussed next.

3.11.2 Galactic Cosmic Ray Flux in the Atmosphere

Unlike the discussion in section 2.12 where the ionizing radiation environments from GCR and SPE were treated simply as a source for the terrestrial neutron production, in the aloft segment, these environments will directly impact the electronic systems. So an understanding of the nature of these environments is needed.

Both GCR and SPE constituents are similar conceptually in that they both contain protons and heavier ions produced outside the Earth's geomagnetic field and must traverse the magnetic field and the upper atmosphere to impact the aloft segment. The other similarity is that both consist of a distribution of particle species, each with their own energy spectra. However, that is where

the similarity ends. With the source of the GCR postulated to be external to the solar system, the quantity of the particles is much lower but they have had sufficient acceleration encounters so they are at much higher energies than their Sun-produced equivalents. An SPE can constitute a significant event on the Sun and thereby throw a substantial amount of particle in Earth's direction. This quantity can be orders of magnitude larger than during the nominal times of no SPE.

For atmospheric neutron environments, it is a much simpler process of presenting the environment. Once a maximum latitude is chosen and the minimum neutron energy required to produce the effect is determined (generally >10 MeV), then a simple plot of neutron flux as a function of altitude can be given (see fig. 57). For GCR and SPE environments, it is not this simple.

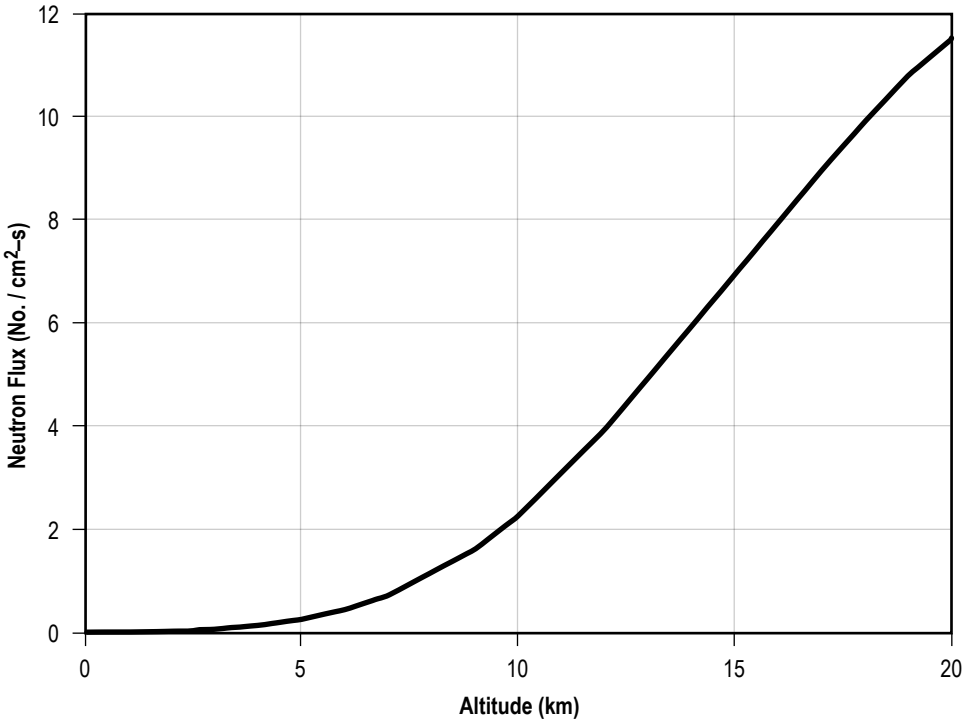

Figure 57. Plot of the atmospheric neutron flux as a function of altitude for >10 MeV neutrons.

These environments consist of protons that can provide a similar plot (see fig. 58) since they produce effects through spallation events as do the neutrons. The only difference for protons is that an altitude is selected and the proton energy spectrum is presented. However, these environments also contain heavier ions that produce effects through direct ionization that is a function of the ion's atomic number, its energy, and the material it is interacting with. As a result, a different parameter is needed to deal with these issues. To deal with the ion species, energy, and target material, a parameter called the linear energy transfer (LET) is used. The LET is how much energy an ion deposits as a function of depth in the given target material. Since most electronics used currently are made from silicon, LET is typically presented for silicon. The calculation of this parameter is based on how ion stop in material; details of this can be found in reference 85. A typical example of this environment is shown in figure 59.

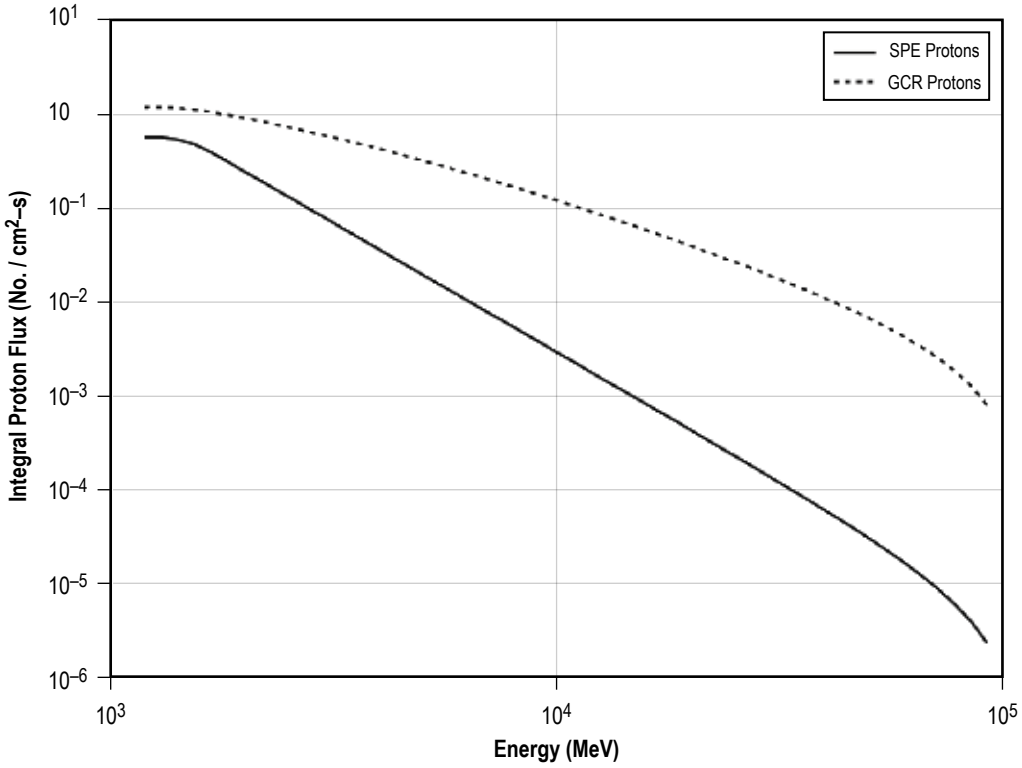

Figure 58. Plot of the proton flux as a function of energy for an altitude >200 km.

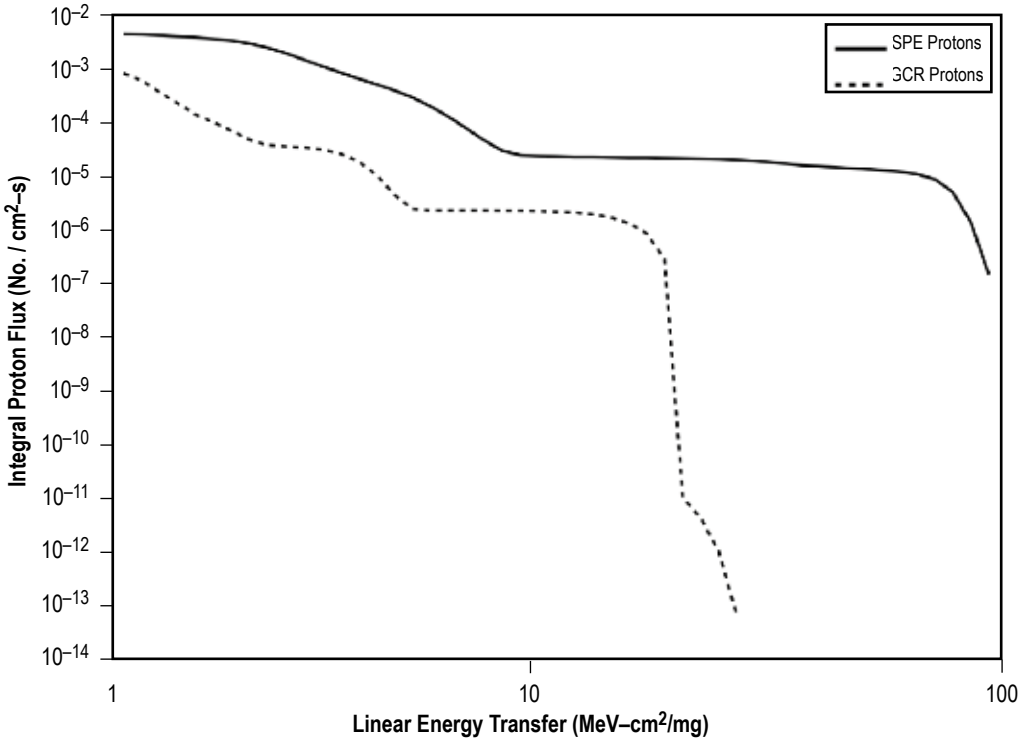

Figure 59. Plot of the heavy ion flux as a function of LET for an altitude >200 km.

3.11.3 Aloft Ionizing Radiation Effects

The effects of ionizing radiation on electronic systems can be divided into two categories: cumulative effects and transient effects. Cumulative effects are those that require exposure to the environments over time to produce an effect. Transient effects are those that can be induced at any time during a mission and can require nothing more than a single particle passing through an electronic device to produce the effect (that can either be temporary or permanent). As with the ground-based segment, the exposure time in the aloft segment is short and the ionizing radiation levels are small as compared to those in space, the cumulative effects for the terrestrial segments of a mission are negligible and will not be discussed here.

The only transient effect that is applicable to space systems is a SEE. SEEs are effects in microelectronics that are induced by the passage of a single particle through the part. Discussion of the basic concepts of SEE is presented in section 2.12.3.

3.11.4 Aloft-Based Effects

In addition to the atmospheric neutrons producing SEEs, the aloft segment will also have to deal with high-energy protons and heavy ions (from GCR and SPE, as discussed above). Similar to the atmospheric neutrons, the protons must rely on spallation events to produce SEE. However, the direct interaction of the heavy ions depositing energy as they traverse sensitive regions of the electronic device will give every ion the possibility of producing an SEE. Therefore, it should be expected that the aloft segment will be dominated by the heavy ion-induced SEE. This will indeed be true for any electronics that will be expected to operate in the upper regions of the aloft segment. If, on the other hand, required operation is complete by 20 km in altitude, then, as with the ground effects, only the atmospheric neutrons will play a role (albeit at a much higher rate than on the ground).

It should be understood that the rate of SEEs will be an additive function of all the environments that a system will be exposed to. As discussed above, there will be regions of the aloft environment that will be dominated by one environment over the other so that its event rate only need be considered. The caveat here is that the required region of operation may encompass many or all of these regions, implying that all SEE-producing environments must be part of the analysis. So in addition to the neutron-based analysis reference given in section 2.12.4, references 86 and 87 should be consulted for an understanding of proton-induced SEE and references 88–90 for heavy-ion-induced SEE.

3.12 Lightning Aloft

Lightning, either triggered or natural, may occur in the vertical domain from ground level up to a typical maximum altitude of around 15 km (49.2×10^3 ft). The highest probability events occur between ground level and approximately 7 km (23×10^3 ft). Refer to section 2.8 for detailed information on lightning flash densities and considerations for external and internal lightning environment.

4. NEAR EARTH SPACE ENVIRONMENTS

The natural space environment refers to the environment as it occurs independent of the presence of a spacecraft; thus, it includes both naturally occurring phenomena (such as AO and atmospheric density, ionizing radiation, plasma, etc.), and a few man-made factors (such as orbital debris). The space environment covers all the environments ranging from approximately 90 km up to 10 R_e.

5. LOW EARTH ORBIT SPACE ENVIRONMENTS (90 to 2,000 km)

5.1 Thermosphere

The region of the Earth's atmosphere lying between approximately 90 and 500 km is known as the thermosphere. The neutral gases in the thermospheric region are in a diffusive equilibrium and are typically referred to as the D (50 to 90 km), E (90 to 160 km), and F (160 to 500+km) layers. At an altitude over 100 km, plasmas (charged particles) are generated due to photoionization of the ambient neutral atmosphere of the solar photons and by magnetospheric particles interacting with the thermosphere. Details of the plasma environment and its characteristics are described in section 5.4.

The neutral atmosphere in this region is most conveniently described in terms of a mean, with spatial and temporal variations about that mean. For space vehicle operations, the neutral atmosphere is significant because (1) even at its low density, it produces torques and drags on the vehicle, (2) the density height profile of the atmosphere above 100 km altitude modulates the flux of trapped radiation encountered, as explained in the ionizing radiation section, and the orbital debris, as explained in their respective sections, and (3) the AO may erode and chemically change those surfaces which are exposed to it.

5.1.1 Thermospheric Process

The temperature in the lower thermosphere increases rapidly with increasing altitude from a minimum at 90 km. Eventually it becomes altitude independent at upper thermospheric altitudes. This asymptotic temperature, known as the exospheric temperature, is constant with altitude due to the extremely short thermal conduction time. The thermospheric gases are heated by the absorption of the solar extreme ultraviolet (EUV) radiation. At the lowest thermospheric altitudes, the absorption of ultraviolet (UV) radiation is also important. The EUV and UV radiation initially heats only the dayside thermosphere, and although conductive and convective processes act to redistribute some of this energy, a large temperature gradient always exists between the daytime and the nighttime thermosphere. An average daytime exospheric temperature is 1,060 K, and an average nighttime exospheric temperature is 840 K. The longitudinal temperature gradient causes a wind to flow from the dayside to the nightside thermosphere, with speeds typically reaching 100 m/s.

An additional heat source for the thermosphere is the interaction of the Earth's magnetic field at distances of several Earth radii, in the region known as the magnetopause, with the solar wind. The solar wind is a stream of high-speed plasma emanating from the Sun. This interaction causes energetic particles to penetrate down into the lower thermosphere at high geographic latitudes and directly heat the thermospheric gas. These energetic particles are also responsible for

the aurora seen at these high latitudes. In addition, electric fields mapped down from the magnetosphere onto the high latitude ionosphere cause electric currents to flow. The term 'ionosphere' refers to the small fraction of the thermosphere that remains ionized due to solar radiation. It never totally disappears at night, and during daylight hours the ionization density never exceeds more than 1% of the neutral density. These electrical currents lose energy through ohmic or joule dissipation and heat the neutral thermospheric gas. The ions also collide directly with the neutral gas, setting the whole gas into motion. At these high latitudes, the wind speeds generated by this process can be very large, at times as large as 1.5 km/s. Eventually viscous effects dissipate these winds, and their lost kinetic energy provides an additional heat source for the neutral thermospheric gas.

The high-latitude heat sources are effective during both the day and night. Although an intermittent source of energy for the thermosphere, they can at times exceed the global EUV energy absorbed by the thermosphere. In addition, although the energy is deposited at high latitudes (>60° or so), the disturbance effects are transmitted to lower latitudes through the actions of winds and waves. However, the disturbance effects at low latitudes are significantly smaller than they are at higher latitudes. The high latitude ionospheric currents that flow perturb the geomagnetic field, so that such disturbances, which can be detected by ground-based magnetometers, are referred to as geomagnetic storms.

Whenever the neutral thermospheric gas is heated, it expands radially outward. Because the undisturbed thermospheric density decreases with increasing altitude, an outward expansion of the gas results in an increase of density at high altitudes. Thus, the daytime thermospheric density is greater than the nighttime density, while during times of geomagnetic storms, the high latitude density is greater than it is during undisturbed periods. This anisotropic heating leads to the so-called diurnal and polar bulges, which were first inferred from the increased drag experienced by orbiting satellites.

Below the turbopause (located at approximately 105 km altitude), the atmosphere is well mixed by turbulence, so that the composition of the atmosphere does not vary with altitude. Above the turbopause, however, diffusion becomes so rapid that the altitude variation of the various species becomes dependent on molecular mass, with the result that composition varies with altitude. Thus, the number densities of the heavier thermospheric species (N_2 and O_2) decrease with increasing altitude much faster than those of the lighter species (H and He). This means that the heavier molecular species dominate in the lower thermosphere, while the lighter atomic species dominate in the upper thermosphere. A typical altitude profile for the individual thermospheric constituents is shown in figure 60. Lifting of the thermosphere will cause the mean molecular weight at a given altitude to increase, while a sinking motion will cause it to decrease.

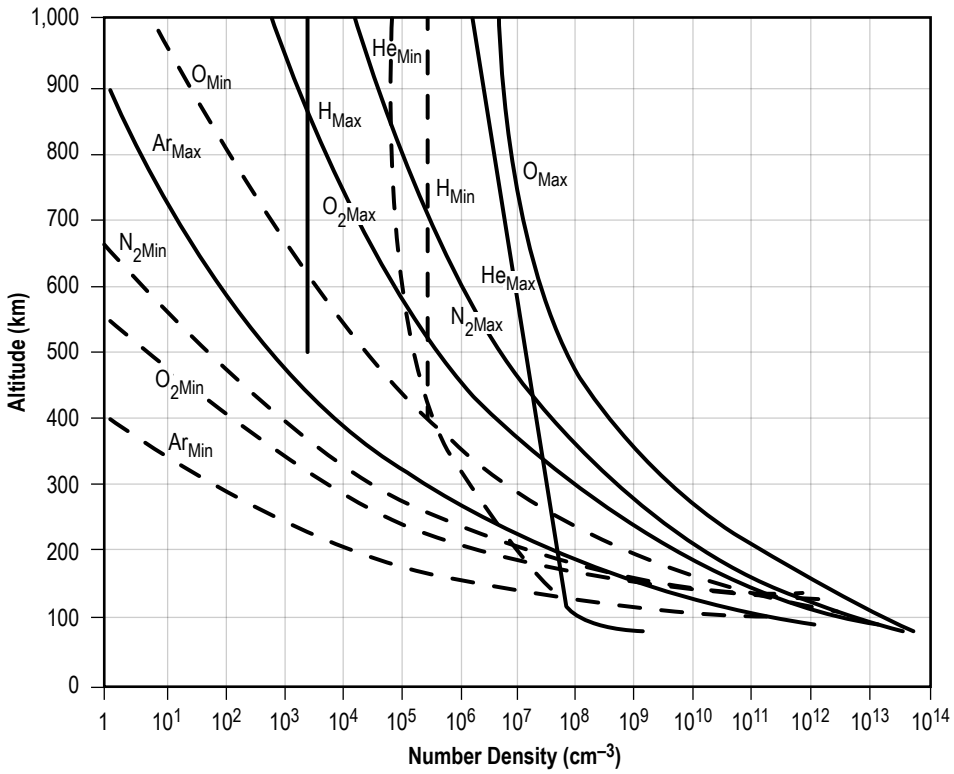

Figure 60. Number density of atmospheric constituents versus altitude.

5.1.2 Variations

In addition to the diurnal variation in the neutral mass density at orbital altitudes, there is a semi-annual variation, a seasonal latitudinal variation in the lower thermosphere, and a seasonal latitudinal variation in the He number density, as well as nonperiodic perturbations associated with variations in solar activity, atmospheric waves, and thermospheric winds. All of these variations are discussed in the following sections.

5.1.2.1 Variations in Solar Activity. While the total amount of solar electromagnetic radiation is nearly constant, the short wavelength portion of the spectrum (EUV and UV) changes substantially with the overall level of solar activity, with the result that the thermospheric density, especially at orbital altitudes, is strongly dependent on the level of solar activity. Thus, there is a (roughly 11 year) variation in the thermospheric mass density, corresponding to the 11-year (more or less) variation in solar activity. Similarly, there is also, on the average, a 27-day variation in density that is related to the mean 27-day solar rotation period although the variation tends to be slightly longer than 27 days early in the cycle when active regions occur more frequently at higher latitude and slightly shorter than 27 days later in the cycle when active regions occur more frequently closer to the Sun's equator. The appearance of coronal holes and active longitudes also affects this average 27-day variation. Changes in the thermospheric density related to changes in the solar output during active periods associated with flares, eruptions, coronal mass ejections (CMEs), and coronal holes can begin almost instantaneously (minutes to hours), although more often a day or more lag is seen. Figure 61 shows typical neutral densities for periods of high and low solar activity.

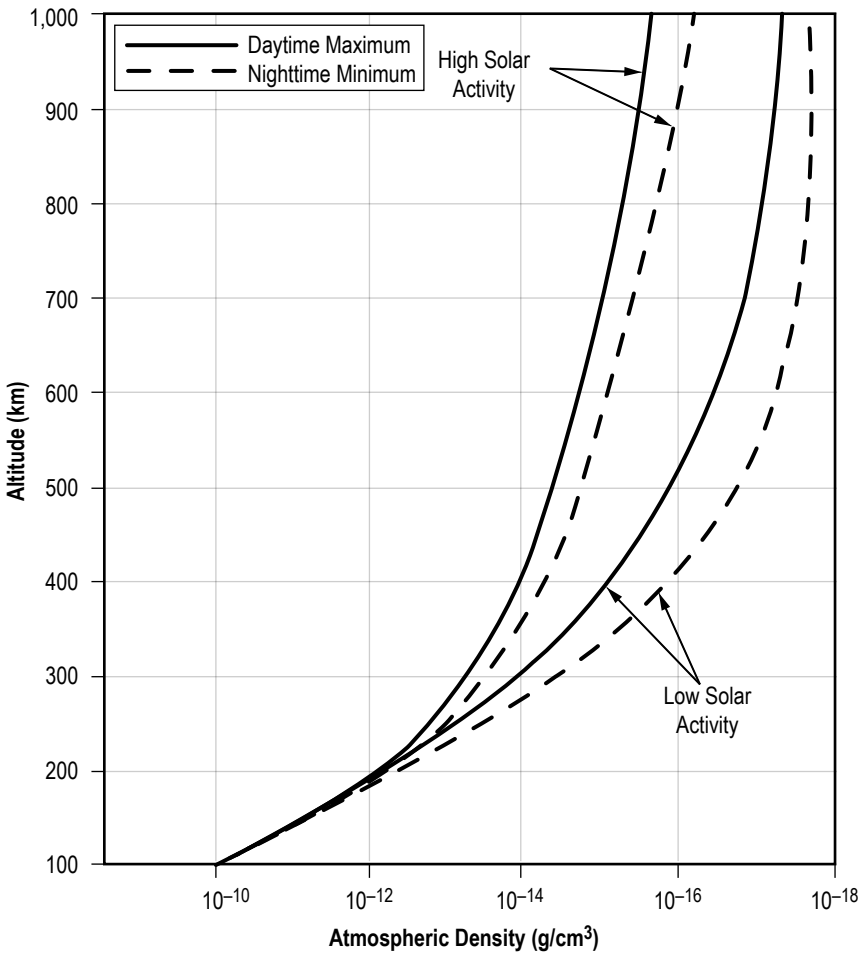

Figure 61. Typical neutral densities for low and high solar activities (the atmospheric density increases toward the left on the abscissa).

5.1.2.2 Variations During Periods of Increased Solar Activity (Flares, Coronal Mass Ejections, and Coronal Holes). As previously described, during periods of increased solar activity the enhanced interaction of the solar wind with the Earth's magnetosphere leads to a high latitude heat and momentum source for the thermospheric gases. Some of this heat and momentum is convected to low latitudes. This episodic type of increased solar activity that usually causes variations in the Earth's magnetic field varies over the solar cycle and usually has two or more major peaks; one during the rise of the cycle and the other with larger peaks during the decline of the cycle. Also, more intense solar cycles seem to have more intense episodic type activity. Finally, there is a seasonal variation associated with this episodic type activity with the density usually being greatest in March (± month) and September (± month) of each year. This variation is possibly related to the path of the Earth in its rotation around the Sun.

5.1.2.3 The Diurnal Variation. The rotation of the Earth with respect to the solar EUV heat source induces a diurnal (24-hr period) variation (or diurnal tide) in the thermospheric temperature and density. Due to a lag in the response of the thermosphere to the EUV heat source, the density at orbital altitudes maximizes around 14:00 LST at a latitude approximately equal to that of the

subsolar point. The lag, which is a function of altitude, decreases with decreasing altitude. Similarly, the density minimum occurs between 03:00 and 04:00 LST at approximately the same latitude in the opposite hemisphere. The diurnal variation is not a predominant effect in the lowest regions of the thermosphere (120 km and below) where the characteristic thermal conduction time is on the order of a day or more.

The various constituents of the thermosphere do not all respond to the diurnal variation of the solar EUV heat source with the same amplitude and phase. The time lag is longer, by as much as 2 hr at orbital altitudes, for the heavier constituents (N_2, O_2, and Ar) than for AO. By contrast, the lighter species' number densities maximize in the early morning hours (03:00 and 07:00 LST, for H and He, respectively). This is due to dynamical (buoyancy) effects.

Harmonics of the diurnal tide are also induced in the Earth's atmosphere. In particular, a semidiurnal tide (period of 12 hr) and a terdiurnal tide (period of 8 hr) are important in the lower thermosphere (below 160 km for the semidiurnal tide and much lower for the terdiurnal tide). These tides are not important at orbital altitudes.

5.1.2.4 Semiannual Variation. This variation is believed to be a conduction mode of oscillation driven by a semiannual variation in joule heating in the high-latitude thermosphere (because of a semiannual variation in the effects on the Earth-atmosphere system of episodic-type variations in solar activity). The variation is latitude independent and is modified by composition effects. The amplitude of the variation is height dependent (30% to 20% and asymmetric about the mean density at 350 km) and variable from year to year, with a primary minimum in July, primary maximum in October, and a secondary minimum in January followed by a secondary maximum in April. It has been found that the magnitude and altitude dependence of the semi-annual oscillation vary considerably from one solar cycle to the next. This variation is important at orbital altitudes.

5.1.2.5 Seasonal-Latitudinal Variations of the Lower Thermosphere Density. This variation is driven in the thermosphere by the dynamics of the lower atmosphere (mesosphere and below). The amplitude of the variation maximizes in the lower thermosphere somewhere between about 105 and 120 km, diminishing to zero at altitudes around 170 km. Although the temperature oscillation amplitude is quite large, the corresponding density oscillation amplitude is small. This variation is not important at orbital altitudes.

5.1.2.6 Seasonal-Latitudinal Variations of Helium. Satellite mass spectrometers have measured a strong increase of He above the winter pole. Over a year, the He number density varies by a factor of 42 at 275 km, 12 at 400 km, and 3 or 4 above 500 km. The formation of this winter He bulge is primarily due to the effects of global scale winds that blow from the summer to the winter hemisphere. The amplitude of the bulge decreases with increasing levels of solar activity, due to the increased effectiveness of exospheric transport above 500 km that carries He back to the summer hemisphere. There is also a very weak dependence of the He bulge amplitude on the magnitude of the lower thermospheric eddy diffusivity.

5.1.2.7 Thermospheric Waves. Fluctuations have been detected in temperature and density measurements throughout the atmosphere from the ground up to at least 510 km. Some of these fluctuations are caused by gravity waves, so named because they are primarily oscillations of the neutral gas for which the restoring force is gravity. A thermospheric gravity wave produces a corresponding wave in the ionosphere known as a traveling ionospheric disturbance.

Thermospheric gravity waves oscillate with periods typically in the range of 30 min to several hours, and have horizontal wavelengths in the range of hundreds of kilometers up to approximately 4,000 km. The density amplitudes of the larger scale waves are larger at higher latitudes and diminish toward the equator. At approximately 200 km altitude, typical values of these amplitudes are 15% of the mean at auroral latitudes and 5% of the mean at equatorial latitudes. The small-scale waves have amplitudes that are essentially independent of latitude. Gravity wave amplitudes generally decrease at greater altitudes in the thermosphere due to dissipation by molecular processes. The larger scale waves survive to greater altitudes than do the smaller scale waves.

5.1.3 Thermospheric Winds

Figures 62 and 63 show the general flow patterns of thermospheric winds between 100 and 700 km as they are currently known. The wind speeds range from 100 to 200 m/s at low latitudes while at high latitudes (greater than approximately 65°) they can be as large as 1,500 m/s or more. Rapid (minutes) change in wind direction (of up to 180°), probably driven by gravity waves, has also been observed.

5.1.3.1 Austral (South Polar Region) Thermospheric Winds. Ground-based observations with Fabry-Perot interferometers have shown that there is a direct relationship between austral thermospheric winds at F-layer altitudes and the interplanetary magnetic field (IMF), particularly in the midnight magnetic local time (MLT) sector. The strength of the zonal component of the austral neutral wind in the MLT midnight sector is directly correlated with the strength and direction of the B_y component of the IMF. The zonal wind in the MLT midnight sector changes direction when the sign of the B_y component of the IMF changes and the speed of the zonal wind in the MLT midnight sector is directly proportional to the strength of the B_y component. Conversely, the meridional wind in the MLT midnight sector is correlated with the B_z component in the IMF. The meridional wind decreases as the B_z component turns northward. When B_z is positive, sunward winds develop in the MLT midnight sector and exceed the strength of the zonal winds.

5.1.3.2 Thermospheric Tide. Models of the tides in the lower thermosphere (90 to 140 km) show the midlatitude semidiurnal tide in the wind has an amplitude of tens of meters per second, maximizing at 50 to 70 m/s at approximately 110 km. Temperature tide amplitudes typically reach a maximum of 10 to 20 K; however, the models do not always agree with observations since a semidiurnal oscillation of approximately 70 K has been measured at low latitudes at 120 km altitude. The best agreement occurs at midlatitude; but in general, the models underestimate both the wind and temperature tidal amplitudes. Phase differences are relatively small for the temperature tide, but are large for the tidal winds, as much as 3 hr. Radio detection and ranging (RADAR) measurements of midlatitude semidiurnal wind tides show maximum amplitudes of 60 to 70 m/s in the 110 to 120 km altitude range.

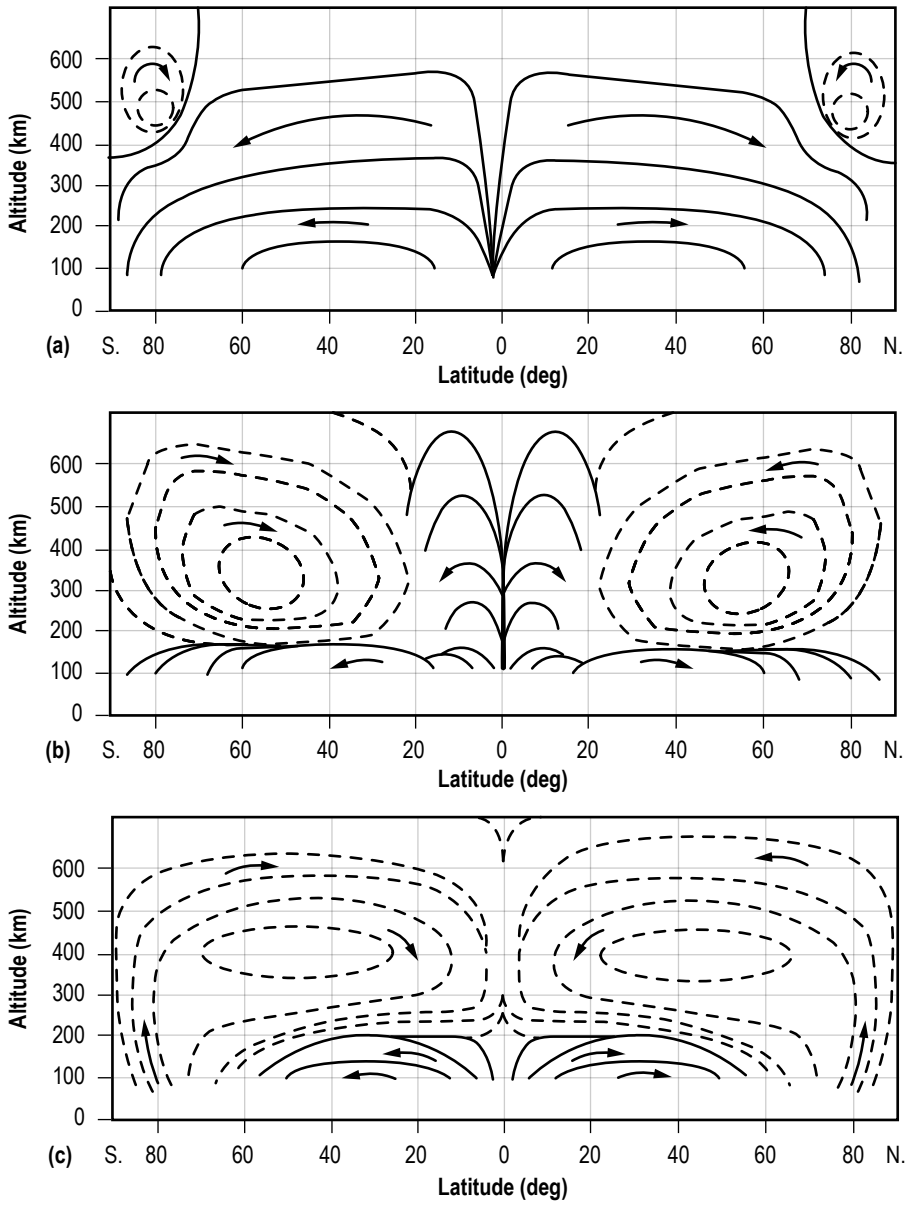

Figure 62. Schematic of the zonal mean meridional circulation in the thermosphere at equinox for various levels of magnetic (auroral) activity (maximum velocities are typically hundreds of meters per second): (a) Quiet, (b) average, and (c) storm.

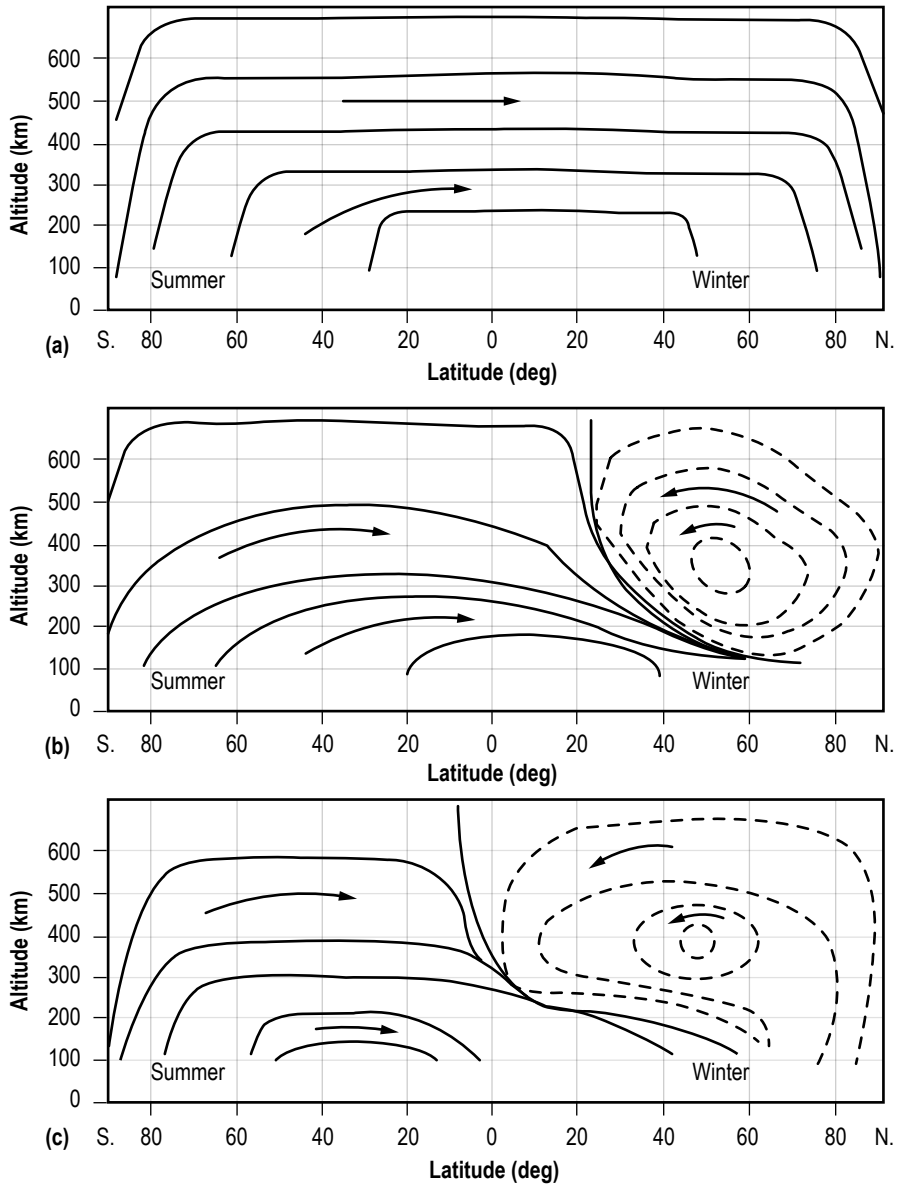

Figure 63. Schematic of the zonal mean meridional circulation in the thermosphere at solstice for various levels of magnetic (auroral) activity (maximum velocities are typically hundreds of meters per second): (a) Quiet, (b) average, and (c) storm.

Values of the maximum midlatitude, annual mean semidiurnal amplitudes, and the altitudes at which they occur are (1) temperature, 25 K at 115 km, (2) northward wind, 50 m/s at 125 km altitude, and (3) eastward wind, 50 m/s at 125 km altitude. The local times of these maxima generally decrease with increasing altitude; temperature leads the meridional wind by approximately 6 hr, while the zonal wind leads the temperature by a few hours.

At middle thermospheric altitudes (300 km), the mean winds are poleward in winter and equatorward in summer. The amplitude of the diurnal component of the mean wind is much greater at solar minimum than at solar maximum, showing that the influence of ion drag more than compensates for the greater EUV input at solar maximum. Typical seasonally averaged wind amplitude for the diurnal tide is approximately 50 m/s. The mean semidiurnal wind tide amplitude averaged over all seasons and solar cycle conditions is approximately 41 m/s.

5.1.3.3 Solar Storm-Induced Effects in the Thermosphere. During magnetic storms and substorms, particle precipitation and the joule dissipation of the high-latitude ionospheric currents heat the neutral gas at altitudes above 110 km. The thermosphere then expands neutral gas densities above approximately 120 km. The energy deposited in the high-latitude thermosphere at such times is significant and can exceed the global EUV absorbed by the thermosphere. It remains an important heat source locally at night in the auroral zones.

The energy generated during a substorm is transferred from high to low latitudes principally by the meridional winds assisted by gravity waves. This high-latitude heating sets up a circulation cell in which gas is lifted in the auroral zone, flows equatorward, sinks at middle to low latitudes, and then returns to the heating region at low altitudes. The sinking causes compressional heating (figs. 62 and 63).

Since the mean molecular weight decreases with altitude, lifting of the gas at auroral latitudes leads to increases in the mean molecular weight at a fixed altitude. Compositional changes also accompany geomagnetic storms and these changes are even observed at middle and low latitudes. In general, during a geomagnetic storm there is a large depletion in AO and an enhancement in O_2 within the auroral ovals. The magnitude of both the AO depletion and the O_2 enhancement is underestimated in current models, with the misrepresentation increasing with the use of daily values of A_p instead of the three hourly values. Analyses, which require instantaneous values of either AO or O_2 within the auroral ovals, should take special precautions in using the available models of the thermosphere.

In one numerical simulation of a geomagnetic substorm it was found that at both 200 and 450 km the latitudinal variations in the mass density during the substorm were relatively insignificant and did not at all reflect the total heat input into the auroral zone. In particular, it was apparent that the global density response was relatively significant (60%) when compared with the 40% increase between the equator and the pole at 450 km. This predominance in the global component was even more pronounced at 200 km and appeared to be in substantial agreement with the satellite drag data. The maximum in the density occurred at 02:00 UTC at high latitudes and shifted toward 08:00 UTC at the equator, with the average time lag of 6 hr deduced from satellite drag data.

In other simulations of geomagnetic substorms, one finds that the heat significantly perturbs the thermosphere at high latitudes and momentum deposited there, with wind speeds approaching 1 km/s in the region of the polar cap and temperatures elevated approximately 500 K in the auroral zones. At lower latitudes the effects are far less dramatic but are still significant. The response is asymmetric with respect to longitude, reflecting the asymmetry of the high-latitude heat sources.

Large-scale disturbances propagate from each auroral region toward equatorial latitudes with a time delay of ≈2 hr at 330 km altitude and ≈5 hr at 125 km altitude. The equatorial thermosphere at 330 km altitude is influenced mainly by the interactions of two converging gravity waves, while at 125 km the thermosphere is influenced by the mean motion of the waves. Equatorial temperature oscillations of magnitude 100 to 200 K occurred at 330 km altitude driven by oscillations in the mean meridional wind of approximately 200 m/s. Temperature enhancements at 125 km were much smaller (60 K) as were the meridional wind speed enhancements (8 m/s). The zonally averaged zonal wind enhancements were found to be confined primarily to the high latitudes.

5.1.3.4 Ionospheric Storm Effects. During and following a geomagnetic substorm, the ionosphere is altered as a consequence of several competing effects. Some of these effects will lead to increases in the ionization density of the F2-region (positive storm effects), and others will lead to decreases in the F2-peak (negative storm effects). These are briefly summarized for the subauroral ionosphere.

5.1.3.4.1 Positive Storm Effects. Traveling atmospheric disturbances, such as gravity waves, will cause a sudden uplifting of the F-layer. Through collisions the neutral disturbances impart to the ions a motion parallel to the geomagnetic field lines. These effects propagate equatorward at speeds of many hundreds of meters per second. The duration of the upward drift is ≈1 hr and is particularly pronounced in the noon/afternoon local time sector.

The large-scale wind circulation will also impart a motion to the ions that is parallel to the geomagnetic field. This effect may last a whole day and is more likely to occur in the daytime.

The expansion of the polar ionization enhancement toward lower latitudes, due for example to particle precipitation, will directly increase ionization densities. It is typically a nighttime phenomenon.

5.1.3.4.2 Negative Storm Effects. Changes in the neutral gas composition, and particularly an increase in the N_2:O ratio, will lead to a depletion of ionization. This is most clearly observed in the morning sector, with an anomalously low rate of ionization after sunrise. The effect may last from many hours to days.

The displacement and expansion of the ionospheric trough region (plasma depletion region) toward lower latitudes creates a steep ionization density drop and is typically observed in the afternoon/evening sector.

Another ionospheric effect of geomagnetic disturbances is the propagation of disturbance effects known as traveling ionospheric disturbances (TIDs). They are characterized by oscillations in the ionization density at the height of the F-layer, driven by gravity wave-driven oscillations in the neutral density and neutral winds.

5.1.4 Solar and Geomagnetic Indices

Various surrogate indices are used to quantitatively assess the levels of solar activity. One of these is the 10.7 cm (2,800 MHz) solar radio noise flux, designated $F_{10.7}$. It is the EUV radiation that heats the thermosphere, but the EUV cannot be measured at the ground. The $F_{10.7}$ can be measured from the ground, and it also correlates quite well with the EUV radiation.

The planetary geomagnetic activity index a_p (or k_p, which is essentially the logarithm of a_p) is an index that is used as a measure of episodic type solar activity. It is based on magnetic field fluctuation data reported every 3 hr at 12 stations between geomagnetic latitudes 48° and 63° and selected for good longitudinal coverage. Although it is the high latitude ionospheric current fluctuations that drive the magnetic field fluctuations as observed at these stations, it is not the magnetic field fluctuations which are driving the thermosphere. Therefore, the correlations between observed density changes and the a_p index are not always good. The daily planetary geomagnetic index (A_p) is the average of the eight 3-hourly a_p values for that particular day.

Table 65 lists 95th percentile, 50th percentile, and 5th percentile of 13-month smoothed values of solar radio noise flux ($F_{10.7}$) and geomagnetic activity index (A_p) throughout a mean 11 years and solar cycle. Figures 64 and 65 show data from this table. The $F_{10.7}$ data are derived from sunspot records for the period 1749 to 1947 with direct $F_{10.7}$ measurements thereafter. The standard deviation about the mean length is 1.23 years in the historical record.

Table 65. 13-month smoothed 10.7 cm solar radio noise flux and geomagnetic activity index over the mean solar cycle, 2002–2028.

	$F_{10.7}$			A_P		
Year	95% Flux	50% Flux	5% Flux	95% A_P	50% A_P	5% A_P
2001.92	194.8914	191.8801	188.925	12.506	11.7432	10.7939
2002	196.7669	189.1827	182.9999	13.1766	11.7679	10.5699
2002.08	196.9785	185.4429	176.684	14.4097	11.9812	10.1947
2002.17	195.6518	181.9426	171.0847	15.5131	12.1699	9.6501
2002.25	194.4169	178.7193	166.3541	16.1222	12.3507	9.6077
2002.33	194.6547	175.4454	161.7553	16.9907	12.5072	9.4901
2002.42	193.8348	171.6151	156.0731	17.2921	12.6248	9.1161
2002.5	190.7193	167.8858	150.27	16.9808	12.8019	8.9714
2002.58	186.5948	164.8723	146.5414	17.4043	12.9949	8.859
2002.67	182.6598	162.174	144.1609	17.1877	13.174	9.054
2002.75	179.5597	159.7874	141.324	16.8001	13.3728	9.2129
2002.83	175.7908	157.2723	140.5153	16.8457	13.578	9.6037
2002.92	169.702	153.3492	137.4805	17.0922	13.712	10.0902
2003	164.4646	148.436	132.9786	17.2449	13.7723	10.4484
2003.08	161.1737	144.2353	128.7686	17.3968	13.9019	10.9643
2003.17	159.4748	140.9991	125.2031	18.2537	13.9794	11.25
2003.25	157.5326	138.1079	121.2903	19.0982	13.9511	11.3494

Table 65. 13-month smoothed 10.7 cm solar radio noise flux and geomagnetic activity index over the mean solar cycle, 2002–2028 (Continued).

Year	$F_{10.7}$			A_P		
	95% Flux	50% Flux	5% Flux	95% A_P	50% A_P	5% A_P
2003.33	154.2465	135.5067	118.2396	19.8833	14.0764	11.4433
2003.42	150.7187	133.3078	116.7739	20.1888	14.2407	10.7039
2003.5	147.9575	130.5241	114.2062	20.3186	14.2686	10.6321
2003.58	146.9935	127.5355	110.8836	20.8846	14.4016	10.9015
2003.67	146.2966	124.94	107.2988	21.5425	14.546	10.7647
2003.75	145.4693	122.1461	102.7479	21.614	14.664	10.6424
2003.83	143.2352	118.6863	98.7188	21.6039	14.8578	11.0628
2003.92	139.9465	115.5923	95.8111	21.9553	15.0998	11.4447
2004	138.4801	113.6259	94.0401	22.4415	15.5881	11.9079
2004.08	137.4264	112.6295	93.3168	22.6438	16.0604	11.9301
2004.17	135.031	111.6439	92.9643	22.065	16.3577	12.2559
2004.25	132.6903	110.6436	92.6502	21.2547	16.5438	12.4453
2004.33	131.172	109.4269	91.8763	21.3053	16.662	12.3896
2004.42	130.113	107.5554	90.2545	21.8257	16.6744	12.4603
2004.5	128.2233	105.2967	88.2664	21.7924	16.8382	13.1595
2004.58	125.0575	103.0319	86.3616	22.8151	17.2108	13.7104
2004.67	121.3224	100.8916	85.1261	23.4261	17.4597	13.7026
2004.75	117.5213	98.7849	84.1752	23.152	17.3417	13.7748
2004.83	114.0496	97.1131	83.5203	23.0656	17.1237	13.6257
2004.92	112.8977	95.9605	82.9042	23.1411	16.7074	13.0105
2005	111.2536	94.6416	82.1568	23.1416	16.1644	12.2215
2005.08	109.2016	92.8183	81.3941	23.7055	15.9137	11.3547
2005.17	106.1988	90.6926	80.2538	24.2181	15.5721	10.3515
2005.25	102.9697	88.6178	78.442	24.6073	15.2582	10.0012
2005.33	100.8023	86.8644	77.5514	24.9149	15.1366	9.749
2005.42	98.4352	85.5441	76.8469	25.1095	15.113	9.602
2005.5	96.0907	84.5975	76.342	25.0809	15.0273	9.8393
2005.58	95.5272	83.9043	75.8852	24.7025	15.0317	10.3193
2005.67	93.9364	82.897	75.251	24.0399	15.0532	10.9187
2005.75	92.3529	81.8942	74.6197	23.4342	15.1428	11.6073
2005.83	90.7838	80.9006	73.9942	23.4186	15.5166	11.5544
2005.92	89.2364	79.9207	73.3773	23.432	15.917	11.2871
2006	87.7179	78.9591	72.7719	23.5028	16.3904	11.4397
2006.08	86.2354	78.0203	72.1809	23.2244	16.6267	11.7461
2006.17	84.7963	77.109	71.6071	22.6938	16.6502	12.1742
2006.25	83.4077	76.2297	71.0536	22.003	16.5419	12.187
2006.33	82.0769	75.3869	70.523	21.045	16.4793	12.4141
2006.42	80.8111	74.5853	70.0183	19.9723	16.356	12.6623
2006.5	79.6174	73.8294	69.5425	19.1145	16.1904	13.226
2006.58	78.5032	73.1238	69.0983	18.788	16.0808	13.8318

Table 65. 13-month smoothed 10.7 cm solar radio noise flux and geomagnetic activity index over the mean solar cycle, 2002–2028 (Continued).

Year	$F_{10.7}$			A_P		
	95% Flux	50% Flux	5% Flux	95% A_P	50% A_P	5% A_P
2006.67	77.4755	72.4731	68.6886	18.9404	16.0814	13.8694
2006.75	76.5418	71.8818	68.3163	19.1498	16.0465	13.8747
2006.83	75.7091	71.3545	67.9844	19.0994	15.9164	12.8981
2006.92	74.9848	70.8958	67.6956	18.6146	15.5736	12.155
2007	74.3759	70.5102	67.4529	18.2498	15.2775	11.6549
2007.08	73.8898	70.2024	67.259	18.0756	15.2119	11.6735
2007.17	73.5336	69.9768	67.1171	18.3813	15.2207	11.9373
2007.25	73.3146	69.8382	67.0297	18.7086	15.1398	11.8384
2007.33	73.24	69.7909	67	19.0527	15.0197	11.7872
2007.42	73.355	69.9227	67.13	18.985	14.8198	11.7797
2007.5	74	70.2773	67.26	18.6472	14.5115	11.7295
2007.58	74.84	70.6636	67.375	17.777	13.8757	11.1745
2007.67	75.665	71.0318	67.505	16.917	13.2474	10.6261
2007.75	76.735	71.4591	67.635	16.0777	12.6342	10.0908
2007.83	78.255	72.0227	67.85	15.2694	12.0436	9.5753
2007.92	79.6	72.6545	68.05	14.5023	11.4831	9.0861
2008	81.055	73.35	68.18	13.7868	10.9604	8.6299
2008.08	83.39	74.1636	68.21	13.1332	10.4828	8.213
2008.17	86.45	75.0864	68.255	12.5519	10.0581	7.8423
2008.25	91.325	76.2727	68.33	12.0531	9.6937	7.5242
2008.33	95.85	77.6682	68.285	11.6472	9.3971	7.2654
2008.42	99.315	79.1364	68.64	11.3445	9.176	7.0723
2008.5	104.58	80.8	68.64	11.1554	9.0378	6.9517
2008.58	110.68	82.7864	68.68	11.09	8.99	6.91
2008.67	116.65	84.9273	68.875	11.3	9.1	6.9
2008.75	124.025	87.1636	68.875	11.605	9.3	7.095
2008.83	132.525	89.5773	68.965	11.695	9.42	7.405
2008.92	139.015	92.1864	69.355	11.9	9.51	7.5
2009	143.575	94.9909	69.8	12.005	9.56	7.495
2009.08	147.915	97.8091	70.13	12.12	9.6	7.28
2009.17	152.24	100.5909	70.815	12.23	9.66	7.17
2009.25	156.96	103.3364	71.18	12.55	9.81	7.05
2009.33	162.115	106.3091	71.35	12.87	10.07	6.93
2009.42	167.195	109.5318	72.115	13.28	10.46	7.12
2009.5	171.485	112.7636	72.73	13.785	10.79	7.515
2009.58	177.305	115.9273	73.29	14.61	11.08	7.79
2009.67	185.155	119.0273	74.03	15.77	11.37	7.63
2009.75	190.17	122.1773	74.26	16.19	11.58	7.61
2009.83	192.75	125.0909	74.635	16.405	11.72	7.495
2009.92	195.38	127.4727	74.955	16.93	11.87	7.47

Table 65. 13-month smoothed 10.7 cm solar radio noise flux and geomagnetic activity index over the mean solar cycle, 2002–2028 (Continued).

Year	$F_{10.7}$			A_P		
	95% Flux	50% Flux	5% Flux	95% A_P	50% A_P	5% A_P
2010	198.32	129.7273	75.275	18.08	12.2	7.52
2010.08	202.925	131.8955	75.455	19.02	12.56	7.58
2010.17	209.115	134.3455	75.45	19.23	12.77	7.57
2010.25	213.23	136.7818	75.13	19.33	13.03	7.67
2010.33	215.93	139.0636	74.895	19.125	13.23	7.575
2010.42	220.385	141.1545	75.19	18.705	13.29	7.595
2010.5	225.015	143.15	75.505	18.595	13.33	7.705
2010.58	227.27	144.85	76.26	19.005	13.5	7.895
2010.67	228.41	146.4909	77.48	18.89	13.57	8.11
2010.75	230.31	147.8773	78.215	17.93	13.63	8.47
2010.83	232.445	148.8136	79.135	18.03	13.84	8.57
2010.92	235.43	149.6545	80.705	18.55	14.05	8.65
2011	238.7	150.0773	82.63	19.165	14.34	8.935
2011.08	240.265	150.4545	84.675	19.67	14.8	9.33
2011.17	238.73	150.8364	85.92	20.395	15.11	9.505
2011.25	236.895	150.9864	86.86	20.395	15.16	9.505
2011.33	238.065	151.2227	88.81	20.385	15.16	9.715
2011.42	238.665	150.5682	90.195	20.585	15.22	9.915
2011.50	236.345	149.1591	92.16	20.875	15.39	10.425
2011.58	232.945	148.0591	93.54	21.265	15.44	11.035
2011.67	229.205	147.4864	94.03	21.345	15.28	11.555
2011.75	227.425	147.4409	95.33	21.465	15.09	11.235
2011.83	227.795	147.4	95.625	21.68	15.08	11.12
2011.92	227.93	147.1455	95.165	22.125	15.09	10.575
2012	226.525	146.7182	95.265	22.88	14.97	10.12
2012.08	224.845	146.2682	96.78	22.58	14.68	9.82
2012.17	224.275	145.6954	97.5	21.42	14.4	9.98
2012.25	224.155	145.1909	97.065	20.685	14.28	10.015
2012.33	223.625	144.7636	96.34	20.15	14.21	10.25
2012.42	222.645	144.0318	96.315	19.72	14.14	10.48
2012.5	220.255	142.9591	96.78	19.615	14.11	10.485
2012.58	216.76	141.3636	95.855	19.41	14.14	10.39
2012.67	213.915	139.7955	95.38	19.2	14.38	10.4
2012.75	211.07	138.6227	96.225	18.99	14.74	10.41
2012.83	207.55	137.6273	97.165	19	14.86	10.2
2012.92	206.55	136.3046	96.225	19.545	14.75	9.755
2013	204.505	134.6091	94.64	20.47	14.87	10.13
2013.08	201.09	132.7545	93.86	22.125	15.28	10.575
2013.17	197.535	131.3545	93.61	23.485	15.59	10.615
2013.25	195.195	130.2955	91.935	24.105	15.78	10.795

Table 65. 13-month smoothed 10.7 cm solar radio noise flux and geomagnetic activity index over the mean solar cycle, 2002–2028 (Continued).

Year	$F_{10.7}$			A_P		
	95% Flux	50% Flux	5% Flux	95% A_P	50% A_P	5% A_P
2013.33	193.375	128.9273	88.495	25.25	16.06	10.95
2013.42	189.625	127.1455	87.745	25.765	16.28	11.135
2013.5	185.14	125.4955	88.815	25.02	16.28	11.38
2013.58	180.715	124.2182	88.35	24.905	16.25	11.595
2013.67	176.815	123.1136	86.96	24.06	16.16	11.74
2013.75	174.555	122.0182	86.045	22.175	16.12	11.725
2013.83	172.735	120.8273	85.715	22.48	16.2	11.92
2013.92	168.58	119.1636	84.79	23.225	16.28	11.675
2014	162.05	117.2045	83.51	23.26	16.27	10.94
2014.08	156.08	115.4	82.49	22.75	16.14	10.65
2014.17	152.515	113.4727	81.905	22.12	15.95	10.68
2014.25	150.32	111.4773	81.91	22.015	15.9	10.685
2014.33	147.975	109.7636	81.56	22.855	16.12	10.645
2014.42	145.065	108.3364	80.395	23.795	16.37	10.705
2014.5	141.97	106.9273	80.525	24.005	16.56	10.695
2014.58	138.355	105.4091	80.205	24.01	16.79	10.59
2014.67	134.54	103.9227	79.515	24.015	16.89	10.485
2014.75	130.145	102.4182	78.975	23.61	16.88	10.19
2014.83	124.09	100.8409	78.15	22.66	16.85	10.34
2014.92	119.11	99.3273	77.105	22.86	16.78	10.54
2015	118.185	98.0273	75.405	23.14	16.89	11.26
2015.08	118.725	96.9227	74.335	23.22	17.17	11.78
2015.17	119.28	95.8682	73.645	22.585	17.34	11.915
2015.25	119.65	95.0182	72.775	21.635	17.25	12.065
2015.33	118.84	94.0227	71.825	21.315	17.06	12.185
2015.42	117.435	92.8727	71.27	21.83	16.85	12.37
2015.5	115.965	91.75	70.815	21.79	16.74	13.21
2015.58	113.915	90.6727	70.375	22.22	16.82	12.98
2015.67	110.18	89.5182	70.275	22.65	16.95	12.75
2015.75	105.11	88.25	70.36	22.43	16.87	12.97
2015.83	102.72	87.2682	70.22	22.445	16.71	12.655
2015.92	101.68	86.5636	70.12	22.77	16.46	12.43
2016	100.195	85.7591	70.175	23	16.07	12
2016.08	98.11	84.7455	70.085	23.565	15.82	11.135
2016.17	96.3	83.5909	70.315	24.23	15.58	10.37
2016.25	94.48	82.5455	69.78	24.955	15.49	10.545
2016.33	93.435	81.7636	69.55	25.475	15.51	10.625
2016.42	92.125	81.0091	69.39	25.69	15.5	10.51
2016.50	91.67	80.2682	69.265	25.58	15.36	10.62
2016.58	91.055	79.5	68.995	25.045	15.26	10.855

Table 65. 13-month smoothed 10.7 cm solar radio noise flux and geomagnetic activity index over the mean solar cycle, 2002–2028 (Continued).

Year	$F_{10.7}$			A_P		
	95% Flux	50% Flux	5% Flux	95% A_P	50% A_P	5% A_P
2016.67	90.46	78.7955	68.68	24.095	15.09	11.005
2016.75	89.77	78.1318	68.405	23.145	14.95	11.155
2016.83	88.885	77.5091	68.305	22.625	15.01	11.075
2016.92	88	76.9636	68.29	22.21	15.15	10.99
2017	87.1	76.4409	68.215	21.89	15.38	11.11
2017.08	85.775	75.8955	67.96	21.46	15.52	11.34
2017.17	84.355	75.4045	67.705	20.83	15.47	11.37
2017.25	82.27	74.8455	67.535	19.99	15.27	11.41
2017.33	79.87	74.1591	67.55	20.08	15.08	11.72
2017.42	78.37	73.4864	67.395	20.175	14.9	11.925
2017.5	77.47	72.8864	67.31	19.875	14.73	11.625
2017.58	77	72.4091	67.21	19.46	14.61	11.54
2017.67	76.87	72.0318	67.18	18.955	14.58	11.145
2017.75	76.655	71.6273	67.165	18.25	14.61	10.55
2017.83	76.485	71.2773	67.105	17.345	14.54	9.755
2017.92	76.165	70.9773	67.075	17.36	14.39	9.44
2018	75.18	70.6818	67.045	17.47	14.27	9.33
2018.08	74.2	70.3682	67.015	17.575	14.2	9.325
2018.17	73.985	70.1364	67.015	17.575	14.09	9.325
2018.25	73.5	69.9	67	17.79	14	9.21
2018.33	73.24	69.7909	67	19.0527	15.0197	11.7872
2018.42	73.355	69.9227	67.13	18.985	14.8198	11.7797
2018.50	74	70.2773	67.26	18.6472	14.5115	11.7295
2018.58	74.84	70.6636	67.375	17.777	13.8757	11.1745
2018.67	75.665	71.0318	67.505	16.917	13.2474	10.6261
2018.75	76.735	71.4591	67.635	16.0777	12.6342	10.0908
2018.83	78.255	72.0227	67.85	15.2694	12.0436	9.5753
2018.92	79.6	72.6545	68.05	14.5023	11.4831	9.0861
2019	81.055	73.35	68.18	13.7868	10.9604	8.6299
2019.08	83.39	74.1636	68.21	13.1332	10.4828	8.213
2019.17	86.45	75.0864	68.255	12.5519	10.0581	7.8423
2019.25	91.325	76.2727	68.33	12.0531	9.6937	7.5242
2019.33	95.85	77.6682	68.285	11.6472	9.3971	7.2654
2019.42	99.315	79.1364	68.64	11.3445	9.176	7.0723
2019.5	104.58	80.8	68.64	11.1554	9.0378	6.9517
2019.58	110.68	82.7864	68.68	11.09	8.99	6.91
2019.67	116.65	84.9273	68.875	11.3	9.1	6.9
2019.75	124.025	87.1636	68.875	11.605	9.3	7.095
2019.83	132.525	89.5773	68.965	11.695	9.42	7.405
2019.92	139.015	92.1864	69.355	11.9	9.51	7.5

Table 65. 13-month smoothed 10.7 cm solar radio noise flux and geomagnetic activity index over the mean solar cycle, 2002–2028 (Continued).

Year	$F_{10.7}$			A_P		
	95% Flux	50% Flux	5% Flux	95% A_P	50% A_P	5% A_P
2020	143.575	94.9909	69.8	12.005	9.56	7.495
2020.08	147.915	97.8091	70.13	12.12	9.6	7.28
2020.17	152.24	100.5909	70.815	12.23	9.66	7.17
2020.25	156.96	103.3364	71.18	12.55	9.81	7.05
2020.33	162.115	106.3091	71.35	12.87	10.07	6.93
2020.42	167.195	109.5318	72.115	13.28	10.46	7.12
2020.5	171.485	112.7636	72.73	13.785	10.79	7.515
2020.58	177.305	115.9273	73.29	14.61	11.08	7.79
2020.67	185.155	119.0273	74.03	15.77	11.37	7.63
2020.75	190.17	122.1773	74.26	16.19	11.58	7.61
2020.83	192.75	125.0909	74.635	16.405	11.72	7.495
2020.92	195.38	127.4727	74.955	16.93	11.87	7.47
2021	198.32	129.7273	75.275	18.08	12.2	7.52
2021.08	202.925	131.8955	75.455	19.02	12.56	7.58
2021.17	209.115	134.3455	75.45	19.23	12.77	7.57
2021.25	213.23	136.7818	75.13	19.33	13.03	7.67
2021.33	215.93	139.0636	74.895	19.125	13.23	7.575
2021.42	220.385	141.1545	75.19	18.705	13.29	7.595
2021.5	225.015	143.15	75.505	18.595	13.33	7.705
2021.58	227.27	144.85	76.26	19.005	13.5	7.895
2021.67	228.41	146.4909	77.48	18.89	13.57	8.11
2021.75	230.31	147.8773	78.215	17.93	13.63	8.47
2021.83	232.445	148.8136	79.135	18.03	13.84	8.57
2021.92	235.43	149.6545	80.705	18.55	14.05	8.65
2022	238.7	150.0773	82.63	19.165	14.34	8.935
2022.08	240.265	150.4545	84.675	19.67	14.8	9.33
2022.17	238.73	150.8364	85.92	20.395	15.11	9.505
2022.25	236.895	150.9864	86.86	20.395	15.16	9.505
2022.33	238.065	151.2227	88.81	20.385	15.16	9.715
2022.42	238.665	150.5682	90.195	20.585	15.22	9.915
2022.5	236.345	149.1591	92.16	20.875	15.39	10.425
2022.58	232.945	148.0591	93.54	21.265	15.44	11.035
2022.67	229.205	147.4864	94.03	21.345	15.28	11.555
2022.75	227.425	147.4409	95.33	21.465	15.09	11.235
2022.83	227.795	147.4	95.625	21.68	15.08	11.12
2022.92	227.93	147.1455	95.165	22.125	15.09	10.575
2023	226.525	146.7182	95.265	22.88	14.97	10.12
2023.08	224.845	146.2682	96.78	22.58	14.68	9.82
2023.17	224.275	145.6954	97.5	21.42	14.4	9.98
2023.25	224.155	145.1909	97.065	20.685	14.28	10.015

Table 65. 13-month smoothed 10.7 cm solar radio noise flux and geomagnetic activity index over the mean solar cycle, 2002–2028 (Continued).

Year	$F_{10.7}$			A_P		
	95% Flux	50% Flux	5% Flux	95% A_P	50% A_P	5% A_P
2023.33	223.625	144.7636	96.34	20.15	14.21	10.25
2023.42	222.645	144.0318	96.315	19.72	14.14	10.48
2023.5	220.255	142.9591	96.78	19.615	14.11	10.485
2023.58	216.76	141.3636	95.855	19.41	14.14	10.39
2023.67	213.915	139.7955	95.38	19.2	14.38	10.4
2023.75	211.07	138.6227	96.225	18.99	14.74	10.41
2023.83	207.55	137.6273	97.165	19	14.86	10.2
2023.92	206.55	136.3046	96.225	19.545	14.75	9.755
2024	204.505	134.6091	94.64	20.47	14.87	10.13
2024.08	201.09	132.7545	93.86	22.125	15.28	10.575
2024.17	197.535	131.3545	93.61	23.485	15.59	10.615
2024.25	195.195	130.2955	91.935	24.105	15.78	10.795
2024.33	193.375	128.9273	88.495	25.25	16.06	10.95
2024.42	189.625	127.1455	87.745	25.765	16.28	11.135
2024.5	185.14	125.4955	88.815	25.02	16.28	11.38
2024.58	180.715	124.2182	88.35	24.905	16.25	11.595
2024.67	176.815	123.1136	86.96	24.06	16.16	11.74
2024.75	174.555	122.0182	86.045	22.175	16.12	11.725
2024.83	172.735	120.8273	85.715	22.48	16.2	11.92
2024.92	168.58	119.1636	84.79	23.225	16.28	11.675
2025	162.05	117.2045	83.51	23.26	16.27	10.94
2025.08	156.08	115.4	82.49	22.75	16.14	10.65
2025.17	152.515	113.4727	81.905	22.12	15.95	10.68
2025.25	150.32	111.4773	81.91	22.015	15.9	10.685
2025.33	147.975	109.7636	81.56	22.855	16.12	10.645
2025.42	145.065	108.3364	80.395	23.795	16.37	10.705
2025.5	141.97	106.9273	80.525	24.005	16.56	10.695
2025.58	138.355	105.4091	80.205	24.01	16.79	10.59
2025.67	134.54	103.9227	79.515	24.015	16.89	10.485
2025.75	130.145	102.4182	78.975	23.61	16.88	10.19
2025.83	124.09	100.8409	78.15	22.66	16.85	10.34
2025.92	119.11	99.3273	77.105	22.86	16.78	10.54
2026	118.185	98.0273	75.405	23.14	16.89	11.26
2026.08	118.725	96.9227	74.335	23.22	17.17	11.78
2026.17	119.28	95.8682	73.645	22.585	17.34	11.915
2026.25	119.65	95.0182	72.775	21.635	17.25	12.065
2026.33	118.84	94.0227	71.825	21.315	17.06	12.185
2026.42	117.435	92.8727	71.27	21.83	16.85	12.37
2026.5	115.965	91.75	70.815	21.79	16.74	13.21
2026.58	113.915	90.6727	70.375	22.22	16.82	12.98

Table 65. 13-month smoothed 10.7 cm solar radio noise flux and geomagnetic activity index over the mean solar cycle, 2002–2028 (Continued).

Year	$F_{10.7}$			A_P		
	95% Flux	50% Flux	5% Flux	95% A_P	50% A_P	5% A_P
2026.67	110.18	89.5182	70.275	22.65	16.95	12.75
2026.75	105.11	88.25	70.36	22.43	16.87	12.97
2026.83	102.72	87.2682	70.22	22.445	16.71	12.655
2026.92	101.68	86.5636	70.12	22.77	16.46	12.43
2027	100.195	85.7591	70.175	23	16.07	12
2027.08	98.11	84.7455	70.085	23.565	15.82	11.135
2027.17	96.3	83.5909	70.315	24.23	15.58	10.37
2027.25	94.48	82.5455	69.78	24.955	15.49	10.545
2027.33	93.435	81.7636	69.55	25.475	15.51	10.625
2027.42	92.125	81.0091	69.39	25.69	15.5	10.51
2027.5	91.67	80.2682	69.265	25.58	15.36	10.62
2027.58	91.055	79.5	68.995	25.045	15.26	10.855
2027.67	90.46	78.7955	68.68	24.095	15.09	11.005
2027.75	89.77	78.1318	68.405	23.145	14.95	11.155
2027.83	88.885	77.5091	68.305	22.625	15.01	11.075
2027.92	88	76.9636	68.29	22.21	15.15	10.99
2028	87.1	76.4409	68.215	21.89	15.38	11.11
2028.08	85.775	75.8955	67.96	21.46	15.52	11.34
2028.17	84.355	75.4045	67.705	20.83	15.47	11.37
2028.25	82.27	74.8455	67.535	19.99	15.27	11.41
2028.33	79.87	74.1591	67.55	20.08	15.08	11.72
2028.42	78.37	73.4864	67.395	20.175	14.9	11.925
2028.5	77.47	72.8864	67.31	19.875	14.73	11.625
2028.58	77	72.4091	67.21	19.46	14.61	11.54
2028.67	76.87	72.0318	67.18	18.955	14.58	11.145
2028.75	76.655	71.6273	67.165	18.25	14.61	10.55
2028.83	76.485	71.2773	67.105	17.345	14.54	9.755
2028.92	76.165	70.9773	67.075	17.36	14.39	9.44
2029	75.18	70.6818	67.045	17.47	14.27	9.33
2029.08	74.2	70.3682	67.015	17.575	14.2	9.325
2029.17	73.985	70.1364	67.015	17.575	14.09	9.325
2029.25	73.5	69.9	67	17.79	14	9.21

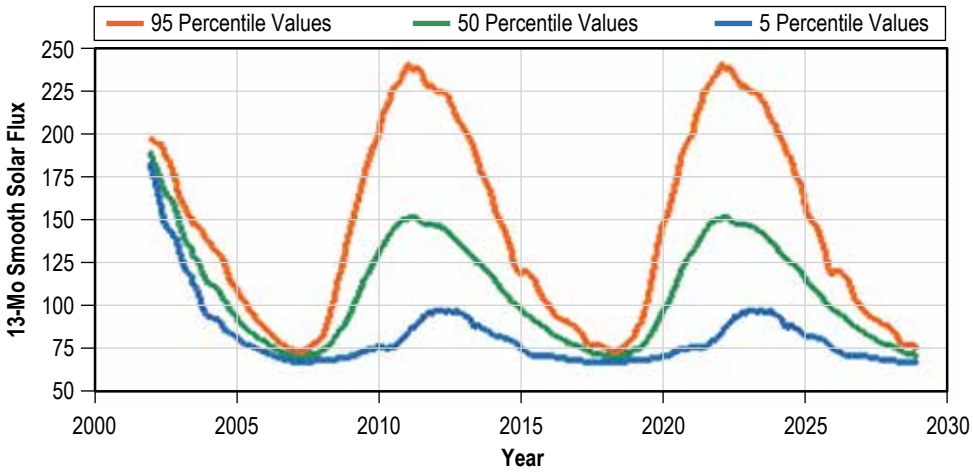

Figure 64. 13-month smoothed values of solar flux ($F_{10.7}$) over the mean solar cycle from 2002–2028.

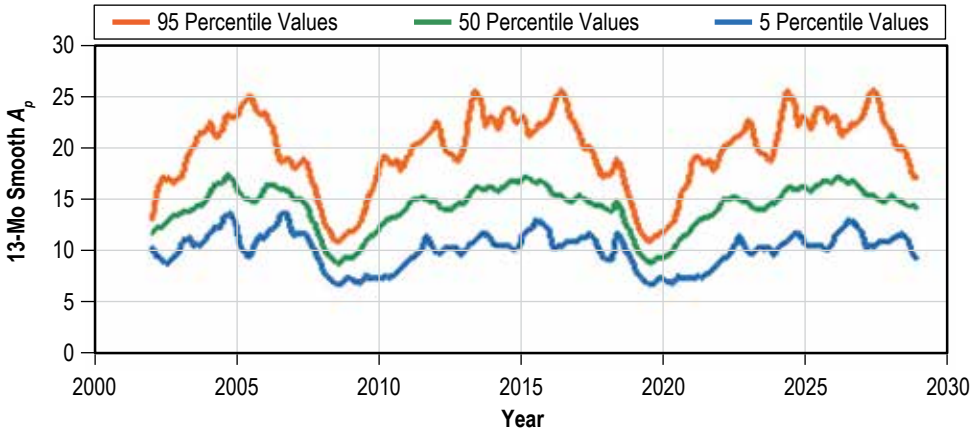

Figure 65. 13-month smoothed values of geomagnetic activity index (A_p) over the mean solar cycle from 2002–2028.

5.1.5 Orbital and Suborbital Neutral Atmosphere Model

5.1.5.1 Marshall Engineering Thermosphere Model. The MET model has been developed to represent, insofar as is practical for engineering applications, the variability of the ambient mass density. It is the standard neutral atmospheric density model used for control and lifetime studies for most NASA spacecraft projects. A description of the model can be found in references 91–96. The MET model is an empirical model with coefficients that were obtained from satellite drag analyses. It is a static diffusion model and is essentially the Smithsonian's Jacchia 1970 model with two additions from the Jacchia 1971 model.[97,98] Inputs to the model are time (year, month, day, hour, and minute), position (altitude and geographic latitude and longitude), the previous day's solar radio flux ($F_{10.7}$), the centered solar radio flux averaged over six solar rotations ($F_{10.7}B$), and a_p index 6 to 7 hours before the time in question. (For some studies, the daily planetary geomagnetic index (A_p) may be used instead of the three hourly a_p values.)

With the exospheric temperature specified, the temperature can be calculated for any altitude between the lower boundary (90 km) and the upper level (2,500 km) of the model from an empirically determined temperature profile. The density for all points on the globe at 90 km altitude is assumed constant, and mixing prevails to 105 km. Between these two altitudes, the mean molecular mass varies as a result of the dissociation of O_2 to AO. At 120 km altitude, the ratio of AO to O_2 is assumed to be 1:5. Density between 90 and 150 km is calculated by integration of the barometric equation. For altitudes above 105 km, the diffusion equation for each of the individual species (O_2, AO, N_2, He, and Ar) is integrated upward from the 105 km level. For H, the integration of the diffusion equation proceeds upward from 500 km altitude. The total mass density is calculated by summing the individual specie mass densities.

The total density is then further modified by the effects of the seasonal-latitudinal density variation of the lower thermosphere below 170 km altitude and seasonal-latitudinal variations of He above 500 km. These two effects have been incorporated in the MET model using equations developed by Jacchia for his 1971 thermospheric model. The final output of the MET model is total mass density, temperature, pressure, individual specie number densities, mean molecular weight, scale height, specific heats, and the local gravitational acceleration. The total mass density, the temperature, and the individual species all have the same phase variation in the MET model (i.e., they all maximize at the same local time). For some studies involving the effects of various species on an orbiting spacecraft where accurate phases of the various species within an orbit are required, it may be necessary to use the Mass Spectrometer Incoherent Scatter (MSIS) model developed by Goddard Space Flight Center. MSIS is a neutral atmosphere empirical model from the surface to lower exosphere.[99] The values given in table 66 define the Earth pressure parameters for space vehicle design performance analyses.

Table 66. Pressure parameters in Earth orbit (ambient pressure in pascal; torr in parentheses).*

Minimum	Nominal**	Maximum	Altitude (km)
4×10^{-5} (3×10^{-7})	8.5×10^{-5} (6.4×10^{-7})	2.3×10^{-4} (1.7×10^{-7})	200
1.8×10^{-7} (1.4×10^{-9})	1.5×10^{-6} (1.1×10^{-8})	1.7×10^{-5} (1.3×10^{-7})	400
3×10^{-8} (2.3×10^{-10})	3.1×10^{-7} (2.3×10^{-9})	6.5×10^{-6} (4.9×10^{-8})	500
1.7×10^{-8} (1.3×10^{-10})	8.3×10^{-8} (6.2×10^{-10})	2.7×10^{-6} (2×10^{-8})	600
4.3×10^{-9} (3.2×10^{-11})	7.5×10^{-9} (5.6×10^{-11})	1.5×10^{-7} (1.1×10^{-9})	1,000
1×10^{-11} (7.5×10^{-14})	–	–	Geosynchronous

* Low- and high-pressure values were computed from the MET model using an orbit average value and assuming a 28.5° orbit inclination. The following inputs were used: 14:00 UTC, $F_{10.7} = 230$, $A_p = 400$.

** Nominal pressure values were taken from U.S. Standard Atmosphere 1976[100] (cf., ref. 101). Geosynchronous pressure values were taken from reference 102. To convert from pascal to torr, multiplyby 7.5×10^{-3}.

5.1.5.2 Statistical Analysis Mode. The statistical analysis mode (SAM) of the MET model was developed for use during those periods when actual values of the daily and 162-day mean values of the 10.7 cm solar radio flux and the global geomagnetic index (a_p) are unknown or unavailable, e.g., when the time of application to a specific problem is sometime in the future. This is particularly true during the design, development, and testing phases of a space vehicle when there are only rough estimates of the 13-month smoothed mean values of these three parameters and no guesses at all about how they should be combined.

One possible procedure that has been used in spacecraft development work is to assume that the daily and the 162-day mean values of the 10.7 cm solar radio flux are both equal to the 13-month smoothed value predicted using a technique developed through a statistical analysis of sunspot data from 1855 to the present.[101] The 13-month smoothed values of a_p are predicted in the same manner. This procedure provides useful estimates of the long-term mean density, subject primarily to the accuracy of the predicted 13-month smoothed input data. For periods shorter than 90 days, the thermospheric properties defined by the use of the 13-month smoothed inputs are no longer representative of the original model outputs using the proper input parameters. For systems that are sensitive to thermospheric effects and variations over a period of a few days or less (e.g., control and pointing systems), representative samples[100] of the proper model inputs taken from the historical data set should be used. Alternatively, for some applications the variations may be treated statistically.

The MET-SAM is the initial step in developing the statistics of these shorter period perturbations in orbital altitude density in addition to providing limits on the magnitudes of the variations that are averaged out through the use of 13-month smoothed solar activity input parameters to the original MET model.

The MET-SAM also provides answers to another frequently asked question: What is the percent of time that the recommended density value will be exceeded during the operational phase of the vehicle? Or, how confident are you that the recommended density value will not be exceeded more than 5% of the time? The answers are crucial in the design of the guidance and control capability, the selection of the altitude at which the vehicle will orbit, and the reboost strategy for payloads put into low Earth orbit (LEO) by the Shuttle. The MET-SAM is also based on the premise that most applications during the development phase primarily require detailed knowledge about the maximum and minimum densities that will be encountered with limits on the magnitude of the variations that occur during monthly periods.

All available daily values of the 10.7 cm solar flux and the three hourly values of a_p were used to calculate values of the global minimum, mean, and maximum exospheric temperatures. The statistics of this new dataset were calculated and the results were indexed to five different levels of solar activity as defined by the values of the 13-month smoothed 10.7 cm solar flux. This makes it possible to statistically include the 3-hr to 90-day variations in these three temperatures using only known or estimated values of the 13-month smoothed 10.7 cm solar flux. MET-SAM is not available for release, so an output summary table of expected density variations is included in table 67. The data in this table present the statistics of the global (spatial) maximum densities for averaging periods as short as 3 hr, the temporal resolution of the a_p dataset. Data in table 67 is reformatted from table C-1 in reference 102.

Table 67. Global maximum density (kg/m^3) for various frequencies of occurrence (percentile) versus altitude $F_{10.7}$ range.

Height (km)	Frequency (percentile)	$F_{10.7}$ Range					
		Bin 1 66–102	Bin 2 102–138	Bin 3 138–174	Bin 4 174–210	Bin 5 210–246	All 6 66–246
250	1	4.39×10^{-11}	6.22×10^{-11}	7.67×10^{-11}	8.89×10^{-11}	1.11×10^{-10}	4.56×10^{-11}
250	5	4.73×10^{-11}	6.7×10^{-11}	8.44×10^{-11}	9.91×10^{-11}	1.16×10^{-10}	5.07×10^{-11}
250	33	5.57×10^{-11}	7.91×10^{-11}	9.94×10^{-11}	1.18×10^{-10}	1.31×10^{-10}	6.91×10^{-11}
250	50	5.94×10^{-11}	8.41×10^{-11}	1.05×10^{-10}	1.24×10^{-10}	1.36×10^{-10}	8.63×10^{-11}
250	67	6.39×10^{-11}	8.99×10^{-11}	1.11×10^{-10}	1.3×10^{-10}	1.42×10^{-10}	1.06×10^{-10}
250	95	7.76×10^{-11}	1.08×10^{-10}	1.26×10^{-10}	1.45×10^{-10}	1.58×10^{-10}	1.39×10^{-10}
250	99	8.67×10^{-11}	1.19×10^{-10}	1.36×10^{-10}	1.53×10^{-10}	1.63×10^{-10}	1.53×10^{-10}
250	100	1.2×10^{-11}	1.53×10^{-10}	1.52×10^{-10}	1.7×10^{-10}	1.74×10^{-10}	1.74×10^{-10}
275	1	2.19×10^{-11}	3.30×10^{-11}	4.23×10^{-11}	5.05×10^{-11}	6.6×10^{-11}	2.29×10^{-11}
275	5	2.39×10^{-11}	3.6×10^{-11}	4.74×10^{-11}	5.76×10^{-11}	7.02×10^{-11}	2.59×10^{-11}
275	33	2.89×10^{-11}	4.39×10^{-11}	5.78×10^{-11}	7.11×10^{-11}	8.17×10^{-11}	3.73×10^{-11}
275	50	3.12×10^{-11}	4.72×10^{-11}	6.18×10^{-11}	7.60×10^{-11}	8.57×10^{-11}	4.87×10^{-11}
275	67	3.4×10^{-11}	5.11×10^{-11}	6.62×10^{-11}	8.07×10^{-11}	9.08×10^{-11}	6.22×10^{-11}
275	95	4.28×10^{-11}	6.38×10^{-11}	7.79×10^{-11}	9.28×10^{-11}	1.04×10^{-10}	8.82×10^{-11}
275	99	4.89×10^{-11}	7.26×10^{-11}	8.52×10^{-11}	1×10^{-10}	1.09×10^{-10}	9.93×10^{-11}
275	100	7.33×10^{-11}	9.94×10^{-11}	9.86×10^{-11}	1.15×10^{-10}	1.18×10^{-10}	1.18×10^{-10}
300	1	1.15×10^{-11}	1.83×10^{-11}	2.44×10^{-11}	2.99×10^{-11}	4.1×10^{-11}	1.21×10^{-11}
300	5	1.27×10^{-11}	2.03×10^{-11}	2.78×10^{-11}	3.49×10^{-11}	4.41×10^{-11}	1.39×10^{-11}
300	33	1.58×10^{-11}	2.54×10^{-11}	3.51×10^{-11}	4.47×10^{-11}	5.29×10^{-11}	2.11×10^{-11}
300	50	1.72×10^{-11}	2.77×10^{-11}	3.79×10^{-11}	4.84×10^{-11}	5.61×10^{-11}	2.87×10^{-11}
300	67	1.9×10^{-11}	3.04×10^{-11}	4.11×10^{-11}	5.21×10^{-11}	6.02×10^{-11}	3.82×10^{-11}
300	95	2.47×10^{-11}	3.94×10^{-11}	4.99×10^{-11}	6.18×10^{-11}	7.1×10^{-11}	5.8×10^{-11}
300	99	2.89×10^{-11}	4.59×10^{-11}	5.56×10^{-11}	6.78×10^{-11}	7.52×10^{-11}	6.72×10^{-11}
300	100	4.64×10^{-11}	6.74×10^{-11}	6.67×10^{-11}	8.08×10^{-11}	8.41×10^{-11}	8.41×10^{-11}
325	1	6.26×10^{-12}	1.05×10^{-11}	1.45×10^{-11}	1.83×10^{-11}	2.62×10^{-11}	6.63×10^{-12}
325	5	7×10^{-12}	1.18×10^{-11}	1.69×10^{-11}	2.18×10^{-11}	2.85×10^{-11}	7.76×10^{-12}
325	33	8.92×10^{-12}	1.53×10^{-11}	2.2×10^{-11}	2.9×10^{-11}	3.53×10^{-11}	1.24×10^{-11}
325	50	9.84×10^{-12}	1.68×10^{-11}	2.4×10^{-11}	3.18×10^{-11}	3.78×10^{-11}	1.75×10^{-11}
325	67	1.1×10^{-11}	1.86×10^{-11}	2.64×10^{-11}	3.47×10^{-11}	4.1×10^{-11}	2.42×10^{-11}
325	95	1.48×10^{-11}	2.51×10^{-11}	3.3×10^{-11}	4.23×10^{-11}	5×10^{-11}	3.93×10^{-11}
325	99	1.76×10^{-11}	2.99×10^{-11}	3.74×10^{-11}	4.73×10^{-11}	5.36×10^{-11}	4.68×10^{-11}
325	100	3.03×10^{-11}	4.69×10^{-11}	4.63×10^{-11}	5.85×10^{-11}	6.15×10^{-11}	6.15×10^{-11}
350	1	3.5×10^{-12}	6.25×10^{-12}	8.92×10^{-12}	1.15×10^{-11}	1.72×10^{-11}	3.74×10^{-12}
350	5	3.97×10^{-12}	7.09×10^{-12}	1.05×10^{-11}	1.40×10^{-11}	1.89×10^{-11}	4.45×10^{-12}
350	33	5.19×10^{-12}	9.41×10^{-12}	1.41×10^{-11}	1.93×10^{-11}	2.41×10^{-11}	7.46×10^{-12}
350	50	5.79×10^{-12}	1.05×10^{-11}	1.56×10^{-11}	2.14×10^{-11}	2.6×10^{-11}	1.1×10^{-11}
350	67	6.53×10^{-12}	1.18×10^{-11}	1.73×10^{-11}	2.36×10^{-11}	2.86×10^{-11}	1.57×10^{-11}
350	95	9.09×10^{-12}	1.64×10^{-11}	2.23×10^{-11}	2.97×10^{-11}	3.59×10^{-11}	2.72×10^{-11}

Table 67. Global maximum density (kg/m^3) for various frequencies of occurrence (percentile) versus altitude $F_{10.7}$ range (Continued).

Height (km)	Frequency (percentile)	$F_{10.7}$ Range					
		Bin 1 66–102	Bin 2 102–138	Bin 3 138–174	Bin 4 174–210	Bin 5 210–246	All 6 66–246
350	99	1.1×10^{-11}	1.99×10^{-11}	2.57×10^{-11}	3.37×10^{-11}	3.9×10^{-11}	3.33×10^{-11}
350	100	2.03×10^{-11}	3.34×10^{-11}	3.29×10^{-11}	4.32×10^{-11}	4.58×10^{-11}	4.58×10^{-11}
375	1	2.01×10^{-12}	3.78×10^{-12}	5.6×10^{-12}	7.43×10^{-12}	1.16×10^{-11}	2.15×10^{-12}
375	5	2.3×10^{-12}	4.35×10^{-12}	6.71×10^{-12}	9.2×10^{-12}	1.28×10^{-11}	2.6×10^{-12}
375	33	3.09×10^{-12}	5.94×10^{-12}	$9.27\text{-} \times 10^{-12}$	1.31×10^{-11}	1.67×10^{-11}	4.6×10^{-12}
375	50	3.48×10^{-12}	6.67×10^{-12}	1.04×10^{-11}	1.47×10^{-11}	1.83×10^{-11}	7.01×10^{-12}
375	67	3.97×10^{-12}	7.58×10^{-12}	1.16×10^{-11}	1.64×10^{-11}	2.03×10^{-11}	1.05×10^{-11}
375	95	5.72×10^{-12}	1.09×10^{-11}	1.54×10^{-11}	2.12×10^{-11}	2.63×10^{-11}	1.92×10^{-11}
375	99	7.07×10^{-12}	1.36×10^{-11}	1.8×10^{-11}	2.44×10^{-11}	2.89×10^{-11}	2.41×10^{-11}
375	100	1.38×10^{-11}	2.42×10^{-11}	2.38×10^{-11}	3.24×10^{-11}	3.47×10^{-11}	3.47×10^{-11}
400	1	1.17×10^{-12}	2.33×10^{-12}	3.58×10^{-12}	4.87×10^{-12}	7.88×10^{-12}	1.26×10^{-12}
400	5	1.36×10^{-12}	2.71×10^{-12}	4.36×10^{-12}	6.15×10^{-12}	8.83×10^{-12}	1.55×10^{-12}
400	33	1.87×10^{-12}	3.81×10^{-12}	6.19×10^{-12}	9.04×10^{-12}	1.18×10^{-11}	2.89×10^{-12}
400	50	2.13×10^{-12}	4.33×10^{-12}	6.99×10^{-12}	1.03×10^{-11}	1.3×10^{-11}	4.57×10^{-12}
400	67	2.46×10^{-12}	4.98×10^{-12}	7.93×10^{-12}	1.16×10^{-11}	1.46×10^{-11}	7.06×10^{-12}
400	95	3.66×10^{-12}	7.4×10^{-12}	1.08×10^{-11}	1.53×10^{-11}	1.95×10^{-11}	1.38×10^{-11}
400	99	4.61×10^{-12}	9.4×10^{-12}	1.28×10^{-11}	1.8×10^{-11}	2.16×10^{-11}	1.77×10^{-11}
400	100	9.59×10^{-12}	1.78×10^{-11}	1.74×10^{-11}	2.46×10^{-11}	2.66×10^{-11}	2.66×10^{-11}
425	1	6.89×10^{-13}	1.46×10^{-12}	2.32×10^{-12}	3.24×10^{-12}	5.45×10^{-12}	7.49×10^{-13}
425	5	8.1×10^{-13}	1.72×10^{-12}	2.87×10^{-12}	4.17×10^{-12}	6.17×10^{-12}	9.38×10^{-13}
425	33	1.15×10^{-12}	2.48×10^{-12}	4.2×10^{-12}	6.33×10^{-12}	8.47×10^{-12}	1.84×10^{-12}
425	50	1.32×10^{-12}	2.85×10^{-12}	4.79×10^{-12}	7.26×10^{-12}	9.41×10^{-12}	3.02×10^{-12}
425	67	1.55×10^{-12}	3.31×10^{-12}	5.49×10^{-12}	8.26×10^{-12}	1.07×10^{-11}	4.84×10^{-12}
425	95	2.37×10^{-12}	5.1×10^{-12}	7.66×10^{-12}	1.12×10^{-11}	1.46×10^{-11}	1×10^{-11}
425	99	3.05×10^{-12}	6.6×10^{-12}	9.27×10^{-12}	1.34×10^{-11}	1.64×10^{-11}	1.32×10^{-11}
425	100	6.75×10^{-12}	1.32×10^{-11}	1.29×10^{-11}	1.89×10^{-11}	2.06×10^{-11}	2.06×10^{-11}
450	1	4.13×10^{-13}	9.24×10^{-13}	1.52×10^{-12}	2.18×10^{-12}	3.82×10^{-12}	4.51×10^{-13}
450	5	4.91×10^{-13}	1.1×10^{-12}	1.91×10^{-12}	2.86×10^{-12}	4.36×10^{-12}	5.75×10^{-13}
450	33	7.13×10^{-13}	1.64×10^{-12}	2.88×10^{-12}	4.48×10^{-12}	6.14×10^{-12}	1.18×10^{-12}
450	50	8.3×10^{-13}	1.9×10^{-12}	3.32×10^{-12}	5.2×10^{-12}	6.87×10^{-12}	2.02×10^{-12}
450	67	9.83×10^{-13}	2.23×10^{-12}	3.85×10^{-12}	5.97×10^{-12}	7.88×10^{-12}	3.36×10^{-12}
450	95	1.56×10^{-12}	3.55×10^{-12}	5.5×10^{-12}	8.32×10^{-12}	1.11×10^{-11}	7.34×10^{-12}
450	99	2.04×10^{-12}	4.69×10^{-12}	6.77×10^{-12}	1.01×10^{-11}	1.26×10^{-11}	9.88×10^{-12}
450	100	4.8×10^{-12}	9.91×10^{-12}	9.71×10^{-12}	1.47×10^{-11}	1.61×10^{-11}	1.61×10^{-11}
475	1	2.5×10^{-13}	5.91×10^{-13}	1.01×10^{-12}	1.48×10^{-12}	2.7×10^{-12}	2.75×10^{-13}
475	5	3.01×10^{-13}	7.14×10^{-13}	1.29×10^{-12}	1.98×10^{-12}	3.12×10^{-12}	3.56×10^{-13}
475	33	4.48×10^{-13}	1.09×10^{-12}	2×10^{-12}	3.21×10^{-12}	4.49×10^{-12}	7.71×10^{-13}
475	50	5.27×10^{-13}	1.28×10^{-12}	2.33×10^{-12}	3.76×10^{-12}	5.07×10^{-12}	1.37×10^{-12}

Table 67. Global maximum density (kg/m^3) for various frequencies of occurrence (percentile) versus altitude $F_{10.7}$ range (Continued).

Height (km)	Frequency (percentile)	$F_{10.7}$ Range					
		Bin 1 66–102	Bin 2 102–138	Bin 3 138–174	Bin 4 174–210	Bin 5 210–246	All 6 66–246
475	67	6.32×10^{-13}	1.52×10^{-12}	2.72×10^{-12}	4.36×10^{-12}	5.88×10^{-12}	2.36×10^{-12}
475	95	1.04×10^{-12}	2.5×10^{-12}	4×10^{-12}	6.23×10^{-12}	8.47×10^{-12}	5.45×10^{-12}
475	99	1.38×10^{-12}	3.37×10^{-12}	4.99×10^{-12}	7.64×10^{-12}	9.7×10^{-12}	7.49×10^{-12}
475	100	3.45×10^{-12}	7.52×10^{-12}	7.35×10^{-12}	1.15×10^{-11}	1.27×10^{-11}	1.27×10^{-11}
500	1	1.54×10^{-13}	3.82×10^{-13}	6.73×10^{-13}	1.02×10^{-12}	1.93×10^{-12}	1.71×10^{-13}
500	5	1.87×10^{-13}	4.67×10^{-13}	8.75×10^{-13}	1.39×10^{-12}	2.25×10^{-12}	2.24×10^{-13}
500	33	2.85×10^{-13}	7.33×10^{-13}	1.4×10^{-12}	2.32×10^{-12}	3.32×10^{-12}	5.07×10^{-13}
500	50	3.38×10^{-13}	8.68×10^{-13}	1.64×10^{-12}	2.74×10^{-12}	3.78×10^{-12}	9.32×10^{-13}
500	67	4.1×10^{-13}	1.05×10^{-12}	1.94×10^{-12}	3.22×10^{-12}	4.42×10^{-12}	1.67×10^{-12}
500	95	6.94×10^{-13}	1.77×10^{-12}	2.93×10^{-12}	4.7×10^{-12}	6.53×10^{-12}	4.07×10^{-12}
500	99	9.43×10^{-13}	2.44×10^{-12}	3.71×10^{-12}	5.85×10^{-12}	7.55×10^{-12}	5.73×10^{-12}
500	100	2.51×10^{-12}	5.75×10^{-12}	5.61×10^{-12}	9.06×10^{-12}	1.01×10^{-11}	1.01×10^{-11}
550	1	6.24×10^{-14}	1.65×10^{-13}	3.08×10^{-13}	4.88×10^{-13}	1×10^{-12}	6.91×10^{-14}
550	5	7.61×10^{-14}	2.05×10^{-13}	4.13×10^{-13}	6.92×10^{-13}	1.19×10^{-12}	9.21×10^{-14}
550	33	1.19×10^{-13}	3.39×10^{-13}	7×10^{-13}	1.24×10^{-12}	1.85×10^{-12}	2.25×10^{-13}
550	50	1.45×10^{-13}	4.09×10^{-13}	8.39×10^{-13}	1.49×10^{-12}	2.13×10^{-12}	4.44×10^{-13}
550	67	3.22×10^{-13}	9.13×10^{-13}	1.85×10^{-12}	3.28×10^{-12}	4.69×10^{-12}	1.3×10^{-12}
550	95	4.63×10^{-13}	1.32×10^{-12}	2.45×10^{-12}	4.23×10^{-12}	6.1×10^{-12}	1.48×10^{-12}
550	99	5.95×10^{-13}	1.72×10^{-12}	2.93×10^{-12}	4.99×10^{-12}	6.8×10^{-12}	3.86×10^{-12}
550	100	1.49×10^{-12}	3.84×10^{-12}	4.18×10^{-12}	7.24×10^{-12}	7.55×10^{-12}	5.86×10^{-12}
600	1	2.78×10^{-14}	7.48×10^{-14}	1.47×10^{-13}	2.42×10^{-13}	5.36×10^{-13}	3.07×10^{-14}
600	5	3.38×10^{-14}	9.47×10^{-13}	2.02×10^{-13}	3.55×10^{-13}	6.49×10^{-13}	4.1×10^{-14}
600	33	5.35×10^{-14}	1.63×10^{-13}	3.6×10^{-13}	6.75×10^{-13}	1.06×10^{-12}	1.04×10^{-13}
600	50	6.53×10^{-14}	2×10^{-13}	4.4×10^{-13}	8.33×10^{-13}	1.24×10^{-12}	2.18×10^{-13}
600	67	1.47×10^{-13}	4.5×10^{-13}	9.82×10^{-13}	1.85×10^{-12}	2.76×10^{-12}	6.66×10^{-13}
600	95	2.17×10^{-13}	6.84×10^{-13}	1.34×10^{-12}	2.47×10^{-12}	3.71×10^{-12}	7.76×10^{-13}
600	99	2.87×10^{-13}	9.19×10^{-13}	1.65×10^{-12}	2.98×10^{-12}	4.2×10^{-12}	2.31×10^{-12}
600	100	8.09×10^{-13}	2.3×10^{-12}	2.48×10^{-12}	4.55×10^{-12}	5.51×10^{-12}	4.49×10^{-12}
650	1	1.42×10^{-14}	3.64×10^{-14}	7.28×10^{-14}	1.24×10^{-13}	2.93×10^{-13}	1.55×10^{-14}
650	5	1.7×10^{-14}	4.63×10^{-14}	1.02×10^{-13}	1.88×10^{-13}	3.62×10^{-13}	2.02×10^{-14}
650	33	2.62×10^{-14}	8.12×10^{-14}	1.9×10^{-13}	3.77×10^{-13}	6.17×10^{-13}	5.11×10^{-14}
650	50	3.18×10^{-14}	1.01×10^{-13}	2.37×10^{-13}	4.76×10^{-13}	7.37×10^{-13}	1.11×10^{-13}
650	67	7.14×10^{-14}	2.3×10^{-13}	5.34×10^{-13}	1.07×10^{-12}	1.65×10^{-12}	3.52×10^{-13}
650	95	1.07×10^{-13}	3.64×10^{-13}	7.57×10^{-13}	1.47×10^{-12}	2.65×10^{-12}	4.19×10^{-13}
650	99	1.45×10^{-13}	5.06×10^{-13}	9.55×10^{-13}	1.82×10^{-12}	2.78×10^{-12}	1.42×10^{-12}
650	100	4.52×10^{-13}	1.41×10^{-12}	1.51×10^{-12}	2.91×10^{-12}	3.56×10^{-12}	2.93×10^{-12}
700	1	8.27×10^{-15}	1.93×10^{-14}	3.81×10^{-14}	6.59×10^{-14}	1.64×10^{-13}	8.96×10^{-15}
700	5	9.67×10^{-15}	2.43×10^{-14}	5.38×10^{-14}	1.02×10^{-13}	2.05×10^{-13}	1.13×10^{-14}

Table 67. Global maximum density (kg/m^3) for various frequencies of occurrence (percentile) versus altitude $F_{10.7}$ range (Continued).

Height (km)	Frequency (percentile)	$F_{10.7}$ Range					
		Bin 1 66–102	Bin 2 102–138	Bin 3 138–174	Bin 4 174–210	Bin 5 210–246	All 6 66–246
700	33	1.42×10^{-14}	4.26×10^{-14}	1.03×10^{-13}	2.15×10^{-13}	3.66×10^{-13}	2.67×10^{-14}
700	50	1.7×10^{-14}	5.32×10^{-14}	1.3×10^{-13}	2.76×10^{-13}	4.45×10^{-13}	5.87×10^{-14}
700	67	3.78×10^{-14}	1.22×10^{-13}	2.97×10^{-13}	6.26×10^{-13}	1.01×10^{-12}	1.92×10^{-13}
700	95	5.66×10^{-14}	1.99×10^{-13}	4.34×10^{-13}	8.92×10^{-13}	1.45×10^{-12}	2.34×10^{-13}
700	99	7.66×10^{-14}	2.85×10^{-13}	5.63×10^{-13}	1.13×10^{-12}	1.7×10^{-12}	8.85×10^{-13}
700	100	2.58×10^{-13}	8.86×10^{-13}	9.33×10^{-13}	1.92×10^{-12}	2.39×10^{-12}	2×10^{-12}
750	1	5.48×10^{-15}	1.14×10^{-14}	2.14×10^{-14}	3.67×10^{-14}	9.43×10^{-14}	5.86×10^{-15}
750	5	6.24×10^{-15}	1.4×10^{-14}	3×10^{-14}	5.74×10^{-14}	1.2×10^{-13}	7.08×10^{-15}
750	33	8.65×10^{-15}	2.38×10^{-14}	5.82×10^{-14}	1.26×10^{-13}	2.22×10^{-13}	1.53×10^{-14}
750	50	1.01×10^{-14}	2.97×10^{-14}	7.41×10^{-14}	1.64×10^{-13}	2.72×10^{-13}	3.27×10^{-14}
750	67	2.23×10^{-14}	6.79×10^{-14}	1.7×10^{-13}	3.75×10^{-13}	6.23×10^{-13}	1.08×10^{-13}
750	95	3.23×10^{-14}	1.13×10^{-13}	2.56×10^{-13}	5.52×10^{-13}	9.32×10^{-13}	1.36×10^{-13}
750	99	4.33×10^{-14}	1.66×10^{-13}	3.39×10^{-13}	7.15×10^{-13}	1.11×10^{-12}	5.66×10^{-13}
750	100	1.52×10^{-13}	5.66×10^{-13}	5.9×10^{-13}	1.27×10^{-12}	1.6×10^{-12}	1.36×10^{-12}
800	1	3.94×10^{-15}	7.33×10^{-15}	1.29×10^{-14}	2.16×10^{-14}	5.58×10^{-14}	4.17×10^{-15}
800	5	4.4×10^{-15}	8.79×10^{-15}	1.78×10^{-14}	3.36×10^{-14}	7.14×10^{-14}	4.9×10^{-15}
800	33	5.8×10^{-15}	1.43×10^{-14}	3.41×10^{-14}	7.51×10^{-14}	1.36×10^{-13}	9.54×10^{-15}
800	50	6.63×10^{-15}	1.76×10^{-14}	4.35×10^{-14}	9.91×10^{-14}	1.7×10^{-13}	1.93×10^{-14}
800	67	1.44×10^{-14}	4.01×10^{-14}	1×10^{-13}	2.28×10^{-13}	3.92×10^{-13}	6.38×10^{-14}
800	95	2×10^{-14}	6.66×10^{-14}	1.54×10^{-13}	3.47×10^{-13}	6.06×10^{-13}	8.2×10^{-14}
800	99	2.62×10^{-14}	9.93×10^{-14}	2.08×10^{-13}	4.6×10^{-13}	7.31×10^{-13}	3.67×10^{-13}
800	100	9.2×10^{-14}	3.68×10^{-13}	3.8×10^{-13}	8.7×10^{-13}	1.1×10^{-12}	9.52×10^{-13}
850	1	2.99×10^{-15}	5.17×10^{-15}	8.49×10^{-15}	1.36×10^{-14}	3.42×10^{-14}	3.14×10^{-15}
850	5	3.3×10^{-15}	6.05×10^{-15}	1.13×10^{-14}	2.07×10^{-14}	4.39×10^{-14}	3.64×10^{-15}
850	33	4.22×10^{-15}	9.28×10^{-15}	2.1×10^{-14}	4.62×10^{-14}	8.56×10^{-14}	6.49×10^{-15}
850	50	4.74×10^{-15}	1.12×10^{-14}	2.67×10^{-14}	6.15×10^{-14}	1.08×10^{-13}	1.22×10^{-14}
850	67	1.02×10^{-14}	2.53×10^{-14}	6.14×10^{-14}	1.43×10^{-13}	2.51×10^{-13}	3.95×10^{-14}
850	95	1.35×10^{-14}	4.13×10^{-14}	9.56×10^{-14}	2.22×10^{-13}	4.01×10^{-13}	5.21×10^{-14}
850	99	1.71×10^{-14}	6.16×10^{-14}	1.31×10^{-13}	3×10^{-13}	4.9×10^{-13}	2.42×10^{-13}
850	100	5.75×10^{-14}	2.43×10^{-13}	2.48×10^{-13}	5.94×10^{-13}	7.59×10^{-13}	6.63×10^{-13}
900	1	2.33×10^{-15}	3.86×10^{-15}	5.98×10^{-15}	9.11×10^{-15}	2.18×10^{-14}	2.45×10^{-15}
900	5	2.56×10^{-15}	4.44×10^{-15}	7.74×10^{-15}	1.35×10^{-14}	2.79×10^{-14}	2.81×10^{-15}
900	33	3.22×10^{-15}	6.48×10^{-15}	1.36×10^{-14}	2.94×10^{-14}	5.5×10^{-14}	4.72×10^{-15}
900	50	3.58×10^{-15}	7.67×10^{-15}	1.71×10^{-14}	3.92×10^{-14}	6.97×10^{-14}	8.28×10^{-15}
900	67	7.62×10^{-15}	1.71×10^{-14}	3.92×10^{-14}	9.11×10^{-14}	1.63×10^{-13}	2.58×10^{-14}
900	95	9.73×10^{-15}	2.69×10^{-14}	6.11×10^{-14}	1.44×10^{-13}	2.68×10^{-13}	3.48×10^{-14}
900	99	1.2×10^{-14}	3.97×10^{-14}	8.45×10^{-14}	1.99×10^{-13}	3.33×10^{-13}	1.62×10^{-13}
900	100	3.71×10^{-14}	1.63×10^{-13}	1.65×10^{-13}	4.17×10^{-13}	5.38×10^{-13}	4.76×10^{-13}

Table 67. Global maximum density (kg/m^3) for various frequencies of occurrence (percentile) versus altitude $F_{10.7}$ range (Continued).

Height (km)	Frequency (percentile)	$F_{10.7}$ Range					
		Bin 1 66–102	Bin 2 102–138	Bin 3 138–174	Bin 4 174–210	Bin 5 210–246	All 6 66–246
950	1	1.86×10^{-15}	3.01×10^{-15}	4.48×10^{-15}	6.51×10^{-15}	1.46×10^{-14}	1.95×10^{-15}
950	5	2.04×10^{-15}	3.43×10^{-15}	5.63×10^{-15}	9.26×10^{-15}	1.85×10^{-14}	2.23×10^{-15}
950	33	2.54×10^{-15}	4.8×10^{-15}	9.37×10^{-15}	1.94×10^{-14}	3.62×10^{-14}	3.63×10^{-15}
950	50	2.8×10^{-15}	5.58×10^{-15}	1.16×10^{-14}	2.58×10^{-14}	4.61×10^{-14}	5.98×10^{-15}
950	67	5.95×10^{-15}	1.23×10^{-14}	2.64×10^{-14}	6×10^{-14}	1.08×10^{-13}	1.78×10^{-14}
950	95	7.39×10^{-15}	1.85×10^{-14}	4.05×10^{-14}	9.62×10^{-14}	1.82×10^{-13}	2.43×10^{-14}
950	99	8.85×10^{-15}	2.67×10^{-14}	5.61×10^{-14}	1.35×10^{-13}	2.29×10^{-13}	1.1×10^{-13}
950	100	2.49×10^{-14}	1.11×10^{-13}	1.12×10^{-13}	2.91×10^{-13}	3.79×10^{-13}	3.39×10^{-13}
1,000	1	1.5×10^{-15}	2.41×10^{-15}	3.50×10^{-15}	4.89×10^{-15}	1.02×10^{-14}	1.57×10^{-15}
1,000	5	1.64×10^{-15}	2.73×10^{-15}	4.3×10^{-15}	6.73×10^{-15}	1.27×10^{-14}	1.8×10^{-15}
1,000	33	2.04×10^{-15}	3.73×10^{-15}	6.81×10^{-15}	1.34×10^{-14}	2.45×10^{-14}	2.87×10^{-15}
1,000	50	2.25×10^{-15}	4.27×10^{-15}	8.26×10^{-15}	1.76×10^{-14}	3.12×10^{-14}	4.54×10^{-15}
1,000	67	4.77×10^{-15}	9.3×10^{-15}	1.86×10^{-14}	4.07×10^{-14}	7.36×10^{-14}	1.29×10^{-14}
1,000	95	5.83×10^{-15}	1.34×10^{-14}	2.79×10^{-14}	6.55×10^{-14}	1.26×10^{-13}	1.77×10^{-14}
1,000	99	6.83×10^{-15}	1.88×10^{-14}	3.84×10^{-14}	9.26×10^{-14}	1.6×10^{-13}	7.63×10^{-14}
1,000	100	1.74×10^{-14}	7.67×10^{-14}	7.71×10^{-14}	2.09×10^{-13}	2.75×10^{-13}	2.48×10^{-13}

Use of the data in this table also makes it possible for the design engineers to easily accomplish any required trade studies while managers will be able to determine just what risks they will be taking. For applications that require density values other than the global maximum or for questions concerning the application of the data in engineering analyses, contact personnel of MSFC Natural Environments Branch. Table 67 also shows the median value of the global maximum density for the altitude and the 10.7 cm solar flux bin indicated, computed over the POR. It also gives the median (50th percentile) global maximum density and several other percentile levels of the global maximum density. Percentile refers to the fraction of time the density was equal to or less than the indicated value. These data may be used directly to indicate the magnitude of the variations in the global maximum density that occurs over a period of a few days. If appropriate for the application, an additional increment may be added to account for model inaccuracies and variations related to other sources. To obtain a conservative (upper limit) estimate, recommendation is made to assume that these additional variations are Gaussian with a standard deviation equal to 0.2 times the total density. To understand the frequency of occurrence of these variations, table 68 provides the probabilities of encountering intervals of 10 and 30 days without exceeding the indicated percentile level. (As with table 67, only solar and geomagnetic variations are considered.)

Table 68. Probabilities of achieving a time interval without encountering thermospheric density level above a given percentile value.

Probability of Going at Least 10 Days Without Exceeding the Indicated Percentile Density Level (Random Start)				
13-mo	Percentile Level			
Smoothed $F_{10.7}$ Range	66%	90%	95%	99%
66 to 102	0.13	0.46	0.63	0.86
102 to 138	0.21	0.55	0.71	0.9
138 to 174	0.28	0.55	0.68	0.89
174 to 210	0.35	0.6	0.75	0.93
210 to 246	0.38	0.65	0.76	0.87
Probability of Going at Least 30 Days Without Exceeding the Indicated Percentile Density Level (Random Start)				
13-mo	Percentile Level			
Smoothed $F_{10.7}$ Range	66%	90%	95%	99%
66 to 102	0.03	0.23	0.4	0.72
102 to 138	0.05	0.28	0.48	0.76
138 to 174	0.08	0.33	0.44	0.77
174 to 210	0.12	0.37	0.52	0.82
210 to 246	0.12	0.38	0.57	0.75

Probabilities for other time intervals can be estimated from figure 66. If one of these higher percentile levels is exceeded, it typically drops back down within a short time (hours, a few days at most). The distributions are highly skewed; once a level has been exceeded, it is usually exceeded again within a few days. On the other hand, if the Sun is quiet, it may remain so for several months.

5.1.5.3 Earth Global Reference Atmospheric Model. The Earth-GRAM that was developed by MSFC's Natural Environments Branch provides a single continuous representation of the neutral atmosphere from the Earth's surface to orbital altitudes. Earth-GRAM is described more fully in section 3.9 and in reference 103.

5.1.6 Spacecraft Effects

Density of the neutral gas is the primary atmospheric property that affects a spacecraft's orbital altitude, lifetime, and motion. Even though space is thought of as a vacuum, there is enough matter to impart a substantial drag force on orbiting spacecraft. Unless the vehicle's propulsion system compensates for this drag force, the altitude will decay until reentry occurs. Density effects also directly contribute to the torques experienced by the spacecraft due to the aerodynamic interaction between the spacecraft and the atmosphere, and thus must be considered in the design of the spacecraft attitude control system.

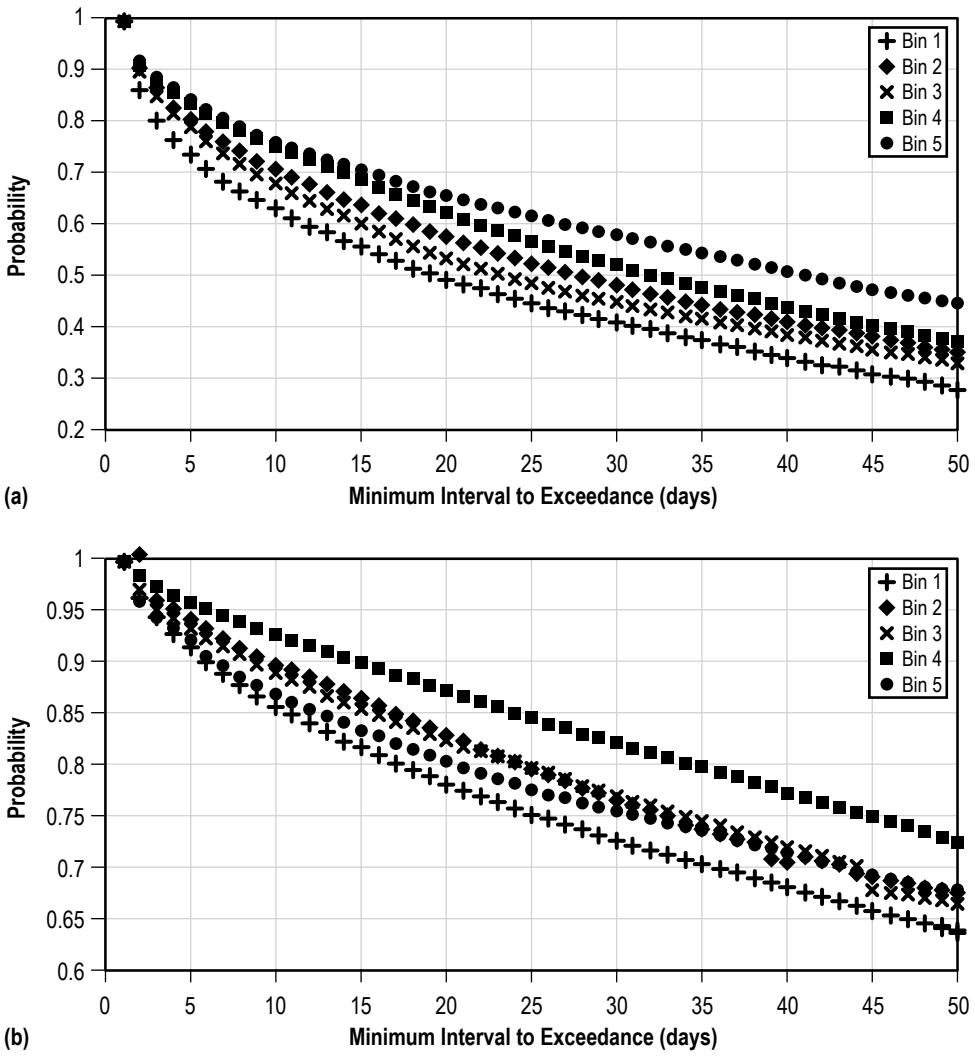

Figure 66. Probability of meeting or exceeding a given time interval without exceeding the (a) 95th percentile density or (b) 99th percentile density (bins represent a range of $F_{10.7}$: (1) 66–102, (2) 102–138, (3) 138–174, (4) 174–210, and (5) 210–246).

Many materials used on spacecraft surfaces are susceptible to attack by AO, a major constituent of the LEO thermosphere region. Due to photodissociation, oxygen exists predominantly in the atomic form and varies with altitude, solar activity, and other effects discussed in section 5.1.2. Simultaneous exposure to the solar UV radiation, micrometeoroid impact damage, sputtering, or contamination effects can aggravate the AO effects, leading to serious deterioration of mechanical, optical, and thermal properties of some material surfaces. Spacecraft glow is a related phenomenon, which may be of concern for optically sensitive experiments. Optical emissions are generated from metastable molecules that have been excited by impact on the surface of the spacecraft. Investigations show that the surface acts as a catalyst, thus the intensity is dependent on the type of surface material.

5.1.7 Atomic Oxygen

In the thermosphere, AO is formed by solar UV radiation dissociating oxygen molecules into free oxygen atoms and is the dominant neutral species from approximately 100–500 km altitude dependent on solar activity (fig. 60). At high solar activity AO can be ≈90% of the atmosphere at 500 km. Oxygen atoms alone are highly corrosive, combining with most materials they encounter. At LEO velocities, the AO flux experienced by a spacecraft is essentially a stream of AO with energies of ≈5 eV. Since the degree of spacecraft surface degradation is directly proportional to the total integrated flux or fluence, a spacecraft should be provided with AO protection optimized for the AO environment in which they will operate for the planned mission life, plus an operating margin to allow for variations in orbital conditions or for reasonable mission extensions. Thus, spacecraft operating for short periods in LEO and spacecraft bound for high orbits or interplanetary trajectories may require far less AO protection than spacecraft designed to operate for long durations in LEO.

The AO fluence for long-duration missions depends on several mission parameters including spacecraft altitude, attitude, orbital inclination, and mission duration. The spacecraft AO flux present during a mission can vary significantly for mission durations of a few months to years and thus affect AO fluence calculations. Thermosphere density variations such as the semiannual variation and those associated with solar activity (sec. 5.1.2) can be a major contributor to AO flux variations in addition to spacecraft altitude changes. To capture these variations, the AO flux can be determined from the MET or MSIS thermosphere models at the location of the spacecraft for appropriate time intervals and integrated over the mission timeline to obtain the AO fluence. This technique was used to determine the AO requirement for the International Space Station (ISS) by using the baseline 90 days to 277.8 km altitude strategy.[104] An AO density time profile was determined for the lifetime of the ISS using the MSIS thermosphere model and then integrated to yield an annual average AO ram fluence value of 5×10^{21} particles/cm^2-yr. For periods on the order of 30 days or less, short-term (daily) density variations become important in AO flux calculations. For the ISS, a short-term daily ram fluence value of 4.4×10^{19} particles/cm^2-day was determined.

5.2 Thermal Environment

A summary of key design factors for the thermal environment is displayed in table 69.

The thermal environment definition provided here was extracted from NASA Technical Memorandum NASA/TM—2001–211221,[105] which was based on analysis of the extensive database available from the Earth Radiation Budget Experiment (ERBE).[106–108] Twenty-eight monthly datasets of 16-s resolution wide field data were obtained and analyzed to produce a new set of environmental parameters. One parameter set was derived specifically for 51.6° inclination orbits and incorporated into the environment definition and requirements for the ISS program.[109,110] More general results keyed to three orbital inclination ranges, 0° to 30°, 30° to 60°, and >60°, were documented in NASA/TM—2001–211221,[105] and these are repeated here. Because they were derived from the same datasets with essentially identical methodology, the definition presented here should lead to system designs that are fully compatible with ISS even though there are slight differences due to the different inclination ranges.

Table 69. Summary of key design factors.

Parameter	Source	Select Based On
For estimates of long-term average and hot/cold conditions:		
Solar constant	Section 5.2.1.1	Season of year or desired extreme
Albedo / long-wave radiance pair(s)	Tables 72–74	Orbit inclination, α/ε ratio, desired extreme and averaging time
Albedo correction	Table 71	Orbital beta angle
For evaluation of thermal time constant dependent conditions (see secs. 5.2.2.4 to 5.2.2.6)		
Solar constant	Section 5.2.1.1	Season of year or desired extreme
Albedo / long-wave radiance pair(s)	Tables 72–74; or for noncritical applications, table 75	Orbit inclination, α/ε ratio, system criticality, desired extreme and averaging time. STEM analysis may be helpful
Albedo correction	Table 76 and section 5.2.2.2.1	Orbital beta angle or SZA

Technically, the work with the ERBE data was undertaken to provide a more detailed statistical description of the variations of the thermal environment than previously was available. Greater use of lightweight structures sensitive to rapid thermal fluctuations greatly increased the importance of this information. Also, since application of these results depends upon the thermal time constants of the system being designed, a companion document, Simple Thermal Environment Model (STEM),[111] was developed to aid in selecting environment parameters that most appropriately apply to a specific application.

5.2.1 Fundamental Thermal Environment Parameters

Space vehicles in Earth orbit receive radiant thermal energy from three sources and reflect or radiate it to the cold sink of space. The three primary sources are the incoming solar radiation, Earth-reflected solar energy (albedo radiation), and outgoing long-wave radiation (OLR) emitted by the Earth and atmosphere. If one considers the Earth and its atmosphere as a whole and averages over long periods, the incoming solar energy and outgoing long-wave radiant energy are essentially in balance; the Earth/atmosphere is very nearly in radiative equilibrium with the Sun. However, it is not in balance everywhere on the globe and important variations exist with respect to local time, geography, and atmospheric conditions. A space vehicle's motion with respect to the Earth results in its viewing only a 'swath' across the full global thermal profile. Hence, the vehicle sees these variations as functions of time and responds in accordance with the thermal time constants of the hardware systems.

5.2.1.1 Solar Constant. The direct solar flux is the greatest source of heating for most spacecraft. The mean value of this solar flux at mean Earth-Sun distance is termed the 'solar constant.' Specifically, the solar constant is defined as the radiation that falls on a unit area of surface normal to the line from the Sun, per unit time and outside of the atmosphere, at 1 astronomical unit (AU) (mean Earth-Sun distance). However, as seen by an Earth-orbiting spacecraft, the incoming solar flux is not quite constant; two factors influence its variability. First, the amount of radiant energy emitted by the Sun is known to vary slightly throughout the 11-year solar cycle.

The exact amount differs from cycle to cycle but is estimated to be only a fraction of a percent. Second, the slightly elliptical orbit of the Earth about the Sun results in a variation in the solar flux incident on the Earth or upon an Earth orbiting spacecraft. This ±1.7% departure from the mean distance leads to an approximate ±3.4% difference in radiation. That is, a few days following winter solstice, 3.4% more solar energy falls on a unit area normal to the line from the Sun at the outside of the atmosphere; just after summer solstice the amount is 3.4% less. The solar constant recommended in this TM corresponds to the value recommended by the World Radiation Center (WRC) in Davos, Switzerland, and is based on a summary of eight measurements made from 1969 to 1980:[112,113]

Hot case: $S_{hot} = 1{,}414\ W/m^2$

Median case: $S_o = 1{,}367\ W/m^2$ = solar constant

Cold case: $S_{cold} = 1{,}322\ W/m^2$.

This variation from median to hot or cold case covers the Earth-Sun distance variation. An additional ±5 W/m^2 could be added (subtracted) to account for measurement uncertainties and solar cycle variations, but is not included in the above values.

5.2.1.2 Solar Irradiance. Table 70 presents the solar spectral irradiance in tabular form for the range from 0.14 to 50 mm. This table was published in American Society for Testing and Materials Designation: E490-00a,[114] entitled Standard Solar Constant and Zero Air Mass Solar Spectral Irradiance Tables. These tables define the zero air mass solar spectral irradiance for use in thermal analysis, thermal balance testing, and other tests of spacecraft and spacecraft components and materials. Typical applications include the calculation of solar absorptance from spectral reflectance data and the specification of solar UV exposure of materials during simulated space radiation testing. This standard does not purport to address all of the safety concerns, if any, associated with its use. It is the responsibility of the user of this standard to establish appropriate safety and health practices and determine the applicability of regulatory limitations prior to use.

5.2.1.3 Albedo. The fraction of incident solar energy reflected (or scattered) by a planet back into space is termed the albedo. Values typically are expressed as a fraction or percent. For spacecraft in LEO and in this TM, the term is more precisely defined as the 'local bolometric' albedo. Bolometric implies wavelength independence, i.e., the albedo representing the integrated short wavelength band. Local is used because it is a characteristic of only a small portion of the planetary surface; the portion viewed by a spacecraft close to Earth. Values presented in this TM are derived from wide field measurements made by the Earth Radiation Budget Satellite (ERBS) at 610 km altitude and the National Oceanic and Atmospheric Administration (NOAA) 9 and 10 satellites at, respectively, 849 and 815 km. Altitude dependence has been removed by transforming the data to a standard surface, where the 'top of atmosphere' is considered to be approximately 30 km above the Earth's surface.[100] 'Top of atmosphere' represents the virtual source of the albedo radiation and the outgoing long-wave radiation.

Table 70. Solar spectral irradiance-standard curve, abridged version.

λ	E_λ	$D_{0-\lambda}$	λ	E_λ	$D_{0-\lambda}$
0.14	9.833×10^{-2}	–	0.57	1,797	31.39
0.16	0.3195	3.1×10^{-4}	0.58	1,801	32.71
0.18	2.042	2×10^{-3}	0.59	1,758	34.01
0.2	10.83	1.1×10^{-2}	0.6	1,745	35.29
0.22	44.93	5.2×10^{-2}	0.62	1,663	37.78
0.23	49.64	8.7×10^{-2}	0.64	1,610	40.18
0.24	51.83	0.12	0.66	1,527	42.48
0.25	59.81	0.16	0.68	1,485	44.68
0.26	129.1	0.23	0.7	1,438	46.82
0.27	222.1	0.36	0.72	1,360	48.87
0.28	212.9	0.52	0.75	1,272	51.76
0.29	441	0.76	0.8	1,132	56.16
0.3	526	1.12	0.9	882.6	63.53
0.31	634.5	1.54	1	719.7	69.4
0.32	746.5	2.05	1.2	487.1	78.23
0.33	948.7	2.67	1.4	342.5	84.3
0.34	947.3	3.36	1.6	243.5	88.59
0.35	969.5	4.06	1.8	167.1	91.6
0.36	985.2	4.78	2	115	93.66
0.37	1,129	5.55	2.2	81.73	95.1
0.38	1,091	6.36	2.4	58.78	96.13
0.39	1,093	7.16	2.6	43.86	96.88
0.4	1,518	8.12	2.8	33.43	97.45
0.41	1,712	9.3	3	25.93	97.88
0.42	1,740	10.56	3.2	20.45	98.22
0.43	1,625	11.79	3.4	16.36	98.49
0.44	1,826	13.06	3.6	13.26	98.71
0.45	2,030	14.47	3.8	10.87	98.89
0.46	2,077	15.97	4	8.977	99.03
0.47	2,049	17.48	4.5	5.674	99.3
0.48	2,057	18.98	5	3.691	99.47
0.49	1,955	20.45	6	1.879	99.68
0.5	1,948	21.88	7	1.022	99.78
0.51	1,911	23.29	8	0.6041	99.84
0.52	1,806	24.65	10	0.2663	99.9
0.53	1,861	26	15	6.106×10^{-2}	99.96
0.54	1,861	27.36	20	1.755×10^{-2}	99.98
0.55	1,867	28.72	50	1.769×10^{-3}	100
0.56	1,808	30.07			

λ = wavelength (μm).

E_λ = solar spectral irradiance averaged over small bandwidth centered at λ, (W • m^{-2} m^{-1}).

$D_{0-\lambda}$ = percentage of the solar constant (1,366.1 W • m^{-2}) associated with wavelengths shorter than λ.

To evaluate the albedo radiation for any satellite at a known altitude the thermal analyst simply assumes the source is at this level, i.e., Earth radius +30 km, not Earth surface. Obviously, a spacecraft only receives reflected (albedo) radiation when a portion of the Earth or atmosphere seen by the spacecraft is sunlit. Albedo radiation has approximately the same spectral shape as the Sun's spectrum, which approximates a blackbody with a characteristic temperature of 5,777 K.

Albedo is highly variable across the globe and is dependent on the distribution of reflective properties of the surface and the amount and type of cloud cover. Reflectivity increases with increased cloud cover. Continental areas generally have higher albedo values than ocean areas. Because of snow and ice cover, decreasing solar elevation angle, and increasing cloud cover, albedo tends to increase with latitude if viewed on a large scale. From the spacecraft design perspective, the most important systematic albedo variation is with SZA that, when averages are used, depends on the spacecraft's beta angle. Care must be taken to correctly account for this effect, especially near the terminator (reference sec. 5.2.1.5 on geometric factors).

5.2.1.4 Outgoing Long-Wave Radiation. In addition to direct solar and reflected (albedo) solar radiation, the third primary component of a spacecraft's thermal environment is the OLR emitted by the Earth itself. This Earth-emitted thermal radiation is a combination of radiation emitted in infrared wavelength bands by atmospheric gases and radiation emitted by the Earth's surface and cloud tops but is partially absorbed in the atmosphere. Thus, the spectral distribution is somewhat complex. For the purpose of spacecraft thermal analysis, however, it is generally sufficient to assume a graybody spectrum corresponding to a temperature in the 250 K to 300 K range.

OLR is not constant over the globe, but the localized variations are much less severe than for albedo. Outgoing long-wave radiation is principally influenced by the temperature of the Earth's surface and the amount of cloud cover. A warmer region of the Earth's surface emits more radiation than a colder area. On a large scale, highest values of OLR occur in tropical and desert regions (regions of the globe receiving the maximum solar heating) and decrease with latitude. Increasing cloud cover tends to lower OLR because cloud tops are cold and clouds effectively block upwelling radiation from the Earth's warmer surface below.

The diurnal effects on OLR as experienced by a satellite were studied in this analysis. For low inclination orbits (<60°), inclusion or exclusion of the nighttime data and changes in SZA cutoff made no significant difference in the net OLR distribution functions. Thus, for these orbits no special accounting for diurnal effects is needed. This is not true, however, for high-inclination orbits. Passage over the nighttime and lighted but high SZA polar regions contributes significantly to the low (cold case) OLR populations. This effect was overlooked in earlier studies, which only checked diurnal variations at low inclination.[111,112]

5.2.1.5 Geometric Factors

5.2.1.5.1 Orbital Altitude and 'Top of Atmosphere.' The OLR and albedo radiation received on a satellite surface diminishes as its altitude increases, i.e., as the satellite moves away from the source. This effect is accounted for as part of the 'view factor' in thermal calculations.

Derived OLR and albedo data measurements from satellites at several altitudes (610, 815, and 849 km) were corrected to the apparent source surface (30 km above Earth surface) or 'top of atmosphere.' Thus, in applying these data, the analyst should assume a source at $R_e + 30$ km, where R_e is the Earth's radius, 6,378.14 km equatorial. Failure to do so leads to a slight underestimate of the OLR and albedo radiation by a factor of:

$$F_a = \frac{\left(R_e + A\right)^2}{\left(R_e + 30\,\text{km} + A\right)^2}\,, \tag{48}$$

where A is the orbital altitude. The error is quite small ($F_a = 0.9911$ at $A = 300$ km) and decreases (F_a approaches 1) with increased altitude.

5.2.1.5.2 Orbital Inclination, Beta Angle, and Solar Zenith Angle. Orbital inclination refers to the angle between the Earth's polar vector and the vector normal to the satellite's orbit plane. Thus, an equatorial orbit has an inclination of zero; a perfect polar orbit has an inclination of 90°. The orbital beta angle is the minimum angle between the satellite's orbit plane (the closest to a Sun-pointing vector possible in the plane) and the Sun-Earth vector. The beta angle can be thought of as the solar elevation angle with respect to the orbit plane. The angle between the Sun-Earth vector and the Earth-satellite vector is termed the SZA. The SZA is zero when the Sun is directly above the satellite (Earth-satellite-Sun in a straight line) and 90° when a satellite is directly over the terminator. Except for special Sun synchronous cases, the SZA varies rapidly over an orbit; the minimum SZA is equal to the absolute value of the beta angle.

5.2.2 Technical Background

This TM provides recommendations on the selection of natural thermal environment parameters for use in design of spaceborne systems. The recommendations are based on analysis of data from the ERBE. The results provide a comprehensive and accurate statistical picture of the thermal environment encountered in LEO. In addition to the material summarized below, additional details are available in the STEM User's Guide.[111]

5.2.2.1 Earth Radiation Budget Experiment. The ERBE is a multisatellite experiment with the primary objective of global data collecting such Earth radiation budget parameters as incident sunlight, reflected sunlight (albedo), and OLR. This experiment was selected because of its thorough coverage and high-quality data. The experiment consists of three satellites: the low-inclination ERBS and two NOAA Sun-synchronous satellites. The data used here are from the active cavity, flat plate radiometers in the fixed, nonscanning, and wide field-of-view mode. This type of instrument was chosen because it directly measures the albedo and OLR as they would be received by a spacecraft surface. The available, separated data sets are daily averaged values (S-4), hourly averaged values (S-10), and raw 16-s instrument measurements along the ERBS or NOAA satellite trajectory (S7). The S-4 and S-10 data products were inappropriate for this application because the averaging times are too long compared to the thermal time constant of typical space systems. Therefore, the design criteria presented below are based on 28 files, representing 1 month

of 16-s data each of S-7 data obtained directly from the ERBE Program Office. The measurements, made from November 1984 through July 1987, represented all seasons well.

5.2.2.2 Details of Application

5.2.2.2.1 Albedo Correction for Solar Zenith Angle. Often in scientific studies of the Earth and Earth radiation balance results are based on albedo data associated with a restricted range of SZA centered about zero for improved accuracy. In these cases and to a first approximation, albedo may be assumed to be independent of SZA, i.e., the scattering is Lambertian or equal in all directions. This approximation was also assumed in the past for most spacecraft engineering applications even though it is less appropriate for this application. For large SZA, the Earth reflects radiation more strongly in the forward direction than to the sides or backward. The effect on albedo can be significant; thus, ERBE data quality and the capability of current engineering analysis methods warrant an improved approach. For low and medium inclination orbits, which see a wide range and rapidly changing SZA, the correction is most significant for subsystems with short thermal time constants (<10 min). For certain Sun-synchronous orbits (those flying near the terminator), the SZA is always relatively large and the correction is important to even orbit-average albedos.

Treatment of this topic in the scientific literature is generally 'scene specific,' e.g., it depends on geographic features in the field of view, data generally not available to the design engineer. Also, the algorithms tested did not fully remove the zenith angle dependence from this data set. Therefore, a zenith angle correction was derived specifically for this data set in a manner specifically tuned to the analysis tools most commonly used for engineering analysis: Thermal Radiation Analyzer System, Thermal Desktop, and Thermal Synthesizer System. Used with this correction and the proper parameters for the ERBS and NOAA satellites, these tools should accurately reproduce the measurements.

The correction term, derived from 4 months of data restricted to the –30 to 30 latitude band, was verified by testing another 4 months of data to wider latitude bands. This removes the SZA dependence to within ± 0.04. The correction is:

$$\text{Albedo(SZA)} = \text{albedo(SZA} = 0) + \text{correction} \tag{49}$$

$$\text{Correction} = \left[C_4(\text{SZA})^4 + C_3(\text{SZA})^3 + C_2(\text{SZA})^2 + C_1(\text{SZA}) \right], \tag{50}$$

where SZA is the solar zenith angle in degrees and the albedo is expressed as a fraction:

$$C_4 = 4.9115 \times 10^{-9} \tag{51}$$

$$C_3 = 6.0372 \times 10^{-8} \tag{52}$$

$$C_2 = -2.1793 \times 10^{-5} \tag{53}$$

and

$$C_1 = 1.3798 \times 10^{-3}. \tag{54}$$

Figure 67 illustrates the albedo correction term as a function of SZA. To evaluate the albedo at a specific SZA, this term must be added to the SZA = 0 albedo values presented in the tables. Correction terms to obtain orbital average albedo values are provided in table 71.

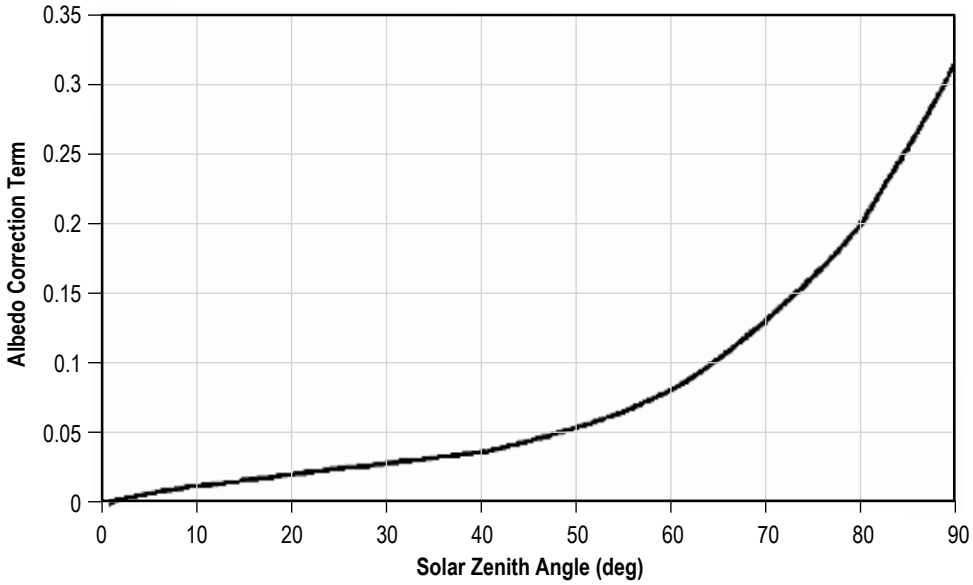

Figure 67. Albedo correction term, *C*(SZA), as a function of SZA.

Table 71. Values of orbital average albedo correction term, <*c*>[113] (add this correction to the SZA = 0 albedo value).

Orbital Beta Angle (°)	Orbital Average Albedo Correction <c>
0	0.04
10	0.04
20	0.05
30	0.06
40	0.07
50	0.09
60	0.12
70	0.16
80	0.22
90	0.31

5.2.2.2.2 Temporal and Orbital Variations. For any satellite system, different portions of the hardware have different thermal response times, ranging from a few minutes to hours. Conceptually, the thermal performance of these systems could be analyzed by inputting either a real or simulated time series of albedo and OLR values, solar exposure, and internal heat sources, all having a time resolution finer than the shortest system time constant. In practice, however, the usual design objective is only to ensure that the system remains within a selected operational temperature range, not to model its detailed temporal variability. Thus, high resolution time series analysis is not warranted. The problem can be solved with adequate accuracy by modeling only the primary orbital variations (light to dark cycles) and assuming extreme albedo and OLR values appropriate to the thermal time constant(s) of the system. The systematic dependence of albedo on SZA, discussed above, must also be considered, especially for short time-constant systems.

To provide appropriate values of extreme albedo and OLR for this analysis approach, running means of the albedo and OLR variations, transformed to top of the atmosphere (30 km) to remove the altitude dependence, were derived from the ERBE data sets. The results are latitude dependent, so the choice of appropriate values for a particular mission depends on the orbital inclination of the satellite in question. Since the satellite inclination seldom equals the inclination of the ERBE satellites, approximation is required to deal with this mismatch. Fortunately, the latitude dependence is sufficiently weak that adequate resolution is obtained by dividing the possible range of inclinations into three regions and deriving a single set of albedo and OLR extremes for each region. The inclination ranges selected are 0° to 30°, >30° to 60°, and >60°.
Running averages are presented for times ranging from a few seconds to 24 hr. Averaging periods to 10 days failed to show substantial variation from the 24-hr results.

There is no albedo radiation, and thus no albedo data, when the satellite is over the dark side of the Earth. Also, at high SZA values the albedo showed a great deal of scatter that would have distorted the distributions, thus these data were excluded from consideration. Thus, there were two data sets: a paired set containing both OLR and concurrent albedo values and a larger unpaired set of OLR data that included the dark side and high SZA data. Comparison of the total (unpaired) OLR data set with the paired OLR subset shows a significant difference in the OLR distributions for high inclinations. As illustrated by figure 68, the difference between the paired and unpaired data sets is negligible for the low inclination orbits. For the middle (30° to 60°) inclinations, the difference is becoming obvious but hardly significant for engineering applications. The mean differs by only 8 W/m^2 between the unpaired and paired 60° data and, more importantly, the upper and lower limits are very similar and are also very similar to the 30° data limits. The separation is more significant at 90° inclinations. In this case the unpaired data set is approximately three times the size of the paired set. A large fraction of the data is excluded because much of the time the SZA is greater than 65° over polar regions. More problematic is the substantial difference in the extreme cold-side values, which clearly must be accounted for in the thermal design process.

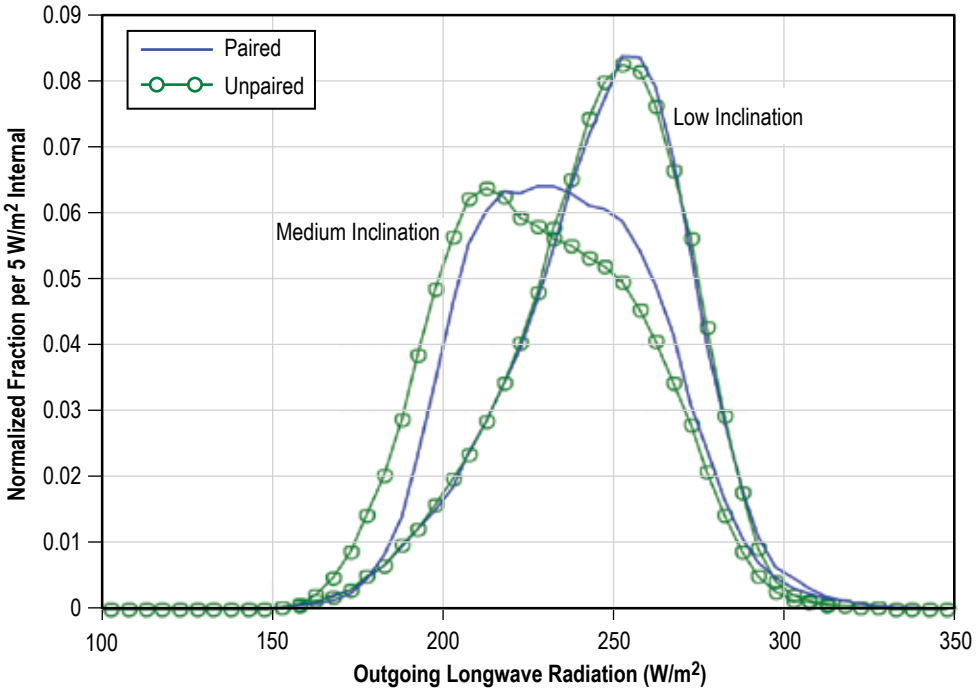

Figure 68. OLR distributions for low inclination (≤30°) and medium inclination (30° to ≤60°) orbits, 128-s averaged paired and unpaired data.

5.2.2.3 Engineering Values for Critical Applications. For critical applications, the designer generally likes to select environment design points associated with some defined risk of occurrence during the mission lifetime. For example, he might select a design point associated with a 5% (or 1% or 0.01%…any reasonable value for the particular application) probability of being encountered during the design life of the system. Unfortunately, this type of information cannot be derived from the limited data set available for this study. The required data set would cover a very long time compared to the mission design life—so long that multiple independent samples, each the duration of the design life, could be drawn from the data set. A distribution function can then be formed of the extreme values encountered in each draw. In this work, 28 monthly data sets drawn from a 33-month period were studied; 10 months were sampled twice by two separate satellites. Typical mission design lifetimes are usually 1 to 10 years. This data set is large enough to provide only a distribution of extremes for mission lifetimes of approximately 1 week or less. Thus, this data resource is limited to a selection of design point recommendations of expected extremes of the distributions (one for each system time constant—averaging time) of the total data. These worst case values are appropriate for critical applications, i.e., situations where the temperature limit is not to be exceeded. Use should be coupled with a design margin selected considering the application, level of confidence in the design analysis, and comparison of mission life to duration of database.

For noncritical applications, i.e., applications where the design limit may be exceeded, a certain fraction of the time, less extreme environmental parameters based on the information provided in the next section may be selected.

In all cases, the percentiles indicated represent the distributions from this single data set. Thus, they are to be associated with the fraction of time the values are expected to be exceeded; not the probability that they will be exceeded over a mission lifetime.

Selection of the extremes of these distributions to define critical engineering minima and maxima involves an arbitrary process of deciding where to cut the tails of the distributions. As with any data set of this type, the larger the data set the more extreme the values that appear in the distribution tails. Generally, the 0.04 and 99.96 percentile values (equivalent to ~ $\pm 3.3\ \sigma$ if a Gaussian distribution) were selected as engineering worst case points for practical applications. One point in 2,500 is above this upper limit and one point is below this lower limit. OLR values in the tails of the distributions reached 20 to 25 W/m^2 beyond these percentile values for the 16- and 128-s running mean data, and ~5 W/m^2 for the 30-min running means. At longer averaging times the number of independent data points diminishes to <2,500 and collapses the tails. The interpolated 0.04 or 99.96th value may actually lie slightly outside the minimum (or maximum) value observed. In these cases the extreme observed value was selected. For the long averaging times there is usually an approximate 5 W/m^2 difference between the first (or 99th) percentile values, extremes of the data set, and the interpolated 0.04 (or 99.96th). Likewise, the albedo data tends to show the same characteristics on the hot side of the distributions. The albedo data reaches 0.04 to 0.08 above the engineering values for the shortest averaging times and less for the longer average data. The cutoff is naturally sharp on the cold side of the albedo distribution.

Once one engineering extreme value has been identified, either OLR or albedo, the next step is to determine the proper value of the other parameter used to form a pair. As illustrated by the contour plots of 128-s running mean paired-data distributions (figs. 69–71), the albedo and OLR data are partially correlated. Low OLR values tend to be paired with high albedos; high OLR values tend to be paired with low to moderate albedos. To select an appropriate albedo to pair with the extreme hot OLR, for example, paired data sorted into bins ranked by both OLR and albedo value were done. The highest OLR value bins were selected until at least 0.04% of the data set was accumulated; the associated albedo values were then averaged to find the match for the OLR engineering maximum pair (tables 72–74). The same process is used to find the engineering minimum OLR, high and low albedo cases.

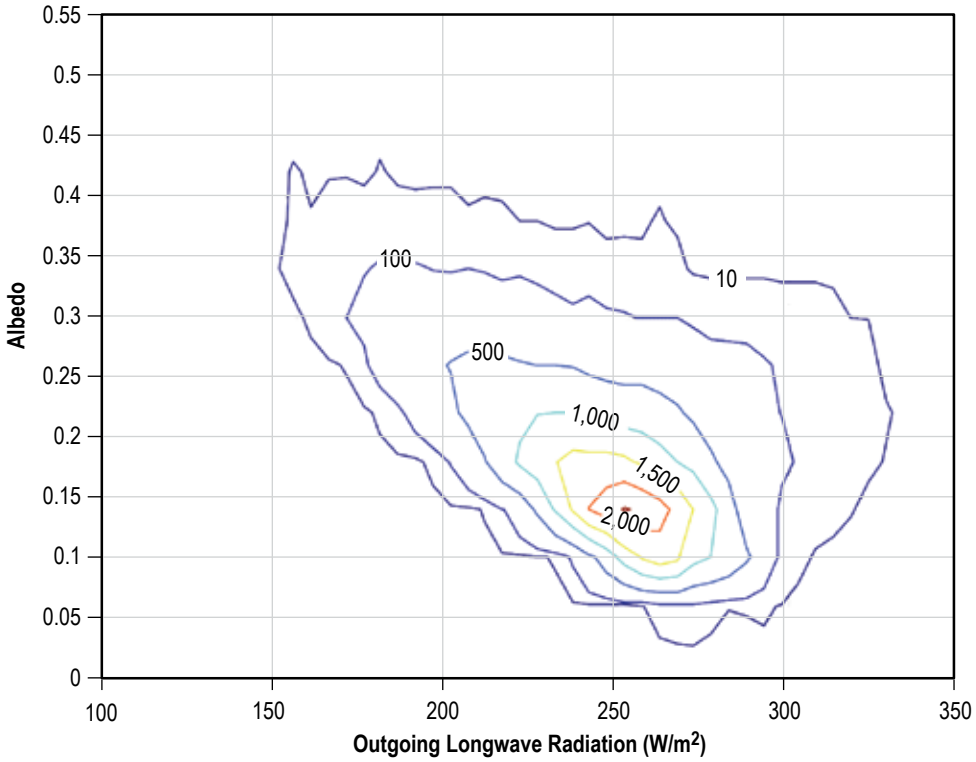

Figure 69. Albedo-OLR correlation for low inclination orbits, 128-s averaged data (contour intervals indicate relative frequency of occurrence).

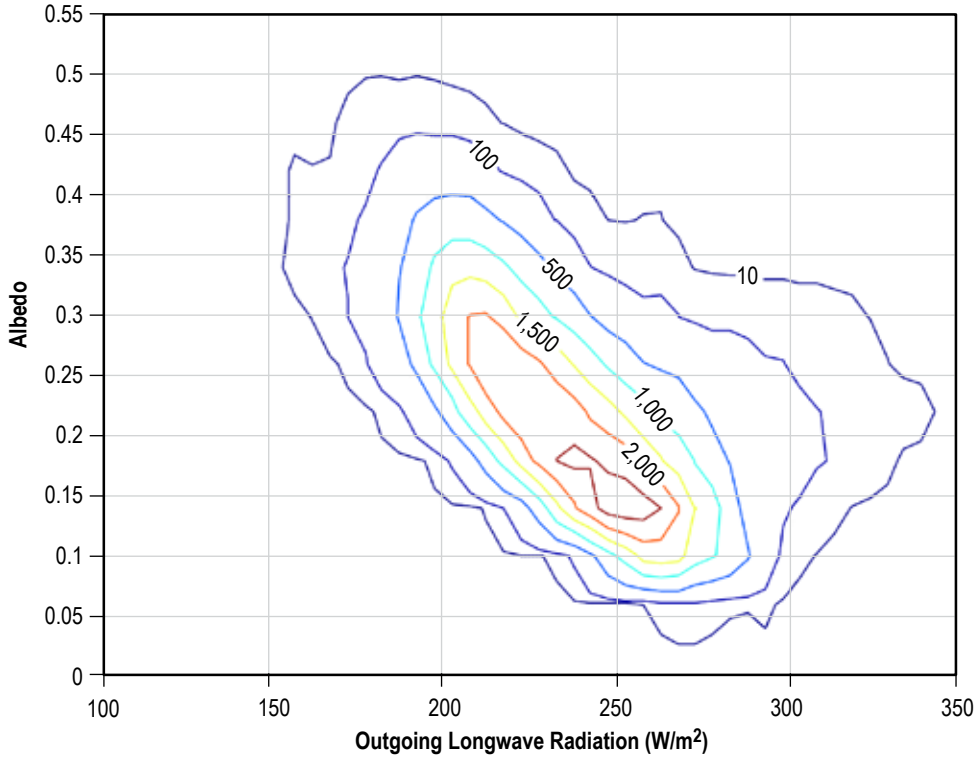

Figure 70. Albedo-OLR correlation for medium inclination orbits, 128-s averaged data (contour intervals indicate relative frequency of occurrence).

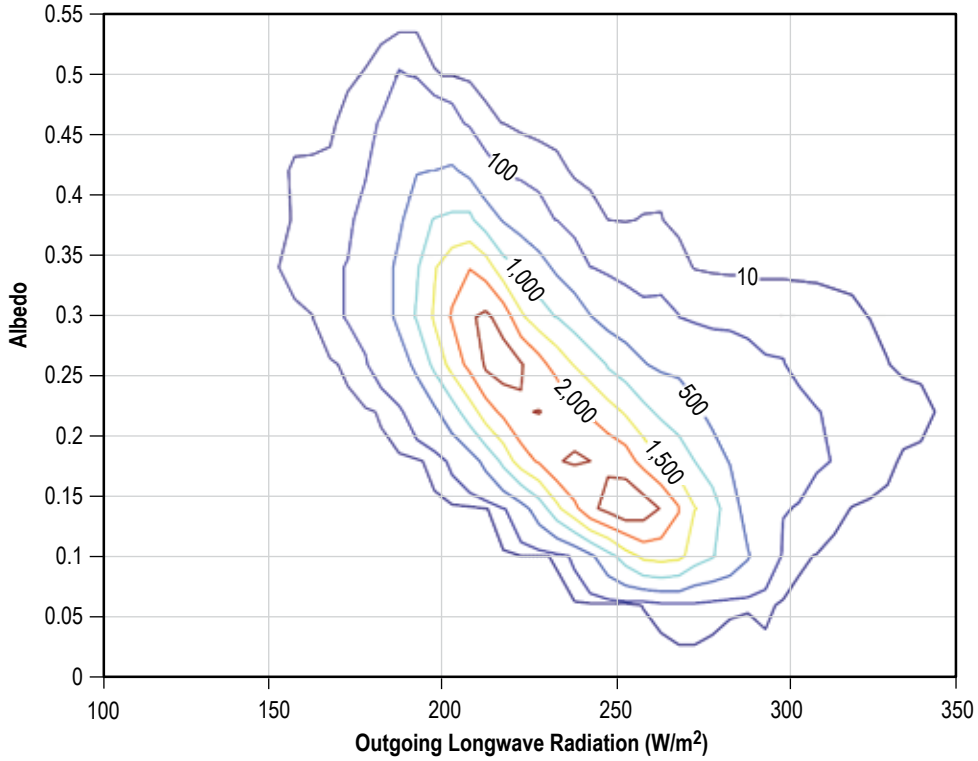

Figure 71. Albedo-OLR correlations for high inclination orbits, 128-s averaged data (contour intervals indicate relative frequency of occurrence).

Table 72. Albedo, OLR pairs for critical systems in low inclination orbits (albedo and OLR values are referenced to the 'top of the atmosphere,' R_e + 30 km).

Averaging Time	Cold Cases		
	Minimum Albedo Alb ⇔ OLR (W/m^2)	Combined Minimum Alb ⇔ OLR (W/m^2)	Minimum OLR Alb ⇔ OLR (W/m^2)
16 s	0.06 ⇔ 273	0.13 ⇔ 225	0.4 ⇔ 150
128 s	0.06 ⇔ 273	0.13 ⇔ 226	0.38 ⇔ 154
896 s	0.07 ⇔ 265	0.14 ⇔ 227	0.33 ⇔ 173
30 min	0.08 ⇔ 261	0.14 ⇔ 228	0.3 ⇔ 188
90 min	0.11 ⇔ 258	0.14 ⇔ 228	0.25 ⇔ 206
6 hr	0.14 ⇔ 245	0.16 ⇔ 232	0.19 ⇔ 224
24 hr	0.16 ⇔ 240	0.16 ⇔ 235	0.18 ⇔ 230
Averaging Time	Hot Cases		
	Maximum Albedo Alb ⇔ OLR (W/m^2)	Combined Maximum Alb ⇔ OLR (W/m^2)	Maximum OLR Alb ⇔ OLR (W/m^2)
16 s	0.43 ⇔ 182	0.3 ⇔ 298	0.22 ⇔ 331
128 s	0.42 ⇔ 181	0.29 ⇔ 295	0.22 ⇔ 326
896 s	0.37 ⇔ 219	0.28 ⇔ 291	0.22 ⇔ 318
30 min	0.33 ⇔ 219	0.26 ⇔ 284	0.17 ⇔ 297
90 min	0.28 ⇔ 237	0.24 ⇔ 275	0.20 ⇔ 285
6 hr	0.23 ⇔ 248	0.21 ⇔ 264	0.19 ⇔ 269
24 hr	0.22 ⇔ 251	0.2 ⇔ 260	0.19 ⇔ 262
Mean Albedo: 0.18		Mean OLR: 246	

Table 73. Albedo, OLR pairs for critical systems in medium inclination orbits (albedo and OLR values are referenced to the 'top of the atmosphere,' $R_e + 30$ km).

Averaging Time	Cold Cases		
	Minimum Albedo Alb ⇔ OLR (W/m^2)	Combined Minimum Alb ⇔ OLR (W/m^2)	Minimum OLR Alb ⇔ OLR (W/m^2)
16 s	0.06 ⇔ 273	0.15 ⇔ 213	0.4 ⇔ 151
128 s	0.06 ⇔ 273	0.15 ⇔ 213	0.38 ⇔ 155
896 s	0.08 ⇔ 262	0.17 ⇔ 217	0.34 ⇔ 163
30 min	0.12 ⇔ 246	0.18 ⇔ 217	0.27 ⇔ 176
90 min	0.16 ⇔ 239	0.19 ⇔ 218	0.3 ⇔ 200
6 hr	0.18 ⇔ 238	0.19 ⇔ 221	0.31 ⇔ 207
24 hr	0.19 ⇔ 233	0.2 ⇔ 223	0.25 ⇔ 210
Averaging Time	**Hot Cases**		
	Maximum Albedo Alb ⇔ OLR (W/m^2)	Combined Maximum Alb ⇔ OLR (W/m^2)	Maximum OLR Alb ⇔ OLR (W/m^2)
16 s	0.48 ⇔ 180	0.31 ⇔ 267	0.21 ⇔ 332
128 s	0.47 ⇔ 180	0.3 ⇔ 265	0.22 ⇔ 331
896 s	0.36 ⇔ 192	0.28 ⇔ 258	0.22 ⇔ 297
30 min	0.34 ⇔ 205	0.28 ⇔ 261	0.21 ⇔ 282
90 min	0.31 ⇔ 204	0.26 ⇔ 257	0.22 ⇔ 274
6 hr	0.31 ⇔ 212	0.24 ⇔ 248	0.21 ⇔ 249
24 hr	0.28 ⇔ 224	0.24 ⇔ 247	0.21 ⇔ 245
Mean Albedo: 0.22		Mean OLR: 234	

Table 74. Albedo, OLR pairs for critical systems in high inclination orbits (albedo and OLR values are referenced to the 'top of the atmosphere,' $R_e + 30$ km).

Averaging Time	Cold Cases		
	Minimum Albedo Alb ⇔ OLR (W/m^2)	Combined Minimum Alb ⇔ OLR (W/m^2)	Minimum OLR Alb ⇔ OLR (W/m^2)
16 s	0.06 ⇔ 273	0.16 ⇔ 212	0.4 ⇔ 108
128 s	0.06 ⇔ 273	0.16 ⇔ 212	0.38 ⇔ 111
896 s	0.09 ⇔ 264	0.17 ⇔ 218	0.33 ⇔ 148
30 min	0.13 ⇔ 246	0.18 ⇔ 218	0.31 ⇔ 175
90 min	0.16 ⇔ 231	0.19 ⇔ 218	0.26 ⇔ 193
6 hr	0.18 ⇔ 231	0.2 ⇔ 224	0.27 ⇔ 202
24 hr	0.18 ⇔ 231	0.2 ⇔ 224	0.24 ⇔ 205
Averaging Time	Hot Cases		
	Maximum Albedo Alb ⇔ OLR (W/m^2)	Combined Maximum Alb ⇔ OLR (W/m^2)	Maximum OLR Alb ⇔ OLR (W/m^2)
16 s	0.5 ⇔ 180	0.32 ⇔ 263	0.22 ⇔ 332
128 s	0.49 ⇔ 184	0.31 ⇔ 262	0.22 ⇔ 331
896 s	0.35 ⇔ 202	0.28 ⇔ 259	0.2 ⇔ 294
30 min	0.33 ⇔ 204	0.27 ⇔ 260	0.2 ⇔ 284
90 min	0.28 ⇔ 214	0.26 ⇔ 244	0.22 ⇔ 250
6 hr	0.27 ⇔ 218	0.24 ⇔ 233	0.22 ⇔ 221*
24 hr	0.24 ⇔ 224	0.23 ⇔ 232	0.2 ⇔ 217*
Mean Albedo: 0.23		Mean OLR: 211	

* Dark side OLR data were included to reach these figures; thus, they may underestimate the maximum to always-daylight Sun synchronous satellites by perhaps 15 W/m^2.

From the spacecraft perspective, however, what proves to be the extreme hot or cold case for a particular system depends on the emissivity of the spacecraft surfaces and its absorptivity for solar radiation. Depending on the ratio between these parameters, the extreme spacecraft temperatures may be associated with extreme OLR cases, extreme albedo cases, or some intermediate 'combined' case where both OLR and albedo run high (or low) together, but neither is near its individual extreme. To provide hot and cold combined extremes, points where normalized variates for albedo and OLR are equal were determined and the 0.04 and 99.96 percentile points from this subset were identified to provide the cold and hot combined extremes. A normalized variate is the deviation from the mean value divided by the standard deviation of the distribution, i.e., $x_N = (x - x_m)/\sigma_x$, where x_N is the normalized variate, x_m is the mean of x in the distribution, and σ_x is the standard deviation. Basically, take the distributions of two variables, OLR and albedo (illustrated in figs. 71–73), select the subset defined by $OLR_N = ALB_N$, and find the 0.04 and 99.96 percentile points in the tails. The resulting values for engineering extreme cases of albedo and OLR are given in tables 72–74 for low, medium, and high inclination orbits. These tables provide engineering values for critical applications of albedo and OLR for various averaging times (time constants) and extreme types (extreme albedo case, extreme OLR case, and extreme 'combined' case).

5.2.2.4 Engineering Margin for Critical Systems. Examination of the OLR distribution tails for the 16- and 128-s averaging times reveals a similarity. The most extreme observations average 17 W/m^2 outside the 0.04 or 99.96 percentile values, while the 1 and 99 percentile values average 26 W/m^2 to the inside. Reference figure 72 for an illustration. Considering that LEO satellites traverse about 120 km per 16-s interval, this is to be expected. The wide field viewing satellite sees the same scene for several sequential 16-s intervals. For longer averaging times, the numerical averaging process causes the tails to shrink. In an 896-s interval the satellite traverses over 6,600 km, thus, many scene types are included in the average. The extreme data point is about 8 W/m^2 outside the 0.04 or 99.96 percentile values while the 1 and 99 percentile values are displaced about 18 W/m^2 toward the inside. The distributions for longer intervals cut off even more sharply.

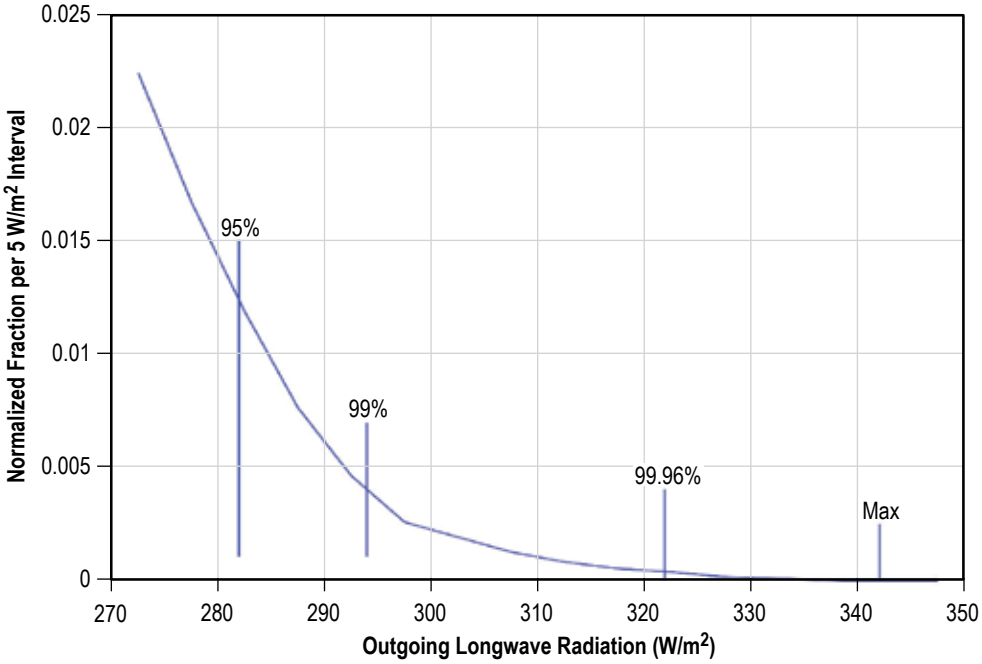

Figure 72. Hot side tail of the 128-s average OLR distribution for low inclination orbits.

Note: The basic confidence limit in the OLR data is about 5 W/m^2; widths of the distribution tails are at most a few multiples of the measurement uncertainty.

Examination of the albedo distribution tails reveals the same characteristics on the hot (high albedo value) side, except the tails are narrower in comparison to the basic measurement uncertainty of approximately 0.02. For the 16- and 128-s intervals, the separations between the 99th and 99.96th percentiles average 0.07, between the 99.96th and the extreme observations, 0.06. Because the cold side cuts off very sharply, there is no tail; separations between the minimum observation, the 0.04, and first percentiles are 0.02 or less.

One key factor in selecting the critical system design point was the shape of the tails and the relationship to the measurement uncertainty. Another key factor was the probable encounter frequency for exceeding the worst case. This is also termed the 'return time' or the mean time between exceedances. Selecting the 0.04 percentile implies that one in 2,500 data points lays outside the design point. If these points were uncorrelated and random, the expectation is to encounter one every 2,500 by 16 s or 11 hr (for the 16-s averaging time data). In fact, the points are not usually isolated, so the return time will be longer. However, comparing the 16- and 128-s distributions reveals the 16-s points exceeding the worst case are unlikely to be in groups larger than eight, thus, the average return time must be <2,500 by 128 s (89 hr). Eighty-nine hours is short compared to the duration of most space experiments and missions. Selecting the 0.04 and 99.96 percentile values as design points is not being overly conservative. A reasonable expectation exists that these values will actually be encountered. In fact, if a system is critically sensitive to such short-duration fluctuations in the environment, i.e., a tether might become brittle and break, it is appropriate to design not only for the worst case limits but also with some appropriate margin. On the other hand, if the system is sensitive in only a noncritical sense, i.e., a temperature exceedance results in a momentary loss of science data, it may suffice to have little or no design margin at the worst case environment and simply tolerate the occasional loss of data. Similar arguments can be made for longer averaging times. Coupled with the collapse of the tail width to within a factor of 2 or less of the measurement uncertainty, the same conclusion is apparent.

5.2.2.5 Design Conditions for Noncritical Systems. For applications where thermal excursions beyond the design point can be easily tolerated, design values associated with the 5th and 95th percentiles are provided in table 75 and as an optional output from the STEM tool. Table 75 gives albedo (Alb)-OLR pairs for thermal analysis sensitivity studies. The albedo extreme type cases are 5th percentile (cold) and 95th percentile (hot) albedos and an associated OLR (obtained by averaging the OLRs paired to the albedos outside the indicated percentile). Combined (Comb) types are pairs with equal normalized variates identified with the 5th or 95th percentile (reference sec. 5.2.3). OLR extreme types were obtained in the same manner as the albedo extreme types but with the parameters switched. One may expect system temperatures to lie outside values derived with parameters from this table for a small fraction of the total mission duration. This fraction cannot be specified but should be on the order of a few percent. Table 76 provides pulse-averaged SZA correction terms for albedo for pulses beginning at or symmetrical about solar noon. That is, the average was taken from solar noon to the time indicated, assuming a 90-min circular orbit and using the method in STEM. As the numbers indicate, the correction term is not a strong function of orbit position because the average has been weighted with cosine (SZA) in accordance with variation of albedo energy. Example albedo-OLR profile for low inclination orbit, beta of 40º. (This is an 'albedo extreme' hot case with pulse averaged SZA corrections included. The initialization and base albedo is the 5,400 s value, 0.28, plus the 0.07 orbit average SZA correction. Data are from tables 75 and 76.)

Table 75. Albedo-OLR pairs for noncritical applications.

Extreme Type	Avg. Time (s)	Cold Case Data						Hot Case Data					
		30°		60°		90°		30°		60°		90°	
		Alb	OLR	Alb	OLR	Alb	OLR	Alb	OLR	Alb	OLR	Alb	OLR
Alb	16	0.09	270	0.1	267	0.1	267	0.29	205	0.36	201	0.38	197
Alb	128	0.09	267	0.1	265	0.1	265	0.29	211	0.35	202	0.37	199
Alb	896	0.1	261	0.13	252	0.14	252	0.26	225	0.29	213	0.28	213
Alb	1,800	0.12	257	0.16	242	0.17	244	0.24	234	0.27	223	0.26	223
Alb	5,400	0.13	249	0.18	238	0.18	230	0.22	246	0.26	229	0.24	219
Alb	21,600	0.15	241	0.19	233	0.19	230	0.2	252	0.25	231	0.23	224
Alb	86,400	0.16	240	0.19	235	0.19	230	0.2	252	0.25	232	0.23	224
Comb	16	0.15	236	0.19	227	0.2	225	0.21	260	0.23	240	0.24	237
Comb	128	0.16	237	0.19	227	0.2	225	0.21	260	0.23	240	0.24	238
Comb	896	0.16	237	0.2	226	0.2	227	0.21	261	0.23	241	0.23	240
Comb	1,800	0.16	237	0.2	225	0.2	226	0.21	258	0.23	240	0.23	242
Comb	5,400	0.16	237	0.2	225	0.21	224	0.2	258	0.23	241	0.23	232
Comb	21,600	0.17	237	0.2	226	0.21	226	0.19	255	0.23	242	0.22	230
Comb	86,400	0.17	236	0.2	226	0.2	225	0.19	257	0.23	241	0.23	230
OLR	16	0.3	195	0.33	183	0.35	164	0.17	285	0.17	280	0.17	280
OLR	128	0.29	198	0.33	184	0.34	164	0.17	284	0.17	279	0.17	279
OLR	896	0.26	209	0.28	189	0.27	172	0.18	279	0.18	264	0.18	263
OLR	1,800	0.23	216	0.25	200	0.25	190	0.18	274	0.2	258	0.2	258
OLR	5,400	0.2	225	0.23	209	0.24	202	0.19	268	0.21	254	0.21	242
OLR	21,600	0.18	231	0.23	212	0.23	205	0.19	261	0.21	242	0.21	216
OLR	86,400	0.17	233	0.23	212	0.23	207	0.18	258	0.21	241	0.21	215

Table 76. Pulse-averaged SZA correction terms for albedo assuming a 5,400-s orbit.*

Beta Angle	MaximumTime From Solar Noon			
	128 s	448 s	896 s	1,350 s or More (Orbit Average)
0	0.01	0.02	0.03	0.04
10	0.01	0.02	0.03	0.04
20	0.02	0.02	0.04	0.05
30	0.03	0.03	0.04	0.06
40	0.04	0.04	0.05	0.07
50	0.05	0.06	0.07	0.09
60	0.08	0.09	0.1	0.12
70	0.13	0.13	0.15	0.16
80	0.2	0.21	0.22	0.22
90	0.31	0.31	0.31	0.31

* Add the indicated correction to the value for SZA = 0.

Fifth and 95th percentile reference points are associated with the percentile from the distribution of a single parameter, albedo or OLR. System temperature is determined by several parameters including albedo and OLR, plus the absorptance/emittance ratio. Thus, it cannot be said that system temperatures derived using 5th/95th percentile reference points will be exceeded 5% of the time, for the correlation is only approximate. Also, the reference here is to the fraction of time the conditions will be exceeded, not to risk of exceedance during mission lifetime.

5.2.2.6 Applications and the Simple Thermal Environment Model. A simple method for incorporating this information into design specifications and requirements documents was devised by Dr. Eugene Ungar and his colleagues at Johnson Space Center on behalf of the ISS Program. For ISS, they were dealing with a complex vehicle with multiple components requiring thermal analysis and control, each with different thermal time constants. The approach was to specify two sets of albedo and OLR value profiles that would drive the thermal analyses. Each profile covered an initialization time plus one orbit. One set was a functional set: conditions during which the components must function within specification. The other was an extreme set: components were required to return to a proper functioning condition after the conditions were applied and then removed. Each set consisted of four albedo-OLR profiles, two hot (max albedo and max OLR cases), and two cold (low albedo and low OLR cases). Each profile consisted of albedo-OLR pairs from tables 72–74. An example, not from the ISS, is provided in figure 73. The figure illustrates an albedo extreme hot case for low inclination orbit with pulse-averaged SZA correction terms added to the albedo. For specification writing, typically, profiles without SZA corrections are provided because the system will usually fly at multiple beta angles.

Several points are important about this approach. First, the profiles are tied to specific orbits with the hot or cold short duration pulses modeled as step functions. The hot case albedo and OLR step functions are specified to encompass orbital noon so the maximum short-term values are encountered at the time of greatest heating. Likewise, the cold case step functions are applied at the opposite side of the orbit, orbital noon plus 180°, when the vehicle is in a shadow or at least the albedo radiation is at minimum. By locking the pulse locations with respect to the orbit, the SZA correction is known and can be applied at the time the specification is derived rather than requiring the analyst to determine the correction. In this illustration, and in the ISS cases, each pulse is modeled as a double square step function, one on top of the other to represent two time constants. Of course, actual variations are not simple step functions. The TESTSTEM routine in STEM gives a good indication of hardware response when using step functions compared to measured profiles. Finally, the orbit is preceded by an initialization period with conditions set at the 90-min average conditions (hot or cold) of interest. Thus, the model temperatures are stabilized before the short period pulses are applied.

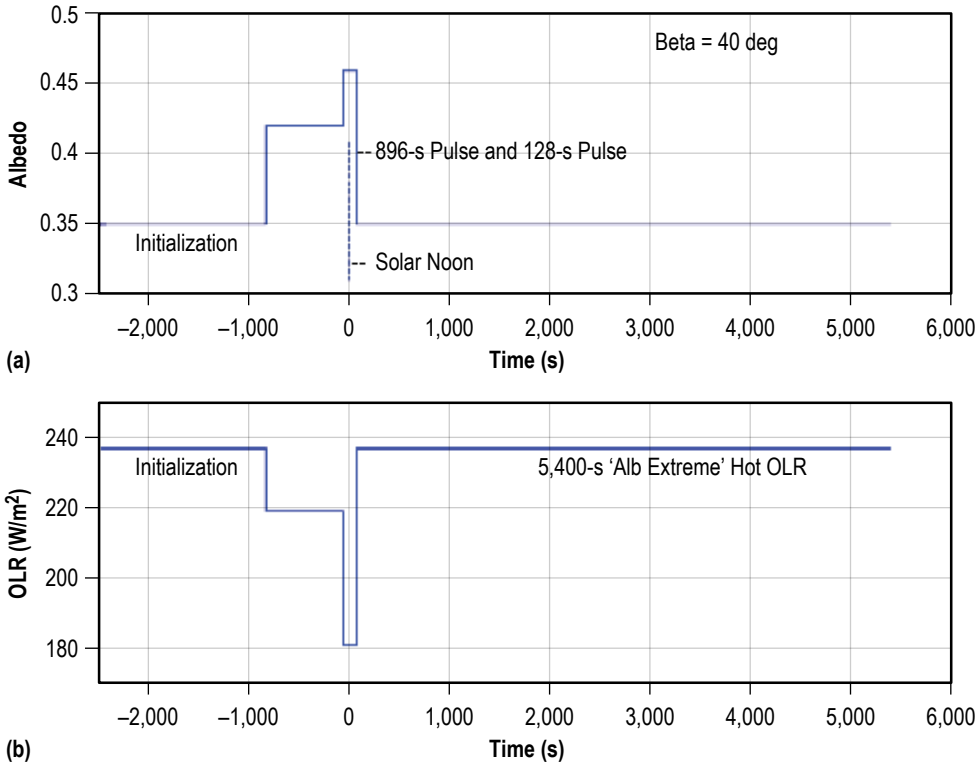

Figure 73. Example low inclination orbit, beta of 40º: (a) Albedo profile and (b) OLR profile.

The ISS approach is especially useful for a situation like ISS where a single set of albedo/OLR conditions need to be specified for a variety of hardware elements. However, in simpler cases, i.e., a single hardware element and surface treatment, this approach can lead to unneeded analysis when the extreme hot and cold cases can be selected directly.To aid this process and to identify cases when a combined albedo/OLR case leads to the temperature extremes, a STEM was developed. STEM is fully documented[111] and provides a shortcut by:

(1) Estimating the thermal time constant for the hardware.

(2) Selecting, based on the absorptance/emittance ratio for the surface, whether extreme albedo, extreme OLR, or combined extreme conditions, yields extreme system temperatures.

(3) Providing the complete set of thermal parameters to model the thermal environment with correct time constant, SZA correction, etc.

STEM accomplishes this shortcut by analyzing the energy balance for a simple spherical satellite. Provision is made for inclusion of internal energy sources. Data in tables 72–74 are used and return values suitable for returning the extreme temperatures, hot and cold, when used in actual system analysis. As an option, STEM also outputs reference points associated with the 5th and 95th percentile extremes (reference sec. 5.2.2.5). This option is included primarily to aid the

analyst in determining the sensitivity of system temperature to environmental inputs near the limits of the distribution. Use as a design specification is only recommended for rare, noncritical circumstances where periodic excursions beyond the design limit can be easily tolerated. In STEM output, the SZA corrections are applied to the albedo values and associated locations are identified in the orbit.

Note that since STEM models the system as a sphere, the environmental parameters selected might not yield the extreme temperatures in a thermal analysis of a system with complex geometry. For example, reflected radiation from adjacent spacecraft surfaces could alter the balance. Thus, when the system involves complex geometry and the extreme temperatures derived from STEM for the different types of environmental conditions are close to one another, the analyst should check system performance using alternate types of environmental extremes, not just conditions identified by STEM. STEM will identify the alternate extremes if the user resets the cold case and hot case parameter switches.

5.3 Geomagnetic Field

The Earth's natural magnetic field (or geomagnetic field) comes from two sources: (1) Currents inside the Earth, which produce 99% of the field at the surface, and (2) currents in the magnetosphere. The Earth's magnetic field can shield the Earth from certain radiations and it can trap charged particles. The magnetosphere has a lower boundary of the ionosphere and an upper one defined by the magnetopause, which is the interface between the Earth's magnetic field and the solar wind. Most (99.9%) of the solar wind particles do not penetrate the magnetopause but are deflected and flow around the magnetosphere.

A dipole magnetic field configuration dominates the magnetic field topology within a few R_e of the planet. The dipole center is approximately 400 km from the center of the planet. The geomagnetic axis is inclined at approximately 11.7° to the Earth's rotational axis. The Earth's magnetic field greatly affects thermal, plasma, radiation, and other environments in space, particularly in the LEO region. The specific environment is affected by the charged particles trapped through the magnetic field lines and the deflections of the low energy cosmic rays. These effects will be specifically described in each respective environment section. In this section, a few simple approximations to the Earth's main geomagnetic field used in the past to curve fit simple radiation models will be discussed. Recent spherical harmonic models used to curve fit the Earth's main geomagnetic undisturbed field from zero to 2,000 km in altitude will be presented.

The strength of Earth's dipole magnetic field varies. Surface magnetic fields are approximately 0.3 G (3×10^{-5} T) at the equator and 0.6 G (6×10^{-5} T) at the poles. Due to the difference between the Earth's rotational axis and the magnetic axis, and the offset of the dipole described above, the field intensity is low in the region near 20 °S. latitude and 50 °W. longitude. This is referred to as the South Atlantic Anomaly (SAA). The magnetic field direction at the equator is nearly horizontal pointing north. At the magnetic North Pole, it points down into the Earth. Beyond an altitude of approximately 2,000 km, strong currents in the magnetosphere cause deviations from the near-Earth dipolar field. In addition to the general magnetic field variation, the geomagnetic storms caused by solar activity can change the magnetic field strength.

The interaction of the Earth's magnetic field at very great distances (several R_e) with the solar wind is one of the heat sources for the neutral thermospheric region. The solar wind is a stream of high-speed plasma emanating from the Sun. This interaction causes energetic particles to penetrate down into the lower thermosphere at high geographic latitudes and directly heat the thermospheric gas.

Based on magnetic field fluctuation data reported every 3 hr at 12 stations between geomagnetic latitudes 48° and 63° and selected for good longitudinal coverage, the planetary geomagnetic activity index a_p (or k_p, which is essentially the logarithm of a_p) as a measure of episodic type solar activity is used. Although it is the high latitude ionospheric current fluctuations that drive the magnetic field fluctuations as observed at these stations, it is not the magnetic field fluctuations that are driving the thermosphere. Therefore, the correlations between observed density changes and the a_p index are not always good. The daily planetary geomagnetic index, A_p, is the average of the eight 3-hourly a_p values for that particular day.

The aurora is primarily produced by high energy charged particles precipitating into the atmosphere along magnetic field lines. At high latitudes, the ionosphere is strongly coupled to the magnetosphere and to the solar wind. The transition from closed to open field lines and the influx of energetic particles profoundly affects the ionospheric plasmas. The boundary region, the auroral oval, is marked by the beautiful display of auroras. Surrounding the magnetic poles, the oval extends to near 75° geomagnetic latitude at noon and 65° at local midnight. On the nightside, the oval is well marked by a depletion of electron density, the so-called trough. On the dayside, one finds a region of enhanced densities just inside the oval, the so-called magnetospheric cleft. The electron density at the tip of the cleft is almost an order of magnitude greater than it is at the bottom of the trough. During magnetic storms, the trough moves equatorward approximately 2° per unit increase in K_p. The region inside the oval is the polar cap.

5.3.1 Models

The magnetic field of the Earth has been investigated by satellite for several decades. Data obtained were sufficient to apply for model development with its average strength and shape during different levels of overall magnetic activity. A summary of key design factors is displayed in table 77.

Table 77. Summary of key design factors (geometric field).

Parameter	Source	Select Based On
For prediction of geomagnetic field:		
Geomagnetic field	IGRF (sec. 5.3.1.1)	Plasma, charged particles
Geomagnetic field effects and guidelines:		
Plasma effects	Section 5.3.2	Section 5.4
EMF potential	Section 5.3.2	Section 5.4
Trapped high energy particle	Section 5.3.2	Section 5.5

5.3.1.1 International Geomagnetic Reference Field. A current version of the International Geomagnetic Reference Field (IGRF) is recommended to predict the magnetic field strength for regions where the field retains the dipolar configuration (typically for altitudes less than approximately geostationary orbit). The IGRF model is the empirical representation of the Earth's magnetic field for scientific use recommended by the International Association of Geomagnetism and Aeronomy. The IGRF model represents the main (core) field without external sources. The model employs the usual spherical harmonics expansion of the scalar potential in geocentric coordinates. The IGRF model coefficients are based on all available data sources, including geomagnetic measurements from observatories, ships, aircraft, and satellites. In combination with the IGRF coefficient sets, different subroutines have been used to determine the components of the magnetic field vector and the *L*-value at a given location. The National Space Science Data Center (NSSDC) version uses a FORTRAN field calculation subroutine to calculate magnetic field components and SHELLG to calculate McIIwain's *L* parameter. Both subroutines were developed by G. Kluge at the European Space Operations Center. The program BILCAL produces tables of the geomagnetic field strength, vector components (B-abs., B-north, B-east, B-down, declination, inclination), equatorial/ minimum field strength (B0), dipole moment, and L-value in latitude, longitude (geodetic), altitude, or year (decimal). The code can calculate the magnetic field at a given position and time or it can calculate the maximum and average magnetic fields during an orbit. Most Earth/Sun parameters remain constant for hundreds of years; however, the magnetic field strength changes significantly every 5 to 10 years. Thus, it is important to use a recent version of the model to correctly determine the magnetic field. The IGRF prediction of the Earth's magnetic field is shown in section 5.3.2.

5.3.2 Geomagnetic Field Effects

The Earth's magnetic field exerts a strong influence on space environmental phenomena, such as plasma motions, electric currents, and trapped high energy charged particles. This influence has important consequences to spacecraft design and performance. The IGRF prediction of the Earth's magnetic field is shown in figures 74 and 75.

The geomagnetic field influences the motions of particles within the Earth's orbital environment and also deflects incoming high energy particles, such as those associated with cosmic rays. These high energy particles may charge spacecraft surfaces causing failure of or interference with spacecraft subsystems. Due to the dipole field geometry, the magnetic field strength is lowest over the southern Atlantic Ocean, which leads to a higher concentration of trapped radiation in this region. It is in the vicinity of the SAA that a spacecraft may encounter electronic 'upsets' and instrument interference. An accurate depiction of the geomagnetic field is also needed to properly size magnetic torquers, which are used in guidance, navigation, and control (GN&C) systems. Potentials can be induced across spacecraft through the $V \times B \bullet L$ electromagnetic force (EMF) or magnetic induction effect. The magnitude of this potential depends on the magnetic field strength (B) direction relative to the spacecraft velocity vector (V) and the orientation and size of the spacecraft (L).This effect has been used to generate power and propulsion with long conductive tethers.

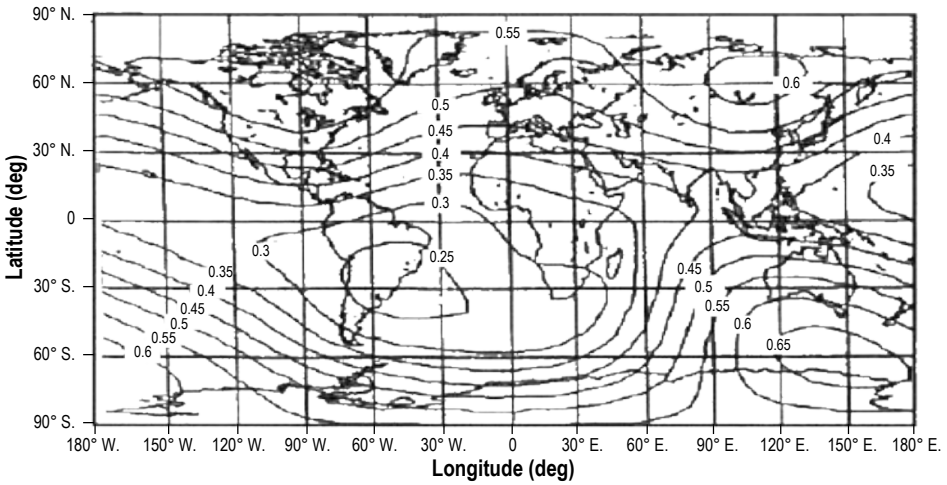

Figure 74. IGRF prediction of the Earth's magnetic field at sea level.

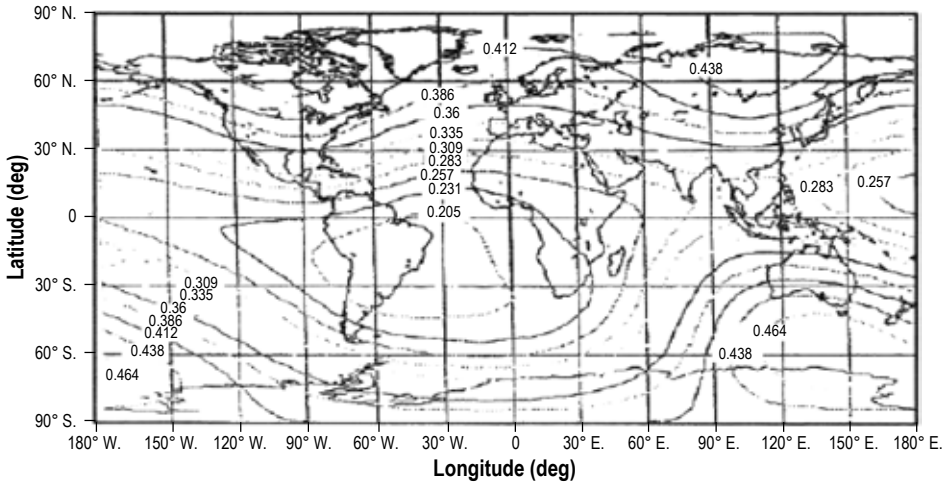

Figure 75. IGRF prediction of the Earth's magnetic field at 650 km altitude.

Geomagnetic storms may also affect orbiting spacecraft. Disturbances in the geomagnetic field which last one or more days are called geomagnetic storms. When a geomagnetic storm occurs, large numbers of charged particles are dumped from the magnetosphere into the atmosphere. These particles ionize and heat the atmosphere through collisions. The heating is first observed minutes to hours after the magnetic disturbance begins. The effects of geomagnetic heating extend from at least 300 km to well over 1,000 km and may persist for 8 to 12 hours after the magnetic disturbance ends.

The response of the Earth's field during a full geomagnetic storm cycle is a combination of effects that includes both an initial distortion and field compression followed by an overall decrease in the field intensity. When the CME (or enhanced solar wind) first arrives, the initial effect is to compress the Earth's magnetic field which increases the field intensity. This is variously

called a 'storm sudden commencement' or 'geomagnetic sudden impulse' but the event is transient and only lasts for a few minutes to tens of minutes but rarely longer than an hour. Geosynchronous orbit (GEO) spacecraft may end up outside of the magnetosphere during this phase if they are located on the dayside of the Earth and the magnetopause (boundary of the magnetosphere) is compressed inside of GEO. However, this is not the main phase of the storm that comes next.

Large storms are typically driven by CMEs during the phase when the IMF inside the CME has a strong southward-directed field component (the IMF B_z component). Since a $B_z < 0$ field orientation is opposite that of the Earth's field, magnetic field annihilation occurs at the dayside of the Earth's magnetosphere and magnetic flux is transferred to the tail, increasing the size of the polar cap and moving the GCR and SPE cutoff latitude towards the equator. In addition, the excess flux in the tail is unstable and the excess energy is released in the form of a geomagnetic storm that drives plasma into the Earth's inner magnetosphere, increasing the intensity of the Earth's ring currents. The ring current generates a perturbation magnetic field in the opposite direction of the Earth's ambient field so the total field intensity is reduced. This phase can last for many hours to days.

5.4 Plasma Environment

Plasmas are quasi-neutral gases in space with an approximately equal number density of ions and electrons. The charged species interact through the electromagnetic field and exhibit a collective behavior. Movements of individual particles are controlled to a great extent by the Earth's magnetic field and electric field. Their collective behavior and movement, however, generate electric and magnetic fields that, in turn, affect the particle's motion and the motion of other charged particles. Only a few percent of neutral gases are ionized in the lower ionosphere. Essentially all are ionized in the outer regions of the Earth's magnetosphere. In some areas, the plasma can be relatively cold (~1,000 K), and dense, such as in the ionosphere region, while the hot (~10^8 K) tenuous plasma exist at very high orbits.

Slightly below the region discussed in the thermospheric environment section that marks the lower boundary of the thermosphere, and associated changes in composition of the neutral species, there is an important transition related to the electromagnetic properties of the gas. At roughly 90 km altitude, there is a division between the lower turbulent neutral gas mixture region where all the meteorological processes occur and the upper region where solar irradiation produces partially ionized plasma composed of AO, N_2, O_2, He, H, atomic oxygen ion (O^+), hydrogen ion (H^+), helium ion (He^+), nitrous oxide ion (NO^+), molecular oxygen ion ($O_2{}^+$), nitrogen ion ($N_2{}^+$), and electrons. This upper region is electrically neutral, with the most abundant neutral being AO and the most abundant ion being O^+ up to approximately 1,000 km altitude where H^+ and He^+ become dominant elements. The properties of the nonionized fraction are discussed in section 5.1.

Section 5.4.1 defines the plasma regimes in the near Earth space. Derivations of plasma characteristics from basic distribution functions are introduced in section 5.4.2. Sections 5.4.3 to 5.4.5 describe the plasma properties in the ionospheric LEO region, the auroral region, and the polar region.

Plasma interactions can be quite complicated, and there are significant differences between a space vehicle's interactions with the relatively low energy plasma in the ionosphere and at very high orbits, and in the auroral regions where the higher energy plasma characteristic of higher altitudes penetrates to LEO. Examples of plasma interaction effects with space vehicles are solar array/power system degradation, contamination, ionospheric scintillation, and spacecraft charging. Details of the plasma effects are shown in sections 5.4.6 and 5.4.7. Most commonly used analysis tools and computer models to obtain the environmental properties and to assess the engineering performance effects are described in section 5.4.8. A summary of key design factors for plasma environments is displayed in table 78.

Table 78. Summary of key design factors (ambient/energetic plasma condition).

Parameter	Source	Select Based On
For prediction of ambient/energetic plasma conditions:		
Plasma density	IRI, GeoSpace models (sec. 5.4.8)	Spacecraft charging
Plasma temperature	IRI/GeoSpace models (sec. 5.4.8)	Spacecraft charging
Plasma measurements and spacecraft charging guidelines evaluation for spacecraft charging:		
Plasma density	Tables 79–81	Spacecraft charging
Plasma temperature	Tables 79–81	Spacecraft charging
Charging predictions	NASCAP/NASCAP-2K (sec. 5.4.8)	Spacecraft charging
Other plasma effects and guidelines:		
Power system / solar array	Section 5.4.6.1	Electrical power
Contamination	Section 5.4.6.2	Spacecraft
Plasma emissions	Section 5.4.6.3	Communication
Ionospheric scintillation	Section 5.4.6.4	Communication/GPS
Secondary plasma effects EMF	Section 5.4.6.5	Charging/communication
	Section 5.4.6.6	Charging

5.4.1 Plasma Ionosphere

The ionosphere is characterized by its low temperature and high density relative to the plasma populations within the magnetosphere and its predominantly O^+ composition due to the terrestrial origin of the ions. The equatorial extension of the ionosphere is predominantly composed of lighter ions, H^+ and He^+, and is usually referred to as the plasmasphere (sec. 5.4.1.1).

5.4.2 Plasma Characteristics

Plasmas are usually described by their density (expressed as electron number density, n_e / m^3), the chemical composition of the ions (often expressed as percentage of total ions), and the electron and ion temperatures (expressed in Kelvin, or as energy, in electron volts). The high energy particles (megaelectron volt range) that also may be present cannot be so described, and they interact differently with a vehicle than the plasma. They are discussed in section 5.5, ionizing radiation environment.

Maxwellian velocity distribution functions have been shown to provide a useful mathematical approximation of the plasma characteristics. Collisions between species in LEO are sufficiently frequent for the gas to assume a thermodynamic equilibrium and the distribution of velocities for individual species may be described by a function of the form:[115]

$$f_i(v) = n_i\left(\frac{m_i}{2\pi kT_i}\right)^{3/2}\exp\left[-\frac{m_i\left(v-u_i\right)^2}{2kT_i}\right], \tag{55}$$

where v is particle velocity and the ith species (i = electron and ion) is characterized by the number density n_i, mass m_i, temperature T_i, and bulk flow velocity u_i.

The advantage of using equation (55) as a description of the plasma environment rather than specifying a complete velocity or energy dependent flux spectra is that the conditions in the plasma are characterized for each species by only a few parameters: density, mass, temperature, and bulk flow velocity.

Plasma characteristics are obtained from equation (55) by computing the velocity 'moments' of the velocity distribution. Of greatest interest are the first four moments:

(1) Number density: $$M1 = n_i = \int v^0 f_i(v)d^3v\,, \tag{56}$$

(2) Number flux: $$M2 = EF_i = \int v^1 f_i(v)d^3v\,, \tag{57}$$

(3) Energy density: $$M3 = ED_i = \int v^2 f_i(v)d^3v\,, \tag{58}$$

and

(4) Energy flux: $$M4 = EF_i = \int v^3 f_i(v)d^3v\,. \tag{59}$$

Multiple Maxwellian distributions may be used in the case where plasma may not be adequately described by equation (55) and its moments in equations (56)–(59). For example, the low-density plasma of GEO collisions are very rare and the gas will never be truly Maxwellian. Even in this environment it has been shown that a double Maxwellian provides a useful description of the plasma:[115,116]

$$f_i(v) = n_{i,1}\left(\frac{m_{i,1}}{2\pi kT_{i,1}}\right)^{3/2}\exp\left[-\frac{m_{i,1}\left(v-u_{i,1}\right)^2}{2kT_{i,1}}\right] + n_{i,2}\left(\frac{m_{i,2}}{2\pi kT_{i,2}}\right)^{3/2}\exp\left[-\frac{m_{i,2}\left(v-u_{i,2}\right)^2}{2kT_{i,2}}\right]. \tag{60}$$

Typically, equations (55) or (60) are implemented in standard charging analysis codes and the engineer simply needs to input the appropriate set of plasma density and temperatures along with an estimate of the relative velocity between the plasma and the spacecraft. Plasma characteristics will therefore be described in terms of these parameters throughout the rest of this discussion.

5.4.3 Low Inclination Ionosphere

The ionospheric plasma is generated principally by photoionization of the ambient neutral atmosphere by solar photons on the sunlit side of the Earth and by magnetospheric particles interacting with the thermosphere at high latitudes over an altitude range of 100 to 200 km. Short-term temporal variations in the solar photon input at a fixed location on the Earth may vary from hours in the case of solar flares to the diurnal variation in solar illumination due to the rotation of the Earth. Long-term modulation of the UV-EUV photon flux over the approximately 11-year solar cycle leads to substantial variations in the composition and density of the ionospheric plasma. Transport of the plasma is strongly controlled by the geomagnetic field and magnetospheric electric fields. Hence, plasma characteristics vary with geomagnetic latitude, altitude, local time, season, and level of solar and geomagnetic activity, but only weakly with geomagnetic longitude. The plasma density decreases at night when the loss of solar UV photons fails to maintain the production of free ions and electrons. The plasma density tends to be greater in the equatorial regions than in the polar regions, with a local minimum near the geomagnetic equator at the center of the equatorial anomaly. Plasma temperatures (thermal energy) are approximately 1,000 K during the day, but two to three times that in the morning and evening.

Composition of the ionospheric plasma mirrors that of the neutral atmosphere since it is photoionization of the neutrals that produces the most common ionic species. The most common neutral species found in the upper atmosphere include AO, N_2, O_2, He, and H so it is not surprising to find that the most common ionospheric constituents are O^+, H^+, He^+, NO^+, $O_2{}^+$, $N_2{}^+$, and electrons. The dominant constituent of the neutral atmosphere is AO while ion populations are dominated by O^+ up to altitudes of 500 to 1,000 km, where H, He, H^+, and He^+ finally occur in greater numbers.

Ionospheric structure is generally discussed in terms of three fundamental altitude regimes, which differ, in addition to differences in neutral gas properties and in the depth of penetration of solar UV radiation. The regions are referred to as the D (50 to 90 km), E (90 to 160 km), and F (160 to 500^+ km) regions.

5.4.3.1 Ionospheric Density. Above the D layer, the neutral gases are in diffusive equilibrium; however, layering of the electron density profile is exhibited within these regions due to competing particle production, loss, and transport processes. The highest electron densities are at the F2 layer peak, 250 to 350 km at mid-latitudes and 350 to 500 km at equatorial latitudes. The density in the E layer, typically located at 100 to 160 km altitude, is an order of magnitude less than the F2 layer peak. Under certain conditions, a valley or an F1 ledge can be observed between these two layers. The density in the D layer, below the E layer peak, decreases rapidly with decreasing altitude. Figure 76 demonstrates the global plasma density (m^{-3}) at 400 km of altitude using the International Reference Ionosphere (IRI90) model for plasma prediction. Values are for June 21 and solar minimum conditions ($F_{10.7} = 70$) at 00:00:00 UTC. Figure 77 describes the noon-midnight cross section of plasma density (m^{-3}) as a function of altitude from 150 to 700 km for June 21 and solar minimum conditions ($F_{10.7} = 70$) at 00:00:00 UTC from IRI90 model prediction.

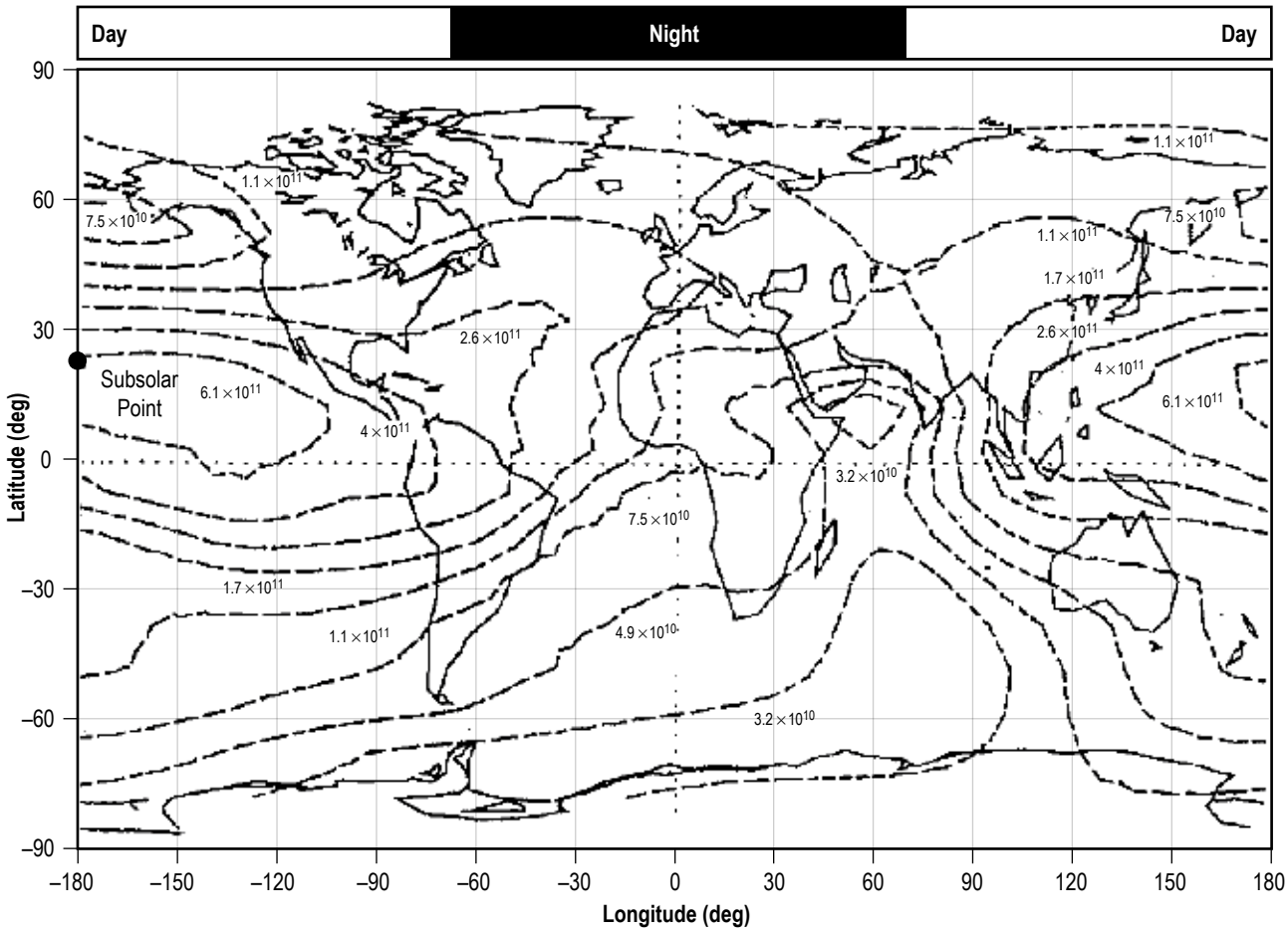

Figure 76. Plasma density (m^{-3}) at 400 km.

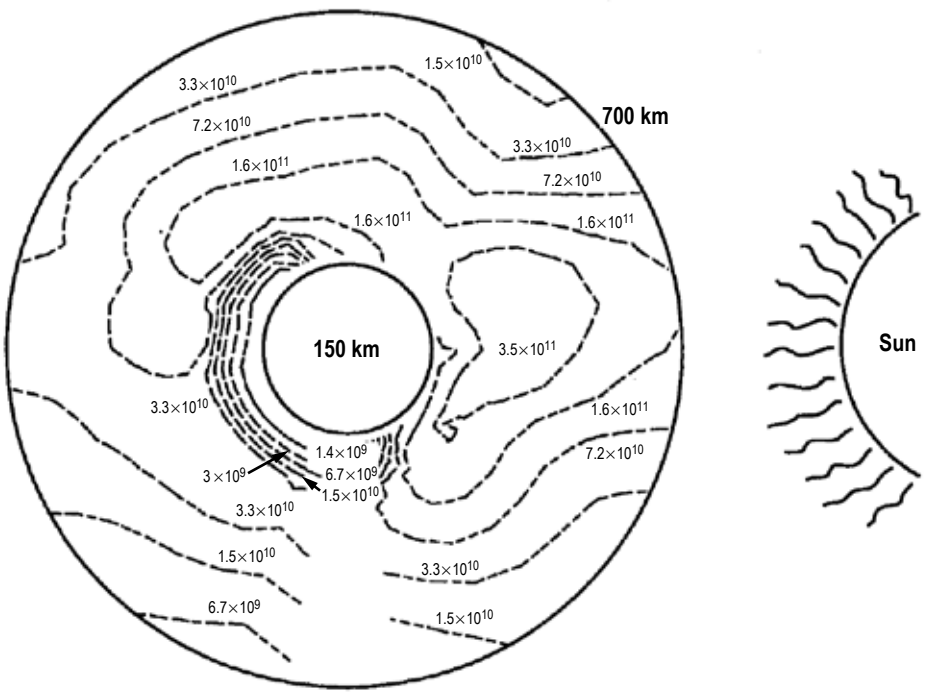

Figure 77. Noon-midnight cross section of plasma density (m^{-3}) as a function of altitude from 150 to 700 km for June 21 and solar minimum conditions (demonstration only).

In the D layer, ionization is primarily caused by solar x-rays and depends strongly upon the SZA. The highest values, 10^8 to 10^9 m^{-3}, occur around summer noon. Below approximately 70 km altitude, ionization by cosmic rays is the major electron source; therefore, the electron density is negatively correlated with the solar cycle below 70 km and positively correlated above.

The E layer is composed primarily of AO ions and electrons, the result of ionization of the predominantly AO neutral atmosphere by solar EUV radiation. The daily maximum is near noon, the seasonal maximum is in the summer, and density varies directly with solar activity. The nighttime density is more than an order of magnitude less than the daytime density due to loss of the ionized species through recombination. Although thin and patchy, a sporadic E layer, Es, with a density that can exceed the E and F2 peaks, occurs irregularly.

The F region consists of the overlapping F1 and F2 layers. The F1 layer, at approximately 150 to 200 km altitude, is of lesser importance. It is under strong solar control. The density distribution in the F layer is generally determined by transport processes, ambipolar diffusion, electrodynamic drift, and neutral wind drag because neutral densities decrease rapidly with increasing altitude. Therefore, the F2 layer peak and the topside ionosphere are highly variable, with 10% to 30% day-to-day variations in density. The F2 layer peak density maximizes in the afternoon in winter. There are two crests at ±15° magnetic latitude with a minimum at the magnetic equator in a latitudinal profile of the F layer. At night and higher altitudes, the two crests merge into a single

crest at the magnetic equator. The so-called 'fountain effect' causes this 'equatorial anomaly.' The charged particles are pushed upward by the equatorial electric field where they then drift downward along magnetic field lines.

A wide variety of ionospheric irregularities have been observed, predominantly at high latitudes and during the equatorial nighttime. The plasma fluctuations range in scale from hundreds of kilometers down to centimeters. Plasma instabilities play an important role in the generation of medium scale (kilometers) and small scale (meters) irregularities. Examples of irregularities are patches of enhanced ionization in the E region (sporadic E) and of depleted ionization in the F region (spread F). Spread F is most frequently observed in the equatorial nighttime ionosphere. The irregularities cause signal fluctuations in traversing radio waves, known as scintillations.

5.4.3.2 Ionospheric Temperature. The main source of energy for the terrestrial ionosphere is EUV radiation from the Sun. Ionospheric electrons are heated most efficiently, and their temperature exceeds the temperature of the ions and neutrals. Electron temperatures increase from approximately 300 K at 100 km altitude to approximately 3,500 K at 800 km altitude. Ion temperatures are close to the neutral temperature below approximately 400 km altitude and increase toward the electron temperature above that altitude. Below 150 km altitude, the high neutral densities and the high collision frequencies result in the same temperature for electrons, ions, and neutrals. During nighttime, the temperatures of all species are similar in magnitude. Figure 78 demonstrates the electron temperature at 400 km of altitude. Values are for June 21 and solar minimum conditions ($F_{10.7} = 70$) at 00:00:00 UTC. Results are from IRI90 with default options. Figure 79 describes the noon-midnight cross section of electron temperature (electronvolt) as a function of altitude from 150 to 700 km for June 21 and solar minimum conditions and solar minimum conditions ($F_{10.7} = 70$) at 00:00:00 UTC from IRI90 model prediction.

In general, plasma temperatures are lowest at the geomagnetic equator and increase toward higher latitudes. The greater temperatures at high latitudes are due to the additional energy input to the atmosphere from precipitating particles and Joule heating (due to currents flowing in the ionosphere) in the auroral zones. At low altitudes, however, the electron temperature peaks at the magnetic equator, reaches minimum values at approximately ±20° latitude, and then increases toward higher latitudes. This behavior is the mirror image of the equatorial anomaly of the electron density and illustrates the strong anti-correlation between electron density and temperature.

On the average, ionospheric temperatures increase from an almost constant nighttime value to an almost constant daytime value. The most significant departure from this behavior is the early morning peak in electron temperature. It is most pronounced at the magnetic equator at approximately 300 km altitude (the peak temperature exceeds the daytime value by a factor of 2 or 3); its magnitude decreases rapidly toward higher and lower altitudes and toward higher latitudes. The temperature peak is a result of the sharp increase in solar heating coupled with the still low electron densities from the preceding night.

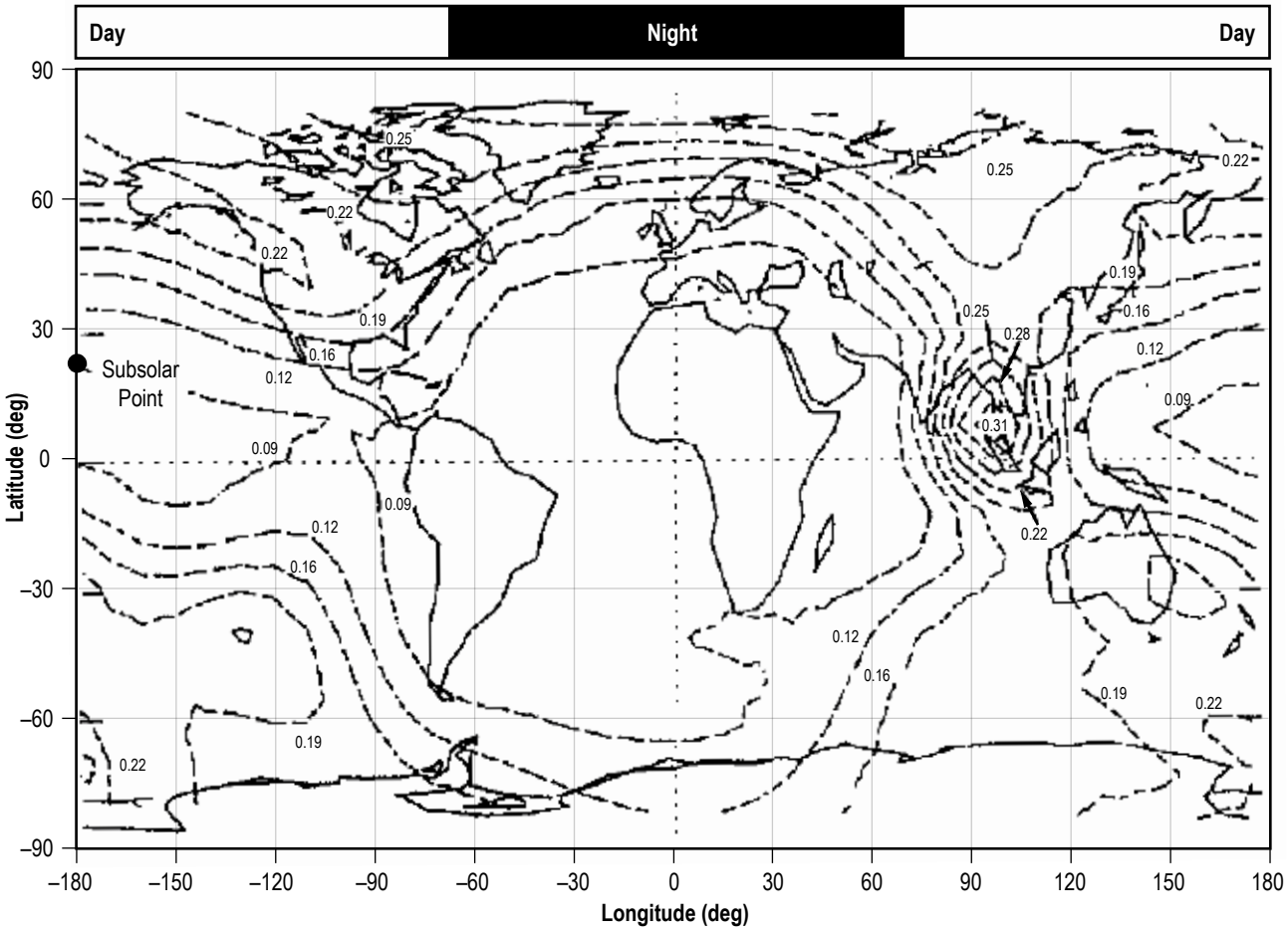

Figure 78. Electron temperatures (eV) at 400 km.

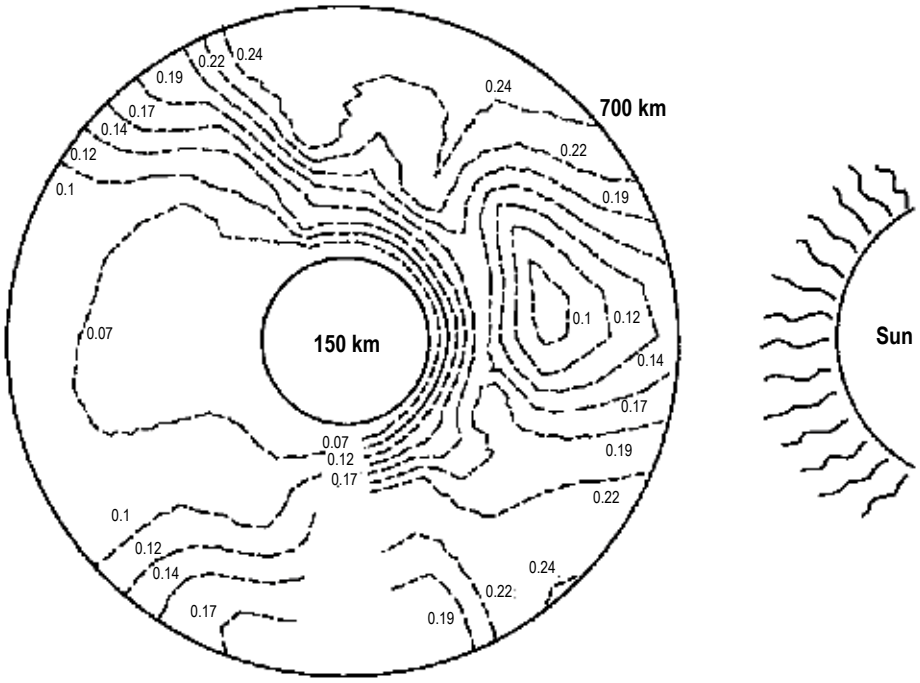

Figure 79. Noon-midnight cross section of plasma temperature (eV) as a function of altitude from 150 to 700 km.

The electron temperature is almost unaffected by the solar cycle, in contrast to the increase of almost all other neutral and ionized parameters. This again is a result of the close coupling with the electron density, which determines both energy gain and loss of the electron gas. The simultaneous increase of both terms leaves the electron temperature nearly unchanged.

5.4.3.3 Spacecraft Charging in Ionosphere. The plasma electrons have much less mass than the positive ions. Since, at a given energy, the thermal velocity is inversely related to the square root of the particle mass, the thermal electron flux to passive spacecraft surfaces and structure is greater than the corresponding thermal ion flux. As a result, surfaces tend to accumulate negative charge. At low latitudes in LEO, where the plasma is relatively dense and of low energy, equilibrium is established within a few volts negative to the reference plasma potential. Thus, charging of passive surfaces is usually not a problem in this regime. However, for active surfaces, e.g., solar arrays and structure tied electrically to them, arcing and related significant effects can occur, depending upon the grounding scheme and the magnitude of the spacecraft-imposed voltages. More details of specific plasma interactions are discussed in section 5.4.6, plasma effects, and in section 5.4.7, spacecraft charging.

5.4.4 Auroral Region

The auroral region is defined as the area between approximately 60° to 75° magnetic latitude. Along auroral field lines a variety of phenomena is observed, including high energetic ionospheric upward ions, high energetic downward acceleration of magnetospheric electrons, perpendicular electrostatic shocks, and intense wave emissions. Sharply defined regions of low electron

densities are a common feature of auroral zone crossings from the predusk hours until the early morning hours. The energy of these precipitated electrons can be on the order of several tens of kiloelectron volts. Electron densities in this region are strongly depleted in relation to the adjacent polar cap and plasmaspheric densities and form a low-density cavity. Minimum densities in this auroral cavity frequently fall to values below 3×10^5 m^{-3} and rarely exceed 3×10^6 m^{-3}.

The plasmas in the polar region (above 60° geomagnetic latitude) have a significant energy contribution from both magnetospheric particle precipitation and current-driven heating. Plasma in the high latitude regions is often more similar to the magnetospheric plasma than to the ionospheric plasma at low latitudes. The ionosphere is strongly coupled to the magnetosphere and to the solar wind. The transition from closed to open field lines and the influx of energetic particles profoundly affects the ionospheric plasma. The boundary region, the auroral oval, is marked by the beautiful display of auroras. Surrounding the magnetic poles, the oval extends to near 75° geomagnetic latitude at noon and approximately 60° at local midnight. On the nightside, the oval is well marked by a depletion of electron density, the so-called trough. On the dayside, one finds a region of enhanced densities just inside the oval, the so-called magnetospheric cleft. The electron density at the tip of the cleft is almost an order of magnitude greater than it is at the bottom of the trough. During magnetic storms, the trough moves equatorward 2° per unit increase in K_p. The region inside the oval is called the polar cap.

Spacecraft in high inclination orbits will encounter the precipitating auroral particle fluxes as they pass through the auroral oval. One result of these fluxes is the increase of local plasma density by a factor of up to 100 over regions of tens of kilometers in latitudinal dimension and hundreds or thousands of kilometers in longitudinal dimension in the auroral regions (60° to 75° magnetic latitude). These enhancements occur between approximately 100 and 250 km altitude (reference fig. 80). Above 250 km, the thermal plasma may be depleted above intense auroral in the midnight sector, falling far below $1\times10^{10}/m^3$. In this region, there is no clear distinction between magnetospheric and ionospheric phenomena. There is a very wide range of scales, both spatially and temporally, present in the dynamics. Small scale (meters to decameters) irregularities exist and move with the prevailing ambient plasma drift. Ionion and ion-neutral collisions in the lower thermosphere tend to make the temperature distribution isotropic while anisotropies still remain at higher altitudes (near 600 km). Plasma property anisotropies are introduced by the geomagnetic field.

5.4.4.1 Auroral Morphology. Aurora occurs in all three altitude regimes, D, E, and F, with the E layer dominant in terms of total auroral precipitation energy deposition. Electron density profiles in the auroral region are dependent upon the energy distribution of the incident precipitating particles, while the auroral emissions are dependent upon the photochemistry of the auroral ionosphere, as well as the energy distribution of the precipitating particles. The spectrum of the precipitating particles determines the altitude at which the particle energy is deposited and, therefore, the applicable photochemistry since neutral composition and density depend strongly on altitude. Enhanced electron densities are produced by impact ionization due to precipitating electron fluxes. The auroral E region extends approximately 2° farther equatorward than the F region, and this extension is formed by proton precipitation, in contrast to the mainly electron precipitation that forms the F region. There is a strong seasonal and local time control of the auroral ionosphere.

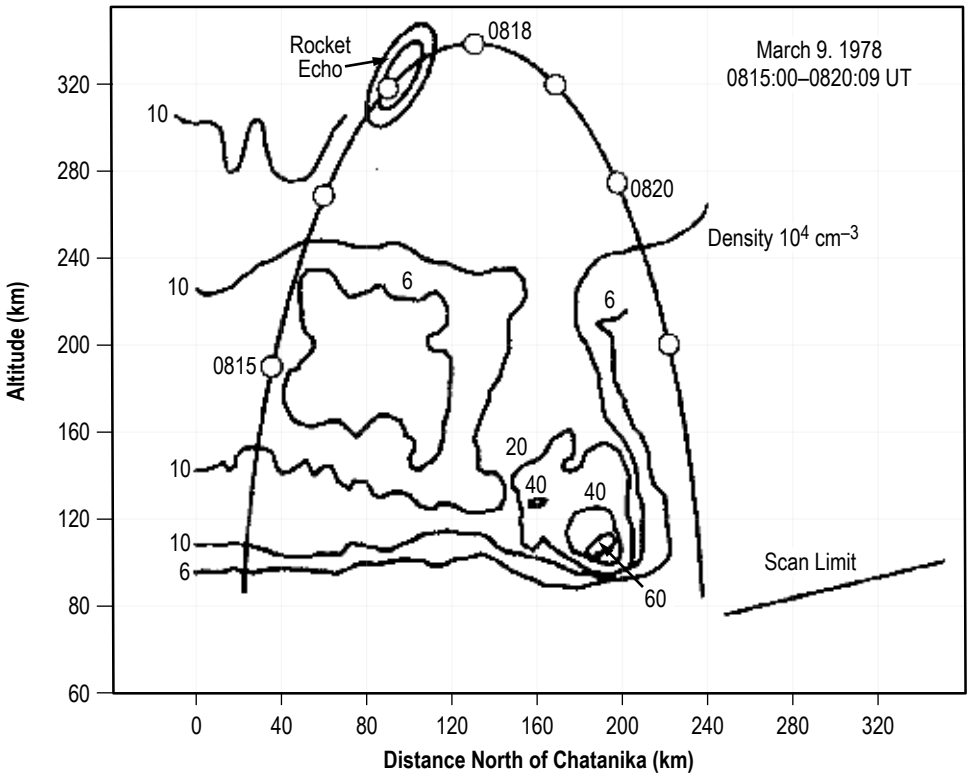

Figure 80. Ionospheric electron density in an aurora ($\times 10^4$ n_e/cm^3).[117]

The aurora occurs at all local times in the auroral ovals that are rings at approximately 65° magnetic latitude around each magnetic pole. The most intense and energetic fluxes occur near local midnight. The location of the aurora and its intensity vary with solar (and resulting magnetospheric) activity. Plots of the average integral energy flux and the average energy of precipitating electrons are presented in polar spectrogram format in an MLT-corrected geomagnetic latitude coordinate system for each of four levels of K_p in figures 81–84. Plots apply to both poles. A statistical analysis of the probability of encountering various levels of aurora particle flux may be found in reference 118, and a detailed discussion of auroral occurrence of morphology may be found in reference 119.

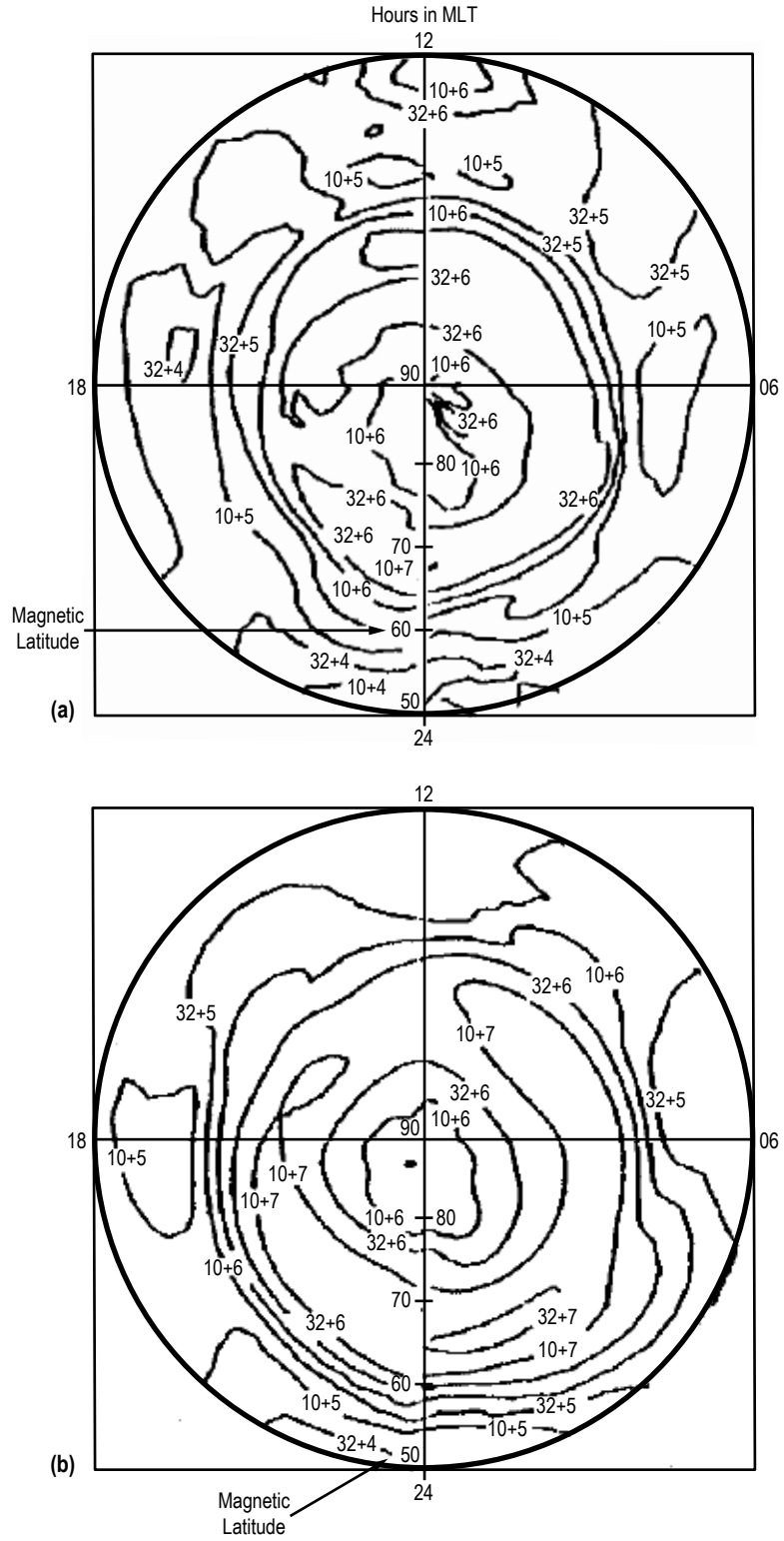

Figure 81. Average integral precipitating electron energy flux: (a) $K_p = 0$ and (b) $K_p = 2$ (polar plots are in corrected geomagnetic coordinates, electron flux is in units of KeV/cm^2-s-sr—demonstration only).

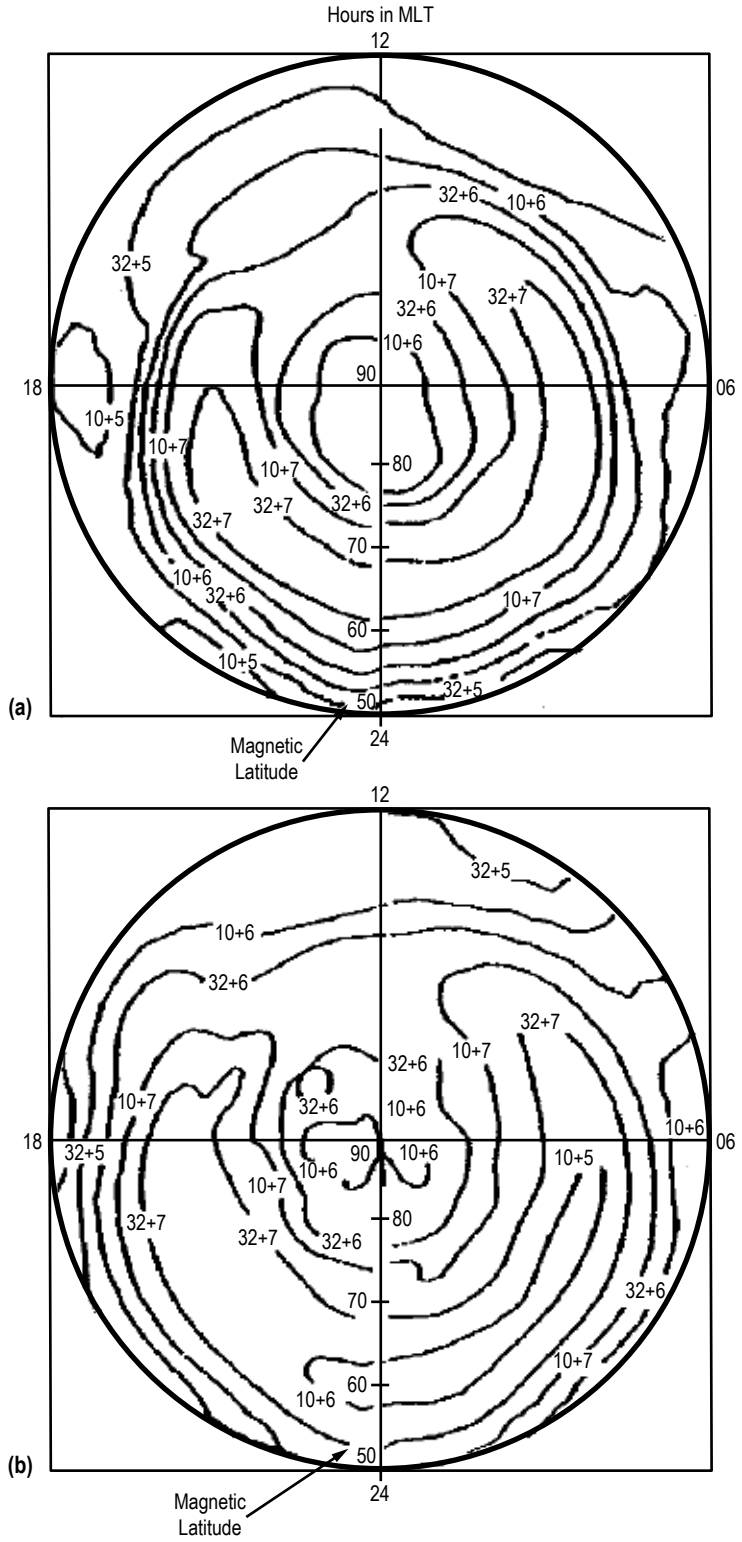

Figure 82. Average integral precipitating electron energy flux: (a) $K_p = 4$ and (b) $K_p = 6$ (the polar plots are in corrected geomagnetic coordinates, electron flux is in units of KeV/cm^2-s-sr—demonstration only).

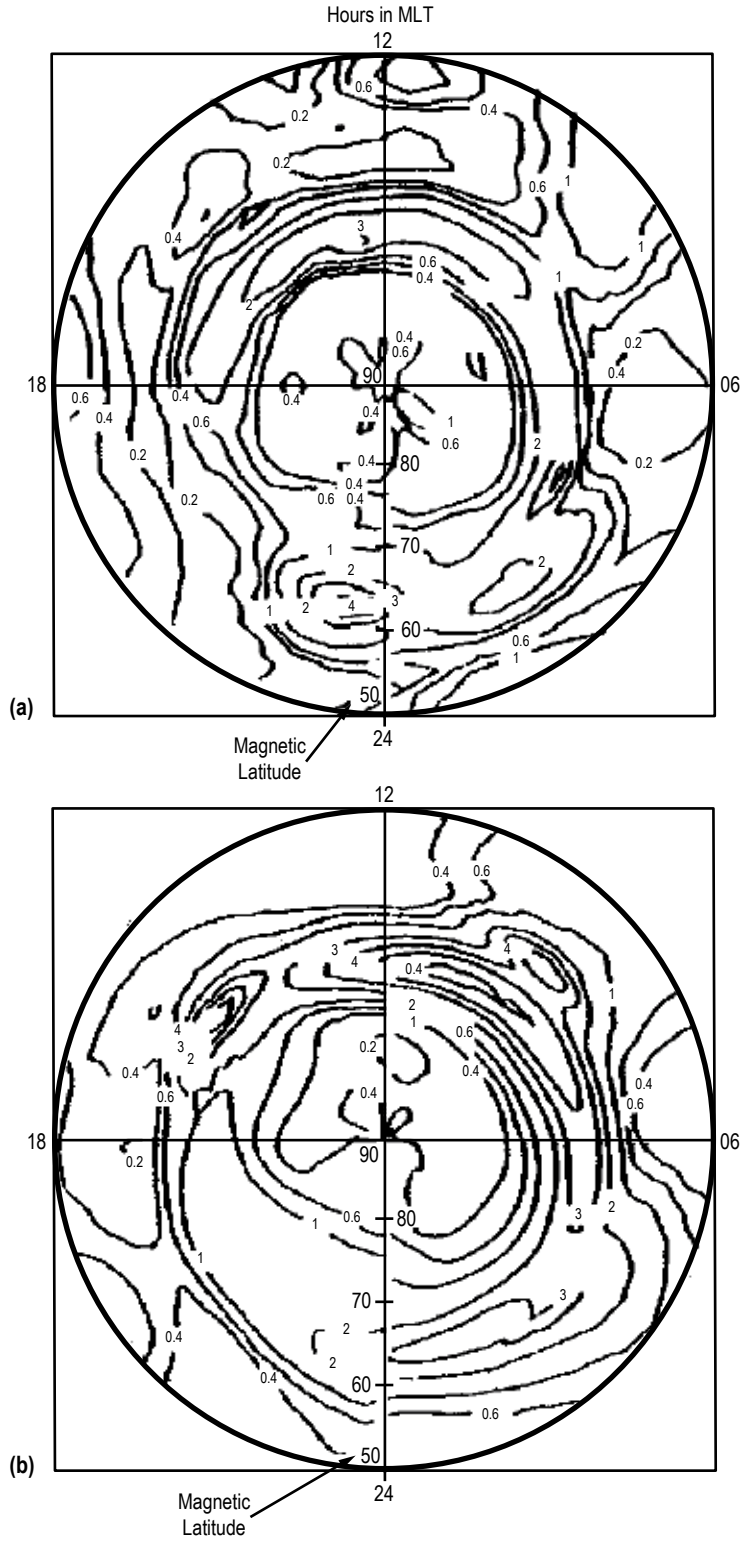

Figure 83. Average integral energy (KeV) of precipitating electrons: (a) $K_p = 0$ and (b) $K_p = 2$ (polar plots are in corrected geomagnetic coordinates —demonstration only).

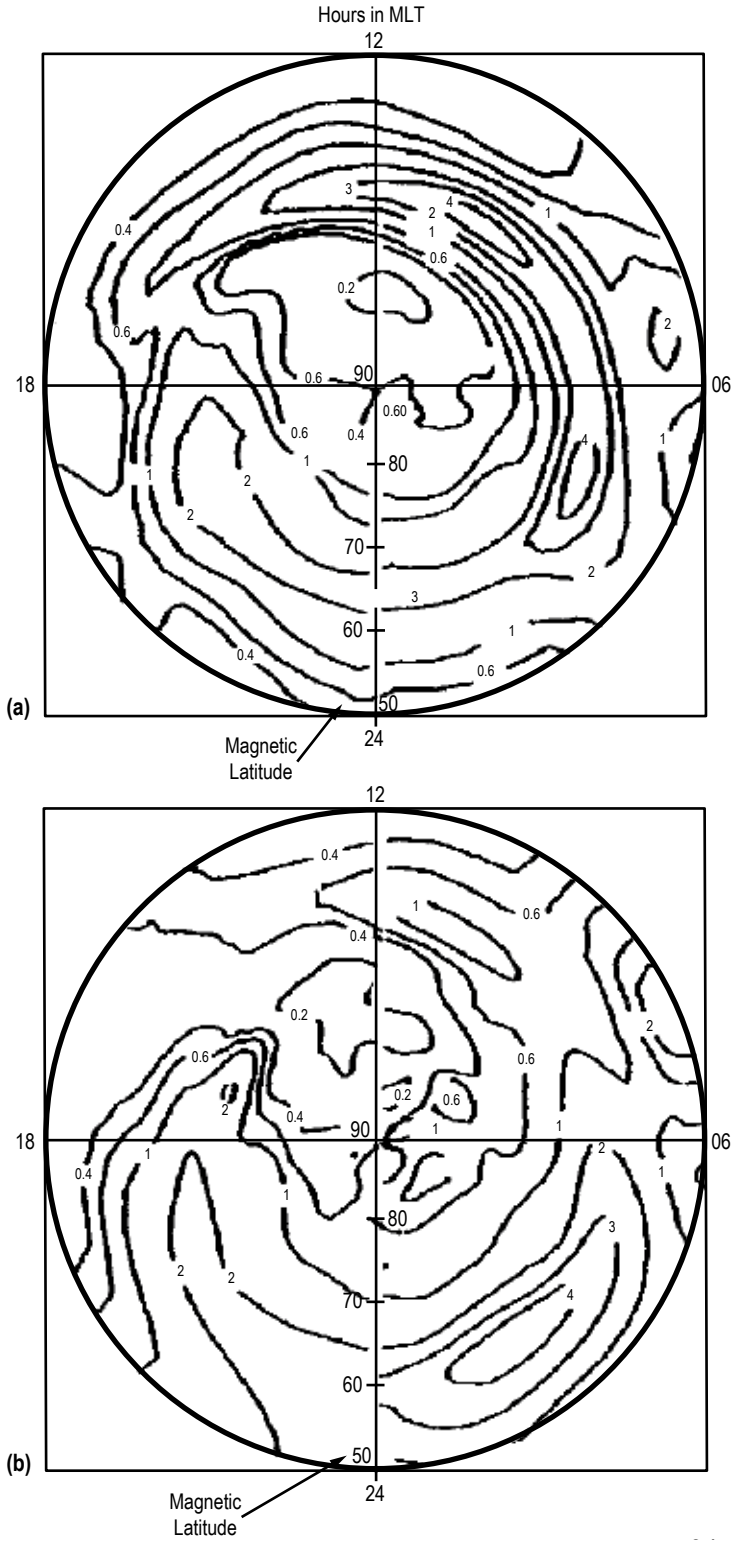

Figure 84. Average integral energy (KeV) of precipitating electrons: (a) $K_p = 4$ and (b) $K_p = 6$ (polar plots are in corrected geomagnetic coordinates—demonstration only).

In the dayside auroral zone, magnetic field lines extend to the dayside magnetopause and provide direct access for the shocked solar wind plasma in the magnetosheath to the topside ionosphere. Strong coupling between the neutral and ionized components of the thermosphere drives winds in the dayside auroral ionosphere anti-sunward across the polar cap toward the nightside ionosphere. The strong ionospheric heating associated with this process generates the largest outflows of ionospheric plasma anywhere at the Earth and forms a global scale 'ion fountain' across the polar cap. Global electric current systems flow along magnetic field lines into and out of the auroral ionosphere. Where these are most intense and in the upward direction, they exceed the capacity of the plasma to carry them with thermal motions, and discharges occur in which electrons are accelerated downward and ions are accelerated upward. These discharges greatly enhance the brightness of the aurora where the electrons are incident and produce outward-flowing ion beams that are far out of local thermodynamic equilibrium and unstable, generating natural plasma wave noise at a variety of frequencies.

There are three distinct magnetospheric states that govern the auroral environment activities: (1) Quiet magnetosphere state, (2) active polar cap state, and (3) active auroral oval state, described in sections 5.4.4.1.1 through 5.4.4.1.3.

5.4.4.1.1 Quiet Magnetosphere State. In this state, the energy input from the solar wind is minimized by a configuration that minimizes magnetic recombination on the dayside. A weak but northward IMF B_z is typical. The auroral oval has the following characteristics:

- Visually small in diameter and circular.
- Somewhat expanded near the dawn and dusk regions.
- Relatively thin near midnight.

5.4.4.1.2 Active Polar Cap State. At this time, characteristics of this state are still controversial, and more detailed observational data are required before a consensus can be reached. However, it is believed that it occurs during strongly northward IMF B_z conditions and is characterized by the presence of:

- Sun-aligned arcs.
- Additional magnetic field-aligned current systems.
- Distortions or disruptions in the traditional two-cell polar convection patterns.

5.4.4.1.3 Active Auroral Oval State. The southward IMF B_z plays a prominent role in this state. Auroral boundaries are active, with rapid poleward movement of the poleward boundary and less rapid equatorward movement of the equatorward boundary during the expansion phase of magnetic substorms.

Although there is some controversy, it appears as if the optical signature of this poleward movement ends before the ground signature of the electrojet activity ceases. The equatorward particle precipitation boundaries move equatorward with increasing geomagnetic activity. The ion boundaries are equatorward of the electron boundaries in the disk/evening sector, while the electron boundaries are ahead in the morning sector. The electron boundaries are equatorward of the

ion boundaries at all local times except the disk when the geomagnetic activity is very low, very quiet times.

Auroral features are also very active in this state. During the expansion phase of an auroral substorm, the poleward and equatorward motions of the nighttime aurora can begin at localized sites in local time, primarily between 22:00 and 24:00 hr LST. Sometimes an 'eye-shaped' structure with substantial north-south structures embedded can form as the expansion proceeds in the east-west as well as north-south directions. The configuration of the east-west expansion is a function of the condition of the IMF.

At the most extreme portion of the poleward expansion, the arcs can intensify rapidly and form vortices along the arc's length. Westward traveling surges (WTSs) have been observed to propagate nearly 7,000 km. Sometimes WTS activity is the predominant auroral response to substorm activity.

5.4.4.2 Electrodynamics and Convection. There are many statistical or empirical, as well as several theoretical, models of the convection and/or electric fields in the auroral zones. Specific use will dictate which model should be used in engineering analyses. Most of these models stress the importance of the IMF B_y, the dawn-dark component of the IMF, in controlling the dayside convective patterns. Results of analyses have shown that substantial structure can be present within the distribution of field-aligned currents. Results of studies have also shown that:

(1) In the morning sector, the westward electrojet is dominated on the poleward side by strong electric fields (with low auroral luminosity and conductivity) and on the equatorward side by large conductivity values. The equatorward side is also the region of precipitating electrons (upward electrical currents).

(2) On the evening side of the eastward electrojet, the reverse trend is observed.

(3) The westward electrojet is also centered in the region of highest auroral luminosity, while the eastward electrojet is in the region of the lowest luminosity.

(4) The brightest auroral regions are associated with upward electrical currents, both in the evening and morning sectors.

(5) The polar cap potential is modified rapidly by changing IMF conditions; however, the nightside auroral zone response is delayed substantially.

(6) Conductivity gradients play crucial roles in the formation of auroral surges.

(7) Once again, understanding the characteristics of the global aurora is progressing rapidly. However, there are many differences between models and observational data, and the use of any empirical/statistical/theoretical model will be highly dependent upon the application. Care should be utilized in the selection of the 'proper' model and experts in the field should be consulted.

5.4.4.3 Transient Fluxes in Polar Low Earth Orbit. In polar LEO, the important transient and energetic fluxes occur in the auroral zone. Figure 85 shows typical aurora fluxes from rocket measurements at approximately 320 km.

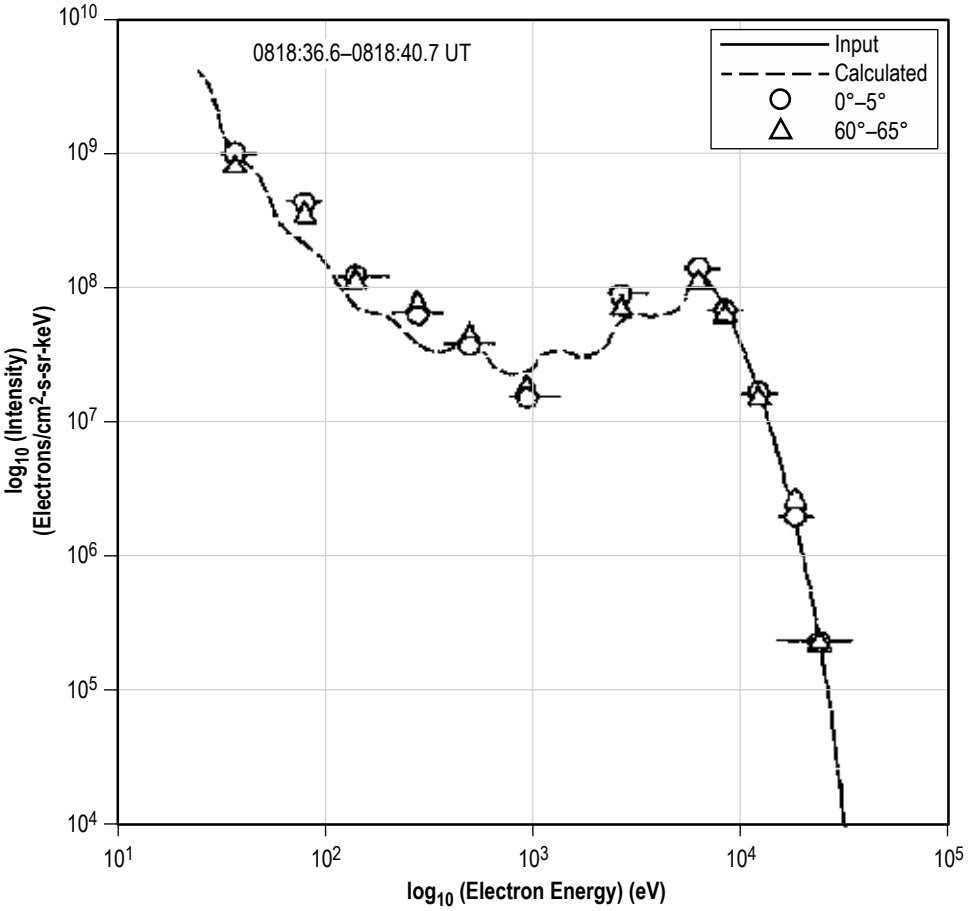

Figure 85. Auroral electron intensity (center of arc).

Auroral fluxes have been shown to be responsible for spacecraft charging at low altitudes in the polar regions.[120,121]

Examples of the plasma environments during intervals when the Defense Meteorological Satellite Program (DMSP) weather satellites have experienced charging to negative potentials less than –100 V are given in table 79. A common feature in all these examples is:

- Thermal plasma density $<10^4$ cm^{-3}.
- Large integral number flux of energetic electrons.
- Spacecraft in eclipse.

Table 79. Charging environments in low Earth polar orbits.

Ambient Plasma			
$N_{1,e}$ (cm^{-3})	$kT_{1,e}$ (keV)	$N_{1,i}$ (cm^{-3})	$kT_{1,i}$ (keV)
125	~ 0.15	2.35	29
190	~ 0.15	2.35	29
180	~ 0.15	2.35	29
Energetic Plasma			
$N_{2,e}$ (cm^{-3})	$kT_{2,e}$ (keV)	$N_{2,i}$ (cm^{-3})	$kT_{2,i}$ (keV)
3.9	10.1	0.16	0.327
3.2	14.4	0.16	0.327
4.9	4.2	0.16	0.327

Gussenhoven et al.[121] defined the 'high energy' electrons as $E \geq 14$ keV and found that charging typically occurs when the energetic electron flux exceeds 10^8 electrons/cm^2-s-sr. Anderson and Koons[120] similarly examined a strong charging event observed on a DMSP spacecraft that was associated with an instrumentanomaly. The ambient plasma density was <100 cm^{-3} and fluxes of energetic electrons peaked in the 30 keV channel on the DMSP particle detectors, the greatest energy sampled by the instruments.

5.4.4.4 Spacecraft Charging in Auroral Region. In the near auroral ionospheric region, the important transient and energetic fluxes occur in the auroral zone. Spacecraft passing through the auroral zone can be charged to large negative potentials by energetic electrons precipitating from the magnetosphere. This occurs because large surface potentials are required to retard this flux and allow equilibrium (defined in this context as no net current to the spacecraft) to be achieved. Also in this region, conditions occur in the wake of large structures, or they may occur naturally so that the entire vehicle is involved, where the low energy plasma density is depleted. This makes it ineffective in balancing the current from the high energy electron flux, and the charging process is enhanced. This is similar to the situation in GEO where the plasma is very energetic but tenuous. Sun/shade effects become important to the point that potentials as large as several kilovolts can develop between sunlit and shaded surfaces (depending on geometry and material properties).

Table 80 lists examples of ambient plasma at 350 to 600 km altitude in three latitude zones (0° to 30°, 30° to 50°, and 50° to 70°). Density (Ne, #/m^3), and temperature (Te, eV) values are placed in latitude bins based on the absolute value of the spacecraft latitude (i.e., Southern and Northern Hemisphere data from equivalent latitudes are grouped into a single latitude range). Within each latitude range the percentile Ne, Te values are computed by sorting the data into monotonically increasing order and identifying the data value that corresponds to 1%, 10%, …90%, and 99% of the Ne, Te values.

Table 80. Ambient plasma at 350–600 km altitude in three latitude zones (0°–30°, 30°–50°, and 50°–70° inclination).

Plasma Environment—Day								
Latitude Range		1%	5%	10%	50%	90%	95%	99%
10° to 30°	Ne (m^{-3})	1.62×10^{10}	3.27×10^{10}	4.26×10^{10}	2.3×10^{11}	1.09×10^{12}	1.61×10^{12}	2.57×10^{12}
	Te (eV)	0.082	0.097	0.106	0.195	0.307	0.386	0.537
30° to 50°	Ne	2.1×10^{10}	2.62×10^{10}	4.36×10^{10}	3.16×10^{11}	1.3×10^{12}	1.83×10^{12}	2.71×10^{12}
	Te	0.086	0.092	0.107	0.211	0.351	0.41	0.574
50° to 70°	Ne	9.2×10^{9}	3.19×10^{10}	5.92×10^{10}	1.61×10^{11}	8.57×10^{11}	1.48×10^{12}	2.65×10^{12}
	Te	0.074	0.097	0.116	0.174	0.267	0.374	0.558
Plasma Environment—Night								
Latitude Range		1%	5%	10%	50%	90%	95%	99%
10° to 30°	Ne	3.4×10^{9}	1.47×10^{10}	1.67×10^{10}	1.18×10^{11}	5.32×10^{11}	8.97×10^{11}	1.7×10^{12}
	Te	0.057	0.068	0.069	0.104	0.214	0.334	0.416
30° to 50°	Ne	9.69×10^{9}	1.76×10^{10}	2.91×10^{10}	2.68×10^{11}	8.06×10^{11}	1.37×10^{12}	3.05×10^{12}
	Te	0.065	0.07	0.076	0.135	0.317	0.388	0.533
50° to 70°	Ne	5.18×10^{9}	7.75×10^{9}	2.56×10^{10}	8.72×10^{10}	8.11×10^{11}	1.61×10^{12}	2.77×10^{12}
	Te	0.06	0.063	0.074	0.097	0.318	0.409	0.516

Table 81 demonstrates high energy plasma environment extremes for the spacecraft charging design consideration at auroral region (50° to 70° inclination) and at 350 to 600 km of altitude. More details of specific plasma interactions are discussed in section 5.4.6, plasma effects, and in section 5.4.7, spacecraft charging.

Table 81. Plasma environment at 50°–70° inclination and 350–600 km altitude.

Energetic Plasma					
$N_{nominal}$ (cm^{-3})	$T_{nominal}$ (eV)	Charging Time (min)	$N_{extreme}$ (cm^{-3})	$T_{extreme}$ (eV)	Charging Time (min)
1.05	10,000	1	1.05	30,000	5

5.4.5 Plasmas in Polar Cap

The polar cap is the region of the Earth's ionosphere and magnetosphere poleward of the auroral oval where magnetic field lines do not connect to the conjugate hemisphere as they do at lower latitudes. Instead, magnetic field lines connect to the solar magnetic field in interplanetary space or extend deep into the magnetotail. Particle fluxes on polar cap field lines tend to be much smaller than at lower latitudes because the open field lines do not support the trapped particle populations that exist on closed field lines. Electric fields, currents, and particle precipitation within the polar cap respond quickly to changes in solar wind conditions due to the relatively direct connection between the terrestrial field within the polar cap region to the solar field in interplanetary space.

Spacecraft within the polar cap encounter plasma environments originating from a number of sources. Magnetosheath electrons with energies of approximately 100 eV penetrate to ionospheric altitudes where they are referred to as the 'polar rain.' Polar rain electrons typically exhibit energy fluxes on the order of approximately 10^{-2} erg/cm^{2}s and densities of only approximately 1/m^3. These values are much less than the energy flux and density within the magnetosheath source region because only a fraction of the population can reach the ionospheric altitudes. Polar rain precipitation is most intense near the cusp and weakens toward the central polar cap. An upward-moving polar wind electron and ion flux is also observed on polar cap field lines. The source of these particles is ionospheric plasma escaping from the polar ionosphere, which is accelerated upward along open magnetic field lines. The low energy ion component of the polar wind exhibits both field-aligned and conical distributions. Finally, sporadic events associated with polar cap auroral arcs are encountered within the polar cap, characterized by an intense localized precipitating electron flux and upward-flowing ions consistent with the acceleration of electrons and positive ions by parallel electric fields.

5.4.5.1 Ionosphere and Polar Wind. Density structures in both E and F regions showed that, in darkness, the ratio of enhanced density to the background density remained constant for many tens of hours and that the vortices only disappeared when they were convected into regions of sunlight or auroral precipitation.

There are systematic differences between the winter electron density signatures in the topside ionosphere in the southern and northern polar regions with the Southern Hemisphere having the lower densities. The region above the polar ionosphere contains mainly ionospheric plasma flowing generally away from the Sun across the polar cap and upward into the magnetosphere. Only weak fluxes of energetic components of the solar wind plasma enter the polar cap region, sometimes referred to as 'polar rain.'

The light ion component of the ionospheric plasma, which flows upward into the magnetosphere even without solar wind energy inputs, is referred to as the polar wind. The heavy ion component responds to the following:

- Energy inputs from the solar wind.
- Heat-driven thermospheric dynamics.
- Solar cycle in UV inputs to the thermosphere.
- Magnetic activity.

This combined light and heavy ion source of plasma to the magnetosphere provides much of the material from which the energetic particle populations are generated. Theoretical research on this area has shown that results are highly model dependent and that 2D models produce different results than 3D models. Caution in use of models is strongly advised.

The polar cap region becomes active in Sun-aligned auroral arcs when the IMF is northward. Field-aligned electrodynamic systems, which close in the ionosphere, are associated with these arcs. Plasma drift inside the arcs is primarily anti-sunward, while outside the arcs both sunward and anti-sunward drifts occur.

A wide variety of ionospheric irregularities have been observed at high latitudes at nighttime. The plasma fluctuations range in scale from hundreds of kilometers down to centimeters. Plasma instabilities play an important role in the generation of medium scale (kilometers) and small scale (meters) irregularities. Examples of irregularities are patches of enhanced ionization in the E region (sporadic E) and of depleted ionization in the F region (spread F). Spread F is most frequently observed in the equatorial nighttime ionosphere. The irregularities cause signal fluctuations in traversing radio waves, known as scintillations.

Influx of solar plasma into the tail of the magnetosphere, sometimes preceded by solar flares, can cause complex ionospheric disturbances (storms). The most consistent pattern is an enhancement in D region ionization. These effects are most dramatic at auroral latitudes, but significant modifications in the ionosphere occur at all latitudes. A particularly severe event, called a polar cap absorption event, is due to energetic protons from the Sun producing ionization at altitudes as low as 40 to 60 km over the polar cap and causing a radio communications blackout over a considerable period.

5.4.6 Plasma Effects for Design Consideration

This section describes the plasma effects that might degrade the spacecraft performance except for spacecraft charging. The major plasma effect, spacecraft charging, will be separately discussed in the next section.

5.4.6.1 Power System/Solar Array. Negatively grounded solar arrays operating in the relatively dense plasmas in LEO will experience a current drain on the power system as a result of losses through coupling to the plasma. This will become more severe as systems are enlarged and operating voltages are raised. Arcing of solar arrays in plasmas could lead to damage and electrical noise. Arcing becomes likely when the array is in a contaminated environment. Attraction of the ambient ions by negatively charged areas of the array could lead to sputtering and mass loss rates that may limit the lifetime of components, especially those designed for long duration operation.

5.4.6.2 Contamination. Contamination will be a critical issue in future missions and can be divided into two areas of concern. The first is that of spacecraft contamination, where material properties may be changed, thermal control systems affected, delicate sensing equipment damaged, etc. The relatively dense atmospheric pressure in LEO is important here. The second aspect is that of modification of the ambient atmosphere by outgassing from the spacecraft structure, thruster firings, water dumps, etc. Plasma effects and spacecraft charging can enhance the collection of contaminants especially at higher latitudes where the Debye length is larger.

5.4.6.3 Plasma Emissions. There will be a large scope for the generation and emission of plasma waves, not just by active beam emissions experiments but also by other spacecraft interactions. Plasma wake, spacecraft power leakage, and contaminant ions all provide a source of radio frequency emissions. As spacecrafts become larger and produce more contamination, the possibilities of disturbance, and of a wider range of generation mechanisms, frequencies, and power levels, will also increase.

5.4.6.4 Ionospheric Scintillation. Rapid electron density variations over a period of minutes affect radio waves propagating through the Earth's ionosphere. Changes in the electron density along electromagnetic waves propagating through the ionosphere changes their velocity and transit time. This ionospheric scintillation effect degrades the performance of spacecraft air-to-ground communications systems and adversely affects the accuracy of the Global Positioning System (GPS). Large numbers of solar energetic particles, such as solar protons, can cause rapid changes in the ionospheric density that produces an ionospheric scintillation effect at high latitudes. Particle precipitation in the auroral zone results in increased scintillation in the ionosphere. The auroral oval is usually near the regions of increased ionospheric scintillation.

5.4.6.5 Secondary Plasma Effects. Many plasma interactions not only produce primary effects but also are responsible for secondary effects, acting in synergism with other interactions. As an example, a large structure with a large ion-free wake zone in a flux of energetic electrons could experience high negative charging levels. These in turn could attract contaminant ions to sensitive surfaces and modify the local plasma environment, causing plasma wave emissions that could disrupt sensors and monitors, or even in extreme cases, onboard computers and communications.

5.4.6.6 Electromagnetic Force. While not a plasma effect, discussion of potential differences produced by the $v \times B$ force is given here since the result is an additional potential on spacecraft that must be added to the electron-ion current balance charging to determine the absolute magnitude of the spacecraft potential.

Charge carriers in conductors moving with a velocity (v) through a magnetic field (B) are subject to the Lorenz force,

$$F = q\,(E + v \times B) \quad , \tag{61}$$

that will separate charge. Ionospheric electric fields are typically sufficiently small that the magnetic term dominates and the electric field effects can be neglected. The result is an induction voltage given by:

$$V = (v \times B \cdot L) \tag{62}$$

where L is a vector along the length of the conductor.

At completion of ISS construction, the dimensions of the photovoltaic array wings and truss structures are sufficient to result in induction voltages of ±30 V at high latitudes where the spacecraft velocity is nearly perpendicular to the vertical geomagnetic field. On the Tethered Satellite System-1R shuttle mission, a 20-km-long conductive tether generated voltages of ≈4,000 V, sufficient to arc and destroy the tether.

5.4.7 Spacecraft Charging

Spacecraft charging results from the differential collection of electron and ion currents on or in spacecraft materials when exposed to space plasma and radiation environments. The electric

potential of a spacecraft varies (either positive or negative) as charge accumulates until an equilibrium is established where the net currents to and from the plasma environment are equal. Accumulation of a net negative charge density on spacecraft surfaces (surface charging) and buried inside insulators (bulk charging) generate electric potentials and fields. Electrostatic discharge (ESD) arcs occur when the electric fields associated with the potential gradients exceed the breakdown strength of the insulating materials. ESD is a well known source of spacecraft anomalies and failures. Both the plasma properties and the spacecraft design and operating characteristics influence the process, so knowledge of material electrical properties, spacecraft configuration, and grounding and bonding schemes are all required to determine if there is a spacecraft charging threat to a vehicle design.

Surface charging currents include the collection of ions and electrons from the plasma environment, conduction currents through the surface materials, active current sources such as electron guns or plasma contactors, and a loss of charge from the spacecraft surface due to the photoelectric effect and secondary emissions generated when energetic particles collide with the spacecraft surface. In addition, electrons with energies ranging from approximately 50 keV through a few MeV are capable of penetrating the outer surface of the spacecraft producing internal charging of spacecraft systems and materials. All of these processes are governed by the properties of the spacecraft materials including conductivity, thickness, density, composition, and work function as well as the plasma density, temperature, bulk velocity, presence of energetic particles, and intensity of solar flux within the space environment.

Generally, the space plasma environment can affect spacecraft charging behavior. An accurate definition of plasma properties is essential in determining the severity of these effects because the charging level of a spacecraft is directly related to plasma properties encountered on orbit. The primary charging environment in LEO is believed to be the low energy (<50 keV) particle deposition causing the surface charging which was found in the Maritime European Communications Satellite (MARECS) upsets. The second mechanism, although rarely happening in LEO, is due to the more energetic particle flux (>50 keV). The charged particles can penetrate into dielectric materials or surfaces and discharge at random times when external conditions change or with a dielectric breakdown.

Exposure to high energy (tens of kiloelectronvolts) auroral electron fluxes in the polar regions can lead to high levels of charging on spacecraft, particularly if the current collection occurs in the ion-depleted wake zones. The orientation of the magnetic field will complicate the interaction mechanisms, with fields parallel to the collection surface inhibiting the escape of secondary emitted electrons and enhancing charging.

5.4.7.1 Types of Spacecraft Charging. For the spacecraft designer, all types of charging (i.e., absolute, differential, and internal charging) are of concern:

- Absolute charging is the development of a potential on the spacecraft frame relative to the surrounding space plasma.
- Differential charging is the change in the potential on one part of the spacecraft with respect to another.
- Internal charging (or buried charging) is the potential buildup in the dielectric.

All charging, particularly buried and differential, may produce strong local electrical fields that can give rise to discharges. Arc discharging can cause problems for operating spacecraft. A primary problem is the occurrence of electronic switching anomalies that can be triggered by differential charging related discharges. The discharge-induced transients can cause system failures and, potentially, material damage. A more common anomaly is a phantom command that requires intervention from the ground, possibly results in loss of data and/or expendables, and shortens the operational lifetime of the spacecraft. Discharging can cause increased levels of contamination that result in changes in surface characteristics. The contaminants are attracted to oppositely charged surfaces and the material expelled during a discharge can be deposited on other surfaces. The surface charging on spacecraft can also bias plasma measurements of the space environment.

Recently, it has been found that the transient discharges due to spacecraft charging can lead to continuous arcing, referred to as a sustained arc. This occurs when the initial discharge transitions into a discharge between two closely spaced conductors at different potentials. The sustained arcs, powered by one or more solar array strings, can completely and permanently short out whole array strings. This phenomenon was first seen on the PAS-6 and Tempo-II satellites in GEO, but has also been seen in ground tests under LEO conditions.[122]

A few severe charging events have been observed in the auroral region. During 1983, instruments onboard the DMSP 7 observed in the polar region an absolute potential of –800 V.[123] Since then a few events with higher potentials up to –1.2 kV were observed. The Advanced Earth Observing Satellite-II polar orbiting satellite lost over 80% of its power due to a discharge in an auroral event that led to arc tracking in a cable bundle.[124] Furthermore, theory predicts that the larger spacecraft of the future will develop even higher potentials. Auroral charging differs from geosynchronous charging in that charging currents tend to be much higher; the vehicle is in a charging environment for only seconds, and the charging rate and the potential reached depend on the vehicle size. Auroral charging is more severe the lower the ambient thermal plasma density is because it tends to slowly discharge the charge caused by the fluxes of high energy auroral electrons. In addition, two-body and wake effects can become important. Also, differential charging between vehicles or a shuttle orbiter and an astronaut during extravehicular activity (EVA) is of concern.

Spacecraft charging in LEO equatorial orbits is produced by currents collected by exposed high voltage conductors, and is thus a function of the spacecraft power system voltages. While spacecraft charging is usually less severe in LEO than the GEO charging produced by solar substorms, it may be just as damaging as studies have shown that arcing voltage thresholds are lower in the LEO plasma than in GEO.[125–127]

Combining extreme plasma conditions (e.g., maximum/minimum temperature and density) for each region does not constitute the worst case situation because the extreme plasma density and the extreme temperature may not occur coincidentally. This worst case environment depends on variations of solar activities and the geomagnetic storm levels. The plasma environment in high altitude orbit is a dynamic medium that exhibits large, daily property variations. Essentially all major parameters can vary over at least 2 orders of magnitude daily. Dynamic changes in the plasma environment can produce large potential differences on spacecraft that might not otherwise

develop during time-stationary plasma conditions. Figure 86 presents the NASA worst case environment to be used in analysis of internal charging issues. Analysis of discharge events on spacecraft in geostationary or geostationary transfer orbits have shown that electron fluxes at internal dielectric breakdown must typically be sufficient to provide a fluence of 2×10^{10} electrons/cm^2 in 10 hr.[128] However, lower charging rates can lead to breakdown under extremely cold temperatures.

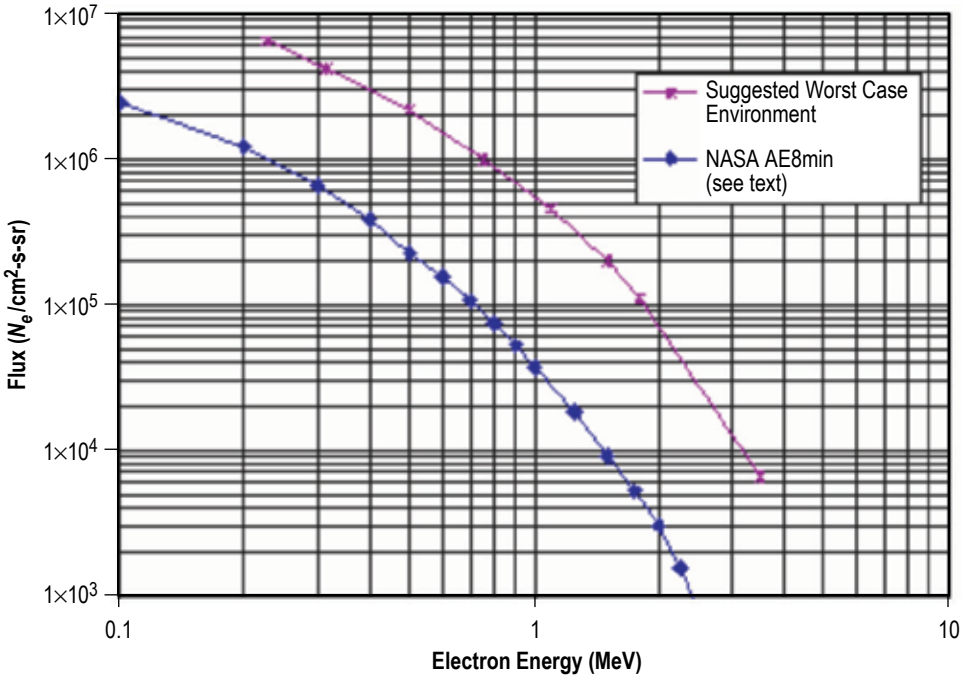

Figure 86. NASA worst case spacecraft charging environment for internal charging issues.

5.4.7.2 Spacecraft Charging Mitigation. Mitigation of charging effects is possible through sound design of the spacecraft systems and structure.[129] A fundamental rule is to ground all conducting surfaces to a common point to reduce the possibility of differential charging. Ideally, all surface materials should be at least partially conductive and the use of dielectric materials on spacecraft surfaces should be avoided as much as possible. If the use of dielectric materials is required (e.g., for a thermal characteristic), the materials can be treated with conductive coatings or impregnated with conductive materials. Electrical filters should be used to protect sensitive circuits from stray currents produced by electrical discharges.

Processes for consideration of the plasma environment by the satellite designer and its possible impact on a spacecraft system follow:

- Determine the plasma environment to which the spacecraft will be exposed during its mission lifetime.
- Determine the magnitude of the satellite floating potential, differential charging, and internal charging in the average and extreme environments. A spacecraft charging analysis utilizing a charging computer code is generally required to obtain useful results.

- Determine if the magnitude of the charging is sufficient to potentially lead to detrimental effects to the spacecraft materials and systems.

- Determine what design steps are necessary to mitigate the effects of charging.

- Determine if charging is likely to be a problem to a spacecraft is a complex problem. Estimates of the average and extreme environments the spacecraft will encounter throughout its intended mission are required to determine the range of floating and differential potentials that are to be expected on the spacecraft structure as well as levels of internal charging.

Knowledge of the materials to be used in the construction of the spacecraft is required and insight into the design of individual systems is required to determine if the charging and associated effects can be tolerated by the spacecraft systems. Designers considering spacecraft charging for the first time may consult a number of excellent references on the subject including Kasha,[123] DeForest,[130] Garrett,[131] Purvis et al.,[129] and Garrett and Spitale.[132] The collection of papers edited by Garrett and Pike,[133] Kasha,[123] and Tribble[134] provide outstanding introductions to the subject of the plasma environment and spacecraft charging.

5.4.8 Plasma Environments and Spacecraft Charging Models

Most commonly used models both for specifying the conditions in the plasma environment and for analyzing spacecraft interactions with the environment are described in the following subsections. Users may also select from a variety of models that have been accepted by the plasma community for spacecraft design purposes.

5.4.8.1 Plasma Environment Models. A wide variety of ionospheric models are currently available.[135] Selection of individual models and their use will require consultation with an ionospheric specialist since a variety of inputs and assumptions are required to obtain meaningful and valid results.

5.4.8.1.1 International Reference Ionosphere. One of the most commonly used computer codes for design work is the IRI model.[136] The IRI model describes the ionosphere plasma properties in the 85 to 1,000 km altitude range for geomagnetic latitudes up to approximately 60°. Both the electron and ions (O^+, NO^+, O_2^+, O_2^-) densities and temperatures can be calculated as a function of latitude, longitude (geomagnetic or geocentric), time of day, day of year, altitude, and solar $F_{10.7}$ radio flux. The error bars on the model during quiet times are a factor of 2 to 4 of the indicated values at altitudes below the F2 peak, and these are primarily the result of small-scale variations in the ionosphere. Above the F2 peak, problems with the scale height could lead to error bars of up to a factor of 10.

The IRI90 was used to generate figures 76–79. The IRI2000 is the most current version and is frequently updated by the plasma community. Different options are suitable to different applications; care should be exercised in this selection. Models of the ionosphere have not progressed to the point where they can be used for reliable forecasts of future conditions, especially those related to magnetic storm and substorm dynamics. Major questions of convection patterns are still

unanswered. Even the static conditions predicted by the IRI90 model frequently do not match observational data perfectly. IRI90 is a climatic model giving average conditions. Great care must be exercised in the use of all ionospheric models.

5.4.8.1.2 GeoSpace. AF-GeoSpace, v.2.0 is a computer model developed by the U.S. Air Force Research Laboratory (AFRL) to facilitate the assessment of space environmental hazards by bringing often-used environmental models together under the umbrella of a user-friendly and graphics-intensive master program. One of the modules recommended here for the auroral environment is the Auroral Precipitation Model in GeoSpace. The AURORA science module is a compilation of statistical models of auroral ion and electron precipitation derived from measurements made by USAF particle detectors flown on the DMSP and P78-1 satellites. PL-GEOSpace uses functional representations for the following:

- Integral electron number and energy flux.
- Electron-produced, height-integrated Hall and Pederson conductivities.
- Integral ion number and energy flux, which were derived using the statistical models presented.

The PL-GEOSpace code is distributed on CD–ROM and is available free of charge upon request through the AFRL.

5.4.8.2 Space Charging Analysis Models. Charging calculations are typically complex and require the use of time-dependent computer models. The most common analysis program in use today is NASA/Air Force Spacecraft Charging Analyzer Program-2000 (NASCAP-2k). Other codes include the Sensit, Environments Work Bench, Spacecraft Charging Handbook, and the Space Environment Information System codes (Equilibrium Potential code (EQUIPOT), and others).

5.4.8.2.1 NASCAP-2k. NASCAP-2k is the next generation spacecraft charging analysis code. It is a comprehensive update to the original NASCAP spacecraft charging codes written 20 years ago. NASCAP-2k is a collaborative project between NASA and the AFRL that builds upon the Air Force's DynaPAC charging algorithms. The model replaces 3D spacecraft charging codes for all environments in GEO, LEO, Auroral Charging, and interplanetary environments.

Satellites orbiting in LEO (excluding polar orbiting satellites) should use the spacecraft charging code NASCAP-2k LEO option for any charging analysis.[117] LEO is typically defined as a satellite orbiting within an altitude of 100 to 1,000 km. NASCAP-2k LEO option is the appropriate code for these satellites, less than ±51° latitude, and where the Debye length (typically in the order of 1 cm for this region) is small compared to the size of the spacecraft. This 3D code utilizes space charge limited particle collection. This type of current collection is appropriate in regions where the plasma is denser and means the space charge actually limits the range of potentials on the spacecraft. NASCAP-2k LEO option is appropriate to use for satellites with solar arrays configuration. It contains a solar array power system model that can determine the solar array currents. It is strongly encouraged for any satellite with solar arrays biased greater than approximately –100 V orbiting in a LEO to perform a spacecraft charging analysis.

Subsets of a low Earth-orbiting spacecraft are those in polar orbits (greater than ±51° ±5° latitude) where spacecraft are exposed to fluxes of auroral particles. The auroral part of NASCAP-2k code also utilizes space charge limited particle collection. It is a 3D code specifically designed to incorporate the ambient LEO orbit plasma density, as well as the hotter environment from the plasma brought to low altitudes by the open magnetic field lines. The auroral component of NASCAP-2k also incorporates the satellite wakes into charging calculations. This charging code is appropriate for satellites orbiting in short Debye-length plasmas.

5.5 Low Earth Orbit (90 to 2,000 km) Ionizing Radiation Environments and Effects

Once the space vehicle is above 200 km it is considered to be in space. Under 2,000 km, it would be considered to be in the low Earth region and if in orbit, it would be in LEO. This section represents the transition from the upper reaches of the terrestrial environment to the LEO region of space.

5.5.1 LEO Ionizing Radiation Environments

Sections 2.12.1 and 3.11.2 described the processes involved in understanding the ionizing radiation environments that will be encountered in the terrestrial segments. The discussion in section 3.11.2 is still valid for the region from 90 to 200 km of this section. Additionally, the discussion in that section on the GCR and SPE environment is applicable to this segment with the exception that those environments will now be seen without atmospheric shielding effects. Variation from the terrestrial environments to the space environments will be discussed next.

5.5.2 LEO Environments

The near-Earth radiation environment can be divided into a trapped radiation environment and transient radiation environments. A depiction of these environments is shown in figure 87. The trapped environment is due to the Earth's magnetic field confining charged particles to certain regions of space. These regions are termed the Van Allen Belts. Nominally there will be one proton and two electron belts (inner and outer) though this can temporarily change with large solar events. The transient environments are due to the effects of the Sun (solar wind and solar particle events) and GCRs. A 2D artist's depiction is shown in figure 88 and a 3D model-based view of these trapped belts is shown in figure 89.

Sections 2.12.1 and 3.11.2 have dealt with the transient ionizing radiation environment in sufficient detail. Therefore, this section will concentrate on the trapped particle environments.

Figure 90 shows the approximate regions of space the various radiation environments occupy. Since boundaries of the bands are not sharp transitions, the indicated numbers should be considered approximations. The trapped radiation belts extend from approximately 500 km to about 12 R_e (roughly 76,000 km). Normally, over this range there are two electron bands (with different population and energy spectra) and one proton band. As shown in figure 89, however, sometimes a departure from normalcy occurs. Figure 89 is based on data from a severe solar event in 1989 that formed a third electron belt (between the inner and outer zones) and a second proton belt (higher in altitude) lasting for many weeks.

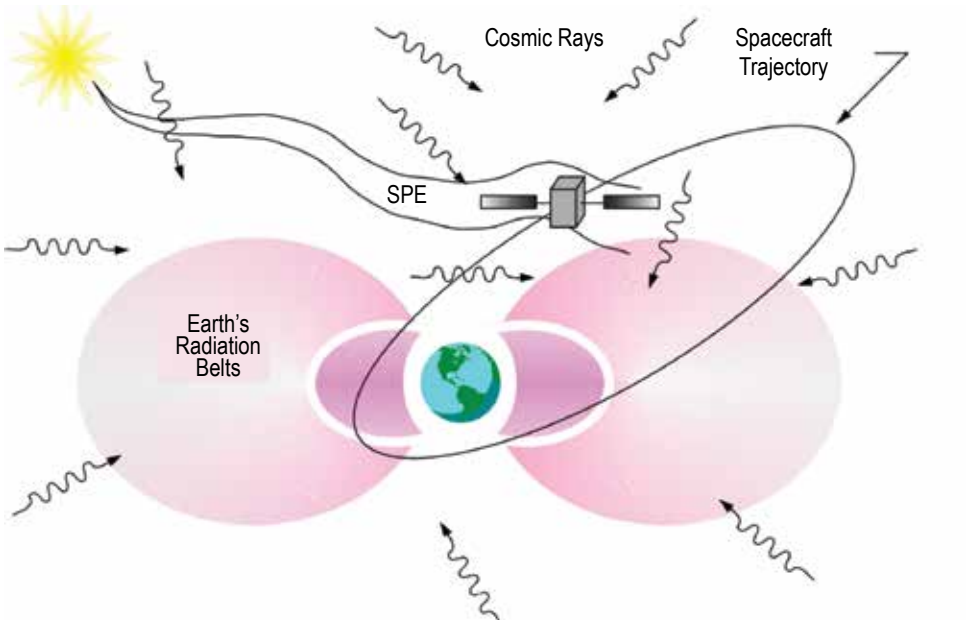

Figure 87. Depiction of all the radiation types that a spacecraft can experience, including the inner and outer trapped radiation belts, solar particle event, and galactic cosmic radiation.

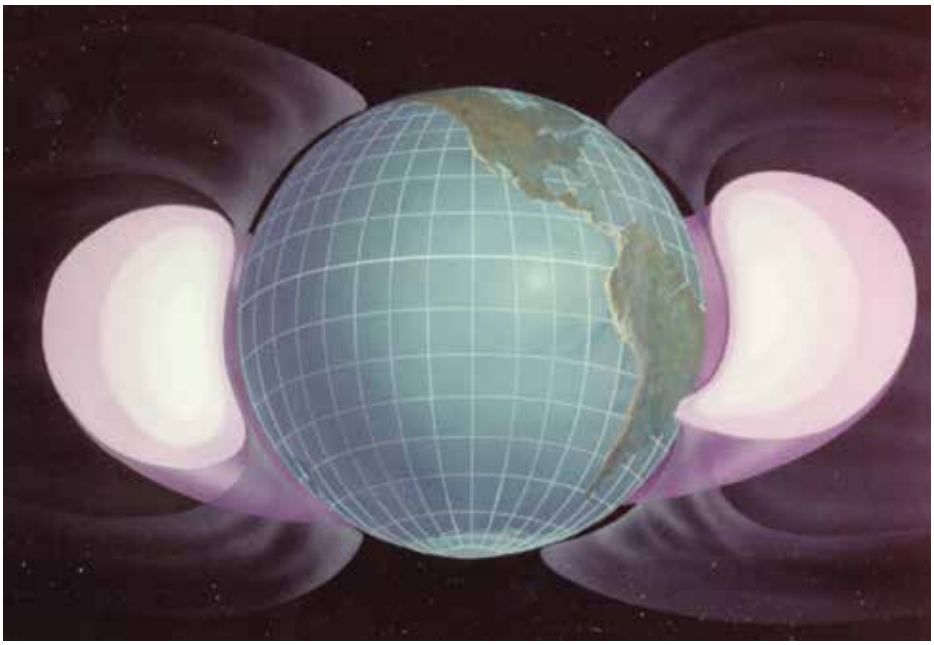

Figure 88. Two-dimensional artist's depiction of the trapped radiation environment.

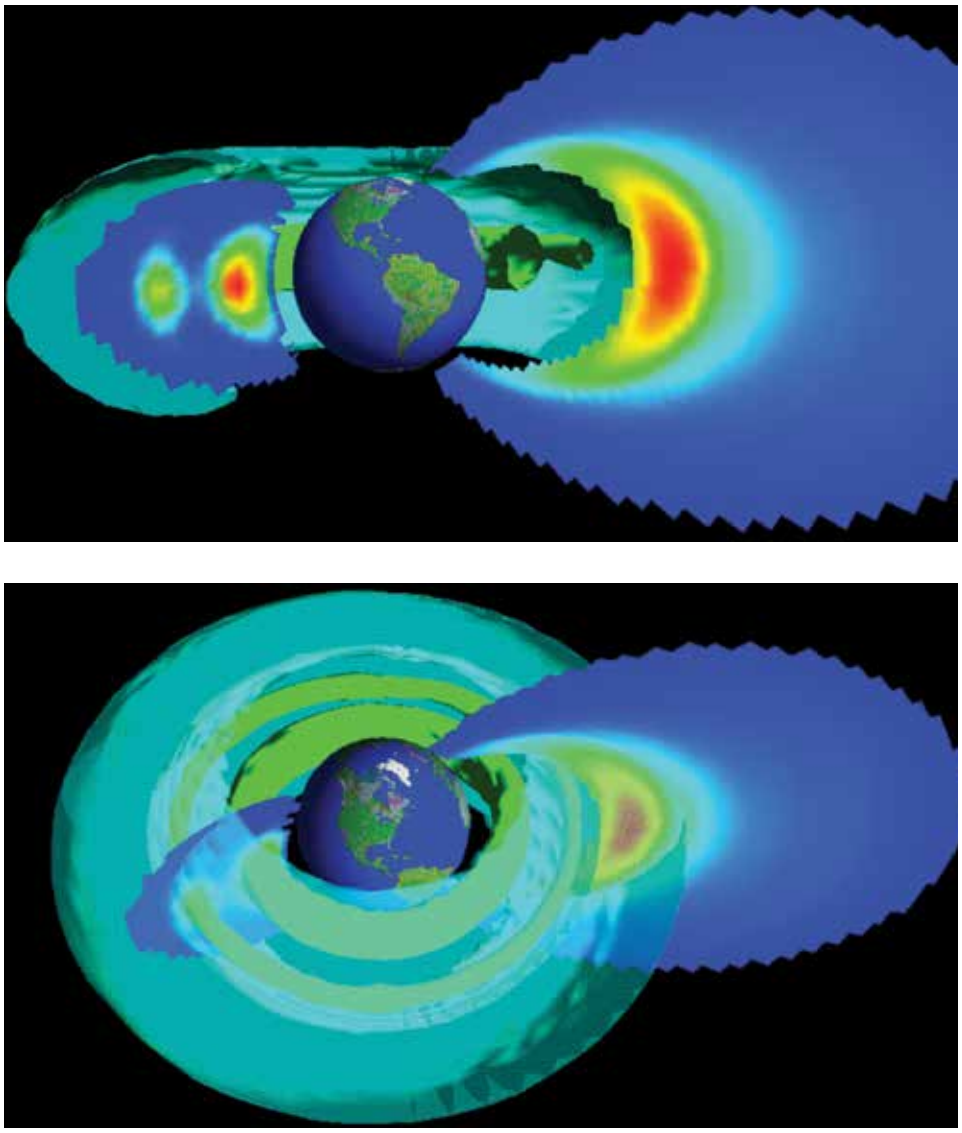

Figure 89. Three-dimensional views of the trapped radiation environment: (a) The true toroidal shape of the radiation belts, with transparent green representing the outer electron belt and solid green the proton belts (data from a particularly strong storm event where a second proton belt was formed), and (b) edge-on view shows cross-sectional data for the belt regions with low to high density represented by blue to red.

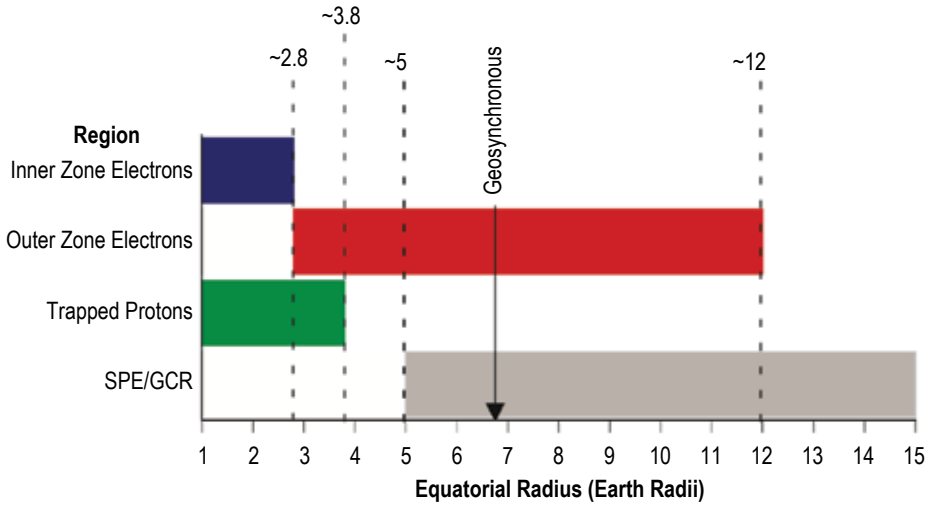

Figure 90. Pictogram showing regions of space where radiation types are significant. Regions are plotted as a function of the equatorial radius, in Earth radii (~6,370 km), because the belts vary with the magnetic field that changes with increasing inclination off the equator.

A specific region of space that warrants special coverage is the SAA. The Earth's magnetic field axis does not point to geographic north (and does not pass directly through the center of the Earth. The combination causes a deformation of the magnetic field over the South Atlantic (magnetic field lines dip lower in altitude) and over Southeast Asia (field lines are higher in altitude). The net effect, the harshness of the radiation belts, is seen at lower altitudes in the SAA region (see fig. 91). Thus, for spacecraft in LEO, this region tends to dominate the observed radiation environment. For systems at higher altitudes, however, this effect is less significant.

Another important point is that the orbit of a spacecraft can take it into and out of the radiation belts. Figure 92 shows the electron environment as a function of time for a satellite in low Earth polar orbit.It is evident there are times of radiation exposure followed by times of no exposure.

Therefore, depending on the orbit or trajectory of the space vehicle, and mission time, the vehicle will be exposed to trapped electrons and/or trapped protons environments. The exposure levels and the respective energy spectra for these particles will be mission specific but will be presented as a differential and integral energy spectra that can be used to analyze for effects that will be discussed next.

5.5.3 LEO Ionizing Radiation Effects

5.5.3.1 Total Ionizing Dose. The term total ionizing dose (TID) implies the dose is deposited to the electronics through ionization effects only. The energy deposited by ionizing radiation moves the electrons of the material to a higher energy state, thus making them available for conduction and mobile inside a nonconductive material. These electrons, or more correctly the positive charge created by the ionization, are the prime cause of the total ionizing dose effects.

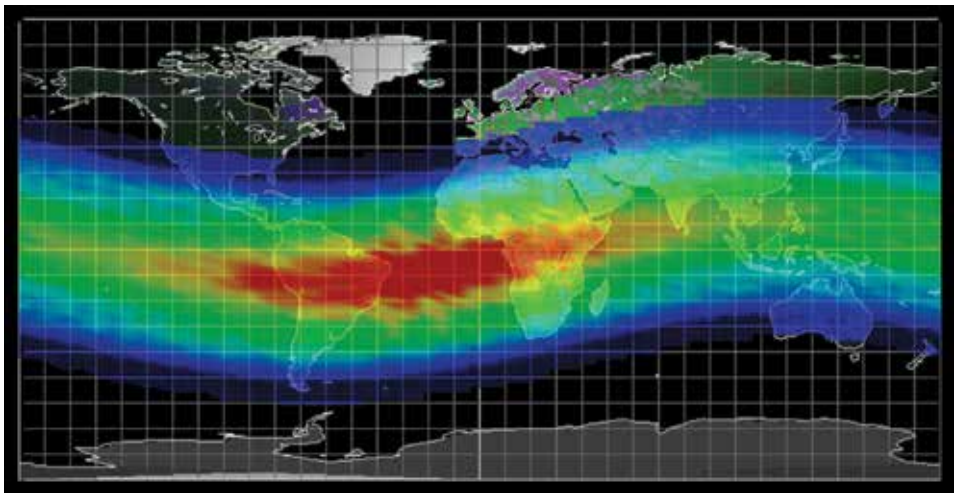

Figure 91. Contour plot of the trapped proton environment overlaying a map of the Earth. Proton density increases from blue to green to yellow to red. Contours are highlighting the SAA where the radiation particle population is high due to the offset nature of the Earth's magnetic field.

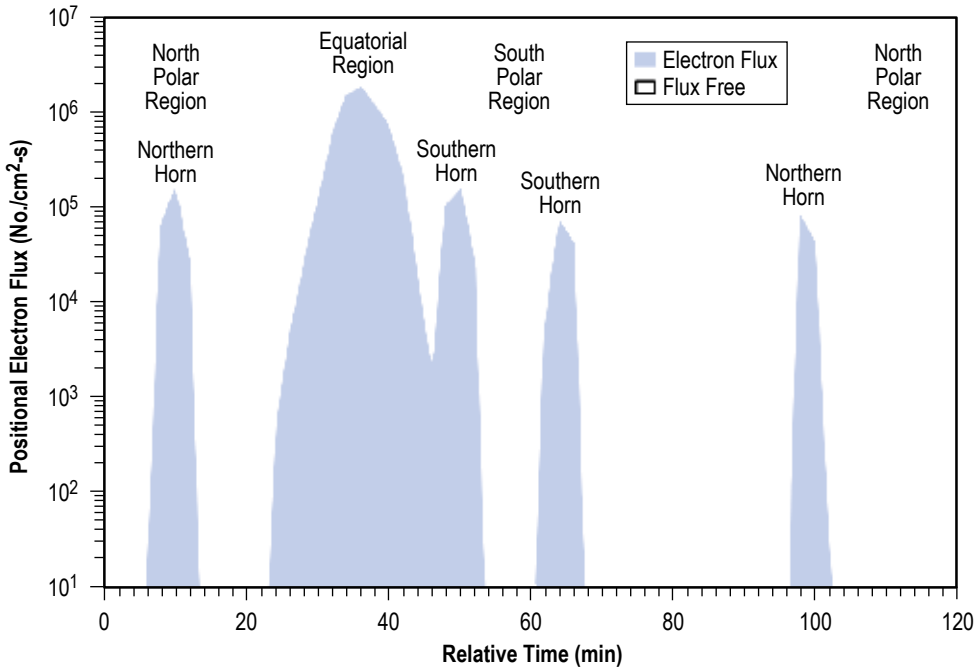

Figure 92. Plot of trapped electron flux as a function of relative orbital time for a 900 km polar orbit. The graph shows the regions of the radiation belts and the noncontinuous exposure (horn identifies regions of space (at high latitudes) where the outer electron belt is seen at lower altitudes).

In general, all types of electronics are susceptible to this ionization but the charge generated inside the semiconductor material can quickly be collected and removed without ill effect (assuming the radiation interaction rate is at the low level of the space environment). If a semiconductor device contains, for example, a silicon dioxide/silicon interface (as in all modern integrated circuits based on complementary metal oxide semiconductor (CMOS) technology), charge generated inside the oxide can become trapped at the interface. This trapped charge, by changing the potential of the interface structure, can lead to increased 'leakage' current or changed operational characteristics of any device using this structure (if this interface exists at a biasing point). Details of this type of cumulative effect can be found in references 137 and 138.

A special consideration for TID comes for a specific technology called linear bipolar devices. Unlike the CMOS technology that uses field effect transistors, linear bipolar devices use bipolar transistors as the switching and amplification elements. For many years it was felt that the sensitivity of this technology to ionizing radiation was good. However, it was discovered that the technology can be susceptible to a cumulative effect of ionizing radiation that is truly dependent on the rate at which the dose is deposited. It was found that the same device would degrade faster with a dose under low dose rate conditions than at higher dose rates. This effect is termed the enhanced low dose rate sensitivity (ELDRS). ELDRS is still a topic of research and the most current information can be found in the December issues of the *IEEE Transactions on Nuclear Science*, containing the papers presented at the Nuclear and Space Radiation Effects Conference held that year. The most current review paper on the ELDRS topic can be found in reference 139.

From an engineering perspective, these cumulative macroscopic effects are important in determining the reliability of electronics to the ionizing dose environment. To determine a part's reliability in this radiation environment, a detailed set of test data is required. Simply testing a part for functionality after exposure to a given radiation level may not be sufficient. Parametric data must be taken with functionality testing over smaller dose steps than one-shot, go/no-go testing. Test data for all parts in a given design must be reviewed for meeting all specifications (not just functionality). This radiation performance change information must be combined with aging and temperature effects. Finally, overall degradation must be compared with actual circuit specification to ensure proper operation throughout mission lifetime.

Test data must also show information useful for mission procured electronics. A high degree of variability in test results is possible for the same parts from the same lot from the same manufacturer. Actual testing should include a number of parts from the same lot and the data should be treated statistically based on observed variability and sample size. Variability results from the attention paid by the manufacturer to designing and building parts while being mindful of the radiation environment. A manufacturer producing a 'rad-hard' part will have a small amount of variability. A mass-produced part for the commercial market, however, can have extreme variations. Therefore, testing should be tailored for the radiation quality of the commercial part (i.e., from accepting previous test data for rad-hard parts to performing piece-part testing). As more and more manufacturers leave the radiation-tolerant market, testing of parts becomes more critical to system design. This process of understanding the test data and the impact on system design is called radiation hardness assurance. A detailed review of this process can be found in reference 140.

In general, TID effects are mitigated through proper use of shielding materials. These effects depend on transfer of energy from the radiation environment. If the particle environment population or its energy is decreased, the effect is lessened, i.e., exactly what shielding does. By forcing the particle to transport through an intervening material, the environment interacts and loses energy (sufficient energy loss can mean the particle never enters the electronics). By appropriately selecting the shielding material and its thickness, mitigation is optimized. Since nothing is free, the cost associated with shielding is weight. Putting weight into orbit costs money. Therefore, the tradeoff is survivability or reliability of electronic systems versus added cost to get systems into space. Also, the effect of shielding is not linear (as shown in fig. 93). At some point, depending on the environment and relative 'hardness' of the electronics, addition of reasonable shielding is no longer effective. It is easily seen from figure 93 that the first few millimeters of aluminum reduces the daily dose by over 2 orders of magnitude. However, to reduce the dose from this point by another factor of 2 requires an additional 50 mm of aluminum, a significant weight addition.Therefore, the only reliable mitigation is replacement of the part with a more tolerant version. A discussion on radiation shield design for space systems can be found in reference 141.

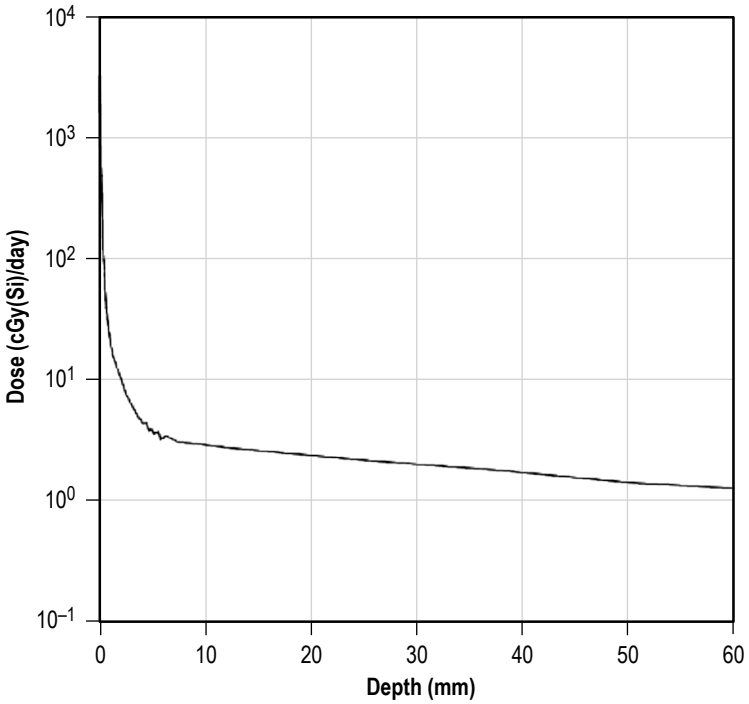

Figure 93. Plot of the total ionizing dose as a function of effective aluminum shield thickness.

5.5.3.1.1 Displacement Effects. The second area of the cumulative effects of radiation is displacement damage. When radiation interacts with the material, either electronically or via direct nuclear interaction, energy is imparted to the atom as a whole. This energy is typically seen as heat by the increasing vibrational motion of the atoms. Or if the energy transfer is sufficiently high, the atom can overcome the binding energy of the crystalline lattice of the material. If this occurs, the

atom is 'displaced' from its normal position to various end locations. Unless the end location is an exact duplicate of the former position, the regular order of the crystalline lattice is disturbed.

Since this regular order gives semiconductor materials their unique properties, the disturbance causes changes in the operation of any device exposed to this environment (level of dose a device is susceptible to varies, but all electronics are affected). This change may add a current path that previously did not exist (allowing increased leakage current) or make conduction more difficult in regions designed for flow. For example, diodes become less effective (two-way current flow becomes easier) and the inherent amplification capabilities of transistors diminish. Similar to the total ionizing dose, effects of displacement damage are cumulative. With a small exposure to a radiation environment, observable effects are small but effects build with exposure time.

The solar cell is an example for this category since it displays these described effects and is a common element to most spacecraft. The solar cell is basically a diode with one side exposed to the illumination of the Sun; photons hit the device, creating electrons. The electric field of the diode (cell) allows the electrons to be collected, thus, generating power. With exposure to radiation, diodes become less effective. Diode leakage current increases, generated electrons 'live' for much shorter time periods, and the internal electric field decreases. All these effects combine to make the solar cell less efficient producing power. Power reductions of 50% are possible depending on solar cell construction and the environment to which the cell is exposed. In general, shielding is effective for mitigating displacement effects, but adding shielding to resolve this solar array problem is difficult. The shielding (called cover glass in this application) must be transparent to the optical photons and make a good optical interface at the solar cell (minimize refractive effects). Even with these conditions met, transmission losses increase with increasing cover glass thickness. Therefore, a balance must be reached between allowable radiation degradation and cell power production efficiency.

A thorough treatment of displacement damage theory and the hardness assurance processes needed for space systems is described in reference 142.

5.5.4 Low Earth Orbit-Based Effects

Both cumulative and transient radiation effects are important for this segment of a space mission. The SEE impacts and analyses are the same as those discussed in section 3.11, so no further discussion is needed here. Section 5.5.3 discussed the cumulative effects of ionizing radiation. Since particles trapped in the Van Allen Belts can produce both TID and displacement damage, this mission segment requires an analysis for both of these types of effects.

5.6 Meteoroid and Orbital Debris Environments

5.6.1 Meteoroid Environment

Meteoroids are natural particles that continually enter space from a variety of sources within the solar system: comets, asteroids, and planets. The cometary particles form the bulk of the particles in the size regime of interest to engineers (>100 mm), of the 'sporadic' meteoroid background, with asteroids contributing the remainder. The cometary/asteroidal ratio is still being investigated; future revisions of this TM will discuss any modifications to this ratio. The planetary component is insignificant by comparison, though it certainly does exist (as evidenced by the Allan Hills 84001 Mars meteorite). For an object in orbit around the Sun in the inner solar system (such as the Earth), the sporadic meteor sky looks similar to figure 94. Note that there are six sources or radiants that can be divided into three groups according to origin. The helion sources, which account for the bulk of the flux, are comprised of particles from a subset of the short period comets called Jupiter family comets (e.g., comets Halley and Encke), whereas the toroidal sources probably derive their material from another subset of the short period comets called Halley family comets. The apex sources derive their material from long period comets. As might be expected, the average speed of meteoroids from the apex sources (~46 km/s) is higher than that of particles coming from the helion radiant (~24 km/s) since the Earth is hitting the apex meteoroids nearly head-on.

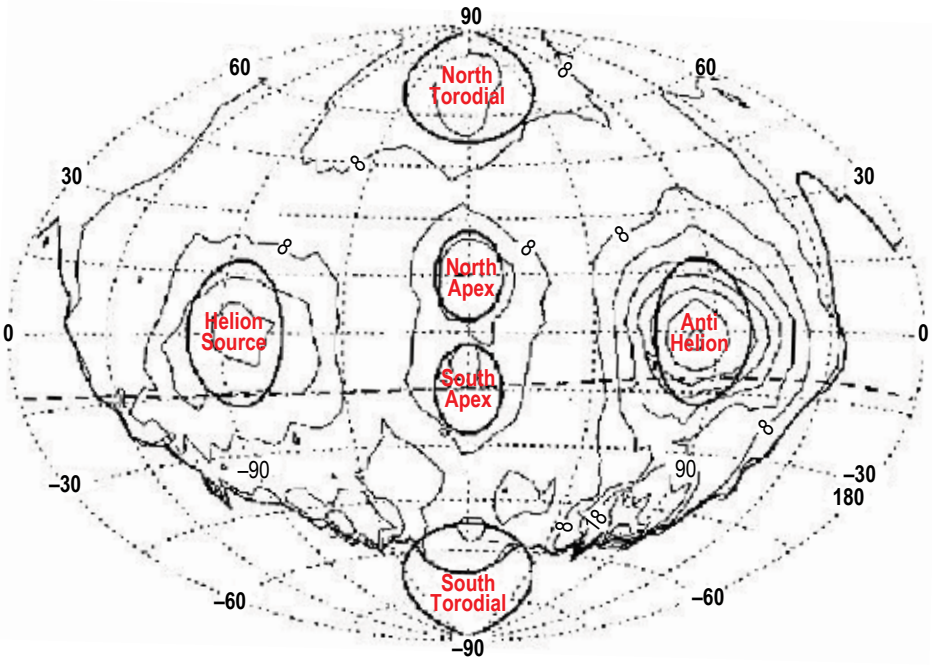

Figure 94. Radiant distribution of meteor sky according to radar (the coordinate frame places the Earth's apex of motion at the center, the solar (helion) direction at a longtitude of –90°, and the north ecliptic pole at latitude 90°).

Figure 94 displays the radiant distribution of the sporadic meteor sky as seen by radar for meteoroids with mass $>10^{-4}$ g encountering the Earth.[143,144] The radiant distribution is based on the Harvard Radio Meteor Project (HRMP) 1969 meteor orbit survey, which has been corrected for various selection effects. Other radar surveys such as the Adelaide radio surveys from 1960–1969, the Kharkov radio survey of 1975, and the recent Canadian Meteor Orbit Radar[145] survey also confirm the locations of these radiants. Particles of sizes >100 μ can do considerable damage to thermal protection systems (TPSs), radiators, windows, and pressurized containers. Some secondary effects might include partial penetration or pitting, local deformation, and surface degradation that cause a failure upon reentry. The speed, mass, density, and directionality of these small particles are important factors for design considerations and mitigation during operations. The shape of the meteoroid and its orientation relative to its trajectory can also affect the degree of the damage, but present knowledge of the meteoroid environment is inadequate to specify these parameters.[146] For the purposes of this environment definition, the assumption is made that meteoroids are spherical in shape.

5.6.1.1 Meteor Showers. In addition to the normal influx of background meteoroids, the Earth (and spacecraft near it) also encounters quasi-periodic meteoritic enhancements caused by streams of material ejected from short period comets that pass near the Earth's orbit. These streams of debris produce the meteor showers observed here on Earth, and normally represent only a modest enhancement over the background (a few percent). However, the density of material in a stream can be increased by a recent entry of the parent comet into the inner solar system, thereby resulting in an enhanced shower (meteor rates of several hundred per hour) or a meteor storm (rates in excess of 1,000 meteors per hour). As might be expected, an enhanced shower or storm presents a time of increased risk for spacecraft. Streams that are notorious for producing enhanced showers or storms at Earth are the Perseids, the Draconids (also called the Giacobinids), and the Leonids. The Leonids are especially famous for producing spectacular meteor storms at 33-year intervals.

Table 82 presents information on those meteor streams that are known to have the potential for causing outbursts at Earth and the Earth-Sun L_1 and L_2 points. It would be appropriate to devote some thought on how to deal with stream activity, whether through design or mitigation procedures, since at least one satellite has been damaged and one effectively killed by encounters with meteor streams.

Table 82. Meteor streams known to produce enhanced or storm level activity.

Stream	Radiant			Time of Maximum Activity
	RA (deg)	Declination (deg)	Speed (km/s)	
Quadrantids	230	49	41	January 3
Cygnids	286	59	25	August 18
Lyrids	271	34	49	April 22
Draconids	262	54	20	October 9
Perseids	46	58	59	August 13
Leonids	152	22	71	November 17–18

In mid-September 1967, the Mariner IV spacecraft was located midway between the orbits of Earth and Mars when it encountered an unknown meteor stream. The onboard meteor counter registered a thousandfold increase in flux for ≈45 min, during which time the spacecraft was slightly torqued about its roll axis and had some of its thermal insulation ripped away. Mariner IV was lucky in that it suffered no major damage; such was not the case with the European Olympus communications satellite in August 1993. During the enhanced shower experienced that year, the Olympus satellite was struck by a Perseid somewhere near its electronics bay. The resulting plasma discharge generated enough current to disable a gyro, causing the satellite to tumble. By the time control was restored some days later, the spacecraft had used practically all of its fuel and was effectively dead as far as its mission was concerned.

It should be noted that even though there are a small number of reported failures, NASA and other scientific spacecraft represent a small fraction of the total satellite surface area; commercial and military satellites account for the majority of exposed surfaces. It is likely that there have been other spacecraft failures resulting from meteoroid impacts; however, insurance or national security concerns often prevent the public release of such information. Still there exist numerous anecdotal reports about attitude anomalies etc.; are these issues the result of a meteoroid strike or faulty thruster? More often the lack of engineering data prevents absolute confirmation of a meteoroid strike. Fortunately, current design practices for Earth-orbiting spacecraft tend to mitigate the meteoroid threat since the primary threat from solid particles is from orbital debris.

5.6.2 Orbital Debris Environment

Orbital debris is man-made material induced by spacecraft that can be as large as spent rocket motors and as small as the dust particles ejected from the nozzles of maneuvering thrusters. Spent satellites, accidental explosions, and collisions between orbiting bodies are contributing towards a rapid increase in this hazard. A serious problem with orbital debris is that it can occur in a size range that is large enough to destroy a spacecraft but is too small to be tracked from the ground. The average impact speed of debris on a spacecraft is 10 km/s, only half that of meteoroids, but the population of debris in typical Earth orbit is much higher than that of meteoroids, making debris a greater hazard for most spacecraft.

NASA's orbital debris program at JSC routinely gathers information about the debris population from the Haystack, Haystack Auxiliary, and Goldstone radars. The debris population is described using statistical sampling from these ground-based radars, which can detect particles as small as a few millimeters in size. Tracking particles smaller than 10 cm is difficult, so statistically sampling the environment provides the most efficient means to develop an engineering debris model. Much of the debris environments are in families of near circular orbits but some are in more eccentric orbits. Using statistical methods, population 'fits' are used to construct debris populations in the Orbital Debris Engineering Model 2000 (ORDEM2000). The populations are functions of altitude, eccentricity, inclination, and size. The biggest unknown with the debris environment along with meteoroids is the shape. Shape and material properties for the debris are important for calculating collision penetrability.[147]

5.6.3 Models/Analysis

5.6.3.1 Meteoroid Environment Models and Analysis. Any accurate model of the meteoroid environment in near-Earth space must properly describe these three aspects of the environment: flux, directionality, and velocity distribution. These three parameters are inseparably intertwined in both the development of a meteoroid model (where crater counts from surfaces exposed in space are converted to the flux versus mass, directionality, and velocity distributions of the model), and in the reverse process where the model is applied to estimate the crater counts to be expected on a future spacecraft.

For example, velocity enters the relationship between crater dimensions and impactor size, as well as the estimation of gravitational focusing. Directionality affects the exposure and crater size evaluations. Unfortunately, it is now known that there are deficiencies in the velocity distributions/assumptions used in older NASA meteoroid models. Improvements in computational techniques, along with new research efforts, have allowed us to incorporate the directionality of the sporadic environment. The previous NASA meteoroid model documented in Space Station Program (SSP) 30425, which assumed an isotropic directionality and three-step speed distribution, should be replaced.

Several researchers in this field have published directional models such as Taylor and McBride,[143] Brown and Jones,[148] and the historical work presented by Elford et al.[149] Also, new models developed by NASA's Meteoroid Environment Office (MEO) and European Space Agency have been designed to remedy many of the earlier mentioned deficiencies. The MEO model is known as the Meteoroid Engineering Model (MEM)[150] and is applicable to spacecraft in Earth orbit and trans-lunar space, spacecraft in lunar orbit, and spacecraft in interplanetary space between 0.2 and 2 AU.

MEM reports the overall meteoroid flux relative to a spacecraft's trjectory; it also reports the flux per second interval, per angular interval, and per input state vector. The output files are designed to be compatible with the BUMPER[151] risk analysis tool. MEM was developed to replace the older Grün model that did not address the directionality of the environment and assumed one average speed at Earth. The directionality and velocity distributions are an important part of accurately modeling the risk to spacecraft and should not be ignored.

5.6.3.1.1 Flux. The interplanetary submodel of MEM (which has no gravitational focusing and planetary shielding effects) yields a flux of meteoroids greater than 10^{-6} g of 5.7 particles/m^2/yr or 6.5×10^{-4} particles/m^2/hr at 1 AU. This is a cross-sectional area flux for a randomly tumbling satellite, where the relevant area is the time-averaged, cross-sectional area. Figure 95 shows the sporadic flux as a function of mass from MEM at 1 AU.

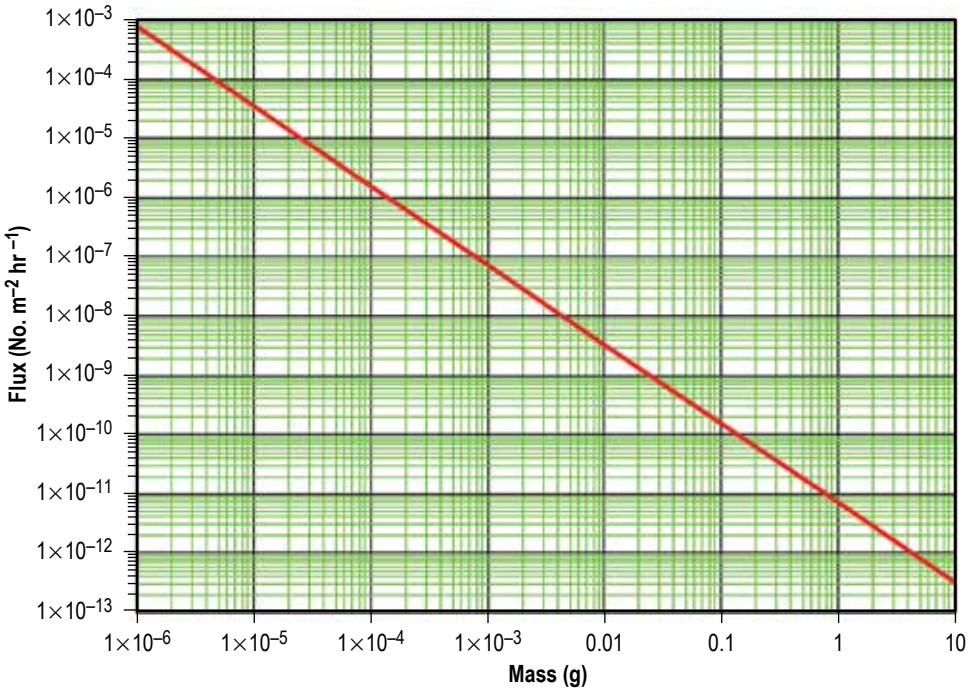

Figure 95. Sporadic meteoroid flux as a function of mass.

This is the flux in terms of mass; meteoroid densities are needed in order to convert to the particle sizes required by penetration equations. Discussion later in this section will cover current efforts to characterize the meteoroid density distribution.

5.6.3.1.2 Directionality. It is now widely documented that sporadic meteors radiate from six distinct sources rather than approaching uniformly from all directions. Imagine a coordinate system in the plane of the Earth's orbit (the ecliptic), with 0° longitude being located at the position of the Sun and 270° being the approximate direction of the Earth's motion. In this system, and without the disturbing effects of Earth's gravity and shielding, background meteors would then be seen radiating from the following six sources:

- One source near the Sun (the helion source).
- One source nearly opposite the Sun (the anti-helion source).
- Two sources near the direction of Earth's velocity (the apex sources).
- Two sources located toward the apex, but 60° above and below the plane of the ecliptic (the toroidal sources).

As it is currently modeled, the flux of meteors from the two helion sources account for approximately 46% of the total flux. The apex sources provide only 3%, and the toroidal sources contribute 45%. These source strengths are currently being updated and at time of publication, this is the best estimate available. The asteroidal component is severely underrepresented and is currently modeled as contributing approximately 6% of the total flux. Table 83 summarizes this directionality information.

Table 83. The six background meteor radiants.

Source	Longitude (deg)	Latitude (deg)	Fraction of Flux
Helion	342	0	0.23
Anti-helion	98	0	0.23
North apex	270	15	0.015
South apex	270	–15	0.015
North toroidal	270	60	0.225
South toroidal	270	–60	0.225

MEM can also calculate the average flux on the surfaces of an oriented spacecraft modeled initially as a basic cube structure. This orientation displays the directionality of the sporadic meteoroids encountered in a 1 AU orbit. Figure 96 shows the importance of surface orientation and directionality effects.

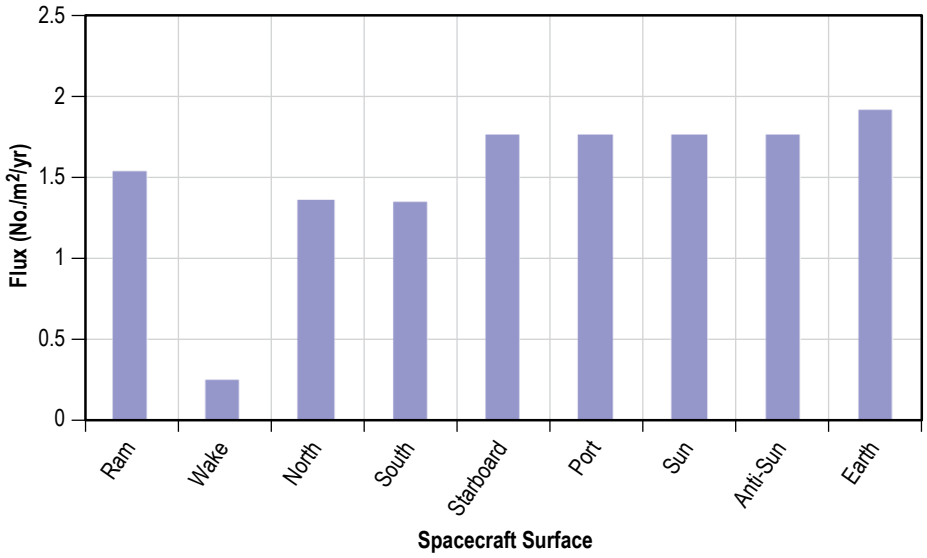

Figure 96. Flux on spacecraft surfaces for limiting mass, 10^{-6} g at a 1 AU orbit (no gravitational focusing or planetary shielding effects are considered).

The basic cube modeled in MEM is oriented with the Ram surface along the velocity vector and the North surface oriented along the angular momentum vector. One thing to notice is that, for a nearly circular orbit, the position vector and velocity vectors will be nearly perpendicular, and therefore the port and Sun surfaces will see the same flux. This will change if the orbit is more eccentric, as will the effects of directionality become more enhanced.

Directionality is a very important issue for spacecraft, as less shielding can be used if the meteoroid threat is shown to be significant on specific surfaces and not over the whole spacecraft. Less shielding saves valuable resources (weight and money). Spacecraft orientation is also another important risk mitigation strategy, and using a directional model to assess orientation will improve any designer's assessment.

5.6.3.1.3 Velocity. Previous velocity distributions and average speeds associated with older meteoroid models suffered from various biases and misapplications between models. Based on best estimates as of this publication, the velocity distribution at Earth as modeled by MEM is given in figure 97.

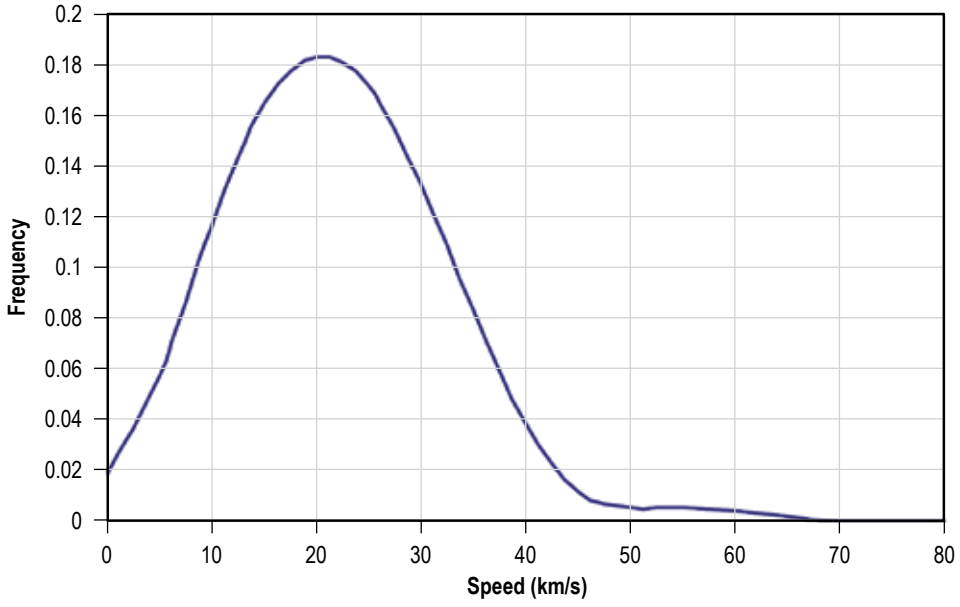

Figure 97. Average meteoroid speed distribution at 1 AU (no gravitational focusing or planetary shielding effects are considered).

This distribution represents the composite of all of the meteoroid sources, weighted for source strength in a circular 1 AU orbit, basically representing what is seen by the Earth but ignoring gravitational focusing and Earth shielding effects.

The composite distribution was derived from individual distributions associated with the sporadic meteoroid sources. If symmetry is assumed among sources of the same type (helion/anti-helion, north apex/south apex, etc.), the velocity distributions can be reduced to four, one for each source. The speed distributions behind MEM have been compared to individual source speed distributions from the HRMP[149] and are in good agreement with the only known published meteor survey, provided the biases in the old HRMP data is accounted for as described in Taylor and McBride.[143] Table 84 shows the average speeds coming from each source, excluding any Earth disturbing forces.

Table 84. Meteoroid average speeds at 1 AU, without Earth focusing or shielding included.

Source	V_{avg} (km/s)
Helion	24
Anti-helion	24
North apex	46
South apex	46
North toroidal	20
South toroidal	20
Asteroidal	5

Notice that while the helion and toroidal sources have nearly the same average velocity, the apex meteoroids have an average speed of approximately 46 km/s, which is twice that of the other sources. Some consideration should be given to surfaces that might face in the apex direction for an extended period of time. Masses being equal, the average apex meteoroid will have 4 times the striking power (relates to penetration) and 16 times the plasma production potential (plasma produced by a meteoroid impact is proportional to v^4) than a meteoroid from the helion sources.

Also, in table 84 there is an asteroidal source average speed. This value came from analysis of orbital distributions of asteroids taken from infrared measurements and was provided by J.C. Liou of JSC.[152] Although the strength of the asteroidal component is underrepresented in current meteoroid models, the average speed is presented for completeness.

The strengths of the individual sources are still a highly debated topic and most important in creating a complete picture of the meteoroid threat. Again, future releases of this definition document will contain revisions as necessary to update the environment based on new information.

5.6.3.1.4 Gravitational Focusing and Planetary Shielding. Meteoroid trajectories can be dramatically altered when approaching a planet. The size of the gravitating body and the flyby geometry will cause the meteoroid trajectories to converge or diverge leaving regions of space behind the planet relatively free of meteoroids or intensely populated.[153] The probability of encounters with meteoroids increases for spacecraft whose orbits cross into these intensely populated regions. The effects of focusing and shielding on sporadic meteoroids (sporadics) is complicated by the fact that sporadics approach from all directions with varying speeds. Therefore, the gravitational field does not focus the sporadic meteoroids to a point. Instead, sporadics are focused to varying distances on the opposite sides of the Earth. Slower moving meteoroids such as those from an asteroidal source are focused more and their trajectories are altered more significantly than fast meteoroids from the apex source.

There have been several methods published and presented that describe the equations and geometries involved in planetary focusing and shielding (M. Matney, Private Communication, 2006).[154,155] While almost all methods accurately describe how the meteoroid trajectories are deflected, the focusing factors do not agree.

The Earth submodel of MEM can then be used to model the gravitationally focused and shielded meteoroids in Earth space out to the lunar sphere of influence. At that point, the Moon becomes the central influencing body on meteoroids, and, for first order calculations, the Earth's focusing effects at that distance are second order at best.

The following figures are examples of how sporadic meteoroids are influenced by the gravity field of the Earth. Plot (a) in figure 98 shows what the sporadic meteoroid environment looks like at 1 AU in a circular orbit around the Sun without the effects of focusing or shielding. Plot (b) shows the sporadic meteoroid environment in LEO at an altitude of 400 km. Both plots are relative to the local spacecraft frame and motion, and show flux intensity as a function of local azimuth and elevation. The darker red colors indicate a higher concentration of meteoroid flux. Also notice in plot (b) that the Earth is obviously shielding a large portion of the meteoroids, and that it is not a straight line cutoff but has a spherical shape due to the aberration effects of spacecraft motion

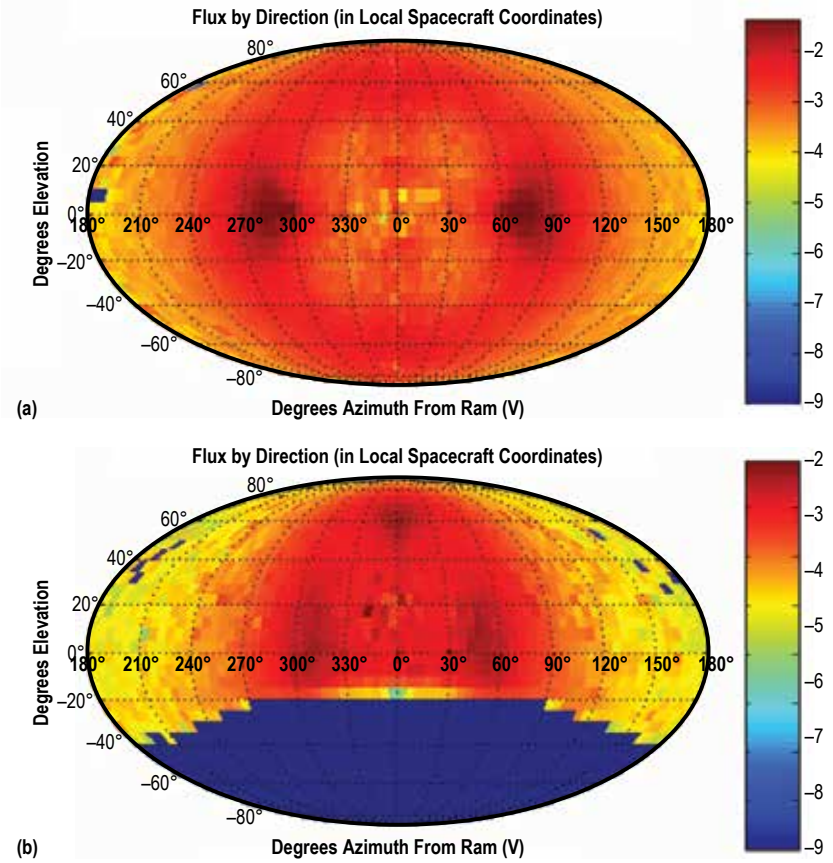

Figure 98. Flux intensity plots of the sporadic meteoroid directionality relative to local spacecraft coordinates moving in circular orbits at (a) 1 AU from the Sun and (b) 400 km above the Earth, respectively.

Table 85 shows the effects of focusing and shielding on a spacecraft in LEO compared to a spacecraft in a circular orbit around the Sun. The specifics of the orbits were described in the preceding paragraph.

Table 85. Flux and average speed values for ram/wake surfaces of spacecraft in circular orbits at 1 AU from the Sun and 400 km above the Earth, respectively.

Circular Orbit	Total Flux From All Directions (No./m^2/yr)	Ram Flux (No./m^2/yr)	Average Ram Speed (km/s)	Wake Flux (No./m^2/yr)	Average Wake Speed (km/s)
1 AU orbit (no focusing or shielding)	5.75	1.52	23.8	0.29	20.9
400 km Earth orbit (with focusing and shielding)	7.59	4.21	24.6	0.09	23.9

5.6.3.1.5 Meteoroid Densities. Meteoroid models of the past have assumed various densities for penetration calculations. It is currently accepted that most meteoroids are cometary in origin; based on the available evidence, such bodies are not homogenous spheres. They are porous conglomerates of ice and dust with a mean bulk density close to water. The hypervelocity effects of these cometary particles probably cannot be adequately represented by the aluminum projectiles used in orbital debris studies; experiments are encouraged to find substitutes that approximate the bulk density. The remainder of the meteoroid population originates from asteroids or, much less frequently, planets. These meteoroids will have a bulk density of approximately 2 g/cm^3 (4.8×10^{-4} lb/in^3); most experimenters use boro-silicate glass or olivine projectiles in hypervelocity tests, as these are thought to be adequate representations of this meteoroid type.

A recent meteoroid radar survey has compiled a database of over 1,000 meteoroids and presented a useful meteoroid density distribution.[156,157] Figure 99 shows these densities.

The following equation and table of values (table 86) are used to fit the density distributions presented in figure 101:

$$y = a\exp\left[-0.5\left(\frac{\ln\left(x / x_o\right)}{b}\right)^2\right]. \tag{63}$$

The mean bulk densities determined by the 3D spherical and overdense theories were 0.6 ± 0.5 and 0.7 ± 0.6 g/cm^3, respectively. These data are valid over the 10^{-6} to 10^{-4} g mass range. These densities are consistent with those determined by other researchers, a summary of which can be seen in SEE/TP-2004-400, section 2.6.[157]

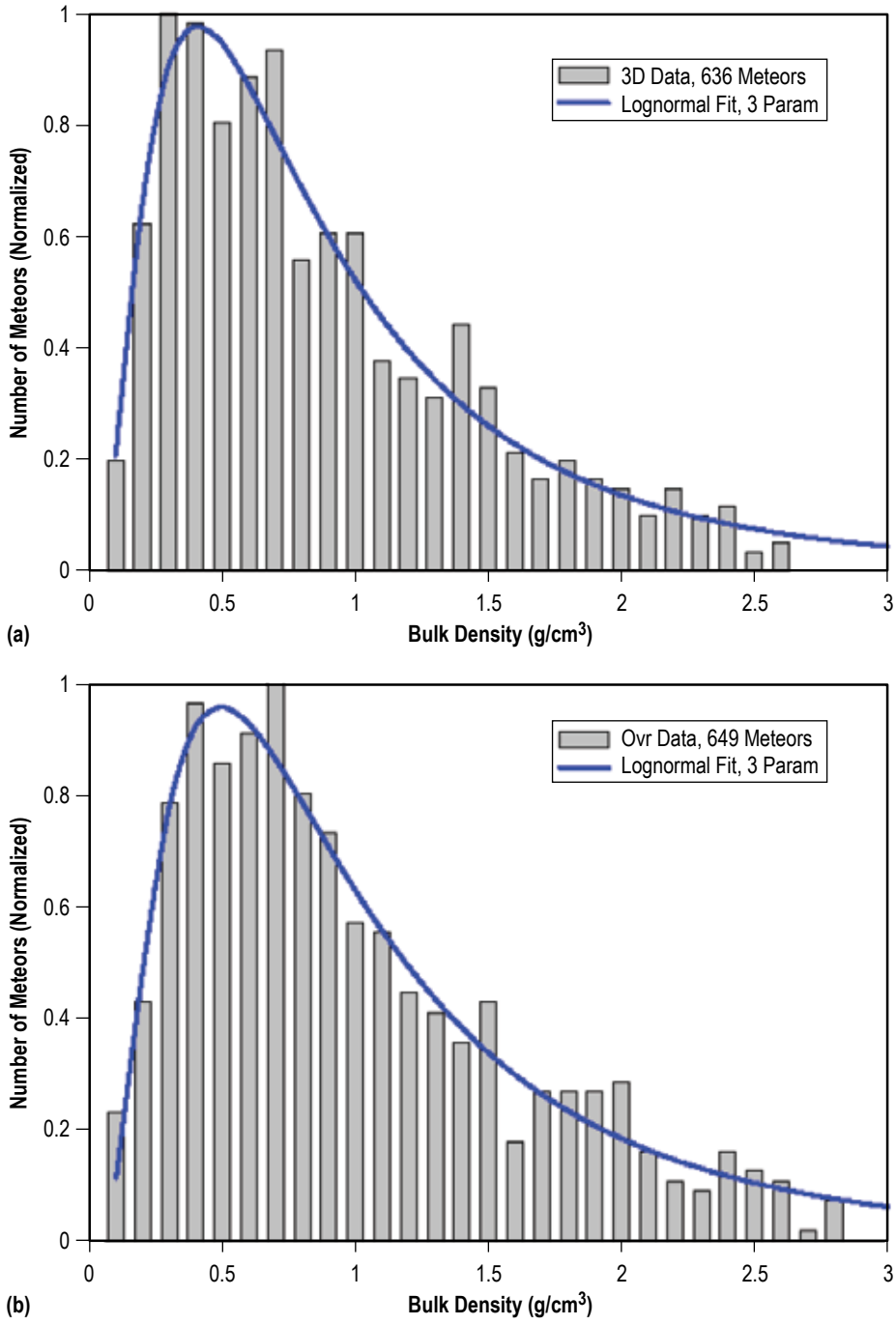

Figure 99. Bulk density histogram of very high frequency head echoes observed by Advanced Research Project Agency long-range tracking and identification radar calculated by (a) the third spherical model and (b) the overdense model.

Table 86. Parameters of the lognormal distribution.

Parameter	3D Spherical Model, R^2=0.9561		Overdense Model, R^2=0.96	
	Value	Standard Error	Value	Standard Error
a	0.9786	0.03362	0.9598	0.02903
b	0.799	0.03185	0.7698	0.02762
x_0	0.4086	0.01612	0.4927	0.01633

To convert from meteoroid mass to size, a spherical shape of particle can be assumed; see the following equation:

$$D = \left(\frac{6 \cdot Mp}{\pi \cdot \rho} \right)^{1/3} , \tag{64}$$

where D is the size of the particle in centimeters, Mp is the mass of the particle in grams, and ρ is the density of the meteoroid found by applying the distributions above.

5.6.3.2 Orbital Debris Environment Model and Analysis. The baseline model for defining the orbital debris environment will be ORDEM2000. ORDEM2000 is an empirical model based on data from a variety of sources. The model describes the orbital debris environment in the LEO region between 200 and 2,000 km altitude. The model is appropriate for those engineering solutions requiring knowledge and estimates of the orbital debris environment (debris spatial density, flux, etc.). ORDEM2000 can also be used as a benchmark for ground-based debris measurements and observations. The executable code for this model is available at the following Web site: <http://orbitaldebris.jsc.nasa.gov/model/engrmodel.html>.[158]

For all documentation, refer to the ORDEM2000 documentation. Particularly important is NASA/TP—2002–210780, the New NASA Orbital Debris Engineering Model ORDEM2000.[152] This Technical Publication documents the technical basis, verification, and validation of the model, and provides the best available information for estimating confidence limits on the environment definition. A detailed study of confidence limits has not been undertaken in the past because of the complexity of the problem and the dependencies on traffic model, satellite breakup rate, breakup locations, and debris population shape and material, all factors where the state of knowledge is very poor. These issues are currently being reviewed and new information will be presented in a forthcoming orbital debris handbook.

A large set of observational data (both in situ and ground based), covering the object size range from 10 μm to 10 m, was incorporated into the ORDEM2000 debris database. A new analytical technique, utilizing a Maximum Likelihood Estimator, was employed to convert observations into debris population probability distribution functions. The small particle portions of the model were based on the orbit distributions derived from the analysis of impact craters on the Long Duration Exposure Facility (LDEF) and on flux measured from the returned surfaces of the space shuttles, as well as other materials returned from space. To relate impact crater dimensions

to the properties of the debris particles, an assumption was made that the particles had the density of aluminum, 2.8 g/cm^3. Therefore, to be consistent with the model, a particle density of 2.8 g/cm^3 should be assumed for orbital debris for particles smaller than 1 cm diameter.

Figure 100 illustrates the orbital debris total flux prediction using ORDEM2000 for an ISS orbit: 51.6° inclination and 407 km circular orbit altitude for the year 2015 for various particle sizes. Figure 101 shows the orbital debris flux in a 28.5° inclination circular orbit at 277.8 km for the year 2015.

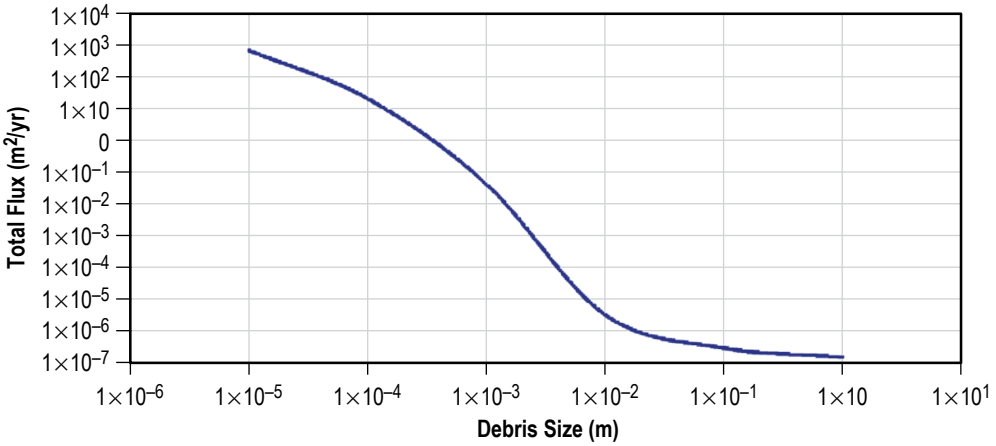

Figure 100. Orbital debris flux prediction using ORDEM2000 for an ISS orbit for the year 2015.

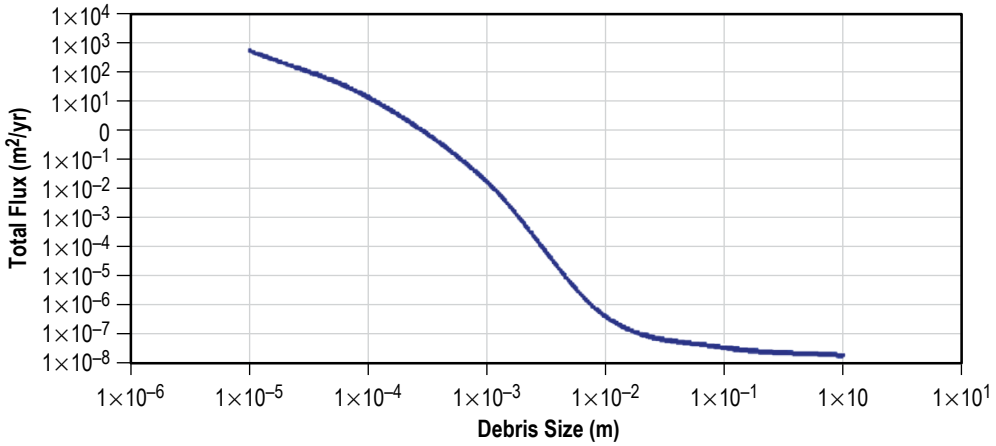

Figure 101. Orbital debris flux prediction using ORDEM2000 for the 28.5° inclination and 277.8 km circular orbit for the year 2015.

The previous figures are only 'snapshots' of the orbital debris environment at specific inclinations and years. ORDEM2000 also produces a directionality plot called the 'butterfly' plot, which is very useful in understanding the directionality of debris in LEO. Changing these inputs to the model will produce different results. Spacecraft designers and users of the environment models are encouraged to understand all the assumptions, limitations, and features of the environment models so that they will be an aid and not a hindrance in performing risk assessments and design options.

5.6.4 Meteoroid and Orbital Debris Protection

The design considerations for meteoroids and orbital debris are much the same, except that orbital debris provides the greatest penetration threat because impact from large (5 to 15 mm) particles are much more likely to be debris, while smaller but very high-speed particles are more likely to be meteoroids. These have the potential to cause electrical damage from impact-induced plasma. In either case, hypervelocity impacts release large amounts of energy with associated flash, plasma, shock waves, secondary debris, etc. capable of causing extensive damage. Even impacts from small particles 'erode' surfaces over time, resulting in degraded performance of solar arrays, optical surfaces, and other exposed components.

The reader should be aware of the following terms frequently used within the meteoroid and orbital debris (M/OD) technical community:

- Critical item: An item whose loss of function or destruction could cause loss of crew or loss of vehicle. Enumeration of these items should be consistent with the Failure Modes and Effects Analysis/Critical Items List usage within the program.

- Penetration: 'Through hole' damage or detached spall damage to an item of interest. The focus on complete through hole damage is a result of historical usage, and confusion can result concerning partial penetration (cratering) that can still result in critical failures of some systems. Perforation is another frequently used word to describe complete penetration creating a through hole. It is best to add clarification if there is any chance of misinterpretation.

- Probability of no penetration: Probability that no M/OD will penetrate an item of interest. To be properly quantified the associated exposure period must also be specified.

- Probability of no critical failure: Probability that M/OD impact will not cause loss of any critical function, either immediately or by secondary or delayed effects. Such loss may be by any mechanism, complete or partial penetration, spall, plasma discharge, shock damage, etc. Application is to the total of all critical functions and failure modes, not individual function or mechanism. Again, the exposure period must also be clearly specified.

Following is a list of options for crew and space vehicle protection that may be useful. Arriving at a safe and cost-effective design for any future space vehicles will doubtless require systems level analysis and planning to arrive at a successful integrated solution.

5.6.4.1 Collision Avoidance. The easiest way to avoid critical damage from a large orbital debris impact is, in many cases, to not get hit. Currently, the Air Force Space Command tracks orbital debris larger than approximately 10 cm in diameter and works with NASA to provide collision avoidance warnings to high value assets, i.e., the Shuttle and the ISS. More importantly, the Air Force has undertaken programs to greatly improve the tracking and warning capabilities of the space surveillance network. The goal is to concurrently increase the precision of the process so that the number of maneuvers needed to maintain the current level of safety does not dramatically increase.

5.6.4.2 Robust Design. Selection of impact-resistant materials and design concepts, especially for the Thermal Protection System (TPS) and other subsystems located on or near the vehicle exterior, goes a long way toward adequate impact M/OD protection. Internal thermal barriers that increase allowable TPS damage before failure; redundant, self-healing, or self-sealing coolant loops; self-shielding structures, etc., may all prove effective. Use of redundant systems is one of the most effective means of increasing overall system reliability from all types of failure modes, and M/OD impact is certainly no exception. Redundant and primary hardware components should be physically separated so that they are unlikely to be harmed by the same impact.

5.6.4.3 Shielding. Shielding is the most common protection system implemented with vehicle design and may be added internally, externally, or it may be deployable. While shielding provides an easy and cost-effective means of protection from the extremely numerous small particles, it becomes significantly more difficult and costly for particles 5 mm in diameter and larger. For each system, the level of shielding to be added must be weighed against the added weight, complexity, and cost. For simple metallic structures (single surfaces and bumper configurations), extensive test data and empirical equations allow the shielding effectiveness to be easily evaluated. However, for complex structures (honeycomb, meshes, and foams) and nonmetallic structures, the body of existing test data is very limited and equations are typically not available. Thus, for these cases, shielding effectiveness must be evaluated by test.

5.6.4.4 Orientation. Both the meteoroid and orbital debris environments are directional, but meteoroids approach from several directions fixed in Earth-Sun coordinates, so a vehicle's orbital motion smoothes out much of the directionality (viewed in vehicle coordinates) over long periods of time; for short duration missions, this may not be the case. On the other hand, the orbital debris flux is highly directional. The flux is nearly all in the local horizontal plane with the specific distribution a function of orbit inclination and altitude. In the ISS orbit at a 51.6° inclination and a 450 km altitude, the flux peaks from 30° to 60° either side of the spacecraft velocity direction. The selection of a vehicle aspect ratio and adoption of an operating orientation that minimizes the area presented to the flux will help minimize the threat. Shield location, thermal radiator orientation, and the location of critical components with respect to other structures should all be determined with the directionality of the debris threat in mind. Clearly, the orientation during the greatest duration of on-orbit segments of the mission, e.g., while docked to the ISS, is the most important.

5.6.4.5 Crew Escape. A hypervelocity impact from a large object on the core of a vehicle would most certainly be so energetic that the spacecraft would be completely and instantaneously

destroyed. However, such impacts are very rare compared to impacts from smaller objects, or impacts to exterior structure, which cause extensive damage to critical systems but leave much of the vehicle intact. Therefore, it is important to consider M/OD impact when developing the overall configuration of the vehicle, especially the crew compartment and life support systems. If the crew is protected from the initial impact and life support can be maintained, various options may be available to save the crew, including:

- Safe haven with rescue by another vehicle.

- Safe abort, if there is still reentry capability.

- Abort to ISS if the vehicle and station are docked, or if rendezvous is possible.

Two important aspects are:

- Configuration development and contingency planning that allow for rescue.

- Damage isolation and protection/inerting of onboard stored energy in order to prevent the amplification and propagation of damage following the initial impact.

5.6.4.6 Operational Protection—Meteoroids. In effect, one designs a vehicle to withstand only the sporadic meteor background and the average meteor shower environment. However, models such as MEM incorporate a yearly average shower flux for design purposes. The occasional meteor outburst or storm is mitigated operationally. For the most important showers, modern computer models enable meteor shower activity to be forecast with adequate accuracy well in advance. These forecasts project both the magnitude and duration of the enhanced shower or storm period, enabling the vehicle managers to decide upon the appropriate course of action. Actions that have been adopted by current spacecraft include:

- No launches during enhanced meteor activity (Space Shuttle during 1993 Perseids and 1998 to 2001 Leonid showers).

- No EVAs during enhanced meteor activity (ISS, 2001 Leonids).

- Solar arrays turned edge-on to direction of meteor stream (numerous unmanned vehicles).

- Sensitive surfaces and optics pointed away from direction of meteor stream (Hubble Space Telescope, Chandra X-ray Observatory, other vehicles).

5.6.4.7 Pressurized Tanks and Volumes. Hypervelocity impacts release very large amounts of energy in a very small space and time. One of the key considerations in M/OD protection is ensuring that the hot plasma flash and pressure wave created by this energy do not trigger additional damage by interaction with other onboard stored energy sources. Examples include burning of flammable materials; explosion of stored propellants, high-pressure bottles, high-pressure lines, or batteries; and release of pressurized gasses leading to unwanted propulsion and 'unzipping' of

the walls of pressurized volumes. Design measures for mitigating these risks include, in addition to adding shielding, dumping unneeded propellants, inerting stored energy devices, using self-sealing tanks and lines, employing automatic leak detection, and implementing isolation systems.

5.6.4.8 Damage Detection and Fault Isolation. Automatic damage detection and fault isolation capability are standard methods of improving system reliability that are also important for the M/OD problem. Quick detection and isolation of a breached system may prevent a serious loss of critical fluids. On-orbit damage detection and perhaps repair could be very important for protecting systems such as large propellant tanks where the failure might not be otherwise evident until a later phase of the flight, reentry for instance.

5.6.4.9 Wire Routing and Shielding. One easily overlooked problem area is the vulnerability of unprotected wires to meteoroid or debris impact. Very small (and thus numerous) particles are often capable of penetrating wire insulation and coaxial shielding, as well as cutting the wire itself. On low-voltage wires, breaching the insulation may not be problematic, but for voltages above ≈100 V, the plasma created by the impact can initiate a sustained short that would burn out the wire or power source. Structure penetrations by larger particles create a cone of secondary debris that can also damage wires and cable bundles. For these reasons, redundant wires/cables in critical systems should be separated by sufficient distance to ensure that they are not taken out by a single impact, more than 30 cm, if possible. In addition, cable shielding should be reviewed and augmented if necessary to prevent damage to the insulation from small particle and secondary particle impact.

5.6.4.10 Radiator Design. Design measures have been taken to shield STS thermal radiators from M/OD penetrations, as shown in figure 102. Similar considerations may be useful for future space programs.

Additional radiator system upgrades include:

- Double-layer beta cloth sleeve added to panel interconnect flex lines and hard external lines.
- Automatic isolation valves added to each loop (port and starboard).

5.6.4.11 Window and Surface Degradation. Impact craters from the multitude of small particles that continually bombard external vehicle surfaces are also small, typically 3 to 5 times the diameter of the generating particle. Thus, damage to surfaces accumulates relatively slowly and degradation is often not a problem; however, there are some exceptions. One exception is the windows, where optical properties are important and crack propagation is an issue. On the average, three windows were replaced on the Shuttle for every two flights. Thought should be given to window protection and easy replacement. Another exception is certain types of laminated materials. Experience on LDEF showed that impacts caused delamination in some materials to diameters 50 to 100 times the diameter of the impact crater. A third potential issue is synergistic effects. Atomic oxygen and plasma (arcing) effects may be triggered or enhanced by M/OD impacts in some cases.

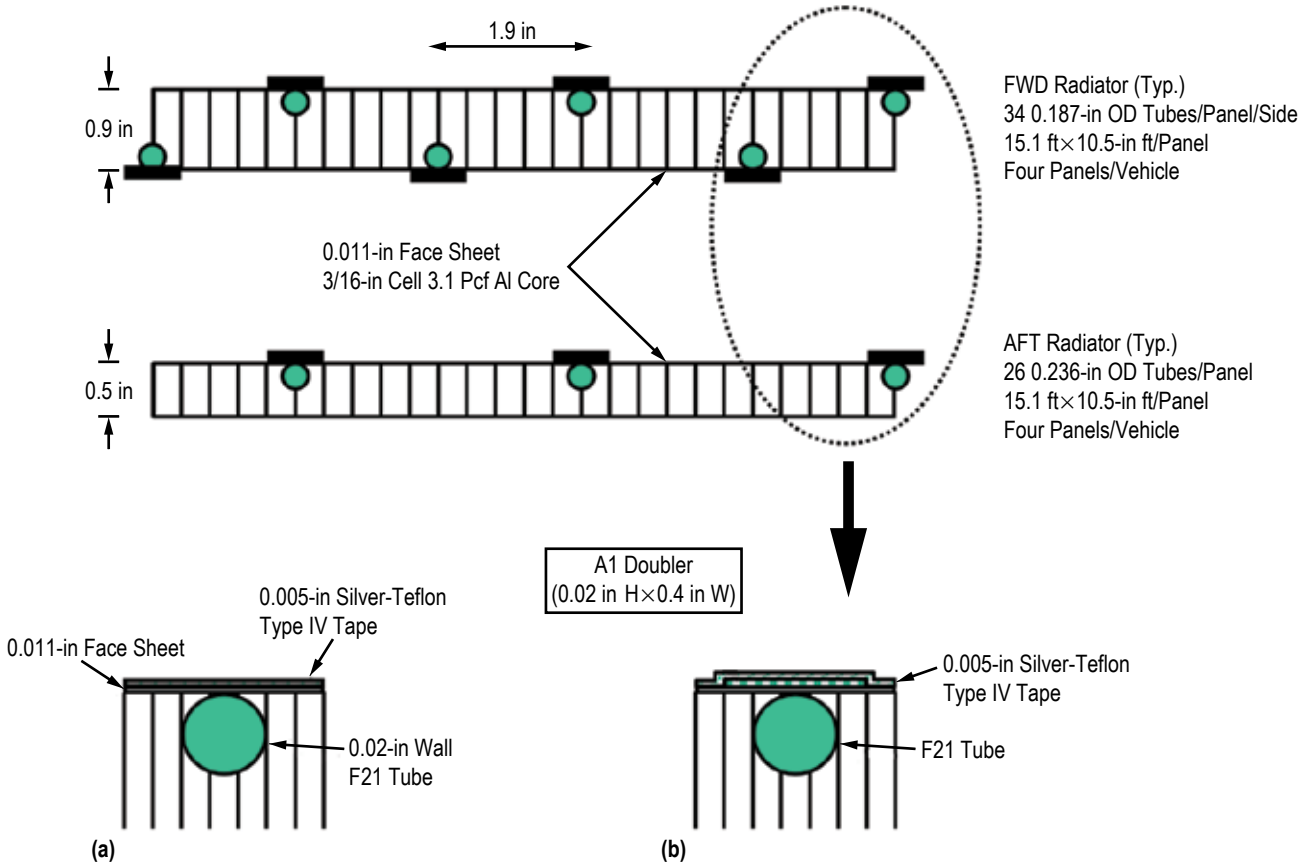

Figure 102. Design measures to shield STS thermal radiators from M/OD penetrations: (a) Before M/OD and (b) after M/OD.

5.6.4.12 Plasma Effects. The apparent fate of the Olympus spacecraft in 1993 (discussed in sec. 5.6.1.2) illustrates a less obvious, yet potentially dangerous effect of meteoroid impact upon a vehicle surface: plasma discharge. Plasma is released in all hypervelocity impacts, but the plasma produced goes as v^4, whereas the total energy goes as v^2. High-speed meteoroids from streams such as the Leonids and Perseids (especially if they strike a spacecraft with a substantial surface potential), can produce intense conducting plasma that can result in a large electrical discharge in and around the spacecraft surface. Should this discharge be near electronic devices, disruption or destruction of the devices may result. This threat is mitigated by both the operational methods noted above, and, more importantly, by good electrical design from a spacecraft charging, electromagnetic interference, and compatibility point of view.

5.7 Gravitational Field

Since the advent of Earth satellites, there has been a considerable advancement in the accurate determination of the Earth's gravitational field. The current knowledge regarding the Earth's gravitational field has advanced far beyond the normal operational requirements of most space

missions. Adequate accuracy for determining most spacecraft design values of gravitational interactions is obtained with the central inverse square field:

$$\vec{F} = \frac{\mu_E m}{r^2} \hat{r} \ , \tag{65}$$

where

$\vec{F}$ = vector force acting on a particle (N)
μ_E = gravitational constant for the Earth
m = mass of particle (kg)
$\hat{r}$ = unit vector pointing from the center of the Earth to the particle
r = distance between particle and center of Earth (m).

The above central force model accurately represents the gravitational field to approximately 0.1%. If this accuracy is insufficient for particular program needs, a more detailed model of the gravitational field can be used that accounts for the nonuniform mass distribution within the Earth, the primary effect of which is the precession of the plane of the orbit. This model gives the gravitational potential, V, to an accuracy of approximately a few parts in a million. The gravitational acceleration is expressed in terms of the negative gradient of the potential. The potential is then expressed using harmonic expansion:

$$\vec{F} = m\vec{g} = m\left(-\vec{\nabla} V\right) , \tag{66}$$

where

$\vec{F}$ = vector force acting on a particle (N)
m = mass of particle (kg)
$\vec{g}$ = accelerator vector
$\vec{\nabla}$ = vector differential operator.

The formula for V is shown below:

$$V(r,\phi,\lambda) = \mu_e / r \left\{ \left(\Sigma\Sigma R_e / r \right)^n P_{nm}(\sin\phi) \left[C_{nm} \cos(m\lambda) + S_{nm} \sin(m\lambda) \right] \right\} , \tag{67}$$

where

ϕ = geocentric declination
λ = east longitude.

For the Marsh et al.[159] model discussed below,

μ_E = 3.9860064×10^{14} Nm^2/kg
R_e = 6,378.137 km
Z = the Z component of the spacecraft geocentric position vector.

The coefficients C_{nm} and S_{nm} are the harmonic coefficients of the potential function, and P_{nm} represents the associated Legendre functions of the first kind of degree n and order m. Because $\sin\phi = Z/r = \nu$, it is simply a function cosine and the associated Legendre function may be expressed as:

$$P_{nm} = \frac{\left(1-\nu^2\right)m/2}{2n\,n!}\frac{d^{n+m}\left(\nu^2-1\right)}{d\nu^{n+m}}\,. \tag{68}$$

5.7.1 Spacecraft Effects

Accurate predictions of the Earth's gravitational field are a critical part of mission planning and design for any spacecraft. The Earth's gravitational field will affect spacecraft orbits and trajectories. Gravity models are used to estimate the gravitational field strength for use in designing the GN&C pointing subsystem, and for designing the telemetry, tracking, and communications. The available gravitational models have sufficient accuracy for estimating the gravitational field strength for spacecraft planning and design including rendezvous and docking missions.

5.7.2 Gravity Recovery and Climate Experiment Earth Gravity Model GGM02C

Gravitational models of the Earth are continually being updated and upgraded. Currently, gravitational models are available for varying degrees of accuracy. For operational applications and other situations where computer resources are a premium, 'best fit' approximations to the highest accuracy model may be utilized, which minimize the computational requirements yet retain the required accuracy for the specific application.

The Earth gravity field recommended for use is the Gravity Recovery and Climate Experiment (GRACE) Earth gravity model (GGM02C). This is a 200th spherical harmonic degree and order model that combines approximately a year of GRACE K-band range rate, attitude, and accelerometer data with surface gravity and mean sea surface information. The model was produced by Byron Tapley et al. at the University of Texas[160] and released on October 29, 2004.

6. MEDIUM AND HIGH EARTH ORBITS (2,000 km TO 10 R_e)

6.1 Thermosphere

Reference section 5.1 for more information about the thermosphere. Gases are negligible in the region 2,000 km to 10 R_e.

6.2 Thermal Environment

The description of the thermal environment in section 5.2 still applies above 2,000 km. However, the dominant cause of the very short duration variations in long wave and albedo are caused by the motion of the satellite over the changing terrain below. The data in section 5.2 were derived from measurements made by satellites in the 610 to 850 km range. When orbiting above 2,000 km, the greater distance to Earth and increased area viewed will tend to smooth out the short period variations of albedo and long-wave radiation.

6.3 Geomagnetic Field

A dipole magnetic field configuration dominates the magnetic field topology within a few R_e of the planet. The dipole field is generated in the Earth's liquid outer core and controls plasma and energetic particle populations throughout the inner magnetosphere. Significant distortions appear in the dipole field configuration at distances beyond 4 to 6 R_e from the Earth due to currents produced by the interaction of the solar wind with the outer regions of the magnetosphere. The boundary between the magnetosphere and the solar wind, the magnetopause, is characterized by a current sheet (the 'Chapman-Ferraro current') that provides the force balance between the inward-directed dynamic pressure of the external solar wind and the outward-directed stress of the Earth's magnetic field. The dipole center is approximately 400 km distance from the center of the planet. The geomagnetic axis is inclined at approximately 11.7° to the Earth's rotational axis.

The interaction of the geomagnetic field at very great distances (several R_e) with the solar wind is one of the heat sources for the neutral thermospheric region. The solar wind is a stream of high-speed plasma emanating from the Sun. This interaction causes energetic particles to penetrate down into the lower thermosphere at high geographic latitudes and directly heat the thermospheric gas.

A general description of the geomagnetic field is provided in section 5.3. While the description provided there is generally applicable above 2,000 km, different models may be used to provide quantitative information about the field in the 2,000 km to 10 R_e region.

6.3.1 Geomagnetic Field Model

Satellites (IMP, Highly Eccentric Orbiting Satellite, International Sun-Earth Explorer, Potentials of Large Spacecraft in Auroral Regions (POLAR), GEOTAIL, etc.) investigated the magnetic field of the Earth for several decades. Data obtained were sufficient to apply to model development with its average strength and shape during different levels of overall magnetic activity.

6.3.1.1 Tsyganenko Model. The Tsyganenko model is the most used empirical global magnetic field model for applications above 2,000 km. The Tsyganenko model is a semi-empirical, best-fit representation for the magnetic field based on a large number of satellite observations. The model includes the contributions from external magnetospheric sources: ring current, magnetotail current system, magnetopause currents, and large-scale system of field-aligned currents. The latest models include T95 and T96_01.[161,162] All of these realistic models start from the official IGRF model, which is improved by adding magnetospheric current systems that modify it toward the true, observed configuration. In the series of figure 103, the magnetospheric topology is seen to be dependent on the season. The K_p index in this study is taken to be 2.

6.3.2 Geomagnetic Field Effects

The Earth's magnetic field exerts a strong influence on space environmental phenomena including ionizing radiation and plasma activities, electric currents, and trapped high-energy charged particles. This influence has important consequences to spacecraft design and performance. Details of the geomagnetic field effects are discussed in section 5.3.2.

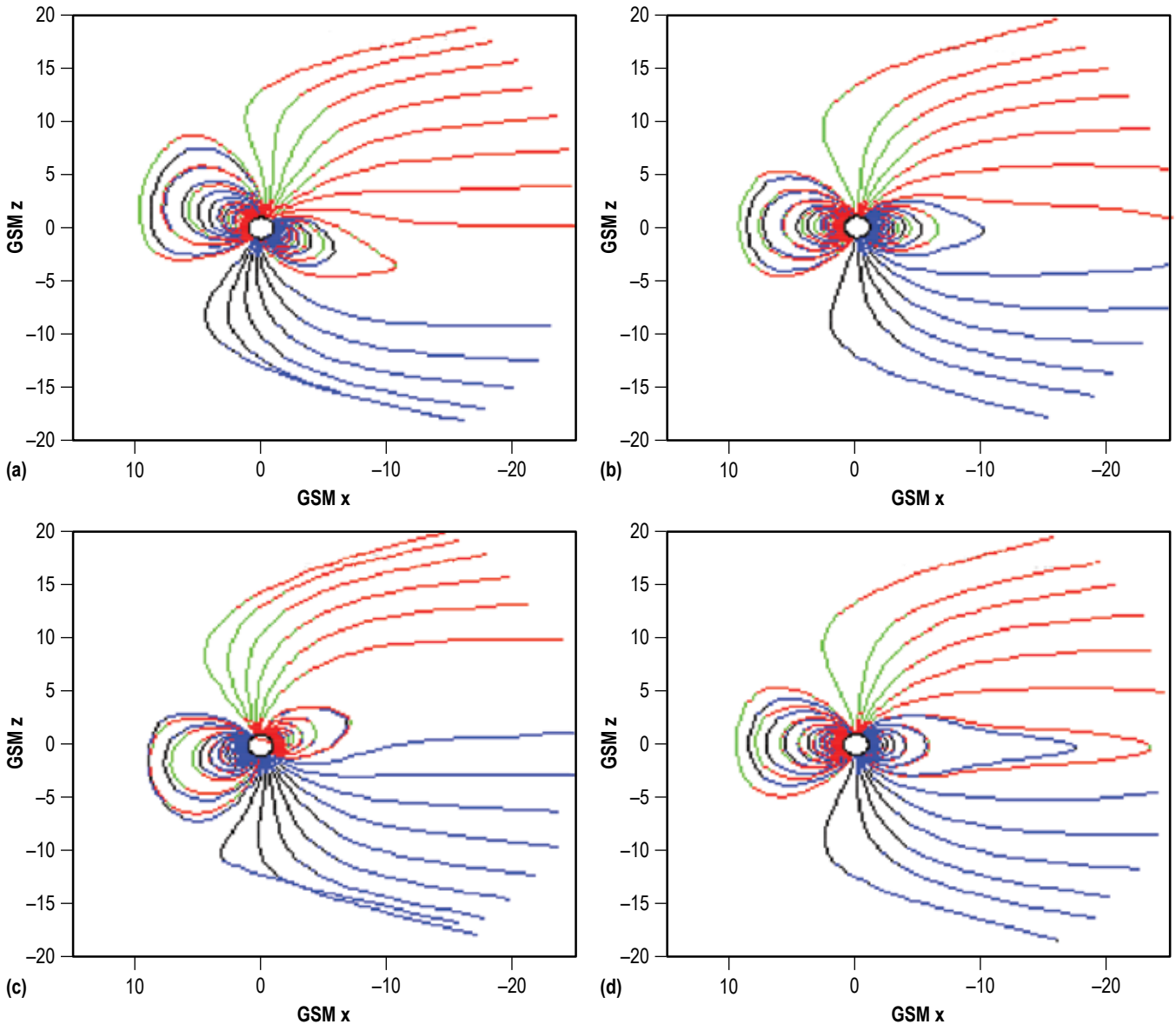

Figure 103. Earth's magnetic field from Tsyganenko model during $K_p = 2$ for different seasons: (a) Winter, (b) spring, (c) summer, and (d) fall.

6.4 Plasma Environment

A summary of key design factors for the plasma environment is displayed in table 87.

Table 87. Summary of key design factors.

Parameter	Source	Spacecraft Design Consideration Factors
For prediction of ambient/ energetic plasma conditions:		
Solar winds	Section 6.4.3/table 88	Spacecraft charging
Plasma density	Figure 108	Spacecraft charging
Plasma temperature	Figure 108	Spacecraft charging
Plasma measurements and spacecraft charging guidelines evaluation for spacecraft charging:		
Plasma density	Figure 109	Spacecraft charging
Plasma temperature	Figure 109	Spacecraft charging
Charging predictions	NASCAP/GEO/section 6.4.7	Spacecraft charging

Note: For other plasma effects and guidelines see section 5.4.6.

6.4.1 Plasma Regimes in Near Earth Space

Figure 104 illustrates the main features of the magnetosphere, the region of space dominated by the terrestrial magnetic field. The dipole field, dominant near the Earth, is compressed by the solar wind flow on the dayside and stretched into the extended magnetotail on the nightside of the Earth. The dipole field is generated in the Earth's liquid outer core and controls plasma and energetic particle populations throughout the inner magnetosphere. This schematic illustrates the main features of the near-Earth (<20 R_e) magnetosphere in the noon-midnight plane. The field is offset from the Earth's center of mass by approximately 400 km and inclined approximately 11° with respect to the rotation axis of the solid Earth.[134] Significant distortions appear in the dipole field configuration at distances beyond 4 to 6 R_e from the Earth due to currents produced by the interaction of the solar wind with the outer regions of the magnetosphere. The magnetopause, a boundary between the magnetosphere and the solar wind, has a current sheet (the Chapman-Ferraro current). The current sheet provides the force balance between the inward-directed dynamic pressure of the external solar wind and the outward-directed stress of the Earth's magnetic field.

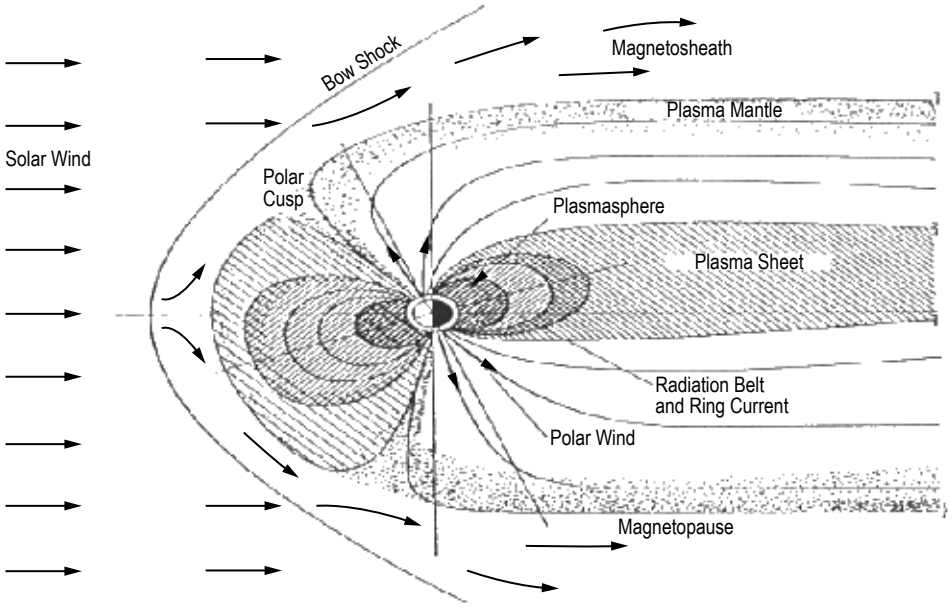

Figure 104. Near-Earth magnetosphere.

Above the ionopause/plasmapause boundary (defined by the sharp density gradients at the outer reaches of the plasmasphere), but within the region of closed magnetic field lines, the plasma is still dominated by photoionized terrestrial particles, but energy input from the solar wind-magnetosphere interaction may accelerate particle-producing regions of energetic ions and electrons within the magnetosphere.

The solar wind significantly compresses the geomagnetic field on the dayside of the Earth, and the dayside magnetopause is typically 10 to 14 R_e from the Earth in the direction of the Sun. Approximately 2 to 3 R_e upstream of the dayside magnetosphere is a shock wave (the 'bow shock') formed where the supersonic solar wind flow is abruptly decelerated upon encountering the magnetosphere. The temperature of the solar wind plasma increases upon traversing the bow shock, as its forward motion is converted to random thermal energy, and its density increases as the plasma stagnates and builds up in front of the magnetosphere in the subsolar region. Plasma in the magnetosheath (the region between the bow shock and the magnetopause) flows around the magnetopause in the same sense as the free solar wind flow. Anti-sunward of the Earth, the solar wind interaction stretches the geomagnetic field for at least several hundred Earth radii, forming the extended magnetotail. The magnetotail has been detected by satellites as far as 500 to 1,000 R_e from the Earth.

The GEOTAIL satellite was launched on July 24, 1992, to study the structure and dynamics of the tail region of the magnetosphere with a comprehensive set of scientific instruments. For this purpose, the orbit has been designed to cover the magnetotail over a wide range of distances, 8 to 210 R_e from the Earth. This orbit also allows us to study the boundary region of the magnetosphere as it skims the magnetopause at perigees. Another spacecraft mission, the Chandra spacecraft, flies with a perigee of 10,000 km, an apogee of 140,000 km with the magnetic latitude of the

orbit inclination at the beginning and the end of the mission between 28.5° and 52°. The spacecraft may encounter the solar wind, plasma sheet, polar cap, auroral, and radiation belt regions within a single orbit. This indicates that the spacecraft will experience several different regimes in orbit.

Some regions in the magnetosphere are well defined and have distinguishable boundaries. Others have particle populations that overlap, making identification difficult. Further complicating the picture are the dynamic properties of this area of space. For example, during a geomagnetic storm, plasma sheet particles can rapidly move in the midnight sector, which causes many of the regions to change size, shape, and plasma composition. Plasma regions that may encounter the charging phenomenon include polar cusp, auroral region, radiation belt, magnetotail, plasma sheet, and plasmasphere. The characteristics of plasmas in each region vary depending upon time, location, geomagnetic storm, and solar activity. The magnetospheric region and characteristics have been described in several publications.[115,163,164] A brief description of the plasma environment characteristics in each region of the magnetosphere is provided in the following sections.

6.4.1.1 Plasmasphere. The plasmasphere extends out to as little as 2 to 3 R_e and, under quiet conditions on the evening side, to more than 6 R_e depending on space conditions and varying region boundaries. The actual extent of the plasmasphere is variable and depends on space weather activity. High levels of activity erode the plasmasphere and the plasmapause (the outer edge of the plasmasphere) moves inwards towards Earth; long periods of quiet allow the plasmasphere to expand outward towards geostationary orbit and beyond. The plasma within the plasmasphere contains cold (1 to 30 eV) and dense (>10 cm^{-3}) plasma surrounding the Earth. During periods of high magnetic activity, the plasmasphere recedes inward, well within the geosynchronous altitude. The plasmapause is characterized by a steep gradient in low energy plasma density. The plasma density can drop by over 3 orders of magnitude within approximately a 1,000 km band in the equatorial plane. Data obtained from Orbiting Geophysical Observatories' five measurements indicated a composite of several typical plasmapause crossings representing different levels of magnetic activity.[165] The plot of H^+ concentration versus L value represents all of the outbound passes in the local time region from midnight to 04:00 hours during the Dynamics Explorer-1 mission (reference fig. 105).

6.4.1.2 Plasma Sheet. The plasma sheet lies beyond the plasmapause and is clearly identifiable on the nightside, where it extends down tail to several tens of R_e. The temperature of charged particles in this region can go to several tens of kiloelectronvolts. The plasma density is normally <1 cm^{-3}. The plasma sheet expands and contracts during solar and magnetic activity. During high activity periods, the earthward edge of the plasma sheet in the equatorial plane can extend inward to <5.5 R_e; during prolonged magnetically quiet periods, the inward edge can lie beyond 10 R_e.

6.4.1.3 Ring Current. The ring current, defined as a western electric current that flows above the geomagnetic equator, is located in the outer Van Allen radiation belt. The ring current, composed primarily of hot trapped ions with energies approximately 10 to 100 keV, lies mostly earthward of the inner edge of the plasma sheet. The outer boundary of the ring current is dependent on particle energy, equatorial pitch angle, and local time. A partial ring current can also exist in the midnight region near geosynchronous altitude.

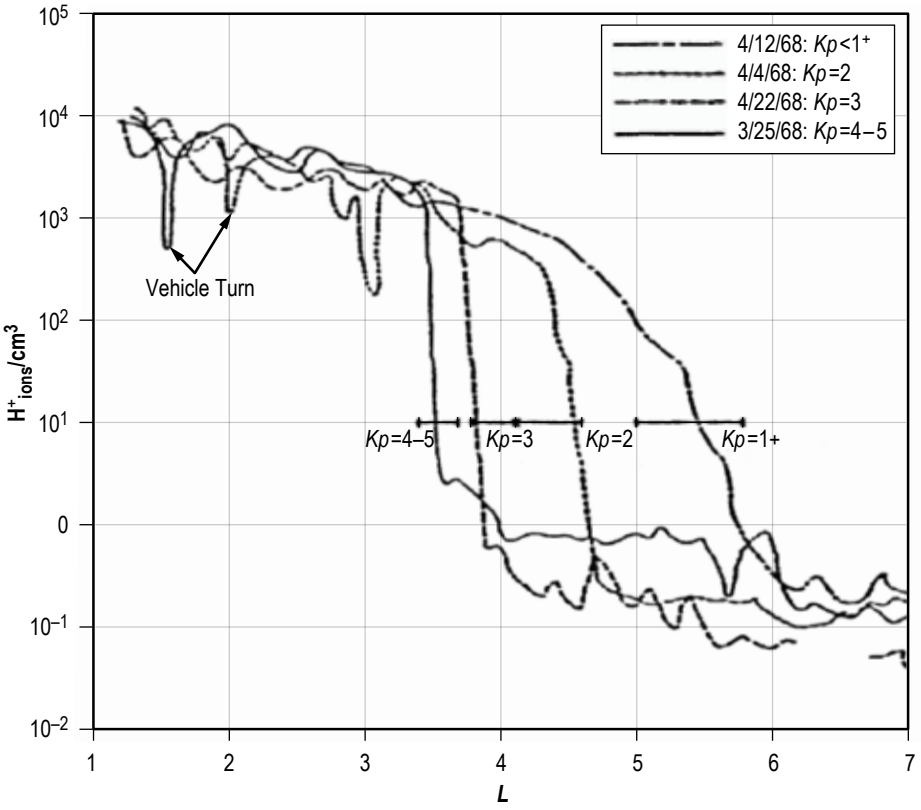

Figure 105. A composite of several typical plasmapause crossings representing different levels of magnetic activity (plots of H^+ versus L represent all of the outbound passes in the local time region from midnight to 04:00.74).

6.4.1.4 Magnetotail. The magnetotail is an extended magnetospheric region on the anti-sunward side of the Earth to at least 100 R_e. The magnetotail is essentially parallel to the solar wind flow in the magnetosheath region. In order to sustain this structure, the tail itself has a two-lobed structure where magnetic field lines from the Earth are divided by the plasma sheet that carries a larger current separating the two regions of oppositely directed magnetic fields.

6.4.1.5 Radiation Belt. The radiation belt of the magnetosphere roughly lies between 1.2 and 6 R_e above the equator in which charged particles (electrons with energies approximately 0.1 to 500 MeV and trace quantities of heavier ions) are trapped by the geomagnetic field. The outer boundary is near the magnetopause on the sunward side (~10 R_e under quiet conditions, ~6 R_e on the nightside); however, due to the distortion of the magnetic field, the boundary may lie well beyond that altitude.

6.4.2 Solar Wind

Solar wind is the plasma source in this region. The solar wind is an extension of the Sun's corona into interplanetary space. As the plasma moves away from the Sun, it expands and cools,

with the electron temperature decreasing from 1 million K (~ 100 eV) in the corona to ~ 100,000 K (~10 eV) near the Earth. The solar wind is supersonic (with speed ranges from 200 to 900 km/s) and consists of electrons, protons, and alphas. These particles coming from the Sun cannot pass through the Earth's magnetosphere and are forced around it. Thus, the solar wind piles up and creates a bow shock in front of the Earth. These parameters vary considerably with time, but are consistent with gross charge quasi-neutrality. The ionic constituents are chiefly protons with a small percentage (~4) of alpha particles. The solar wind can vary markedly on an hourly basis and is highly structured throughout the solar system because of time variations, shocks, CMEs, and flares. Despite this marked variation, it is useful to provide average values for the parameters describing the interplanetary medium near the Earth. Table 88 compares the plasma characteristics near the Earth for low speed, high speed, and average solar wind conditions.

Table 88. Solar wind parameters near the Earth.

Plasma Parameter	Average	Low	High
n (cm^{-3})	8.7	11.9	3.9
u (km/s)	468	327	702
Tp (K)	1.2×10^5	0.34×10^5	2.3×10^5
Te (K)	1.4×10^5	1.3×10^5	1×10^5

6.4.3 Plasma Characteristics

The plasma characteristics, generally described in terms of plasma density and temperature, can be used to define the appropriate particle distribution function shown in section 5.4. The plasma environment in high altitude orbit is a dynamic medium that exhibits large, daily property variations. Essentially, all major parameters can vary over at least 2 orders of magnitude daily. Dynamic changes in the plasma environment can produce large potential differences on spacecraft that might not otherwise develop during time-stationary plasma conditions. The extent of the variations and the expected resulting effects on levels of expected spacecraft charging have been well documented for GEO. In GEO, plasma thermal current densities can be 3 orders of magnitude less than in LEO, so that photoelectron emission from surfaces can play a significant role in balancing currents to a spacecraft. Sun/shade effects become important to the point that potentials as large as several kilovolts can develop between sunlit and shaded surfaces (depending on geometry and material properties).

Currently, the GEOTAIL satellite is orbiting in 9×30 R_e with an inclination of –7° to the ecliptic plane. Figure 106 describes plasma characteristics and its variation during the GEOTAIL mission from February 25, 2005, through March 1, 2005 (plot courtesy of University of Iowa Comprehensive Plasma Instrument team). Each survey plot is a 5-day record of the electron and ion intensities and several parameters derived from those intensities. The measurements are given in a sequence of five panels. From top to bottom, the panels display the following:

- N (cm^{-3}), the ion number density.
- V_x (km/s), the component of the ion bulk-flow velocity along the Earth-Sun line. Positive flow is towards the Sun.

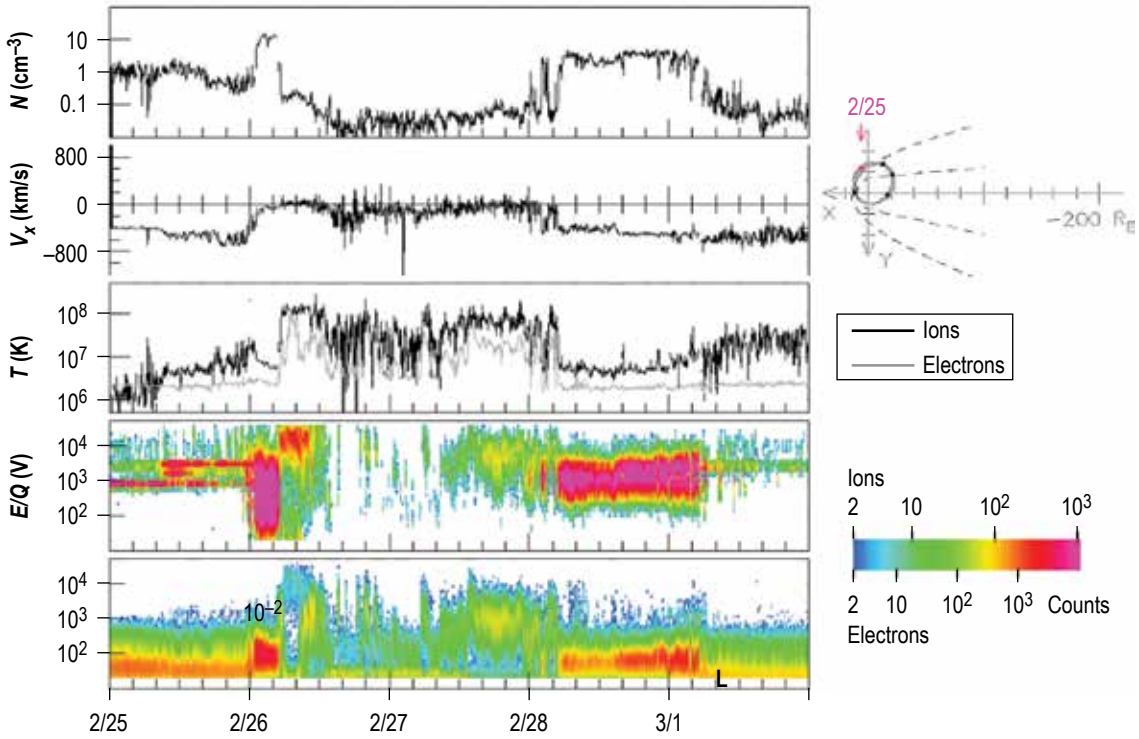

Figure 106. Demonstration of plasma density and temperature variation during the GEOTAIL mission from February 25, 2005, through March 1, 2005 (updates to the plasma environments are planned when new data are available).

- T_i and T_e (K), the respective temperatures of ions and electrons.
- The intensities of positive ions as a function of particle energy.
- The intensities of electrons as a function of particle energy.

6.4.3.1 Geosynchronous Altitude Plasma. The geosynchronous altitude plasma environment is very complex and dynamic. Charged particle flux in geostationary orbit can be quite energetic and is highly variable with magnetic activity, reaching the highest density and temperature during geomagnetic substorms. Plasma parameters listed in table 89 (adapted from ref. 129) represent the average, 90th percentile, and worst case geostationary orbit plasma environments derived from the spacecraft charging at high altitudes (SCATHA) spacecraft mission, assuming bi-Maxwellian representations for the environment. The strongest charging conditions will be encountered in the extreme environments where the high electron flux in the hot plasma environment drive spacecraft potentials to large negative values before equilibrium potentials are established on the spacecraft structure.

Table 89. Geoplasma parameters (adapted from ref. 29).

Parameter	Average Environment*		90% Environment**		SCATHA Worst Case Environment***	
	Electrons	Ions	Electrons	Ions	Electrons	Ions
Number density (No./cm^3)	1.09±0.89	0.58±0.35	2.55	1.16	3	3
Current density (nA/cm^2)	0.115±0.1	3.3±2.1	0.28	6.75	0.501	0.016
Number density, population 1 (No./cm^3)	0.78±0.7	0.19±0.16	1.93	0.453		
Parallel					1	1.1
Perpendicular					0.8	0.9
Temperature, population 1 (eV)	550±320	800±100	1,076	965		
Parallel					600	400
Perpendicular					600	300
Number density, population 2 (No./cm^3)	0.310±0.37	0.39±0.26	0.919	0.818		
Parallel					1.4	1.7
Perpendicular					1.9	1.6
Temperature, population 2 (eV)	8,680±4,000	15,800±5,000	15,260	24,025		
Parallel					25,100	24,700
Perpendicular					26,100	25,600

* Error is 1σ.

** The 90% case is the average + 1.645σ.

*** SCATHA worst case from reference 129.

Spacecraft often encounter the greatest potentials in, and immediately after, eclipse passage.[166] Photoelectron currents are typically significant (if not dominant) contributors to the charging process in the low-density geostationary orbit environments, resulting in positive spacecraft potentials (or at least reducing the magnitude of negative potentials in hot electron environments). The absence of the outgoing photoelectron current in eclipse conditions removes one of the primary currents that balance the incoming electron current from the plasma environment, and the spacecraft must charge to large negative potentials before current balance is established on a spacecraft surface. Differential charging is often a significant issue during eclipse conditions. The electrical resistivity of insulating materials is inversely proportional to temperature, so localized charge densities can accumulate in cold materials where conduction processes are ineffectual in removing the excess charge as the spacecraft surfaces cool during eclipse passage. Charging analyses using the environments provided in table 89 should therefore be examined both for sunlight and eclipse conditions to determine the full range of spacecraft potentials on a spacecraft surface.

6.4.4 Spacecraft Charging Environment

Generally, the space plasma environment can affect spacecraft charging behavior. Combining extreme plasma conditions (e.g., maximum/minimum temperature and density) for each region does not constitute the worst case situation because the extreme plasma density and the extreme

temperature may not occur coincidentally. This worst case environment depends on variations of solar activities and the geomagnetic storm levels. An accurate definition of plasma properties is essential to determine the severity of these effects because the charging level of a spacecraft is directly related to plasma properties encountered on orbit. Properties in GEO orbits have been quantified from various satellite and ground measurement programs. However, for spacecraft with orbits outside these regions, plasma characterization is far more difficult. At geosynchronous altitudes with spacecraft enveloped in a plasma cloud, charge is injected during a magnetic substorm. These plasma clouds have particle densities on the order of 10^6 to 10^7 m^{-3} and energies of tens of kiloelectronvolts. For calculation purposes, measured fluxes can usually be fitted by a Maxwellian or biMaxwellian distribution function shown in section 5.4.

Two regions, geosynchronous altitudes (~6.6 R_e) and low altitude auroral regions (~60° to 75° geomagnetic latitude, reference sec. 5.4), have been identified with plasma energy sufficiently high to charge spacecraft to kilovolts or higher. Probably two different charging mechanisms are involved in GEO charging. Lower energy (<50 keV) particle deposition is believed to cause the surface charging typically found in the MARECS upsets. The second mechanism, due to the more energetic particle flux (>50 keV), can be buried in the dielectric and discharge at random times when external conditions change or with dielectric breakdown. Once charged in this manner, the dielectric can hold its charge for long periods of time.

6.4.4.1 Geostationary Transit and Geostationary Orbits and Internal Charging. Spacecraft in geostationary transfer orbits and geostationary orbits will encounter the strong fluxes of the electron radiation belts. Energetic electrons in the belts with energies of a few megaelectronvolts or greater can penetrate spacecraft shielding and deposit energy in internal systems, creating a susceptibility to anomalies and failures. Electric fields produced by the charge buildup create a hazard to electronic systems from electrostatic discharges and surface materials from arcing. Since electrons of a few hundred kiloelectronvolts deposit their energies near surfaces, and electrons with energies of a few megaelectronvolts can penetrate into materials and deposit energy internally, internal charging can impact internal systems or exposed dielectrics. Many charge-related anomalies in geostationary orbit have been identified with internal charging.

Figure 107 presents the NASA worst case environment to be used in analysis of internal charging issues. Analysis of discharge events on spacecraft in geostationary or geostationary transfer orbits have shown that electron fluxes at breakdown must typically be sufficient to provide a fluence of 2×10^{10} electrons/cm^2 in 10 hr.

6.4.5 Charging Consideration for Spacecraft Design

GEO are used frequently for scientific missions that require long viewing periods without the interference of the Earth's atmospheric effects and magnetic field effects. Typically, satellites flying these orbits are concerned with spacecraft charging and the potentially adverse effects of charging on particular systems. Defining the plasma environment that spacecraft will encounter is the first step in analyzing spacecraft charging in space. Spacecraft charging models require specific characteristics of the plasma environment for analyzing worst case charging levels. These plasma characteristics are generally described in terms of plasma density and temperature and can

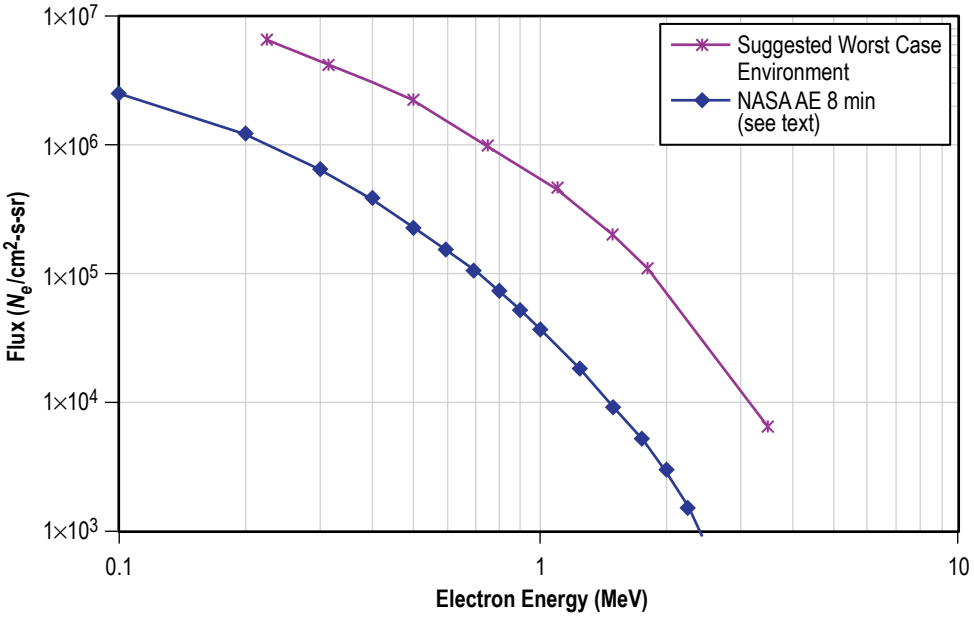

Figure 107. NASA worst case environment for internal charging.

be used to define an appropriate particle distribution for the spacecraft charging analysis. However, defining the worst case plasma/charging environment for the various regions becomes difficult to quantify because of different altitude, latitude, solar activity, geomagnetic storms, sunlight/eclipse effects, and ram/wake effects. Also, several different plasma regions may be encountered during every orbit, each having specific plasma environment characteristics and each bringing about its own detrimental effects. Transient events occur as a spacecraft passes through the boundaries of different regions because of tremendous changes in space plasma characteristics. Therefore, the time spent in crossing different regions needs to be precisely quantified to accurately define overall levels of spacecraft charging. Also, large orbital changes due to gravitational perturbations of the Earth and Moon significantly alter the orbit of high altitude spacecraft from beginning through end of life. All these variations should be considered when specifying worst case plasma environment characteristics for spacecraft charging analyses.

6.4.6 Other Plasma Effects for Design Consideration

Other than the spacecraft charging, plasma effects that might degrade the spacecraft performance include effects to the power system/solar array, thermal control/contamination, plasma emissions, ionospheric scintillation, and secondary plasma effects. Details of these plasma effects are described in section 5.4.6.

6.4.7 Spacecraft Charging Models

NASA/Air Force Spacecraft Charging Analyzer Program-2k (NASCAP-2k) for GEO is one popular spacecraft charging model that is used in evaluating charging analysis in geosynchronous orbits.[117] This 3D code uses an orbit-limited particle collection algorithm appropriate for the low

density and high temperature geosynchronous orbit charging environments. The orbit-limited algorithm is used in low density conditions where the dimensions of the plasma sheath adjacent to the spacecraft structure are sufficiently large and the collection of particles from the plasma depends on the orbital parameters of the individual particles. These conditions are satisfied when the Debye length in the plasma is greater than the radius of curvature of the spacecraft surface, a condition typically met for spacecraft in geostationary orbit.[167]

6.5 Ionizing Radiation Environment

In the region of space from 2,000 km to 10 R_e, the ionizing radiation environment will be composed of the trapped radiation belts, the GCR and SPE. The details of these environments and the effects on electronics are presented in sections 2.12, 3.11, and 5.5.

The middle Earth orbits (MEOs), which range to about 4 R_e, are in the heart of the trapped radiation belts with very high radiation levels. From a TID and displacement damage (DD) perspective, the trapped radiation environments will dominate the GCRs and SPEs (except for an extremely large solar event). In the high Earth orbits (HEOs), which range from 4 to 10 R_e, the trapped electron belt still provides a significant source of the ionizing radiation but the orbits are now beyond the trapped proton belt. For TID, the trapped electron belt will still be the primary source of dose for the lightly shielded electronics. Once shielding thicknesses reach about 5 mm of equivalent aluminum thickness, the electrons are effectively screened out and the dose driver for both TID and DD will be solar particle events. It should also be pointed out that, at these altitudes, the geomagnetic screening is weakening significantly and the SPE particles are almost entirely unscreened.

From a SEE point of view, the rate drivers for the MEO will be the SPEs, GCRs (under non-SPE conditions), and the trapped protons, for those electronics that are sensitive to proton SEE. Upon reaching the HEO altitudes, the trapped protons are no longer a SEE threat and therefore the only sources for SEE are GCRs (under nominal conditions) and SPEs. It should be noted, as stated above, that the HEO have very little protection from the Earth's geomagnetic field. Therefore, the GCR rates will be higher than those at MEO levels and the rates due to SPE can increase substantially (orders of magnitude). For these mission segments, it is often best to be conservative in design by having systems that can deal with event rates from a worst case unscreened SPE (at least the high criticality systems). If the system is capable of surviving and/or operating under these conditions, then performing under the lower rates of GCR and trapped protons will already be in the design.

6.6 Meteoroid and Orbital Debris Environments

6.6.1 Meteoroid Environment

Refer to section 5.6.1 for general discussion of the meteoroid environment. This description is still valid for this region of space.

6.6.2 Orbital Debris Environment

Refer to section 5.6.2 for general discussion of the orbital debris environment. This description is still valid for this region of space with the exception of the modeling capabilities. ORDEM2000 does not model the debris region above 2,000 km, although debris is still present out to GEO. The orbital debris model is being expanded to cover as much of this unmodeled region as possible.

In a 1999 United Nations (UN) report on space debris, it is stated that the population of large space debris in and near the GEO region is well known for spacecraft and upper stages. The probability for collision between these objects is much lower than in LEO because of their fewer numbers, leading to a wider spatial distribution with lower average relative speeds (500 m/s). Since spacecraft and upper stages continue to be left in orbits above and below GEO, the number of uncontrolled intact objects intersecting this GEO region is increasing at a very slow rate. Collisions between objects in GEO are still possible because of the close distances between active spacecraft at specific longitudes.

Smaller debris less than 1 m in diameter near the GEO region is poorly defined. At the time of the 1999 UN report,[168] two breakups of a spacecraft and an upper stage were recorded. It was anticipated that the resulting smaller debris pieces would be perturbed into new orbits (possibly reducing the time in GEO, but increasing the relative collision velocity), making the flux contribution near constant with inclination change. It is believed that in many cases the debris fragments would be widely dispersed in both altitude and inclination.

Since there is no natural removal mechanism for spacecraft in GEO, there is a risk that active spacecraft could be damaged by these dead satellites or their fragments from breakup events. This annual collision probability for an average operational satellite with other catalogued objects is estimated at 10^{-5}.[168]

6.7 Gravitational Field

Reference section 5.7 for the gravitational field in LEO and section 8.5 for lunar gravity.

7. CISLUNAR SPACE ENVIRONMENTS

The cislunar section covers those environments in lunar space (10 to 60 R_e).

7.1 Lunar Exosphere (Lunar Atmosphere)

The Moon has an atmosphere attributed to interactions of the solar wind and solar photons with the lunar surface, coupled with contributions from volatile materials introduced by meteor impact.[169] The total number density of neutral species that have been detected on the lunar surface is $\leq 10^5$/cm, although undetected species may contribute additional density.[170] The lunar atmosphere is more properly termed an 'exosphere' due to the low density of gas atoms. Interactions of individual atoms are dominated by the lunar surface and altitude distributions are governed by ballistic motions rather than atom-atom interactions. The dominant species is Ar at densities of approximately 4×10^5/cm^3 with He being the dominant minor species contributing 2×10^3/cm^3 to 4×10^5/cm^3 to the exospheric density. Other minor species include $<5\times10^2$/cm^3 oxygen atoms, approximately 70/cm^3 sodium (Na) atoms, approximately 16/cm potassium atoms, and <17/cm^3 hydrogen atoms.[170] The density of Na and potassium (K) are time dependent with variations attributed to solar wind modulated photo-desorption[171] and enhancements in metallic species during meteor storms.[172–174] Searches for additional exospheric species have been conducted with negative results including magnesium (Mg),[175] silicon (Si), aluminum, calcium (Ca), iron (Fe), and titanium (Ti).[176]

7.2 Solar Wind (Interplanetary Fields)

Solar wind is the primary source of lower energy charged particles in the interplanetary region of space. Its outflow starts in the lower corona and the velocity steadily increases as the plasma moves radially outward away from the Sun. The formation of shocks in the planetary medium can have important consequences for planetary magnetospheres and ionospheres because the strong impulsive force associated with shock impact on planetary magnetic fields induce electric fields within the magnetosphere and magnetic fields associated with the shock structures control the rate at which energy flows from the solar wind into the Earth's magnetosphere, ionosphere, and thermosphere. Shocks can form where CME interact with the ambient solar wind and when a fast solar wind stream overtakes a slower moving solar wind. The solar wind density and velocity can vary markedly on time scales from minutes to hours and even days, giving rise to variations in solar wind structure throughout the solar system. Solar wind plasma generally takes 2 to 3 days to reach the Earth from the Sun at average speeds, although high-speed CME flows may arrive in times of less than a day. Near the Earth, the speed ranges from 200 to 900 km/s and the density varies from 1 to 80 cm^{-3} with extreme low densities <0.1 cm^{-3} and high densities over 100 cm^{-3}. The highest solar wind flow speeds on the order of a few 1,000 km/s are found in CMEs. As the plasma moves away from the Sun, it expands and cools, with the electron temperature decreasing from 1 million K

in the corona to approximately 100,000 K near the Earth. The interplanetary magnetic field (IMF) also decreases with distance from the Sun, from approximately 1 G at the Sun's surface to approximately 3×10^{-5} G near the Earth. Table 90 compares the plasma characteristics near the Earth for low speed, high speed, and average solar wind conditions.

Table 90. Solar wind parameters near the Earth.

Parameter	Average	Low Speed	High Speed
n (cm^{-3})	8.7	11.9	3.9
u (km/s)	468	327	702
T_p (K)	1.2×10^5	0.34×10^5	2.3×10^5
T_e (K)	1.4×10^5	1.3×10^5	1×10^5

7.3 Plasma Environments

Earth's magnetotail extends to distances well beyond lunar orbit at 60 R_e from the Earth (magnetotail environments are well ordered at L2 distances of 236 R_e and have been detected at distances of 500 to 1,000 R_e). The Moon is immersed in the solar wind flow approximately 73.5% of the time,[177] with the remaining time approximately equally split between the Earth's magnetosheath and magnetotail.[178] This section describes the characteristics of the solar wind, magnetosheath, and magnetotail plasma environments that will impact vehicles in transit to the Moon from the Earth. Plasma characteristics will be perturbed in the vicinity of the Moon due to charging of the lunar surface and formation of the lunar wake (sec. 8.2.1), and the properties provided in this section should be applied in those conditions.

7.3.1 Solar Wind

A summary of the solar wind plasma environments is given in table 91 (adapted from ref. 179).

Table 91. Average solar wind properties.

Parameter	Mean	σ	Most Probable	Median	5%–95% Limit
N (#/cm^3)	8.7	6.6	5	6.9	3 to 20
V (km/s)	468	116	375	442	320 to 710
$T_p\times10^4$ (K)	12	9.1	5	9.5	0.98 to 30
$T_e\times10^4$ (K)	14	3.9	12	13	8.9 to 20
$T_\alpha\times10^4$ (K)	58	50	12	45	6 to 154
N_α/N_p	0.047	0.019	0.048	0.047	0.017 to 0.078

Statistical differential flux spectra for solar wind plasma at 1 AU are given in figure 108 for (a) electrons and (b) ions. These environments are computed from data obtained by the Ulysses spacecraft solar wind plasma experiment plasma and heliosphere instrument for spectra, composition, and anisotropy at low energy energetic particle instruments. Ulysses data were obtained over a range of distance from 1 to 5.4 AU, but all data in this figure have been scaled to 1 AU for computation of the statistical flux. Differential flux values from over 12 years of the Ulysses mission are sorted within individual energy bins into increasing flux order, and values are extracted for the 50% (black), 90% (blue), 95% (green), and 99% (yellow) flux environments. In addition, the red line in both plots indicates the maximum (100%) value in each energy bin. The solid (dashed) lines indicate flux impacting the Sun side (dark side) of the Moon. The electron flux in this model environment is isotropic at the highest energies and only exhibits flux directionality at energies below 0.01 keV. In contrast, the solar proton flux is anisotropic with the largest flux, ions of a few kiloelectronvolts, impacting the illuminated side of the Moon. Plasma flux approaching the backside of the Moon is approximately 5 orders of magnitude less than the flux on the Sun side (see sec. 8).

Charging of the lunar surface due to differential collection of ion and electron currents from the plasma environment and emission of photoelectrons from the illuminated surface will modify the spectrum of particles that reach the surface. Halekas et al.[180] report nightside

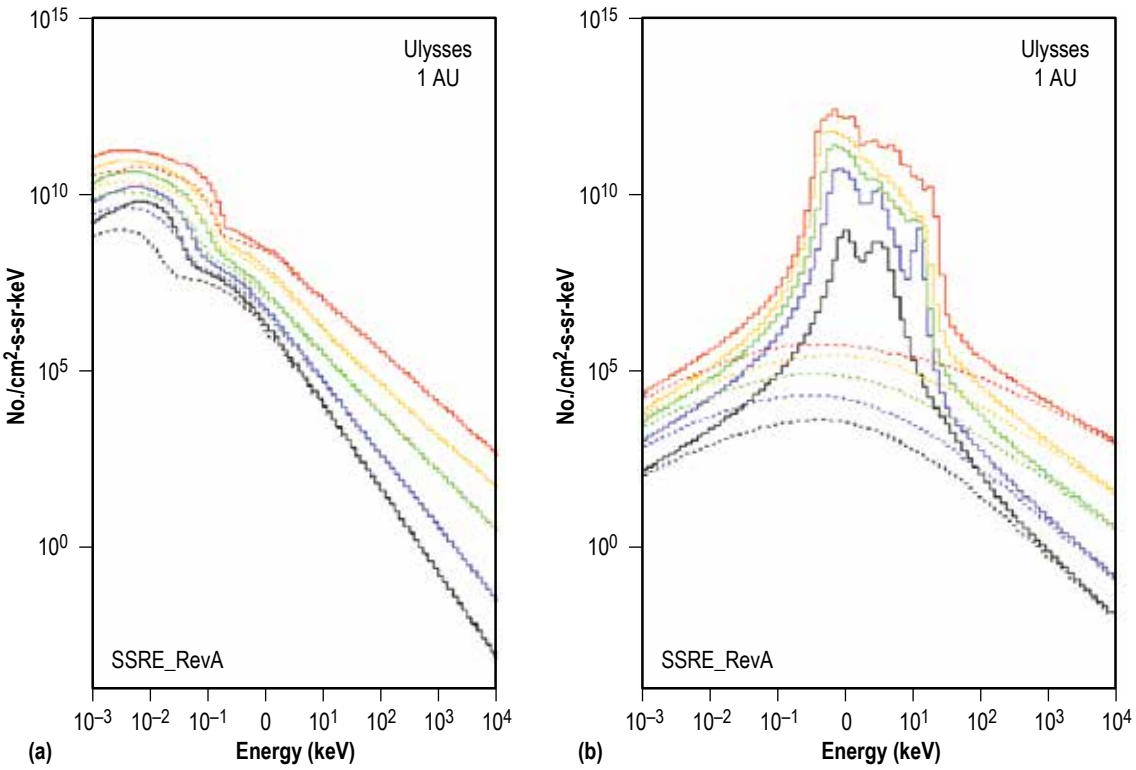

Figure 108. Statistical solar wind flux: (a) Electrons and (b) ions are represented Maxwellian environments at low energies with nonthermal tails extending megaelectronvolt energies.

potential differences of approximately –35 V between the Lunar Prospector (LP) satellite and the lunar surface and note that the satellite may in fact be charged relative to the ambient plasma, suggesting even greater lunar surface potentials. These results are consistent with ion measurements from the Apollo 14 Superthermal Ion Detector Experiment (SIDE) that suggested potentials of approximately 100 V negative exist near the terminator.[181] Recently, Halekas et al.[182] report statistical analyses of the LP electron reflectometer (ER) data that demonstrate the existence of >500 V negative lunar surface potentials. Most of the charging events occur in shadow and the large charging events are rare, although they do occur in both sunlight and shadow. The extreme charging events appear to be correlated with exposure of the lunar surface to plasma sheet environments within the magnetotail. They are strongly correlated with characteristics of the incident electrons instead of localized variations in properties of the lunar surface, suggesting the charging flux is the primary control of the surface charging phenomenon.

7.3.2 Magnetosheath and Magnetotail

Figure 109 shows plasma environments for a 6-month period in 1993, obtained from the Comprehensive Plasma Instrument Hot Plasma analyzer within 25 R_e of the Earth-Sun line, over distances from –50 R_e to beyond –200 R_e. Data are from the University of Iowa/Comprehensive Plasma Instrument onboard the GEOTAIL satellite for the first 180 days in 1993. Values for all GSE Y and Z distances are plotted on the same axis. Data gaps are due to the sparce sampling of deep tail plasma regimes during the four deep tail passes represented in the data set.[183] Environments represented in the figure are primarily magnetosheath and magnetotail plasma environments due to the large dimensions of the bow shock at distances beyond –50 R_e. Radial trends are largely lacking in the plasma moments, and parameters appropriate for lunar distances of 60 ± 10 R_e are essentially the same throughout the distant magnetotail to nearly L_2 at –236 R_e. Statistics from the entire data set are included in figure 109 and in table 92.

7.3.2.1 Extreme Electron Flux Environment for Internal (Bulk) Charging Evaluations. The electron flux environment at the lunar surface is estimated by analyzing solar wind measurements taken by the Charged Particle Measurement Experiment (CPME) on the Interplanetary Monitoring Platform 8 (IMP-8) satellite. The satellite was placed in a near-circular orbit around the Earth in October 1973 with a radius of approximately 35 R_e. The period of the satellite is approximately 12 days, of which 60% of its period is in the solar wind and the remaining time is in the magnetosheath and magnetosphere. IMP-8 provides a reasonable estimate of extreme internal charging environments for lunar operations even though the spacecraft orbits the Earth at approximately half the distance to the Moon. This happens because the origins of the high flux environments are typically solar energetic particle events (flares and CMEs) that exhibit minimal spatial variations over the scale of Earth-to-Moon distances. It should be noted that charging behavior of the lunar surface (positive in the sunlit hemisphere and negative in the dark hemisphere) will perturb plasma populations and may alter the free-field environments reported in this section. More detailed analyses of the surface electron populations are required to obtain bulk charging environments for the lunar surface.

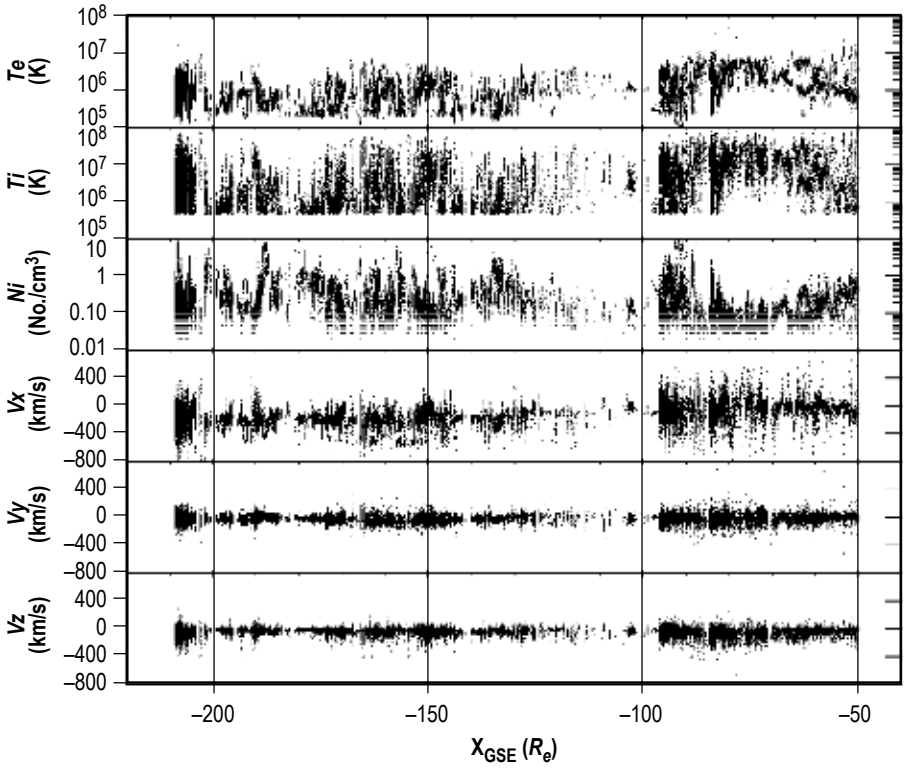

Figure 109. Survey of magnetotail and magnetosheath plasma characteristics (data are from the University of Iowa/comprehensive plasma instrument (CPI) onboard the GEOTAIL satellite for the first 180 days in 1993. Values for all GSE *y* and *z* distances are plotted on the same axis.

Table 92. Magnetosheath and magnetotail plasma parameters.

Cumulative Probability	*Ni* (#/cc)	*Ti* × 10 (K)	*Ti* × 10^4 (K)	*Vx* (km/s)	*Vy* (km/s)	*Vz* (km/s)
Magnetosheath Parameters*						
5	0.283	18.6	3.12	–519	–93.6	–52.3
33	0.687	75.5	20.6	–383	–50	–15.8
50	1.006	92.7	31.2	–311	-32.9	–7.21
67	1.645	110	41.8	–272	–12.1	–0.88
99	8.684	461	111	–112	75.1	35.3
Boundary Layer Parameters*						
5	0.108	30.9	6.03	–297	–61.2	–68.8
33	0.235	90.3	39.8	–199	–18.8	–23.6
50	0.316	114	60.7	–167	–5.67	–12
67	0.44	165	84.9	–139	6.87	–1.9
99	2.286	1,220	272	2.49	74.4	58.7
Lobe Parameters*						
5	0.01	93.7	75.2	–194	–119	–202
33	0.069	405	151	–50.5	–23	–79.3
50	0.107	627	205	–24	–5.62	–55.4
67	0.166	1,180	303	11.5	–33.6	–28.5
99	0.62	5,880	1,650	330	208	124
Plasma Sheet Parameters*						
5	0.015	185	60	–378	–104	–148
33	0.096	472	130	–134	–25.4	–58
50	0.146	708	169	–62	–4.87	–36
67	0.196	1,100	228	–10.1	14.7	–17.4
99	1.361	4,740	753	308	154	81

* Based on analysis of GEOTAIL CPI records.[183]

Data collection ended in October 2001, providing approximately 28 years of data covering two complete solar cycles. The CPME instrument has three electron detection channels that measure electron fluxes in three energy ranges (0.22–2.5, 0.5–2.5, and 0.8–2.5 MeV). From these measurements, maximum electron flux environments are determined for various durations of interest. Daily average fluxes are used in the analysis. Higher temporal resolution data were analyzed for variations in flux due to measurements in the magnetosphere. No significant variations were observed due to magnetosphere boundary crossings.

Figure 110 shows the daily average electron flux bounds and the maximum flux observed for various durations as a function of electron energy. The CPME measurements are fitted with the function of form: $F=AE^{\gamma}$. F is the flux (#/cm^2-s-ster-MeV), E is the electron energy (MeV), and A and γ are fitting parameters. Fluxes of higher electron energies are obtained by extrapolation of the CPME data. Table 93 provides values of A and γ for the curves in figure 110.

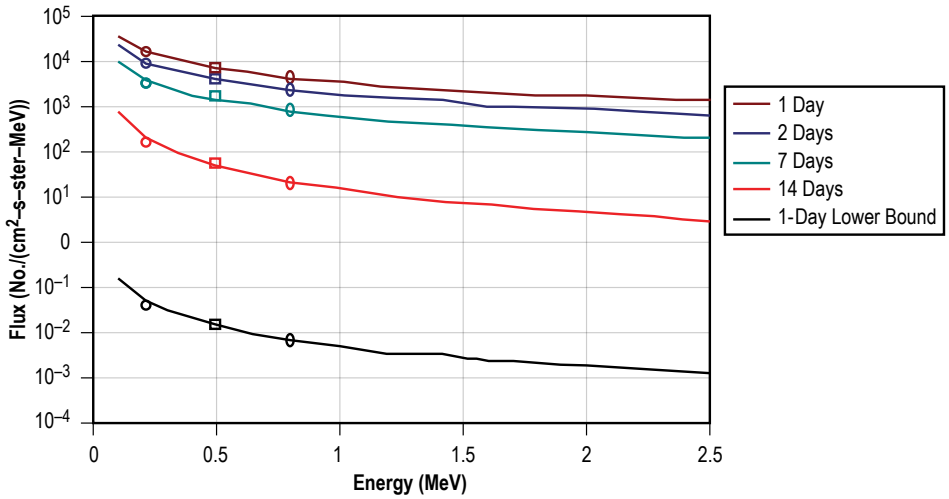

Figure 110. Maximum measured electron flux by the CPME instrument from 1973 to 2001 corresponding to durations equal to the number of days indicated. CPME instrument measurements are plotted along with curve fit (see table 93).

Table 93. Equation and coefficients for the maximum electron flux events (refer to fig. 110).*

Event Duration (days)	Flux (#/(cm^2-s-ster-MeV))=$A\,E^{\gamma}$			
	1	2	7	14
A	3,700	2,000	660	16
γ	–1	–1.1	–1.2	–1.7

E = Electron Energy (MeV)

* Refers to maximum measured flux by the CPME instrument for events with durations equal to the number of days indicated.

Figures 111–114 show the flux associated with each of the durations in figure 112 for a given number of observed events in the data set. This provides an indication of the frequency of events for lower fluxes less than the maximum values provided in figure 110. Tables 94–97 provide the function parameters associated with the curves in the associated figures.

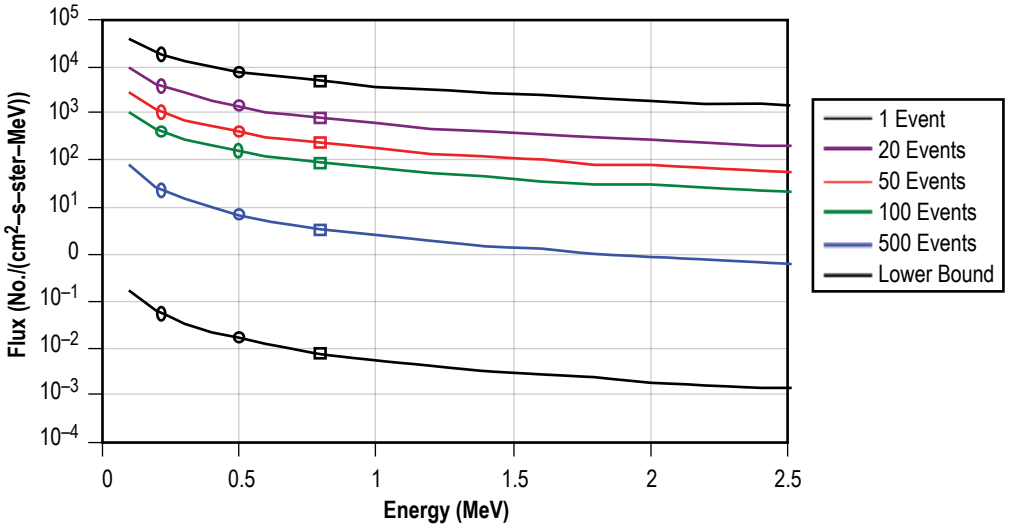

Figure 111. Flux values obtained from the CPME instrument data associated with the number of 1-day events the given flux was greater than or equal to that indicated by the number of events curve. CPME instrument measurements are plotted along with curve fit (see table 94).

Table 94. Equation and coefficients for average daily electron flux bounds (refer to fig. 111).*

Number of Events	Flux (#/(cm^2-s-ster-MeV))=$A\,E^{\gamma}$					
	1	20	50	100	500	All
A	3,700	610	170	65	2.5	0.0055
γ	–1	–1.2	–1.2	–1.2	–1.5	–1.5

E = Electron Energy (MeV)

* Flux values obtained from the CPME instrument data associated with the number of days the given flux was greater than or equal to that indicated by the number of events curve.

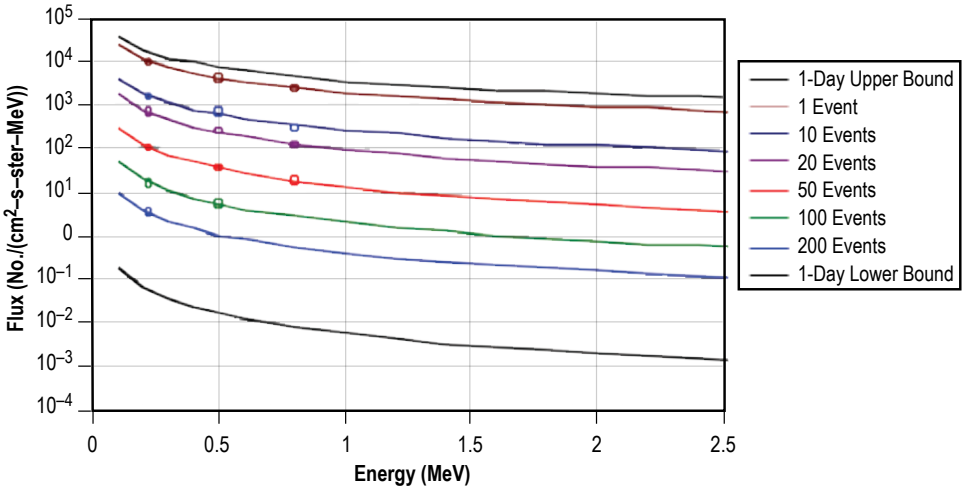

Figure 112. Flux values obtained from the CPME instrument data associated with the number of 2-day duration events that the given flux was greater than or equal to that indicated by the number of events curve. CPME instrument measurements are plotted along with curve fit (see table 95).

Table 95. Equation and coefficients for 2-day duration electron flux events (refer to fig. 112).*

Number of Events	Flux (#/(cm^2-s-ster-MeV))=$A\,E^{\gamma}$					
	1	10	20	50	100	200
A	2,000	610	170	65	2.5	0.4
γ	–1.1	–1.2	–1.3	–1.4	–1.4	–1.4

E = Electron Energy (MeV)

* Flux values obtained from the CPME instrument data associated with the number of 2-day duration events that the given flux was greater than or equal to that indicated by the number of events curve.

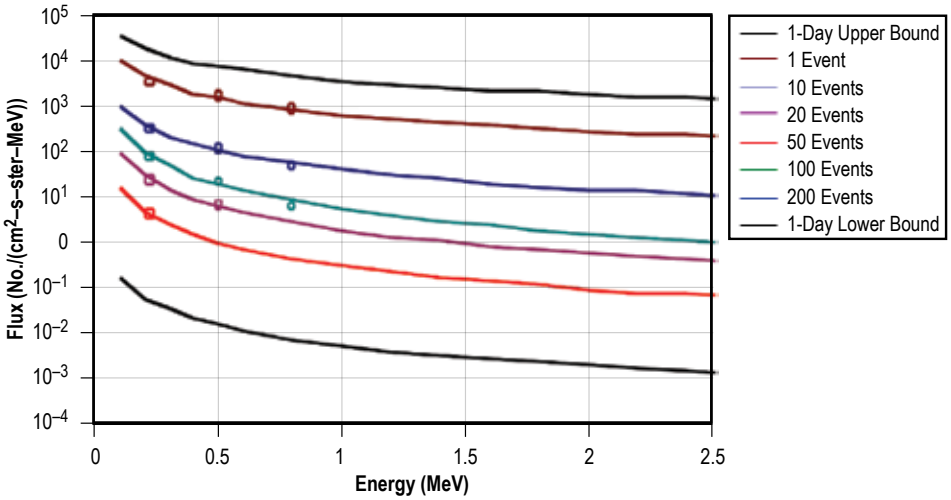

Figure 113. Flux values obtained from the CPME instrument data associated with the number of 7-day duration events that the given flux was greater than or equal to that indicated by the number of events curve. CPME instrument measurements are plotted along with curve fit (see table 96).

Table 96. Equation and coefficients for 7-day duration electron flux events (refer to fig. 113).*

Number of Events	Flux (#/(cm^2-s-ster-MeV))=$A\,E^{\gamma}$				
	1	2	10	20	50
A	660	40	5.5	1.9	0.32
γ	–1.2	–1.4	–1.8	–1.7	–1.7

E = Electron Energy (MeV)

* Flux values obtained from the CPME instrument data associated with the number of 7-day duration events that the given flux was greater than or equal to that indicated by the number of events curve.

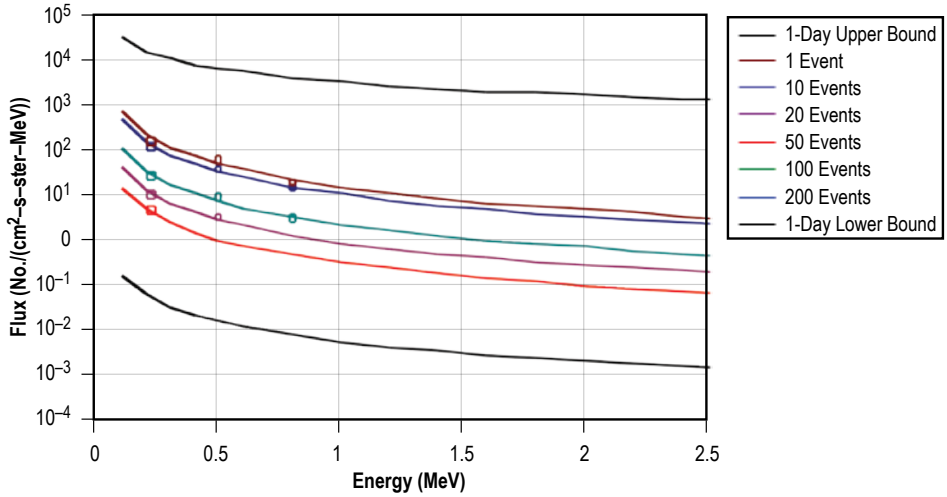

Figure 114. Flux values obtained from the CPME instrument data associated with the number of 14-day duration events that the given flux was greater than or equal to that indicated by the number of events curve. CPME instrument measurements are plotted along with curve fit (see table 97).

Table 97. Equation and coefficients for 14-day duration electron flux events (refer to fig. 114).*

Number of Events	Flux (#/(cm²-s-ster-MeV))=$A\,E^{\gamma}$				
	1	2	4	12	20
A	16	11	2.3	0.9	0.32
γ	–1.7	–1.7	–1.7	–1.7	–1.7

E = Electron Energy (MeV)

* Flux values obtained from the CPME instrument data associated with the number of 14-day duration events that the given flux was greater than or equal to that indicated by the number of events curve.

7.4 Ionizing Radiation Environment

In the region of space from 10 to 60 R_e, the ionizing radiation environment will be composed of GCRs and SPEs. For the small section between 10 to 12 R_e, there is some exposure to the outer electron belt, but it is weakening rapidly with altitude. The details of these environments and the effects on electronics are presented in sections 2.12, 3.11, and 5.5.

The main impact at these altitudes is that the Earth's geomagnetic screening is no longer there. All the external environments (GCRs and SPEs) will be at full strength when interacting with any electronic systems. For total ionizing dose (TID), the trapped electron belt will only be a source of dose for the lightly shielded electronics and for altitudes <12 R_e. Beyond this altitude, the dose driver for both TID and DD will be unscreened SPEs.

From a SEE point of view, the only sources for SEE are unscreened GCRs (under nominal conditions) and unscreened SPEs. For these mission segments it is often best to be conservative in design by having systems that can deal with events rates from a worst-case unscreened SPEs (at least the high criticality systems). If capable of surviving and/or operating under these conditions, then performing under the lower rates of GCRs will already be in the design.

7.5 Meteoroid Environment

Refer to section 5.6.1 for general discussion of the meteoroid environment. This description is still valid for this region of space. For mission trajectories from the Earth to the Moon, the meteoroid environment can be described by the Earth submodel of MEM. Once the mission trajectory reaches the lunar sphere of influence, roughly 60,000 km from the Moon's center, meteoroids are primarily gravitationally focused and shielded by the Moon, so the lunar submodel of MEM would be applicable. Within the lunar sphere of influence, the Earth's gravity field has a small effect on meteoroids and is not modeled in the lunar submodel of MEM. For discussion of the meteoroid environment in lunar orbit, see section 9.8.

8. LUNAR SPACE ENVIRONMENTS

This section covers those environments in lunar space, lunar orbit, and on the lunar surface (10 to 60 R_e).

8.1 Thermal Environments

The lack of atmosphere, water, and slow rotation rate of the Moon leads to a substantially more severe thermal environment on the lunar surface than on the Earth. The same conditions result in an equally severe thermal environment—both hot and cold—in lunar orbit. In eclipse above the dark side, a satellite lacks direct solar radiation and receives only a few watts per square meter from the cold lunar surface. On the sunlit side near the subsolar point, the satellite receives both direct solar radiation and a nearly equal amount of energy in the infrared spectrum from the lunar surface.

8.1.1 Solar Constant

The solar constant, as defined in section 5.2.1.1, applies to lunar orbit. However, there is an enhanced range of variation due to changes in Moon-Sun distance caused by the Moon orbiting the Earth. This motion adds or subtracts up to 405,504 km to the variations in the Earth-Sun distance considered in section 5.2.1.1, so the effective solar constant range is as follows (does not include a $\pm$5 W/m^2 measurement uncertainty):

- Maximum solar flux: 1,421 W/m^2.
- Mean solar flux: 1,367 W/m^2 (solar constant).
- Minimum solar flux: 1,315 W/m^2.

For the near side of the Moon, average values of the normal albedo are provided by Dollfus and Bowell[184] for wavelengths from 0.327 to 1.050 μ.To convert these data to an average bolometric value, the data were averaged weighted by the solar spectrum as approximated by a blackbody curve for 5,780 K. The resulting value is:

- Average bolometric normal albedo = 0.12 (lunar near side).

Local surface variations will cause an orbiting spacecraft to experience short-term variations about this value. These could range from a low of 0.07 to a high of 0.2.The average reflectivity is 164 W/m^2 with a maximum of 285 W/m^2 and minimum of 91 W/m^2 for the near side.

The surface of the far side of the Moon is dominated by ‘lunar highlands’ terrain that tends to be somewhat brighter than the near side, which has numerous darker maria. For the far side, local normal albedo data are available for the waveband at 750 nmi from the UV/visible camera

(UV/Vis) instrument from the Clementine mission. Noting that the curve fit of albedo against wavelength for the near side[184] data crossed 750 nmi essentially right at the average value, 0.12, it can be assumed that the 750 nmi normal albedo will be a close approximation to the normal bolometric albedo. Thus, the resulting value is:[185]

• Average bolometric normal albedo = 0.15 (lunar far side).

Temporal variation about this value will be ±0.05. The average reflectivity is 154 W/m^2 with a maximum of 285 W/m^2 and minimum of 131 W/m^2 for the far side.

The ranges of variation quoted here should bound the values seen by low-orbiting spacecraft. In higher orbits, some spatial averaging will occur and the range of variation will diminish somewhat.

8.1.2 Lunar Long-Wave Radiance

Analysis of the long-wave infrared camera data from the Clementine mission[185] indicates that the radiance from the Moon, as viewed by a nadir-looking spacecraft, can be well represented by a simple Lambertian thermal balance model. The term Lambertian implies equal scattering in all directions. Given the slow rotation rate of the Moon, effects of thermal inertia on the surface can be neglected for this application. On this basis, the thermal balance at the lunar subsolar point can be expressed by the Stefan-Boltzmann law:

$$\varepsilon\sigma T_S^4 \approx (1-\bar{a})S_o / R_L^2 \ , \tag{69}$$

where

ε = long-wave emissivity of the surface, assumed to equal 1
σ = Stefan-Boltzmann constant (5.67×10^{-8} W/m^{2}K^4)
T_s = lunar surface temperature at the subsolar point
$\bar{a}$ = average lunar normal bolometric albedo = 0.15
S_o = average solar constant at 1 AU from section 5.2.1.1.

On the sunlit side, the solar irradiance varies as cosine (cos)(i), where i is the solar incidence angle (the angle between the Moon-Sun vector and the Moon-satellite vector). A good approximation for the gross lunar surface temperature variation is therefore:

$$T \approx T_s \cos^{1/4}(i) \ . \tag{70}$$

As a result the lunar long-wave radiance on the sunlit side is:

$$I_{LW} \approx \varepsilon\sigma T^4 \approx (1-\bar{a})S_o \cos(i) \ . \tag{71}$$

The uncertainty and range of variation due to local albedo effects is approximately 270 W/m^2 at the subsolar point. This corresponds to a ±20 K surface temperature variation. As the solar

incidence angle increases to ~80°, the range of surface temperature variation increases to ~60 K but the irradiance variation is much less than at the subsolar point because of the power law.

On the dark side, the first part of this expression still applies:

$$I_{LW} \approx \varepsilon \sigma T^4 \ , \tag{72}$$

with the dark side temperature equal to 100 K, ±20 K. The analyst may wish to add an interpolation over the small discontinuity at $i = 90°$.

8.2 Plasma Environments

8.2.1 Lunar Plasma (Solar Wind, Magnetosheath, and Magnetotail) Environments

Solar wind plasma energies are too low to produce bulk damage in thick materials but may degrade surface properties of thermal control coatings and multilayer insulation (including optical properties required for heat rejection). They may also degrade material integrity of thin materials used for thermal control systems, regolith 'sandbags,' or other lunar system design features. Should surface optical, thermal, or electrical properties be identified as critical to crew exploration vehicle (CEV) function, then evaluation of solar wind and magnetospheric plasma radiation damage should be conducted to determine the magnitude of the effect.

There are three types of lunar space plasma environments that the designer must consider: solar wind, magnetotail, and magnetosheath.

The Moon's orbit is inclined approximately 5.1° from the ecliptic plane, yielding a maximum distance of $\pm 5.3\ R_e$ that the Moon can be located above or below the ecliptic plane. The magnetotail is approximately circular in cross section at lunar distances and the radius of the magnetopause (the boundary between the magnetotail and the magnetosheath) ranges from 20 to 30 R_e.[186]

The magnetotail is aligned with the solar wind, approximately 4° from the Sun-Earth line in the plane of the ecliptic, so the Moon must past through the magnetotail once each month. Bow shock dimensions are even larger, with the mean radius varying from 40 to 70 R_e (or more) at lunar orbit.[187] Using values of R_e for the magnetopause (RMP) = 25 R_e and Rozetka Bortovoi Seti (bow shock radii) = 50 R_e for the magnetopause and bow shock radii, respectively, the fraction of the lunar orbit inside the bow shock is 26.5%, the fraction inside the magnetotail is 13.2%, and the fraction between the bow shock and magnetopause is 13.3%. The balance of the Moon's orbit, 73.5%, is spent in the solar wind. For many reasons, one will see a more severe charging environment inside the bow shock than in the solar wind.

Plasma environments are based on mean solar wind values from Feldman et al.[188] and magnetosheath and plasma sheet plasma moment statistics reported by Minow et al.[189] Plasma electron and ion spectra are reconstructed from the moments given in table 98 using Kappa distribution functions with a value of $\kappa = 3.5$ for all species to provide a nonthermal tail to the distribution functions and corresponding differential flux spectra. Magnetotail encounters are all conservatively

Table 98. Moments for lunar plasma environment.

Environment	N_p (#/cm^3)	N_α/N_p	N_e (#/cm^3)	T_p ($\times 10^4$ K)	T_α ($\times 10^4$ K)	T_e ($\times 10^4$ K)	V_c
Solar wind	8.7	0.047	N_p+2N_α	12	58	14	468
Magnetosheath	1	0.047	N_p+2N_α	92.7	370.8	31.2	311
Plasma sheet	0.15	0.047	N_p+2N_α	708	2,832	169	62

assumed to be plasma sheet environments, which add a conservative high-energy environment (although many magnetotail encounters are likely to be the low flux, lower energy lobes above or below the plasma sheet).

The electron environment shown in figure 115(a) is a power law dominated by high flux at low energies. Ion fluences given in figure 115(b) exhibit two peaks: a lower energy peak near 1 keV due to protons and a higher energy peak due to He ions. Assumptions are that the Moon spends 73.5% of the time in the solar wind, 13.3% of the time in the magnetosheath, and 13.2% of the time in the magnetotail—taken to be the plasma sheet. The lunar 10-year plasma fluence environments are given in tabular form in table 98 for use in developing TID tests of material surface properties or bulk properties of thin materials.

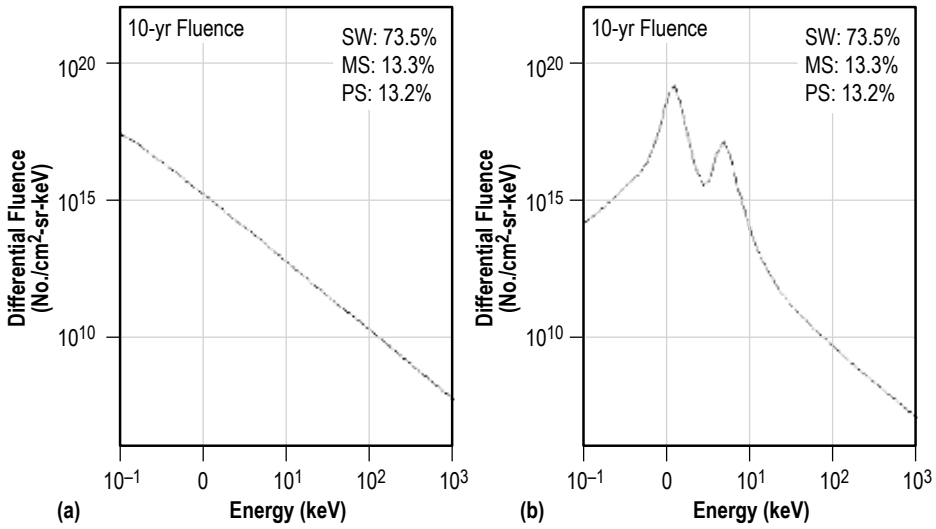

Figure 115. Lunar 10-year, free field plasma fluence: (a) Electron and (b) ion fluence environment for sunward-facing surfaces of the lunar surface.

These free-field environments provide the plasma flux at 60 R_e from the Earth in the absence of the perturbations caused by the Moon. Spacecraft in lunar orbit or systems used in lunar surface operations will see significant perturbations to the free-field environments due to shielding by the Moon, as well as photoelectron production on illuminated surfaces.

8.2.2 Lunar Wake Plasma

The lunar wake is a plasma cavity in the solar wind on the anti-solar side of the Moon. With no intrinsic magnetic field and only a tenuous lunar atmosphere, the solar wind plasma is absorbed, for the most part, on the dayside when it comes into contact with the lunar surface, leaving a plasma void on the nightside.[190] When the solar wind plasma directly collides with the Moon, a very low-density region called a lunar wake is formed behind the body of the Moon. The solar wind IMF passes through the Moon with only a slight inductive interaction with the more electrically conducting interior and reemerges into the plasma void of the solar wind wake. The IMF variation is expected to cause significant differences in the structure of the lunar wake. The extent of the wake and its topology is dependent upon the IMF direction. The system of currents that result from formation of the plasma void slightly amplifies the magnetic field within the wake and depresses the field at the wake boundary. At the boundary of the wake, electrons with greater thermal speed rush into the wake region faster than ions, creating an ambipolar electric field and a potential drop along the flanks of the wake that slows the energetic electrons and accelerates ions into the central wake region.

Al'pert,[191] using a kinetic approach, started the theoretical study of the lunar wake. Explorer 35 and the Apollo subsatellites made the first measurements of the lunar wake, albeit with very low resolution. They were able, however, to detect a significant depletion in density behind the Moon. Recently, the WIND and LP satellites observed the plasma density structure of the lunar wake when the satellites passed behind the Moon at a distance of 6 to 8 lunar radii (R_L). The WIND spacecraft made transits across the wake at distances beyond approximately 6 R_L. The result showed that a depletion of plasma density occurred widely behind the Moon.[192] The observation of the lunar wake by the 3D Plasma and Energetic Particle investigation (WIND/3DP) experiment showed:

- Significant ion and electron depletions.
- Rarefaction waves traveling away from the wake.
- Increased electron temperatures and constant ion temperatures.
- Counterstreaming ion beams.
- An increase in magnetic field strength.
- A number of electromagnetic and electrostatic waves.[193–196]

The various regions encountered through the wake at approximately 6 R_L are shown schematically in figure 116. A trailing compression wave is introduced in the plasma penumbra region to account for the changes in flow direction. The results can be summarized as follows:

- A plasma cavity (or plasma umbra), not entirely empty of plasma, is located within the Moon's optical shadow and particle densities are low, <0.5 cm^{-3}.
- The plasma penumbral region, externally bounded by a rarefaction wave (Mach cone inclined of 11°), is populated by plasma with increasing temperatures, decreasing densities, and variable flow velocities.
- The isotropic background of energetic solar particles follows IMF lines and is partially occulted by the Moon.

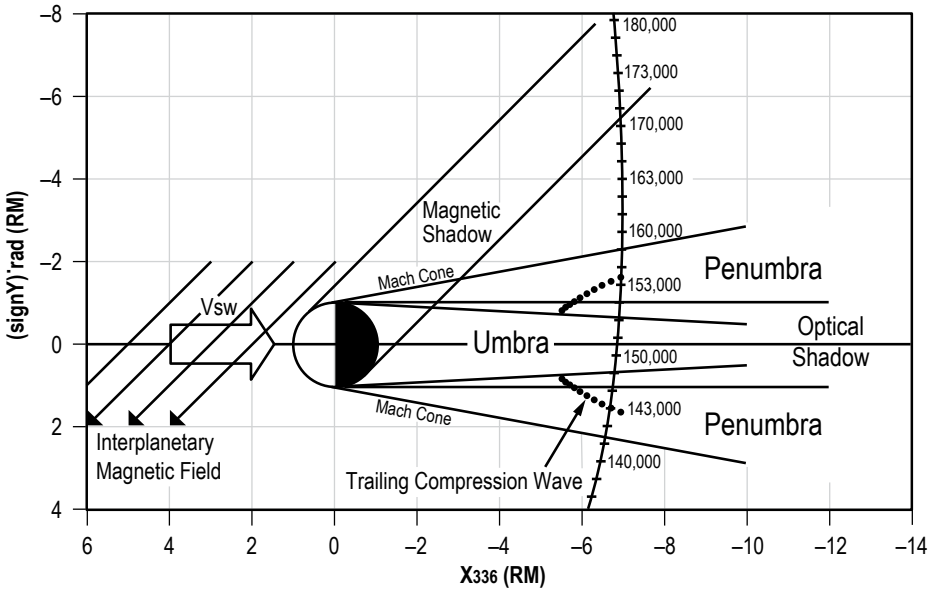

Figure 116. Schematic view of the solar wind-Moon interaction as deduced from the WIND/3DP results on December 27, 1994.

As the plasma is convected downtail, the wakeward beams fill the lunar tail with cold plasma. The rate of the wake refilling depends on the orientation of the IMF. The evolution of the lunar wake in simplified geometry can be simulated via an electromagnetic particle-in-cell code.[197] This simulation begins immediately downstream of the Moon, before the solar wind has refilled the wake region, then evolves in the solar wind rest frame. The electrons immediately begin to move into the void but are trapped by two potential wells, thus generating vortices in phase space on both sides of the wake, between which counterstreaming electron beams interact. Ion beams are generated after the lighter electrons have moved into the void, creating a two-stream distribution that mixes in phase space due to the potentials created by the electron two-stream instability. The simulations are consistent with both Wind observations and the results of earlier electrostatic simulations that focus only on the ion dynamics.

8.2.3 WIND Observations of the Distant Wake

Launched on November 1, 1994, the WIND spacecraft passed behind the Moon on December 27, 1994. At the time, the Moon was immersed in the planetary medium and a large amount of new data were collected by the WIND/3DP experiment. Wind in situ observations[192,196] show a plasma density dropout region extending to at least 6 R_L down tail. The solar wind properties observed before and after the WIND pass in the lunar environment are $N_p \sim 5$ cm^{-3}, $V_p \sim$ 500 km/s, and $T_p \sim 8\times10^4$ K. Near-Earth IMF variations show an almost constant IMF magnitude, slightly increasing from 7 to 8 nT during the Wind pass near the Moon.[196] This demonstrated the plasma characteristics (density and velocity) during the lunar wake crossing, as shown in figure 117.

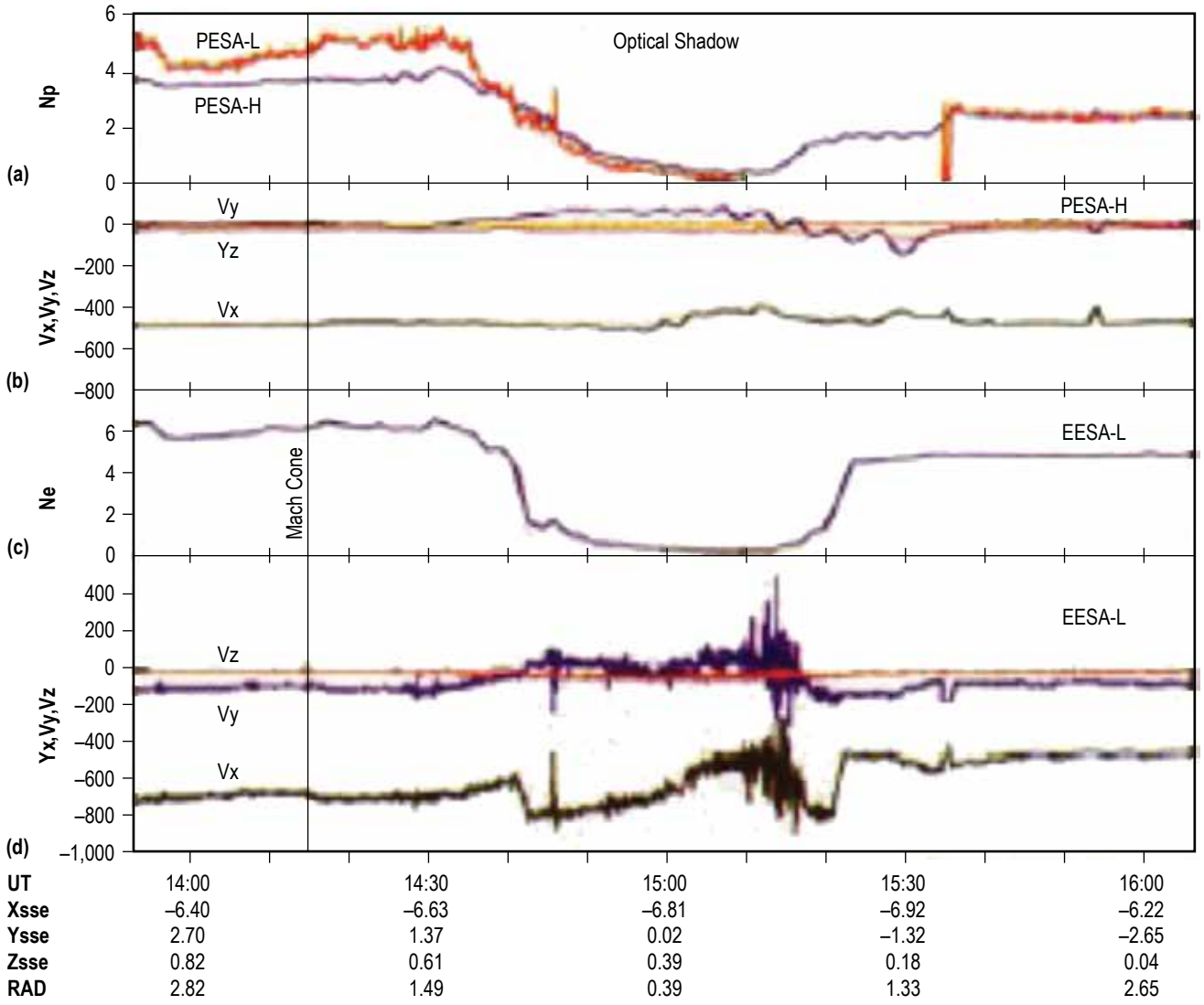

Figure 117. Plots of WIND/3DP plasma data during the lunar wake crossing in December 27, 1994:[196] (a) *Np*, (b) *Vx*, *Vy*, *Vz*, (c) *Ne*, and (d) *Vx*, *Vy*, *Vz*.

As shown in panel (a) of figure 117, the ion density *Np* is approximately 4 to 5 cm^{-3} in the interplanetary medium, before 14:15 UTC. Beginning at 14:15 UTC, the ion density increases slightly up to 5 cm^{-3}. At 14:32 UTC, *Np* begins to decrease toward a marked minimum of 0.5 cm^{-3}, reached at about 14:52 UTC, i.e., inside the optical umbra region. Between 14:55 and 15:15 UTC, the ion densities reach minimum and then gradually increase, finally reaching its interplanetary value of 2.5 cm^{-3} at approximately 15:36 UTC. Panel (b) shows the directions of the ion flow. Only small modifications of external flow are noted in the wake; deflection of the flow direction as measured by the *Vy* component is outward directed during the inbound penumbra crossing. This result indicates that no significant flow component is needed to partially fill the plasma cavity. Indeed, it may be due to the expansion of the solar wind plasma owing to its thermal motion. The ion plasma temperature is increased at 14:40 UTC, followed by a sharp cooling between 15:00 and 15:12 UTC (not shown in fig. 117).

In panel (c), the crossing of the wake is evidenced by a sharp decrease in the electron density *Ne* down to <0.5 cm^{-3}, between 14:50 and 15:17 UTC, roughly simultaneous with the crossing of the optical shadow. In panel (d), a significant *Vy* component away from the wake is again detected within the plasma void, well correlated with the associated ion flow. It is worth mentioning that during the entire wake crossing, the magnetic field direction was not strongly influenced by the downstream flow.

Similar results reported by Ogilvie et al.,[192] shown in figure 118, indicate the observations of the lunar plasma wake from the WIND spacecraft on December 27, 1996, at a downstream distance of 6.5 R_L. The plasma number densities show reductions clearly associated with the Moon. The minimum densities measured are approximately 20 times lower than the solar wind densities measured just before entry into the wake. While the electron temperature increases in the wake by a factor of approximately 4, the ion temperature remains fairly constant. As the system attempts to restore pressure balance,[198] the magnetic field exhibits a corresponding gradual increase. The magnetic field rises slightly as reported earlier. Within the region where the plasma is significantly depleted, two distinct proton distributions are simultaneously detected. The ions are accelerated along the direction of the IMF by an electric field of the order 2×10^4 V/m. Each appears as a cold beam, narrow in velocity space, one convecting with a speed slightly faster than the ambient solar wind and the other convecting slightly slower.

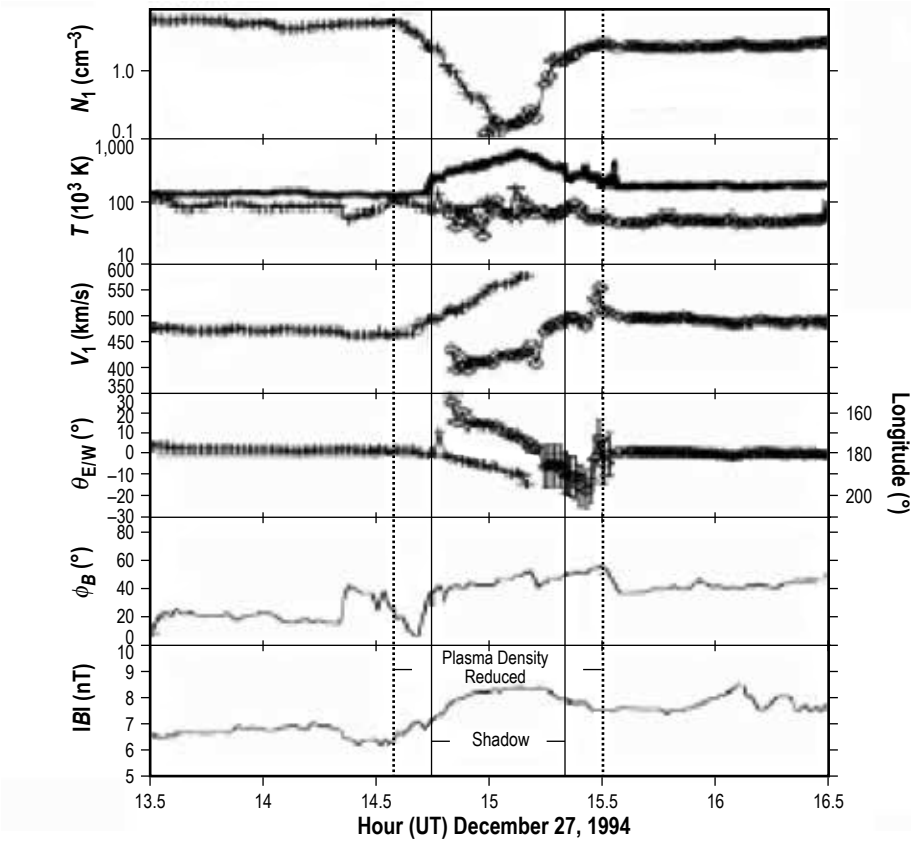

Figure 118. Plasma and magnetic field parameters for lunar wake crossing.[192]

Figure 119[199] shows the in situ observations in the lunar wake by the WIND spacecraft at ~25 R_L on November 13, 1996. Figure 119(a) shows a gray-scale plot of the magnetic field fluctuation spectrum as a function of time and frequency. The overlaying dark curve denotes the local proton gyrofrequency. Panel (b) shows the gray-scale plot of the ion spectrum as a function of time and energy. Panels (c) and (d) show the three components and magnitude of the magnetic field. Panel (e) shows the density profile. Panel (b) clearly shows counterstreaming ion beams[192] as an important feature of the wake tail region.

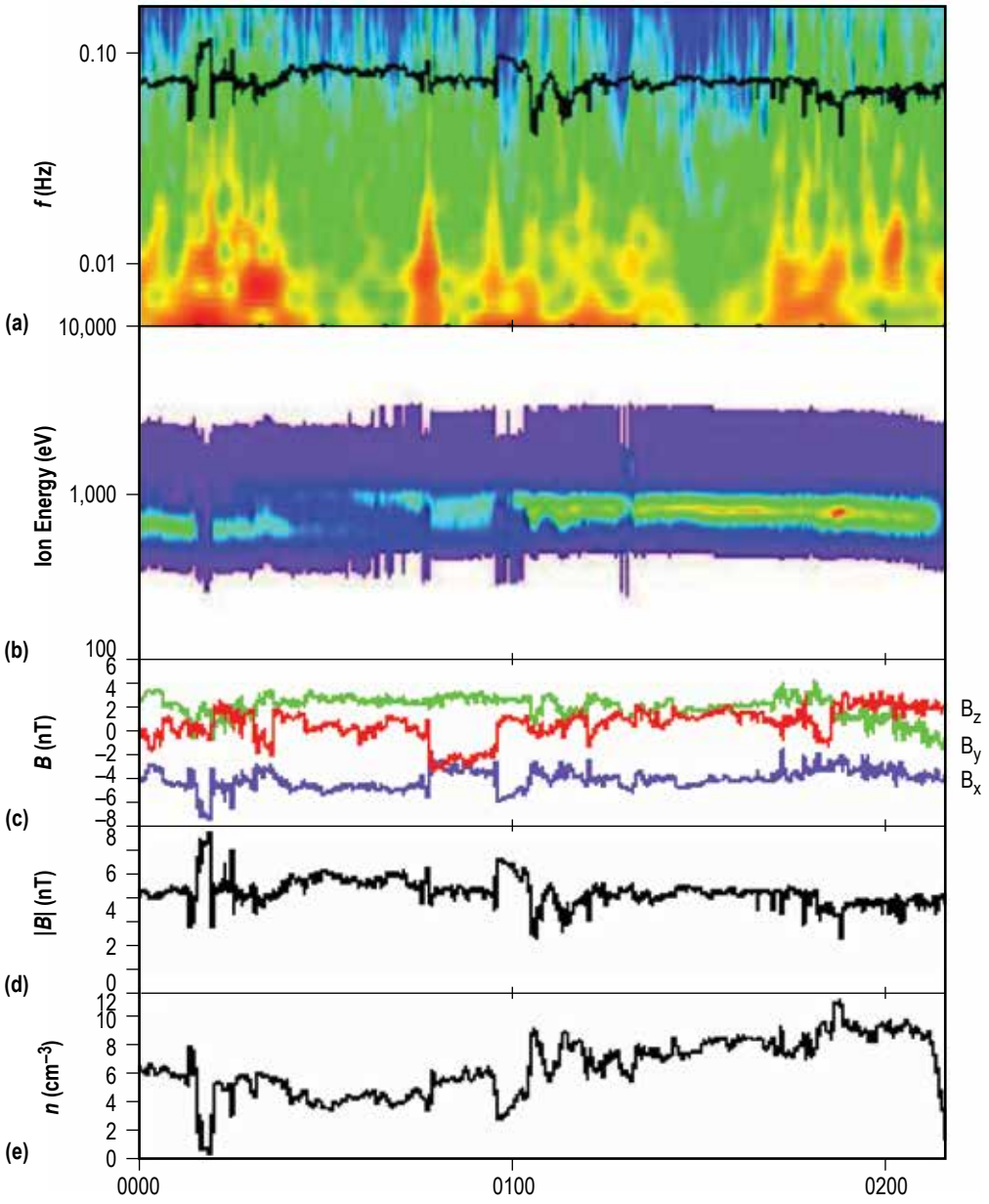

Figure 119. WIND spacecraft data from the moon wake tail encounter on November 13, 1996 (spacecraft distance from the Moon center was approximately 25 R_L).[199]

Results of the simulation study by Trávníček et al.,[199] with the focus on the deep lunar wake (up to 40 R_L), show that two beams of counterstreaming plasma fill the lunar wake with the relatively cool, inhomogeneous and highly anisotropic plasma. As the plasma moves into the cavity, two rarefaction waves propagate away from the wake's center, forming edges of the lunar tail structure. The streaming plasma is subject to velocity filtering as hotter plasma moves faster into the cavity than colder plasma. The current associated with this plasma expansion is responsible for the enhancement of the magnetic field in the cavity of rarefied plasma. The enhanced magnetic field cools down the streaming plasma. The plasma convects further downtail and a region-enhanced density is formed in the wake's center where the magnitude of the magnetic field decreases.

8.2.4 Plasma Interactions and Effects

Counterstreaming electrons were reported during NOZOMI's second lunar swing-by.[200] These events can be categorized into two types from the characteristics of the electron distribution function:

(1) Counterstreaming electrons with a velocity distribution similar to that of the solar wind electrons, but its phase space density ratio to the solar wind electrons decreases as a function of velocity.

(2) Counterstreaming electrons that are thermalized and have a flux comparable to or dominating that of the solar wind electrons.

The origin of counterstreaming electrons observed in the first event is the lunar wake region, where the electrostatic potential drop associated with the ambipolar plasma expansion reflects the solar wind electrons. The energy of the reflected electrons reaches 480 eV, so that the magnitude of ambipolar electrostatic potential is estimated to be at least 480 V. The value of 480 V is consistent with the value of 400 V concluded by Ogilvie et al.[192] based on the accelerated solar wind proton data from the WIND spacecraft. As for the second event, the electron energy spectrum implies that the solar wind electrons have thermalized at the downstream region. There are two candidates for the thermalization mechanisms: the terrestrial bow shock and the interaction region of the solar wind ions in the downtail of the Moon. When solar wind protons passing both sides of the terminator of the Moon interact with each other behind the void region, the two-stream instability can easily develop. After the thermalization of the solar wind electrons, the considerable amount of the solar wind electrons can be reflected back. Both cases can account for the observed counterstreaming electrons of the second event.

Ogilvie et al.[192] detected the counterstreaming beam distribution, creating a two-stream instability. Analysis of the two-stream instability generated by the counterstreaming particle beams from either side of the wake[197,201] revealed that the instability is largely due to the presence of the counterstreaming electrons. Previously, it was believed the instability was generated by the presence of counterstreaming ions.

Various types of electrostatic and electromagnetic plasma waves, in both upwake region and in the waketail itself, are reported.[193–195] In general, these observations show that kinetic processes are important in the lunar plasma environment. A characteristic feature of the lunar wake is the presence of two counterstreaming ion beams drawn in from either flank.

Clack et al.[202] observed both ion components exhibit an extreme temperature anisotropy, often with $T(\perp) \sim 10T(\parallel)$. The anisotropy is greatest in the central wake region. It appears that the anisotropy arises through the conservation of adiabatic invariants as solar wind plasma expands to fill in the cavity behind the Moon. Despite their large anisotropy, the proton distributions appear stable to the cyclotron instability. Correlated field and flow directional changes show that the wake geometry is dependent upon the prevailing magnetic field orientation.

8.2.4.1 Lunar Prospector Observations of the Inner Wake. In contrast to WIND that passes through the outer wake region, the LP spacecraft made a large number (>6,000) of crossings through the wake close to the Moon (between 20 to 115 km). The LP had a magnetometer and electron spectrometer onboard, and thus could detect the electron depletion and magnetic perturbations from the wake. Further, based on the systematic shift in the electron energy distribution function, LP could infer the potential change in crossing from solar wind into the wake plasma void. These near-surface transits through the wake flanks are valuable, providing unique insight into the plasma expansion process in a location close to where the wake is formed. The primary results of LP include the following:[180]

- The electron density was found to exponentially decrease by a factor of 1001,000 from a subsolar angle of 90° (terminator) to 180° (antisolar point).

- The electron temperature was found to progressively increase by a factor of 6–8 from a subsolar angle of 90° (terminator) to 180° (antisolar point).

- The inferred electrostatic potential was found to be slightly positive on the dayside (tens of volts), pass through zero volts at a subsolar angle of 75°, and become progressively more negative with increasing subsolar angle. At 90° (terminator), the potential was typically approximately –20 V but dropped as low as –300 V over the lunar nightside (subsolar angles >150°).

Figures 120–122 summarize the results stated above. In essence, with >6,000 passages, LP effectively mapped out the wake region close to the Moon. The views are centered as if looking down the tail of the wake back towards the Moon, with 0° latitude and 0° longitude being the antisolar point.

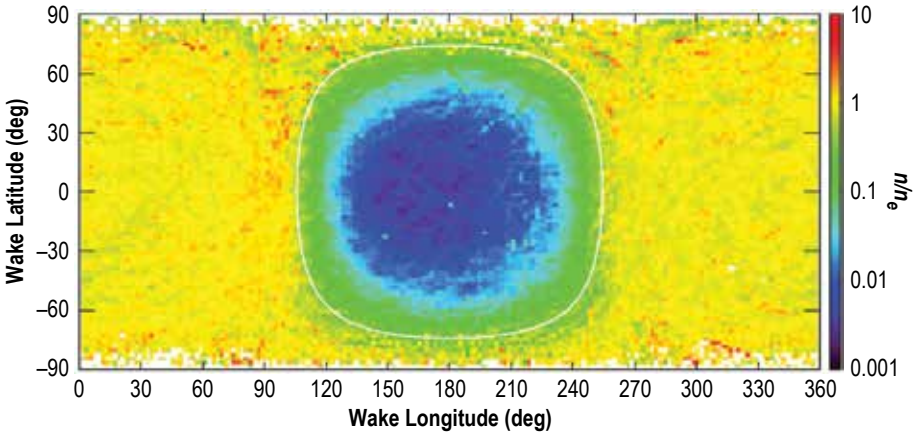

Figure 120. Normalized LP electron density measurements from altitudes of 20 to 115 km, binned by wake longitude and latitude (white circle shows the solar wind flow terminator).[203]

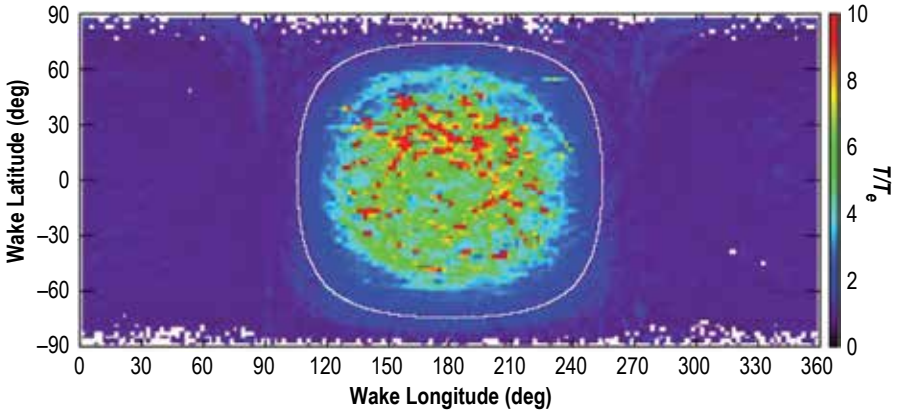

Figure 121. Normalized LP electron temperature measurements from altitudes of 20 to 115 km, binned by wake longitude and latitude (white circle shows the solar wind flow terminator).[203]

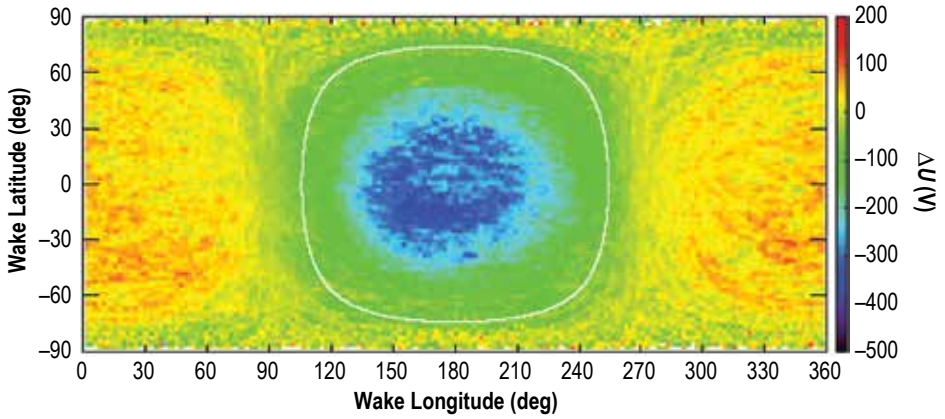

Figure 122. Electrostatic potential measurements from altitudes of 20 to 115 km, binned by wake longitude and latitude (white circle shows the solar wind flow terminator). [203]

Halekas et al.[180] demonstrated that the modified self-similar plasma expansion process described by Samir et al.[204] best fits the observations. The modification involved the use of solar wind kappa distributions rather than Maxwellians, which then gave a realistic fit to the observed solar wind temperature increase. Given a plasma void immediately following plasma absorption by the Moon, electrons will thermally diffuse into the wake ahead of the more massive ions. As a consequence, an ambipolar electric field develops that attempts to slow the electron inward flow and accelerate ions into beams that then catch up to the electrons. The self-similar model predicts the plasma density given this progressive charge neutrality loss, *E*-field development, and ion beam formation. Halekas et al.[180] found that observations and the theoretical model matched very closely.

Unfortunately, LP did not include a direct current (DC) *E*-field measurement system or an ion spectrometer. Theories have also suggested that the ions accelerated via the plasma expansion process into the wake never fully catch up to the electrons, creating an electron cloud and a region of enhanced *E*-fields.These added instruments would be able to discern any subtle loss of plasma neutrality.

8.2.4.2 Simulations. Based on the WIND transits of the wake,[194,197] a series of simulations of the plasma expansion process were run and compared to actual measurements. The codes were fully kinetic allowing the development of electrostatic fields that operate in the plasma expansion region. Figure 123 shows the results of a particle-in-cell simulation. Farrell et al.[205] assumed that the solar wind magnetic field lay across the wake. The following simulated features were noted:

- A deep plasma void that extended back to beyond 32 R_L.
- The development of an intense ambipolar electric field along the wake flank, in the region <4 R_L of the Moon.
- Wake replenishment by an ion-ion beam instability that acts to slow the ion beams emitted into the central region by the wake flank. The structure of the trailing streamers is associated with wake replenishment that starts in the central region and progressively moves toward the flanks.

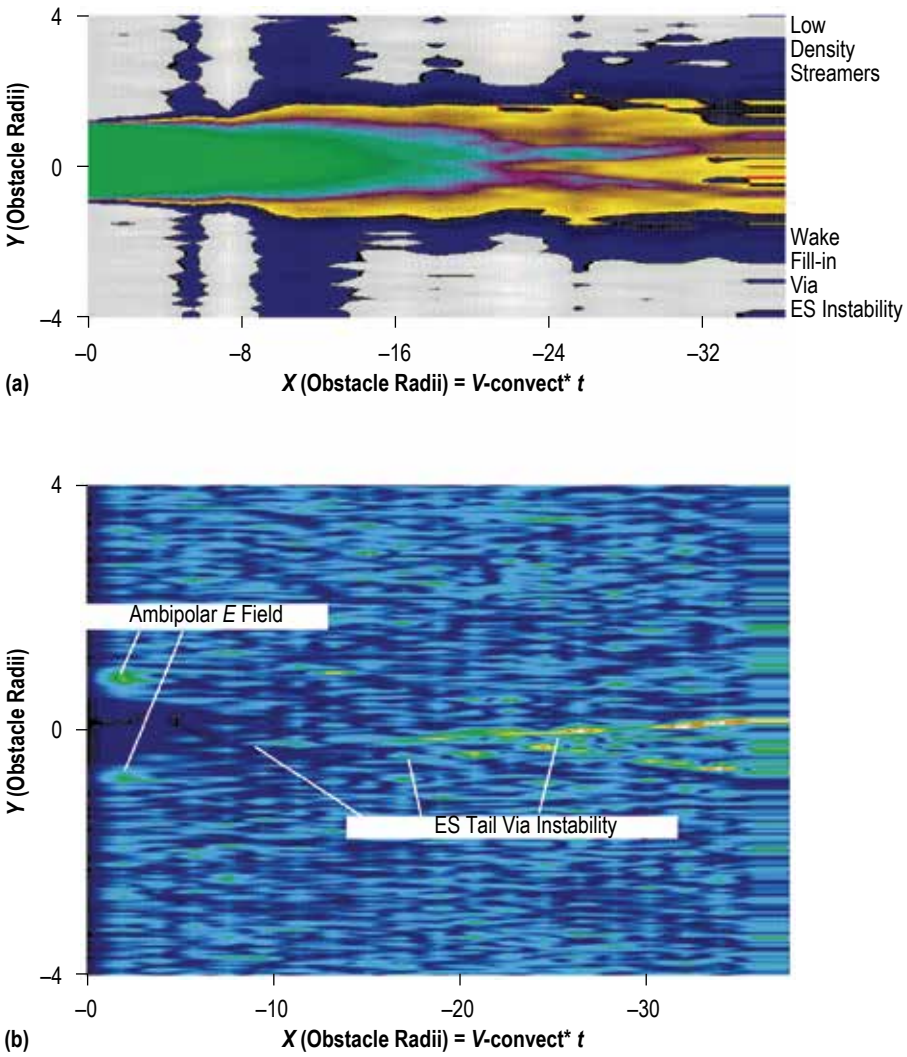

Figure 123. Kinetic simulation of the lunar wake showing the formation of the void region and associated electrostatic fields (development of strong ambipolar *E*-fields appear along the wake flank near the Moon): (a) Ion wake density and (b) wake electric field.[205]

Both the density and temperatures simulated in the model compared almost identically to those actually measured by the WIND spacecraft at the 6.5 R_L crossing location. Figure 124 is a comparison of WIND measured and simulated densities and ion beam velocities across the feature. Note that the density dropout is nearly one-to-one and the ion flow speeds (two beams coming from opposite flanks) vary nearly identically between measurement and simulation.

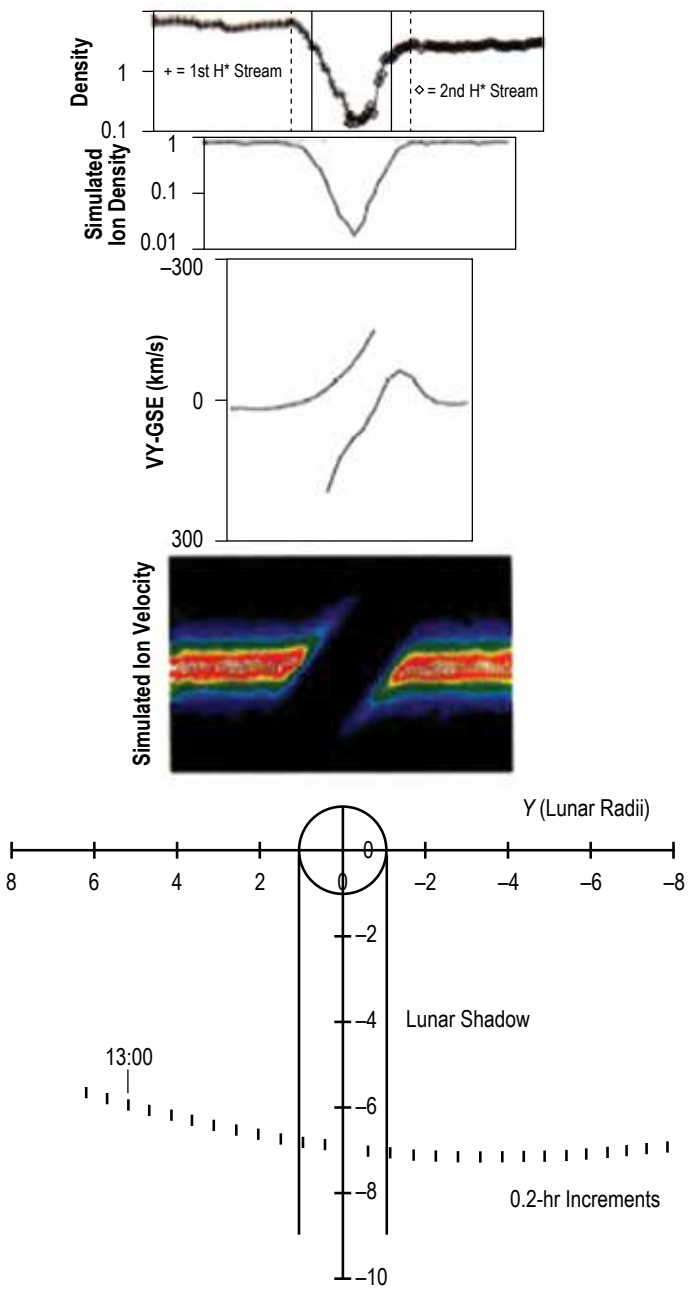

Figure 124. Comparison of wind density and simulation density along with wind ion beams and simulation ion distributions for the December 24, 1994, wake encounter near 7 R_L (development of two separate beams appears in both measured and modeled sets).[205]

8.2.5 Plasma Wake Interactions and Spacecraft Effects

Traditional spacecraft surface charging, which can occur for the CEV, lunar landers, lunar EVAs, and lunar habitats occurs from high-energy electrons impinging on spacecraft surfaces. The following factors influence the amount of charging:

- Potential of the surface.
- Secondary and photoemission characteristics of the surface materials.
- Bulk and surface resistivities of surface materials.
- Flux and spectrum of the impinging electrons.
- Geometry of the spacecraft (i.e., where the spacecraft dielectrics and conductors are located, which are in sunlight and which are in shade).
- Grounding schemes and floating conductors.
- Spacecraft wakes.
- Other factors.

For a description and mitigation techniques for spacecraft charging, see the references listed in section 5.4.7.2.

Passages of spacecraft into the lunar wake region are made both in darkness (no photoemission) and into a very tenuous plasma environment. As a consequence, the most serious concern is spacecraft charging effects. Halekas et al.[203] demonstrated that the LP spacecraft charges to a few hundred volts negative during wake passages. During a solar storm when a flux of energetic particles is expected, the spacecraft could charge even more negative. As such, there should be a special emphasis on spacecraft charging practices, including tying all surfaces to a chassis ground and verifying that any carbon composite systems are coated with conductive paints (that tie to ground). The objective is to keep any part of the spacecraft from charging to a differential voltage relative to other well-grounded systems.

Recent analyses by Halekas et al.[180] of the lunar surface charging measured from counterstreaming electrons on LP in 1998 have shown that in solar energetic particle events, when the Moon is in the magnetotail, shadowed areas can charge up to potentials of ~ –4.5 kV. It is expected that spacecraft or landers deeply immersed in the lunar wake may charge to similar levels. Such large potentials may have important consequences for surface expeditions near the lunar poles.

8.2.6 Magnetosphere Plasma Interactions and Spacecraft Effects

As shown in table 98, the plasma sheet consists of a low density but very warm plasma component. A concern is spacecraft charging in the warm plasma, which will tend to make unlit surface charge to large negative values (relative to sunlit surface that have photoemission processes). As such, there should be a special emphasis on spacecraft charging practices, including tying all surfaces to a chassis ground and verifying that any carbon composite systems are coated with conductive paints (that tie to ground). The objective is to keep any part of the spacecraft from charging to a differential voltage relative to other well-grounded systems.

8.3 Ionizing Radiation Environment

The lunar space ionizing radiation environments are the same as those discussed in section 6.5 for 60 R_e. Since the Moon does not have any magnetic field that could provide any geomagnetic screening, the ionizing radiation environment will be composed of the unscreened GCRs and SPEs. The details of these environments and the effects on electronics are presented in sections 2.12, 3.11, and 5.5.

8.4 Lunar Gravity

Detailed gravity models of the type needed for precise orbit determination are derived from tracking data from orbiting spacecraft. For Earth there are, of course, many satellites and extensive data sets. However, for the Moon this is not the case. Suitable data are available from the Lunar Orbiters (I–V), Apollo 15 and 16 and their subsatellites, Clementine, and LP. These data are limited in two important aspects: (1) Orbit inclinations are limited to low inclination (<30°) and polar inclinations and (2) no direct tracking data are available from the backside passages. As a result, expected errors in the geoid reach 30 mm on the far side at mid-high latitudes, and orbit propagation errors will be greatest for the 40° to 70° and 130° to 160° inclination ranges. The situation cannot be improved until additional data from new missions become available.

Details and accuracy of the lunar gravity field require more careful consideration for lunar spacecraft design than is typically needed for Earth-orbiting spacecraft. Because there is no lunar atmosphere, lunar missions may use lower orbits (≤100 km) where the gravity variations have the greatest effect. Also, the variations represent a greater fraction of the total field. Without station keeping, a satellite placed in circular polar lunar orbit at 100 km will impact the surface in approximately 160 days. If the initial polar orbit is at 50 km, the lifetime is only approximately 50 ± 5 days, depending upon initial longitude. A more extreme example, the propulsionless Apollo 16 subsatellite, which was released into a near circular 100 km orbit at a low (10°) inclination, impacted the surface after only 36 days. For higher altitude orbits (≥200 km), the details of the field become much less critical for design applications and it becomes appropriate to use truncated or simplified models for many applications.

8.4.1 Lunar Gravity Design Model

The Gravity Recovery and Interior Laboratory lunar gravity model is currently under evaluation for use by the Exploration program.

The gravitational potential of the Moon is expressed in terms of a spherical harmonic expansion with normalized coefficients $\left(\overline{C_{nm}}, \overline{S_{nm}}\right)$ in the form:

$$U = \frac{GM}{r} + \frac{GM}{r}\sum_{n=2}^{\infty}\sum_{m=0}^{n}\left(\frac{a_c}{r}\right)^n \overline{P_{nm}}(\sin\phi)\left[\overline{C_{nm}}\cos(m\lambda) + \overline{S_{nm}}\sin(m\lambda)\right], \tag{73}$$

where GM is the lunar gravitation constant (universal gravitation constant times the lunar mass), $\overline{P_{nm}}$ represents the fully normalized associated Legendre polynomials, a_c is the reference radius of the Moon (1,738 km) for the model specified, ϕ is the latitude, and λ is the longitude.

The model selected for design applications is the LP150Q model. The LP150Q lunar gravity field is a 150th spherical harmonic degree and order model that was developed using all available data from past U.S. missions to the Moon, including the Lunar Orbiter missions (I–V), the Apollo 15 and 16 subsatellites, Clementine, and all LP Doppler and range data. The LP data include all 100 km altitude data from the primary mission (which lasted for approximately 1 year) and all extended mission data consisting of 1 month at an average altitude of 40 km and 6 months at an altitude of 30 km. The model was produced by Alex Konopliv at the Jet Propulsion Laboratory.

Trajectory and navigation related model information must be used in the design of reference trajectories and in the development of baseline operational navigation strategies. Adequate sensitivity analysis is needed to ensure that the design will cover the range of DRMs. The gravity field is available on-line at <https://pds-geosciences.wustl.edu/geodata/lp-l-rss-5-gravity-v1/lp_1001/sha/>.[206]

The LP150Q model should not be simply truncated to fewer terms for applications requiring lower fidelity. A lower order model must be generated by fitting a complete data set with fewer terms.

It is important that the proper astrodynamic constants and coordinates be used in conjunction with the model when optimum accuracy is needed. For the DE403 JPL ephemeris, the Earth gravitation constant is:

$$GM_{\text{Earth}} = 398{,}600.435608 \text{ km}^3/\text{s}^2 = 0.888769245056500600 \times 10^{-9} \text{ AU}^3/\text{day}^2 \ . \qquad (74)$$

The ratio of the mass of the Earth to the mass of the Moon is 81.300585 and the lunar radius is 1,738 km. Carranza et al.[207] discuss conversion between the DE403 coordinates and the International Astronomical Union 1994 coordinates. At the lunar surface, the shift between these two systems is approximately 700 m.

Errors intrinsic in the model are predominately due to data limitations. Thus, resulting errors in orbit propagation are very dependent on the orbit being considered. The errors will be small when the orbit matches closely to one of the satellite orbits used in developing the model, but they are much larger for inclinations far from those covered by the data set or when the orbit periapse is on the lunar far side. Near-polar and near-equatorial inclinations are represented in the data set, so errors for similar orbits can be anticipated to be only approximately 20 m radially and on the order of 1 km along track for a 2-day simulation at 100 km.However, for inclinations between 30° and 80°, the errors increase such that the radial error can reach 500 m for a similar 2-day simulation. Orbit determination errors are discussed in detail in Carranza et al.[207]

Note that this specification is not intended for operations, and hopefully new models incorporating direct measurements from the lunar backside will be available prior to crewed missions.

As discussed above, for high orbit applications, this 100×100 coefficient model is more complex than will be needed for many hardware design applications and it may be appropriate to use a truncated set of coefficients, especially in preliminary and noncritical applications. The average truncation error in orbit eccentricity for the last 7 days of a 30-day orbit propagation from initially circular polar orbits is illustrated in figure 125. Three curves are presented for orbits beginning at 50, 100, and 400 km altitude and 0° longitude. For the 50 km case, the effect of various initial longitudes (initial right ascension) was also investigated. The error variation due to initial longitude was ±2% at 40°×40° resolution, and ±10% at 20°×20° resolution, about the values indicated on the graph. Thus, the variations, with respect to initial right ascension, are roughly equivalent in magnitude to going from 50 to 100 km initial altitude. Truncation errors for nonpolar orbits may be different.

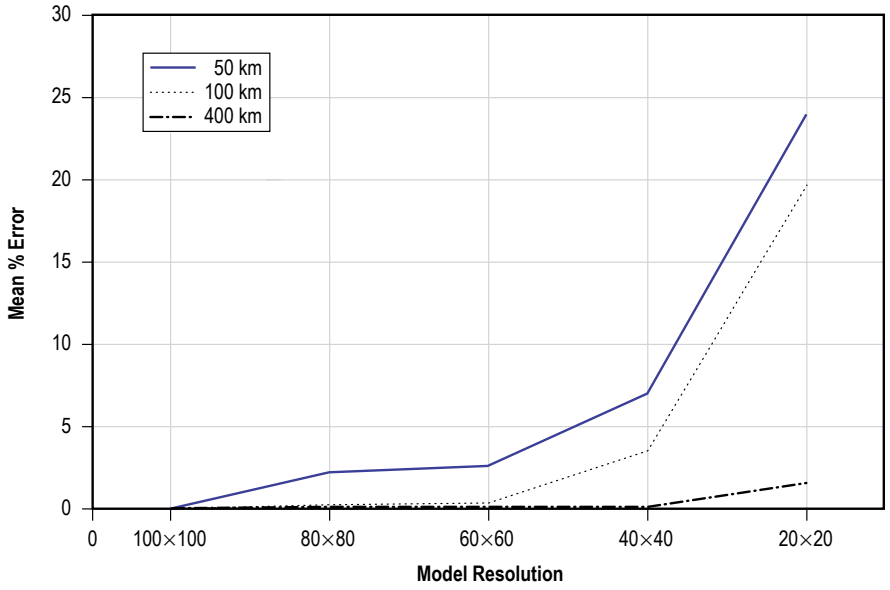

Figure 125. Indication in the growth in truncation error relative to orbit propagation with the 100×100 model (30-day propagation of circular polar orbits beginning at 0° longitude and 50, 100, and 400 km altitude. The graph shows average error in eccentricity over the last 7 days of the simulation).

8.5 Lunar Eclipse

A lunar eclipse occurs when the Earth is between the Sun and the Moon, and the Earth's shadow falls on the Moon. The Moon's orbit is 5° inclined with respect to the Earth's orbit around the Sun. This results in a lunar eclipse occurring only when the ascending or descending nodes fall

in the ecliptic during a full moon. Lunar eclipse tables can be found at <http://eclipse.gsfc.nasa.gov/lunar.html> for the years 1901 through 2100.[208] There may be up to five lunar or solar eclipses in a year but the combined total of both will never exceed seven.

There are three types of lunar eclipses: penumbral, partial, or total. During a penumbral eclipse, the Moon only encounters the penumbral shadow. A partial eclipse will have only part of the Moon going through the penumbral and umbral shadows. However, during a total eclipse, the Moon experiences all three types of events during the eclipse: penumbral, partial, and total. Light is refracted in the Earth's atmosphere and will give the Moon an orange, red, blue-green, or purple hue while totally immersed in the umbra. The color is dependent on atmospheric conditions on Earth while the Moon is experiencing totality.

The stellar apparent magnitude is a numerical value of the observed brightness of a celestial object as seen from Earth. A full moon has an apparent magnitude of –12.6 (the brighter an object the lower the numerical value), while the Moon during totality ranges from –3.5 to 1.5.[209] These numbers are derived using an eclipse model[209] during mid eclipse. Using these computed values, the solar flux can be calculated during an eclipse from the following equations:

$$\Delta m = m_{\text{eclipse}} - m_{\text{full moon}} = m_1 - m_0 \tag{75}$$

calculates the decrease in apparent magnitude during an eclipse and

$$\underline{I_0} = 10^{\frac{\Delta m}{2.5}} \tag{76}$$

calculates the ratio of brightness of a full moon to the eclipsed Moon I_1.

By setting the $\text{eclipse}_{\text{flux}}$ equal to 1,367 W/m^2, the solar flux during a lunar eclipse can then be calculated using the average I_0/I_1 solar flux at the Moon of 1,367 W/m^2. This corresponds to 0.03% to 0% of solar flux reaching this region. This is of concern to a spacecraft orbiting the Moon if the spacecraft is dependent on solar energy.

During the years 2018–2035, the worst case lunar eclipse occurs on June 26, 2029. Using the data from this eclipse as an example, a spacecraft in a circular orbit would experience totality for the following altitudes versus times around the Moon and would experience worst case minimum solar flux for times indicated in table 99.

Table 99. Projected worst case minimum solar flux during lunar eclipse, June 26, 2029.

Orbit Altitude (km)	Totality (min)	No Solar Flux (Worst Case) (min)
100	188	233
500	197	242
1,000	177	234

9. LUNAR SURFACE ENVIRONMENTS

This lunar environment section covers those environments in lunar space 10 to 60 R_e.

The lunar surface is covered with a 'soil' called the regolith. It is formed from continuous bombardment of the surface materials by micrometeoroid impacts, and is modified by the solar UV flux, the solar wind, radiation, and other weathering factors.

The Moon can be divided into two major terrain classes on the basis of composition and age: (1) The Highlands and (2) the Mare (plural Maria). The Highlands and Mare terrains have very different morphologies due to the length of time each type of terrain has been exposed to meteorite bombardment (the 'exposure age'). See figure 126.

Figure 126. Near side of the Moon—the bright rayed crater in the southern highlands is Tycho (fig. 127) (courtesy of NASA).

9.1 Principal Surface Features—Lunar Highlands

Lunar highlands were originally formed as the Moon accreted and consist of plutonic rocks that have been modified by impact. The shallow crust consists of a megaregolith (kilometer thickness) formed during the early heavy bombardment composed of thick deposits of basin ejecta, and a meter scale regolith. Compositionally, the highlands are 'anorthositic.' See figure 127.

Figure 127. Central southern highlands—the fresh crater at center left with the central peak and terraced rim is Tycho (courtesy of NASA).

The maria have relatively smooth lava surfaces that formed after the end of the heavy bombardment, hence they are relatively less cratered than the older highland terrain. Compositionally, the maria can be considered 'basaltic.' Because they postdate the heavy bombardment, they have a relatively thin regolith compared to the highland terrain. See figure 128.

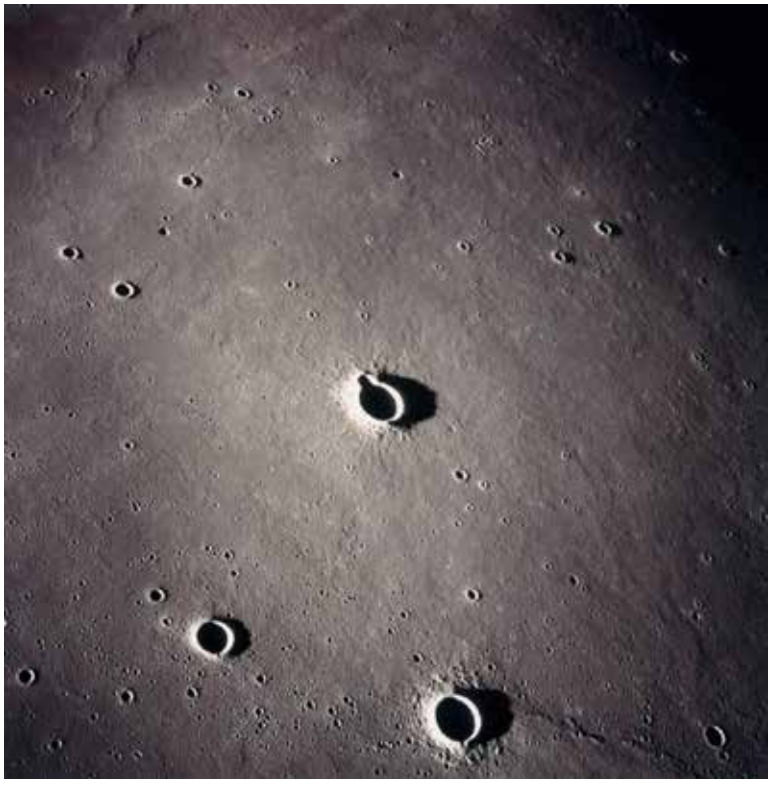

Figure 128. A portion of Oceanus Procellarum, including the craters Schiaparellic and Schiaparellie—a typical mare surface with relatively few impact craters (courtesy of NASA).

9.2 Surface Feature Properties

9.2.1 Crater Size Distributions

Crater size frequency distributions have been compiled for the highlands and mares areas on the lunar surface from both orbital and surface imaging data. These data were compiled primarily for scientific purposes (e.g., to estimate the relative and absolute age of an area). As a result, such compilations typically focus on craters having diameters >1 km. A few of those compilations have been made which include craters down to the submeter size range. These analyses were done with Surveyor surface images, a few very high resolution lunar orbiter images, and now using the Lunar Reconnaissance Orbiter (LRO) Lunar Reconnaissance Orbiter Camera (LROC) images. It is the craters whose diameters are in the tens of centimeters to hundreds of meters scale that are relevant to landing and surface operations.

On a level surface, at diameters less than about 300–500 m, the craters are in steady state, in equilibrium, or saturated in terms of the frequency. This means that, as time passes, each new impact destroys an existing impact and the frequency remains more or less constant. Figure 129 illustrates the size frequency distribution for a number of sites. The red line denotes the steady state level and it can be seen that the observed frequency of craters does not extend above this value. For a typical intercrater area, the frequency of 1-m-diameter craters is ~10/100 m^2; for 10-m craters, it is ~0.1/100 m^2.

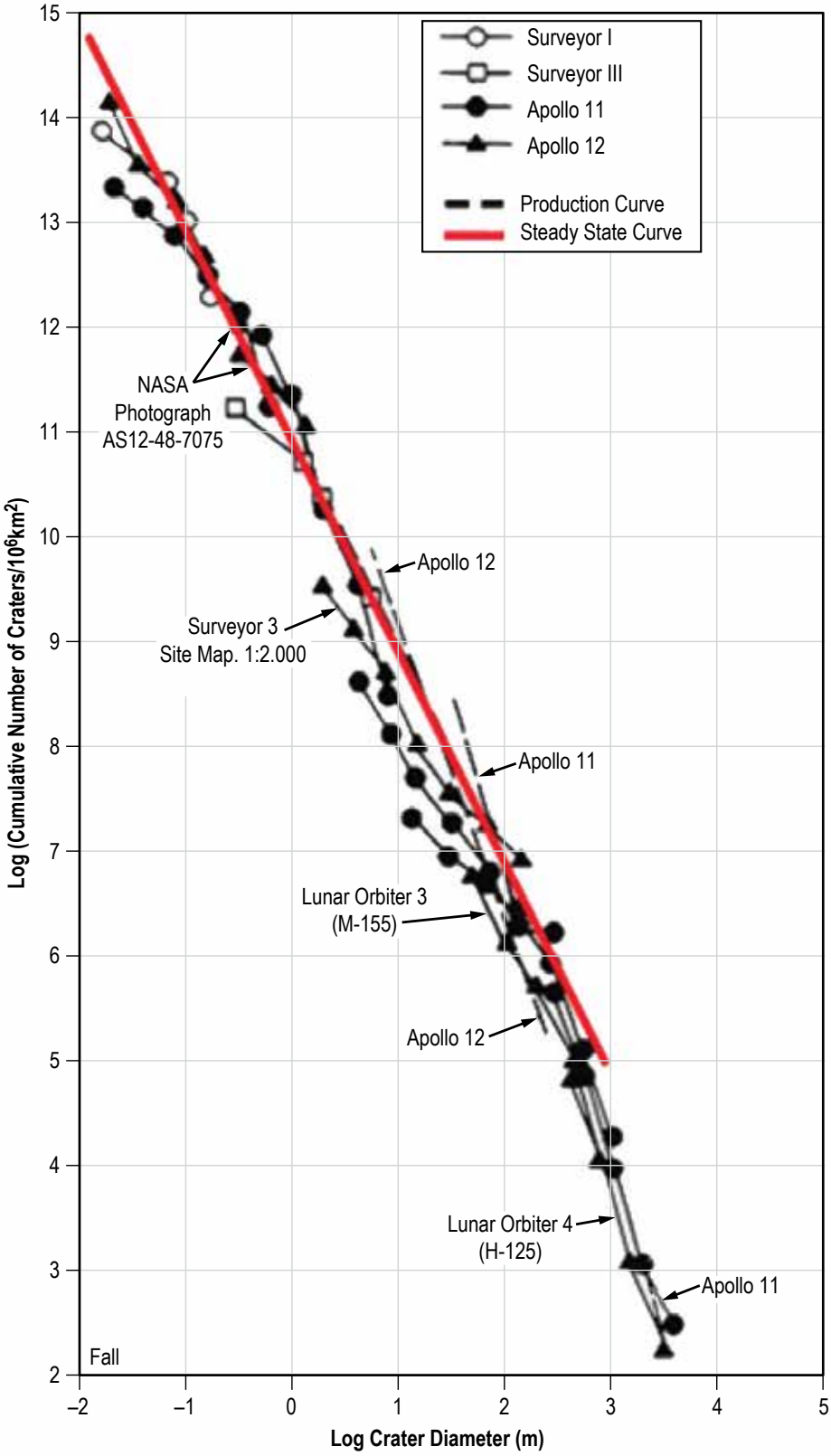

Figure 129. Crater size frequency distributions for several areas. The red line denotes the steady state or equilibrium condition. At diameters <200–300 m, the surface is in approximate equilibrium.[210]

On a surface having slopes, the frequency of craters at the relevant diameters is significantly less than the value that would be expected based on the absolute formation age of that surface. Figure 130 illustrates a mare surface under low Sun. The roughness is exaggerated by the low illumination angle; the Sun is 2.8° above the horizon. The area labeled A is a very old 1,500-m-diameter impact crater which is almost completely infilled. The gentle slopes on the interior wall have very few impact craters. This lack of craters and the texture on the surface ('elephant skin') is the result of micrometeoroid-induced downslope creep of the regolith. This creep is sufficiently active to remove most craters. It is also observed on steeper slopes covering larger area.

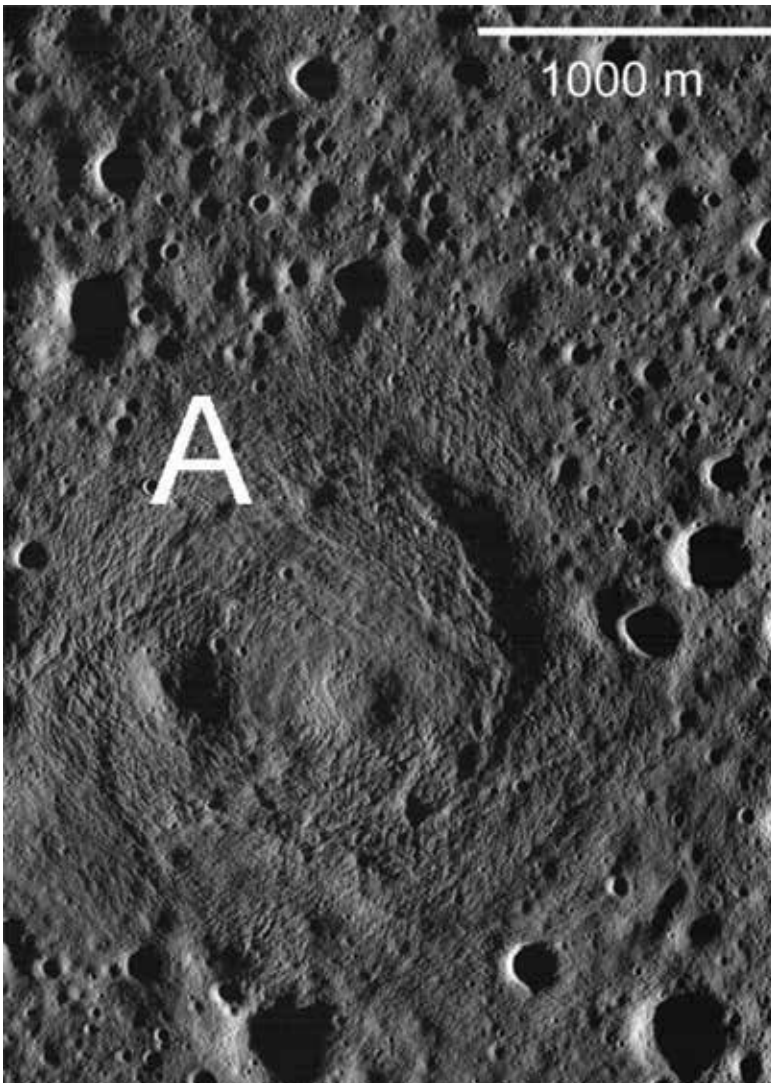

Figure 130. Mare surface in northwest mare imbrium under very low illumination; Sun is illuminating from the right. The cratered nature of mare surface is evident. Due to the low Sun, even the older shallow craters are apparent. 'A' is an old 1,500 m crater. Creep of the regolith down the interior slopes has removed small diameter craters and produced the observed texture (LROC M116465524RE) (courtesy of NASA/GSFC/Arizona State University).

The topography of an impact crater is a function of its age; as the crater ages, the rim height decreases and the floor becomes shallower due to erosion by micrometeoroid impact.

For craters ~<700–800 m diameter, the initial depth/diameter relationship is:[211]

$$R_a = 0.15 D_a^{0.88} \ , \tag{77}$$

where R_a = depth (km), relative to external surface, not from the rim, and D_a = diameter (km).

9.2.2 Rock Size Distributions

The distribution of rocks on the lunar surface is not random but rather is tied directly to the geology and geologic history of the region. Rocks are typically found associated with the ejecta of fresh craters, within the interiors of craters, and along scarps of exposed bedrock (e.g., rille walls). There are a few random rocks scattered across the surface that represent distal ejecta-clasts launched from impact events. Compilations of the size-frequency distribution of rocks for different areas using Lunar Orbiter images have been compiled by Cintala and McBride,[212] Bart and Melosh,[213,214] and Cameron and Coyle,[215] (G. Bart, "Lunar surface geology from analysis of impact crater and their ejecta," unpublished dissertation, University of Arizona, 2007).

On the lunar mare, the surface is composed of a fragmental, impact-derived regolith that is of the order of a few meters thick. Impact craters that formed entirely within the regolith (i.e., those with depths less than a few meters) excavate only regolith material and typically do not have rocks scattered around the rim. As the diameter of the crater increases and its depth increases, the crater excavates through the regolith into the underlying basalt and ejects rocks around the crater rim (fig. 131).

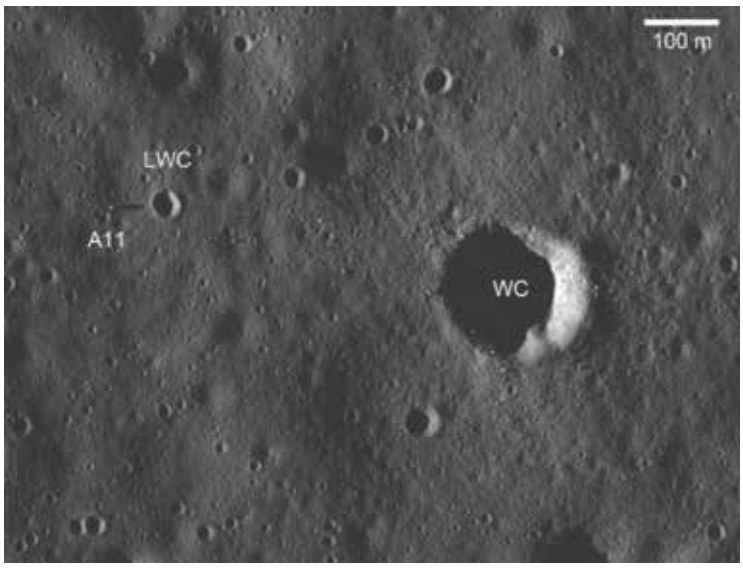

Figure 131. West Crater—fresh impact crater east of the Apollo landing site with rocks scattered around the rim. A11: Apollo 11 LM descent stage, LWC: Little West Crater (visited by Armstrong), and West Crater: WC (M117338434R) (courtesy of NASA/GSFC/Arizona State University).

Figure 132 illustrates rock maps for a number of craters showing the distribution of rocks around the craters. These figures from Bart and Melosh[214] were compiled from Lunar Orbiter images and illustrate the variation in the total number of rocks as well as the spatial distribution of rocks around the craters.

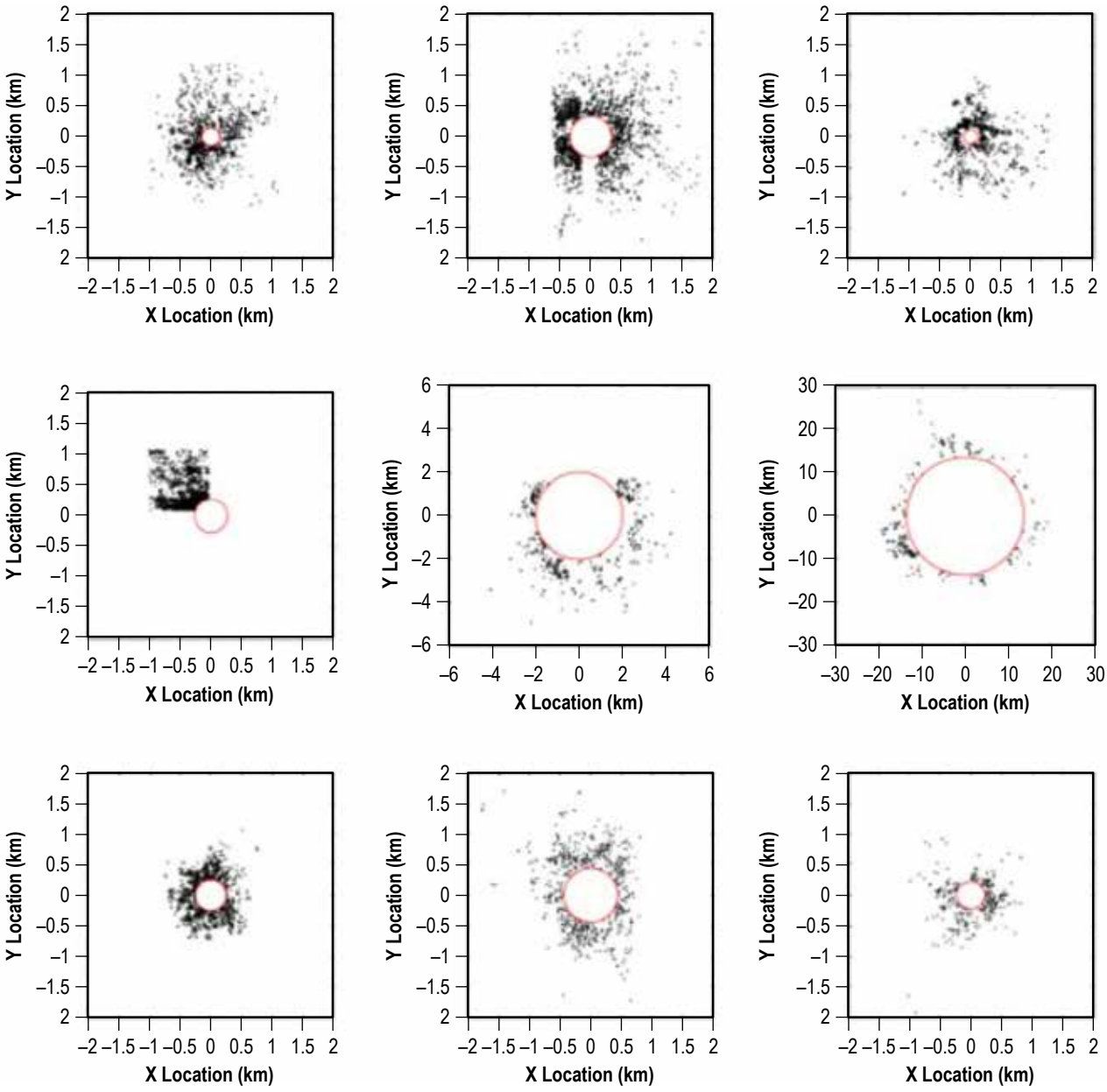

Figure 132. Map of rock locations around lunar craters showing the range of spatial distributions. Red circle denotes the crater rim (three from Bart and Melosh).[214]

Over time, the flux of micrometeorites slowly breaks down the rocks into smaller and smaller particles. A number of craters are observed on the mare in which rocks are not present (or rarely present) around the rim but whose interiors have large number of rocks (fig. 133). There is no reason to suspect that the degradation process of rocks within the crater and around the rim should be any different, thus in these cases, the rocks presumably are being derived from bedrock exposed in the crater walls.

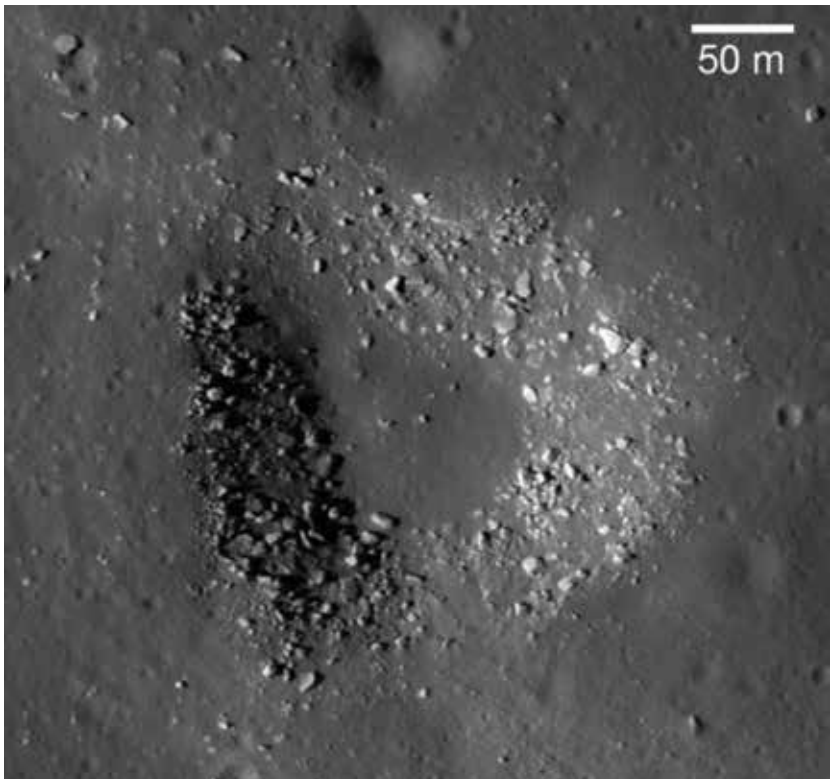

Figure 133. Impact crater with rocky inner wall; note the presence of rocks along the inner wall compared with the exterior where rocks are rare to absent (LROC image M1194490911) (courtesy of NASA/GSFC/Arizona State University).

Within the highlands, the same impact-generated regolith is formed as on the mare. However, in this case, the original target material is an impact-derived debris formed by the ejecta of large basins (the so-called megaregolith). In this case, there is not an intact bedrock surface that can be excavated and thus rocks are not as frequent.

Surface rock counts have been compiled using orbital and landed images. These analyses have suffered from two different types of problems. The orbital data have typically been of a resolution too low to resolve the rocks that are the most common hazards to landing and operations (i.e., the large rocks tens of meters are easy to recognize and avoid). Images from landed robotic spacecraft (Surveyor, Luna) have a limited range over which data can be acquired and thus may not be representative of a larger area (i.e., Surveyor) or of poor quality (i.e., Luna). Surface images from the Apollo program allowed for detailed high-resolution data to be collected. Figure 134 illustrates the average cumulative size-frequency distributions for rocks near the Surveyor spacecraft.

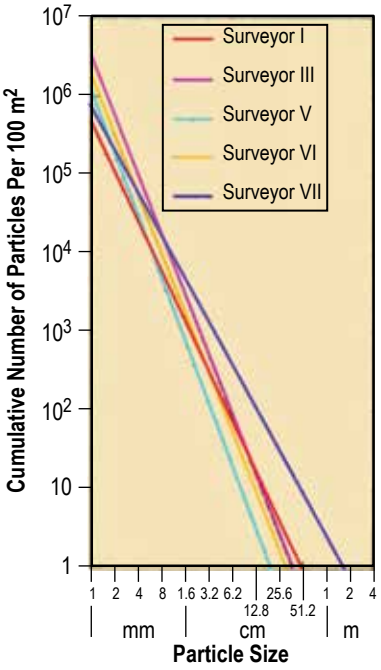

Figure 134. Cumulative size-frequency distributions for rocks near the Surveyor spacecraft derived from surface images.

During the Apollo traverses, panoramic image sequences were acquired at each of the sampling stations. From these image sequences the number and distribution of rocks within 10 m (32.8 ft) were compiled to produce maps of the rock distribution. These maps were presented in the Preliminary Science Reports of each mission. Unfortunately, the original data have been lost and the figures show only two size classes (10–20 cm and 20–50 cm) as well as the actual size of the largest rocks. Figure 135 illustrates the maps for three of the stations (4–6).

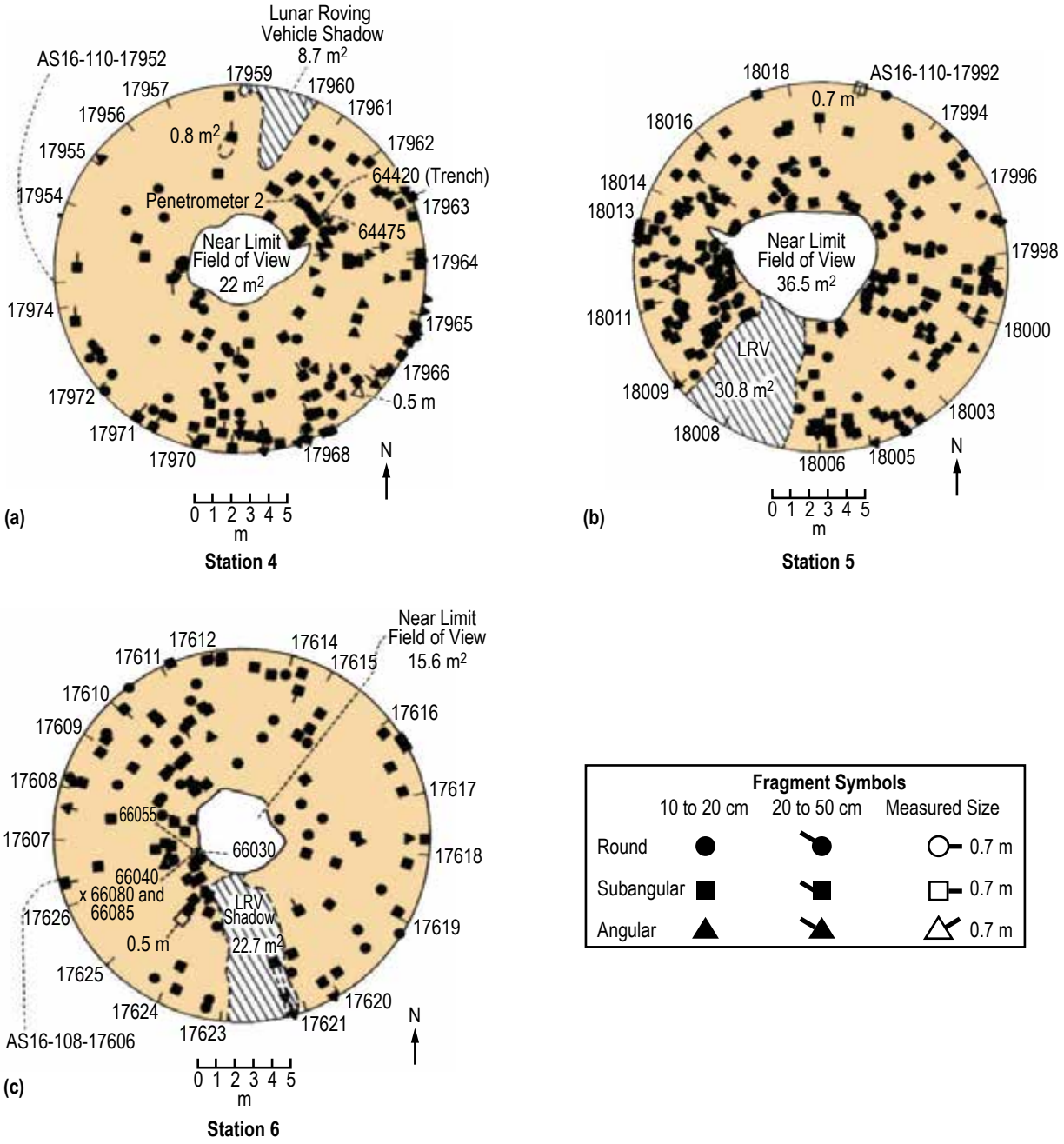

Figure 135. Maps of the rock distributions at the Apollo 16 landing site. Figures are from the Apollo 16 Preliminary Science Report: (a) Station 4, (b) station 5, and (c) station 6.[216]

The data that are illustrated in a few of the rock maps were also published as cumulative size-frequency curves. But again, the original data have been lost and only a few points are plotted on each curve. Figure 136 illustrates the cumulative size-frequency distributions for Apollo 16 stations 4–6.

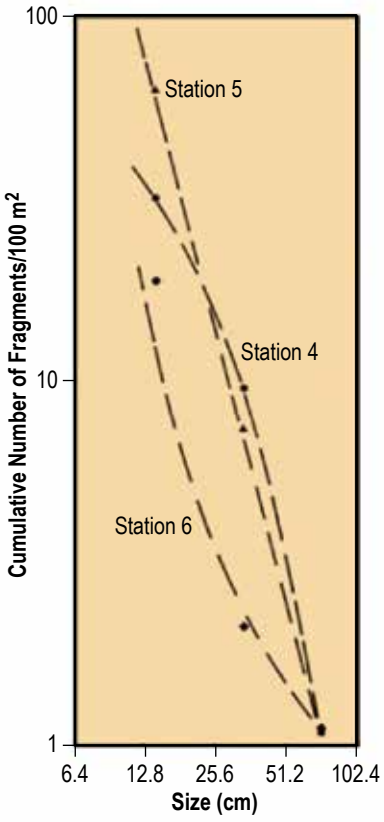

Figure 136. Cumulative size-frequency distributions for rocks at stations 4–6 at the Apollo 16 landing site. [216]

Cintala and McBride[212] compiled data for rocks at the Surveyor sites. They grouped the rocks as those within craters (such as those shown in fig. 135) and those between craters. Figure 137 illustrates their data for the Surveyor 7 site. A large counting was surveyed, such that the largest block counted was of the order 70 m.

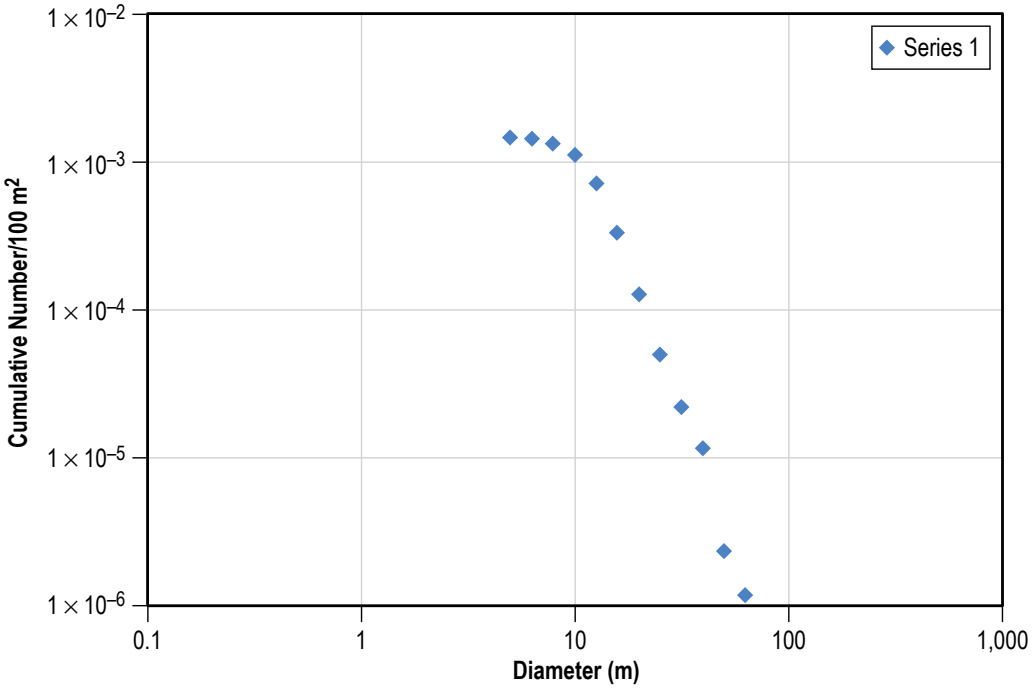

Figure 137. Cumulative size-frequency distribution for rocks around the Surveyor 7 landing site based on lunar orbiter data (data from Cintala and McBride[212]).

The LROC provides much higher resolution data than were available for most of the lunar orbiter images;[217] these data are also better controlled in terms of position and image calibration. In addition, multiple lighting angles are available for many sites to allow for an assessment of the influence on lighting angle on rock recognition. The image scale for an LROC narrow angle camera image is 0.5 m/pixel from the nominal mapping orbit (50 km). Thus, rocks of the order of 2 m can be resolved. Rock frequency data collected for a number of sites illustrate the variation in size range of the rocks, the spatial distribution, and the statistics of the population.

Figures 138–150 present a number of different areas, followed by table 100 summarizing the data. These data represent a range of areas with variable geology and rock distribution. In some cases the data are for rocks around craters; in other cases, the data indicate the distribution for intercrater areas (plains units between craters excluding rocks directly associated with ejecta).

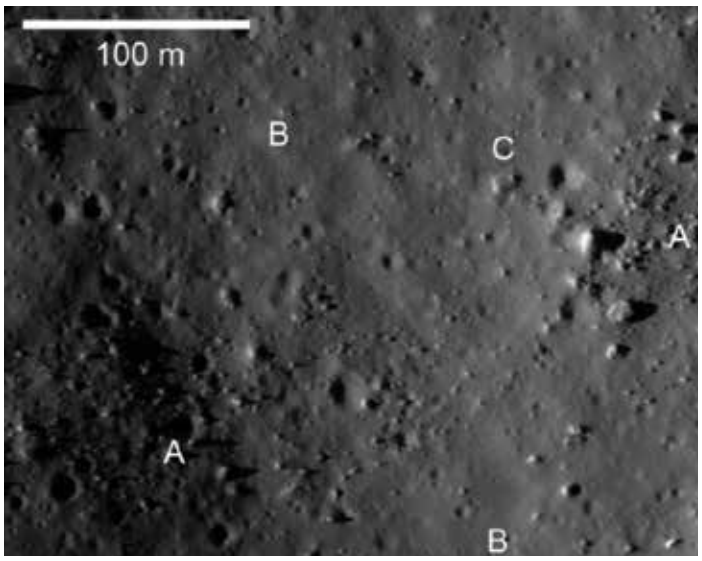

Figure 138. Western rim of North Ray Crater at the Apollo 16 landing site: A, lobes of blocky ejecta extending from the rim; B, areas between rocky lobes with fewer blocks; and C, partially buried blocks (LROC image: M1173925411) (courtesy of NASA/GSFC/Arizona State University).

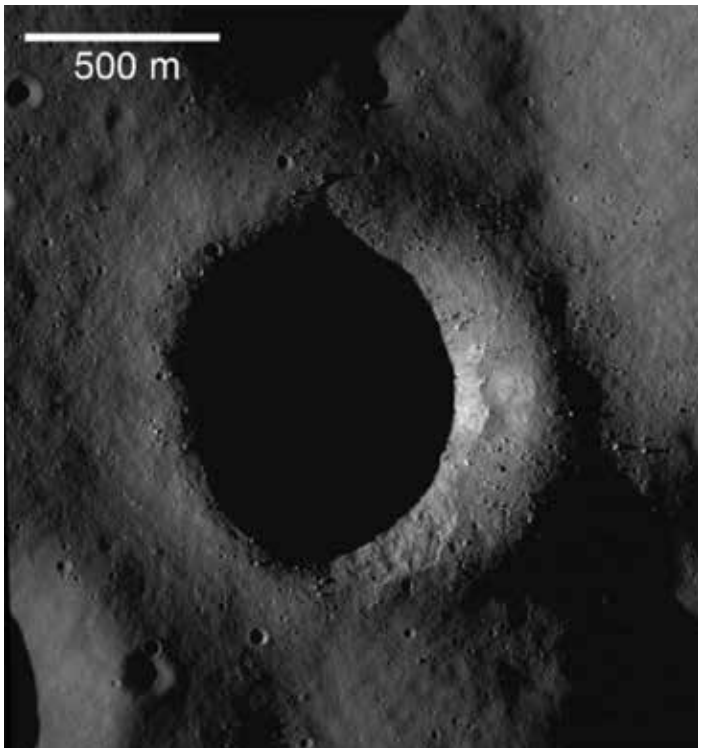

Figure 139. NRC at the Apollo 16 landing site. Counting area is the area to the west of the crater rim. (LROC image M1173925411) (courtesy of NASA/GSFC/Arizona State University).

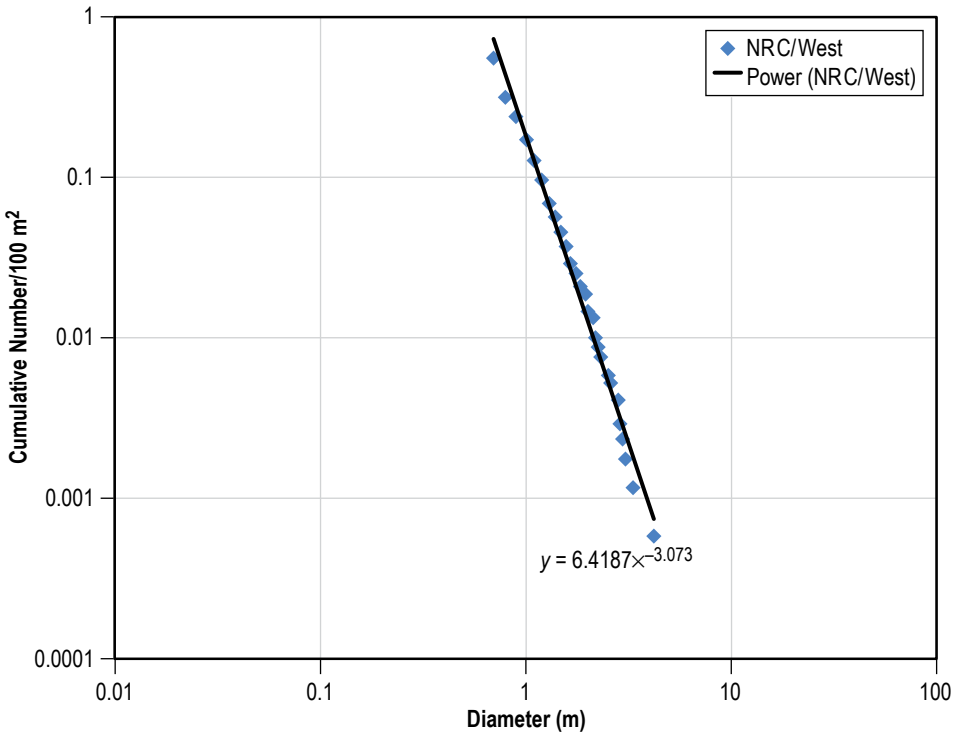

Figure 140. Cumulative size frequency distribution for rocks on the western rim of NRC (area shown in fig. 138).

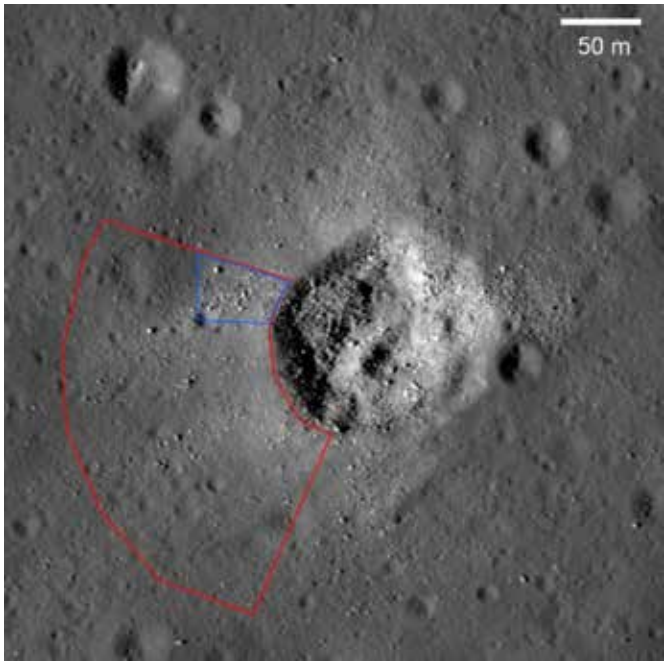

Figure 141. Concentric crater with diameter of 130 m. Area outlined in red indicates the total area counted; area outlined in blue is subarea with higher rock frequency (LROC image M1194490911), crater at –11.8721 °S./.339.432 °E. (courtesy of NASA/GSFC/ Arizona State University).

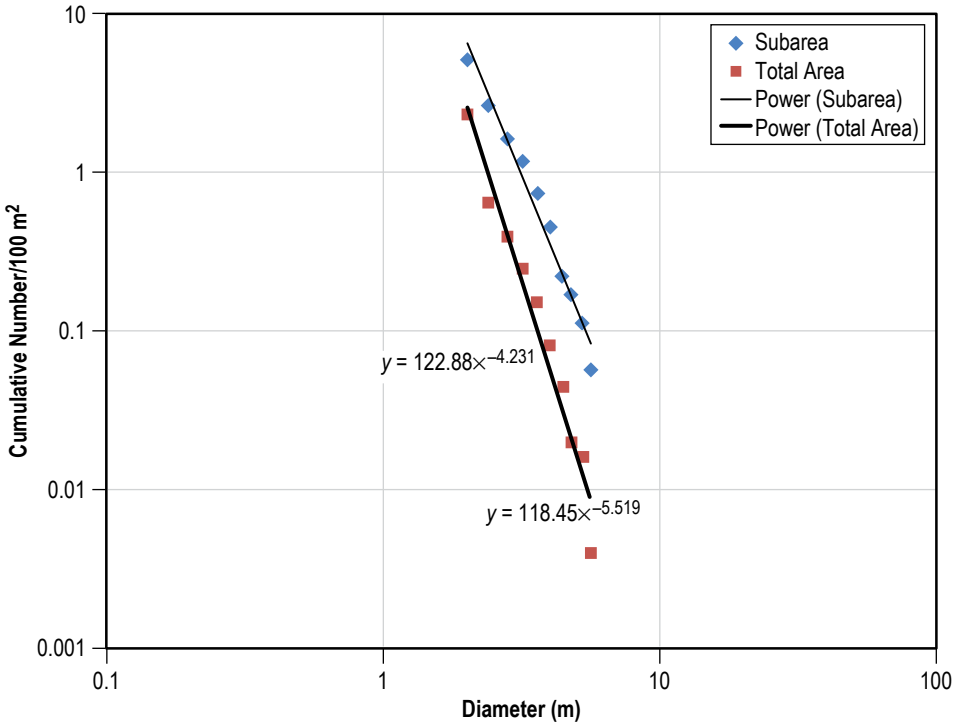

Figure 142. Size frequency distribution of ejected rocks for the crater illustrated in figure 143. Subarea is outlined in blue; total area in red in figure 141.

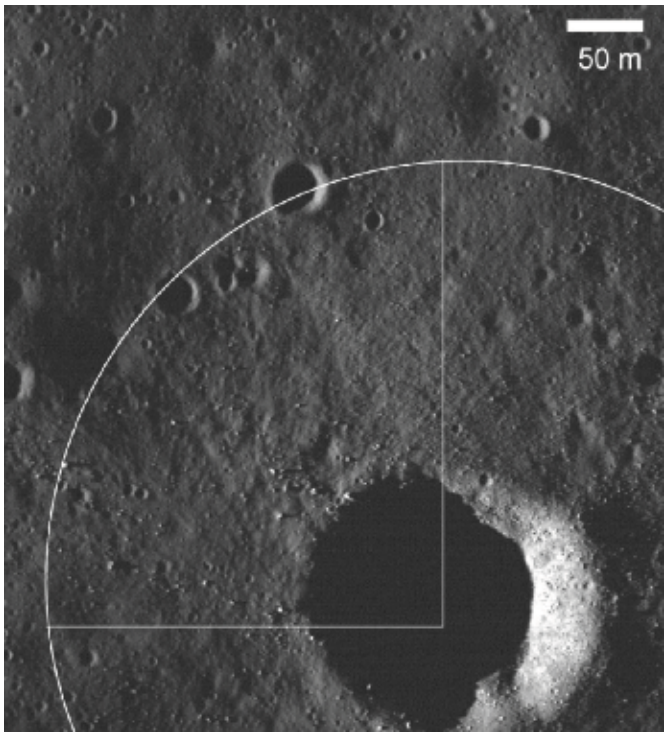

Figure 143. Counting area is the northwest quadrant of West Crater (LROC image M117338434R) (courtesy of NASA/GSFC/ Arizona State University).

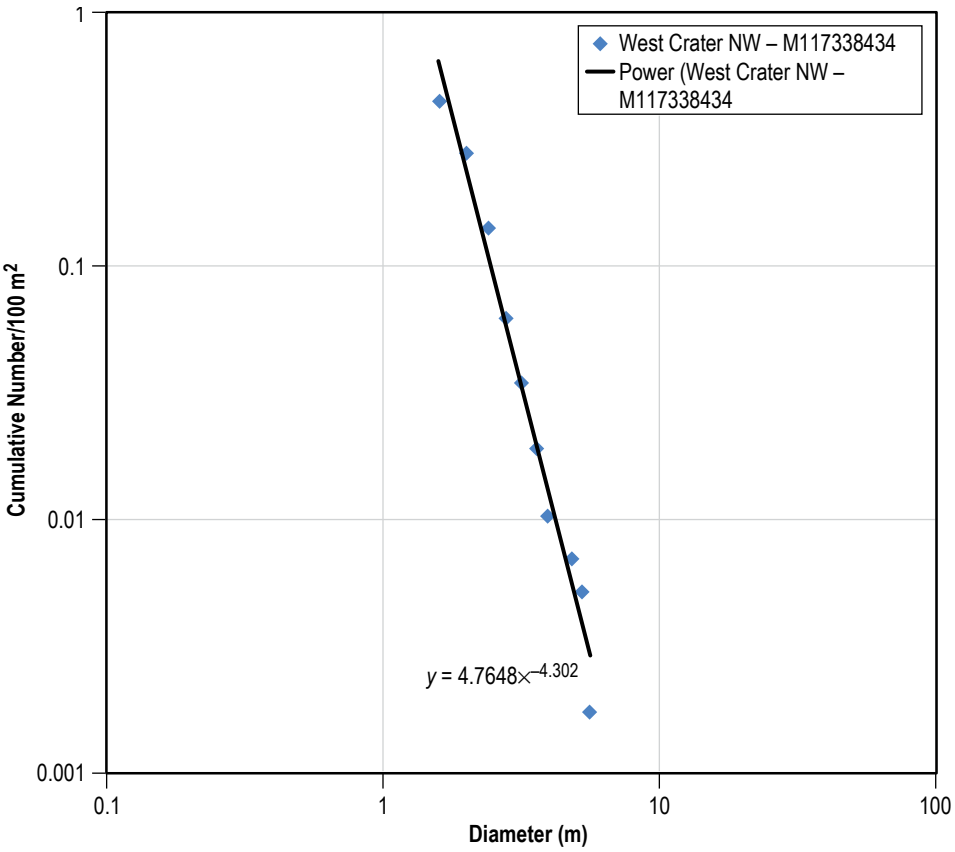

Figure 144. Cumulative size-frequency distribution for the northwest quadrant of the ejecta of West Crater.

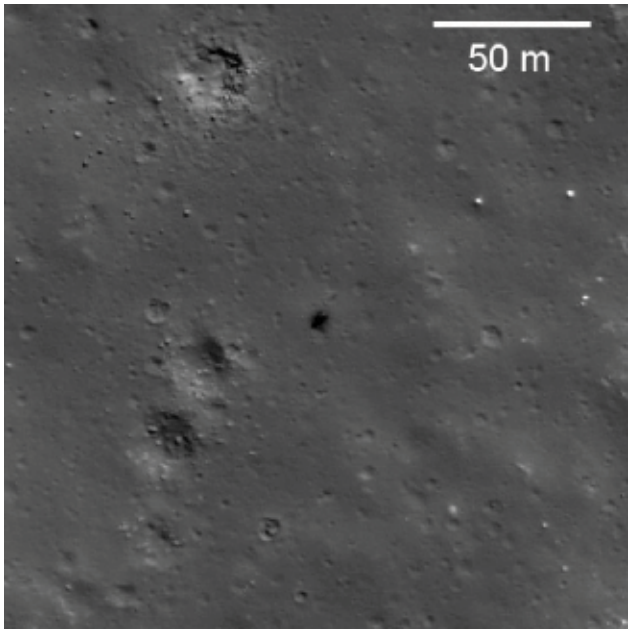

Figure 145. Area surrounding the Surveyor VII landing site (LROC image M157668488RE) (courtesy of NASA/GSFC/Arizona State University).

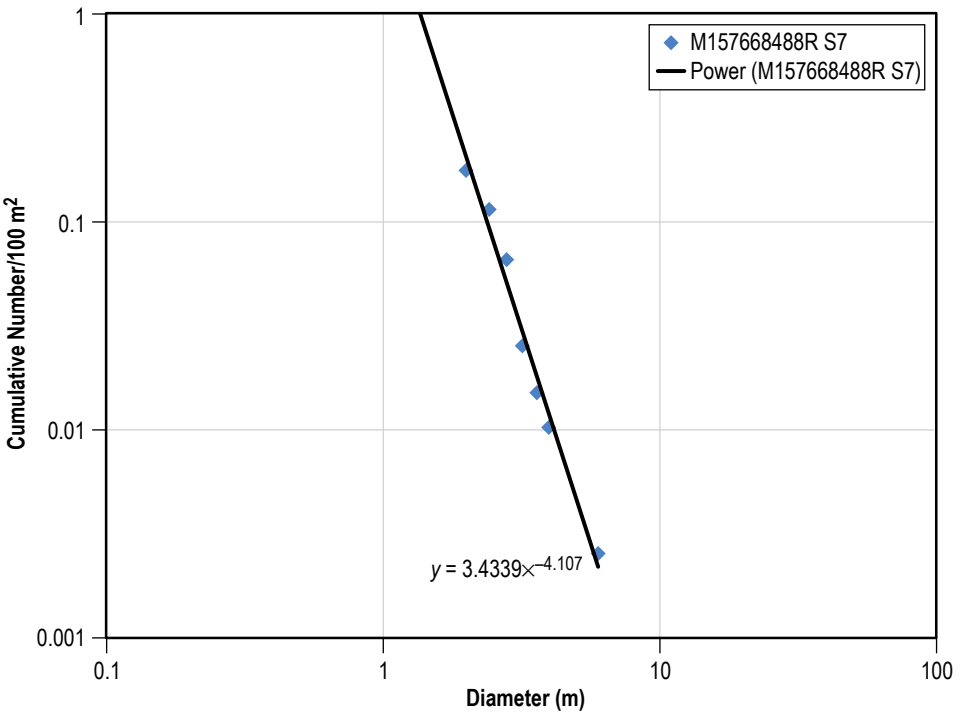

Figure 146. Cumulative size-frequency for rocks in the area outlined in figure 143. Counts exclude rocks within craters.

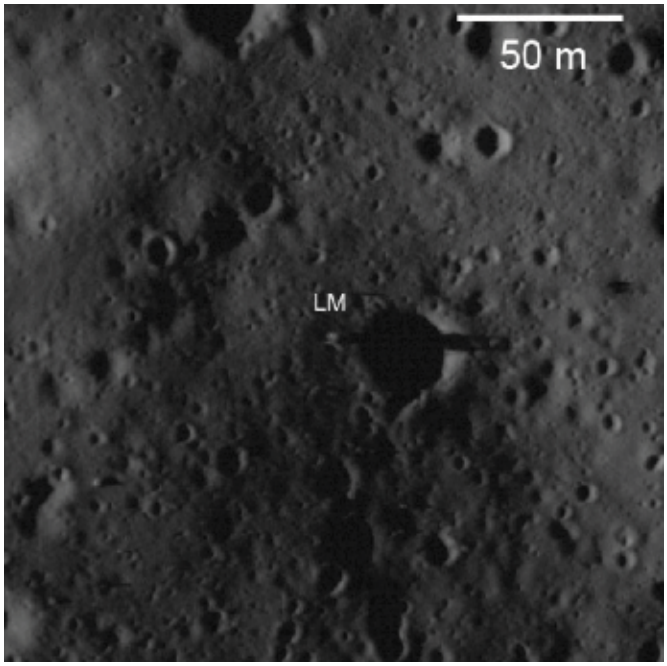

Figure 147. Area surrounding the Apollo 16 landing site; LM descent stage (LROC image M117392541L) (courtesy of NASA/GSFC/ Arizona State University).

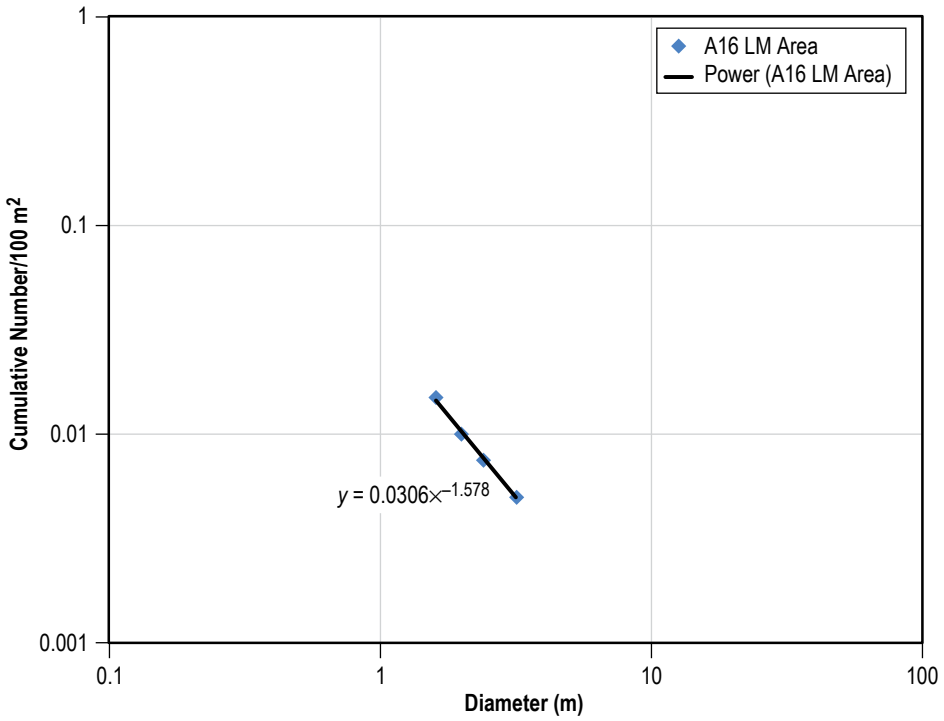

Figure 148. Cumulative size-frequency distribution of rocks observed around the Apollo 16 landing site.

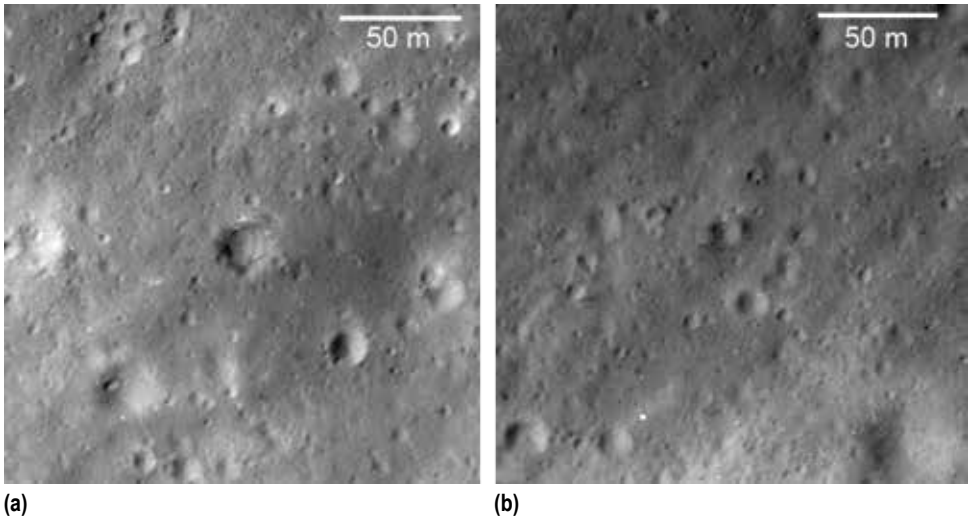

Figure 149. Apollo 16 landing sites: (a) Station 5 and (b) station 6 (LROC image: M122108795L) (courtesy of NASA/GSPC/University of Arizona).

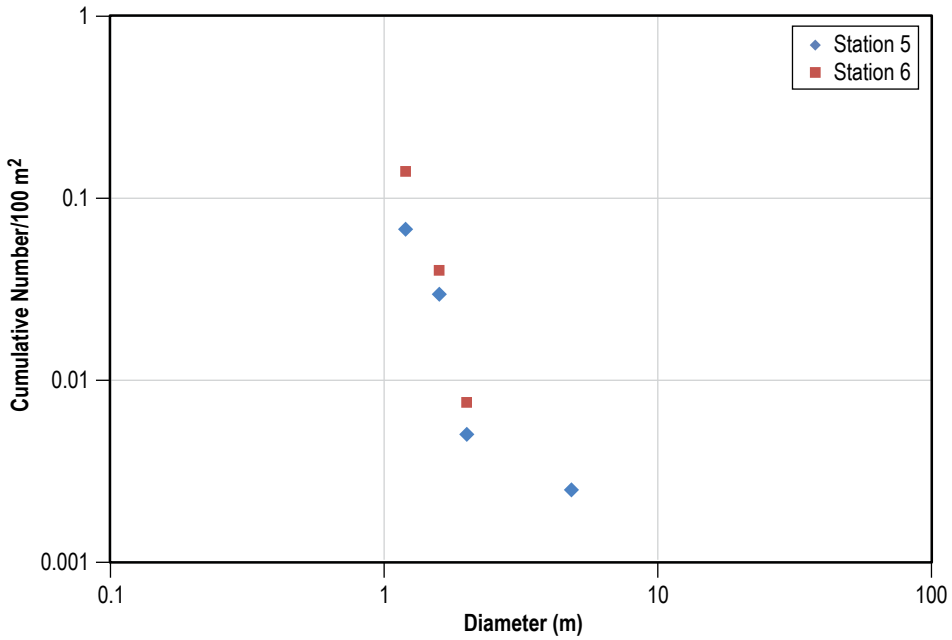

Figure 150. Cumulative size-frequency distributions of rocks at stations 5 and 6 of the Apollo 16 landing site.

Table 100. Rock frequency data.

Region	Frequency of Rocks		Distribution Slope
	10 cm	1 m	
North Ray West Rim	7,558	6	–3.1
West Crater NW quadrant	95,509	5	–4.3
Concentric Crater total	39,132,272	118	–5.5
Concentric Crater subarea	40,595,809	122	-4.3
Surveyor VII	43,932	3	–4.1
Apollo 16 landing area	1.2	<0.1	–1.6
Apollo 16 station 5	13	<0.1	–2.3
Apollo 16 station 6	183,986	0.4	–5.6

9.2.3 Slope Distributions

The distribution of slopes on the lunar surface is primarily a function of the baseline over which the slope is measured. For long baselines, the cratered highlands are rough with a large distribution of slopes whereas the maria are smooth. However, at short baselines, both the mare and the highlands are rough with similar slope distributions. It is the presence of small diameter craters (in the meter to hundreds of meters size range) which controls the slope distribution, and both the maria and the highlands are saturated with craters in this diameter range.

9.3 Regolith Composition and Characteristics

9.3.1 Lunar Regolith Properties

The lunar regolith is a fragmentary material produced on the lunar surface over billions of years by the impact of meteoroids. Each impact event shatters the surface material creating a fine-grained layer whose thickness and properties are a function of age. There are, in fact, two competing processes, the impact events break up the surface into the smaller pieces while at the same time melting small particles and fusing them into composite particles (agglutinates).

Regolith is taken to mean the entire fragmental layer on the lunar surface. A somewhat inconsistent nomenclature has developed that refers to specific size fractions. The definitions adopted here are listed in table 101.

Table 101. Particle size nomenclature.

Particle Name	Size Range	
	(mm)	(φ)
Rock	>10	< –3.32
Coarse fine	1–10	0 to –3.32
Fine fines/soil	<1	>0
Dust	<0.05	>4.32
$\varphi = -\log_2(d)$, where d is the particle diameter		

When considering analyses of the regolith (e.g., chemical, mineralogic, and physical properties), it is critical to recognize that the data were compiled from very small samples of specific size fractions. Most regolith samples were sieved at JSC after return from the Moon into the following size fractions: >10 mm, 10–4 mm, 4–2 mm, and <1 mm. Most of the laboratory data have been collected using particles <1 mm. Study of the >1 mm size fraction is so limited that it is difficult to compare with analyses of the <1 mm size fraction. For Luna and Apollo core material, data are for the <0.25 mm fraction. No data on size fractions >1 mm have been included in attempts to infer bulk properties of the regolith. Except for a few rock fragments, the average size of a rock clast in the regolith is <250 μ. It is difficult to determine the petrology of such fragments and hence the chemistry has been used to infer the petrology of the rock fragment (i.e., individual minerals have not actually been determined).[203,205,218–272]

9.3.1.1 Size-Frequency Distributions. Particle size-frequency distributions were compiled on a large number of lunar regolith samples (e.g., fig. 151). These data were collected for small aliquots of size subsampled material. They do not represent the size-frequency distribution for the bulk regolith.

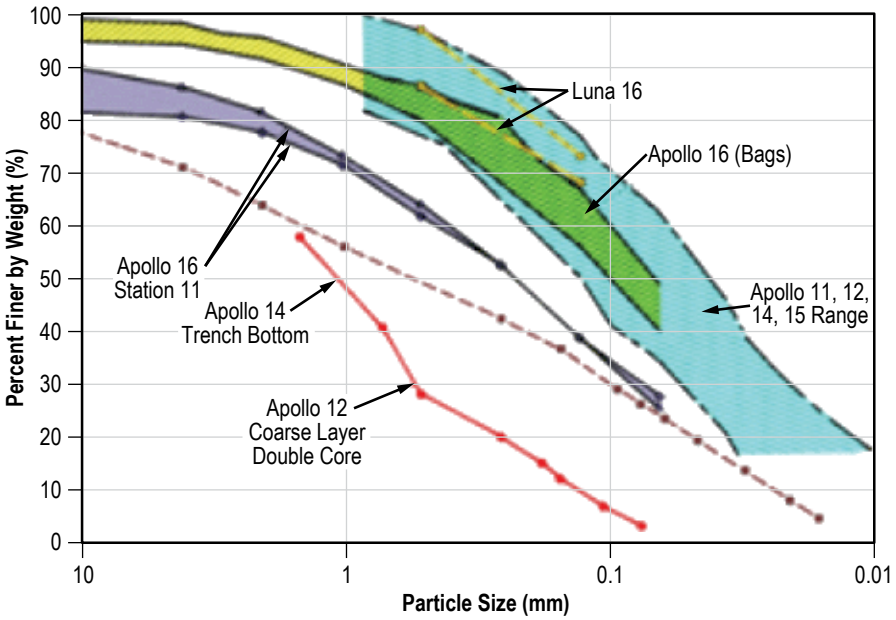

Figure 151. Cumulative size-frequency distribution of regolith grain size from a variety of samples. Note the very coarse material from the Apollo 12 double core and the Apollo 14 trench.[216]

Figure 151 shows the size-frequency distribution for several lunar samples. Bands illustrate the variability in samples from a given site. Also illustrated are two very coarse samples (lower layer Apollo 14 trench; coarse layer Apollo 12 double core tube). Table 102 lists the dust component particle size frequency as illustrated in figure 151.

Table 102. Particle size frequency distribution for the dust component as illustrated in figure 151.

Sample	Fraction of Total Mass					Total Sample Mass (g)	Mean Grain Size	
	>10 mm	4 –10 mm	2–4 mm	1–2 mm	<1 mm		<1 cm Fraction (μ)	<1 mm Fraction (μ)
A10002	0.039	0.016	0.023	0.031	0.891	476.3	–	52
A14003	0.021	0.031	0.03	0.039	0.879	1,077.9	129	99
A14141	–	0.154	0.14	0.113	0.594	48	616	123
A14163	–	0.038	0.038	0.056	0.867	5,126.3	76	56
A15220	–	0.023	0.019	0.008	0.95	305.2	–	43
A15270	–	0.005	0.016	0.025	0.954	837.1	–	94
A15400	0.83	0.013	0.01	0.008	0.14	618.3	330	61
A61180	–	0.034	0.035	0.053	0.878	177.9	94	64
A61220	0.055	0.114	0.104	0.069	0.658	92.7	216	68
A62280	0.043	0.051	0.047	0.078	0.781	279.6	134	70
A64500	0.052	0.04	0.04	0.047	0.821	603.6	104	65
A68500	0.002	0.029	0.042	0.063	0.865	602.6	106	68
A70180	0.737	0.003	0.005	0.007	0.248	633.1	67	58
A71500	0.074	0.019	0.025	0.032	0.85	706.6	83	65
A72140	0.005	0.011	0.008	0.022	0.953	237.1	57	50
A72500	0.004	0.011	0.018	0.033	0.935	735.3	67	57
A73240	0.007	0.091	0.059	0.061	0.784	245.9	127	51
A74220	–	0.102	0.018	0.071	0.809	9.6	–	41
A78220	–	0.006	0.011	0.022	0.96	236.5	50	45
A78500	0.124	0.022	0.018	0.024	0.812	884.7	46	41

9.3.1.2 Particle Shape. Regolith particles exhibit a range of sizes and shape because of the manner in which they form. Meteoroids of various sizes have bombarded the surface for billions of years, shattering the rocks and creating finer and finer particles over time. Micrometeoroids, which also break down particles, can also create larger particles (agglutinates) due to the welding of particles by the impact-induced melt. Table 103 lists grain-specific properties.

Table 103. Summary of grain-specific properties (<1 mm size fraction).

Property	Value	Units	Notes	Sources
Sorting	1.99 to 3.73 range	φ	Very poorly sorted	Reference 255
Skewness	0 to 0.3 range		Nearly symmetric to slightly coarsely skewed	
Elongation	01.32 to 1.3835 range 1.35 average		Somewhat elongated	
Flatness	01.17 to 1.37 range			
Aspect ratio	0.3 to 0.9 range 0.55 average		Slightly to medium elongation	
Roundness	0.19 to 0.29 range 0.21 average		Subangular to angular	
Volume coefficient	0.32 to 0.35 range 0.3 average			
Specific surface area	0.4 to 0.78 range 0.5 average	$m^2\ g^{-1}$		

Depending upon the size fraction considered <1 cm versus <1 mm, the mean value can vary by a few to a hundred microns. There can also be variations between splits of individual samples. Pyroclastic material is typically much finer with more spherical particles and better sorting:

- Elongation: Elongation is defined as the ratio of the major to intermediate axes of the particle, or length to width. Particles with values of the ratio <1.3 are considered equant, and particles whose ratio is >1.3 are elongate. Measurements of elongation on individual particles (sized 44–2,300 μm) ranged from 1.31 to 1.39.

- Aspect ratio: In geotechnical studies, aspect ratio is inversely related to elongation. It is defined as the ratio of the minor axis to the major axis of an ellipse fitted to the particle by a least-squares approximation. Measurements of the aspect ratio of individual particles (sized 1.25–30 μm) range from 1 (equant) to <0.1 (very elongate), with most values falling in the range 0.4 to 0.7 (slightly to moderately elongated).

- Roundness: Roundness is defined as the ratio of the average of the radii of the corners of the particle image to the radius of the maximum inscribed circle. Measurements of roundness on individual particles (sized 44–2,300 μm) had average roundness values from 0.19 to 0.26.

- Volume coefficient: Volume coefficient is defined as the volume of a particle divided by the cube of the diameter of the circle that encloses the same area as the particle profile. Measurements of volume coefficient of individual particles (sized 60–733 μm) range from 0.24 to 0.37, with an average value of approximately 0.3; this value corresponds approximately to a prolate spheroid with a major-to-minor axis ratio of 3:1. The volume coefficient for a sphere is >0.52, well above the measured values for lunar particles.

- Specific surface area: Specific surface area (SSA) is defined as the surface area of a particle divided by its mass. It is a measure of both the size and the shape of the particle. A 'soil' consisting of spheres with the same submillimeter particle size distribution as lunar soil would have an SSA of approximately 0.065 m^2/g. Lunar soil particles have measured SSA values of 0.02 to 0.78 m^2/g, with a typical value of 0.5 m^2/g. The relatively large SSA of lunar soils is indicative of the extremely irregular, reentrant particle shapes.

9.3.2 Physical Properties

The mechanical properties of the lunar regoliths have been established by a combination of in situ measurements on the lunar surface, laboratory measurements of the properties of returned lunar samples, and theoretical analysis. Table 104 lists a summary of bulk geotechnical properties with notes indicating the source of the information.

- Bulk density: The bulk density (ρ) of the regolith is defined as the mass of material in a given volume usually expressed as g/m^3 or kg/m^3. The density of the regolith has been determined by analysis of the returned core and drill tubes, by analysis of boot, boulder and rover tracks, penetration resistance, and in situ measurements by Surveyor, Luna, and Lunokhod spacecraft. Figure 152 illustrates the density as a function of depth for several Apollo drill cores. There is a general increase in the bulk density with depth. These values represent minimum values. If larger volumes were considered, intact rocks would be incorporated into the volume and the net bulk density would be greater.

- Specific gravity: The specific gravity (G) of a particle is a ratio of its mass to the mass of an equal volume of water at 4 °C. To determine the specific gravity of the regolith, a volume of material is weighed and then immersed in a fluid to determine its volume. Since it is a ratio, it is unitless.

Table 104. Summary of bulk regolith properties.

Property	Value	Units	Notes	Sources
Bulk density (ρ)	1.58 ± 0.05: 0–30 cm 1.74 ± 0.05: 30–60 cm	g/cm^3	Intercrater areas	Reference 273 (table 9.4)
Relative density (D_R)	74 ± 3: 0–30 cm 92 ± 3: 30–60 cm	%	Intercrater areas	Reference 273 (table 9.6)
Specific gravity (G)	3.1	–	Based on limited number of bulk samples	Reference 273 (table 9.3)
Porosity (n)	49 ± 2: 0–30 cm 44 ± 2: 30–60 cm	%	Calculated	Reference 273 (table 9.5)
Void ratio (e)	0.96 ± 0.07: 0–30 cm 0.78 ± 0.07: 30–60 cm	–		Reference 273 (table 9.5)
Permeability (Q)	1–7 $\times 10^{12}$	m^2	Firing of Surveyor vernier engines on surface	Reference 274
Diffusivity	7.7 He, 2.3 Ar, 1.8 Kr	cm^2/s	Measured on simulant function of gas species	Reference 275
Friction angle (φ)	30–50	°		Reference 273 (table 9.11, 9.12)
Cohesion (c)	0.1–1	kPa		Reference 273 (table 9.11, 9.12)
Thermal conductivity (k)	1.5 $\times 10^2$ A15 1.72–2.95 $\times 10^{-2}$ A17 1.5 $\times 10^{-3}$ for 0–2 cm	W/mK		Langseth et al.[276, 277]
Thermal diffusivity (κ)	0.002–0.008 @ 300 K	cm^2/s	Temperature and density dependent	Horai and Winkler[278]
Heat capacity (specific heat)	TBD	J/gK	Temperature dependent	TBD
DC electrical conductivity	<10^{-10} @ 400 K <10^{-25} @ 100 K <10^{-9} upper 5 km	Mho/m	Rock values, lower for soil. Temperature dependent lab analysis and in situ	Reference 273 (table 9.15), Reference 279
Relative dielectric permittivity (k)	2.8 @ 1.58 g cm^{-3} 3.11 @ 1.74 g cm^{-3}	–	Function of density, temperature, and frequency	Reference 273, p. 536, Reference 280
Loss tangent	0.0057 @ 1.58 g cm^{-3} 0.0066 @ 1.74 g cm^{-3}	–	Function of density, temperature, frequency, and chemistry	Reference 273, p. 545.
Compression index (C_c)	0.3: loose 0.05: dense 0.01 to 0.11: range	–	Lab measurement on 1.2 to 200 g samples	Reference 277 (tables 9.9 and 9.10)
Recompression index (C_r)	0.003: average 0 to 0.013: range	–	Lab measurement on 1.2 to 200 g samples	Reference 273 (table 9.9)
Coefficient of lateral stress (K_o)	0.45: normally consolidated 3–5: below a few meters 0.7: recompacted	–	Lab measurement on 1.2 to 200 g samples	Reference 273 (table 9.9)
Modulus of subgrade reactions (k)	8: average 1 to 100: range	kPa/cm	Based on in situ observations of boot prints	Reference 273 (fig 9.37)

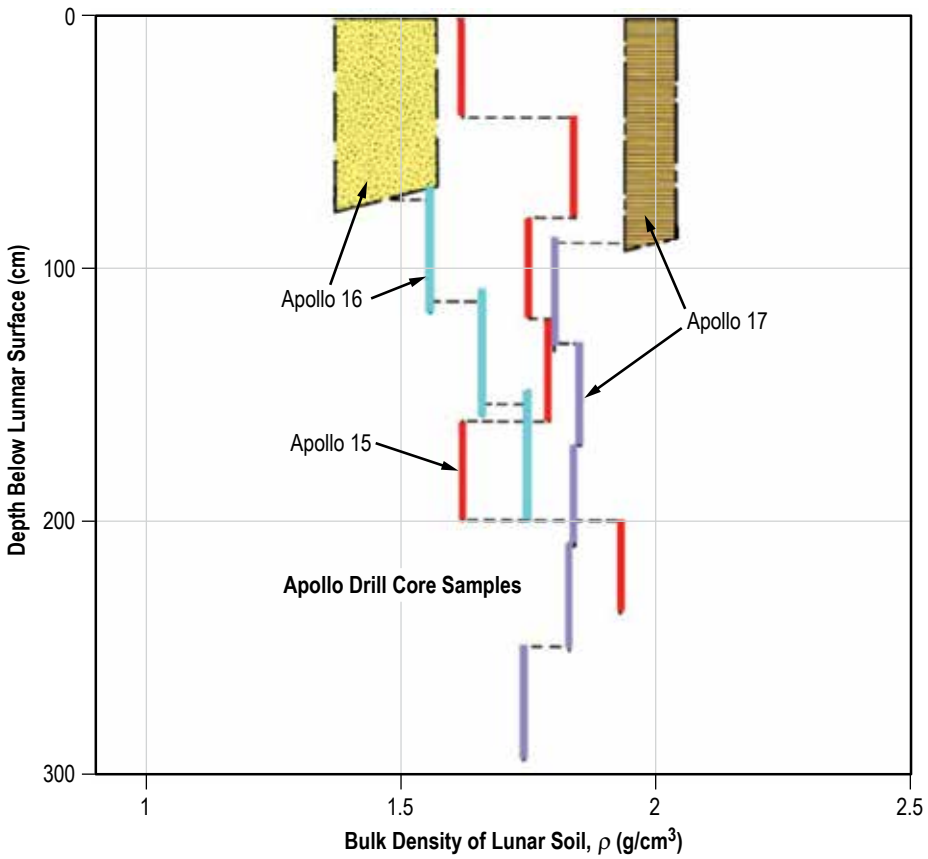

Figure 152. In situ bulk density of the regolith based on drill core samples from the Apollo 15, 16, and 17 missions. The abrupt increases and decreases result from different layers at different depths[273] (Copyright ©1991, Cambridge University Press, reprinted with permission of Cambridge University Press).

- Relative density: The relative density (D_R) is a function of the degree of packing of the individual particles in a granular medium. For mass of spherical particles, the relative density would be a minimum if the particles were arranged in face-centered packing and a maximum in a hexagonal close packing. Figure 153 illustrates the average relative density as a function of depth. The parameter is expressed as a percentage,

$$D_R = \left[\frac{e_{\max} - e}{\left(e_{\max} - e_{\min} \right)} \right] \times 100\% \ , \tag{78}$$

where

e = void ratio of regolith its present configuration
$e_{\max}$ = maximum void ratio at which the regolith can be placed
$e_{\min}$ = minimum void ratio at which regolith can be placed.

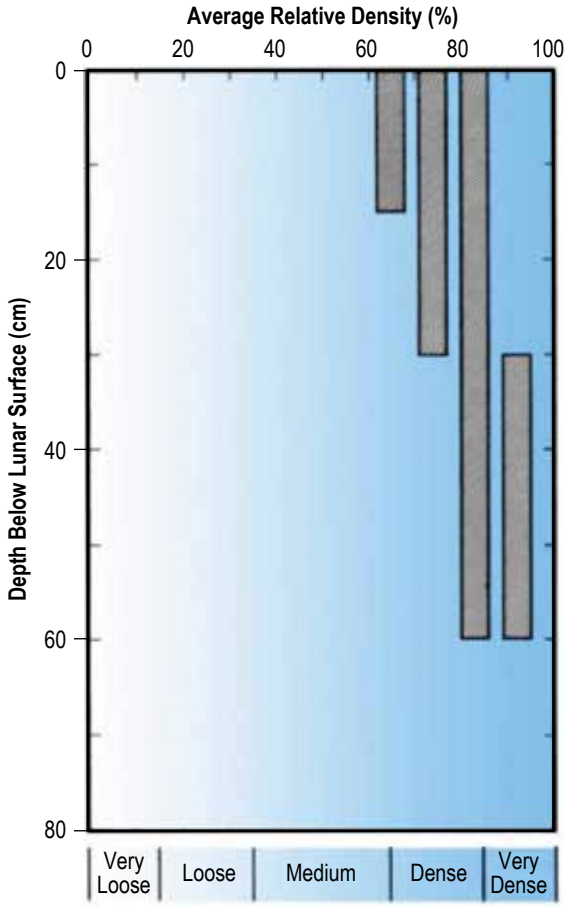

Figure 153. Relative density as a function of depth (modified from fig. 9.20 in ref. 273) (Copyright ©1991, Cambridge University Press, reprinted with permission of Cambridge University Press).

• Porosity: The porosity (n) is defined as the volume of void space divided by the total volume, and related to the bulk density and the specific gravity. The parameter is expressed as percent:

$$n = 1 - \left[\frac{\rho}{(G\rho_w)} \right], \tag{79}$$

where

ρ = bulk density
G = specific gravity
ρ_w = density of water.

• Void ratio: The void ratio (e) is the volume of the void space between particles to the volume of the solid particles (including subgranular porosity). The parameter is unitless:

$$e = \left[\frac{n}{(1-n)} \right], \tag{80}$$

where

n = porosity.

The relations between void ratio (e), relative density (D_R), and porosity is illustrated in figure 154 for a number of lunar samples, a lunar simulant, and for uniform spheres with different packing.

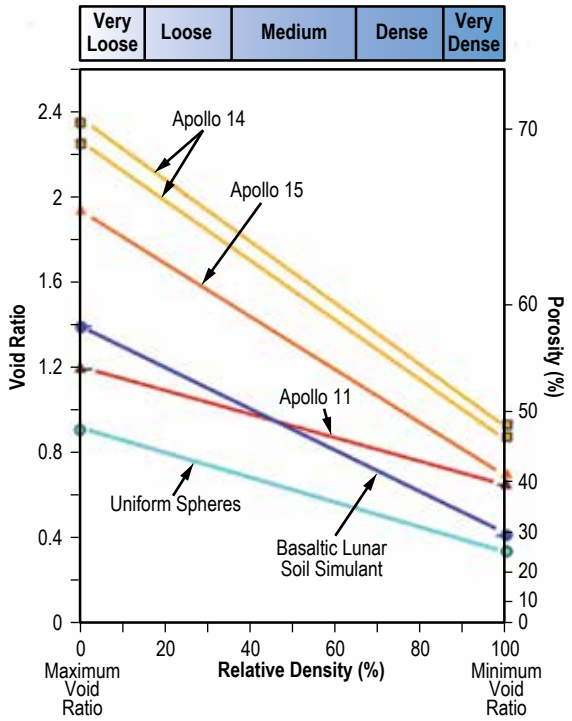

Figure 154. Void ratio and porosity as a function of relative density for lunar samples. Also shown is a function for ideal, variably packed uniform spheres. There is considerable scatter among the lunar samples (modified from fig. 9.18 in ref. 273) (Copyright ©1991, Cambridge University Press, reprinted with permission of Cambridge University Press).

- Permeability and diffusivity: These parameters relate to the movement of a fluid (either liquid or gas) through the regolith. These values have not been directly measured on lunar regolith but rather are inferred from other observations.

- Permeability: The coefficient of permeability defines the flow quantity through the regolith as a function of the fluid pressure gradient. The value cited in table 104 was derived from the test firing of the Surveyor 5 vernier engine on the lunar surface and the permeability to depth of 25 cm was deduced.[281] This value is considered to be consistent with the fine-grained nature of the regolith.

The simplest case is an incompressible, nonreactive fluid and is given by Darcy's law:

$$Q = K\left[\frac{\left(\rho g_m\right)}{\mu}\right] iA \ , \tag{81}$$

where

Q = flow rate (m^3/s)
K = absolute permeability (m^2)
ρ = density of the fluid (kg/m^3)
g_m = gravity (m/s^2)
μ = fluid viscosity (Ns/m^2)
i = hydraulic gradient
A = cross-sectional area normal to fluid flow direction (m^2).

- Diffusivity: Gas diffusivity defines molecular flow through the regolith in response to a gradient in the concentration of a species. Diffusivity depends on the species composition, pressure, and temperature and the particle size and shape distribution. Data in table 104 were derived using He, Ar, and Kr in with a lunar simulant under vacuum conditions.[275] These data indicate that the diffusivity for these gases is proportional to the absolute temperature and molecular weight of the gas.

- Friction angle: The angle of internal friction relates the shear stress and normal stress at which failure occurs. It is a measure of the regolith's ability to withstand shear stress, and determined experimentally. The manner in which the angle is calculated is illustrated in figure 155.

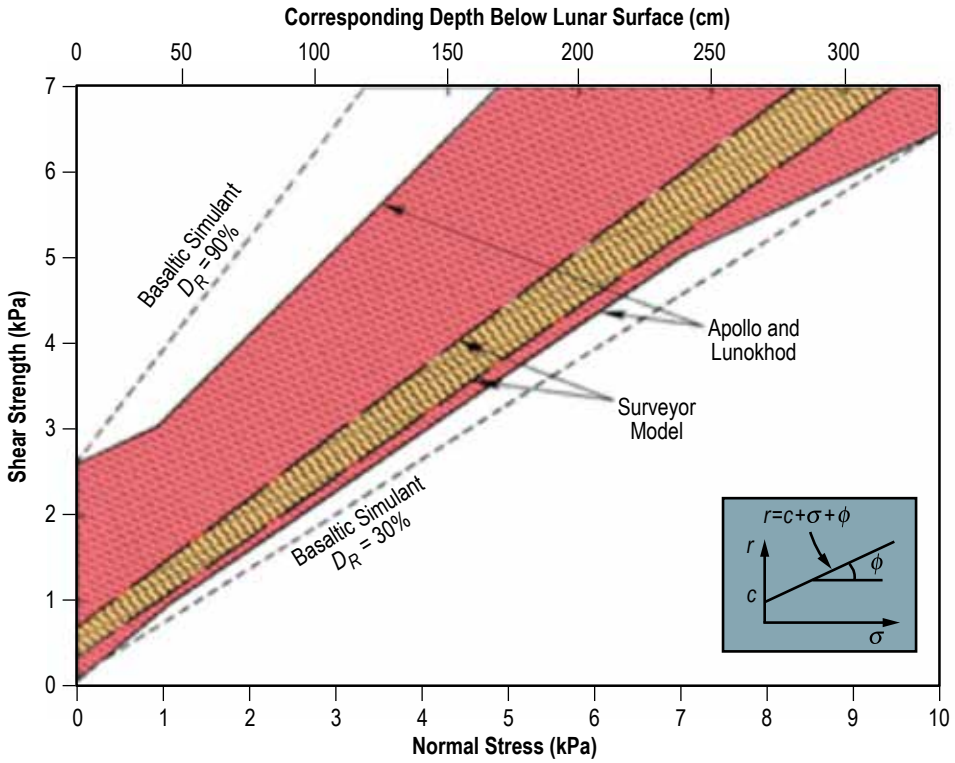

Figure 155. Normal shear stress versus shear strength. The slope of the relation defines the friction angle (inset) (modified from fig. 9.26 in ref. 273) (Copyright ©1991, Cambridge University Press, reprinted with permission of Cambridge University Press).

- Cohesion: Cohesion is the component of shear strength that is independent of interparticle friction; it is the strength when the confining pressure is zero. Variations in the cohesion of the regolith can be accounted for by differences in the relative density of the regolith.

- Thermal conductivity: Thermal conductivity (k) is the ability of the material to conduct heat. Thermal conductivity data were collected in situ on the lunar surface as part of the heat flow experiment and for returned samples in the laboratory.

  The upper 1–2 cm of the regolith has extremely low conductivity, about a factor of 10 lower than the bulk regolith. Overall, the bulk lunar regolith has very low conductivity; it is similar to aerogel and about a factor of 10 less than dry silica sand.

- Heat capacity: Heat capacity (C) is a measure of the amount of heat that is required to change the temperature of a body by a given amount. Specific heat capacity refers to the amount of heat required to change the temperature a given amount of mass.

Heat capacity is defined as

$$C = \frac{\Delta Q}{\Delta T} , \tag{82}$$

where

ΔQ = amount of heat
ΔT = temperature change.

For comparison, water has a specific heat capacity of 4.1855 J/gK.

• Thermal diffusivity: The thermal diffusivity (κ) is a measure of the rate at which material adjusts to changes in the temperature of the surroundings:

$$\kappa = \frac{k}{\left(\rho C_p\right)} , \tag{83}$$

where

κ = thermal conductivity (W/mK)
ρ = density (g/m^3)
C_p = heat capacity (J/kgK).

Materials with high thermal diffusivity adjust to the changes in the surrounding thermal environment rapidly.

Thermal diffusivity has been measured on a number of lunar samples. The values measured at atmospheric pressure are greater than those measured in a vacuum; values measured in vacuum are relevant to the Moon. Data indicate that basalts, which are denser and less fractured, have higher values than breccias, which are less dense and fractured.

Each investigation compiles the data for an individual rock sample and then a curve is fit to the data. Typically the expression has the form of:

$$\kappa = A + BT + \frac{C}{T^2} + DT^2 , \tag{84}$$

where

T = temperature (K)
A, B, and C = constants.

Lunar samples have diffusivities at 300 K of 0.001 to 0.008/cm^{2}s. For comparison, rocks have a thermal diffusivity of ~10^{-2}/cm^{2}s.

9.3.2.1 Derived Physical Properties. Following are some physical property descriptions:

- Compressibility: The compressibility of the material is an indication of the volume change that occurs when a confining stress is applied. At low stresses, the volume change is accommodated by particle movement and reorientation. At higher stresses, the volume change results from particle deformation or breakage.

- Compression index: The compression index (C_c) is defined as the decrease in void ratio when the confining stress is increased by an order of magnitude (fig. 156):

$$C_c = -\left[\frac{\Delta e}{\left(\Delta \log \sigma_v\right)}\right], \tag{85}$$

where

Δe = change in void ratio
$\Delta \log \sigma_v$ = log change of applied vertical stress.

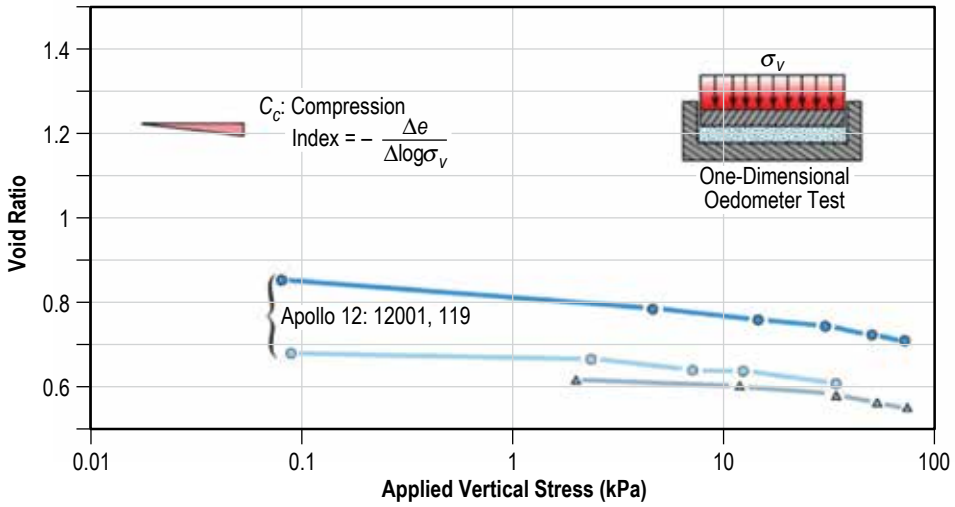

Figure 156. Compressibility measurements on Apollo 12 samples. Inset shows a diagram of a 1D oedometer for measuring compressibility (modified from fig. 9.21 in ref. 273) (Copyright ©1991, Cambridge University Press, reprinted with permission of Cambridge University Press).

- Recompression index: The recompression index (C_r) indicates the slope of the rebound-reload curve. It results when the sample expands after unloading and then is compressed again in the next compression cycle, as illustrated in figure 157.

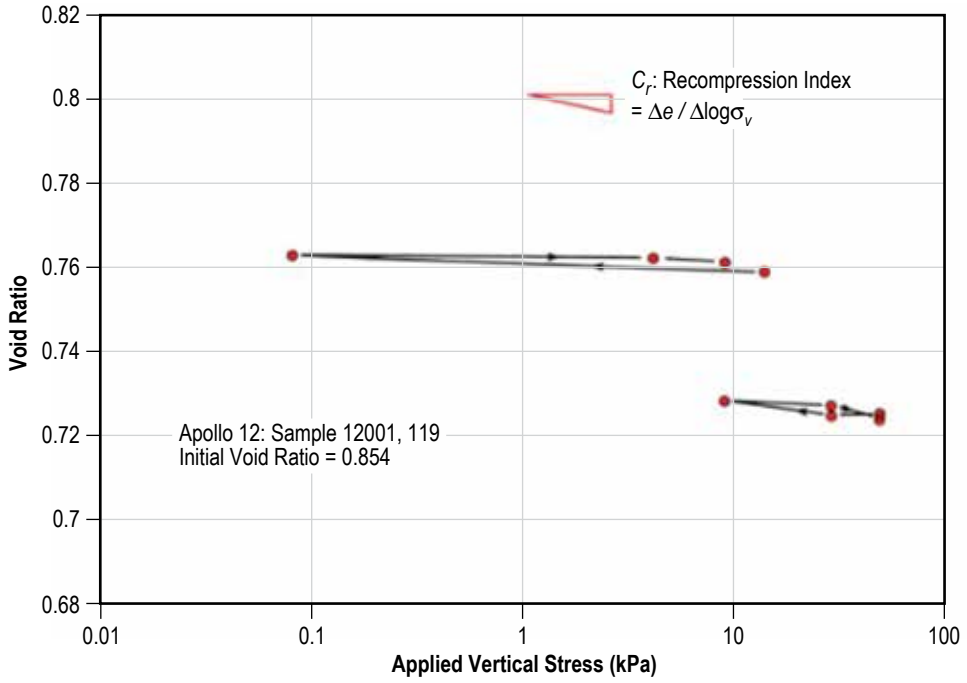

Figure 157. Change in void ratio as a function of applied vertical stress. The arrows indicate the changes in void ratio as the sample is loaded and then unloaded.[273] (Copyright ©1991, Cambridge University Press, reprinted with permission of Cambridge University Press).

• Coefficient of lateral stress: The coefficient of lateral stress (K_0) defines the ratio of horizontal stress to vertical stress. This value has not been measured on the Moon, but the assumption is made that the lunar regolith is normally consolidated. As the parameter is a ratio, it is unitless:

$$K_0 = \frac{\sigma_h}{\sigma_v} \ , \tag{86}$$

where

σ_h = horizontal stress
σ_v = vertical stress.

• Shear strength: The shear strength (τ) of the regolith is measure of the stability of the regolith against failure. It is typically defined in terms of the Mohr-Coulomb equation:

$$\tau = c + \sigma \tan \phi \ , \tag{87}$$

where

c = cohesion (kPa)
σ = normal stress (kPa)
ϕ = friction angle (°).

- Bearing capacity: Bearing capacity is the ability of the regolith to support a load. Bearing capacity is discussed in two categories: ultimate bearing capacity and allowable bearing capacity. Ultimate bearing capacity is the maximum possible load that can be applied without causing gross failure. For a 1-m footing, the ultimate bearing capacity is approximately 6,000 kPa. Allowable bearing capacity defines a smaller load that can be applied without exceeding a given amount of settlement. Both ultimate and allowable bearing capacity can be further defined into static and dynamic regimes.

A parameter that is used to calculate the allowable static bearing capacity is the modulus of subgrade reaction (k). This parameter has been calculated from astronaut boot prints and has an average value of 8 kPa/cm.

- Slope stability: Slope stability is a factor of consideration in construction, either in the excavation of the regolith or the construction of an embankment or pile. For stability analyses, a factor of safety (FS) is calculated:

$$FS = N\left[\frac{\left(\rho g_m h\right)}{c}\right], \tag{88}$$

where

N = stability number (function of friction angle and the slope angle)
ρ = regolith density
g_m = lunar gravity
h = slope height.

9.3.3 Regolith Composition

The composition of the regolith can be defined in terms of chemistry and mineralogy/lithology. In terms of both chemistry and mineralogy/lithology, the composition depends upon both basement rock (basaltic mare, anorthositic highlands, or pyroclastics) and the grain size. With a given site (e.g., the Apollo 11 mare site), the chemistry and mineralogy/lithology of the material in the regolith is a direction function of the grain size range under consideration.

9.3.3.1 Chemistry. An analysis of the chemistry does not necessary imply a specific mineralogy, although a specific mineralogy does imply an approximate chemistry. In a simple example, both graphite and diamond are composed of carbon. Knowing the sample was composed of carbon does not allow a determination of the mineralogy and hence the history of the sample. On the other hand, if one knows the mineralogy, both the bulk chemical composition and the geologic history of the material can be determined.

Chemical compositions are typically expressed as oxides, although the elements do not necessarily occur in such forms. Trace elements are usually reported as ppm (parts per million) or ppb (parts per billion), depending upon the species. Again, this does not necessarily indicate that the elements occur as native species. Tables 105 and 106 list the bulk and trace element compositions for a number of Apollo samples, respectively.

Table 105. Bulk element compositions of Apollo samples.

Major Oxides (wt %)								
Element	**Apollo 11**	**Apollo 12**	**Apollo 15 KREEP-rich**	**Apollo 17 Orange Glass**	**Apollo 17 Light Mantle**	**Apollo 14 Fra Mauro**	**Apollo 16 Cayley Fm**	**Luna 20 Highlands**
SiO_2	42	46.1	46.7	38.7	45.1	47.7	44.9	45.2
TiO_2	7.5	2.7	1.5	8.8	1.3	1.7	0.59	0.49
Al_2O_3	13.5	12.6	16.4	6.5	21.3	17.4	26.7	22.8
FeO	15.8	16.5	12.2	22.3	8.3	10.5	5.44	7.3
MnO	0.21	0.21	0.16	0.29	0.11	0.14	0.07	0.11
MgO	7.9	10.2	10.4	14.5	9.8	9.4	6	9.5
CaO	12	10.3	11.2	7.5	12.9	10.9	15.3	14.4
Na_2O	0.44	0.46	0.46	0.37	0.43	0.7	0.46	0.35
K_2O	0.14	0.24	0.21	0.077	0.144	0.52	0.121	0.07
Cr_2O_3	0.3	0.38	0.34	0.7	0.22	0.2	0.111	0.19
P_2O_5	0.1	0.3	0.22	0.06	0.13	0.49	0.12	0.12
S	0.11	0.08	0.08	0.05	0.06	0.1	0.07	–
∑	100.1	100	99.8	99.8	99.9	99.8	99.9	100.5
Is/FeO*	78	55	65	1	65	65	82	–

* Is/FeO is a measure of regolith maturity; increasing maturity with increasing number.[282]

Table 106. Trace element compositions of Apollo samples.

Trace Element Composition (ppm)								
Element	Apollo 11	Apollo 12	Apollo 15 KREEP-rich	Apollo 17 Orange Glass	Apollo 17 Light Mantle	Apollo 14 Fra Mauro	Apollo 16 Cayley Fm	Luna 20 Highlands
Li	12	17	9	11	10	27	8	6
Na	3,200	3,400	3,400	2,800	3,200	5,200	3,400	2600
P	400	1,300	1,000	300	600	2,100	540	500
K	1,100	2,000	1,700	640	1,200	4,300	1,010	600
Sc	63	39	24	49	17	22	9.5	16
V	65	110	85	130	40	55	25	45
Cr	2,100	2,600	2,300	4,800	1,500	1,400	760	1,300
Mn	1,600	1,700	1,300	2,200	900	1,100	540	900
Co	29	43	41	62	90,032	35	31	30
Ni	200	200	260	90	270	370	440	230
Zn	24	7	25	250	15	25	26	50
Ga	4.5	4.2	4.2	–	2.8	6	3.6	–
Rb	2.8	6.2	5.8	1.1	3.4	15	2.9	1.6
Sr	163	137	140	209	152	179	176	139
Y	115	131	90	49	58	242	46	26
Zr	300	480	380	190	220	880	180	110
Nb	19	29	23	15	13	55	13	–
Cs	0.11	0.3	0.26	0.12	0.18	0.65	0.14	0.09
Ba	170	390	280	80	170	800	140	90
La	16	34	25	6.4	15	67	13	6.9
Ce	47	89	68	19	39	176	34	17
Pr	7	12	9	3	5	24	4.5	2.4
Nd	38	55	39	18	26	105	21	11
Sm	13	16	12	6.6	7.3	30	6	3.1
Eu	1.77	1.75	1.45	1.84	1.24	2.5	1.2	0.91
Gd	17	20	13	9	9	35	8	4
Tb	2.9	3.5	2.3	1.5	1.5	6.2	1.2	0.64
Dy	19	22	15	9	10	39	8	4.2
Ho	4.6	4.8	3.4	1.8	2.1	8.7	1.7	0.9
Er	11	13	9	5	6	23	5	2.7
Tm	1.7	1.9	1.3	0.7	0.9	3.5	0.7	0.4
Yb	10.6	12.3	8.5	4.2	5.5	22	4.3	2.5
Lu	1.54	1.74	1.24	0.61	0.78	3.1	0.61	0.38
Hf	10	13	10	5	6	23	4.5	2.5
Ta	1.3	1.5	1.1	1	0.7	3	0.55	0.3
W	0.2	0.7	1.2	–	–	1.7	<0.5	64
Ir	7	7	7	0.8	12	13	15	10
Au	2.9	3.5	4	0.3	5	7	10	3.4
Th	2	5.8	4.2	0.5	2.6	13	2.2	1.3
U	0.51	1.5	1.2	0.16	0.73	3.5	0.62	0.33

- Apollo 11: Data are based on sample 10084 and some data for 10085 and 10010, both of which are nearly identical to 10084.[283]

- Apollo 12: Data from typical samples 12001, 12023, 12029, 12041, 12042, 12044, 12057, and 12070 which are very similar in composition (e.g., FeO range: 15.9%–17.1%; Th range: 5.3–6.3 ppm).

- Apollo 15 KREEP-rich: Data are from six samples from station 6. Station 6 regolith contains the greatest proportions of KREEP-rich materials and thus has the largest concentration of incompatible elements.

- Apollo 17 Orange Glass: Data from 74220 taken near Shorty Crater at station 4. This soil is the most anomalous in the collection as it consists almost entirely of pyroclastic glass beads with some 'normal' soil (drive tube 74001/74002).

- Apollo 14 Fra Mauro: Based on data for all samples except 14141. Apollo 14 are very similar in composition (e.g., Fe range: 10.1%–10.9%; Th range: 12.3–13.6 ppm).

- Apollo 16 Cayley Fm: Mean of data from all 24 samples of mature soil. This composition probably best represents surface of Cayley Fm (Korotev[284]). Compositional range of mature soils is moderate (e.g., FeO range: 4.4%–6%, Th range: 1.6–2.5 ppm) and mainly represents variations in the relative abundance of anorthosite.

- Luna 20 Highlands: Based on all available data.

9.3.3.2 Mineralogy/Lithology. Since the regolith is simply a layer of fragmental material derived largely from the underlying bedrock, it is a mixture of fragments of the bedrock, individual mineral grains derived from rocks, and agglutinates (small fragments formed by welding together of other grains) (table 107). Figure 158 illustrates these data in a graphical form.

Table 107. Modal volume abundance of particles in the 1,000–90 μ size range for different sites.

Modal Abundance (Vol. %) for 1,000–90 μ Size Fraction									
	10,084	**12,001**	**12,033**	**15,221**	**14,163**	**64,501**	**67,641**	**76,501**	**22,001**
Mineral Fragments									
Pyroxene + olivine	4.2	18.3	26.3	16.1	2.6	1	0.5	17.3	8.9
Plagioclase	1.9	3.9	9.9	13.1	5.1	32.1	12.2	15.2	14.7
Opaque	1.1	0.2	1.3	0.1	–	–	1.1	2.8	0.1
Lithic Fragments									
Mare basalt	24	12.9	7.5	3.1	2.2	0.3	0.5	9.2	6.9
ANT	0.4	1	1.3	2.6	2.9	5	21.7	0.5	3.5
LMB	0.8	0.1	0.3	0.6	0.3	2.1	30.7	6.3	0.5
Feldspathic basalt (KREEPY)	1.1	0.5	–	0.4	0.6	1.6	1.6	0.2	1.4
RNB/POIK	–	2.3	3.7	2.7	10.9	8.3	7.9	8.1	2.2
Fused Soil									
DMB	7.5	9.5	11.9	13.3	19.3	13.9	11.1	4.2	10.6
Agglutinate	52	40.1	17	36.9	45.7	29.1	8.5	29.2	16.6
Glass Fragments									
Orange/ black	2.7	0.5	1.5	0.4	–	0.7	0.5	1.6	–
Yellow/ green	0.8	2.8	0.2	4.5	2.9	1.2	–	1.3	0.9
Brown	–	1.5	7.8	0.3	–	–	–	–	0.2
Clear	1.3	1	–	1.5	1.3	1.4	–	0.8	0.6
Devitrified glass	1.8	5	10.8	4.1	6.1	3.4	3.2	2.2	5.4
Others	0.3	0.5	0.5	0.3	–	–	0.5	1.1	0.3
Total	99.9	100.1	100	100	99.9	100.1	100	100	100.1
N	625	823	666	1,000	311	942	189	820	634

ANT= anorthosite, norite, troctolite

LMB = light matrix breccia

RNB/POIK = recrystallized norite breccia / poikilitic breccia

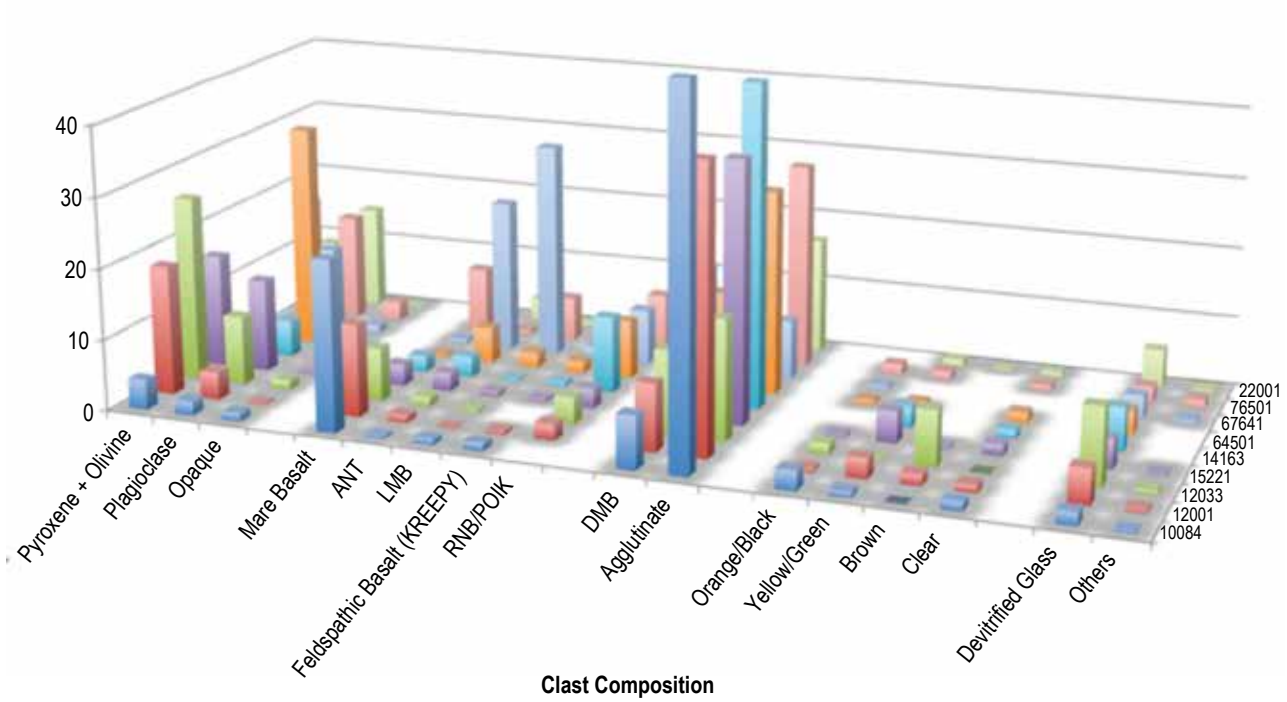

Figure 158. Grain composition in regolith samples. *x* axis lists the component composition, *y* axis lists the different samples (data from table 107).

9.3.4 Lunar Regolith Electrical Properties

9.3.4.1 Introduction. Theoretical considerations and observational evidence acquired from Apollo, as well as subsequent lunar missions, indicates that the lunar surface and dust grains are electrostatically charged by the incident solar UV radiation and the solar wind plasma.[285,286] On the lunar dayside of the Moon, the dust is believed to be charged positively by photoelectric emissions with the incident solar UV radiation, and predominantly negatively by the incident solar wind electrons on the nightside. There is considerable evidence to indicate that the charged fine lunar dust grains, smaller than a few microns in size, are levitated and transported to high altitudes and transported over long distances across the lunar terminator.[287–290] The lunar dust, with its toxic nature and high adhesive characteristics, constitutes a major source of hazard for humans and the mechanical systems in human and robotic exploration of the Moon.

Although the basic principles and the underlying sources of the observed lunar dust phenomena are recognized, the extent and the details of the lunar dust charging, levitation, and transportation process remain poorly understood. The current theoretical models do not satisfactorily explain the observed lunar dust phenomena. A more definitive knowledge of the lunar dust phenomena with acquisition of the basic data is needed for engineering solutions and development of mitigating strategies.

9.3.4.2 Lunar Dust Charging Processes. The charging of the lunar regolith is a complex process and can be accomplished by many different means. The lunar regolith is typically a non-conductive material suggesting that it can be charged readily by many different means. Electrostatic charging of the lunar regolith and dust can be done by photoelectric emissions produced by UV radiation at wavelengths near 200 nm on the dayside, leading to positively charged grains, with substantial electrostatic charging taking place when the dust is bombarded by soft x-rays with a wavelength <100 nm. Electron or ion collisions on the nightside of the lunar surface produce negatively charged dust grains due to low-energy electrons (<100 eV) impact, and positively charged dust grains due to high-energy electron impact. These different charge states are typically driven by variations in the secondary electron yield of the dust grains.

Triboelectric charging is the other charging process that must be considered. Triboelectric charging of dust grains by contact charging is a process in which electrons are transferred from a solid material with high work function to one with a lower work function, and occurs during landing of a lunar vehicle or movement of an astronaut over the regolith. Triboelectric charging can be exacerbated by trying to remove the dust through brushing, dusting, or blowing. Triboelectric charges can build up rapidly because there is no atmosphere to discharge through, and the regolith is electrically insulating (i.e., there is no common 'ground' for electrical equipment). The dust forms unique morphologies, is loosely packed, and is electrically and thermally insulating. The experience of the Apollo astronauts was that the dust is very adherent and abrasive, and hindered the effectiveness of even those very short missions. Mitigation of the effects of charge and dust must be a priority for any mission planned for a long stay on the lunar surface. The source of the problem is twofold: induced charging through triboelectric effects and interactions with naturally occurring background charge.

9.3.4.3 Electrical Properties for Charging Analysis. The typical electrical properties required to conduct a surface charging analysis of the lunar regolith and lunar dust using the NASCAP and NASCAP-2K are bulk resistivity of the lunar regolith, surface resistivity of the lunar regolith, secondary electron data, photoemission data, and physical properties. This section is designed to address only the bulk resistivity, surface resistivity, secondary electron data, and photoemission data of the bulk lunar regolith and dust grains. The physical properties of the lunar regolith such as atomic number, atomic mass, density, and size distribution are addressed in sections 9.3.1 and 9.3.2.

The lunar surface temperature typically varies from approximately –150 to 150 °C, depending upon shadowing of the Sun. Because electrical properties of insulators are highly dependent upon temperature, the electrical properties needed for charging analysis should include the temperature dependence. Where possible, this dependence has been incorporated.

9.3.4.3.1 Measured Bulk (Dust) Electrical Properties. Most of the known bulk electrical properties of the lunar surface fines have been made on samples taken in the Apollo era, either on the lunar surface or on samples returned to the Earth and held in the Lunar and Planetary Institute, a division of the Universities Space Research Association. These measurements are few and were made on samples from the locations of the sites of the Apollo landings. Thus, the coverage over the lunar surface is limited. The values given below are generally based on direct measurements. Where this is not so, it is noted.

9.3.4.3.2 Bulk Conductivity of Lunar Regolith. All of the electrical conductivity data that are known were measured from samples retrieved during Apollo missions 14–16.[291] The samples were brought back to the Earth where they were tested in the laboratory. One sample retrieved during the Apollo 15 missions was tested over a wide temperature range and showed temperature dependence. For the most part, the data show the lunar regolith to be a good insulator. Table 108 shows data measured on various lunar samples.[291] The crust of the Moon has an average conductivity of about 10^{-7} to 10^{-8} mho/m.

Table 108. Direct current electrical conductivity of lunar rocks.

Lunar Sample	σ_0* (mho/m)	E_0** (eV)	σ_1 (mho/m)	E_1 (eV)
10048	3.5	0.896	2.66×10^{-3}	0.559
12002,85	13	1.09	1.8×10^{-4}	0.48
15058	134	1.374	2.78×10^{-3}	0.593
15418	137	1.509	9.84×10^{-2}	0.971
15555	36.8	1.04	1.27×10^{-2}	0.604
68415	1.27×10^{8}	2.64	–	–
68815	14.2	1.366	–	–

* Conductivity.
** Activation energy.
Data for sample 12002 is from Olhoeft et al.;[247] the rest of the data are from Schwerer et al.[243]

Figure 159 shows a temperature dependence of electrical conductivity measured on a soil from the Apollo 15 site (sample 15301,38).[251,291] The temperature dependence shown is characteristic of amorphous type samples typical of the lunar regolith. Also shown in figure 159 is the temperature dependence of an Apollo 16 rock (sample 65015,6),[247] which was similar in form to that of soil. However, the temperature dependence of the electrical conductivity measured on the remaining lunar rocks was found to be given by table 108.

9.3.4.3.3 Bulk Conductivity (Cryogenic Temperature). The conductivity is temperature dependent. Using data from a variety of samples, Olhoeft et al.[250] and Schwerer et al.[245] derived the following relation:

$$\text{DC conductivity} = \sigma_0 e^{\left(\frac{-E_0}{kT}\right)} + \sigma_1 e^{\left(\frac{-E_1}{kT}\right)} \text{mho/m} \ , \tag{89}$$

where

k = Boltzmann's constant = 8.6176×10^{-5} eV/K
E_0, E_1 = activation energies
σ_0, σ_1 = conductivities.

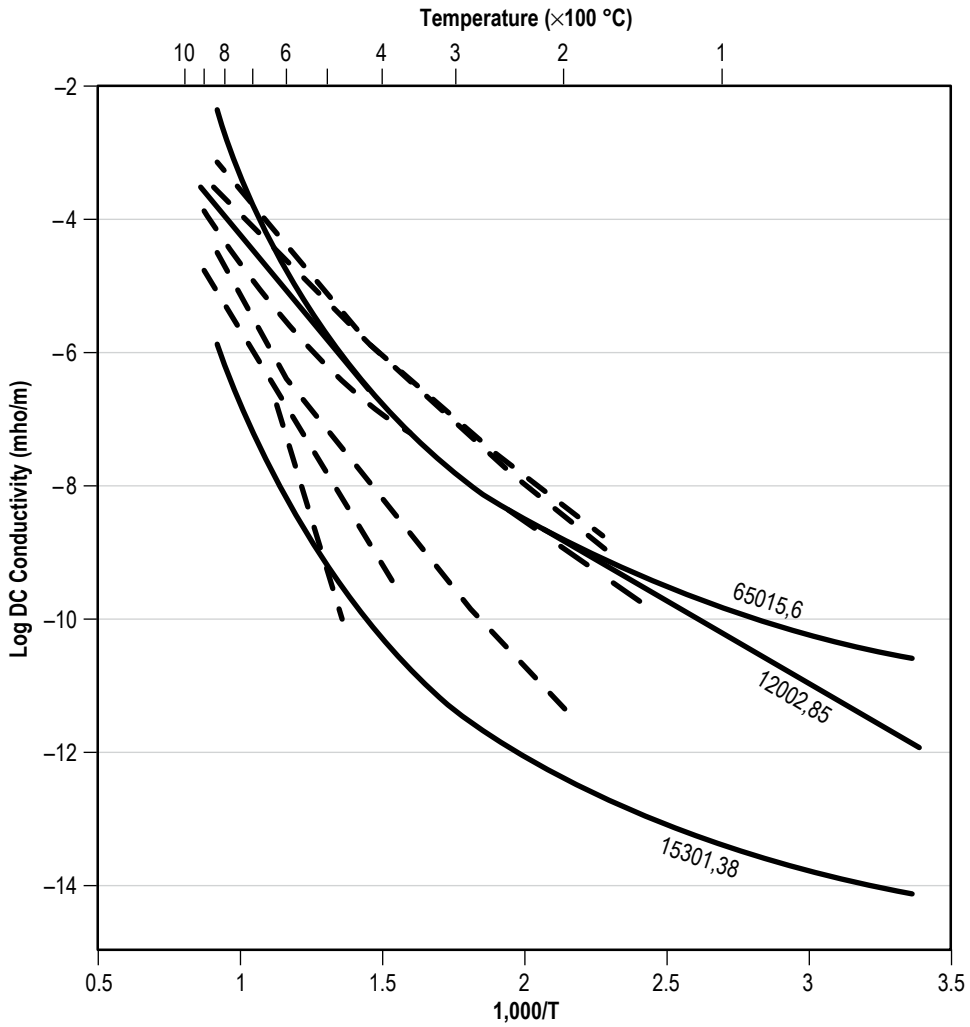

Figure 159. Temperature dependence of lunar soil samples (Apollo 15) and lunar rock samples (Apollo 16) (Copyright ©1991, Cambridge University Press, reprinted with permission of Cambridge University Press).

9.3.4.3.4 Dielectric Constant.

• Dielectric permittivity: Dielectric permittivity (k) is a measure of the ability of the regolith to maintain electrical charges physically separated by a distance. The relative permittivity is the ratio of permittivity of the material to the permittivity of a vacuum. The value is related to the density of the material. Unlike the loss tangent, the permittivity does not show a relation with the amount of titanium dioxide (TiO_2) and ferrous oxide (FeO).

Laboratory measurements on a variety of returned lunar materials indicate that for all of the data, the following relation is observed:

$$k = 1.919^{\rho}\,, \tag{90}$$

where ρ = material density (g/cm^3).

For soils alone, they define a somewhat different relation:

$$k = 1.871^{\rho}, \tag{91}$$

where ρ = material density (g/cm^3).

• Loss tangent: The loss tangent of a material quantifies its dissipation of electromagnetic energy. The parameter refers to the angle in a complex plane between the lossy component of an EM field and its lossless component. For the laboratory analysis of lunar regolith samples, the loss tangent is a function of both the density of the material and the amount of FeO + TiO_2.

Expressed as a function of only density for all data:

$$\text{Loss tangent} = 10^{[0.44*(\rho-2.943)]}, \tag{92}$$

where ρ = density (g/cm^3).

Expressed as a function of only density for lunar soils:

$$\text{Loss tangent} = 10^{[0.42*(\rho-2.903)]}, \tag{93}$$

where ρ = density (g/cm^3).

When the FeO + TiO_2 composition is considered, as well as the density, the following two expressions are determined:

• For all data:

$$\text{Loss tangent} = 10^{[(0.038\times M)+(0.312*(\rho-3.26))]}, \tag{94}$$

where

ρ = density (g/cm^3)
M = % FeO + TiO_2.

• For only soil data:

$$\text{Loss tangent} = 10^{[(0.027\times M)+(0.273*(\rho-3.058))]}, \tag{95}$$

where

ρ = density in g/cm^3
M = % FeO + TiO_2.

9.3.4.4 Lunar Surface Potential. Solar radiation and plasma are directly incident on the lunar surface, affecting the near-surface electrical environment. The situation is especially complex at the polar regions where surface photoelectric currents are reduced (due to large solar radiation/surface incidence angles), and solar wind plasma currents are reduced in the trailing lunar plasma void or 'wake' region (sec. 8.2.2). As recent LP measurements indicate, the unlit lunar surface potential is also affected strongly by solar storms. The impact on any landed system will be described below.

9.3.4.4.1 Surface and Near-Surface Electrical Environments. Figure 160 shows the near-surface electrical environment. It is characterized by three major regions: dayside, nightside, and terminator/polar regions.

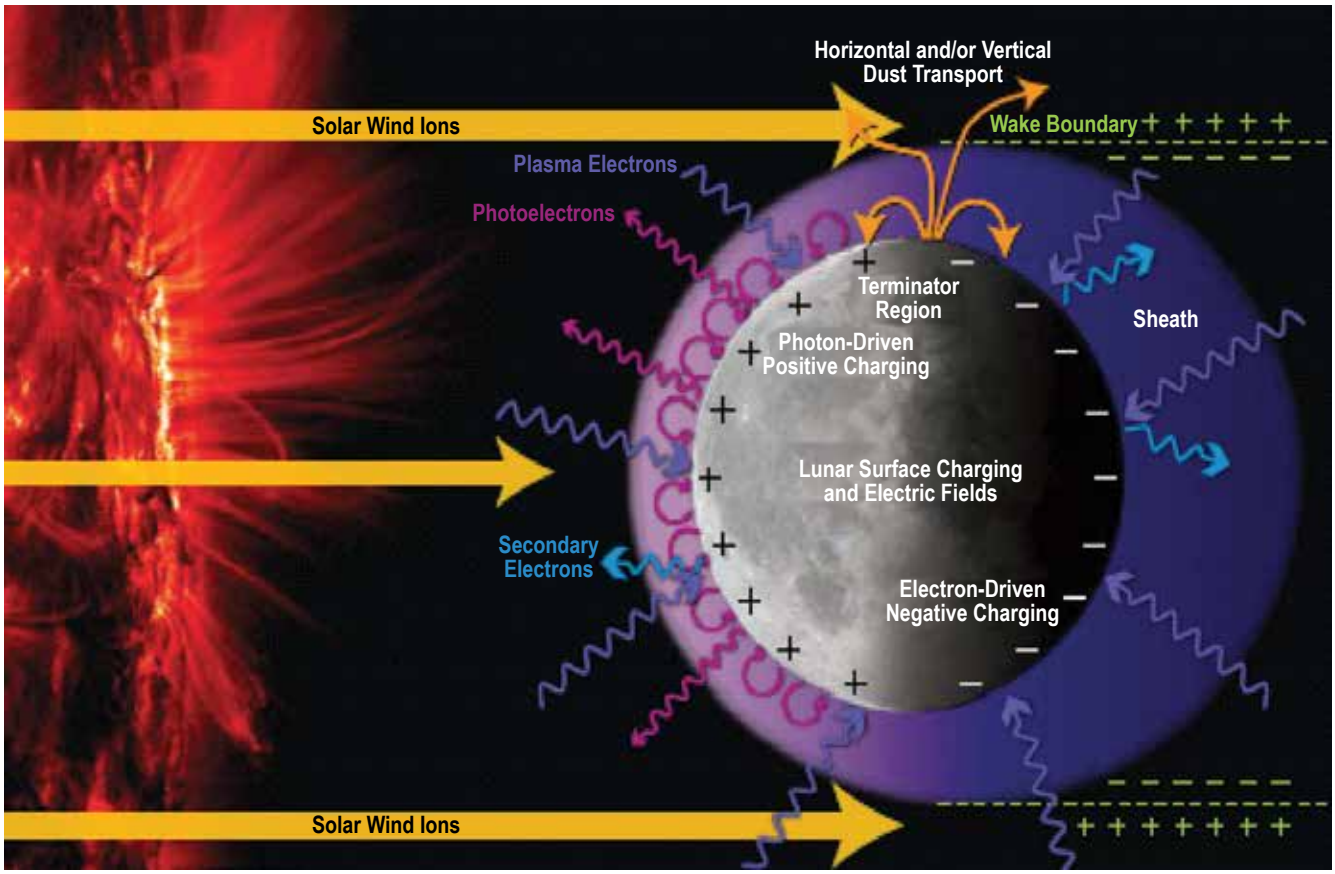

Figure 160. Lunar near-surface electrical environment.[292]

9.3.4.4.1.1 Dayside region. Solar photon radiation is directly incident on the lunar surface, releasing a population of low-energy electrons from the surface called photoelectrons. [263] The nominal emitted electron current, Jph, for direct solar incidence is approximately 4 μA/m^2, assuming a photo-conversion of the lunar regolith of approximately 0.1. These photoelectric currents dominate over incoming solar wind electron and ion currents. Since the surface boundary requires current balances (i.e., the net flux of all currents equals zero), the surface will charge a few volts positive to draw the photoemitted electrons back toward the surface. Typically, the surface potential is shielded by the electrons and ions in the plasma on the spatial scale of a Debye sheath length, which for the lunar dayside is approximately 0.5 m.[263]

9.3.4.4.1.2 Nightside region. Since there are no photoelectrons, the nightside surface potential is defined by the current balance between inflowing plasma electrons and ions. For comparable temperatures (i.e., solar wind temperature of kT/e ~ 10 eV), the electrons will have a higher thermal velocity than the more massive ions, making the nightside electron flux greater than the ion flux. As a consequence, the nightside surface potential will be negative to slow the electrons and attractions.

However, the situation is compounded by the nightside surface's exposure to the low-density lunar wake trailing the Moon. As a consequence, the surface can charge strongly negative to values < –100 V. Figure 161 shows a model of the surface potential and electric field at the terminator and in the plasma void/wake region.[259] In this region, the ambient plasma density is getting progressively lower (to <1% of that in the solar wind) and the electron temperature is progressively increasing, reaching many factors times their solar wind ambient temperature. The nightside surface potential varies approximately as:

$$\phi \sim -\frac{kT_e}{e}\ln(A,B,C)\ , \tag{96}$$

where A is the ratio of electron density to ion density (n_e :n_i), B is the square root of the ratio of electron to ion temperatures ((T_e :T_i)$^{1/2}$ and progressively increases from 1 to 4 as a function of subsolar angle), and C is the square root of the ratio of ion-to-electron mass ((m_i :m_e)$^{1/2}$ ~ 43 for protons). For a quasi-neutral plasma ($n_e \sim n_i$), the value of ln ($A{\cdot}B{\cdot}C$) is on the order of ~5. Thus, the surface potential is $\phi \sim -5\ kT_e/e$, and can become strongly negative deep in the nightside as illustrated in figure 161. Clearly, the increase in potential is a strong function of electron temperature, which is found to steadily increase with subsolar angle (or distance from the wake flank) due to velocity filtration of non-Maxwellian solar wind electrons. This T_e increase is confirmed with LP observations.[180] This progressive temperature increase is illustrated in figure 161(d). The Debye sheath in the nightside region varies from ~10 m just nightside of the terminator to >500 m at the antisolar point.[180]

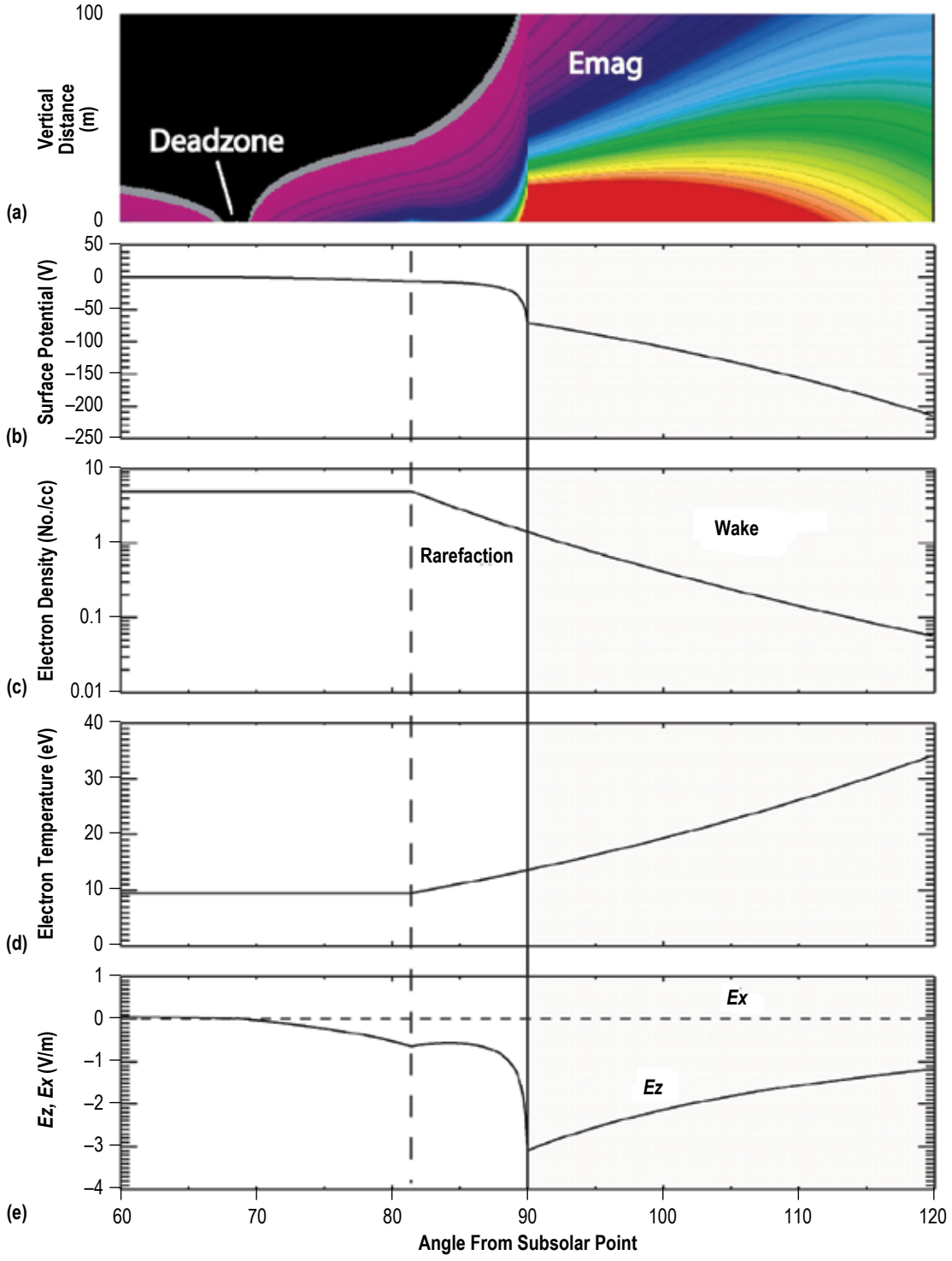

Figure 161. A model of the near-surface *E*-field, associated surface potential, ambient electron plasma density and temperature above the sheath, and surface electric field in the terminator. [260]

The model calculations shown in figure 161 assumes a quasi-neutral plasma with $n_e \sim n_i$. However, in the plasma expansion process into the void (described in sec. 8.2.3), the low mass electrons diffuse into the void region ahead of the ions and establish an ambipolar *E*-field to force the ions to 'keep up.'[264] However, simulation of the process[197,258,260] suggests that there are regions near the leading edge of the expansion where the ions never fully catch up, creating an electron cloud along this leading edge where $n_e \gg n_i$.[205,266] This electron cloud region will also be incident with the lunar surface, creating a local region of very strong negative charging where the ion-devoid electron cloud intercepts the surface. For $n_e \sim 10\, n_i$, the surface potential decreased by another factor of 2.3, and $\phi \sim -11\, kT_e/e$, extending to values in the many hundreds of volts negative for a surface immersed in the electron cloud region.

9.3.4.4.1.3 Terminator/polar region. Due to the transition from dayside/positive to nightside/negative potentials, terminator regions (including the poles) possess very complicated electrical geometries. As indicated in figure 161, the surface potential makes a steep transition and the local *E*-field in the near-surface region can be 1–5 V/m. Local topography plays a large role in the formation of the surface potential, since both photoemission and solar wind (which is flowing quasi-perpendicular to the surface normal) will be influenced by terrain. Mountains and crater walls will both obscure sunlight and block solar wind flow (a solar wind orographic effect) leading to large negative potentials on leeward-facing unlit surfaces.[259]

9.3.4.4.2 Validation of Model Results—Past Data Sets. Current balance models[259,265] like that shown in figure 161 indicate evidence for strong nightside surface charging. These models have been validated, in part, by previous missions to the Moon. The SIDE flown as an Apollo lunar surface experiments package (ALSEP) on Apollo 12, 14, and 15 had the ability to measure surface potentials via the acceleration of local ions by surface fields. Benson et al.[256] mapped the surface potentials across the terminator and found variations very similar to those modeled with potentials dropping below –100 V at terminator crossings. The orbiting LP ER can remotely sense nightside negative surface potential via surface-ejected electron beams and surface-reflected electrons. The electron beams are created by secondary processes at the surface, but then are repulsed from the negatively charged surface and move along connecting magnetic field lines out to the spacecraft. Large negative potentials are consistently detected in nightside regions (many hundreds of volts negative)[203] and terminator regions had potentials that were moderately negative (~ –35 V).[262]

9.3.4.4.3 Temporal Effects: Solar Storms and Passages Into the Magnetosphere. The LP ER recently detected surface potentials on the lunar nightside that were below –4 kV in association with a passing solar energetic particle event, typical of that which occurs with the most intense solar storms.[203] The detection is from electron beams that are created by secondary processes at the surface and ejected via the surface potential. When LP is magnetically connected to the Moon, these electron beams stream directly to the spacecraft along the low conductivity field line. The nightside surface potential just prior to the storm was ~ 700 V and the change in potential to > –4 kV storm values occurs on time scales of hours. The Moon was located in the solar wind during these times. It is believed that the large influx of energetic electrons charge the surface to anomalous large negative values. Hence, the same energetic relativistic particles that pose a radiation hazard to astronauts are also capable of altering the surface potential, posing a system charging risk.

The Moon spends approximately 73.5% of its orbit in the solar wind but passes through the magnetotail for approximately 13%–25% of its orbit. In this plasma, there is not a substantial flow, but the plasma is both of very low density and very warm (see table 98). This combination makes the anti-sunward surface charge to large negative values approaching –1,000.0 V.[263] The LP confirms the presence of these large negative potentials with geomagnetic tail crossing, with the number of surface-ejected electron beams with energy >500 eV increasing during the crossings (indicating an electron ejecting surface potential of <–500 V). See figure 162.

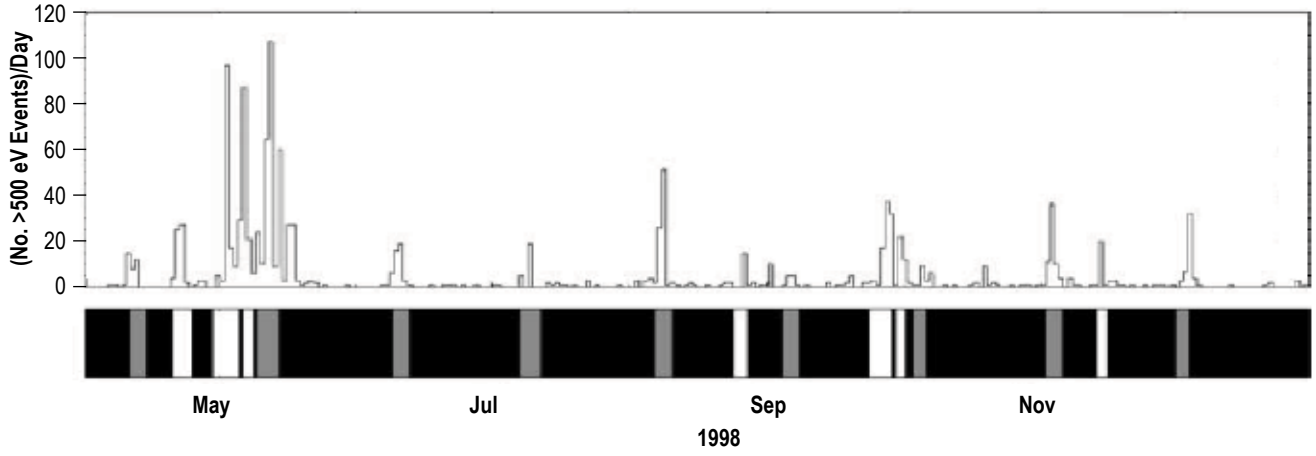

Figure 162. Number of surface-ejected electron beams with energies >500 eV as a function of time (white bars at the bottom indicate times of solar storm events (solar energetic particle events with solar storms); gray bars indicate passages through the geomagnetic tail).[263]

9.3.4.4.4 Effects on Landed Operations: Roving, Power Systems, and Dust. The surface potential and its fluctuations in solar storms can affect landed systems in three ways: roving and charge dissipation, lunar surface power system, and lunar dust.

9.3.4.4.4.1 Roving and charge dissipation. As astronauts rove, they will accumulate triboelectric charge (frictional or contact electricity) with the regolith. In sunlit regions, the photoelectric and ambient plasma currents can dissipate astronaut charge on time scales of <0.01 s. However, in unlit regions where solar wind flow is obstructed (by a large mountain or inside a crater such as Shackleton or Shoemaker), there are little natural environmental currents to remediate any tribocharge buildup. Within the cold craters, the conductivity of the regolith can become as low as 10^{-14} S/m, rendering them insulators (unable to deliver the needed currents). Recent studies indicate that the dissipation time in unlit craters could be as large as 10,100 s. Hence, a rover (continuous charging) or astronaut (charging with each step with a cadence of a second) will charge faster than can be dissipated. As a consequence, roving systems in unlit regions can become ESD hazards.

9.3.4.4.4.2 Lunar surface power system. Any polar base will spend some fraction of time in darkness and away from the photoelectric sheath. Consequently, the region is susceptible to solar

storm-induced variations in surface potential. Given the poor conductivity of the lunar regolith (making it a poor electrical 'ground'), a potential difference can develop between the surface and objects located on the unlit surface during storms. To date, there are no direct measurements of this effect and modeling is just beginning to address this issue. In essence, an object in the unlit region is sitting on an insulator. Consequently, it is recommended that there are clear ground paths for all landed system components to reduce the effect of differential charging, especially during solar storms when the ground and landed components will develop potential differences relative to each other.

Any system venturing into a polar crater should also be aware that the surface in the unlit region is strongly negative relative to any voltage referenced at the crater rim (in daylight). Thus, the use of a tether for power will have a ground reference to the sunlit region where the power source is located, but the surface surrounding the exploration system could be many hundreds of volts negative relative to the system ground (referenced to a topside location). Some consideration should be given to mitigating this ESD risk.

9.3.4.4.4.3 Lunar dust. At terminator/polar regions, where electric fields are expected to be large (see fig. 161), the dust environment becomes active. The Lunar Ejecta and Meteorite (LEAM) experiment, an Apollo 17 lunar surface experiments package, detected incidence of highly energetic lifted dust grains with speeds >100 m/s at both terminator crossings Berg et al.[267] The dust was detected in all directions but was primarily moving in nightside directions. The activity peaked at the terminators but extended well into the nightside. Naturally lifted dust grains were detected by LEAM at a rate of one every couple of minutes. Since LEAM was relativity insensitive to low-energy dust, it is anticipated that there is a progressively larger flux of natural dust at progressively lower speeds (a distribution of dust that increases with density at decreasing velocities) and that LEAM is detecting only the most energetic lofted grains at the 'tail' of the distribution. However, landed instrumentation is required to confirm this possibility. The naturally lifted lunar dust is an indicator of locations where near-surface electric fields may become large.

Figure 161 indicates that driving *E*-fields may indeed peak where LEAM dust is most active at the terminator. Such an electrical environment would also have an impact on any anthropogenically lofted dust since there is an induced potential on both the roving astronaut and the dust that may further increase their electrostatic attraction.

9.3.4.5 Photoelectric Emission of Lunar Fines. Photoelectron emission is affected by surface properties. Attempts were made to mitigate possible contamination of lunar samples from Apollo 14 and 15 before measurements of photoemission measurements from the lunar fines were made. References 268 and 269 give information on laboratory results for the photoelectric yield versus wavelength for samples of lunar surface fines from Apollo 14 and 15. In situ behavior is likely to be different because of potentials on the particles in the fines not present in the laboratory environment and possibly a different packing on the lunar surface. There are no measurements of this property from the lunar surface. This yield function has to be folded with the Sun's spectra in the 500 to 2,500 Å range in order to obtain the total photoemission from the lunar surface.

9.3.4.6 Secondary Electron Emission—Bulk Material. Secondary electron emission from a semi-infinite slab of material as a result of electron impact can be represented approximately by the Sternglass formula:

$$\delta \cong C\delta_{\max}\left(\frac{E}{E_{\max}}\right)\exp\left(-2\sqrt{\frac{E}{E_{\max}}}\right), \tag{97}$$

where

δ = number of secondary electrons emitted per incident electron
C = constant (7.4)
$\delta_{\max}$ = maximum number of secondary electrons emitted per incident electron
E = energy of incident electron
$E_{\max}$ = energy at which the maximum yield occurs.

Preliminary secondary electron emissions from Apollo 14 and 15 can be found in references 293 and 269.

9.3.4.7 Triboelectric Charging. As a result of motion both through and over lunar regolith, a moving body, such as a rover or an astronaut, will experience triboelectric charging. The basic mechanism involved in triboelectric charging is well understood. Triboelectric charging, also known as tribocharging or the triboelectric effect, is an example of contact charging, wherein surfaces become electrically charged after making contact with each other. Often associated with frictional contact, such as rubbing, the effect actually requires only that the materials come into contact and then separate. The strength of the resulting charge as well as the polarity acquired by each of the two materials depends on material properties. While the most important of these is known to be electron work function, such properties as surface roughness and temperature can compound the problem. For this reason, attempts to predict the actual response of engineering systems are often only partly successful and generally require testing under realistic conditions.

At its source, then, the magnitude of the effect depends on the difference in work function between the materials involved. While the effective work function of lunar dust is not known, and probably differs from that of available simulant, it is believed to be approximately equivalent to that of platinum. What is not known is how sensitive vehicle charging is to this parameter. It is conceivable that careful attention to work function in the selection of materials and coatings could considerably reduce the charging problem at its source. While most of the emphasis has been paid to moving rovers, and it is this case that the best information is currently available, it is increasingly recognized that contact and movement of crewmembers' boots with regolith results in charge transfer that is implicated in significant dust adhesion to boots and the lower parts of space suits.

For the case of triboelectric charging of rovers, experiments at Glenn Research Center (GRC) in support of Mars Pathfinder showed that a rover wheel turning in simulant in a Martian atmospheric environment would lead to overall charging in excess of 100 V with transients observed that were 2 to 3 times that much.[239,240] Mars has a tenuous atmosphere, therefore it was

possible to partially mitigate the charging through the addition of a microdischarge point. GRC-provided discharge points were installed on the Pathfinder rover and have been installed on both Mars Exploration Rovers now operating on Mars. A more efficacious solution was developed for the Mars 2001 rover, Marie Curie. That package, the Mars Experiment on Electrostatic Charging (MEEC), used a small dot of radioactive Americium 241 to partially ionize the atmosphere in front of the rover. MEEC was built and delivered to JPL, but the mission was cancelled.[241]

Triboelectric charging is expected to be more severe on the lunar surface. On Mars, it is the presence of roughly 7 torr of CO_2 that allows charge to be bled off. On the Moon, the presence of hard vacuum does not allow mitigation that might be achieved through discharge points, whether they are added or consist of naturally occurring sharp points on the vehicle body. The radioactive dot solution also works by partially ionizing atmosphere and will be ineffective on the Moon.

In addition to triboelectric charging caused by motion, operations on the lunar surface must deal with a naturally occurring background charge. The distribution of charge in the lunar environment is not well understood. Tribocharging has been studied to date assuming that the natural environment was initially neutral and that charge separation and transfer resulted in charging. This is the case for Mars, but on the Moon the environment may already be charged.

9.3.5 Contamination

Contaminants on the lunar surface are described in table 109.

Table 109. Contamination of the lunar surface.

Contaminant Type	Description	Prevalence	Systems at Risk
Particulate	Adhered regolith/ dust	Ubiquitous	Mechanical, EVA, life support, power, thermal control surfaces, optics
Particulate	Dust fallout	Sporadic	Power, thermal control surfaces, optics
Particulate	Micrometeoroid	Sparse/continuous	Power, thermal control surfaces, optics
Molecular	Impact melt vapor	Sparse/continuous	Power, thermal control surfaces, optics
Particulate	Micrometeoroid-induced spallation	Very sparse	Power, thermal control surfaces, optics
Molecular	Condensed gas	Shadowed regions	Optics
Molecular	Solar nuclei	Dayside/sporadic	Optics
Molecular	GCR nuclei	Sparse/continuous	Optics

9.3.5.1 Lunar Regolith as a Contaminant. By far, the greatest natural contamination source on the lunar surface is the regolith. From a contamination perspective, the whole Moon is a sea of potential foreign object debris, which is of concern to any mechanical systems. Additionally, even moderate size fines (>5 μ) can tend to adhere tenaciously to surfaces due to charging. Bulk charging is predicted to be positive on the dayside and negative on the nightside, so adhesion properties will change from day to night. Similarly, any triboelectric charging of the regolith may differ from day to night.

At the leading and trailing terminators, rapid changes in charging conditions may allow dust dynamics to occur, lofting submicron particulate kilometers above the surface. Such lofted particulate would then settle in a fairly broad fallout zone. The LEAM experiment of Apollo 17 accidentally detected particle events at lunar dawn and dusk which were determined to be charged dust. Measurements of actual diurnal fallout rates would be necessary to predict the level and size distribution of this natural particulate contamination. Preliminary estimates of the column density of dust to produce Apollo-observed horizon glow would allow for as high as 1% obscuration of surfaces from fallout of 0.1–0.5 μ particulate. Fallout onto some surfaces could allow accumulation of particulate on every cycle (where the particulate tends to stick, or is shaded, etc.), such that in 1 year there could be over 10% total obscuration. But even after 10 years a surface completely covered in submicron dust particles might appear clean to the unaided eye, though it would be absorbing over wavelengths determined by the dust mineral species.

9.3.5.2 Micrometeoroids. There is a somewhat higher flux of micrometeoroids on the lunar surface than the interplanetary flux of surrounding space. Over time, this may allow a significant buildup of micrometeoroid contamination of surfaces exposed on the Moon. The constituent elements of this particulate (as described in the micrometeoroid section) will become embedded in surface layers but will cover the surface at a cumulative level of <1% over 10 years of exposure (estimated from LunaRef meteoroid fluence of 5,000/yr m^2 for masses in the 10^{-12} g range). However, localized contamination can be quite high near a rare, larger impact.

The high velocity of micrometeoroids imparts energy upon impact that produces, at minimum, a localized melt vaporization zone. Vaporized ejecta may then condense on cold surfaces in the immediate vicinity. For micrometeoroids of greater mass, affected area of impact increases accordingly, eventually reaching the point where the energy of impact can cause spallation of debris from the surface. In cases where the surface is loose regolith with fines, the ejecta will include such dust particles, which will create a fallout field in the vicinity (with submicron diameter dust having the widest fallout zone).

9.3.5.3 Condensed Gas. In the cold, shadowed regions and on the nightside, some gas species will tend to condense on surfaces. The densities of these gases on the lunar surface are extremely low, so it would take years to accumulate an appreciable molecular layer, and then only if permanently shadowed. However, the lunar poles are likely repositories of these condensed and frozen gases.

9.3.5.4 Implanted Nuclei. The solar wind, made up mostly of protons (and electrons) will, over time, implant a subsurface layer of hydrogen atoms. The flux of protons has a fairly continuous lower energy component but can increase dramatically with SPEs. There is a similar but more tenuous flux from GCR that would penetrate deeper and be more dispersed than the higher density, lower energy solar protons. Such a layer of implanted hydrogen could eventually affect optical systems, though it would more likely be a detriment to surface finishes, perhaps causing flaking of metals through hydrogen embrittlement. Though hydrogen would be the predominant implanted species, iron nuclei could actually cause more of a problem as an eventual contaminant.

9.3.6 Transient Lunar Phenomena

Transient activity on the Moon has been reported by visual observers for many years although documented events are very rare and are often disputed. Hazes and red glows are the most frequent. Flashes from meteoroid impacts on the Moon have been recorded,[243] but the other transient lunar phenomena (TLPs) are so poorly documented and uncertain that no design or operational planning regarding these questionable phenomena is appropriate.

9.3.7 Lunar Interior and Moonquakes

9.3.7.1 Introduction. The seismic activity of the Moon was determined using the Passive Seismic Experiment (PSE) that was part of the ALSEP package on missions 11, 12, 14, 15, and 16. The seismometer at the Apollo 11 site failed a few weeks after deployment. The remaining stations continued in operation until October 1977. The stations form an approximate equilateral triangle approximately 1,100 km on a side; the Apollo 12 and 14 sites forming the southwest corner, Apollo 15 the northern corner, and Apollo 16 the southeast corner (fig. 163). In addition to the passive experiments, active seismic experiments were conducted on the Apollo 17 Lunar Seismic Profiling Experiment and the impact of the S-IVB stages and upper stages of the lunar module (LM) were also used as active sources.

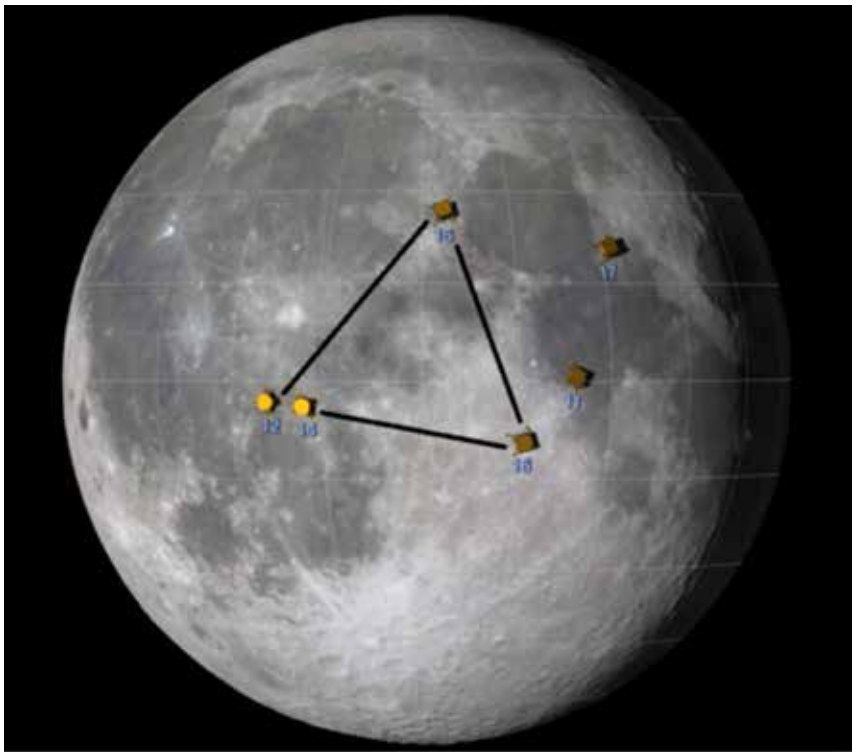

Figure 163. Location of ALSEP seismometers. Lunar image with landers courtesy of NASA GSFC Visualization Studio.

9.3.7.2 Seismometer. Each station consisted of four seismometers: three low-frequency components that formed a triaxial set (one vertical, two horizontal) with a peak sensitivity of 0.45 Hz and a fourth seismometer sensitive to vertical motion with a peak sensitivity of 8 Hz (high-frequency component). The instruments are capable of detecting ground motion of 0.05 nm. The deployed instrument is illustrated in figure 164.

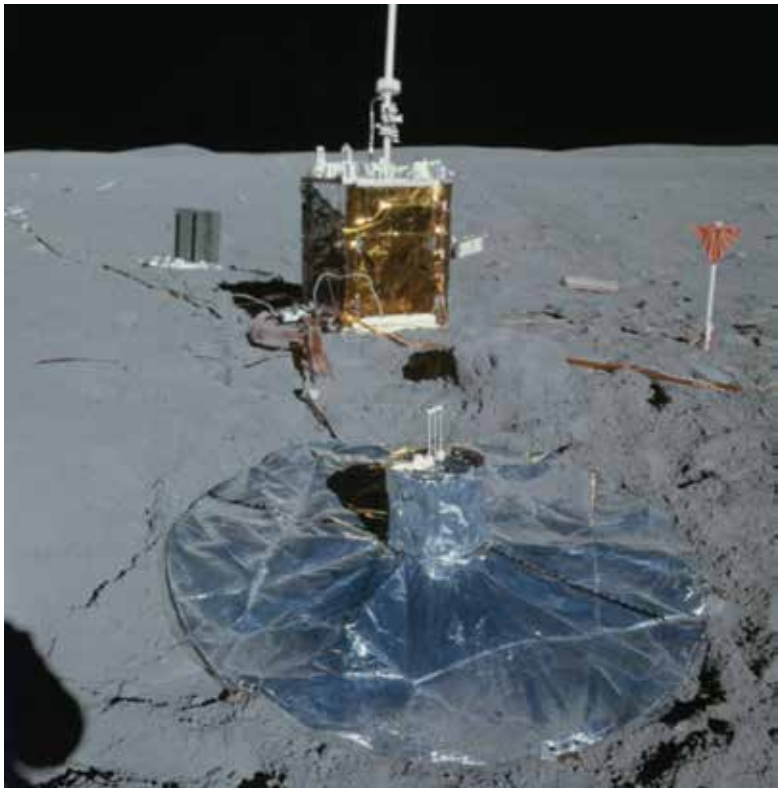

Figure 164. Passive seismic experiment at the Apollo 16 site (courtesy of NASA).

9.3.7.3 Seismic Events. During the nearly 8 years of operation, the PSE recorded in excess of 12,500 events (table 110). These events can be categorized as deep moonquakes, shallow moonquakes, and impact events. Table 110 lists the events. The seismic energy released in the Moon is approximately 2×10^{10} J/yr compared with 10^{17}–10^{18} J/yr on the Earth. The short interval of time during which data were collected suggests that the lunar energy release might be as high as 10^{14} J/yr but still many orders of magnitude lower than the Earth.

Table 110. Seismic events on the Moon detected by the Apollo 16 PSE.

Number of Seismic Events Detected	Total*	Major Events**
Artificial impacts	9	5
Meteoroid impacts	1,743***	95
Shallow moonquakes	28***	7
Deep moonquakes	3,145***	9
Unclassified events	7,300***	–

* These data do not include signals detected only by short-period seismometer or large number of events recorded only at the Apollo 16 site.
** Signal amplitude >10 nm at two or more stations.
*** Numbers as of 1982. [294] Subsequent analysis has indicated that additional events may be retrievable from the data.

9.3.7.3.1 Deep Moonquakes. These are the most abundant type of events. They have small magnitude (typically ~1) and occur approximately half-way between the surface and the center of the Moon at depths of 800 to 1,000 km (range 700 to 1,200 km). Their occurrence is strongly linked to tides raised by the Earth and the Sun and are suggested to be caused by dissipation of tidal energy. Almost all events have been located on the front side; the highlands terrain on the far side either lacks such events or the signals are attenuated and not detectable. These quakes occur in localized groups ('nests') within a volume of approximately $1 \times 1 \times 1$ km. There are approximately 2 to 300 quakes in each nest.

9.3.7.3.2 Shallow Moonquakes. These events have the highest energies but are rare (approximately four events per year). A total of 28 events were recorded in 8 years, 2 of which had magnitudes close to 5. Focal depths were not determined but are estimated to be 50 to 200 km. The occurrence of these events is unrelated to tides, hence is considered tectonic in origin and shows similar characteristics to terrestrial intraplate earthquakes. The events produce P and S arrivals suggesting that the events occur at some depth below the surface. The temporal frequency of shallow quakes can be found in reference 294; The location of the shallow moonquakes can be found in reference 295.

9.3.7.3.3 Thermal Moonquakes. Thousands of very small seismic events that are detectable only to distances of a few kilometers are caused by temperature variations near or at the surface. They may be spatially associated with young craters and large rocks.

9.3.7.3.4 Natural Impact Events. Meteoroids in the size range of 0.1 to 1,000 kg have been detected in the long-period data; more numerous events have been detected by the short-period seismometers. These are not all random events but tend to be clustered in time (20% of the events occurred within 3% of the time). Large events were detected between April and July, while smaller events were associated with meteor showers. The largest events indicate meteoroids of ~5 tons; seven events were recorded that were formed by bodies >1 ton, impacting the Moon.

9.3.7.3.5 Artificial Impact Events. For several Apollo missions, the S-IVB booster and the upper stage of the LM were targeted at the Moon to produce artificial impact events with sufficient energy to probe the lunar interior.

9.3.7.3.6 Unclassified Events. Unclassified events are those whose origin could not be determined. Table 111 lists the frequency and energy of moonquakes and earthquakes.

Table 111. Frequency and energy of moonquakes and earthquakes.

Parameter	Moon	Earth
Event frequency	5 per year (shallow, $m > 2.2$) 500 per year (deep, $m > 1.6$)	10^4 ($m > 4$)
Energy released by largest event	2×10^{12} J (shallow) 1×10^{18} J (deep)	10^{21} J
Magnitude of largest event	4.8 (shallow) 3 (deep)	9.5
Seismic energy release	2×10^{12} J/yr (shallow) 8×10^{8} J/yr (deep)	10^{25} J/yr

9.3.7.4 Seismic Risk. The seismic events that present risk to a lunar base are those associated with relatively strong shallow moonquakes and impacts. The primary issue with impacts is the impact event itself rather than the resulting seismic energy.

Shallow quakes occur at depths of less than 100 km and average four per year. The likelihood that a randomly chosen site would experience a quake with magnitude Mb > 4.5 within 100 km of that point is estimated at 1 in 400 year.

9.3.8 Lunar Volcanism

Lunar volcanism is the result of partial melting of the lunar interior (mantle) and eruption of these melts onto the lunar surface. Volcanic products include lava flows (called 'maria' when they fill large impact basins) and pyroclastic deposits that created volcanic glass beads such as the Apollo 17 orange glass. Lava flows cover about 17% of the lunar surface, primarily filling topographic lows on the nearside.[296] Lunar basalt classification is based on three distinguishing geochemical indices (Ti, Al, and K);[297] however, remote sensing data sets have shown that the full range of mare basalt composition and ages has not yet been sampled.[298] Knowledge of the duration of lunar volcanism comes from (1) radiometric dating of meteorites and samples from the Apollo and Luna missions, and (2) crater counting statistics of mare surfaces from remote sensing data. Lunar volcanism reached its maximum volumetric output between 3.8 and 3.2 giga years ago (Ga),[299] but began as early as 4.3 Ga[300–303] and may have persisted until as recently as 1.2 Ga.[304] There is currently no evidence of volcanic activity on the Moon.

9.4 Lunar Poles

The lunar poles have a unique environment because of the small value of the lunar obliquity (1.5°). Thus, the Sun never rises much above (or sets much below) the horizon. The relatively constant illumination geometry creates locations of near-permanent (possibly permanent) sunlight and areas of permanent shadow (crater interiors). Areas of permanent shadow have very low temperatures (perhaps approximately 50 K).

The heavily cratered morphology of both poles suggests they are 'anorthositic' highlands terrain. The South Pole lies just beyond the rim of the South Pole Aitken Basin. Figures 165 and 166 show the north and south polar regions in visible and in radar illumination.

9.4.1 Solar Illumination Conditions

Topographically high areas in the polar region have the potential to be permanently or nearly permanently illuminated if they are high enough to remain illuminated by the Sun when it is 1.5 below the nominal horizon. Similarly, depressions such as craters can remain in permanent shadow if they are deep enough.

Analysis of images acquired over the North and South Poles (primarily Clementine, with additional data from Lunar Orbiter, Galileo, and Small Missions for Advanced Research in Technology-1, have allowed an assessment of the lighting conditions.[305]

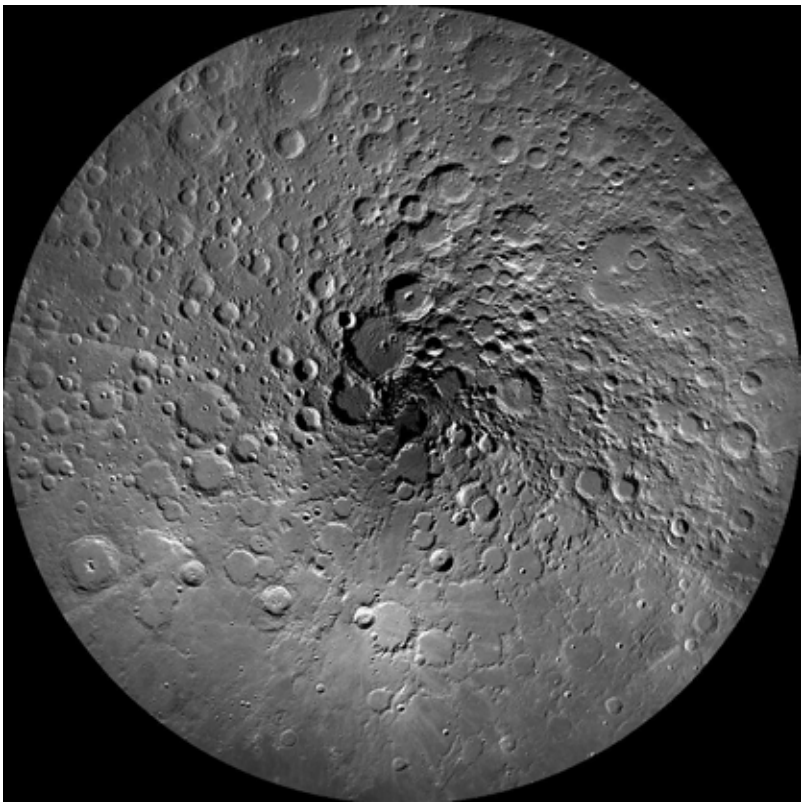

Figure 165. North Pole mosaic from Lunar Reconnaissance Orbiter (courtesy of NASA/GSFC/Arizona State University).

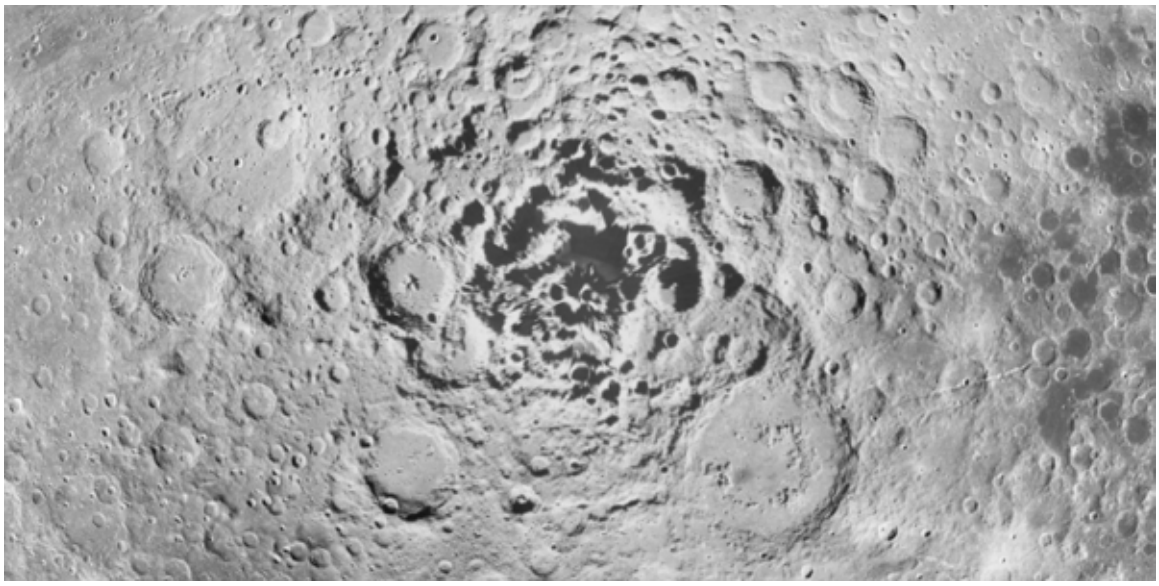

Figure 166. South Pole mosaic from Clementine (courtesy of NASA).

9.4.2 Volatile Traps

Areas within permanent shadow are thought to have such low temperatures that they become cold traps for normally volatile elements and compounds. Any atomic or molecular species that enters the cold trap will be stored there permanently unless energized with sufficient kinetic energy to escape ballistically (e.g., meteor impact).

Because of the presence of water at the poles, there may be some significant water or hydration in the minerals there. Hydrated minerals are very rare or nonexistent at other lunar sites.

Because of the differences in the temperature, chemistry, lighting, electrical, and other conditions at the poles, results of robotic precursors to manned missions will help preclude unfortunate surprises when manned missions land. A robotic lander would help immensely in finding out how much the polar surface differs from that in the equatorial regions and would greatly help reduce the risks involved with landing in unknown conditions.

The Lunar Crater Observation and Sensing Satellite impacted a Centaur upper stage followed by a sensing satellite into the permanently shadowed crater Cabeus in October 2009. There were significant water and other volatile signatures detected by the sensing satellite.[249] In addition, a significant amount of mercury (Hg) was also detected in the plume by the Lyman-alpha mapping project instrument on the LRO.[306,307]

9.5 Lunar Dust

What is popularly called the lunar dust is actually the very fine material in the lunar regolith. For its properties, see sections 9.3.1 through 9.3.4.

9.6 Thermal Environment

Since there is no moderating atmosphere, surface temperatures are extreme. At the Apollo 17 site the temperature ranged from 384 K during the day to 102 K just before sunrise. A detailed study of infrared radiation at 11 μ from the eclipsed lunar surface revealed over a thousand small anomalously warm regions.

There is an approximate anticorrelation between infrared eclipse temperature and albedo. Local high temperature anomalies have been interpreted as due to the presence of an excess of bare rocks on the surface.

The spectral distribution of sunlight is approximately blackbody at 5,760 K. Energy flux at the Earth-Moon system is 1.97 cal/(cm^2min) or 1,371 ± 5 W/m^2. Other than direct sunlight, the most important sources of radiant flux at the Moon are earthshine (sunlight reflected from the Earth) and thermal radiation from the Earth's surface and atmosphere.

9.6.1 Surface Temperature

The surface temperature on the lunar surface varies as a function of latitude due to the fact that toward the poles, the Sun illuminates the surface at a lower angle. Figure 167 illustrates generalized temperature as a function of time and latitude.

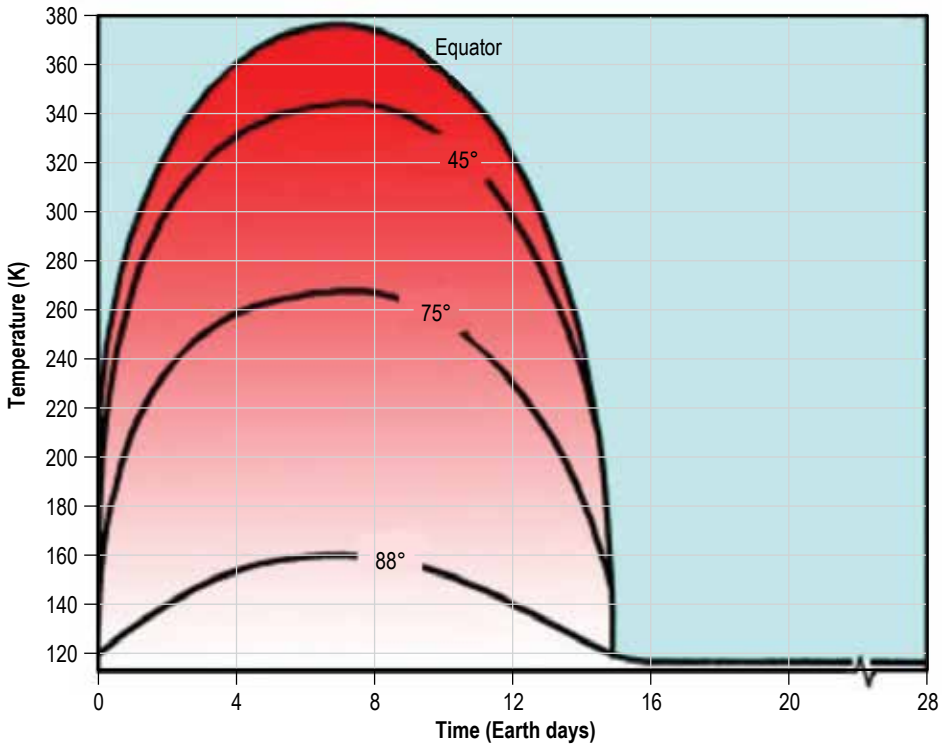

Figure 167. Generalized temperature as a function of time and latitude.

The radiative heat input into the surface Q_{in} (W/m^2):

$$Q_{in} = (1 - A(\mu))S\cos\theta \ , \tag{98}$$

where

$A(\mu)$ = directional hemispherical albedo (reflectivity)
S = solar constant
θ = angle relative to surface normal.

The solar constant (S) varies from 1,315 to 1,412 W/m^2 (minimum in July; maximum in January). This is orders of magnitude greater than the heat flow from the interior of 2 to 4×10^{-6} W/cm^2.

The surface temperature is a function of the thermal loading and the thermal properties of the regolith. The thermal loading varies over a period of 709 hr (a lunar day). For a given set of thermal properties, the surface temperature curve depends only on the thermal inertia (I) in units of J/(m^2 s$^{1/2}$ K):

$$I = \sqrt{(K\rho C_p)} \ , \tag{99}$$

where

K = thermal conductivity (J/(smK))
ρ = density (kg/m^3)
C_p = specific heat (J/(kg K)).

Thermal conductivity data for the lunar regolith were determined in several ways: modeling the decay of the thermal disturbance caused by the insertion of the heat flow probes, heat dissipation from active heating of regolith, and analysis of returned samples. Data from the heat flow probes may not accurately reflect values for the bulk regolith due to disturbance of the physical properties during insertion of the heat flow probes. Values determined in the laboratory may also not reflect the bulk regolith because of the limited sample size and lower densities. Conductivity also has a temperature dependence. Thermal diffusivity is estimated from models of the attenuation of annual temperature amplitude as a function of depth and transient thermal events associated with probe insertion.

Thermal conductivity and diffusivity both vary as a function of temperature. The relation among these different parameters for Apollo 12, sample 12001 and two different densities can be found in reference 308. Table 112 shows the thermal properties of the lunar regolith.

The resulting surface temperatures vary very little within the range of these parameters except for small differences at night. Figure 168 shows the calculated lunar surface temperature for rock and regolith over a lunar day. Table 113 lists the temperature variations across the lunar surface. The lunar thermal inertia is so low that the surface daytime temperature is in thermal equilibrium with absorbed solar radiation flux. At the equator, the subsolar point temperature would be approximately 387 K, but a radiometric measurement would indicate a temperature of 409 K because the surface does not radiate energy uniformly.

Table 112. Thermal properties of the lunar regolith.

Parameter	Units	Value	Notes
Conductivity <6 cm	W/cmK	0.6×10^{-4}	Very low at the surface
Conductivity >50 cm	W/cmK	$0.9–1.3 \times 10^{-4}$	Increases with depth
Diffusivity	Cm/s	$0.74–1 \times 10^{-4}$	Attenuation of annual temperature amplitude
Thermal gradient	K/m	0.79–2.52	Significant variation between Apollo 15 and 17, and between probes at each site
Specific heat	W s/gK	0.67	

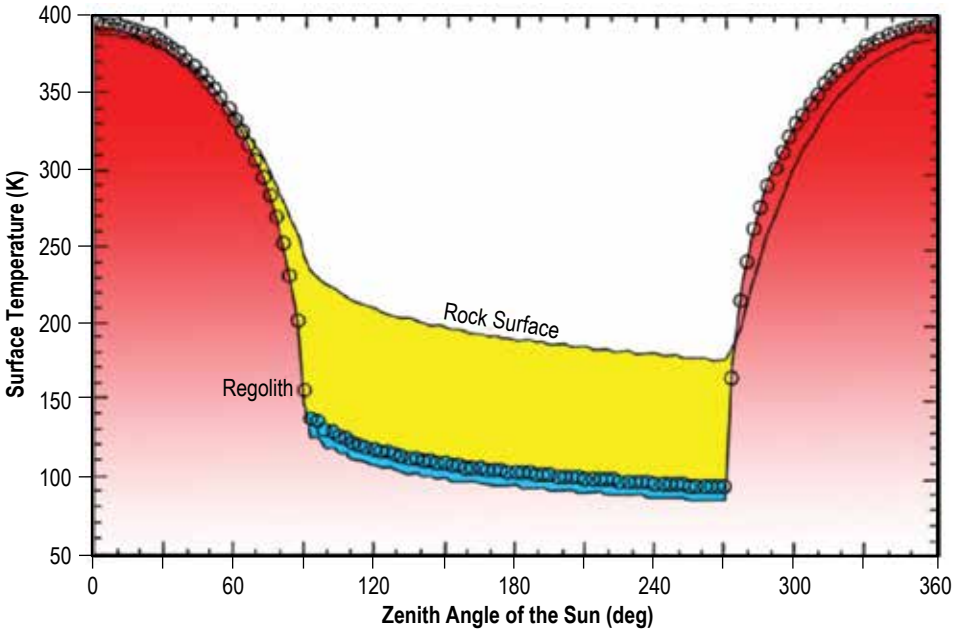

Figure 168. Surface temperature as a function of time; when the thermal properties of the regolith are considered the lowest, nighttime temperature can vary. (Circles represent lunar sample values; the lower solid line represents values for a mature regolith; and the upper solid line represents values for a theoretical rock surface. The blue area illustrates the difference in temperature between immature and mature regolith; the yellow area illustrates the difference between a regolith-covered and rock-covered surface.)

Table 113. Lunar surface temperatures.

Temperature	Shadowed Polar Crater	Other Polar Areas	Nearside Equatorial	Farside Equatorial	Mid-Latitude
Average temperature	40 K	220 K	254 K	256 K	$220 < T < 255$ K
Monthly range	None	±10 K	±140 K	±140 K	±110 K

Clementine long-wavelength infrared data (8–9.5 μ) shows that a Lambertian temperature model provides a good approximation of the temperature observed from orbit below a spacecraft. The relation is a function of $\cos^{1/4}(i)$ where i is the solar incidence angle.

9.6.2 Subsurface Temperature

The Apollo 15 and 17 heat flow experiments provide information on the temperature and thermal conductivity of the regolith with depth over different time scales. Long-term monitoring of the subsurface temperature shows that it consists of three components; diurnal, annual, and aperiodic.

The diurnal variation (period 29.53 days) is observed close to the surface and affects the upper 30 cm. The annual variation extends to a depth of 200 cm at the Apollo 17 site. An additional aperiodic effect caused by the disturbance of the surface by the crew resulted in a slow, long-term increase in the subsurface temperature. Figure 169 illustrates temperature variation as a function of depth at the Apollo 15 and 17 landing sites.

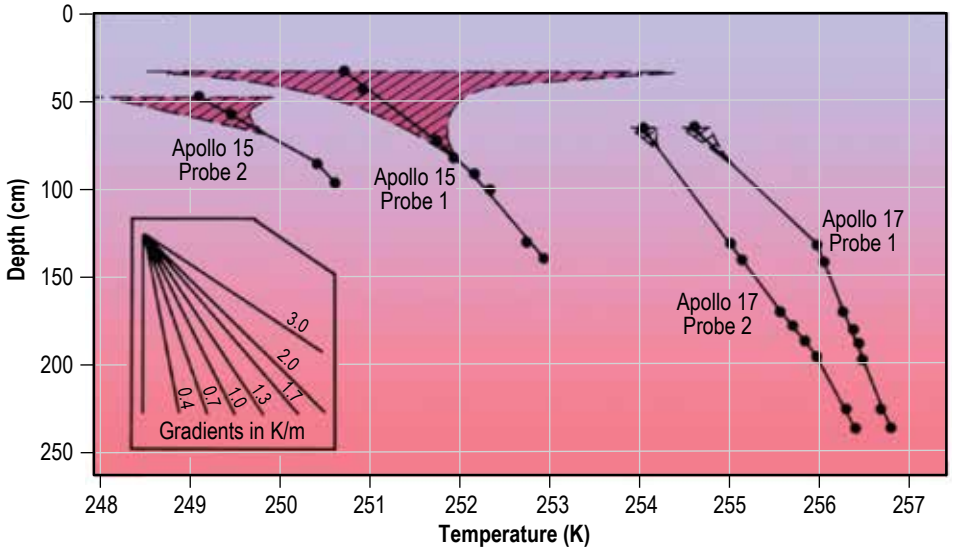

Figure 169. Temperature variation as a function of depth at the Apollo 15 and 17 landing sites (hatched areas show day-to-night temperature variations). Below approximately 50 cm, there is essentially no temperature variation due to the day-night cycle (adapted from fig. 3.9)[291] (Copyright © 1991, Cambridge University Press, reprinted with permission of Cambridge University Press).

9.7 Ionizing Radiation Environment

With one exception to be discussed next, the lunar surface ionizing radiation environments are the same as those discussed in section 9.3 for lunar space. Since the Moon does not have any magnetic field that could provide any magnetic screening, the ionizing radiation environment will be composed of the unscreened GCRs and SPEs. The details of these environments and the effects on electronics are presented in sections 2.12, 3.11, and 5.5.

9.7.1 Lunar Neutron Environment

GCRs generate neutrons through inelastic collisions with atoms in the lunar soil. These neutrons lose energy through collision with other atoms, a process that is called thermalization. The lunar neutron environment has a continuous energy spectrum from the thermal range, approximately 2.5×10^{-8} MeV through the high-energy range at approximately 1,000 MeV. The peak flux occurs at the most probable spallation energy of approximately 2 MeV.

Albedo neutrons produced by GCR interactions with the lunar surface were measured by the neutron spectrometer (NS) and gamma ray spectrometer (GRS) instruments on the LP mission while the spacecraft was in orbit around the Moon in 1998 and 1999. The spacecraft was inserted into a 100 km altitude circular, polar lunar orbit on January 11, 1998, and the first set of neutron observations was obtained at an altitude of 100 km from January 16, 1998 to October 5, 1998. A second set of lower altitude measurements between 10 km and 50 km from the lunar surface was obtained between December 20, 1998 and July 28, 1999.[308] The mission was terminated on July 31, 1999, with disposal of the spacecraft through a commanded crash of the vehicle into the lunar surface in the Moon's southern polar region.

During the mission, thermal neutrons (>0.4 eV) and epithermal neutrons (0.4 to 100 eV) were measured by the NS. Two other channels, the wide band (0 to 500 eV) and fast neutrons (0.6 to 8 MeV) were measured by the GRS. Maurice et al.[308] and Feldman et al.[309] describe the instrument and data sets.

The lunar surface neutron spectrum was not measured directly, but those indirect measurements of the escaping flux at 30 km, along with knowledge of the GCR environment, were used to model the lunar surface neutron environment. The Monte Carlo N-Particle eXtended code was used to predict the spallation response of lunar soil to the GCR environment and the results were matched to the measured neutron spectra at 30 km.[310] Figure 170 presents the flux as a function of landing site soil composition.

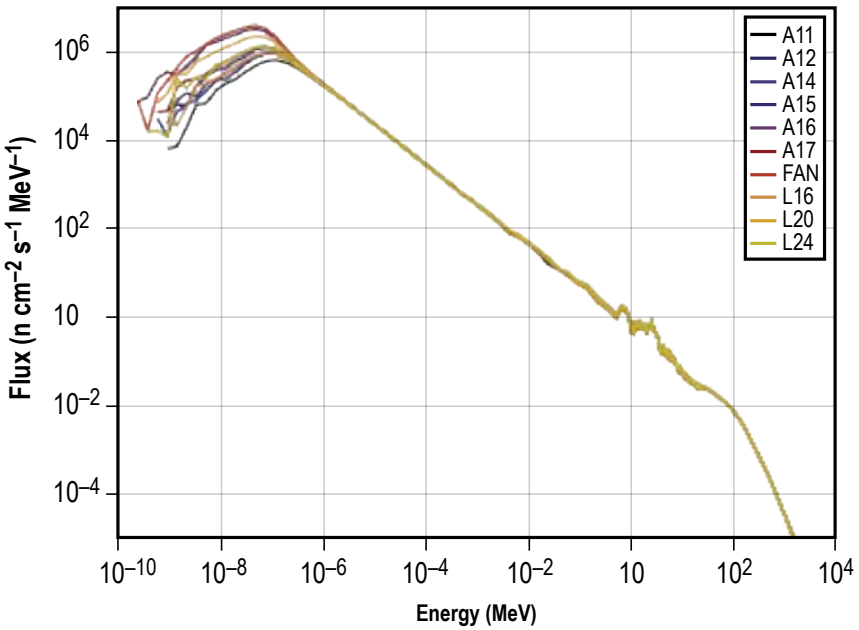

Figure 170. Lunar neutron spectrum in terms of neutron differential flux (n/cm^2/s/MeV) as a function of energy) MeV and lunar soil composition.[310]

9.8 Meteoroid Environment

For a general description of the meteoroid environment including showers, flux, directionality, speed, and densities, see section 4.6. The general description of the environment does not change near the Moon, just the effects of shielding and focusing due to the Moon's mass.

9.8.1 Flux

The Moon's relatively weak gravitational pull does not significantly focus or enhance the meteoroid flux in its vicinity; indeed, simple calculations assuming an isotropic environment show that the flux enhancement is of the order of 2% or less, much smaller than other uncertainties in the environment. Shielding is still significant, though. Still, for accuracy in modeling the shielding and focusing effects, a lunar submodel of MEM is available. The lunar submodel of MEM models the primary meteoroid flux, speed, and directionality for spacecraft in orbit around the Moon out to the Moon's sphere of influence (which extends out to roughly 60,000 km from the lunar center). These output files can then be incorporated into BUMPER (meteorid and orbit debris risk assessment tool) for risk analysis. Figure 171 shows the average flux on the surfaces of an oriented cube-like spacecraft. Figure 171 was generated using 1,500 randomly drawn state vectors over a 2-week period corresponding to a lunar equatorial 100 km altitude orbit.

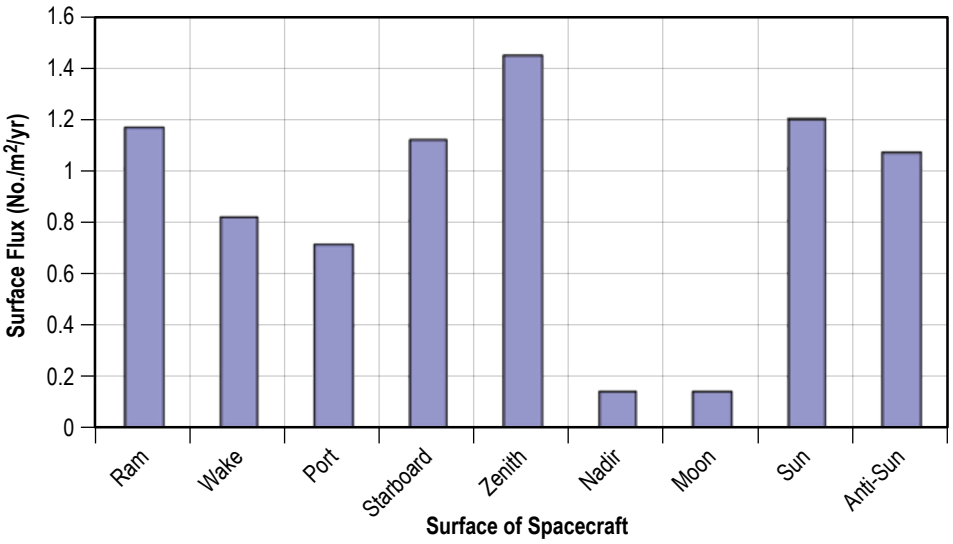

Figure 171. Effects of directionality for an oriented cube-like spacecraft in low lunar orbit, with focusing and shielding.

Figure 172 represents the flux of meteoroids as a function of diameter. To convert diameter to mass in grams, use the following relationship (also found in sec. 5.6):

$$D = \left(\frac{6 \cdot Mp}{\pi \cdot \rho} \right)^{1/3} , \tag{100}$$

where ρ is the density of the meteoroid and for most purposes can be assumed to be 1 g/cm^3.

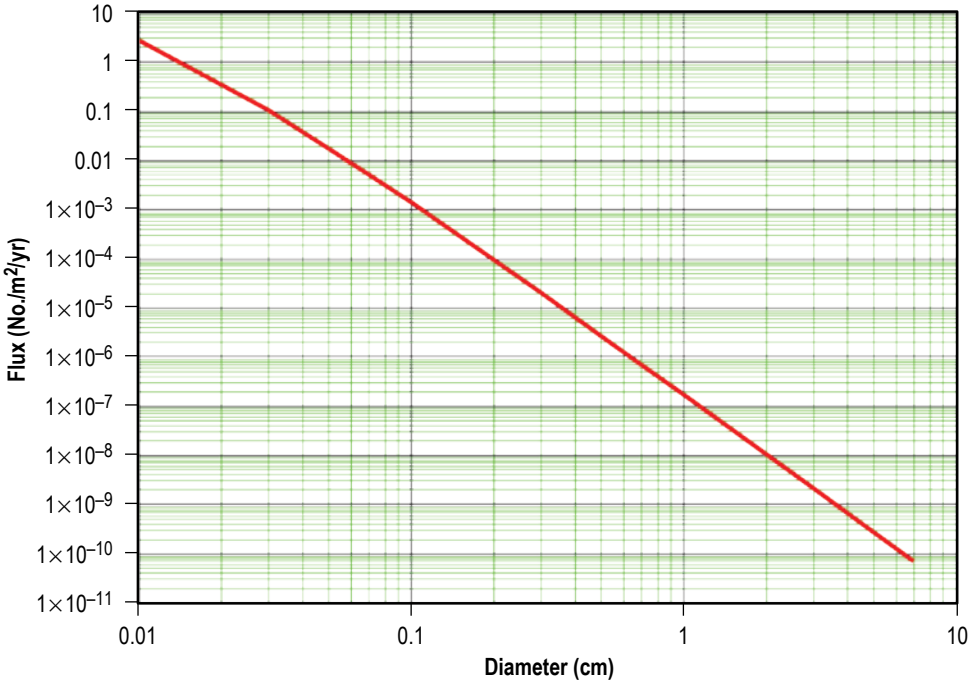

Figure 172. Meteoroid surface area flux near the Moon as a function of particle size (no correction has been made for lunar shielding, and the particle sizes were computed assuming a density of 1 g/cm^3).

Table 114 shows the interplanetary meteoroid flux at Earth's distance (1 AU) as a function of particle size.

Table 114. Interplanetary meteoroid flux at Earth's distance (1 AU) as a function of particle size.

Diameter (cm)	Mass (g)	Flux (No. m^{-2} yr^{-1})
0.01	5.24×10^{-7}	2.639
0.03	1.41×10^{-5}	0.1
0.05	6.55×10^{-5}	1.7×10^{-2}
0.07	1.8×10^{-4}	5.09×10^{-3}
0.1	5.24×10^{-4}	1.3×10^{-3}
0.3	0.014	1.96×10^{-5}
0.5	0.065	2.61×10^{-6}
0.7	0.18	6.87×10^{-7}
1	0.524	1.66×10^{-7}
3	14.137	2.05×10^{-9}
5	65.45	2.64×10^{-10}
7	179.594	6.84×10^{-11}

Note: Diameters are computed assuming a meteroid density of 1 g/cm^3.

Figure 172 ignores the directional nature of the meteoroid environment, which could have significant effects. This is currently being investigated. See figure 173.

Figure 173 shows the directional nature of the meteoroid environment relative to a stationary observer at the lunar pole and lunar equator. The sporadic meteoroid environment is tied to the solar direction, therefore the intensity of incoming meteoroid fluxes varies by latitude, longitude, and lunar phase.

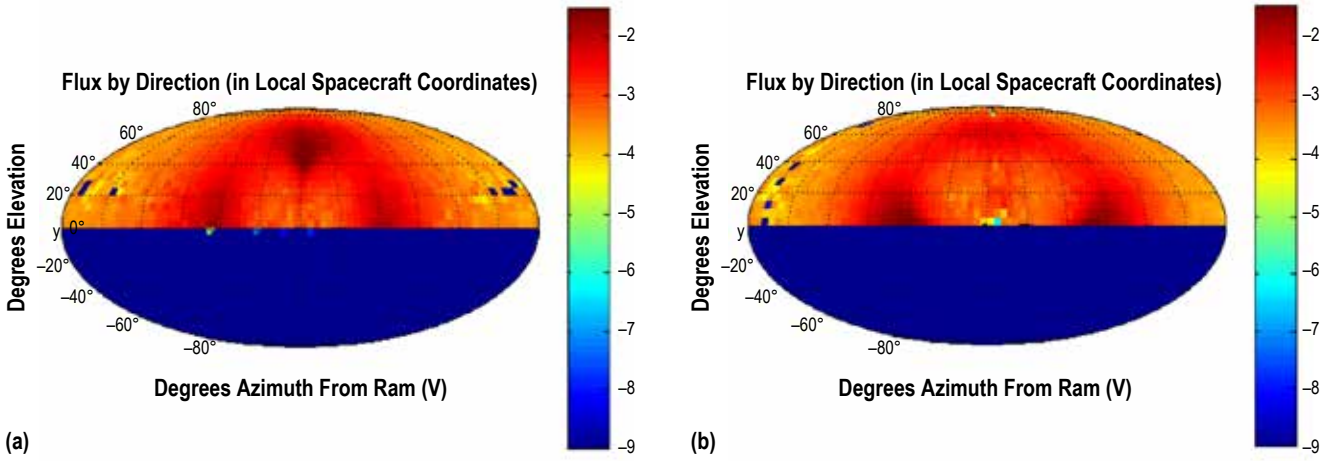

Figure 173. Example of the directionality of the meteoroid environment for stationary observer at (a) lunar Equator and (b) lunar North Pole.

9.8.2 Lunar Shielding

For a discussion involving shielding and focusing from a primary body, see section 5.6. An example of lunar shielding and focusing at the surface is shown in figure 173, specifically the zero flux from negative elevations.

9.8.3 Density

For a discussion on meteoroid densities, see section 5.6.

9.8.4 Speed

The velocity of meteoroids in near-Earth space is still the subject of considerable debate; the Grün model used to derive the fluxes given previously assumes a single speed, 20 km/s, for all meteoroids. An actual speed distribution, derived from photographic observations of large meteors, is given in NASA TM-4527,[311] Natural Orbital Environment Guidelines for Use in Aerospace Vehicle Development, and NASA Special Publication (SP) 8013, Meteoroid Environment Model-1969[312] (Near-Earth to Lunar Surface), but many researchers now believe that it underestimates the number of fast meteoroids. The speed distribution given by the new LunarMEM is used, which seems to best match the available observational data. This distribution for particles greater than and including 10^{-6} g is shown in figure 174.

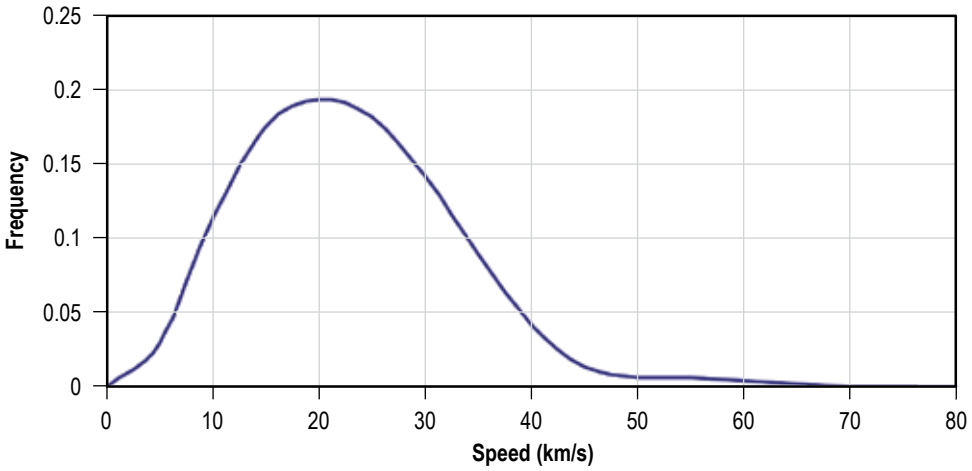

Figure 174. Average impacting meteoroid speed distribution in lunar space, no gravitational focusing no lunar shielding.

The velocity distribution of meteoroids impacting the Moon is roughly the same as that of meteoroids just outside the Earth's gravitational influence. Figure 175 compares the normalized velocity distribution for the lunar surface to that of meteoroids in lunar space or roughly interplanetary space at Earth's distance from the Sun. The only noticeable difference is at the slower speeds, where the Moon's weak gravity can accelerate the meteoroids by an additional kilometers per second. The minimum meteoroid impact speed with the lunar surface is set by conservation of energy to be the same as the lunar escape speed –2.38 km/s.

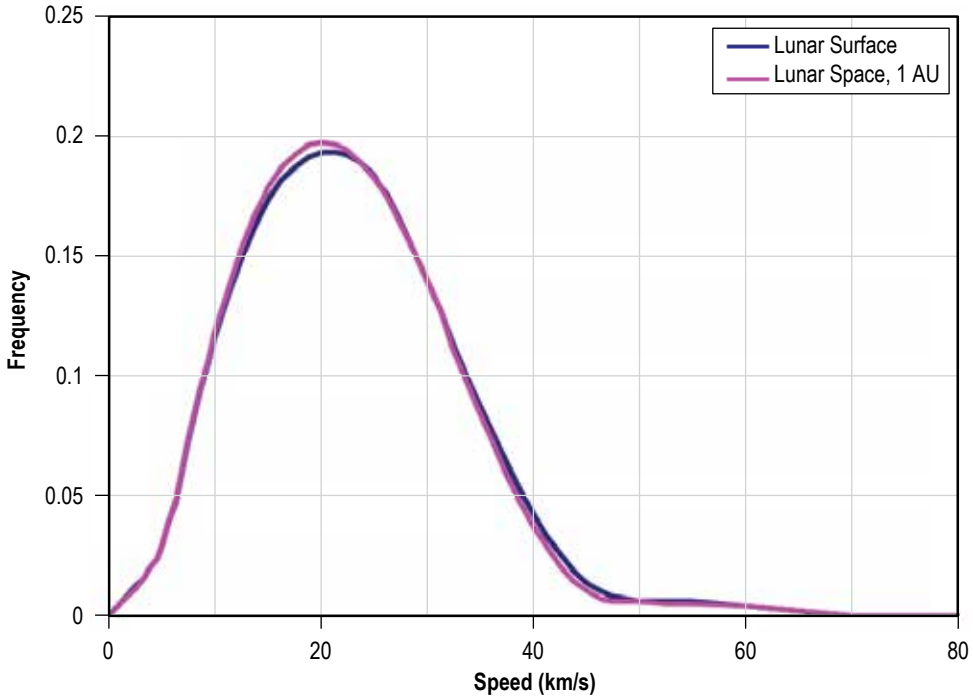

Figure 175. Comparison of meteoroid speed distributions at the lunar surface and in lunar space at 1 AU.

9.8.5 Meteor Showers

The meteor showers experienced by lunar orbiting spacecraft or surface sites are essentially the same as for Earth-orbiting spacecraft; however, the times of maxima will be offset by as much as several hours and the meteor activity could be orders of magnitude different, depending on the Moon's proximity to the meteor stream. The Moon's average distance is over 3 times greater than the width of a typical meteor stream, so it is quite possible for lunar space to experience much more activity than recorded by Earth-bound observers.

9.8.6 Lunar Secondaries

Meteoroids striking the surface produce craters, thereby generating ejecta, which comprise an additional component of the lunar meteoroid environment. The following is taken from section 3.2 of NASA SP-8013,[312] the model used in the Apollo program, which may overestimate the flux of secondaries. Work is currently proposed to refine this environment definition.

Ejecta bulk density is assumed to be 2.5 g/cm^3 and the average velocity is set to 0.1 km/s (100 m/s). With these assumptions, the average annual cumulative flux of ejecta or secondaries having masses greater than m is given by:

$$F_{\text{ejecta}} = 10^{-10.75-1.2 \log m} \quad , \tag{101}$$

where F_{ejecta} is No./m^{2}s and m is in g.

A more detailed analysis of the risk posed by the ejecta requires consideration of the cumulative flux as a function of speed. NASA SP–8013[313] gives a flux expression for each of three velocity ranges as shown in table 115.

Table 115. Cumulative ejecta flux versus velocity.

Velocity Range (km/s)	Cumulative Ejecta Flux	Adopted Ejecta Speed (km/s)
$0.1 \le V_{\text{ejecta}} < 0.1$	$F_{\text{ejecta}}=10^{-10.75-1.2 \log m}$	0.05
$0.1 \le V_{\text{ejecta}} < 0.25$	$F_{\text{ejecta}}=10^{-11.88-1.2 \log m}$	0.175
$0.25 \le V_{\text{ejecta}} < 1$	$F_{\text{ejecta}}=10^{-13.41-1.2 \log m}$	0.625

Measured: F_{ejecta} (No./m^{2}s) and m (g).

REFERENCES

1. Johnson, D.L. (ed.): "Terrestrial Environment (Climatic) Criteria Handbook for Use in Aerospace Vehicle Development 2008 Revision," NASA/TM—2008–215633, NASA Marshall Space Flight Center, AL, December 2008.

2. NASA National Space Transportation System (NSTS) 07700, Vol. X, Book 2, Rev. M: "Space Shuttle Flight and Ground System Specification," Vol. X, App. 10.10, Natural Environment Design Requirements, June 9, 1999.

3. Fichtl, G.H.; Kaufman, J.W.; and Vaughn, W.W.: "Characteristics of Atmospheric Turbulence as Related to Wind Loads on Tall Structures," *J. Spacecraft and Rockets*, Vol. 6, No. 12, pp. 1396–1403, December 1969.

4. Johnson, D.L.: "Natural Environment Data Base for the National Aerospace Plane Program," NASP-FS-FDR#072390, NASA Marshall Space Flight Center, AL, July 1990.

5. NERD Ground Winds and Low Level Wind Shear - Background and Analyses, NASA ES-42-1-93, NASA Marshall Space Flight Center, Huntsville, AL, 1993.

6. National Solar Radiation Database, 1991-2005 Update, Users Manual, National Renewable Energy Laboratory Technical Report, NREL/TP-581-41364, April 2007.

7. Geer, I.W.: *Glossary of Weather and Climate: With Related Oceanic and Hydrologic Terms,* Vol. 2, American Meteorological Society, 272 pp., 1996.

8. "Climatological Summaries: Visibilities Below 1/2 Mile and Ceilings Below 200 Feet," SRDS Report No. RD-69-22, Vol. 2, National Weather Records Center, Asheville, NC, June 1969.

9. NASA Kennedy Space Center, KSC Online: Weather Status Reports, <http://www-pao.ksc.nasa.gov/kscpao/status/weatstat/2005/months.htm>, January 5, 2006.

10. Wheeler, M.M.; Atchison, M.K.; Schumann, R.; et al.: "Analysis of Rapidly Developing Fog at the Kennedy Space Center, 1986-1990, Final Report," Applied Meteorology Unit/ENSCO, Inc., under contract NASA10-11844, October 29, 1993.

11. Corrosion Technology Laboratory, NASA Kennedy Space Center, <http://corrosion.ksc.nasa.gov/index.htm>.

12. Williamson, E.L.; and Dickinson, M.J.: Local Atmosphere Salt Profile, Shuttle Study Task No. 0031, <http://corrosion.ksc.nasa.gov/lasp.htm>, July 1974, June 1975, and October 1976.

13. Report on Relative Corrosivity of Atmospheres at Various Distances From the Seacoast, MTB 099-74, NASA Kennedy Space Center, <http://corrosion.ksc.nasa.gov/pubs/099-74.pdf>, January 16, 1980.

14. Woodock, A.H.: "Salt nuclei in marine air as a function of altitude and wind force," *J. Meteor.*, Vol. 10, pp. 362–371, 1953.

15. Lovett, R.F.: "Quantiatative measurement of air borne sea-salt in the North Atlantic," *Tellus*, Vol. 30, pp. 358–363, 1978.

16. Goodloe, C.C.: "Lightning Protection Guidelines for Aerospace Vehicles," NASA/TM—1999–209734, NASA Marshall Space Flight Center, AL, May 1999.

17. Boccippio, D.J.; Cummins, K.L.; Christian, H.J.; and Goodman, S.J.: "Combined Satellite- and Surface-Based Estimation of the Intracloud—Cloud-to-Ground Lightning Ratio over the Continental United States," *Mo. Wea. Rev.*, Vol. 129, pp. 108–112, January 2001.

18. Reap, R.M: "Analysis and Prediction of Lightning Strike Distributions Associated with Synoptic Map Types over Florida," *Mo. Wea. Rev.*, Vol. 122, pp. 1698–1715, August 1994.

19. Harms, D.E.; Boyd, B.F.; Lucci, R.M.; and Maier, M.W.: "Weather Systems Supporting Launch Operations at the Eastern Range," Paper 98-0744, AIAA 36th Aerospace Sciences Meeting and Exhibit, Reno, NV, January 12–15, 1998.

20. Standard for Facility Grounding and Lightning Protection, KSC-STD-E-0012E, NASA Kennedy Space Center, Titusville, FL, August 1, 2001.

21. Roeder, W.P.; Sardonia, J.E.; Jacobs, S.C.; et al.: "Lightning Launch Commit Criteria at the Eastern Range/Kennedy Space Center," Paper 99-0890, AIAA 37th Aerospace Sciences Meeting and Exhibit, Reno, NV, January 11–14, 1999.

22. Krider, E.P.; Christian, H.J.; Dye, J.E.; et al.: "Natural and Triggered Lightning Launch Commit Criteria," Paper 8.3, 12th AMS Conference on Aviation and Range Meteorology, Atlanta, GA, January 29–February 2, 2006.

23. Garner, T.; Lafosse, R.; Bellue, D.; and Priselac, E.: "Problems Associated with Identifying, Observing, and Forecasting Detached Thunderstorm Anvils for Space Shuttle Operations," *Proc. 7th Conference on Aviation, Range, and Aerospace Meteorology*, Long Beach, CA , pp. 302–306, February 2–7, 1997.

24. SAE Aerospace Recommended Practice: "Aircraft Lightning Zoning," SAE ARP5414, SAE International, December 2000.

25. SAE Aerospace Recommended Practice: "Aircraft Lightning Environment and Test Waveforms," SAE ARP5412, SAE International, December 1999.

26. Environmental Conditions and Test Procedures for Airborne Equipment, Sec. 22, Lightning Induced Transient Susceptibility, and sec. 23, Lightning Direct Effects, DO-160E, Radio Technical Commission for Aeronautics, December 20, 2005.

27. Turpin, R.: "Hurricane Havens Handbook for the North Atlantic Ocean: XXX. Port Canaveral, FL," NAVENVPREDRSCHFAC TR 82-03, Updated 1999.

28. Johnson, D.L.; and Rawlins, M.A.: "Hurricane Properties for the ER and Mid-Florida Coastal Sites," AMS Paper 6.5, 9th Conference on Aviation Range and Aerospace Meteorology, Orlando, FL, 2000.

29. Garza, A.L.: "1985-1998 North Pacific Tropical Cyclones Impacting the Southwestern United States and Northern Mexico: An Updated Climatology," NOAA Technical Memorandum, National Weather Service Western Region, WR-258, 1999.

30. Caires, S.; and Sterl, A.: "A New Nonparametric Method to Correct Model Data: Application to Significant Wave Height from the Era-40 Re-Analysis," *J. Atmos. Oceanic Tech.*, Vol. 22, pp. 443–459, 2005.

31. Caires, S.; Sterl, A.; Bidlot, J.-R.; et al.: "Intercomparison of Different Wind-Wave Reanalyses," *J. Climate*, Vol. 17, pp. 1893–1913, 2004.

32. Hsu, Y.L.; Rogers, W.E.; Kaihatu, J.M.; and Allard, R.A.: "Application of SWAN in the Mississippi Sound," *Proc. Sixth Int. Wksp. on Wave Hindcasting and Forecasting*, Monterey, CA, Meteorological Service of Canada, pp. 395–403, November 6–10, 2000.

33. Caires, S.; and Sterl, A.: "Climatology, Variability, and Extrema of Ocean Waves – The Web-Based KNMI/ERA-40 Wave Atlas," *Proc. 25th Int. Conf. on Offshore Mechanics and Arctic Engineering*, Hamburg, Germany, American Society of Mechanical Engineers, OMAE2006-92568, 2006.

34. European Centre for Medium-Range Weather Forecasts, <www.ecmwf.int>, 2013.

35. National Oceanic and Atmospheric Administration, National Data Buoy Center, <www.ndbc.noaa.gov>, 2013.

36. The Coastal Data Information Program, Integrative Oeanography Division, <http://cdip.ucsd.edu/>, 2013.

37. Demirbilek, Z.; and Vincent, L.: "Water Wave Mechanics," in: Demirbilek, Z., *Coastal Engineering Manual, Part II*, Hydrodynamics, Chapter II-1, Engineer Manual 1110-2-1100, U.S. Army Corps of Engineers, Washington, DC, 2002.

38. Schwartz, M.L. (ed.): *Encyclopedia of Coastal Science*, Springer Netherlands, 914 pp., 2005.

39. U.S. Navy Hindcast Spectral Ocean Wave Model Climatic Atlas: North Atlantic Ocean, NAVAIR 50-1C-538, Naval Oceanography Command Detachment, Asheville, NC, October 1983.

40. U.S. Navy Hindcast Spectral Ocean Wave Model Climatic Atlas: North Pacific Ocean, NAVAIR 50-1C-539, Naval Oceanography Command Detachment, Asheville, NC, March 1985.

41. Caires, S.; Sterl, A.; and Gommenginger, C.P.: "Global ocean mean wave period data: Validation and description," *J. Geophys. Res*., Vol. 110, C02003, doi:10.1029/2004JC002631, 2005.

42. Sorensen, R.M.: *Basic Wave Mechanics for Coastal and Ocean Engineers*, John Wiley & Sons, Inc., 284 pp., 1993.

43. Cote, L.J.; Davis, J.O., Markes, W.; et al.: "The directional spectrum of a wind generated sea as determined from data obtained by the Stereo Wave Observation Project," *Meteorological Papers*, New York University College of Engineering, Vol. 2, No. 6, 88 pp., 1960.

44. Reynolds, R.W.; Rayner, N.A.; Smith, T.M; et al.: "An Improved In Situ and Satellite SST Analysis for Climate," *J. Climate*, Vol. 15, pp. 1609–1625, 2002.

45. Pidwirny, M.: "Fundamentals of Physical Geography, 2nd Edition," Okanagan University College, <http://www.physicalgeography/fundamentals.net>, 2006.

46. National Oceanographic Data Center, United States Department of Commerce, <http://nodc.noaa.gov>, 2013.

47. Van Dorn, W.G.: "Source Mechanism of the Tsunami of March 27, 1964," *Proc. 9th Alaska: Coastal Eng. Conf.*, Lisbon, pp. 166–190, 1964.

48. Stein, R.S.; and Yeats, R.S.: "Hidden Earthquakes," *Scientific American*, Vol. 260, pp. 48–57, June 1989.

49. Frankel, A.D.; Peterson, M.D.; Mueller, C.S.; et al.: "Documentation for the 2002 Update of the National Seismic Hazard Maps," USGS, Open-file Report 02-420, 2002.

50. Mullineaux, D.R.: "Preliminary Map of Volcanic Hazards in the Conterminous United States," USGS, Misc. Field Inv. MF-786, scale 1:7,500,000, 1976.

51. Bolt, B.A.; Horn, W.L.; Macdonald, G.A.; and Scott., R.F.: *Geologic Hazards*, Springer-Verlag, New York, 328 pp., Chapter on evaluation of volcanic hazards, 1975.

52. Scott, T.M.: Environmental Geology Series, Orlando Sheet, Florida Geology Survey MS 85, 1978.

53. Dibblee, Jr., T.W.: *Geology of the Rogers Lake and Kramer Quadrangles, California*, *USGS Bull. 1089-B*, pp. 73–139, 1960.

54. Droste, J.B.: "Clay Minerals in the Playa Sediments of the Mojave Desert, California," California Division of Mines and Geology Special Report 69, 19 pp., 1961.

55. Mortan, D.M.: "Geologic Hazards in Southwestern San Bernardino County, California," California Division of Mines and Geology Special Report 113, 40 pp., 1976.

56. Real, C.R.; Toppozada, T.R.; and Parke, D.L.: "Earthquake Epicenter Map of California, 1900–1974," California Division of Mines and Geology, MS39, 1978.

57. Cousineau, R.D.; Crook, R., and Leeds, D.J.: "Investigation of Seismicity and Related Effects at NASA Ames-Dryden Flight Research Facility, Computer Center, Edwards, California," NASA-CR-170415, November 1985.

58. Stassinopoulos, E.G.: "Microelectronics for the Natural Radiation Environments of Space, Chapter I: Radiation Environments Of Space," *Proc. 1990 IEEE NSREC Short Course*, Reno, NV, July 16, 1990.

59. Barth, J.L.: "Applying Computer Simulation Tools to Radiation Effects Problems, Section Ii: Modeling Space Radiation Environments," *Proc. 1997 IEEE NSREC Short Course*, Snowmass Village, CO, July 21, 1997.

60. Normand, E.; and Baker, T.J.: "Altitude and latitude variations in avionics SEU and atmospheric neutron flux," *IEEE Trans. Nucl. Sci.*, Vol. 40, No. 6, pp. 1484–1490, December 1993.

61. Gordon, M.S.; Goldhagen, P.; Rodbell, K.P.; et al.: "Measurement of the flux and energy spectrum of cosmic-ray induced neutrons on the ground," *IEEE Trans. Nucl. Sci.*, Vol. 51, No. 6, pp. 3427–3434, December 2004.

62. Measurement and Reporting of Alpha Particle and Terrestrial Cosmic Ray-Induced Soft Errors in Semiconductor Devices, JEDEC Standard JESD89A, Electronic Industries Alliance, October 2006.

63. Bieber, J.W.; Clem, J.; Evenson, P.; et al.: "Largest GLE in Half a Century: Neutron Monitor Observations of the January 20, 2005 Event," *Proc. 29th International Cosmic Ray Conference*, Vol. 1, pp. 237–240, 2005.

64. Messenger, G.C.; and Ash, M.S.: *The Effects of Radiation on Electronic Systems*, 2nd ed., Springer, May 14, 1992.

65. Edwards, R.; Dyer, C.; and Normand, E.: "Technical standard for atmospheric radiation single event effects (SEE) on avionics electronics," *Proc. 2004 IEEE Radiation Effects Data Workshop,* Atlanta, GA, July 22, 2004.

66. Merceret, F.J.: "Rapid Temporal Changes of Midtropospheric Winds," *J. Appl. Meteor.*, Vol. 36, No. 11, pp. 1567–1575, doi: http://dx.doi.org/10.1175/1520-0450(1997)036<1567:RTCOMW>2.0.CO;2, 1997.

67. Merceret, F.J.: "The Coherence Time of Midtropospheric Wind Features as a Function of Vertical Scale from 300 m to 2 km," *J. Appl. Meteor.*, Vol. 39, pp. 2409–2420, 2004.

68. Smith, O.E.; and Austin, L.: "Space Shuttle Response to Ascent Wind Profiles," *J. Guid. Contr. Dynam.*, Vol. 6, No. 5, pp. 355–360, Sept.–Oct. 1983.

69. Adelfang, S.I.; Smith, O.E.; and Batts, G.W.: "Ascent Wind Model for Launch Vehicle Design," *J. Spacecraft Rock.*, Vol. 31, No. 3, pp. 502–508, May–June 1994.

70. Barbré, Jr., R.E.: "Characteristics of the Spliced KSC Doppler Radar Wind Profiler Database," Jacobs ESSSA Group, ESSSA-FY13-1935, November 2013.

71. Leslie, F.W.; and Justus, C.G.: "The NASA Marshall Space Flight Center Earth Global Reference Atmospheric Model—2010 Version," NASA/TM—2011–216467, 132 pp., June 2011.

72. Malcher, J.; and Kraus, H.: "Low-level Jet Phenomena Described by an Integrated Dynamic Planetary Boundary Layer (PBL) Model," *Boundary-Layer Meteor.*, Vol. 27, pp. 327–343, 1983.

73. Leahy, F.B.: "Discrete Gust Model for Launch Vehicle Assessments," American Meteorological Society, 13th Conference on Aviation, Range, and Aerospace Meteorology, New Orleans, LA, March 2008.

74. Flying Qualities of Piloted Aircraft, MIL-STD-1797A, August 24, 2004.

75. Chalk, C.R.; Neal, T.P.; Harris, T.M.; et al.: "Background Information and User Guide for MIL-F-8785B(ASG), Military Specification - Flying Qualities of Piloted Airplanes," AFFDL-TR-69-72, August 1969.

76. Adelfang, S.I.; and Smith, O.E.: "Wind Gust for Shuttle Ascent, Part II," White Paper prepared for Electromagnetics and Aerospace Environments Branch (EL23) in support of Shuttle Systems Integration Office, March 25, 1997.

77. Johnson, D.L.: "Wind Gust Procedure for Shuttle Ascent," NASA Marshall Space Flight Center Memorandum EL23 (13-97), March 25, 1997.

78. Justus, C.G.; Campbell, W.C.; Doubleday, M.K.; and Johnson, D.L.: "New Atmosphere Turbulence Model for Shuttle Applications," NASA TM-4168, NASA Marshall Space Flight Center, AL, 52 pp., January 1990.

79. Range Reference Atmosphere 0–70 km Altitude, RCC Document 361-83, Meteorology Group Range Commanders Council, Cape Canaveral, FL, February 1983.

80. Adelfang, S.I.; and Smith, O.E.: "Gust Models for Launch Vehicle Ascent," AIAA Paper 98-0747, 36th Aerospace Sciences Meeting, Reno, NV, January 1998.

81. Edwards AFB, California, Range Reference Atmosphere 0- to 70-km Altitude, RCC Document 366-83, Meteorology Group Range Commanders Council, Defense Technical Information Center, 209 pp., 1983.

82. Anderson, G.P.; Chetwynd, J.H.; Clough, S.A.; et al.: "AFGL Atmospheric Constituent Profiles (0-120 km)," AFGL-TR-86-0110, Environmental Research Papers, No. 954, AFGL, Hanscom Air Force Base, MA, May 15, 1986.

83. Smith, M.A.H.: "Compilation of Atmospheric Gas Concentration Profiles from 0 to 50 km," NASA TM-83289, NASA Langley Research Center, March 1982.

84. Kent, G.S.; and Yues, G.K.: "The Modeling of CO_2 Lidar Backscatter from Stratospheric Aerosols," *J. Geophys. Res.*, Vol. 96, No. D3, pp. 5279–5292, 1991.

85. Ziegler, J.F.; Biersack, J.P.; and Ziegler, M.D.: *SRIM, The Stopping and Range of Ions in Matter*, Lulu Press Co., Morrisville, NC, 683 pp., January 1, 2008.

86. Marshall, P.W.; and Marshall, C.J.: "Proton Effects and Test Issues for Satellite Designers," *Proc. 1999 IEEE NSREC Short Course*, Sec. 3, 1999 IEEE Radiation Effects Data Workshop, Norfolk, VA, July 12–16, 1999.

87. Peterson, E.L.: "The SEU Figure of Merit and Proton Upset Rate Calculations," *IEEE Trans.Nucl. Sci.*, Vol. 45, No. 6, p. 2550, December 1998.

88. Peterson, E.L.: "Single-Event Analysis and Prediction," *Proc. 1997 IEEE NSREC Short Course Notes*, Snowmass Village, CO, July 1997.

89. Weller, R.A.; Reed, R.A.; Warren, K.M.; et al.: "General Framework for Single Event Effects Rate Prediction in Microelectronics," *IEEE Trans. Nucl. Sci.*, Vol. 56, No. 6, pp. 3098–3108, December 2009.

90. Pellish, J.A.: "Single-Event and Total Dose Testing for Advanced Electronics," *Proc. 2012 IEEE NSREC Short Course Notes*, Norfolk, VA, July 2012.DC, 1985.

91. Owens, J.K.; Niehuss, K.O.; Vaughan, W.W.; and Shea, M.A.: "NASA Marshall Engineering Thermosphere Model - 1999 Version (MET-99) and Implications for Satellite Lifetime Predictions," *Adv. Space Res.*, Vol. 26, No. 1, pp. 157–162, 2000.

92. Johnson, D.L.; and Smith, R.E.: "The 1985 MSFC/J70 Orbital Atmosphere Model and Data Bases for the MSFC Solar Activity Prediction Technique," NASA TM-86522, Washington, DC, 1985.

93. Hickey, M.P.: "The NASA Marshall Engineering Thermosphere Model," NASA CR-179359, Washington, DC, 1988.

94. Hickey, M.P.: "An Improvement in the Integration Procedure Used in the NASA Marshall Engineering Thermosphere Model," NASA CR-179389, Washington, DC, 1988.

95. Smith, R.E.: "The Marshall Engineering Thermosphere (MET) Model: Technical Description," NASA/CR—1998–207946/VOL1, NASA NASA Marshall Space Flight Center, AL, 1998.

96. Owens, J.K.: "NASA Marshall Engineering Thermosphere Model - Version 2.0," NASA/TM—2002–211786, NASA NASA Marshall Space Flight Center, AL, 2002.

97. Jacchia, L.G.: "New Static Models of the Thermosphere and Exosphere with Empirical Temperature Profiles," Smithsonian Astrophysical Observatory Special Report No. 313, Smithsonian Institution, Astrophysical Observatory, May 6, 1970.

98. Jacchia, L.G.: "Revised Static Models of the Thermosphere and Exosphere with Empirical Temperature Profiles," Smithsonian Astrophysical Observatory Special Report No. 332, Smithsonian Institution, Astrophysical Observatory, 1971.

99. Hedin, A.E.: "Extension of the MSIS Thermospheric Model into the Middle and Lower Atmosphere," *J. Geophys. Res.*, Vol. 96, p. 1159, 1991.

100. U.S. Standard Atmosphere, 1976 (NOAA Document S/T 76-1562), COESA, compiler; NOAA/NASA/U.S. Air Force, collaborators, Washington, DC, 1976.

101. Hickey, M.P.; and Smith, R.E.: "Ninety-Day Solar and Geomagnetic Activity Input Files or Thermospheric Variation Simulation: Simulation Data Files/Research 2," NASA CR PHY-92R031, Contract NAS8-38333, 1992.

102. Anderson, B.J. (ed); and Smith, R.E. (compiler): "Natural Orbital Environment Guidelines for Use in Aerospace Vehicle Development," NASA Technical Memorandum 4527, NASA NASA Marshall Space Flight Center, AL, pp. 7-1 to 7-74, June 1994.

103. Justus, CG.; and Johnson, D.L.: "The NASA/MSFC Global Reference Atmospheric Model - 1999 Version (GRAM-99)," NASA/TM—1999–209630, Marshall Space Flight Center, Huntsville, AL, May 1999.

104. Boeder, P.: "Models and Methodology for Atomic Oxygen Requirements Development," ISS VEAIT Report No. 2-8FIA-HB-044-PAB, March 7, 1995.

105. Anderson, B.J.; Justus, C.G.; and Batts, G.W.: "Guidelines for the Selection of Near-Earth Thermal Environment Parameters for Spacecraft Design," NASA TM—2001–211221, NASA Marshall Space Flight Center, AL, September 2001.

106. Barkstrom, B.R.; and Smith, G.L.: "The Earth Radiation Budget Experiment: Science and Implementation," *Rev. Geophys.*, Vol. 24, No. 2, pp. 379–390, May 1986.

107. Barkstrom, B.; Harrison, E.; Smith, G.; et al.: "Earth Radiation Budget Experiment (ERBE Archives and April 1985 Results)," *Bull. Amer. Meteorol. Soc.*, Vol. 70, No. 10, pp. 1254–1262, 1989.

108. Bess, T.D.; and Smith, G.L.: "Earth Radiation Budget: Results of Outgoing Long-wave Radiation from Nimbus-7, NOAA-9, and ERBS Satellites," *J. Appl. Meteorol.*, Vol. 32, No. 5, pp. 813–824, 1993.

109. "Space Station Program Natural Environment Definition for Design," SSP 30425, NASA Space Station Program Office, Johnson Space Center, Houston, TX, February 8, 1994.

110. Anderson, B.J. (ed.); and Smith, R.E.: "Natural Orbital Environment Guidelines for Use in Aerospace Vehicle Development," *NASA TM-4527*, NASA Marshall Space Flight Center, AL, June 1994.

111. Justus, C.G.; Batts, G.W.; Anderson, B.J.; and James, B.F.: "Simple Thermal Environment Model (STEM) User's Guide," NASA/TM—2001–211222, NASA Marshall Space Flight Center, AL, October 2001.

112. Fröhlich, C.; and Brusa, R.W.: "Solar Radiation and Its Variation In Time," *Solar Phys.*, Vol. 74, pp. 209–215, 1981.

113. Fröhlich, C;. and Wehrli, C.: "Spectral Distribution of Solar Irradiance from 25000 nm to 250 nm," World Radiation Center, Davos, Switzerland, 1981.

114. ASTM E490-00a, "Standard Solar Constant and Zero Air Mass Solar Spectral Irradiance Tables," ASTM International, December 2000.

115. Rosenbauer, H.; Grunwaldt, H.; Montgomery, M.D.; et al.: "HEOS-2 Plasma Observations in the Distant Polar Magnetosphere: The Plasma Mantle," *J. Geophys. Res.*, Vol. 80, p. 2723, 1975.

116. Garrett, H.B.; and Deforest, S.E.: "An Analytical Simulation of the Geosynchronous Plasma Environment," *Planet. Space Sci.*, Vol. 27, pp. 1101–1109, 1979.

117. Robinson, R.J.; Bering, E.A.; Vondrak, R.R.; et al.: "Simultaneous Rocket and Radar Measurements of Currents in an Auroral Arc," *J. Geophys. Res.*, Vol. 86, No. A9, pp. 7703–7717, 1981.

118. Cho, M.; Saito, K.; and Hamanaga, T.: "Data Analysis of the Polar Plasma Environment for Spacecraft Charging Analysis," *Acta Astronautica*, Vol. 81, pp. 160–173, 2012.

119. Jursa, A.S. (ed.): *Handbook of Geophysics and the Space Environment*, Air Force Systems Command, U.S. Air Force, Springfield, VA, 1985.

120. Anderson, P.C.; and Koons, H.C.: "Spacecraft Charging Anomaly on a Low-Altitude Satellite in an Aurora," *J. Spacecraft Rockets*, Vol. 33, pp. 734–738, 1996.

121. Gussenhoven, M.S.; Hardy, D.A.; Rich, F.; et al.: "High-Level Spacecraft Charging in the Low-Altitude Polar Auroral Environment," *J. Geophys. Res.*, Vol. 90, pp. 11,009–11,023, 1985.

122. Snyder, D.B.; Ferguson, D.C.; Vayner, B.V.; and Galofaro, J.T.: "New Spacecraft-Charging Solar Array Failure Mechanism," *Proc. 6th Spacecraft Charging Technology Conference*, AFRL-VS-TR-20001578, pp. 297–301, September 1, 2000.

123. Kasha, M.A.: *The Ionosphere and Its Interaction with Satellites*, Gordon and Breach, New York, 156 pp., 1969.

124. Kawakita, S.; Kusawake, H.; Takahashi, M.; et al.: "Investigation of an Operational Anomaly of the ADEOS-II Satellite," JAXA-SP-05-001E, *Proc. 9th International Spacecraft Charging Technology Conference,* Tsukuba, Japan, April 4–8, 2005.

125. NASA Technical Standard, NASA-STD-4005, Low Earth Orbit Spacecraft Charging Design Standard, Washington, DC, June 3, 2007.

126. NASA-HDBK-4006, The Low Earth Orbit Spacecraft Charging Design Handbook, NASA Technical Handbook, Washington, DC, June 3, 2007.

127. Cho, M.; Ramasamy, R.; Matsumoto, T.; et al.: "Laboratory Tests on 110-Volt Solar Arrays in Simulated Geosynchronous Orbit Environment," *J. Spacecraft Rockets*, Vol. 40, No. 2, p. 211, 2003.

128. NASA-HDBK-4002, NASA Technical Handbook, Avoiding Problems Caused By Spacecraft On-Orbit Internal Charging Effects, February 17, 1999.

129. Purvis, C.K.; Garrett, H.B.; Whittlesey, A.C.; and Stevens, N.J.: "Design Guidelines for Assessing and Controlling Spacecraft Charging Effects," NASA Technical Paper 2361, NASA Lewis Research Center, Cleveland, OH, 1984.

130. DeForest, S.E.: "Spacecraft Charging at Synchronous Orbit," *J. Geophys. Res.,* Vol. 77, pp. 3587–3611, 1972.

131. Garrett, H.B.: "The Charging of Spacecraft Surfaces," *Rev. Geophys.*, Vol. 19, pp. 577–616, 1981.

132. Garrett, H.B.; and Spitale, G.C.: "Magnetospheric Plasma Modeling (0-100 keV)," *J. Spacecraft Rockets*, Vol. 22, pp. 231–234, 1985.

133. Garrett, H.B.; and Pike, C.P. (eds.): "Space Systems and Their Interactions with Earth's Space Environment," in *Progress in Astronautics and Aeronautics*, Vol. 71, AIAA, New York, 1980.

134. Tribble, A.C.: *The Space Environment*, Princeton University Press, 1995.

135. Schunk, R.W. (ed.): *Solar-Terrestrial Energy Program: Handbook of Ionospheric Models*, Scientific Committee on Solar and Terrestrial Physics (COSTEP), Center for Atmospheric and Space Sciences, 295 pp., August 1996.

136. Bilitza, D. (ed.): "International Reference Ionosphere 1990," National Space Science Data Center 90-22, Greenbelt, MD, 1990.

137. Ma, T.P.; and Dressendorfer, P.V.: *Ionizing Radiation Effects in MOS Devices and Circuits*, Wiley-Interscience, New York, NY, 608 pp., 1989.

138. Oldham, T.R.: "Total Ionizing Dose Effects in MOS Oxides and Devices," *IEEE Trans. Nucl. Sci.*, Vol. 50, No. 3, pp. 483–499, June 2003.

139. Fleetwood, D.M.: "Total Ionizing Dose Effects in MOS and Low-Dose-Rate-Sensitive Linear-Bipolar Devices," *IEEE Trans. Nucl. Sci.*, Vol. 60, No. 3, pp. 1706–1730, June 2013.

140. Fleetwood, D.M.; and Eisen, H.A.: "Total-Dose Radiation Hardness Assurance," *IEEE Trans. Nucl. Sci.*, Vol. 50, No. 3, pp. 483–489, June 2003.

141. Drumm, C.R.; Roeske, S.B.; and Scrivner, G.J.: "Shielding considerations for satellite microelectronics," *IEEE Trans. Nucl. Sci.*, Vol. 43, No. 6, pp. 2790–2796, December 1996.

142. Marshall, P.W.; and Marshall, C.J.: "Proton Effects and Test Issues for Satellite Designers," Sec. IV, *1999 IEEE NSREC Short Course*, July 1999.

143. Taylor, A.D.; and McBride, N.: "A Radiant-Resolved Meteoroid Model," Second European Conference on Space Debris, ESA SP-393, pp. 375–380, 1997.

144. Jones, J.; and Brown, P.: "The Radiant Distribution of Sporadic Meteors," *Planet Space Science*, Vol. 42, No. 2, pp. 123–126, 1994.

145. Campbell-Brown, M.D.; and Jones, J.: "Annual Variation of Sporadic Radar Meteor Rates," *Mon. Not. R. Astron. Soc.,* Vol. 367, No. 2, pp. 709–716, 2006.

146. "Meteoroid Damage Assessment, NASA Space Vehicle Design Criteria (Structures)" NASA/SP-8042, Washington, DC, 50 pp., May 1970.

147. Matney, M.J.; and Stansbery, E.: "What Are Radar Observations Telling Us About the Low-Earth Orbital Debris Environment," *Proc. Third European Conference on Space Debris*, ESA–SP 473, Huguette Sawaya-Lacoste (ed.), Darmstadt, Germany, Vol. 1., pp. 43–48, March 19–21, 2001.

148. Brown, P.; and Jones, J.: "A Determination of the Strengths of the Sporadic Radio-Meteor Sources," *Earth, Moon and Planets*, Vol. 68, pp. 223–245, 1995.

149. Elford, G.W.; and Hawkins, G.S.: "Meteor Echo Rates and the Flux of Sporadic Meteors," *Harvard Radio Meteor Project NASA Research Rep.*, No. 9, 30 pp., 1964.

150. McNamara, H.; Suggs, R.; Kauffman, B.; et al.: "Meteoroid Engineering Model (MEM): A Meteoroid Model for the Inner Solar System," J.M. Trigo-Rodrâiguez (ed.), *Earth, Moon and Planets*, Vol. 95, Nos. 1–4, 2004.

151. "NASA Engineering Safety Committee review for the BUMPER II code," NASA doc ID RP-05-66, Johnson Space Center, Houston, TX, February 8, 1994.

152. Liou, J.C.; Matney, M.J.; Anz-Meador, P.D.; et al.: "The New NASA Orbital Debris Engineering Model ORDEM2000," NASA/TP—2002–210780, Johnson Space Center, Houston, TX, May 2002

153. Peterson, G.E.: *Dynamics of Meteor Outbursts and Satellite Mitigation Strategies*, The Aerospace Press, Reston, VA, 216 pp., 1999.

154. Divine, N.: "Meteoroid Focusing at a Planet," Jet Propulsion Laboratory Interoffice Memorandum 5217-92-86, 1992.

155. Jones, J.; and Poole, L.M.G.: "Gravitational Focusing and shielding of meteoroid streams," *Mon. Not. R. Astron. Soc*., Vol. 375, pp. 925–930, 2007.

156. Drew, K.; Brown, P.G.; Close, S.; and Durand, D.: "Meteoroid Bulk Density Determination Using RADAR Head Echo Observations," *Earth, Moon, and Planets*, Vol. 95, pp. 639–645, 2004.

157. Suggs, R.M.; Cooke, W.; Brown, P.; et al.: "Meteor Properties Database - Final Report," *NASA SEE/TP-2004-400*, August 2004.

158. Orbital Debris Engineering Models, NASA Orbital Debris Program Office, <http://orbitaldebris.jsc.nasa.gov/model/engrmodel.html>.

159. Marsh, J.G.; Lerch, F.J.; Putney, B.H.; et al.: "The GEM-T2 gravitational model," *J. Geophys. Res.*, Vol. 95, pp. 22,043–22,071, 1990.

160. Tapley, B.; Ries, J.; Bettadpur, S.; et al.: "GGM02 - An Improved Earth Gravity Field Model from GRACE," *J. Geodesy*, doi 10.1007/s00190-005-0480-z, 2005.

161. Tsyganenko, N.A.: "Modeling the Earth's Magnetospheric Magnetic Field Confined Within a Realistic Magnetopause," *J. Geophys.Res.*, Vol. 100, pp. 5599–5612, 1995.

162. Tsyganenko, N.A.; and Stern, D.P.: "Modeling the Global Magnetic Field of the Large-Scale Birkeland Current Systems," *J. Geophys.Res.*, Vol. 101, pp. 27,187–27,198, 1996.

163. Herr, J.L.; James, B.F.; and Hwang, K.S.: "Plasma Definition for High Altitude Orbits as Required for Spacecraft Charging Analyses," AIAA 95-0368, 33rd Aerospace Sciences Meeting and Exhibit, Reno, NV, January 9–12, 1995.

164. Hwang, K.S.: "Review of Spacecraft Charging Design Guidelines," An Interim Report to Electromagnetics and Aerospace Environments Branch, EL23, Systems Analysis and Integration Laboratory, NASA Marshall Space Flight Center, AL, July 1995.

165. Chappell, C.R.; Harris, K.K.; and Sharp, G.W.: "A Study of the Influence of Magnetic Activity on the Location of the Plasmapause as Measured by OGO 5," *J. Geophys. Res.*, Vol. 75, p. 50, 1970.

166. Garrett, H.B.; and Gauntt, D.M.: "Spacecraft Charging During Eclipse Passage," in *Space Systems and Their Interactions with Earth's Space Environment, Progress in Astronautics and Aeronautics*, Vol. 71, pp. 227–251, American Institute of Aeronautics and Astronautics, New York, 1980.

167. Hastings, D.; and Garrett, H.: *Spacecraft-Environment Interactions*, Cambridge University Press, Cambridge, UK, 1996.

168. Technical Report on Space Debris, Scientific and Technical Subcommittee of the United Nations Committee on the Peaceful uses of Outer Space, United Nations, NY, A/AC. 105/720, ISBN 92-1-100813-1, 1999.

169. Stern, S.A.: "The Lunar Atmosphere: History, Status, Current Problems, and Context," *Rev. Geophys.*, Vol. 37, pp. 453–491, 1999.

170. Hunten, D.S.; and Sprague, A.L.: "Origin and Character of the Lunar and Mercurian Atmospheres," *Adv. Space Res.*, Vol. 19, pp. 1551–1560, 1997.

171. Potter, A.E.; Killen, R.M.; and Morgan, T.H.: "Variation of Lunar Sodium During Passage of the Moon Through the Earth's Magnetotail," *J. Geophys. Res.*, Vol. 105, pp. 15,073–15,084, 2000.

172. Hunten, D.M.; Cremonese, G.; Sprague, A.L.; et al.: "The Leonid Meteor Shower and the Lunar Sodium Atmosphere," *Icarus*, Vol. 136, pp. 298–303, 1998.

173. Verani, S.; Barbieri, C.; Benn, C.; and Cremonese, G.: "Possible Detection of Meteor Stream Effects on the Lunar Sodium Atmosphere," *Planet. Space Sci.*, Vol. 46, pp. 1003–1006, 1998.

174. Smith, S.M.; Wilson, J.K.; Baumgardner, J.; and Mendillo, M.: "Discovery of the Distant Lunar Sodium Tail and its Enhancement Following the Leonid Meteor Shower of 1998," *Geophys. Res., Lett.*, Vol. 26, pp. 1649–1652, 1999.

175. Stern, S.A.; Parker, J.W.; Morgan, T. H.; et al.: "A Hubble Space Telescope (HST) Search for Magnesium in the Lunar Atmosphere," *Icarus*, Vol. 127, pp. 523–526, 1997.

176. Flynn, B.C.; and Stern, S.A.: "A Spectroscopic Survey of Metallic Species Abundances in the Lunar Atmosphere," *Icarus*, Vol. 124, pp. 530–536, 1996.

177. Neugebauer, M.; Snyder, C.W.; Clay, D.R.; and Goldstein, B.E.: "Solar Wind Observations on the Lunar Surface With the Apollo-12 ALSEP," *Planet. Space Sci.*, Vol. 20, pp. 1577–1591, 1972.

178. Johnson, J.R.; Swindle, T.D.; and Lucey, P.G.: "Estimated Solar-Wind Implanted Helium-3 on the Moon," *Geophys. Res. Lett.*, Vol. 26, pp. 385–388, 1999.

179. Feldman W.C.; Asbridge, J.R.; Bame, S.J.; and Gosling, J.T.: *Plasma and Magnetic Fields from the Sun, in The Solar Output and its Variation*, O.R. White (ed.), Colorado Associated University Press, Boulder, 1977.

180. Halekas, J.S.; Mitchell, D.L.; Lin, R.P.; et al.: "Evidence for Negative Charging of the Lunar Surface in Shadow," *Geophys. Res. Lett.*, Vol. 29, No. 10, pp. 77-1–77-4, 2002.

181. Lindeman, R.; Freeman, J.W.; and Vondrak, R.R.: "Ions From the Lunar Atmosphere," *Proc. 4th Lunar Science Conf.*, March 21–22, 1973, League City, TX, pp. 2889–2896, 1973.

182. Halekas, J.S.; Lin, R.P.; and Mitchell, D.L.: "Large Negative Lunar Surface Potentials in Sunlight and Shadow," *Geophys. Res. Lett.*, Vol. 32, No. 9, doi: 10.1029/2005GL022627, 2005.

183. Minow, J.I.; Blackwell, W.C.; Neergaard, L.F.; et al.: "Charged Particle Environment Definition for Next Generation Space Telescope (NGST): L2 Plasma Environment Statistics," *UV, Optical, and IR Space Telescopes and Instruments VI*, J.B. Breckinridge and P. Jakobsen (eds.), *Proc. SPIE*, Astronomical Telescopes and Instrumentation 2000, March 27–31, 2000, Munich, Germany, pp. 942–953, 2000.

184. Dollfus, A.; and Bowell, E.: "Polarimetric Properties of the Lunar Surface and its Interpretation, Part I. Telescopic Observations," *Astron. & Astrophys.*, Vol. 10, pp. 29–53, 1971.

185. Lawson, S.L.; Jakosky, B.M.; Park, H.-S.; and Mellon, M.T.: "Brightness Temperatures of the Lunar Surface: Calibration and Global Analysis of the Clementine Long-Wave Infrared Camera Data," *J. Geophys. Res.*, Vol. 105, No. E2, pp. 4273–4290, 2000.

186. Howe, Jr., H.C.; and Biinsack, J.H.: "Explorer 33 and 35 Plasma Observations of Magnetosheath Flow," *J. Geophys. Res.*, Vol. 77, pp. 3334–3344, 1972.

187. Bennett, L.; Kivelson, M.G.; Khurana, K.K.; et al.: "A Model of the Earth's Distant Bow Shock," *J. Geophys. Res.*, Vol. 102, pp. 26,927–26,941, 1997.

188. Feldman W.C.; Asbridge, J.R.; Bame, S.J.; and Gosling, J.T.: "Plasma and Magnetic Fields from the Sun," *The Solar Output and its Variation,* O.R. White (ed.), Colorado Associated University Press, Boulder, 1977.

189. Minow, J.I.; Blackwell, W.C.; Neergaard, L.F.; et al.: "Charged Particle Environment Definition for NGST: L2 Plasma Environment Statistics," *Proc. SPIE*, Vol. 13, pp. 942–953, UV, Optical, and IR Space Telescopes and Instruments VI, J.B. Breckinridge and P. Jakobsen (eds.), 2000.

190. Lyon, E.F.; Bridge, H.S.; and Binsack, J.H.: "Explorer 35 Plasma Measurements in the Vicinity of the Moon," *J. Geophys. Res.*, Vol. 72, pp. 6113–6117, 1967.

191. Al'pert, Ja.L.: "Effects Due to Artificial Earth Satellite in Rapid Motion Through the Ionosphere of the Planetary Medium," *Space Sci. Rev.*, Vol. 2, pp. 680–748, 1963.

192. Ogilvie, K.W.; Steinberg, J.T.; Fitzenreiter, R.J.; et al.: "Observations of the Lunar Plasma Wake From the WIND Spacecraft on December 27, 1994," *Geophys. Res. Lett.*, Vol. 23, pp. 1255–1258, 1996.

193. Kellogg, P.J.; Goetz, K.; and Monson. S.J.: "Observations of Plasma Waves During a Traversal of the Moon's Wake," *Geophys. Res. Lett.*, Vol. 23, pp. 1267–1270, 1996.

194. Farrell, W.M.; Fitzenreiter, R.J.; Owen, C.J.; et al.: "Upstream ULF Waves and Energetic Electrons Associated With the Lunar Wake: Detection of Precursor Activity," *Geophys. Res. Lett.*, Vol. 23, No. 10, pp. 1271–1274, 1996.

195. Bale, S.D.; Owen, C.J.; Bougeret, J.-L.; et al.: "Evidence of Currents and Unstable Particle Distributions in an Extended Region Around the Lunar Plasma Wake," *Geophys. Res. Lett.*, Vol. 24, No. 11, pp. 1427–1430, 1997.

196. Bosqued, J.M.; Lormant, N;, Rème, H.; et al.: "Moon-Solar Wind Interaction: First Results From the WIND/3DP Experiment," *Geophys. Res. Lett.*, Vol. 23, No. 10, pp. 1259–1262, 1996.

197. Birch, P.C.; and Chapman, S.C.: "Particle-in-Cell Simulation of the Lunar Wake With High Phase Space Resolution," *Geophys. Res. Lett.*, Vol. 28, No. 2, pp. 219–222, 2001.

198. Ness, N.F.; Behannon, B.W.; Scearce, C.S.; and Cantarano, S.C.: "Early Results From the Magnetic Field Experiment on Lunar Explorer 35," *J. Geophys. Res.*, Vol. 72, pp. 5769–5778, 1967.

199. Trávnícek, P.; Hellinger, P.; Schriver, D.; and Bale, S.D.: "Structure of the Lunar Wake: Two-Dimensional Global Hybrid Simulations," *Geophys. Res. Lett.*, Vol. 32, L06102, doi:10.1029/2004GL022243, 2005.

200. Futaana, Y.; Machida, S.; Saito, Y.; et al.: "Plasma Environment in the Vicinity of the Lunar Wake," *Geophys. Res. Abstracts*, Vol. 5, 09580, European Geophysical Society, 2003.

201. Birch, P.C.; and Chapman, S.C.: "Correction to 'Particle-in-Cell Simulation of the Lunar Wake With High Phase Space Resolution,'" *Geophys. Res. Lett.*, Vol. 28, No. 13, p. 2669, 2001.

202. Clack, D.; Kasper, J.C.; Lazarus, A.J.; et al.: "Wind Observations of Extreme Ion Temperature Anisotropies in the Lunar Wake," *Geophys. Res. Lett.*, Vol. 31, No. 6, CiteID L06812 2004.

203. Halekas, J.S.; Bale, S.D.; Mitchell, D.L.; and Lin, R.P.: "Electrons and Magnetic Fields in the Lunar Wake," *J. Geophys. Res.*, Vol. 110, A07222, doi: 10.1029/2004JA010991, July 2005.

204. Samir, U.; Wright, Jr., K.H.; and Stone, N.H.: "The Expansion of a Plasma Into A Vacuum: Basic Phenomena and Processes and Applications to Space Plasma Physics," *Rev. Geophys. Space Phys.*, Vol. 21, No. 7, pp. 1631–1646, doi: 10.1029/RG021i007p01631, August 1983.

205. Farrell, W.M.; Kaiser, M.L.; Steinberg, J.T.; and Bale, D.: "A Simple Simulation of a Plasma Void: Applications to Wind Observations of the Lunar Wake," *J. Geophys. Res.*, Vol. 103, pp. 23,653, 1998.

206. <https://pds-geosciences.wustl.edu/geodata/lp-l-rss-5-gravity-v1/lp_1001/sha/>, PDS Geosciences Node, Washington Earth and Planetary Remote Sensing Laboratory, University in St. Louis, MO, February 2, 2005.

207. Carranza, E.; Konopliv, A.; and Ryne, M.: "Lunar Prospector Orbit Determination Uncertainties Using the High Resolution Lunar Gravity Models," Paper AAS 99-325, American Astronomical Society (AAS)/American Institute of Aeronautics and Astronautics (AIAA) Astrodynamics Specialists Conference, Girdwood, AK, August 16–19, 1999.

208. NASA Eclipse Web Site, Lunar Eclipse Page, <http://eclipse.gsfc.nasa.gov/lunar.html>, July 8, 2013.

209. Mallama, A.: *Eclipses, Atmospheres and Global Change*, Appendix A, 1996.

210. Apollo 12 Preliminary Science Report, NASA SP-235, NASA Johnson Space Center, Houston, TX, 1970.

211. Pike, R.J.: "Apparent depth/diameter relations for lunar craters," *Proc. 8th Lunar Sci. Conf.*, Houston, TX, March 14–18, 1977, Vol. 3, pp. 3427–2436, Pergamon Press, New York, 1977.

212. Cintala, M.J.; and McBride, K.M.: "Block distributions of the lunar surface: A comparison between measurements obtained from surface and orbital photography," NASA Technical Memorandum 104804, Washington, DC, 41 pp., 1995.

213. Bart, G.D.; and Melosh, H.J.: "Using lunar boulders to distinguish primary from distant secondary impact craters," *Geophys. Res. Lett.*, Vol. 34, L07203, 2007.

214. Bart, G.; and Melosh, H.J.: "Distribution of boulders ejected from lunar craters," *Icarus*, Vol. 209, pp. 337–357, 2010.

215. Cameron, W.S.; and Coyle, G.: "An analysis of the distribution of boulders in the vicinity of small lunar craters," *The Moon*, Vol. 3, pp. 159–188, 1971.

216. Apollo 16 Preliminary Science Report, NASA SP-315, NASA Johnson Space Center, Houston, TX, 1972.

217. Robinson, M.S.; Brylow, S.M.; Tschimmel, M.; et al.: "Lunar Reconnaissance Orbiter Camera (LROC) Instrument Overview," *Space Sci. Rev.*, Vol. 150, pp. 81–124. doi 10.1007/s111214-010-9634-2, 2010.

218. Taylor, L.A.; and Meek, T.T.: "Microwave Processing of the Lunar Soil," *Proc. Int'l Lunar Conf.,* Int'l Lunar Explor. Wrk. Grp. 5, Amer. Astr. Society, Vol. 108, pp. 109–123, 2004.

219. *Lunar Sourcebook: A User's Guide to the Moon,* G.H. Heiken, D.T. Vaniman, and B.M. French (eds.), Cambridge University Press, p. 150, 1991.

220. Grove, D.E.: *Platinum Metal Rev.,* Vol. 47, No. 1, p. 44, 2003.

221. Toutanji, H.; Glenn-Loper, B.; and Schrayshuen, B.: "Strength and Durability Performance of Waterless Lunar Concrete," AIAA 2005-1436, *Proc. 43rd American Institute of Aeronautics and Astronautics*, 43rd AIAA Aerospace Sciences Meeting and Exhibit, Reno, NV, January 10–13, 2005.

222. Fubini, B.; Giamello, E.; Volante, M.; and Bolis, V.: "Chemical Functionalities at the Silica Surface Determining its Reactivity When Inhaled. Formation and Reactivity of Surface Radicals," *Toxicol. Ind. Health*, Vol. 6, No. 6, pp. 571–598, December 1990.

223. Wilson, J.W.; Townsend, L.W.; Schimmerling, W.; et al.: "Transport Methods and Interactions for Space Radiations," NASA RP-1257, Washington, DC, December 1991.

224. Apollo 11 Mission Report, NASA MSC-00171, Manned Spacecraft Center, Houston, TX, p. 12-7, November 1969.

225. Hurowitz, J.A.; Tosca, N.J.; McLennan, S.M.; and Schoonen, M.A.A.: "Production of Hydrogen Peroxide in Martian and Lunar Soils," *Earth and Planetary Letters,* Vol. 255, Nos. 1 and 2, pp. 41–52, 2007.

226. Helsley, C.E.: "Magnetic Properties of Lunar Dust and Rock Samples," *Science*, Vol. 167, pp. 693–695, 1970.

227. Stacey, F.D.; Lovering, J.F.; and Parry, L.G.: "Thermomagnetic properties, natural magnetic moments, and magnetic anisotropies of some chondritic meteorites," *J. Geophy. Res.*, Vol. 66, No. 5, pp. 1523–1534, May 1961.

228. Carrier III, W.D.: "The Four Things You Need to Know About the Geotechnical Properties of Lunar Soil," Lunar Geotechnical Institute, Lakeland, FL, September, 2005.

229. Colwell, J.E.; Batiste, S.; Horanyi, M.; et al.: "Lunar Surface: Dust Dynamics and Regolith Mechanics," *Rev. Geophys.*, Vol. 45, No. 2, doi: 10.1029/2005RG000184, 2007.

230. Fenner, M.A.; Freeman, Jr., J.W.; and Hills, H.K.: "The Electric Potential of the Lunar Surface," *Proc. 4th Lunar Sci. Conf.* (Supplement 4, *Geochemica et Cosmochimica Acta*), Vol. 3, pp. 2877–2887, 1973.

231. Freeman, J.W.; and Ibrahim, M.: "Lunar Electric Fields, Surface Potential and Associated Plasma Sheaths," *The Moon*, Vol. 14, pp. 103–114, September 1975.

232. Freeman, Jr., J.W.; Fenner, M.A.; and Hills, H.K.: "The Electric Potential of the Moon in the Solar Wind," in *Photon and Particle Interactions With Surfaces in Space*," R.J.L. Grard (ed.), *Proc. 6th ESLAB Symposium*, Noordwijk, The Netherlands, D. Reidel Publishing, pp. 363–368, 1973.

233. Goertz, C.K.: "Dusty Plasmas in the Solar System," *Rev. Geophys.*, Vol. 27, pp. 271–292, doi: 10.1029/RG027i002p00271, 1989.

234. Park, J.S.; Liu, Y.; Kihm, K.D.; and Taylor, L.A.: "Micro-morphology and Toxicological Effects of Lunar Dust," *Lunar and Planetary Science XXXVII (2006)*, 2193.pdf, 2006.

235. Reasoner, D.L.; and Burke, W.L.: "Direct Observation of the Lunar Photoelectron Layer," *Proc. 3rd Lunar Science Conference* (Supplement 3, *Geochimica et Cosmochimica Acta*), Vol. 3, pp. 2639–2654, 1972.

236. Reasoner, D.L.; and Burke, W.L.: "Measurement of the Lunar Photoelectron Layer in the Geomagnetic Tail; in Photon and Particle Interactions with Surfaces in Space," R.J.L. Grard (ed.), *Proc. 6th ESLAB Symposium*, Noordwijk, The Netherlands, September 26–29, 1972, D. Reidel Publishing, pp. 369–387, 1973.

237. Wang, X.; Horányi, M.; Sternovsky, Z.; et al.: "A Laboratory Model of the Lunar Surface Potential Near Boundaries Between Sunlit and Shadowed Regions," *Geophys. Res. Lett.,* Vol. 34, No. 16, L16104, doi:10.1029/2007GL030766, 2007.

238. Whipple, E.C.: "Potentials of Surfaces in Space," *Rep. Prog. Phys.*, Vol. 44, pp. 1197–1250, 1981.

239. Siebert, M.; and Kolecki, J.: "Electrostatic Charging of the Mars Pathfinder Rover," AIAA Paper 96-0486, Toledo University, OH, doi: 10.2514/6.1996-486, 1996.

240. Leach, R.N.: "Effect of Pressure on Electrostatic Processes on Mars. Sand and Dust on Mars," NASA CP-10074, Ames Research Center, Moffett Field, CA, p. 36, 1991.

241. Ferguson, D.C.; and Hillard, G.B.: "MEEC, An MSP 2001 Rover Experiment to Measure Electrostatic Charging in the Martian Atmosphere," 31st Lunar and Planetary Science Conference, Houston, TX, March 13–17, 2000, Lunar and Planetary Science XXXI, 1848. pdf, 2000.

242. Schwerer, F.C.; Nagata, T.; and Fisher, R.M.: "Electrical Conductivity of Lunar Surface Rocks and Chondritic Meteorites," *The Moon*, Vol. 2, pp. 408–422, 1971.

243. Schwerer, F.C.; Huffman, G.P.; Fisher, R.M.; and Nagata, T: "Electrical Conductivity and Mossbauer Study of Apollo Lunar Samples," *Proc. 3rd Lunar Sci. Conf.*, pp. 3173– 3185, 1972.

244 Schwerer, F.C.; Huffman G.P.; Fisher, R.M.; and Nagata, T.: "Electrical Conductivity of Lunar Surface Rocks at Elevated Temperatures," *Proc. 4th Lunar Sci. Conf.*, pp. 3151–3166, 1973.

245. Schwerer F.C.; Huffman G.P.; Fisher, R.M.; and Nagata, T.: "Electrical Conductivity of Lunar Surface Rocks; Laboratory Measurements and Implications for Lunar Interior Temperatures," *Proc. 5th Lunar Sci. Conf.*, March 18–24, 1973, Houston, TX, pp. 2673–2687, 1974.

246. Olhoeft, G.R.: "Impulse Radar Studies of Near Surface Geological Structure," *Lunar and Planetary Science X,* pp. 943–945, Lunar and Planetary Institute, Houston, TX, 1979.

247. Olhoeft G.R.: "Applications and Limitations of Ground Penetrating Radar," *Expanded Abstracts, 54th Ann. Int. Mtg. and Expo. of the Soc. of Explor. Geophys.*, pp. 147–148, 1984.

248. Olhoeft, G.R.; and Strangway, D.W.: "Dielectric Properties of the First 100 meters of the Moon," *Earth Planet. Sci. Lett.*, Vol. 24, pp. 394–404, 1975.

249. Olhoeft, G.R.; Strangway, D.W.; and Frisillo, A.L.: "Lunar Sample Electrical Properties," *Proc. 4th Lunar Sci. Conf.*, pp. 3133–3149, 1973.

250. Olhoeft, G.R.; Strangway, D.W.; Pearce, et al.: "Electrical and Magnetic Properties of Apollo 17 Soils," *Eos Trans. AGU*, Vol. 54, p. 601, 1973.

251. Olhoeft, G.R.; Frisillo, A.L.; Strangway, D.W.; and Sharpe, H.: "Temperature Dependence of Electrical Conductivity and Lunar Temperatures," *The Moon*, Vol. 9, pp. 79–87, 1974.

252. Olhoeft, G.R.; Frisillo, A.L.; and Strangway, D.W.: "Electrical Properties of Lunar Soil Sample 15301,38," *J. Geophys. Res.*, Vol. 79, pp. 1599–1604, 1974.

253. Olhoeft, G.R.; Strangway, D.W.; and Pearce, G.W.: "Effects of Water on Electrical Properties of Lunar Fines," *Proc. 6th Lunar Sci. Conf.*, pp. 3333–3342, 1975.

254. Olhoeft G.R.; Schaefer B.,; and Johnson G.R.: "Experimental Measurements of Surface and Volume Scattering Processes at Microwave Wavelengths" (Abstract), in *Lunar and Planetary Science X*, pp. 946–948, Lunar and Planetary Institute, Houston, TX, 1979.

255. *Lunar Sourcebook: A User's Guide to the Moon*, G. H. Heiken, D. T. Vaniman, and B.M. French (eds.), Cambridge University Press, 1991.

256. Benson, J.: "Direct Measurement of the Plasma Screening Length and Surface Potential Near the Lunar Terminator," *J. Geophys. Res.*, Vol. 82, No. 13, p. 1917, 1977.

257. Berg, O.E.; Wolf, H.; and Rhee, J.: "Lunar Soil Movement Registered by the Apollo 17 Cosmic Dust Experiment," *Interplanetary Dust and Zodiacal Light*, H. Elsasser and H. Fechtig (eds.), Springer-Verlag, Berlin, 1976.

258. Birch, P.C.; and Chapman, S.C.: "Particle-in-Cell Simulations of the Lunar Wake With High Phase Space Resolution," *Geophys. Res. Lett.*, 28, p. 219, 2001.

259. Crow, J.E.; Auer, P.L.; and Allen, J.E.: "The Expansion of Plasma Into a Vacuum," *J. Plasma Phys.*, Vol. 14, p. 65, 1975.

260. Farrell, W.M.; Stubbs, T.J.; Vondrak, R.R.; et al.: "The Complex Electric Fields Near the Lunar Terminator: The Near-Surface Wake and Accelerated Dust," *Geophys. Res. Lett.*, Vol. 34, L14201, doi:10.1029/2007GL029312, 2007.

261. Farrell, W.M.; Stubbs, T.J.; Halekas, J.S.; et al.: "Loss of Solar Wind Plasma Neutrality and Affect on Surface Potentials Near the Lunar Terminator and Shadowed Polar Regions," *Geophys. Res. Lett.*, Vol. 35, Issue 5, doi:10.1029/2007GL032653, March 2008.

262. Farrell, W.M.; Stubbs, T.J.; Delory, G.T.; et al.: "Concerning the dissipation of electrically charged objects in the shadowed lunar polar regions," *Geophys. Res. Lett.*, Vol. 35, L19104, doi:10.1029/2008GL034785, 2008.

263. Halekas, J. S.; Delory, G.T.; Brain, D.A.; et al.: "Extreme Lunar Surface Charging During Solar Energetic Particle Events," *Geophys. Res. Lett*., Vol. 34, No. 2, doi: 10.1029/2006GL028517, January 2007.

264. Manka, R.H.: "Plasma and potential at the lunar surface," *Photon and Particle Interactions with Surfaces in Space*, R. J.L. Grard (ed.), Dordrecht, Holland, 1973.

265. Ogilvie, K.W., et al.: "Observations of the Lunar Plasma Wake From the WIND Spacecraft on December 27, 1994," *Geophys. Res. Lett.*, 23, p. 1255, 1996.

266. Stubbs, T.J.; Vondrak, R.R.; and Farrell, W.M.: "A Dynamic Fountain Model for Lunar Dust," *Adv. Space Res.*, Vol. 37, p. 59, 2006.

267. Berg, O.E.; Richardson, F.F.; and Burton, H.: Apollo 17 Preliminary Science Report, NASA SP-330, p. 16, 1973.

268. Feuerbacher, B.; Anderegg, M.; Fitton, B.; et al.: "Photoemission from lunar surface fines and the lunar photoelectron sheath," *Proc. 3rd Lunar Science Conference,* (*Geochim. Cosmochim. Acta* Suppl. 3), pp. 2655–2663, 1972.

269. Willis, R.F., et al.: *Photon and Particle Interaction with Surfaces in Space*, D. Reidel Publ. Co., Dordrecht, Holland, pp. 369–387, 1973.

270. LPI Lunar Engineering Reference Model (Luna Ref), <https://www.lpi.usra.edu/wiki/lunaref>, Lunar & Planetary Institute, USRA, June 10, 2010.

271. Walton, O.R.: "Adhesion of Lunar Dust," NASA/CR—2007–214685, Hanover, MD, 45 pp., April 2007.

272. Apollo-17 Preliminary Science Report, NASA SP-330, NASA Johnson Space Center, Houston, TX, 1973.

273. Carrier, W.D.; Olhoeft, G.R.; and Mendell, W.: "Chapter 9, Physical Properties of the Lunar Surface," *Lunar Sourcebook: A User's Guide to the Moon*, G.H. Heiken, D.T. Vaniman, and B.M. French (eds.), Cambridge University Press, pp. 475–594, 1991.

274. Choate, R.; Batterson, S.A.; Christensen, E.M.; et al.: "Lunar surface mechanical properties," Surveyor Project Part I: Project Description and Performance, JPL Technical Report 32-1265, Jet Propulsion Laboratory, Pasadena, CA, pp. 137–194, 1968b.

275. Martin, R.T.; Winkler, J.L.; Johnson, S.W; and Carrier III, W.D.: "Measurement of conductance of Apollo 12 lunar simulant taken in the molecular flow range for helium, argon, and krypton gases," unpublished report, 1973.

276. Langseth, Jr., M.G.; Clark, Jr., S.P., ; Chute, Jr., J.L.; et al.: "Heat flow experiment," Apollo 15 Preliminary Science Report, NASA SP-289, Johnson Space Center, Houston, TX, pp. 11-1 to 11-23, 1972.

277. Langseth, Jr., M.G.; Keihm, S.J.; and Chute, Jr., J.L.: "Heat flow experiment," Apollo 17 Preliminary Science Report, NASA SP-330, Johnson Space Center, Houston, TX, pp. 9-1 to 9-24, 1973.

278. Horai, K.I.; and Winkler, Jr., J.L.: "Thermal diffusivity of four Apollo 17 rock samples," *Proc. 7th Lunar Science Conference*, Houston, TX, March 15–19, 1976, Vol. 3. (A77-34651 15-91), Pergamon Press, Inc., New York pp. 3183–3204, 1976.

279. Dyal, P.; Parkin, C.W.; and Daily, W.D.: "Lunar electrical conductivity, permeability, and temperature from Apollo magnetometer experiments," *Cosmochemistry of the Moon and Planets*, pp. 447–491, 1974.

280. Olhoeft, G.; and Strangway, D.W.: "Dielectric properties of the first 100 meter of the Moon," *Earth Planet. Sci. Lett.*, Vol. 24, pp. 394–404, 1975.

281. Scott, R.F.; and Ko, H.Y.: "Transient rock-engine gas flow in soil," *AIAA J.*, Vol. 6, pp. 258–264, 1968.

282. Morris, R.V.; Lauer, H.V.; Gooding, J.L.; and Mendell, W.W.: "Spectral Evidence and Implications for the Occurrence of Aluminous Iron Oxides on Mars," *Lunar and Planetary Science XIV*, pp. 526–527, 1983.

283. Korotev, R.L.; and Gillis, J J.: "A new look at the Apollo 11 regolith and KREEP," *J. Geophys. Res.*, Vol. 106, Issue E6, pp. 12,339–12,354, 2001.

284. Korotev, R.L.: "Some things we can infer about the Moon from the composition of the Apollo 16 regolith," *Meteoritics*, Vol. 32, pp. 447–478, 1997.

285. Horányi, M.; Walch, B.; Robertson, S.; and Alexander, D.: "Electrostatic Charging Properties of Apollo 17 Lunar Dust," *J. Geophys. Res.*, Vol. 103, Issue E4, pp. 8575–8580, 1998.

286. Vondrak, R.R.; Stubbs, T.J.; and Farrell, W.M.: "A Dynamic Fountain Model for Dust in the Lunar Exosphere," Paper 4017, Workshop on Dust in Planetary Systems, Lunar and Planetary Institute, Kaua'i, HI, 2005.

287. McCoy, J.E.; and Criswell, D.R.: "Evidence for a High Altitude Distribution of Lunar Dust, *Proc. 5th Lunar Science Conference,* Vol. 3., A75-39540 19-91, Houston, TX, March 18–22, 1974, pp. 2991–3005, 1974.

288. Rennilson, J.J.; and Criswell, D.R.: "Surveyor Observations of Lunar Horizon-Glow," *The Moon*, Vol. 10, pp. 121–142, 1974.

289. Pelizzari, M.; and Criswell, D.: "Differential Photoelectric Charging of Nonconducting Surfaces in Space," *J. Geophys. Res.*,Vol. 12, pp. 5233–5244, 1978.

290. Zook, H.; and McCoy, J.: "Large Scale Lunar Horizon Glow and a High Altitude Lunar Dust Exposphere," *Geophys.Res. Lett.*, Vol. 18, p. 2117, 1991.

291. *Lunar Sourcebook: A User's Guide to the Moon*, G.H. Heiken, D. T. Vaniman, and B.M. French (eds.), Cambridge University Press, p. 305, 1991.

292. Coulter, D.: "Moondust in the Wind," <http://science1.nasa.gov/science-news/science-at-nasa/2008/10 apr_moondust in the wind/>, April 10, 2008.

293. Anderegg, M.; Feuerbacher, B.; Fitton, B; et al.: "Secondary Electron Emission Characteristics of Lunar Surface Fines," Proc. 3rd Lunar Science Conference (Supplement 3, Geochinica et Cosmochimica Acta), Vol. 3, pp. 2665–2669, 1972.

294. Nakamura Y.: "Shallow Moonquakes: How They Compare With Earthquakes," Proc. 11th Lunar Planet. Sci. Conf., Houston, TX, March 17–21, 1980, Vol. 3 (A82-22351 09-91), pp. 1847–1853, 1980.

295. Frohlich, C.; and Nakamura, Y.: "Possible Extra-Solor-System Cause for Certain Luna Seismic Events," *Icarus*, Vol. 185, pp. 21–28, 2006.

296. Head III, J.W.: "Lunar volcanism in space and time," *Rev. Geophys. Space Phys.*, Vol. 14, pp. 265–300, 1976.

297. Neal, C.R.; and Taylor, L.A.: "Using Apollo 17 high-Ti mare basalts as windows to the lunar mantle," *Lunar Science Inst., Workshop on Geology of the Apollo 17 Landing Site*, pp. 40–41 (SEE N93-18786 06-91), 1992.

298. Giguere, T.A.; Taylor, G J.; Hawke, B.R.; and Lucey, P.G.: "The titanium contents of lunar mare basalts," *Meteoritics & Planetary Science*, Vol. 35, No. 1, pp. 193–200, 2000.

299. Shearer, C.K.; and Papike, J.J.: "Origin of Lunar Mare High-Titanium Basalts. Melting of a Deep Hybridized Source or Shallow Assimilation of High-Ti Cumulates?," 30th Annual Lunar and Planetary Science Conference, March 15–29, 1999, Houston, TX, Abstract No. 1365, 1999.

300. Taylor, L.A.; Shervais, J.W.; Hunter, R.H.; et al.: "Pre-4.2 AE mare-basalt volcanism in the lunar highlands," *Earth Planet. Sci. Lett.*, Vol. 66, pp. 33–47, 1983.

301. Dasch, E.J.; Shih, C.-Y.; Bansal, B.M.; et al.: "Isotopic analysis of basaltic fragments from lunar breccia 14321 - Chronology and petrogenesis of pre-Imbrium mare volcanism," *Geochimica et Cosmochimica Acta*, Vol. 51, pp. 3241–3254, 1987.

302. Shih, C.-Y.; and Nyquist, L.E.: “Isotopic and Chemical Constraints on Models of Aluminous Mare Basalt Genesis,” *Abstracts of the Lunar and Planetary Science Conference*, Vol. 20, p. 1002, 1989.

303. Shih, C.-Y.; and Nyquist, L.E.: “Isotopic constraints on the petrogenesis of Apollo 14 igneous rocks,” Workshop on Moon in Transition: Apollo 14, KREEP, and Evolved Lunar Rocks, pp. 128–136, 1989.

304. Schultz, P.H.; and Spudis, P.D.: “The Beginning and End of Mare Volcanism on the Moon,” *Lunar and Planetary Science XIV*, pp. 676–677, 1983.

305. Fincannon, J.: “Characterization of Lunar Polar Illumination from a Power System Perspective,” AIAA-2008-447, 46th AIAA Aerospace Sciences Meeting and Exhibit, Reno, NV, January 7–10, 2008.

306. Gladstone G.R.; and the LAMP team: “Initial Results from the Lyman Alpha Mapping Project (LAMP) Instrument on the Lunar Reconnaissance Orbiter (LRO) Mission,” Abstract No. 2277, 41st Lunar and Planetary Science Conference, 2010.

307. Reed, Jr., G.W.: “Don’t drink the water,” *Meteoritics & Planet. Sci.*, Vol. 34, No. 5, pp. 809–811, September 1999.

308. Cremers, C.J.; Birkebak, R.C.; and White, J.E.: “Thermal Characteristics of the Lunar Surface Layer,” *Int. J. Heat Mass Transfer*, Vol. 15, pp. 1045–1055, 1972.

309. Maurice, S.; Feldman, W.C.; Lawrence, D.J.; et al.: "High-Energy Neutrons From the Moon," *J. Geophys. Res.*, Vol. 105, pp. 20,365–20,375, 2000.

310. Feldman, W.C.; Barraclough, B.L.; Fuller, K.R.; et al.: “The Lunar Prospector gamma-ray and neutron spectrometers, *Nucl. Instrum. Methods Phys.. Res*. *Instrum.* p. 422, pp. 562–566, 1999.

311. Lawrence, D.J.; Feldman, W.C.; Elphic, R.C.; et al: “Improved Modeling of Lunar Prospector Neutron Spectrometer Data: Implications for Hydrogen Deposits at the Lunar Poles,” *J. Geophys. Res.*, Vol. III, p. E08001, 2006.

312. Anderson, B.J. (ed); and Smith, R.E. (compiler): “Natural Orbital Environment Guidelines for Use in Aerospace Vehicle Development,” NASA Technical Memorandum 4527, NASA Marshall Space Flight Center, AL, pp. 7-1 to 7-74, June 1994.

313. Cour-Palais, B.G.: Meteoroid Environment Model—1969 [near earth to lunar surface], NASA Space Vehicle Design Criteria (Environment), NASA/SP-8013, NASA, Washington, DC, March 1969.

REPORT DOCUMENTATION PAGE

Form Approved
OMB No. 0704-0188

1. REPORT DATE *(DD-MM-YYYY)*	2. REPORT TYPE	3. DATES COVERED *(From - To)*
01–10–2016	Technical Memorandum	

4. TITLE AND SUBTITLE

Natural Environments Definition for Design

5a. CONTRACT NUMBER

5b. GRANT NUMBER

5c. PROGRAM ELEMENT NUMBER

6. AUTHOR(S)

H.L. Justh (Ed.), K.M. Altino, R.K. Decker, H.M. Koehler, F.B. Leahy, J.I. Minow, B.C. Roberts, R.M. Suggs, R.J. Suggs, P.W. White, R.E. Barbre, Jr.,* J.W. Howard,* L.N. Parker,* L. Burns,** and R.D. Leach***

5d. PROJECT NUMBER

5e. TASK NUMBER

5f. WORK UNIT NUMBER

7. PERFORMING ORGANIZATION NAME(S) AND ADDRESS(ES)

George C. Marshall Space Flight Center
Huntsville, AL 35812

8. PERFORMING ORGANIZATION REPORT NUMBER

M–1420

9. SPONSORING/MONITORING AGENCY NAME(S) AND ADDRESS(ES)

National Aeronautics and Space Administration
Washington, DC 20546–0001

10. SPONSORING/MONITOR'S ACRONYM(S)

NASA

11. SPONSORING/MONITORING REPORT NUMBER

NASA/TM—2016–218229

12. DISTRIBUTION/AVAILABILITY STATEMENT

Unclassified-Unlimited
Subject Category 46
Availability: NASA CASI (443–757–5802)

13. SUPPLEMENTARY NOTES

Prepared by the Natural Environments Branch, Spacecraft and Vehicle Systems Department, Engineering Directorate
*Jacobs ESSA Group, **Raytheon Jacobs ESSA Group, ***Dynetics

14. ABSTRACT

This Technical Memorandum (TM) defines the natural environment through models and data specifically selected to support engineering and analysis, requirements development, and verification involved in development of exploration concepts and acrhitectures, flight hardware, and new technologies for NASA's Exploration System Development initiatives. Natural environment includes all environmental factors outside the program's influence. This TM covers terrestrial environments (from the Earth's surface to the thermosphere's edge), near-Earth space environments (Earth orbit), and cislunar and lunar environments (lunar orbit and surface).

15. SUBJECT TERMS

natural environment, terrestrial environment, solar radiation, temperature, pressure, density, humidity, aerosols, winds, precipitation, lightning, tropical cyclones, sea state, earthquakes, tsunamis, seiches, volcanoes, ionizing radiation, geomagnetic field, plasma enviornment, meteoroid, orbital debris, lunar environment, solar wind, lunar regolith, lunar dust

16. SECURITY CLASSIFICATION OF:			17. LIMITATION OF ABSTRACT	18. NUMBER OF PAGES	19a. NAME OF RESPONSIBLE PERSON
a. REPORT	b. ABSTRACT	c. THIS PAGE			STI Help Desk at email: help@sti.nasa.gov
U	U	U	UU	439	19b. TELEPHONE NUMBER *(Include area code)* STI Help Desk at: 443–757–5802

National Aeronautics and
Space Administration
IS02
George C. Marshall Space Flight Center
Huntsville, Alabama 35812